Breccia-hosted chemical and mineralogical zonation patterns of the Northeast Zone, Mt. Polley Cu-Ag-Au alkalic porphyry deposit, British Columbia, Canada

by

Heidi Elaine Pass

BSc (Hons)

Submitted in fulfilment of the requirements for the degree of

Doctor of Philosophy

November, 2010

UNIVERSITY
OF TASMANIA

CODES, ARC Centre of Excellence in Ore Deposits at the University of Tasmania

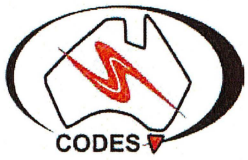

It is not really a mark of distinction for a geologist's writing to be so obscure that a glossary is required for its comprehension.

- Jules Braunstein

Declaration of originality

This thesis contains no material which has been accepted for the award of any other degree or diploma in any tertiary institution and, to the best of my knowledge and belief, contains no copy or paraphrase of material previously published or written by another person, except where due reference is made in the text of the thesis, nor does the thesis contain any material that infringes copyright.

Signature: Date:

Authority of access

This thesis may be made available for loan and limited copying in accordance with the *Copyright Act 1968*.

Signature: Date:

Statement regarding published work

The publishers of the paper comprising Chapter 5 hold the copyright for that content, and access to the material should be sought from the journal of *Economic Geology*. The remaining non-published content of the thesis may be made available for loan and limited copying in accordance with the *Copyright Act 1968*.

Signature: Date:

Abstract

The Mt. Polley alkalic Cu-Ag-Au porphyry was emplaced in the late Triassic to early Jurassic Quesnellia island-arc terrane of the Canadian Cordillera. In the Central Quesnel Belt, Middle Triassic fine-grained oceanic sediments ± limestone were overlain by a thick pile of Late Triassic submarine, alkalic basaltic to andesitic volcanics (Nicola Group), with related subvolcanic intrusions and minor limestones of Late Triassic age. The Mt. Polley Complex is a 6.0 km long by 3.5 km wide, north-northwest-trending, composite alkalic intrusive (and breccia) complex; one of several that are scattered along the length of this terrane, making British Columbia the type location for Au-enriched alkalic porphyry deposits. The Mt. Polley Complex contains silica-undersaturated to silica-saturated pyroxenites, diorites and syenites, but is dominated by monzonites, monzodiorites, and associated breccia bodies, all of which were emplaced during the final stages of arc magmatism, between 209.4 Ma and 195.4 Ma. Mineralization occurred between 209 and 204 Ma. A new model Pb age of 207.8 ± 1.8 Ma for a galena vein is consistent with these ages.

The NEZ is an alkalic Cu-Ag-Au porphyry deposit hosted by the Mt. Polley Complex. Ore is distinctly higher grade than in other ore zones at Mt. Polley, with average Cu grades at 0.8–1.0 percent and Au grades 0.19–0.29 g/t. Mineralization and alteration mostly occurred during magmatic-hydrothermal breccia formation. Chalcopyrite and bornite occur primarily as coarse- to fine-grained breccia cement, with lesser disseminations, veins and replacements. Bornite-rich, pyrite-deficient high-grade zones of mineralization (>1% Cu, up to >5% Cu locally) occur within broader chalcopyrite-rich domains (Cu grades of 0.3 to 1.0 %). Pyrite is the dominant sulfide on the deposit periphery (up to 1–2% locally).

There were five major mineralization and alteration events in the NEZ: 1) early-stage (pre-breccia), 2) main-stage (syn-breccia), 3) post-brecciation late-stage mineralization, 4) barren intrusions, veins and vein breccia, and 5) epithermal-style veins. Main stage alteration and mineralization assemblages are zoned vertically and laterally through the breccia body. Magmatic-hydrothermal brecciation focused the high temperature mineralizing fluids, forming a core of potassic alteration (K-feldspar-magnetite-albite-calcite ± biotite ± augite ± anhydrite ± epidote and Cu-Fe-sulfides) surrounded by a halo of propylitic alteration (pyrite-chlorite-epidote ± albite ± sericite). Calc-potassic (garnet ± epidote) and sodic (albite) alteration assemblages are variably abundant within the broader domains of potassic and propylitic alteration. Alteration minerals are consistent with temperatures >300°C and near-neutral to alkalic pH fluids during stages 1, 2 and 3. Acidic and lower temperature fluids were associated with stages 4 and 5.

Laser-ablation ICP-MS analyses of sulfide trace element contents of the NEZ have shown bornite is enriched in Ag (average 913 ppm), Bi and Se. Chalcopyrite is enriched in Pb, Zn and Se, with Zn concentrations increasing and Pb concentrations decreasing from the centre of the deposit to its margins. Pyrite is enriched in Cu, Zn, Cd, Co, Ni, Se, Te and Au with these elements substituted into the pyrite structure or evenly disseminated as nano-particles. Pyrite contains abundant micro-inclusions of chalcopyrite, galena,

sphalerite, electrum and tellurides. Gold contents were found to be 1–3 orders of magnitude higher in pyrite (0.011–4.32 ppm, plus one outlier of 483.2 ppm) than in chalcopyrite (0.050–1.29 ppm). Gold was mostly below detection limits in bornite. Gold, Pd- and Pt-bearing inclusions were primarily detected in pyrite on the fringes of the deposit. This contradicts the assay data that shows high gold grades are associated with areas rich in bornite and chalcopyrite. This implies that the Au in the high-grade ore zones does not occur in Cu-sulfides, but in another phase, possibly electrum.

The $\delta^{34}S_{sulfide}$ isotopic compositions of main- and late-stage chalcopyrite, pyrite and bornite range from -7.1 to +1.4 per mil, with most between -3 and -4 per mil. Sulfur isotopic compositions of anhydrite and gypsum were between +6.2 and +9.8 per mil, with two outliers of +13.6 and +14.0 per mil. These values, together with the presence of hematite, are consistent with an oxidized (sulfate predominant), high-temperature (>400°C) magmatic-hydrothermal fluid. Limited sulfide geothermometry indicates that ore precipitated at temperatures from ~ 480° to ~ 250°C. The $\delta^{34}S$ values of main-stage sulfides define zonation patterns across the deposit, from low $\delta^{34}S$ values in the core to higher $\delta^{34}S$ values near the deposit periphery. Changes in redox conditions, pH changes, cooling, and water-rock interaction are concluded to have been important processes of ore formation and hydrothermal alteration in the NEZ.

Hydrothermal calcite occurs throughout the paragenesis, and several processes may have contributed to its precipitation, including boiling, CO_2 degassing, pH increase, and water-rock interaction. Calcite $\delta^{13}C$ values range from -0.2 to -10.5 per mil (average -3.0 ‰), and $\delta^{18}O$ values from +4.0 to +20.9 per mil (average +15.4 ‰). The C-O isotopic values are not consistent with simple precipitation from a "normal" magmatically-derived source hydrothermal fluid. Enriched $\delta^{13}C$ values suggest the involvement of a heavy carbon source, such as limestone or seawater. However, $\delta^{18}O$ isotopic data preclude the involvement of meteoric or seawater in the formation of the NEZ, until stage 4.

Lead isotopic data suggest mixing of mantle and crustal sources during mineralization. Main-stage chalcopyrite, pyrite and late-stage galena have $^{206/204}Pb$ values of 18.77–18.92, $^{207/204}Pb$ of 15.56–15.59 and $^{208/204}Pb$ of 38.22–38.32. Strontium isotopic data (0.70331 to 0.70371) provide evidence of a strongly depleted mantle source of Sr with minor crustal input. Epsilon Nd values for main-stage apatite range between +5.9 and +6.5, also indicating a depleted mantle source. Stage 5 carbonate $^{206/204}Pb$ values of 18.96–19.04, $^{207/204}Pb$ of 15.57–15.59 and $^{208/204}Pb$ of 38.26–38.36, from epithermal-textured veins suggest that telescoping of an epithermal environment into the NEZ occurred ~100 m.y. after breccia formation.

The stable and radiogenic isotopic data provide evidence that the silica-undersaturated alkalic Mt. Polley Complex formed due to carbonate assimilation prior to mineralization. This process can explain both the $\delta^{13}C$-$\delta^{18}O$ isotopic data and the silica-undersaturated composition of the magmatic-hydrothermal system. The CO_2 released during assimilation of carbonate could have promoted magmatic-hydrothermal brecciation, thereby leading to high-grade ore formation. Silica-undersaturated alkalic porphyry systems may preferentially form in arc terranes built on a carbonate-bearing substrate or where carbonate platforms are subducted.

Acknowledgements

A PhD is not conducted in isolation, and I have benefited greatly from the knowledge, help and friendship of a large number of people over the past years. While it is not possible to list everyone, I extend my gratitude to each of them.

First, I would like to whole-heartedly thank my primary supervisor, David Cooke. He spent many red pens and many hours unwinding my sentences into the thoughts and ideas on the following pages. Thank you Dave for guiding me through the geology and geochemistry of porphyry deposits and imparting your expertise. Your patience, support and enthusiasm were critical and are greatly appreciated. To his wife Helen, thank you for welcoming me to your home when I first arrived in Hobart and the many dinners over the years.

Whole-hearted thank-yous also go to my supervisors, Garry Davidson and Zhaoshan Chang. I thank Garry for his continued enthusiasm whenever I knocked on his door and for the many inspiring conversations, introducing me to the carbonate assimilation idea, "Touch Footy" and shared veggies from his garden. Zhaoshan gave me two of the best pieces of PhD advice that carried me throughout: "No matter what....just keep going." and "People can't help you until you write it down". I cannot count how many times I repeated these to myself.

Several people have critically reviewed parts of this thesis or provided stimulating and insightful discussions and feedback along the way. Many thanks to Greg Dipple, Julie Hunt, Jim Lang, Ross Large, Roland Maas, Jocelyn McPhie, Chris Rees and John Walshe.

A big thank-you to Imperial Metals Corporation who withstood the "alkalic group" at the mine each year and provided the all-important logistical and financial support that was necessary to conduct this research. Specifically, Linda Bingham, Michelle Brereton, Brenda Emerson, Natasha Gainer, Shelia Jonnes, Patrick McAndless, Steve Roberston, Tim Stubbley and Gary Roste are thanked. A special thank-you to Chris Rees, Lee Ferreira and Chris Taylor, for sharing their ideas and helping me learn the geology of Mt. Polley.

Funding for this research has also been provided in part by NSERC-CRD, Geoscience BC and CODES. The receipt of Geoscience BC and SEG student grants are gratefully acknowledged.

Technical support and advice was given at several stages. Thank-you Keith Dobson and Paul George for your excellent technical support, Christine Cook, Keith Harris and Janet Gabites for producing my stable isotopic data, Karsten Gomez for his patience in producing my microprobe and SEM data, Sebastien Meffre for your assistance with radiogenic isotopes, Steve Micklethwaite for structural geology review, Robert Scott for trace element advice, and David Hutchinson for discussion on PGEs. Karin Orth is thanked for assistance with several analytical techniques and work on the post-breccia vein breccias. Simon Stephens is thanked for his immense talent in the lapidary and always managing to squeeze in a sample at the last minute. June Pongratz is thanked for her assistance with graphics, design, printing and "eagle-eye" reviews. Sarah Gilbert is thanked for her endless patience and guidance with my laser ablation study. Helen Scott, Karen Mollross and Christine Higgins are thanked for taking care of all the financial paper work. Heather Mitchell and the staff at the Science Library are

thanked for their unending resourcefulness with various references and patience with Endnote. Finally, thank-you to Steve Walters and Julie Hunt for letting me write in the relative tranquility of the GEM room.

To all my colleagues, past and present, thank-you for your laughter, keeping me sane, not minding when I wasn't and generally sharing the highs and lows of this experience: Andrea Agangi, Heidi Berkenbosh, Paul Berkenbosh, Fiona Best, Natalee Bonnici, Isabelle Chambefort, Mawson Croaker, Liezl Cuison, Mary Eckhart, Jacqueline Halpin, Emily Johnson, Kit Chun Lai, Sang Qinh, Nathan Fox, Victor Galvan, Sarah Gordee, Julie Hunt, Tim Ireland, Nick Jansen, Ben Jones, Martin Jutzeler, Claire McMahon, Joe Moye, Anita Parbhakar, Lee Robson, Patrick Sack, Abhisit Salam, Bronto Sutopo, Sofia Tetroeva, Helen Thomas, Olga Vasyukova, Adal Vatandoost, Clara Wilkinson, Jamie Wilkinson and the many that I have temporarily forgotten – you are greatly appreciated!

A special thank-you to the other "alkalic project" students: Adam Bath, Jacqueline Blackwell, Kevin Byrne, Amber Henry, Meghan Jackson, Paul Jago, Janina Micko, Wojciech Zukowski and project leaders: Thomas Bissig, Claire Chamberlain, Cari Deyell, Richard Tosdal and Kirstie Simpson for their friendship, invaluable discussions and assistance. I am glad our sponsors meetings are over and I had great adventures globe-trotting with you all.

My *non*-geology friends, primarily from the Tasmania Ultimate Association community were a much needed balance. I thank Ashley Martens and Shavawn Donoghue for starting team BUSH. It was a personal highlight to play for Tassie in three national competitions. To the Clifton Crew: Shannon Trenwith, Stella Just (nee Foley), and Kate Godber, you guys are true "beauties" and I thank you for your generous friendship throughout my studies.

Finally, I'd like to thank my family and friends at home in Canada, especially my parents, Heather and Konrad Pass, who have always believed in their daughter, but never dreamed she would move half a world away to undertake such an adventure. A special thank you to Ross Olsen. It is not what we have in our life, but who we have in our life that counts. I am very grateful for you. Thank-you aunts, uncles, cuzzies and friends (especially Glen, Clayton, Lisa, Lynn and Michelle) for keeping in touch and always welcoming me home so warmly.

Table of Contents

Chapter 1

Introduction

1.1 Preamble

Porphyry deposits are the world's most important source of Cu, accounting for approximately 50 to 70 percent of global Cu production and also one fifth of the world's Au production, amongst other valuable metals (Sillitoe, 2000; Richards, 2003; Seedorff et al., 2005; Sinclair, 2007, Sillitoe, 2010). In Canada, porphyry deposits currently provide more than 40 percent of Cu and approximately 10 percent of total Au production. The Canadian Cordillera is a highly fertile metallogenic environment that hosts several world-class ore bodies, and includes an abundance of porphyry deposits (Fig. 1.1; Nelson and Colpron, 2007).

Porphyry deposits in the Cordillera can be classified in two ways: (1) according to their igneous geochemistry into alkalic and subalkalic categories; and (2) based on their endowment of Cu, Au and/or Mo (Fig. 1.2; McMillan and Panteleyev, 1995). Cu grades in porphyry Cu-Au deposits are comparable to those of the porphyry Cu subtype but Au contents tend to be consistently higher in alkalic deposits (0.2–2.0 g/t, Sinclair 2007, Müller and Groves, 1995; Jensen and Barton, 2000; Sillitoe, 2000). The alkalic chemistry of igneous rocks is the primary condition for distinguishing alkalic deposits from other types of porphyry deposits (Barr et al., 1976; Lang et al., 1995b). There are many definitions of alkalic igneous rocks, most of which overlap. As used here, "alkalic" applies to igneous rocks that have $Na_2O + K_2O$ values above a line defined by $Na_2O + K_2O = 0.3718 * SiO_2 - 14.5$ (Fig. 1.2). These rocks plot in the basanite, trachybasalt, shoshonite, latite and trachyte fields of the IUGS classification scheme for volcanic rocks (Fig. 1.2 all oxides in wt %; MacDonald and Katsura, 1964; LeMaitre et al., 1989).

Most igneous rocks can be classified as either silica-undersaturated, silica-saturated or silica-oversaturated (Table 1.1, Fig. 1.2A; Streckeisen, 1976; Cox et al., 1981; LeMaitre et al., 1989). Rocks with 5 to 20 percent modal quartz are considered slightly oversaturated variants (i.e. "quartz syenite"; Streckeisen, 1976; LeMaitre et al., 1989). Similarly, alkalic porphyry deposits can be subdivided on the basis of their associated igneous rocks into silica-oversaturated to silica-undersaturated sub-types (Lang et al., 1995a; Lang et al., 1995b; Lang and McClaren, 2003; Seedorff et al., 2005). Lang et al. (1992) subdivided the alkalic porphyry deposits of British Columbia into two sub-types, one related to igneous suites which include silica-undersaturated intrusions (i.e. Galore Creek, Copper Canyon, Mt. Polley, Rayfields River) and a second with only silica-saturated to weakly oversaturated intrusions (all others). Both silica-saturated and silica-undersaturated alkalic porphyries are associated exclusively with Cu-Au mineralisation and have

Table 1.1 Comparison of silica-saturation definitions from Streckeisen (1976) and LeMaitre et al. (1989).

Silica content	Modal	CIPW Normative
undersaturated	>10% feldspathoid and no quartz	olivine + nepheline
saturated	<5% quartz *or* <10% feldspathoid	olivine + hypersthene
oversaturated	>5% quartz*	quartz + hypersthene

* Rocks with 5 to 20 percent quartz in the mode are considered slightly oversaturated variants (i.e. "quartz syenite").

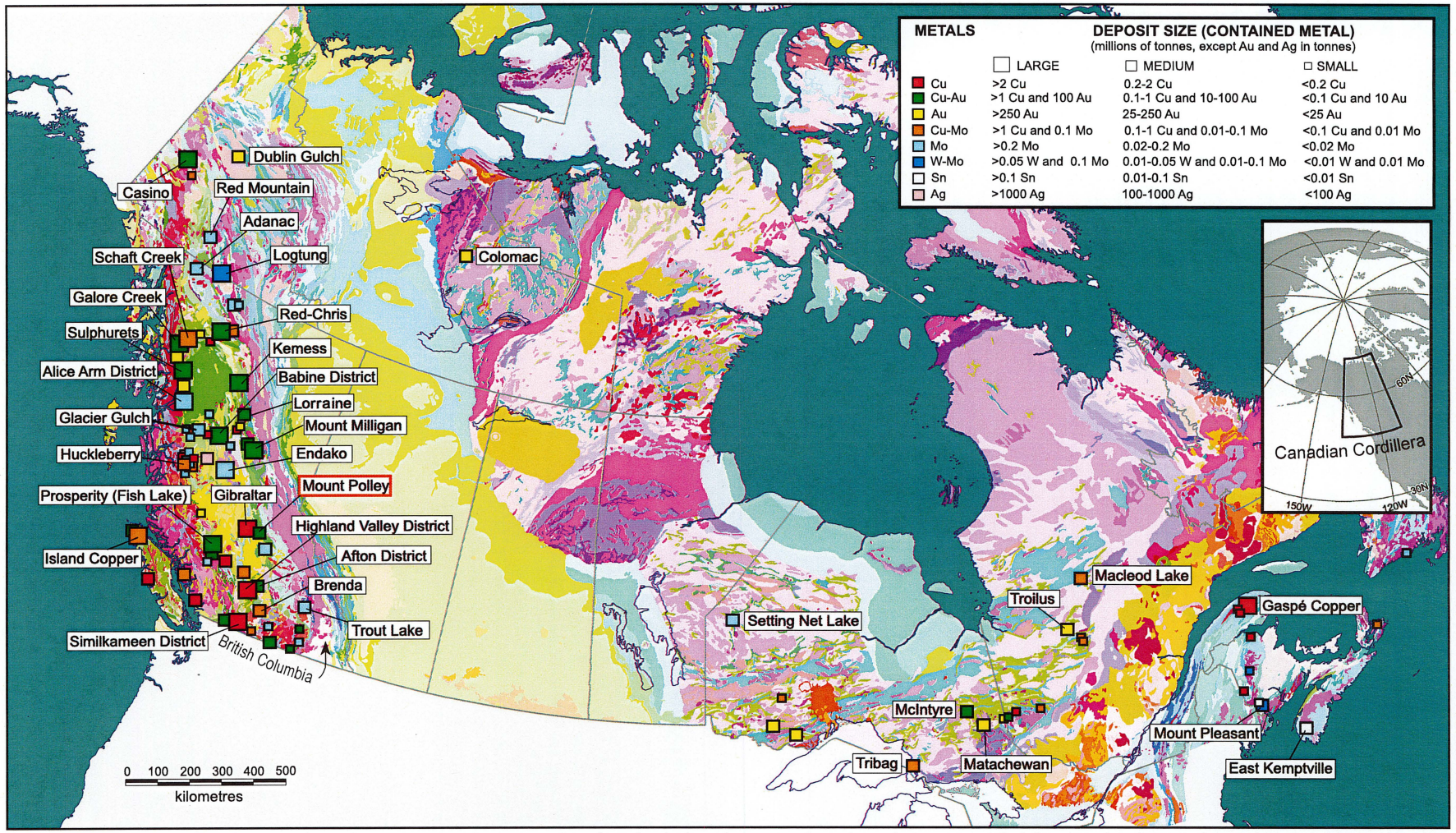

Figure 1.1 Distribution of selected porphyry deposits in Canada showing British Columbia's endowment of porphyry deposits. Modified from Sinclair (2007) after Kirkham and Dunne (2000). Mt. Polley is outlined in red. Geology is from Wheeler et al. (1996) and the detailed legend is provided in Appendix A1. Inset shows the location of the Canadian Cordillera in north-western North America (from Johnston and Borel, 2007).

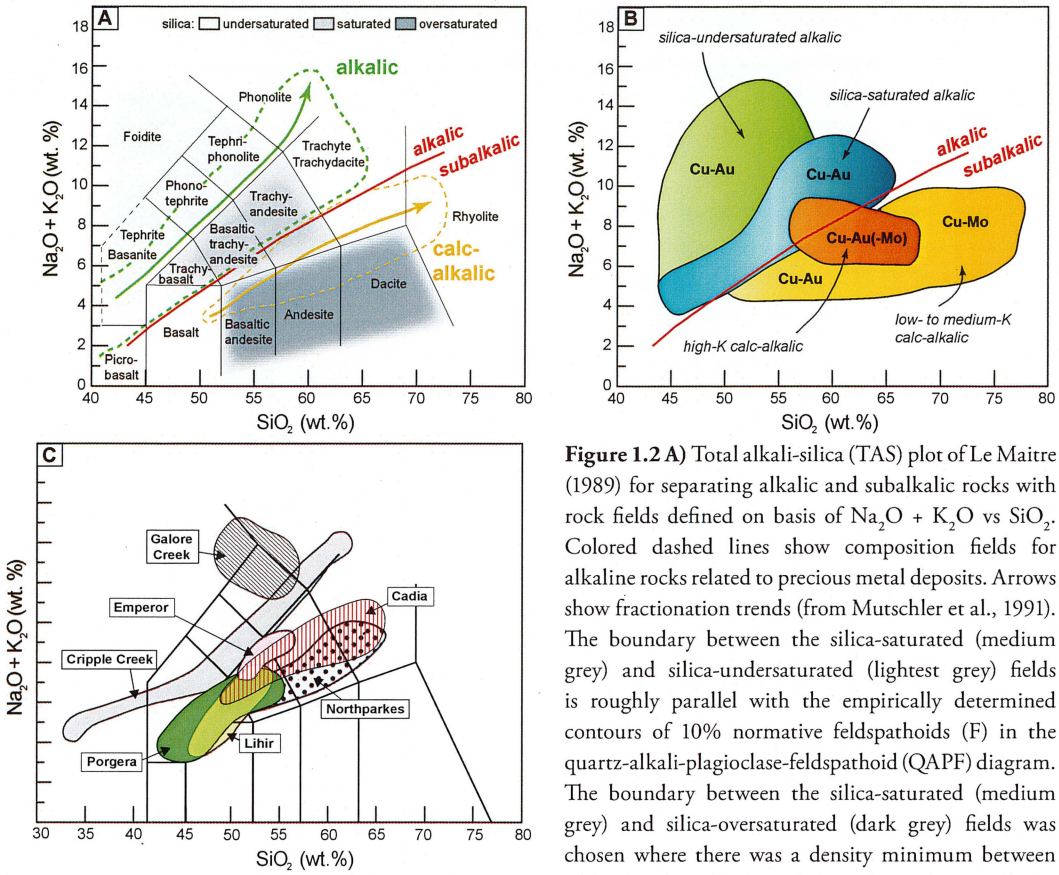

Figure 1.2 A) Total alkali-silica (TAS) plot of Le Maitre (1989) for separating alkalic and subalkalic rocks with rock fields defined on basis of Na_2O + K_2O vs SiO_2. Colored dashed lines show composition fields for alkaline rocks related to precious metal deposits. Arrows show fractionation trends (from Mutschler et al., 1991). The boundary between the silica-saturated (medium grey) and silica-undersaturated (lightest grey) fields is roughly parallel with the empirically determined contours of 10% normative feldspathoids (F) in the quartz-alkali-plagioclase-feldspathoid (QAPF) diagram. The boundary between the silica-saturated (medium grey) and silica-oversaturated (dark grey) fields was chosen where there was a density minimum between rocks that were alkalic and those that were calc-alkalic, as in Le Maitre (1989). **B)** Classification schemes for porphyry deposits by magma chemistry with corresponding metal endowments. Figure courtesy Cooke et al. (2004) from Lang et al. (1995b). **C)** The TAS diagram with geochemical compositions for selected alkalic porphyry and epithermal deposits (Figure modified from Zukowski, 2009; data modified and compiled from Muller, 2001; Jensen, 2003; Wilson, 2003).

potential for valuable by-products such as platinum group elements (PGEs; Fig. 1.2B; Mutschler et al., 1991; Lang et al., 1995b; Economou-Eliopoulos, 2005).

Calc-alkalic porphyry deposits have been intensely studied for decades and models for this deposit type are well-established (i.e. Lowell and Guilbert, 1970; Gustafson and Hunt, 1975; Sillitoe, 1979; Beane and Titley, 1981; Titley and Beane, 1981; Richards, 1995; Sillitoe, 2000; Seedorff et al., 2005). In contrast, while the alkalic suite of porphyry deposits was identified in the mid-1970s (Barr et al., 1976), the alkalic sub-type has only been the subject of detailed research since the mid-1990s (e.g. Schroeter, 1995). The two type locations for alkalic deposits are British Columbia, Canada (e.g. Barr et al., 1976; Schroeter, 1995) and New South Wales in eastern Australia (Lickfold et al., 2003; Wilson et al., 2003; Cooke et al., 2007). Other isolated alkalic deposits are known from the Philippines (Dinkidi; Wolfe, 2001), Greece (Skouries; Kroll et al., 2002), and Colorado (Allard Stock; Werle, 1984), amongst others (Fig. 1.3).

Alkalic rocks are known to occur in a variety of settings globally, but most notably in magmatic arcs associated with convergent margins and in areas of extensional tectonics (Müller and Groves, 1993; McMillan and Panteleyev, 1995; Jensen and Barton, 2000; Sillitoe, 2002). Alkalic magmatism is distinguished from calc-alkalic magmatism by higher CO_2 and SO_2 contents, with relatively smaller proportions of H_2O from partial mantle melts (Bailey and Hampton, 1990; Mutschler et al., 1991). Key characteristics of alkalic hydrothermal systems associated with Au deposits are their hydrous and oxidized fluids, and their apparent ability to produce ideal conditions for Au transportation, extensive carbonatization and voluminous potassium metasomatism (Jensen and

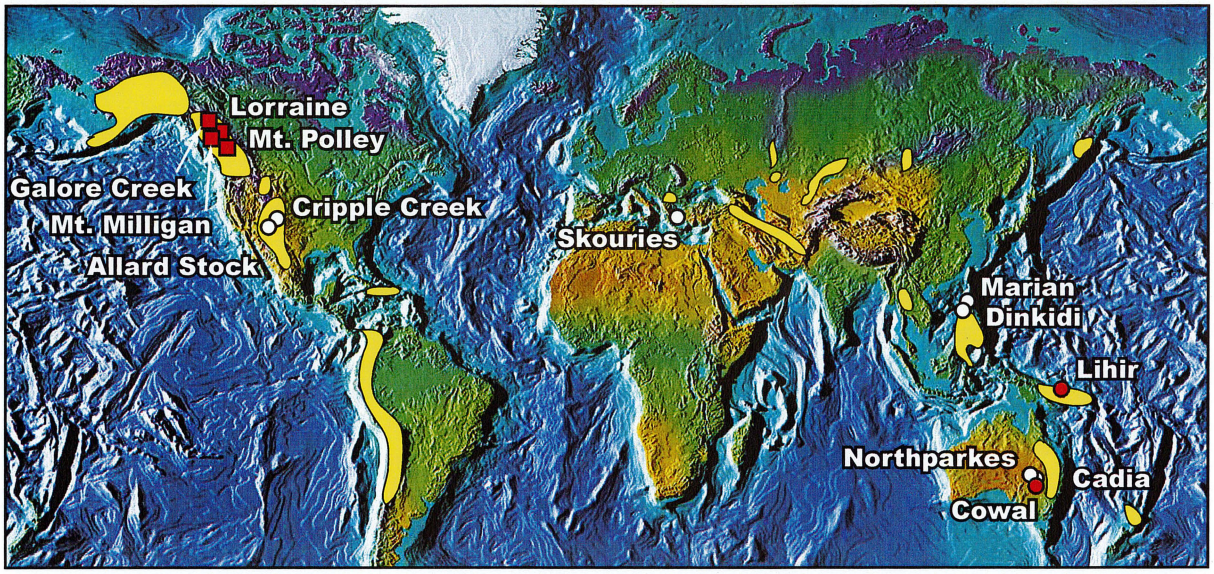

Figure 1.3 Yellow areas cover major porphyry Cu provinces (from Titley and Beane, 1981). Locations of alkalic porphyry (square) and epithermal (circle) deposits that were part of the *Shallow- and Deep-Level Alkalic Minerals Deposit: Developing an Integrated Exploration Model* project are shown in red. Other important alkalic porphyry deposits are in white. World bathymetry map from the National Oceanic and Atmospheric Administration (www.noaa.gov).

Barton, 2000; Sillitoe, 2000).

The alkalic rocks associated with porphyry deposits generally form small, complex, alkalic plutons that are co-magmatic with the enclosing volcanic rocks and can contain moderate volumes of sub-alkalic rocks (Barr et al., 1976; Lang et al., 1995c; Jensen, 2003). Within British Columbia and New South Wales, alkalic deposits occur in clusters locally and specific volcanic belts or terranes regionally (i.e. Copper Mountain-Ingerbelle district, Quesnellia terrane; Cadia District, Molong Volcanic Belt, respectively; Figs. 1.3 and 1.4; Stanley et al., 1995; Jensen and Barton, 2000; Cooke et al., 2007).

In Canada, alkalic porphyry deposits occur along the entire length of the Cordillera, primarily in the Quesnellia and Stikinia terranes (Figs. 1.1 and 1.4; McMillan and Panteleyev, 1995; Mortensen et al., 1995). These two terranes are believed to have some of the highest potential for porphyry deposit discoveries in Canada (Sinclair, 2007). Exploration for alkalic deposits is favored by some companies due to the potentially large metal contents and also because they can be environmentally friendly to mine with their low total sulfides content and high acid-buffering potential (Jensen and Barton, 2000; Sillitoe, 2002).

With regard to metal production in British Columbia up to 2004, 14 alkalic porphyry deposit and/or camps yielded 1.7 million ounces of Au, 3.2 million ounces of Ag and 0.326 million tonnes of Cu (Schroeter et al., 2004). Alkalic porphyry deposits contain a significant component of British Columbia's Au resources, totaling 19 million ounces. Afton-Ajax, Mt. Polley, Galore Creek, Mt. Milligan, Red Chris, Lorraine and Copper Mountain-Ingerbelle deposits are the most well known examples of alkalic porphyry deposits in British Columbia (Fig. 1.4; Schroeter et al., 2004).

While porphyry Cu deposits have been found at many locations around the world (Fig. 1.3), alkalic, silica-undersaturated porphyry deposits are rare globally. British Columbia is the exception to this generalization, because silica-undersaturated deposits are both common and economic (Figs. 1.4 and 1.5). The only currently recognized silica-undersaturated deposits outside of British Columbia, are the Marian and Dinkidi deposits in the Philippines (Fig. 1.3; Knittel, 1987; Wolfe, 2001).

The similarities between alkalic and calc-alkalic porphyry deposits suggest that a continuum of porphyry deposits exists: calc-alkalic Cu-Mo deposits,

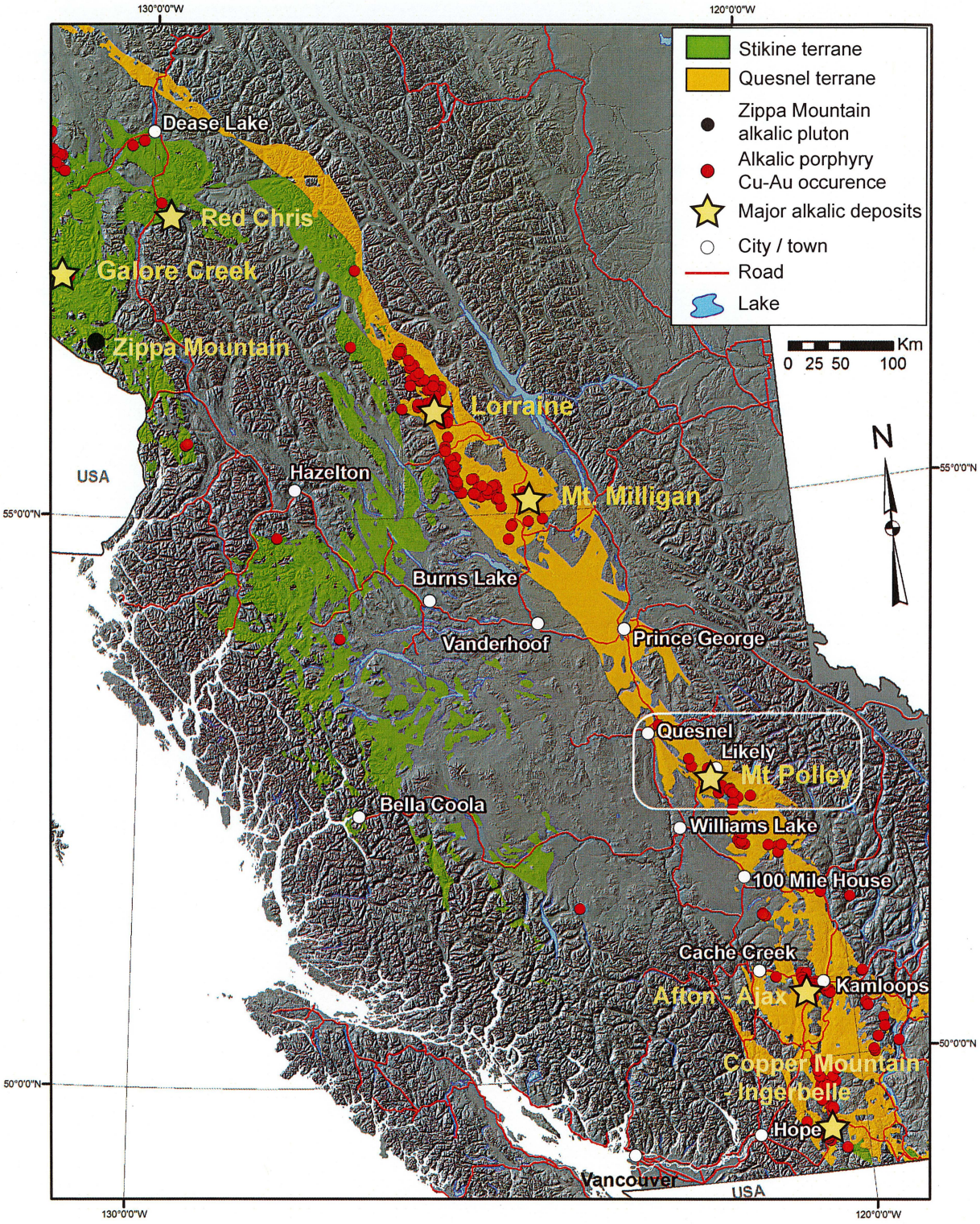

Figure 1.4 Location of the Mt. Polley Cu-Au-Ag porphyry deposit in British Columbia, Canada. Other alkalic porphyry Cu-Au deposits are shown as yellow stars, and mineral prospects as red circles. Location of the Zippa Mountain pluton is marked by a black circle. These are hosted in the Triassic and Early Jurassic Quesnel and Stikine terranes. Figure modified from Tosdal et al. (2008).

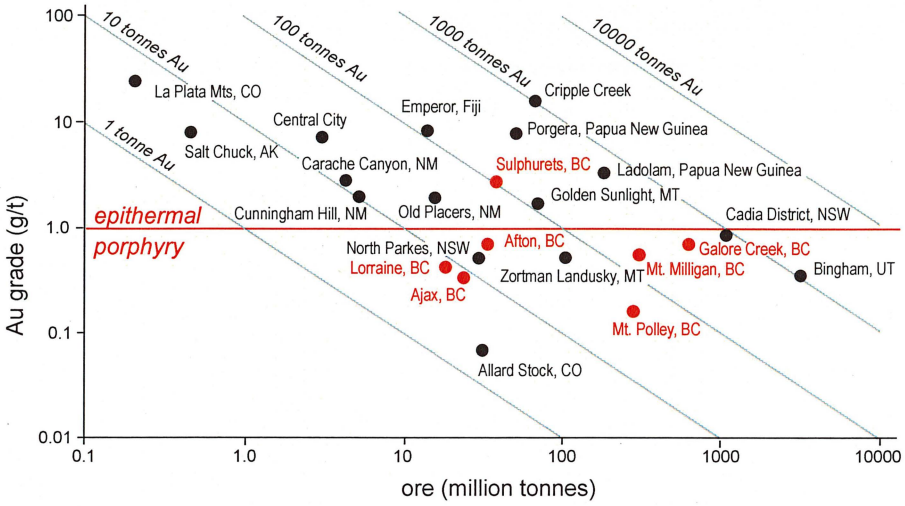

Figure 1.5 Grades and tonnages for selected alkalic porphry and epithermal deposits. Deposits from British Columbia are highlighted in red. Figure modified from Jenson and Barton (2000).

high-potassium calc-alkalic Cu-Mo-Au deposits, silica-saturated Cu-Au alkalic deposits and Cu-Ag-Au silica-undersaturated, highly alkalic deposits (Lang et al., 1995a; Lang et al., 1995b). Alkalic deposits are the Au-enriched end-member of this continuum, with the silica-undersaturated systems more strongly alkalic than their silica-saturated counterparts (Lang et al., 1995a, b, c; Jensen and Barton, 2000; Logan and Bath, 2006).

Despite being part of a continuum, alkalic porphyries have many characteristics that distinguish them from calc-alkalic porphyry deposits, including distinctive and complex hydrothermal alteration and mineralization assemblages, metal zonation and geochemical signatures (Table 1.2 and Appendix A2; Lang et al., 1993; Lueck and Russell, 1994; Smith, 1994; Lang et al., 1995b; Jensen and Barton, 2000; Wilson et al., 2002; Wilson, 2003). Phyllic alteration is typically fault- and fracture-controlled in alkalic porphyries, which lack the pervasive and voluminous phyllic alteration typical of calc-alkalic porphyry deposits (Fig.1.6, compare A to B, C, D; Lang et al., 1995c; Jensen and Barton, 2000; Ossandon et al., 2001; Wilson et al., 2003; Cooke et al., 2007). Complex K-Na-Ca (potassic, sodic, calc-potassic) alteration assemblages typify alkalic porphyry deposits (Fig. 1.6B and C). Hematite (i.e. "red-rock") alteration appears to be a "trademark" of alkalic systems and carbonate can be found throughout the paragenesis. Gold mineralization is most commonly associated with bornite (i.e. Ridgeway, Wilson, 2003) but also chalcopyrite (i.e. Copper Mountain, Stanely et al., 1995; Cadia Hill, Wilson, 2003). Molybdenum usually occurs only in minor to trace amounts, and Mo grades are not typically reported (e.g. Ajax; Ross et al., 1995; Galore Creek, Central Zone, BCMINFILE, 2010). Consistent with a continuum, some deposits exhibit both alkalic and calc-alkalic features, such as Red Chris in northwestern British Columbia (Fig 1.6D; Newell and Peatfield, 1995; Baker et al., 1997; Baker and Thompson, 1998).

The silica-saturated and silica-undersaturated alkalic porphyry Cu-Au deposits of British Columbia (Table 1.3) lack quartz veins, in marked contrast with "classic" porphyry Cu-Au deposits, as well as the silica-oversaturated alkalic deposits of New South Wales (compare Fig. 1.6B and C; Lang and McClaren, 2003). The deposits in British Columbia can also contain abundant carbonate and garnet as alteration and vein minerals in the core of the deposit (Fig. 1.6C; Barr et al., 1976; Lang et al., 1993; Lueck and Russell, 1994; Lang et al., 1995b; Lang et al., 1995c). Carbonate minerals only occur in the outer propylitic halo, and garnet is restricted to metasomatized limestone wallrocks in calc-alkalic deposits (Jensen and Barton, 2000). The causative intrusions lack quartz, and quartz veins are uncommon or absent. This contrasts markedly with "classic" porphyry Cu-Au deposits, where quartz occurs as phenocrysts, a groundmass component and in veins.

An important but under-appreciated part of alkalic porphyry systems is the various types of breccias, which have the potential to provide a link between intrusive, volcanic and tectonic events (Cooke et al., 2006). Breccias in magmatic-hydrothermal systems

Table 1.2 Comparison of geological characteristics of alkalic and calc-alkalic porphyry deposits, based on Lang et al. (1995b), Jensen and Barton (2000), Wilson et al., (2002) and Seedorf et al., (2005). Table modified from Wilson (2003).

Feature	Alkalic	Calc-alkalic
Metal association	Au-Cu; Cu-Au rare Mo	Cu-Au-Mo (high-K) Cu-Mo(-Au), Cu-Au-Mo (med-K)
Sulfide mineral abundance	Lower total sulfides	Higher total sulfides
Ore textures	Early pervasive or micro-fracture-controlled alteration followed by fracture-controlled alteration; higher density of dilatant fractures than is typical of calc-alkalic deposits; breccias	Disseminated or stockwork veined, breccia; weaker association of alteration and mineralization to stockwork zones of dilatant fractures
Ore related alteration	Potassic: bt-or-mt-ab-ch ± ah (extensive K-metasomatism) calc-potassic: at-bt-mt-ep; gt-or-py ± ap ± ah Sodic-calcic: ab-di-ep-ch-cc	Potassic: bt-or-ab ± mt ± ah Phyllic: qz-ms-py
Peripheral alteration	Sodic: ab-ch-py Propylitic: ch-ab-ep-cc	Argillic: mn-il-py Propylitic: ch-ep-cc ± at Advanced argillic: qz-al-dk-pr
Quartz veining	Rare in British Columbia, abundant in New South Wales	Ubiquitous
Related mineral deposit styles	Cu-Au skarn, Au-Ag-Te alkalic epithermal	Cu-Au and Pb-Zn skarn; sediment-hosted Au
Type examples	Galore Creek, Copper Mountain, Mt. Polley, British Columbia; Skouries, Greece; Dinkidi, Philippines	Escondida, Chuquicamata, El Salvador, Chile; Bingham Canyon, USA; Bajo del Alumbrera, Argentina

Mineral abbreviations: ab-albite, at-actinolite, al-alunite, ah-anhydrite, ap-apatite, bt-biotite, cc-calcite, ch-chlorite, di-diopside, dk-dickite, ep-epidote, gt-garnet, il-illite, mt-magnetite, mn-montmorillonite; ms-muscovite, or-orthoclase, py-pyrite, pr-pyrophyllite, qz-quartz

can provide information regarding the chemistry of the mineralizing fluids and the timing and energetics of the system. Detailed descriptions of breccia characteristics can lead to enhanced understandings of the chemical and physical evolution of a hydrothermal system (Davies et al., 2008). Breccias can provide clues to the location of hidden mineralization, and can themselves host high-grade mineralization, with grades up to double of those in the surrounding stock-work or disseminated mineralization (Sillitoe, 1985; Taylor and Pollard, 1993; Sillitoe, 1997, 2002; Seedorff et al., 2005; Eichenlaub and Seedorff, 2008; Tosdal et al., 2008).

1.2 Thesis aims and objectives

To address the challenges outlined above, a three-year, industry-sponsored collaborative research project, *Shallow- and Deep-level Alkalic Mineral Deposits: Developing an Integrated Exploration Model*, was initiated between the Australian Research Council Centre of Excellence in Ore Deposits (CODES) at the University of Tasmania and the Mineral Deposit Research Unit (MDRU) at the University of British Columbia in Canada, in collaboration with the British Columbia Geological Survey (BCGS) and the Geological Survey of Canada (GSC). The project aimed to advance the understanding of the characteristics of individual alkalic systems and integrate that information into a holistic model for the porphyry and epithermal environments.

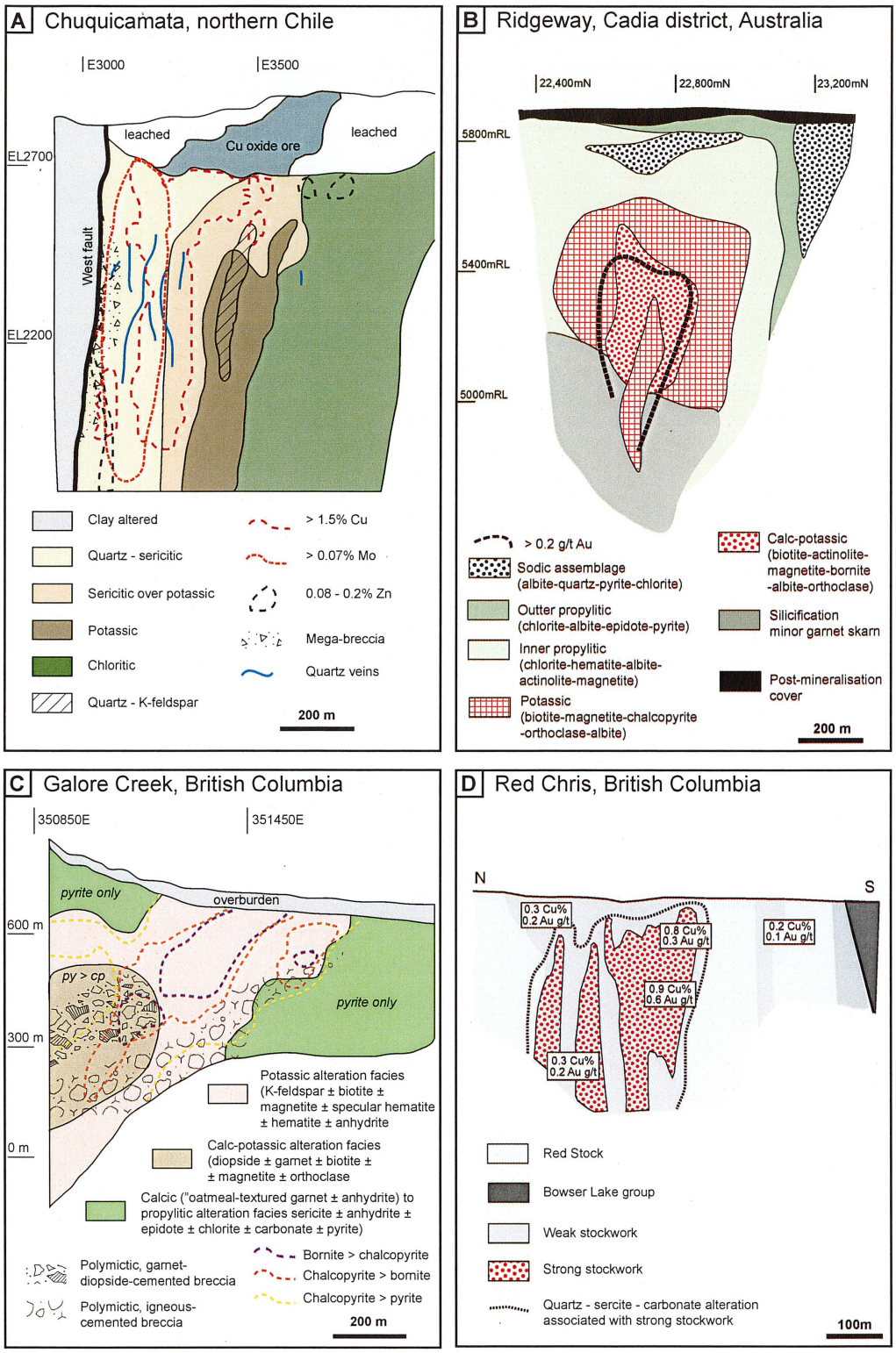

Figure 1.6 Cross sections with distribution of alteration facies in selected calc-alkalic and alkalic porphyry systems (modified from Zukowski, 2009). **A)** Chuquicamata calc-alkalic Cu deposit (cross section 3600N), northern Chile (modified from Ossandon et al., 2001). **B)** Ridgeway silica-oversaturated alkalic Au-Cu deposit, Cadia district, New South Wales, Australia (modified from Wilson, 2003). **C)** Galore Creek (North Au Lens) silica-undersaturated alkalic Cu-Au-Ag deposit, British Columbia, Canada (modified from Micko, 2008). **D)** Red Chris Cu-Au deposit, hosted by an intrusion with composition intermediate between the alkalic and subalkaic, porphyry related intrusive suites in the Cordillera, British Columbia, Canada (modified from Baker et al., 1997). Abbreviations: Cu-copper, Mo-molybdenum, Zn-zinc, Au-gold, py-pyrite, cp-chalcopyrite.

The study involved five PhD and four MSc studies of alkalic porphyry and epithermal deposits in British Columbia, New South Wales and Papua New Guinea (Fig. 1.3).

The easily accessible open-pit mining operation, of Mt. Polley (Fig. 1.3) is an ideal location to study the anatomy and fluid chemistry of a relatively high-grade, breccia-hosted alkalic Cu-Au porphyry deposit. Mt. Polley is significant in that it is a silica-undersaturated to silica-saturated, breccia-hosted system that is spatially and perhaps genetically associated with silica-undersaturated rocks of the nearby Bootjack Stock (Lang et al., 1995b). Alteration and mineralization features in Mt. Polley have affinities to both the silica-saturated and silica-undersaturated alkalic subtypes (Table 1.3; Lang et al., 1995b).

The Northeast Zone (NEZ) is one of more than eight ore zones and prospects that have been identified in the Mt. Polley intrusive and breccia complex (Mt. Polley Complex[1], Fig. 1.7). It is the focus of this PhD study. The NEZ is a small and relatively Au- and Ag-enriched deposit. The principal aim of this PhD study is to determine chemical and mineralogical zonation patterns within the NEZ, such that the fluid composition, fluid source(s) and fluid evolution responsible for carbonate- and sulfide-bearing breccia cement and veins can be elucidated. This will be achieved by:

- Documenting the intrusions and breccias of the NEZ, with the objectives of interpreting breccia formation links between magmatic and hydrothermal ore-forming processes.
- Documenting the detailed paragenetic sequence of breccia cement and veins to evaluate relationships between hydrothermal brecciation, alteration and mineralization.
- Characterize the different styles and temporal occurrences of Cu-Au-Ag mineralization.
- Constraining the fluid chemistry in order to identify likely fluid and magma sources and/or depositional processes using stable (C, O, S) and radiogenic (Pb, Sr) isotope geochemistry.
- Analyzing and mapping the trace element chemistry of sulfides in order to determine the trace element contents of the main sulfide minerals of the NEZ, focusing on Au, Ag and PGE occurrences.
- Developing an integrated genetic model for the NEZ, and commenting on possible exploration implications.

[1] For the purposes of this study, the Mt. Polley Complex does not include the Bootjack Stock.

1.3 Approach and methods

This PhD study included three seasons of fieldwork for a total of five months at the Mt. Polley mine site (July 2005, July–September 2006, and October–November, 2007). Geologic relationships were documented mainly through diamond drill core logging. Only limited time was spent making open pit-scale observations. Pit mapping and an extended study of the structures in the pit were not possible due to access restrictions for safety reasons.

The primary focus of logging was a long-section bisecting the NEZ. Logging of a cross-section was also conducted in the first field season. The long-section contains both high-grade mineralization and peripheral alteration domains, and had not been studied previously by Imperial Metals. To create the long-section, numerous inclined drill holes were clipped 10 m laterally either side of the center line of the section. Graphic core logging was conducted at a scale of 1 cm : 2 m for parts or all of 43 diamond drill holes contained within that clipped window, for a total of 4,898 m. Of this total, approximately 1,300 m of geology ± alteration was logged by other members of the alkalic project (Dr. Kirstie Simpson, Dr. Claire Chamberlain, Prof. David Cooke), prior to the author re-logging these holes for alteration and/or geology, paragenesis and sample collection. The author logged all aspects of the additional 3,598 m. Core was not oriented and therefore systematic structural information was not collected. A list of drill holes and meterage logged and scanned copies of logs from this study are provided in Appendix A3.

Rocks samples were cut length-wise along the cut face from ½ and ¼ core pieces to produce a

Table 1.3 Characteristics of alkalic silica-saturated and silica-undersaturated porphyry Cu deposits. Information from Lang et al. (1993) and Lang et al. (1995a, b) and unless otherwise stated.

Feature	Silica-saturated	Silica-undersaturated
Most abundant rock type	Shoshonitic basalts, andesites and intrusion that range form diorites (usually early and equigranular) to monzodiorites and monzonites (usually later and porphyritic); true syenties rarely developed; intrusions are not zoned (with exception of Copper Mountain stock)	Silica-undersaturated phonolites and syenite porphyries with lesser pyroxenite and monzonite; diorites less common than in silica-saturated deposits (exception is Mt. Polley where diorite host rock forms a separate intrusion from a feldspathoid-bearing syenite); when present as single intrusion, characterized by concentric zoning with a pyroxenite border phase, with syenite core, and planar mineral fabrics of strongly silica-undersaturated systems (Lueck and Russell, 1994; Smith, 1994)
Associated volcanic rocks	Dominated by augite- and plagioclase-phyric basalt and andesite flow, pyroclastics, and volcanic breccia and fragmental rocks; evidence for both subaerial and submarine deposition	As in silica-saturated
	(Feldspathoid-bearing flows and fragmental rocks not observed as in silica-undersaturated)	Feldspathoid-bearing flows and fragmental rocks form part of the local volcanic pile
Igneous chemistry	Less strongly alkalic than silica-undersaturated; may have minor normative nepheline or quartz, compositions project mostly into silica-saturated fields	More strongly alkalic than silica-saturated rocks; strong Fe-enrichment (Lueck and Russell, 1994)
Rock textures	Macroscopically equigranular, seriate, or have only fine-grained porphyritic textures and thin section observation is required to observe the crowded porphyritic texture usually present	Commonly mega-porphyritic (can be up to 25 cm in length)
Phenocrysts	Various combinations of augite, plagioclase, K-feldspar, magnetite, apatite, biotite, and more rarely hornblende.	Pseudoleucite, orthoclase, augite, amphibole, garnet, titanite, plagioclase, apatite, less abundant biotite, and extremely rare zircon;
		Melanite garnet, aegirine-augite, K-feldspar and feldspathoid mineral assemblages, prominent mineral fabric in the form of planar crystal alignment (Lueck and Russell, 1994)
Groundmass minerals	Apatite, magnetite and orthoclase are ubiquitous groundmass minerals; zircon is a common accessory mineral in some intrusions, less commonly titanite	Orthoclase, magnetite, titanite, apatite, biotite is usually minor to absent, but is abundant in some pyroxenites
Magnetite content	High magnetite content (locally up to 15%)	Consistently high; low magnetite (with abundant augite) in barren deposits and high magnetite (and abundant hornblende) in Cu-mineralized deposits (Lueck and Russell, 1994)
Morphology and size	Composite batholiths to isolated occurrences or dike (sill) swarms	Large plutons to dike/sills swarms

Table 1.3 continued

Feature	Silica-saturated	Silica-undersaturated
Alteration	Albite-dominated alteration associated with mineralization more common and widespread than in calc-alkalic deposits; minor late-stage quartz veins, scapolite common in late-stage alteration; major calcite, prehnite and hematite, present, major epidote, local bornite; alteration on average more closely related to dilatant fractures	Potassium-calc-silicate alteration (garnet, diopside, anhydrite, apatite) common and important in silica-undersaturated deposits, but virtually absent in calc-alkalic deposits; early pervasive effects overprinted by fracture controlled potassic alteration assemblages; bornite important; minor calcite and epidote, no scapolite, prehnite or quartz development; alteration on average is less closely related to dilatant fractures
Character of pervasive alteration	Early pervasive Na- and then K-metasomatism largely precedes sulfide mineralization	Early pervasive K-metasomatism largely precedes sulfide mineralization, Na-metasomatism is not well developed
Mineral zonation	Low sulfide core of sodic and/or potassic alteration assemblages, surrounded by higher sulfide propylitic assemblage (can be contemporaneous or overprinting), potassium-calc-silicate assemblages can be in the core or form an intermediate zone	As in silica-saturated
Ore minerals	Cp-(Bn)-Au^0	Cp-Bn-Au^0
	Chalcopyrite is most important, bornite is usually found in core of deposits (excèption is Galore Creek) and associated with Au (or Ag as in Copper Mountain and Mt. Polley); molybdenite, sphalerite, galena are minor to trace minerals; also similar Cu/Au ratios	As in silica-saturated
Mineralization features	Late timing, more abundant dilatant fractures than silica-undersaturated, Cu/Au decrease towards margins, Au:Cu lower than silica-undersaturated	Early timing, very minor dilatant fractures compared to silica-saturated, Cu/Au decreases toward margins, higher Au:Cu than silica-saturated
Breccia	Intrusion breccias associated with early plutonic phases are more common; the magmatic-hydrothermal breccias that do form are syn-mineralization, but only rarely the main host for ore	Magmatic-hydrothermal breccias are more common and include pre-, syn- and post-mineralization varieties and are common a major host to ore grade mineralization
Timing of mineralization	Main-stage mineralization typically occurred from solutions evolved late in local magmatic sequence, and more explosively	Hydrothermal fluids evolved early in sequence of magmatic events via relatively passive fluid release

~1 cm thick slab from which textural relationships and laboratory analyses could be conducted. In addition to graphic logging and rock sample collection, rock characteristics from each drill hole representative of coherent units, contact relationships, breccia characteristics, veining, alteration, textural features and paragenetic relationships were recorded by producing a library of 1,695 scanned images (Appendix A4). In addition to petrographic analyses conducted by the author at CODES, supplementary petrographic data was obtained from internal reports of Imperial Metals Corporation (principally conducted by K. Ross of Panterra Geoservices Inc.).

Laboratory-based methods were used to supplement mineral identification made during core logging and thin section petrography. Scanning electron microprobe (SEM) analyses, electron microprobe (EMP), energy dispersive spectrometry (EDS) and back scattered electron (BSE) imaging of carbonates, sulfides and selected other minerals were carried out at the Central Science Laboratory (CSL) at the University of Tasmania (UTAS) under the supervision of Dr. Karsten

Figure 1.7 Aerial photo of the Mt. Polley Complex in September 2005, showing open pits and mill, looking south. Polley Lake is approximately 670 m wide. Image courtesy of C. Rees (2009, Imperial Metals Corporation).

Goemann. A portable shortwave infrared spectroscopy (SWIR) Terraspec ASD (analytical spectral device) was used to assist with mica, clay and carbonate identification. Staining of rocks slabs with cobaltinitrite was used to assist with K-feldspar identification. This work was conducted at CODES. Stable isotope analyses, including S-isotopic analyses of sulfides and sulfates and C-O isotopic analyses of carbonates were performed by Ms. Christine Cook and Mr. Keith Harris at the CSL at UTAS. Additional C-O isotopic analyses of carbonates were performed by Ms. Janet Gabites at the Pacific Center for Isotopic and Geochemical Research at the University of British Columbia. Radiogenic Pb and Sr data were analyzed by Dr. Roland Maas at the University of Melbourne isotope laboratory. Trace element analyses of Pb, Sr and rare earth elements were conducted by Ms Sarah Gilbert and Ms. Terrie Sawyer at CODES. Unpublished geochronological and radiogenic Nd and additional Sr data was kindly provided by Adam Bath (UTAS) and James Logan (British Columbia Geological Survey). Sulfide trace element analyses were conducted using the CODES laser-ablation inductively coupled plasma mass spectrometry (LA-ICP-MS) facility by the author. Sulfide multi-element grain maps were produced by Ms. Sarah Gilbert and Mr. Shaun Inglis at CODES. Analyses of Cu-sulfide flotation concentrate samples were conducted by Genalysis Laboratory Services Pty Ltd in Western Australia.

1.4 Thesis organization

Following this introduction, there are five chapters that describe and interpret the NEZ of Mt. Polley:

Chapter 2 reviews the tectonic setting of British Columbia, and in particular Quesnellia and describes the regional and local geology and metallogeny of the Nicola Group. A brief review of the geology, geochronology, alteration and mineralization of the Mt. Polley Complex, as documented from previous studies, concludes this chapter.

Chapter 3 presents the results of graphic logging of the geology of the NEZ, including detailed documentation of NEZ breccia. This chapter includes genetic classification of the breccia facies and an interpretation of breccia formation.

Chapter 4 describes the breccia cement, alteration and mineral paragenesis of the NEZ. A detailed paragenetic sequence for mineralization and alteration is provided, together with documentation and interpretation of alteration zonation patterns.

Chapter 5 describes the physiochemical environment of ore deposition and alteration based upon new S, C-O, Pb, Sr and Nd isotopic data for the NEZ.

Chapter 6 concerns the deportment and distribution of trace element compositions of pyrite, chalcopyrite and bornite in the alkalic porphyry environment of the NEZ. Implications for the evolution of hydrothermal fluids and depositional processes are discussed.

Chapter 7 concludes the thesis by presenting a genetic model for the formation of the NEZ specifically and Mt. Polley in general. This model is also discussed from the broader context of the genesis of silica-undersaturated porphyry mineralization. Aspects of the model relevant to exploration are also discussed in addition to recommendations for further research.

1.5 Location and access

The Mt. Polley mine is located in heavily forested and till-covered ground of the Fraser Plateau in south-central British Columbia, latitude 52°33'N; longitude 121°38'W or UTM 592600E, 5823100N (Zone 10, NAD 83) in NTS Map Sheets 093A/5, 6 and 12 (Fig. 1.1). The mine lease encompasses moderate rolling hills between Polley and Bootjack Lakes (Fig. 1.7; Hodgson et al., 1976). Elevations range from 920 m at Polley Lake to 1266 m at the summit of Mt. Polley. The nearest airport is in the town of Williams Lake, 56 km southwest, and Likely is the closest village, 8 km northeast of the mine site. Mt. Polley is accessible year-round via paved provincial highway between 150 Mile House (15 km southeast of Williams Lake on British Columbia Highway 97; Fig. 1.8) and Likely. From Morehead Lake, 12 km of well-maintained gravel road (the Bootjack Forest Access Road), connects the paved road to the main mine site entrance (Fig. 1.8; Rees et al., 2006a).

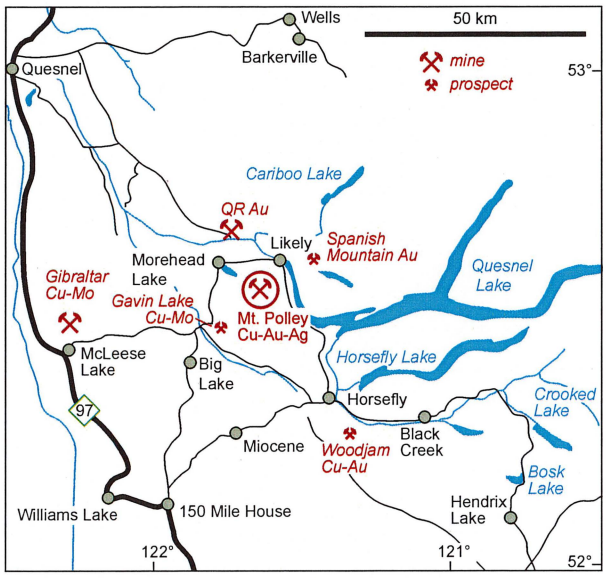

Figure 1.8 Regional geography of the Mt. Polley area showing road access and surrounding mines and prospects. Modified from Rees et al. (2006) after Panteleyev et al. (1996).

1.6 Mt. Polley exploration and mining history

The Mt. Polley mine is located in a region with a long history of mining (Panteleyev, 1987). Since 1859 the region has been the site of historically important placer Au production from the Quesnel River and

its tributaries (Bailey, 1990; Panteleyev et al., 1996). Bedrock exploration in the Quesnel River area was active during the late 1960s and throughout the 1970s, initially for Cu and Cu-Au porphyry deposits followed by Au deposits in the 1980s (Panteleyev, 1987).

A detailed account of past ownership, exploration and mining history of the Mt. Polley mine was provided by Gillstrom (2004) and updated by Rees et al. (2006a). Most of the following is summarized from these references.

Copper mineralization was discovered in what would become the heart of the Cariboo-Bell deposit during follow-up prospecting of an aeromagnetic anomaly on a 1963 provincial government map sheet (Graham, 2003; Gillstrom, 2004). The first claims were staked in 1964 by Mastodon Highland Bell Mines Limited and Leitch Gold Mines. These companies merged in 1966 to form Cariboo-Bell Copper Mines Limited, which conducted geological mapping, soil, geochemical, and geophysical surveys, trenching, and drilling (Gillstrom, 2004).

Between 1964 and 1987 exploration was conducted by several parties including Teck Corporation (1969 to 1979), Highland Crow Resources in 1978 (an affiliate of Teck), and E&B Explorations Inc. from 1981 to 1987 (including joint venture partners Geomex Partnerships and Imperial Metals Corporation as of 1982). During this time exploration included magnetic, seismic, very low frequency-electromagnetic (VLF-EM) and induced polarization (IP) surveys, soil geochemical surveys and geological mapping. Numerous drilling programs over this time generated more than 37,900 m of core drilled in 290 drill holes that intersected generally low-grade Cu porphyry mineralization in the Cariboo and Bell areas (Fig. 1.7; Graham, 2003; Gillstrom, 2004).

In 1987 Imperial Metals Corporation merged with Geomex Partnerships and purchased the remaining interest in the property from Homestake Canada and others. A comprehensive exploration program over the next two years generated 238 diamond drill holes totaling 27,566 m, six bulk samples totaling 130 tonnes, geological mapping and IP surveys (Gillstrom, 2004). This was followed by a feasibility study conducted by Wright engineers in 1990, based on a 5 million tonne per year plant that incorporated new ore reserve calculations, metallurgical testing, geotechnical evaluations and environmental impact assessments.

Imperial Metals bought out Geomex Partnerships and obtained 100% ownership in 1992. A merger with Bethlehem Resources Corporation followed in 1995 and an in-house feasibility study was completed. The Mt. Polley Mining Corporation (MPMC) was formed in April 1996 with financing arranged with Sumitomo Corporation through a joint venture with SC Minerals Canada. Construction of the Mt. Polley mine and mill began in 1996 (Rees et al., 2006b). Construction of this 18,000 tonnes per day facility was completed in June 1997 at a cost of $123.5 million and the open-pit mine opened in 1997 (Graham, 2003). Ongoing drilling, mine planning and exploration activities continued throughout this period, generating an additional 65 core, rotary, percussion or water well holes totally 7,250 m, soil and litho-geochemical surveys, surface mapping and Cariboo pit-wall mapping.

Production at Mt. Polley began in 1997 at Cariboo-Bell, and continued until 2001. During that time the mine was plagued by low Cu and Au prices. From 1998 to 2001, 493 core or percussion holes were drilled for a total of 39,100 m. These holes defined mineralization, determined rock quality and resulted in the discovery of the C2 zone, south of the Cariboo pit, the Southeast Zone and high-grade Cu mineralization north of the proposed Springer Pit. Two pits were in operation in 2001, the Bell and Cariboo (Fig. 1.7). After four and a half years of operation, with production of 370,700 oz Au and 133.9 million lbs of Cu from 27.7 million tons of ore from 55.0 million tons mined milled, operations were suspended in September 2001 due to low metal prices (Graham, 2003; Gillstrom, 2004).

The mill was maintained on standby from 2001 to 2005, pending higher metal prices (Gillstrom, 2004). Exploration continued during this period and in 2003, rising metal prices and changes in provincial government mining policies prompted Imperial Metals to evaluate several prospective targets on site (Graham, 2003; Danielson, 2005). This led to the discovery of the Cu-Au rich Northeast Zone (Wishbone target), approximately 1.5 km northeast of the partially mined

Bell Pit, in August 2003 (Fig. 1.6; Graham, 2003; Rees et al., 2006b). The proposed pit in the NEZ zone was named the Wight Pit after the late George Wight, who was the mine manager at Mount Polley between 1996 and 2003 (Gillstrom, 2004). Development of the Wight pit began in March 2005 and the mine officially re-opened in the fall of 2005 with the Bell and Wight pits feeding the mill (Danielson, 2005).

Mining of the Springer Pit and the Southeast Zone began in 2008 as mining in the Bell pit ceased. Mining activity in the Wight Pit was completed in 2009, although drilling in 2008 defined a high grade pod of mineralization (Kidney zone). Currently drilling is being conducted from the bottom of the pit to provide access for further exploration in the NEZ. Underground mining is being considered for a high-grade resource that is known to exist ~300 to 600 m below the surface, which presently is too deep to be captured by surface mining (Imperial Metals Corporation, 2009a). This part of the NEZ may be the first mineralization to be mined underground at Mt. Polley.

The most recent proven and probable reserves and resources of the Mt. Polley mine are listed in Table 1.4 (Imperial Metals Corporation, 2009b). Current exploration is focused on locating high-grade ore to replace the Wight pit mill feed. Drilling at the Boundary, Southeast and Northeast zones has returned significant intervals of high-grade Cu-Au mineralization. The Pond zone is a high-grade discovery that is expected to be in production by the end of 2009 (Imperial Metals Corporation, 2009a).

In April 2009 Imperial entered into an option agreement with Valley High Ventures Ltd. to acquire a 100% interest in a portion of a claim adjacent to the Boundary zone. The optioned property will facilitate open pit mining of the near-surface mineralization discovered in the Boundary zone (Imperial Metals Corporation, 2009a). From 1997 to 2009, more than 363 Mlbs of Cu, 1.8 Moz of Ag and 0.6 Moz of Au have been produced and mining at Mt. Polley is predicted to continue until late 2015 (Imperial Metals Corporation, 2009a).

1.7 Previous research of the Mt. Polley Complex

Mineralization and alteration zonation patterns of the Mt. Polley property were first documented in the PhD and MSc studies by Morton (1976), Bailes (1977; cited in Bailey, 1988) and Bailey (1978). Geology of the 'Cariboo-Bell' deposit was documented by Hodgson et al. (1976), and Bailey and Hodgson (1979) who identified porphyry Cu mineralization associated with a potassically altered core surrounded by propylitic alteration. Radiometric dating and geological relationships led the authors to interpret a close temporal association of volcanism, plutonism and ore deposition. Fraser (1994a and b; also Fraser et al., 1993, Fraser et al., 1995) conducted her MSc studies at an advanced stage of exploration in the area of the Springer, Cariboo and Bells pit (Fig. 1.7). She identified minor igneous-cemented breccia and abundant hydrothermal breccias genetically related to the emplacement of a crowded plagioclase porphyry. The hydrothermal breccias were found to be the main host to mineralization. Surface mapping conducted by Read (1997; cited in Rees et al. 2005) supplemented Fraser's work, extending geological contacts outside the incipient Cariboo pit in the Core Zone. Geochronogical analyses of zircon and titanite (U-Pb) from the Bootjack Stock and the Mt. Polley Complex constrained their emplacement to the Triassic-Jurassic boundary (Mortensen et al., 1995).

With the discovery of the NEZ and reopening of the mine in 2005, several additional in-house studies were implemented by Imperial Metals. These included petrographic studies of the Springer, Bell, Nordic, Leak and Northeast zones by Ross (2004a; 2004b; 2004c; 2004d; 2004e); reports on the environment and physiochemical conditions of deposition (Bailey, 2004a; Bailey, 2004b), geophysical studies (Shives et al., 2004), and reports on the structure and rock classification of the Wishbone deposit by Taylor (2004) and Blackwell (2005), respectively, surficial geology and till geochemistry of the entire property (Blackwell and Stubley, 2005), breccia classification schemes (Simpson, 2005), and the mining feasibility study of Gillstrom (2004). Key results from these reports are summarized by Rees et al. (2005, 2006). Logan and Mihalnyuk

Table 1.4 Mt. Polley mine proven and probable reserves and resources.

Zone / Pit	Tonnes Ore	Grade			Contained metal		
		Cu (%)	Au (g/t)	Ag (g/t)	Cu (lb) x 1,000,000	Au (oz) x 1,000	Ag (oz) x 1,000
Proven and probable reserves (as of January 1, 2010)[1]							
Boundary	943,313	0.526	0.385	3.247	10.9	11.7	98.5
Springer	33,706,789	0.316	0.263	0.400	235.0	285.0	433.5
Pond	977,671	0.519	0.274	6.787	11.2	8.6	213.3
Southeast	1,585,826	0.187	0.396	0.847	6.5	20.2	43.2
C2	3,284,426	0.284	0.396	n/a[1]	20.63	41.8	n/a[1]
Total reserve	**40,498,025**	**0.318**	**0.282**	**0.606**	**284.2**	**367.3**	**788.5**
Measured, indicated and inferred resources (as of March 30, 2009)[2]							
NEZ and Boundary							
measured	19,631,561	0.580	0.229	4.077	251.02	144.54	2573.23
indicated	2,666,499	0.464	0.267	3.281	27.28	22.89	281.28
inferred	2,366,199	0.372	0.156	2.301	19.41	11.87	175.05
Bell							
measured	9,562,373	0.233	0.238	n/a[3]	49.12	73.17	n/a[3]
indicated	976,160	0.227	0.190	n/a[3]	4.89	5.96	n/a[3]
inferred	828,312	0.236	0.174	n/a[3]	4.31	4.63	n/a[3]
Springer							
measured	18,437,736	0.359	0.297	0.709	145.93	176.06	420.29
indicated	26,536,116	0.300	0.302	0.643	175.50	257.65	548.58
inferred	25,475,566	0.290	0.316	0.561	162.87	258.82	459.49
C2							
measured	5,352,649	0.237	0.363	n/a[3]	27.97	62.47	n/a[3]
indicated	4,045,493	0.240	0.356	n/a[3]	21.40	46.30	n/a[3]
Southeast							
measured	18,421,459	0.180	0.414	1.052	73.02	245.20	623.06
indicated	5,306,026	0.159	0.325	0.978	18.62	55.44	166.84
Pond							
measured	1,477,694	0.379	0.324	5.774	12.34	15.39	274.32
indicated	630,108	0.268	0.257	6.279	3.72	5.21	127.20
Total Resource							
measured / indicated	**113,043,874**	**0.325**	**0.305**	**1.380**	**810.81**	**1110.28**	**5014.84**
inferred	**25,670,077**	**0.295**	**0.299**	**0.688**	**186.59**	**275.32**	**634.54**

[1] Imperial Metals Corporation (2010), [2] Imperial Metals Corporation (2009b), [3] Ag assay values not significant in this zone.

(2005) evaluated the regional and local geologic setting of the Mt. Polley Corporation. A sulfur isotope zonation study of the NEZ was completed by Deyell and Tosdal (Deyell, 2005; Deyell and Tosdal, 2005).

The geochemistry of the Nicola Group (including Mt. Polley) was assessed by Logan and Bath (2006). This work included a melt inclusion study of the volcanic and intrusive rock associated with mineralized and barren alkalic centres in the Mt. Polley area. Logan et al. (2007) and Logan (2009; unpublished data, courtesy imperial Metals Corporation) completed several Ar-Ar (orthoclase, biotite), U-Pb (zircon), and Re-Os (molybdenum) age determinations. Geochronological analyses of the Bootjack Stock were carried out by Bailey

and Archibald (1990), Logan and Mihalnyuk (2005), Bath and Logan (2006), and Logan and Bath (2006).

As part of the current alkalic research project, several conference abstracts and reports have been published that include details of or specifically concern the NEZ: Bath et al. (2006), Chamberlain et al., (2007a; 2007b) and Jackson et al. (2007a; 2007b; 2007c). A MSc thesis on the NEZ was completed by Jackson (2008) which documented the igneous paragenesis and brecciation history of the NEZ from two cross-sections. A review of hydrothermal breccias at Mt. Polley, including the NEZ, was presented by Tosdal et al. (2008). Results of the current PhD study have been presented previously in Pass et al. (2007a; 2007b; 2007c) and Pass et al. (2009). These publications are provided in Appendix A5.

Chapter 2

Regional and Local Geologic Setting

2.1 Introduction

The purpose of this chapter is to introduce and review the tectonic and geologic setting of the Mt. Polley mine from provincial to local scale. The mine is hosted in the Mt. Polley intrusive and breccia complex, which has intruded the volcanic and sedimentary rocks of the Nicola Group. These rocks are part of the Quesnel (Quesnellia) terrane, which extends along the eastern margin of the Intermontane Belt of the Canadian Cordillera (Figs. 1.4 and 2.1). The following section reviews the tectonic setting, geology and metallogeny of Quesnellia, the Nicola Group and the Mt. Polley Complex.

2.2 Terranes of the Britsh Columbia Cordillera

Most of British Columbia is composed of exotic island arcs, oceanic crust, accretionary wedges, and segments of lithosphere that are the product of Middle Proterozoic to Cenozoic accretion to the North America craton (Gabrielse et al., 1991; McMillan et al., 1995; Johnston and Borel, 2007; Nelson and Colpron, 2007). Five morphological belts of differing geological histories comprise the British Columbia Cordillera (Fig. 2.1). From east to west, these are: 1) ancestral North America craton (Laurentia) and foreland passive margin, 2) deformed pericratonic terranes of the Omineca Belt, 3) allochthonous terranes of the Intermontane Belt, which include rifted continental fragments, arcs, and ocean basins consisting primarily of the Stikinia, Quesnellia, Cache Creek and Slide Mountain terranes, 4) Coast Mountain Plutonic Belt, and 5) crustal fragments of the Insular Belt and late accreted accretionary prisms (Fig. 2.1; Gabrielse et al., 1991; McMillan et al., 1995; Johnston and Borel, 2007; Nelson and Colpron, 2007).

2.3 Quesnellia, Stikinia and the Cache Creek terranes

The Quesnellia and Stikinia intraoceanic island-arc terranes are interpreted to have been a single, contiguous oceanic island arc located outboard of the ancestral North American continental margin during Late Paleozoic and Mesozic times (Fig. 2.2A; Mihalynuk et al., 1994; Nokleberg et al., 2000; Nelson and Colpron, 2007). The Cache Creek ocean was located to the south and west of the Stikinia-Quesnellia arc, and the Seventymile–Slide Mountain ocean(s) to the north and east, during Paleozoic and early Mesozoic times (Fig. 2.2A–E; Wernicke and Klepacki, 1988; Mihalynuk et al., 1994; Nokleberg et al., 2000; Johnston and Borel, 2007). The Stikinia-Quesnellia arc arguably formed on the axial or flanking portions of displaced passive pericratonic strata of the Yukon-Tanana (Nisling) and Kootenay terranes, which were previously rifted from the North American cratonal margin (Fig. 2.2A–B; Mihalynuk et al., 1994; Nokleberg et al., 2000; Nokleberg et al., 2005). These metamorphosed continental-margin terranes are mainly clastic-dominated successions containing mafic to felsic volcanic rocks, coeval granitic plutons, and marble (McMillan et al., 1995; Nokleberg et al., 2000). The older parts of the Stikinia and Quesnellia arc(s) began to form in the Devonian to Pennsylvanian, due to subduction of the Cache Creek oceanic plate,

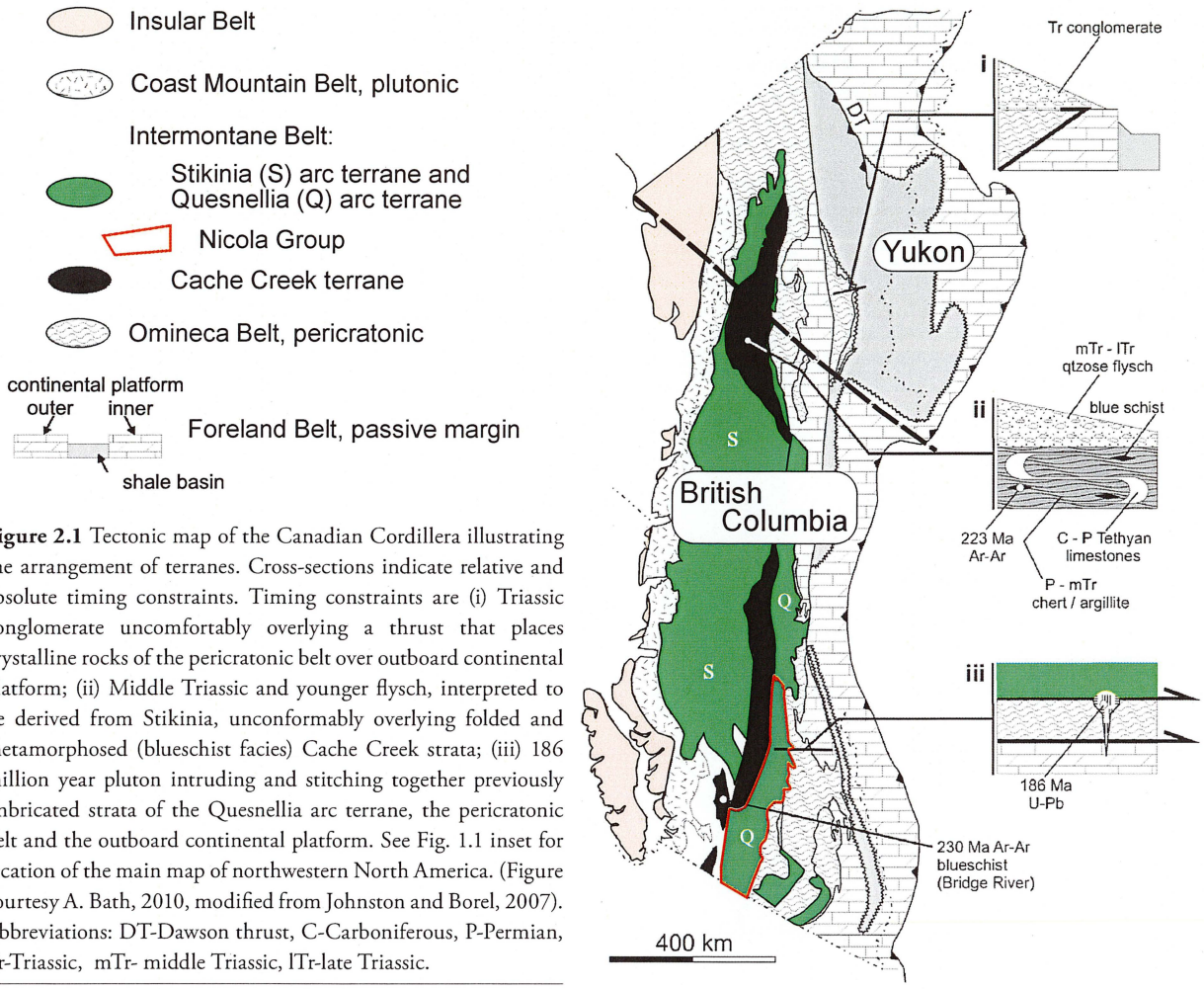

Figure 2.1 Tectonic map of the Canadian Cordillera illustrating the arrangement of terranes. Cross-sections indicate relative and absolute timing constraints. Timing constraints are (i) Triassic conglomerate uncomfortably overlying a thrust that places crystalline rocks of the pericratonic belt over outboard continental platform; (ii) Middle Triassic and younger flysch, interpreted to be derived from Stikinia, unconformably overlying folded and metamorphosed (blueschist facies) Cache Creek strata; (iii) 186 million year pluton intruding and stitching together previously imbricated strata of the Quesnellia arc terrane, the pericratonic belt and the outboard continental platform. See Fig. 1.1 inset for location of the main map of northwestern North America. (Figure courtesy A. Bath, 2010, modified from Johnston and Borel, 2007). Abbreviations: DT-Dawson thrust, C-Carboniferous, P-Permian, Tr-Triassic, mTr- middle Triassic, lTr-late Triassic.

now preserved as the accretionary Cache Creek terrane (Fig. 2.1; Mortimer, 1987; Bailey, 1990; Mihalynuk et al., 1994; Monger and Nokelberg, 1996; Nokleberg et al., 2000; Nokleberg et al., 2005).

In Early to Late Permian times, thick and extensive limestone successions (i.e. Marble Range subterrane; Monger and Berg, 1987) were deposited in the Cache Creek ocean (Mihalynuk et al., 1994; Fig. 2.2D). Seamounts, oceanic plateau with fringing carbonate reefs and banks located on the Cache Creek oceanic plate first collided with the Stikinia-Quesnellia arc in the Lower Triassic (230 Ma or earlier; Fig. 2.2D; Monger, 1977; Johnston and Borel, 2007). While seamount and oceanic plateau accretion did not terminate subduction, they may have allowed large amounts of carbonate-bearing substrate to be subducted beneath the Stikinia-Quesnellia arc (e.g. Dominguez et al., 2000). The major period of arc formation is considered to be Late Triassic (Carnian and Norian; 230–200 Ma, Fig. 2.2E; McMillan and Panteleyev, 1995; Nokleberg et al., 2000; Johnston and Borel, 2007). Alkali basaltic volcanism evolved to intermediate magmatism at the end of the Triassic (Mortimer, 1987). Subduction-related intermediate to felsic plutons intruded the arc during the final stages of Late Triassic to Early Jurassic arc-related igneous activity (Mortimer, 1987; Bailey, 1990; Fig. 2.2E). Arc magmatism is interpreted to have culminated in alkalic-style porphyry mineralization at the Triassic-Jurassic boundary (Fig 2.2E; Mihalynuk, 1999).

Magmatism ended in the Early Jurassic (Sinemurian-Pliensbachian) time as the arc collided with the previously amalgamated pericratonic belt–outer carbonate platform of the foreland passive margin from subduction and(or) obduction of the Seventymile and/or Slide Mountain oceanic plates along the continental margin (Fig. 2.2; Nelson and Mihalynuk, 1993;

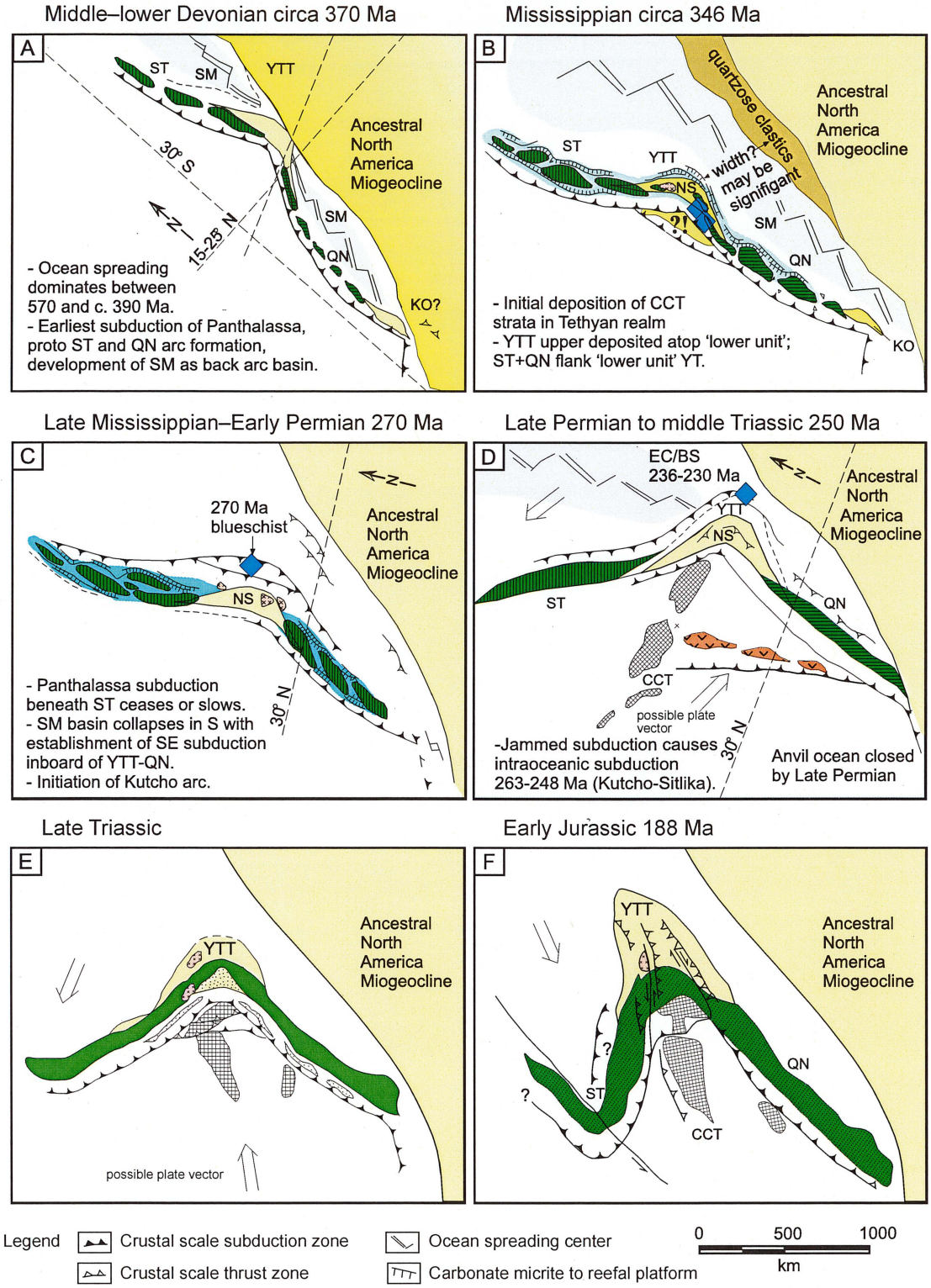

Figure 2.2 Scaled palinspastic maps of the west coast of Ancestral North America at **A)** middle to lower Devonian, **B)** Mississippian, **C)** Late Mississippian to Early Permian, **D)** Late Permian to middle Triassic, **E)** Late Triassic, and **F)** Early Jurassic, as proposed by Mihalynuk (1999). The palinspatic maps show the location of Quesnellia (QN) and Stikinia (ST) arc terranes relative to the pericratonic Yukon-Tanana (YTT), Nisling (NS) and Kootenay (KO). The maps also show the Slide Mountian (SM) terrane assemblages, which is inferred to have formed as a rifted marginal basin that developed landward of Quesnellia and Stikinia arc. The maps also depict the translation and collision of the Cache Creek terrane (CCT) from the Late Permian to the Early Jurassic which is thought to have led to oroclinal folding of the QN-ST arc. Additional acronyms include eclogite (EC) and blueschist (BS; figure modified from A. Bath (2010); modified from M. Mihalynuk, written commun., 2008).

Nokleberg et al., 2000). This resulted in a magmatic hiatus between Upper Triassic and Lower Jurassic volcanism (Monger and Nokelberg, 1996).

The Stikinia-Quesnellia island arc is now located on either side of the Cache Creek terrane (Figs. 1.4, 2.1 and 2.2F). Stikinia is structurally juxtaposed onto Cache Creek to the west, and Quesnellia is thrust over the pericratonic belt to the east. The final arrangement of these terranes is interpreted to have to have occurred during syn- to post-accretion deformation, either from strike-slip displacement from a position at the southern end of Quesnellia to its present position (Wernicke and Klepacki, 1988) or oroclinal bending of the arc due to collision of Cache Creek oceanic plateaus (Fig. 2.2E; Mihalynuk et al., 1994).

2.4 Geology of Quesnellia and the Nicola Group

Quesnellia and Stikinia arc rocks occur in belts that can be correlated along the length of the Cordillera: Nicola Group in southern Quesnellia, Takla Group in central Quesnellia and Stuhini Group in northern Stikinia (Mortimer, 1987; Mihalynuk et al., 1994; Lang et al., 1995b; McMillan et al., 1995; Nokleberg et al., 2000). The main components of Quesnellia are Upper Paleozoic and lower Mesozoic sedimentary, volcanic and plutonic rocks (Fig. 2.3; Bailey, 1990; McMillan et al., 1995; Panteleyev et al., 1996). Quesnellia overlies the Slide Mountain terrane structurally and in part stratigraphcially. The Slide Mountain terrane consists mainly of basalt, diabase and chert with lesser amounts of ultramafic rocks, pillow basalts and minor limestone (Figs. 2.3, 2.4 and 2.5; Struik, 1986; Mortimer, 1987; Gabrielse et al., 1991; McMillan et al., 1995; Panteleyev et al., 1996).

The Paleozoic rocks of Quesnellia are characterized by a fine grained epiclastic sedimentary unit with both oceanic and arc characteristics that are interpreted as basin-fill (Bailey, 1990; McMillan et al., 1995; Panteleyev et al., 1996). The Harper Ranch sub-terrane, composed of Devonian to Permian siliciclastic and volcaniclastic rocks, and limestone successions are the basement of Quesnellia in southern British Columbia, although these rocks do not crop out in the region around Mt. Polley. Harper Ranch comprises a lower volcanic arc succession and carbonate platform succession, preserved as limestone bodies up to 1 km in length (Read and Okulitch, 1977; Monger and Berg, 1987). This lower succession records the inception of arc activity, the growth of an arc edifice, volcanic quiescence and fringing reef construction. The upper member consists of a deepening-up sequence of interbedded, variously argillaceous wackestone, packstone, and grainstone of Sakmarian to Wordian age. A Pennsylvanian unconformity separates the lower and upper members (Read and Okulitch, 1977; Monger and Berg, 1987; Panteleyev et al., 1996). Late Triassic and Early Jurassic island arc magmatic-volcanic and sedimentary strata of the Nicola Group unconformably overly the Paleozoic rocks (Mortimer, 1987; McMillan et al., 1995).

The Nicola Group is the principal assemblage of Quesnellia in south-central British Columbia (Figs. 1.8 and 2.5; Panteleyev et al., 1996). This area is variably known as the Quesnel Belt, Quesnel Trough or Central Quesnel Belt and contains the Morehead Lake and Horsefly map areas and the Mt. Polley property (Fig. 1.8; Morton, 1976; Bailey, 1978; Mortimer, 1987; Panteleyev et al., 1996). The first map of the Morehead Lake area was produced by Bailey (1976), which was updated by Bailey (1987) and by Panteleyev et al. (1996). Panteleyev et al. (1996) completed a comprehensive review of the Central Quesnel Belt that incorporated the findings of theses by Morton (1976), Bailes (1977, cited in Bailey, 1988) and Bailey (1978) as well as British Columbia Geological Survey publications by Fox (1975, cited in Fraser, 1995), Fox and Cameron (1991) Bailey (1975; 1978; 1990), Bloodgood (1987; 1988), Pantelevey (1987, 1988; 1989), Preto (1975, 1977) and Mortimer (1987; 1990) to name a few. Key findings are highlighted below.

The Nicola Group comprises a diverse assemblage of Triassic to Early Jurassic submarine to subaerial volcanic, volcaniclastic, and sedimentary rocks of island arc-marginal basin heritage. In the Central Quesnel Belt, the Nicola Group can be divided into four basic assemblages that have been interpreted to represent a continuous cycle of volcanism-plutonism and erosion

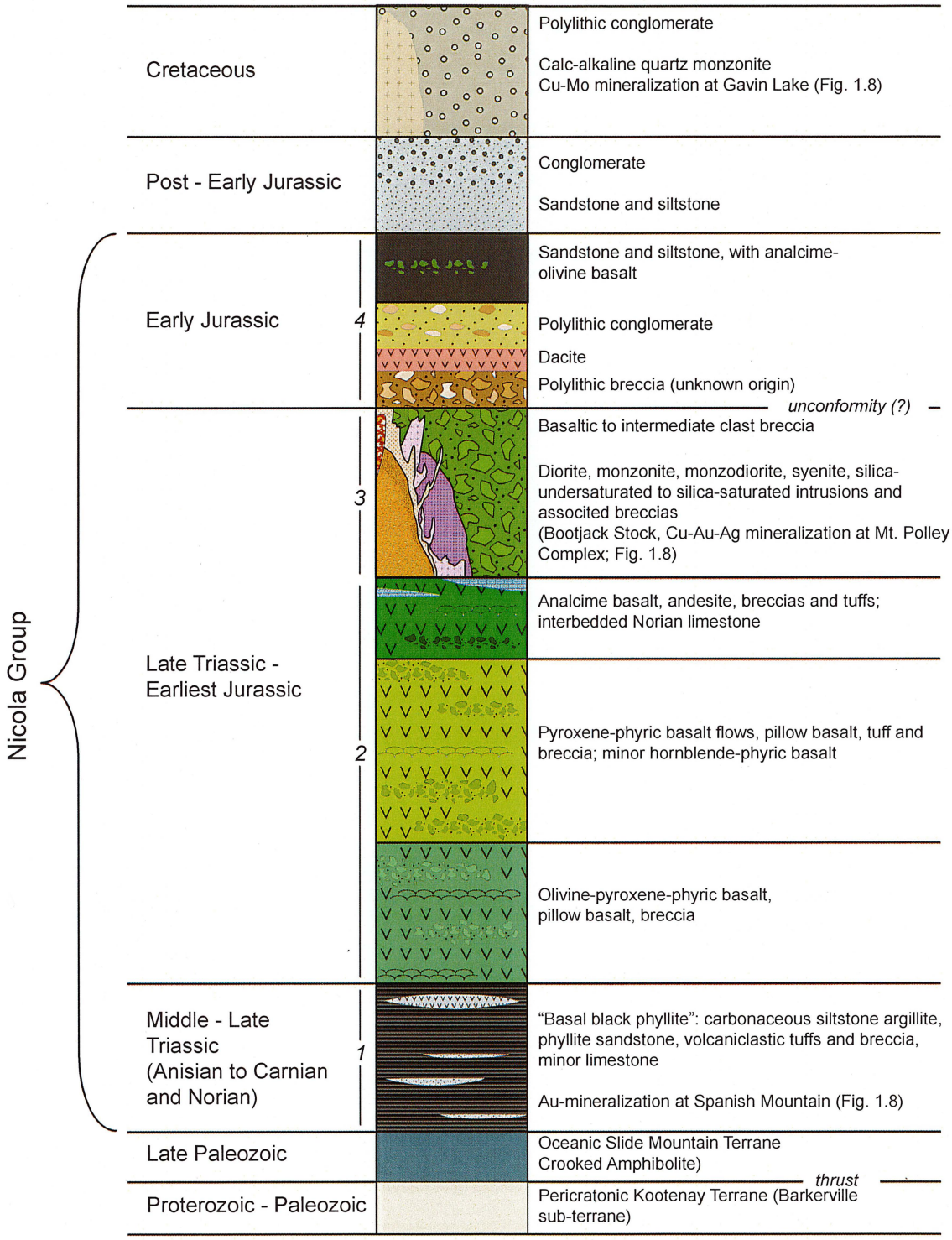

Figure 2.3 Simplified stratigraphic column of Quesnellia (Nicola Group) for the Mt. Polley region. Numbers 1 to 4 correspond to descriptions in the text. Note: the Harper Ranch subterrane is not included in this figure as it does not crop out in the region, although it is part of the Nicola Group to the southeast, and possibly to the north. Image modified from Jackson (2008) after Rees et al. (2005). Data from Bailey (1978), Struik (1986), Bloodgood (1990), Panteleyev et al. (1996), Logan and Mihalynuk (2005), Logan and Bath (2006), and Logan et al. (2007).

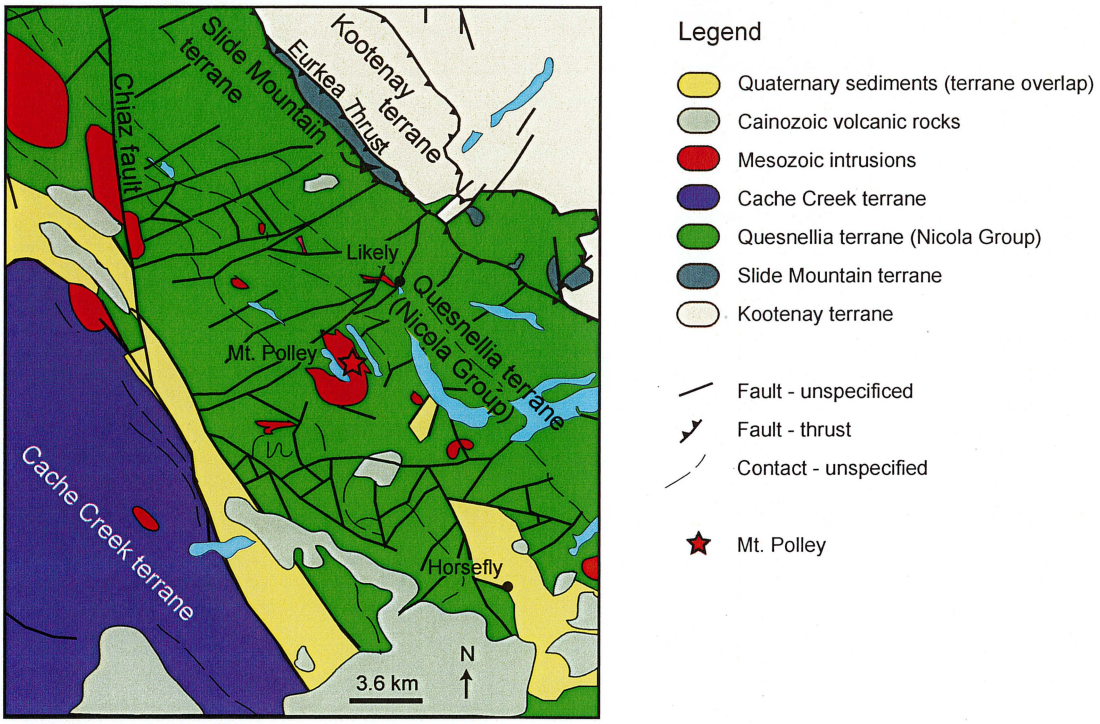

Figure 2.4 Regional geologic map of the Central Quesnel Belt highlighting the three main fault sets of the region: northwesterly-trending, east-northeasterly-trending and north-trending. Redrafted from the MapPlace.ca, British Columbia Geological Survey Geoscience Map (www.empr.gov.bc.ca/Mining/Geoscience/MapPlace/).

(Figs. 2.3 and 2.5; Panteleyev et al., 1996; Logan and Mihalynuk, 2005; Bath and Logan, 2006; Logan and Bath, 2006). These four assemblages are detailed below and shown schematically in Figure 2.3.

The oldest, basal assemblage is comprised of volcano-sedimentary argillitic rocks grading up into siltstone, minor limestone, sandstone and greywacke (Basal black phyllite, unit 1; Fig. 2.3). Local mafic tholeiitic to lesser calc-alkalic volcanic rocks and volcaniclastic rocks occur at the top of the unit. These rocks are primarily olivine and pyroxene basalts that range from alkalic basalt to basaltic trachyandesite compositions (Panteleyev et al., 1996). The volcano-sedimentary assemblages are interpreted to have been deposited on the ocean floor of a restricted marginal basin, now the Slide Mountain terrane (Figs. 2.3, 2.4 and 2.5; Bailey, 1978; Mortimer, 1987; Panteleyev et al., 1996). The volcanic rocks mark the initial stage of arc activity.

A 5.0–6.5 km thick sequence of Carnian-Norian submarine, volcanic alkali basaltic flow and breccia rocks overlies the basal package (unit 2, Fig. 2.3). This thick assemblage shows increasing differentiation up-section beginning with basal olivine-pyroxene-phyric basalt, followed by pyroxene-phyric basalts, with analcite–bearing basalt and basaltic-andesite at the top of the sequence (Fig. 2.3; Panteleyev et al., 1996). Normative calculations indicate the basaltic sequence is silica-undersaturated and alkalic versus subalkalic. Norian age limestone lenses are locally interbedded and/or overlie the basalt (Fig. 2.3; McMillan and Panteleyev, 1995; Orchard, 1995). Debris-flow breccias and tuffs fill intervolcanic depressions and lateral facies variations are characteristic (Panteleyev et al., 1996).

The third assemblage consists of varied volcanic, plutonic breccias and flows and sedimentary rocks of Late Triassic to Early Jurassic age that cut the volcanic rocks of the second assemblage (unit 3, Fig. 2.3). The third assemblage represents more mature arc activity when mafic basaltic magmatism was accompanied or surpassed by more differentiated magmatism and a gradual change took place to more subaerial or shallow water deposition as the arc became emergent.

Included in the third assemblage are calc-alkalic

and alkalic intrusive centres, the latter of which define the axis of the magmatic arc (Figs. 1.8 and 2.5; Barr et al., 1976). Some of these centres are genetically related to porphyry Cu-Mo and Cu-Au mineralization, respectively (Figs. 1.8, 2.3 and 2.5; McMillan et al., 1995), of which the Mt. Polley Complex (with the Bootjack Stock) is the largest known example in the Central Quesnel Belt (Panteleyev et al., 1996). At least 11 other alkalic intrusive complexes characterized by associated pyroxenite and syenite are part of the assemblage (Lueck and Russell, 1994; Lang et al., 1995a). These intrusions are silica-undersaturated to silica-saturated, alkalic, and in many individual cases, well zoned (Lueck and Russell, 1994; Lang et al., 1995a; Coulson et al., 1999). The Zippa Mountain pluton (Fig. 1.4) exhibits the most complete range of features characteristic of the group, whereas, other complexes display them to varying degrees (Monger et al., 1991; Lueck and Russell, 1994; Lang et al., 1995a; Coulson et al., 1999; Coulson et al., 2007).

A clastic assemblage of Early Jurassic to Middle Jurassic polylithic breccia, dacite tuff and volcaniclastic conglomerate of debatable origin overlies the volcanic sequence (unit 4, Fig. 2.3; Bailey, 1988; Monger et al., 1991; Logan et al., 2007). This assemblage forms the upper unit of the Nicola Group. It is variably interpreted to be related to erosion and redistribution of volcanic-derived material (Panteleyev et al., 1996) or as a non-volcanic sedimentary basin fill unit (Bailey, 1988). The geometry and contact relationship between this 196 Ma breccia-bearing unit and the 205 Ma Mt. Polley Complex are unresolved (Logan et al., 2007).

2.5 Local geology

2.5.1 Bootjack Stock

The alkalic, nepheline normative Bootjack Stock is a northwest-trending, elliptical pluton 2.3 by 7.0 km in diameter that crops out approximately 2 km south of the Mt. Polley Complex (Fig. 2.5; Bailey and Hodgson, 1979; Bailey and Archibald, 1990; Fraser et al., 1995). The Bootjack Stock intruded Triassic Nicola Group rocks and is separated from the Mt. Polley Complex by northwest-trending metavolcanic flows, breccias, fine-grained bedded volcaniclastic units of the Nicola Group and a pyroxenite body (Figs. 2.5 and 2.6; Bath and Logan, 2006). The northern extent of the Bootjack stock is unknown due to poor exposure. It is possible that the Bootjack Stock intruded the Mt. Polley Complex or

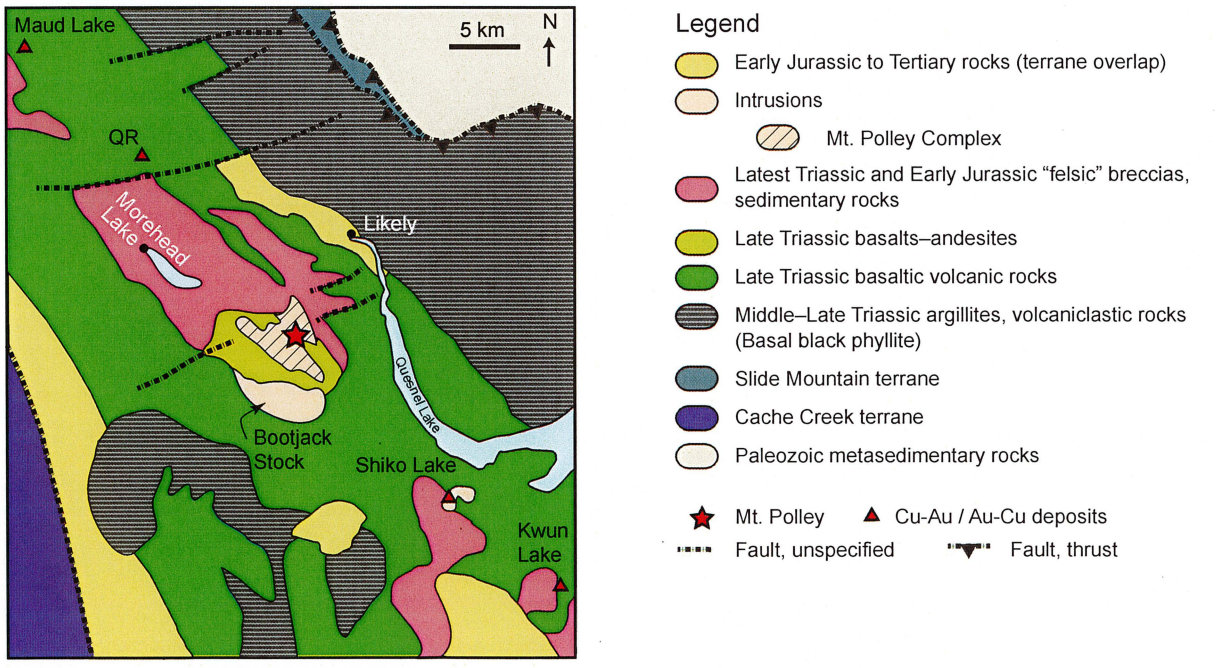

Figure 2.5 Simplified regional geology of Quesnellia surrounding Mt. Polley showing the Triassic–Jurassic intrusions and porphyry Cu-Au deposits. Modified from Rees et al. (2005; 2006; 2008).

vice-versa (Fraser et al., 1995; Bath and Logan, 2006).

The Bootjack Stock is zoned and consists of three main intrusive rock types. It has a rim of medium-grained sparse pseudoleucite melanocratic syenite, and a core of orbicular pseudoleucite syenite (Fig. 2.6C). There is also equigranular coarse- to medium-grained syenite that contains pegmatitic zones and miarolitic cavities (Bath and Logan, 2006).

2.5.2 Mt. Polley Complex

The Mt. Polley Complex is a north-northwest-trending composite alkalic intrusive and breccia complex that has intruded the Nicola Group (Figs. 2.5, 2.6A and B; Fraser et al., 1995; Logan and Mihalynuk, 2005; Bath and Logan, 2006; Rees et al., 2006; Rees, 2009). The Mt. Polley Complex is 3.5 km wide and 6.0 km long. Its immediate host rocks are basalt, andesite, breccias and minor limestone of the Nicola Group (Rees, 2008).

The Mt. Polley Complex contains pyroxenite, diorites and syenites, but predominantly consists of variably equigranular to porphyritic monzonite and monzodiorite intrusive rocks and associated breccia bodies (Figs. 2.6 and 2.7; Fraser et al.,1993; Fraser, 1994; Fraser et al., 1995; Rees et al., 2005, 2006; Logan and Mihalynuk, 2005). Rees et al. (2006) divided the Mt. Polley Complex into 15 coherent and clastic facies that range from early diorites and monzodiorites to plagioclase porphyry, K-feldspar-phyric monzonite and later stage intermediate to mafic augite-phyric porphyry and aphanitic mafic dikes. The local stratigraphy is summarized in Fig. 2.6B (Rees et al., 2006).

Undivided monzonite and monzodiorite (Fig. 2.7) are the major components of the Mt. Polley Complex. Their compositions are highly variable, including rocks defined as 'diorites', 'monzodiorites', 'plagioclase porphyry' and 'syenite' by previous authors (Rees et al., 2006). The 'monzonite-monzodiorite' unit is predominantly equigranular to weakly porphyritic, generally leucocratic, feldspar-rich and depleted in ferromagnesian minerals (Rees et al., 2006). Euhedral to subhedral plagioclase phenocrysts are typically more common than primary K-feldspar phenocrysts. The dominant mafic mineral is augite, with prismatic hornblende less common. Biotite comprises 1 to 2 percent of the rock locally. Accessory minerals include magnetite, titanite and apatite. Staining indicates the presence of 15 to 40 percent K-feldspar, but there is always uncertainty as to how much of this is secondary, as potassic alteration is quite variable, from strong and pervasive to streaky and fracture-controlled, to erratic patches (Rees et al., 2006). The distinction between monzonite and syenite is often difficult to determine due to this widespread K-metasomatism. Rocks termed "syenite" in past reports and maps are thought be strongly K-feldspar altered (Rees et al., 2006), although Logan and Mihalmyuk (2005) reported syenite compositions based on hand sample and petrographic analyses. Abundant millimeter- to centimeter-sized lithic clasts, xenoliths or xenocrysts in the monzonite locally comprise several percent of the rock, but more typically constitute 1 to 2 percent. Primary quartz is very rare to non-existent in all Mt. Polley Complex intrusive rocks.

Numerous small intrusions, including monzonite stocks, plagioclase porphyry, fine to megacrystic K-feldspar-phyric monzonite, augite-phyric and mafic dikes have cross-cut the monzonite-monzodiorite. These intrusions are generally elongate, steeply-dipping and trend north-northwest, with the exception of the augite-phyric and mafic dikes, whose orientations are more variable. Distinctive K-feldspar porphyry dikes (Fig. 2.7E) have a wide distribution in the Mt. Polley Complex, although they are not voluminous. Plagioclase porphyry rocks commonly grade into equigranular monzonite or monzodiorite (Fig. 2.7).

Much of the Mt. Polley Complex consists of breccias which vary considerably in composition, texture and alteration (Rees et al., 2005). The geological complexity has resulted in a diversity of interpretations for the origins of the breccias (Hodgson et al., 1976; Fraser et al., 1995; Bailey, 2004a; Bailey, 2004b; Simpson, 2005; Jackson, 2008). Rees et al. (2005) noted that at least four major genetic classes of breccia are likely to be present in the Mt. Polley Complex: volcaniclastic, phreatomagmatic, hydrothermal and igneous-cemented breccia.

Hydrothermally-cemented and igneous-cemented breccias were recognized by Fraser et al. (1995) in the Central and West Zones of Mt. Polley (Figs. 2.6A and 2.8A). Igneous-cemented breccias were observed to be associated with some intrusive phases (i.e. plagioclase-

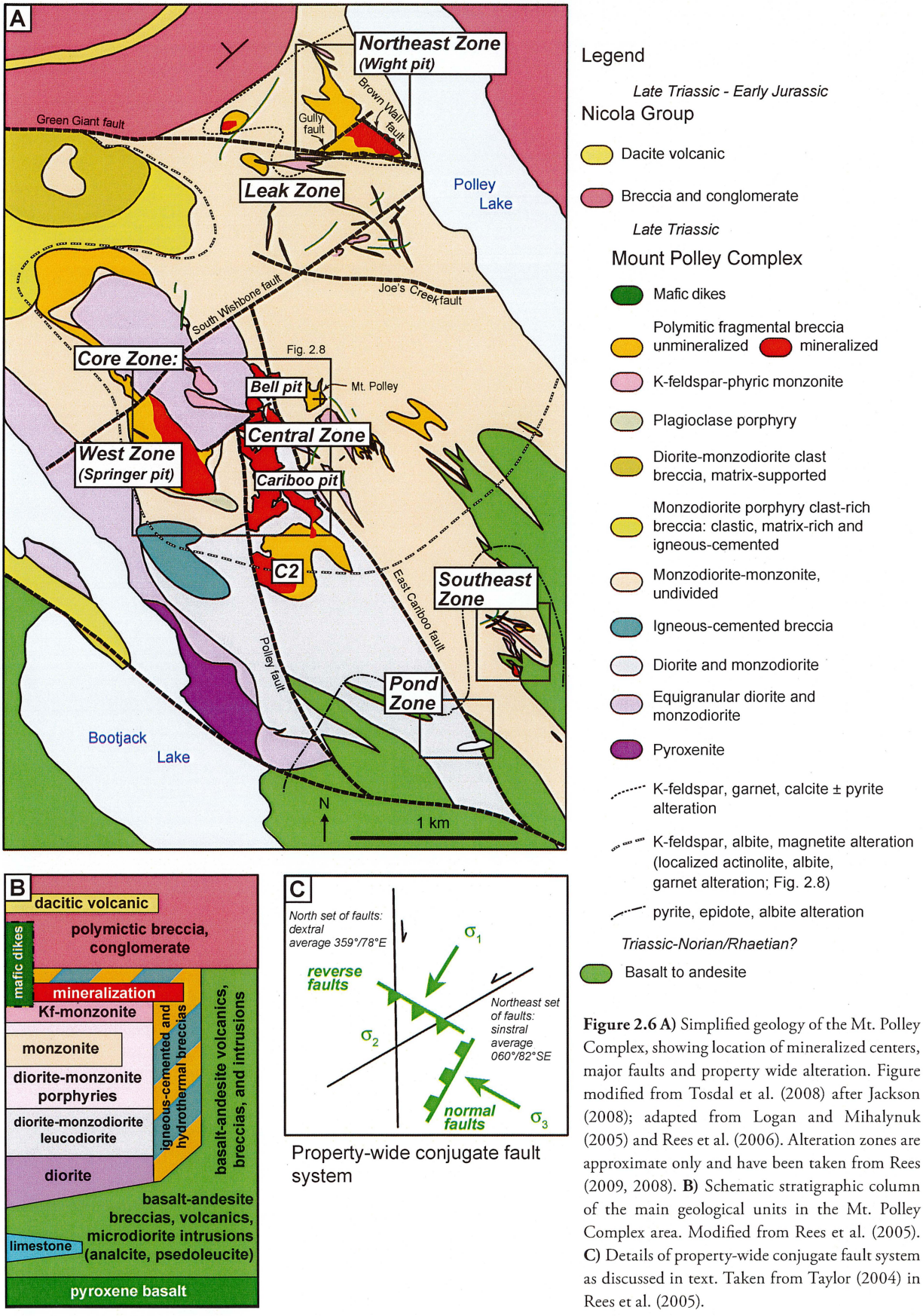

Figure 2.6 A) Simplified geology of the Mt. Polley Complex, showing location of mineralized centers, major faults and property wide alteration. Figure modified from Tosdal et al. (2008) after Jackson (2008); adapted from Logan and Mihalynuk (2005) and Rees et al. (2006). Alteration zones are approximate only and have been taken from Rees (2009, 2008). **B)** Schematic stratigraphic column of the main geological units in the Mt. Polley Complex area. Modified from Rees et al. (2005). **C)** Details of property-wide conjugate fault system as discussed in text. Taken from Taylor (2004) in Rees et al. (2005).

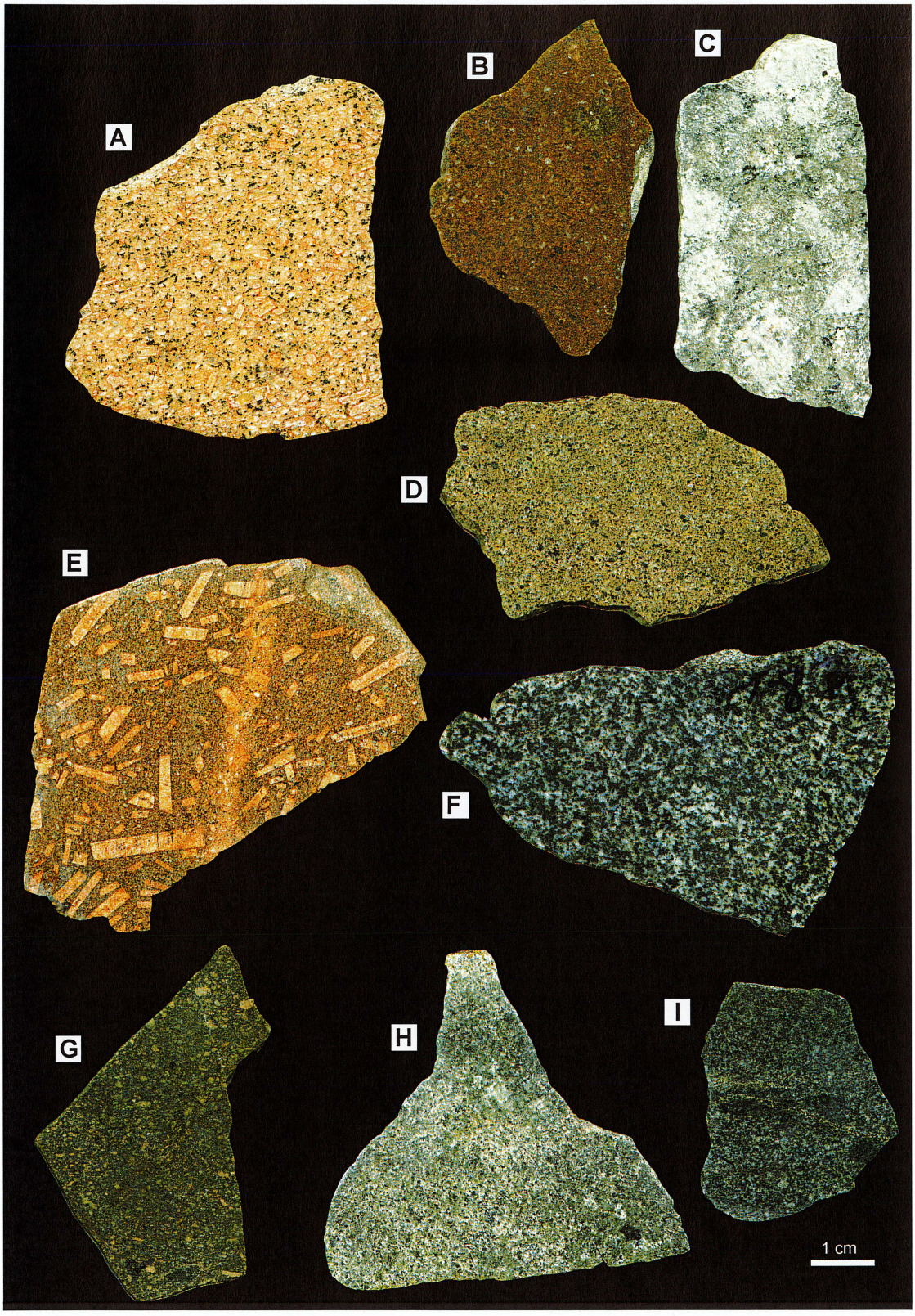

Figure 2.7 Examples of intrusive rocks types from the Mt. Polley Complex (and the Bootjack Stock where indicated): **A)** K-feldspar-phyric monzonite, medium-grained; **B)** monzonite-monzodiorite, altered; **C)** orbicular pseudoleucite nepheline syenite of the Bootjack Stock; **D)** equigranular monzonite, homogeneous; **E)** K-feldspar-phyric monzonite, coarse-grained; **F)** equigranular pyroxene-biotite diorite, coarse grained; **G)** hornblende monzonite-monzodiorite; **H)** diorite-monzodiorite; **I)** diorite, fine grained. Samples courtesy R. Tosdal from C. Rees (2007, Imperial Metals Corporation).

porphyry) and gradational contacts between intrusions and breccias were noted. Igneous-cemented breccia has been mapped in a large area west of the Core Zone, and in several smaller areas elsewhere (Fig. 2.8). These rocks were mapped as "igneous breccia" by Gillstrom (2004), and as volcaniclastic breccia by Hodgson et al. (1976) and Bailey (2004a, b). Abundant hydrothermally-cemented breccias occur on the margin and above plagioclase porphyry intrusions. These hydrothermal breccias were subdivided into four distinct types based on the dominant cement or alteration assemblage: actinolite, biotite, magnetite and albite cemented breccia (Fig. 2.8). Hydrothermally-cemented breccias were previously mapped in the NEZ by Logan and Mihalnyuk (2005), Rees et al. (2005, 2006) and Jackson (2008). The NEZ breccias are described in detail in later chapters.

2.5.3 Geochronology

Constraints on the absolute timing of magmatic and hydrothermal activity in the Mt. Polley Complex and Bootjack Stock (Table 2.1) have been provided by the geochronologic studies of Bailey and Archibald (1990), Mortensen et al. (1995), Logan et al. (2007) and Bath (2010, unpublished data). Earlier regional and local geochronologic studies by Barr et al. (1976), Hodgson (1976), and Mortimer (1990) based on regional correlations, fossil determinations and imprecise radiometric dating techniques were rejected by Logan and Mihalynuk (2005) and Fraser (1994) as they represent cooling and/or resetting ages rather than crystallization ages. This latter data has therefore not been included in this review.

Figure 2.9 displays the data of Bailey and Archibald (1990), Mortensen et al. (1995), Logan et al. (2007) and Bath (2010, unpublished data) in three groups: Bootjack Stock igneous rocks, Mt. Polley Complex mineralization and Mt. Polley Complex igneous rocks. The age of the Bootjack Stock can be constrained by the overlap in results of the three samples to be between 203.5 and 201.1 Ma (grey box, Fig. 2.9, Table 2.1; Bailey and Archibald, 1990; Mortensen et al., 1995). The data for the Mt. Polley Complex is more scattered, but the combined results of these studies, including errors indicate that the Mt. Polley Complex was emplaced between 209.4 and 190.4 Ma, with most of the results between 209 and 201 Ma (Late Triassic). Dating of a dacite volcanic rock of the Nicola Group that overlies the Mt. Polley Complex has constrained the minimum age of the Mt. Polley Complex to 196.7 ± 1.3 Ma (Table 2.1; Figs. 2.3, 2.6A and B). Based on four samples and including error, mineralization in the Mt. Polley Complex is therefore constrained to a 5 Ma window from approximately 209 to 204 Ma (Fig. 2.9). These results are broadly consistent with Mortensen et al.'s (1995) statement that the Mt. Polley Complex was emplaced over a short time period (i.e. <5 Ma). Based on the data presented here, the interval of emplacement could have been longer, perhaps up to 14 million years, around 205 ± 4 Ma.

While mineralization at Mt. Polley is associated with breccias in most ore zones (Table 2.2), Rees (2006) noted that there is no field evidence that the NEZ brecciation-mineralization event was contemporaneous with that of the Central Zone (or other zones) of the Mt. Polley Complex. A new U-Pb date of 207.3 ± 0.3 Ma from apatite in main-stage breccia cement of the NEZ (Bath, 2010, unpublished data), is older than the original 205.2 ± 1.2 Ma age (Logan et al., 2007), but is consistent with Re-Os molybdenum dates from the Southeast and Cariboo pit (206.2 ± 1 Ma and 207.8 ± 1 Ma, respectively; Logan et al., 2007). These dates constrain the Mt. Polley Complex mineralization to approximately 207 Ma. A younger (201.7 ± 0.4 Ma) age was obtained from a diorite clast from the Cariboo pit breccia, inconsistant with the older mineralization age. This discrepancy remains unexplained and additional work is therefore required to resolve the age(s) of mineralization in the Mt. Polley Complex.

2.5.4 Rock classification

Whole rock geochemical studies were carried out on rocks from the Mt. Polley Complex, Bootjack Stock and surrounding Nicola Group by Fraser (1994a), Logan and Mihalynuk (2005), Bath and Logan (2006), Logan and Bath (2006) and Jackson (unpublished data). Figure 2.10A and B presents the geochemical composition of samples from these studies. As a group, the Nicola Group basaltic rocks have the lowest silica contents (43–49 wt %) and moderate to high alkali contents (4–9.5 wt %; Fig. 2.10A, dark grey field). Silica content of the Mt. Polley Complex rocks overlaps with the Nicola Group and continues in a broadly linear

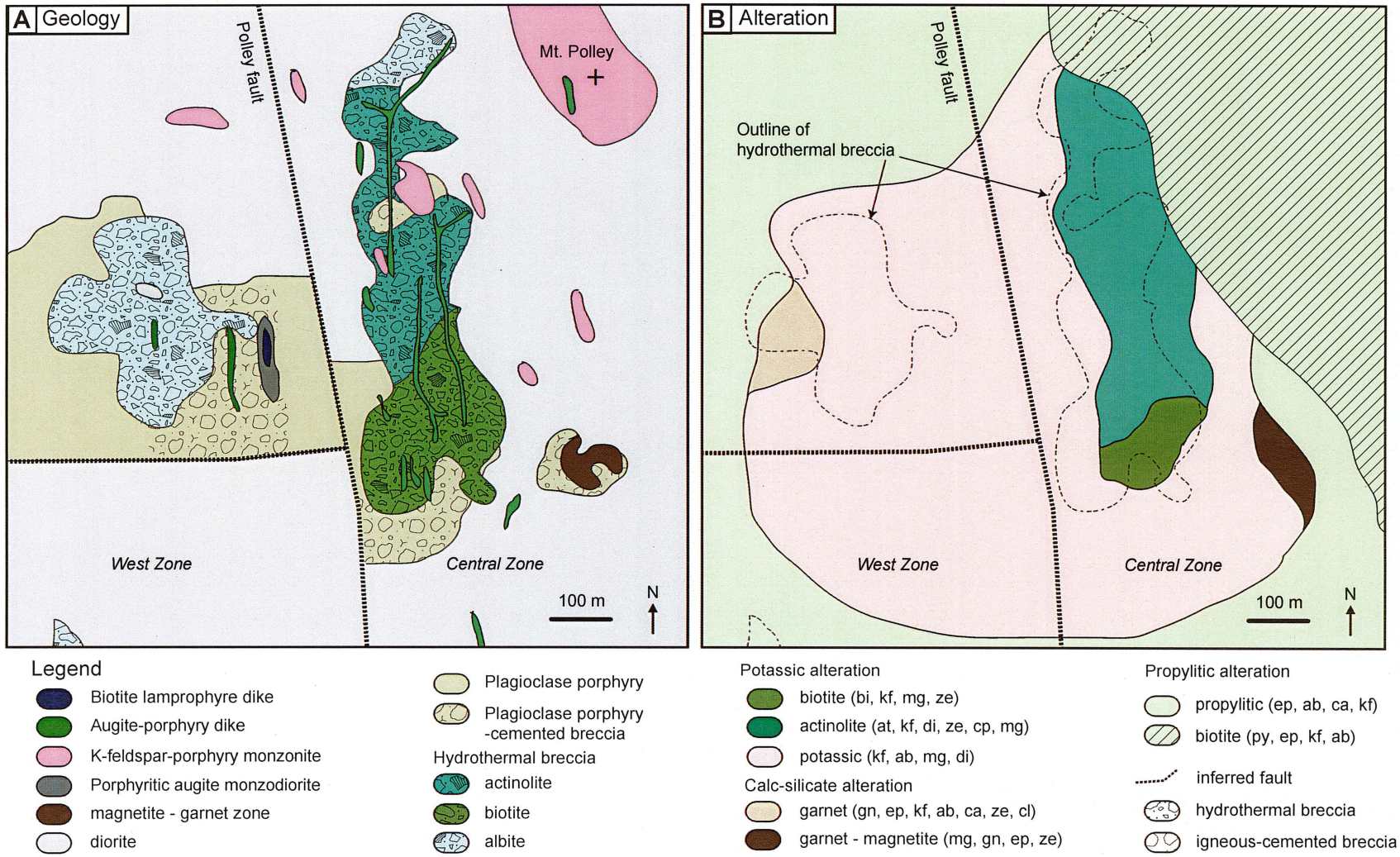

Figure 2.8 Surface geology **A)** and alteration zones **B)** of the West and Central Zones (Core Zone) of Mt. Polley (Fig. 2.6A). The deposit is characterized by multiple northerly-trending intrusions and a series of hydrothermal breccias superimposed on diorite and plagioclase porphyry. A core of actinolite and biotite alteration is surrounded by intensely potassic-altered rocks grading out to calc-silicate and propylitic alteration. Figures modified from Fraser (1994) and Fraser et al. (1995). Mineral abbreviations: ab-albite, at-actinolite, bi-biotite, ca-carbonate, cl-chlorite, cp-chalcopyrite, di-diopside, ep-epidote, gn-garnet, kf-K-feldspar, mg-magnetite, py-pyrite, ze-zeolite.

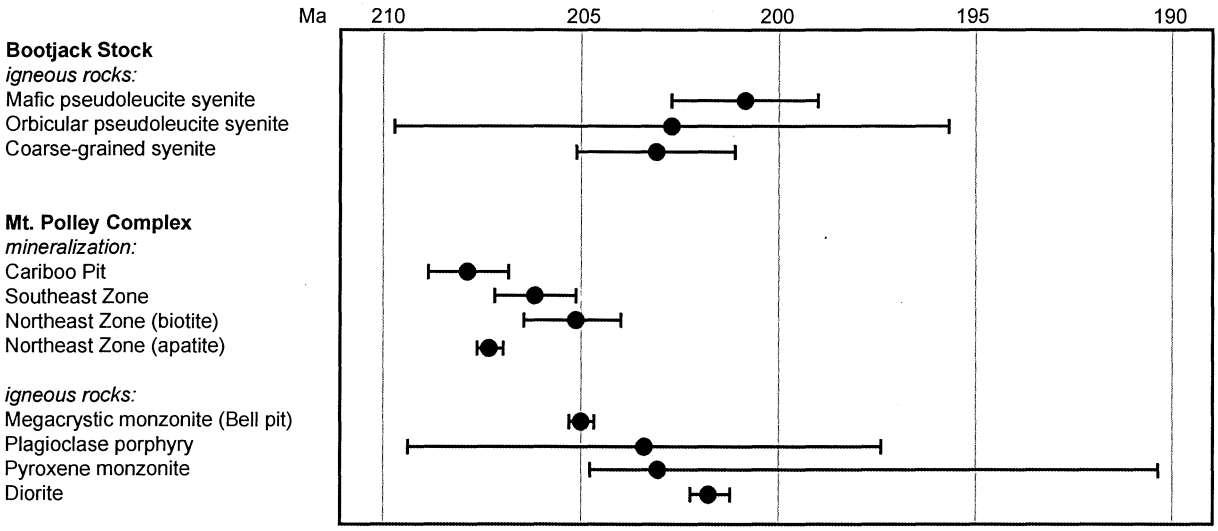

Figure 2.9 Summary geochronology diagram of the Mt. Polley Complex and Bootjack Stock. The shaded grey bar represents the constrained age of the Bootjack Stock. Data is from Table 2.1.

trend to a maximum of 60 weight percent SiO_2 in the K-feldspar-phyric monzonite and plagioclase-phyric porphyry (Fig. 2.10A, medium grey field). Most of the Mt. Polley Complex rocks have similar alkali contents to the Nicola Group rocks, although K-feldspar-phyric monzonite, plagioclase-phyric monzonite and one sample of augite porphyry have alkali contents up to 12 weight percent. Rocks of the Bootjack Stock have restricted silica contents compared to the Mt. Polley Complex and are the most alkali-enriched of the three groups (up to 17 wt % $Na_2O + K_2O$; light grey field, Fig. 2.10A).

The major element chemistry of least altered samples from the Mt. Polley Complex and Bootjack Stock help to discriminate the general compositions of the intrusive rocks and give a rough indication of differentiation amongst the units sampled. Interpretations are, however, made with caution as major elements can and have been mobilized during hydrothermal alteration. Almost all rocks sampled in these studies are alkalic in character using the definition of Irvine and Baragar (1971; Fig. 2.10A and B, red line) and basic to intermediate in terms of their silica content. The diorite, augite-monzodiorite, hornblende-, and augite- monzonite units of the Mt. Polley Complex cluster together near the Nicola Group samples, with more felsic units such as the plagioclase-phyric porphyry and K-feldspar porphyry units plotting at higher silica and alkali contents (Fig. 2.10B; Fraser, 1994a). Monzonite units join these two clusters. Together, rocks from the Mt. Polley Complex appear to form a differentiation trend with local Nicola Group rocks (Figs. 1.2A and 2.10A; Fraser, 1994a; Logan and Bath, 2006). Whether or not the Bootjack Stock also shows a differentiation trend with the Nicola Group rocks is equivocal.

Figure 2.10C shows the Cross-Iddings-Pirsson-Washington (CIPW) normative classification from 97 igneous rock samples from the Mt. Polley Complex, the spatially associated Bootjack Stock and surrounding Nicola Group volcanic rocks. Data are from Logan and Mihalynuk (2005), Bath and Logan (2006), Logan and Bath (2006) and Jackson (unpublished data). Most of the rocks are classified as silica-undersaturated, although there also some samples that are classified as silica-saturated to silica-oversaturated. Mt. Polley has been variably referred to in the literature as an alkalic silica-undersaturated (i.e. Lueck and Russell, 1994; Lang et al., 1995b; Tosdal et al., 2008) and/or silica-saturated complex (i.e. Lang et al., 1995c). Analyses of Mt. Polley rocks from Lang et al. (1995a) using phase relations for silica-saturated and silica-undersaturated igneous rocks are similar to those in Fig. 2.10C and show most results clustering around the alkali-feldspar tie line, although some are silica-undersaturated in composition (Fig. 2.10D). Several other mineralized and unmineralized alkalic complexes in British Columbia also contain

Table 2.1 Geochronology of the Mt. Polley Complex and the Bootjack Stock. Bolded values are considered representative of the age of Mt. Polley Complex emplacement and mineralization.

Rock Unit (Imperial Metals rock unit in brackets)	Location	Age (Ma)	Method/ Mineral	Notes	Reference
Bootjack Stock					
Mafic pseudoleucite syenite (Bns)	middle of pseudoleucite syenite, ~1km south of Bootjack Lake; see maps in Mortensen et al. (1995)	200.8 ± 1.8	Pb/Pb titanite	Imperial Metals Unit: Bootjack Stock nepheline syenite; Mortensen et al. (1995) sample #: 92-G4	Mortensen et al. (1995), Rees et al. (2005)
Orbicular pseudoleucite syenite (Bns)	middle of orbicular pseudoleucite syenite, ~2 km south of Bootjack lake; see maps in Mortensen et al. (1995)	202.7 ± 7.1	U/Pb zircon	Imperial Metals Unit: Bootjack Stock nepheline syenite; Mortensen et al. (1995) sample #: 92-G3	Mortensen et al. (1995), Rees et al. (2005)
Syenite phase (coarse grained)	see map in Bailey and Archibald (1900)	203.1 ± 2.0	Ar/Ar hornblende	Plateau age	Bailey and Archibald (1990)
Mt. Polley Complex *mineralization:*					
Hydrothermal breccia, mineralized (Pbxhm)	Wight Pit, NEZ, UTM 592775E, 5825410N	**207.3 ± 0.3**	U/Pb apatite	Main-stage breccia cement, field sample collected by A. Bath; field #: WB-5(A5), analyzed by R. Maas, University of Melbourne, using MC-ICP-MS	A. Bath (2010, unpublished data)
Hydrothermal breccia, mineralized (Pbxhm)	Cariboo pit, east side	**207.8 ± 1**	Re/Os molybdenum	-	Logan et al., (unpublished data 2009), courtesy Imperial Metals Corporation
Hydrothermal breccia (Pbxhm)	above ramp, SE corner of Cariboo Pit, UTM 592452E, 5823190N	220.8 ± 1.3	Ar/Ar hydrothermal biotite	Hydrothermal biotite, date considered suspect as predates crystallization ages of MPC	Logan et al. (2007)[1]
Hydrothermal breccia, mineralized (Pbx2m)	Southeast Zone	**206.2 ± 1**	Re/Os molybdenum	-	Logan et al., (unpublished data 2009), courtesy Imperial Metals Corporation
Hydrothermal breccia (Pbx1m)	Wight Pit, NEZ, UTM 592436E, 5825412N, WB05-09 290-380 m	**205.2 ± 1.2**	Ar/Ar hydrothermal biotite	Hydrothermal biotite associated with chalcopyrite; interpreted to be the age of mineralization of the NEZ	Logan et al. (2007)[1]
Hydrothermal breccia (Pbx1m)	Wight Pit, NEZ, UTM 592436E, 5825412N, WB05-09 290-380 m	130.7 ± 1.0	Ar/Ar hydrothermal orthoclase	Hydrothermal biotite associated with chalcopyrite; age suspect due to contamination or excess Ar (Logan et al., 2007). Possibly represents younger overprint	Logan et al. (2007)[1]

Table 2.1 continued

Rock Unit (Imperial Metals rock unit in brackets)	Location	Age (Ma)	Method/ Mineral	Notes	Reference
igneous rocks:					
Megacrystic K-feldspar porphyritic syenite (Pkm)	South Bell Pit UTM 592065E, 5823745N	**205.01 ± 0.3**	U/Pb zircon	Suspected to be the causative intrusion to NEZ breccia	Logan et al. (2007)[1]
Pyroxene monzonite (Pdm - monzodiorite)	Satellite stock-peripheral to Mt. Polley Complex, UTM: 589072E, 5824698N	**203.1 +1.6/ -12.7**	U/Pb zircon	-	Logan et al. (2007)[1]
Pyroxene monzonite (Pmdu? - monzonite)	North of Bell Pit, Polley Lake road (km 10), UTM: 589977E, 5825274N	165.2 ± 1.8	Ar/Ar hornblende	Considered suspect due to possible contamination and Ar recoil by Logan et al. (2007); Possible Middle Jurassic thermal overprint.	Logan et al. (2007)[1]
Plagioclase porphyry (Pmdu?)	Central Zone, Cariboo pit see maps in Mortensen et al. (1995)	**203.4 ± 6.0**	U/Pb zircon	Imperial Metals unit: monzonite to diorite, collected pre-mining from breccia body in Cariboo Zone. Interpreted as crystallization age.; Mortensen et al. (1995) sample #: 92-G2	Mortensen et al. (1995), Rees et al. (2005)
Diorite (Pd1/Pd2/Pmdu)	Central Zone, Cariboo pit see maps in Mortensen et al. (1995)	**201.7 ± 0.4**	U/Pb zircon	Imperial Metals Unit: diorite-monzodiorite block (clast) in hydrothermal breccia, collected pre-mining from breccia body in Cariboo pit; Mortensen et al. (1995) sample #: 92-G1	Mortensen et al. (1995), Rees et al. (2005)
Other					
Andesite, mineralogically classified as dacite (Jd-Jurassic dacitic volcanic)	Fry Pan Road, 12.4 km, UTM 591797E, 5826577N	196.7 ± 1.3	U/Pb zircon	Constrains the minimum age of mineralization	Logan et al. (2007),[1] Rees et al. (2005)
Limestone	Nicola Group	Norian Anisian-Ladinian	fossils conodonts	-	Bailey, 1988, Bloodgood, 1990

[1] Using time scale of Palfy et al. (2000)

Abbreviations: Ar-argon, Pb-lead, Re-rhenium, Os-osmium, U-uranium

both silica-saturated and silica-undersaturated to oversaturated rocks that are temporally and spatially coincident (Lang et al., 1995a; Lang et al., 1995c). Examples include the Hogem batholith, which hosts the Lorraine deposit (Bath, 2010), and the Zippa Mountain Pluton (Fig. 2.10D; Coulson et al., 1999; Coulson et al., 2007).

Temporal and genetic relationships between the Bootjack Stock and the Mt. Polley Complex are controversial. The Bootjack Stock has been considered to be petrogenetically related to the Mt. Polley Complex by Hodgson et al (1976), Bailey (1990) and Bath and Logan (2006), with the Bootjack Stock interpreted to be a deeper level-equivalent of the Mt. Polley Complex. In contrast, Fraser (1994) suggested a younger age for the Bootjack Stock based on observations of diorite xenoliths contained within pseudoleucite syenite and orbicular syenite. Chemical and petrographic evidence for the first model, which included the presence of bornite- and chalcopyrite-bearing melt inclusions in all three units of the Bootjack Stock was presented by Bath and Logan (2006). These authors noted that the Bootjack Stock has characteristics that suggest it could possibly be a late fractionate of the causative magma responsible for mineralization at Mt. Polley. However, an unequivocal link was not made by these authors. Geochronologic data (Fig. 2.9, Table 2.1) suggests that while crystallization ages of the Mt. Polley Complex and the Bootjack Stock are similar, it appears that the Bootjack Stock may be slightly younger than the Mt. Polley Complex, apparently precluding it from being the source of Cu and Au for the Mt. Polley Complex. This interpretation is supported by similar geochemical fractionation trends of the Bootjack Stock to those of coeval intrusions from the Mt. Polley Complex, suggesting a cogenetic relationship between the Bootjack Stock and the most fractionated end-member of the Mt. Polley Complex (Bath and Logan, 2006).

2.6 Structure and metamorphism

Deformation and faulting in the area of Mt. Polley in the Central Quesnel Belt can be separated into two categories: (1) subduction related tectonics during the accretion of Quesnellia onto peri-cratonic North America, and (2) a later period of Cretaceous-Tertiary dextral trans-current crustal extension (Bailey, 1989, 1990). The earliest deformation is recorded in the basal sedimentary sequence, exposed to the east of Mt. Polley, and is most prominent in the lower parts of the stratigraphy (Bloodgood, 1987; Bailey, 1989, 1990). The basal black phyllite unit has been deformed into northeast-verging folds with a well-developed slaty to phyllitic penetrative axial planar fabric that dips moderately southwest (Bloodgood, 1987; Bloodgood, 1988). These first phase folds have been overprinted and refolded (Bloodgood, 1988). Structural elements associated with the second phase produced fold interference patterns, with crenulation cleavages dipping to the northwest and southwest (Bloodgood, 1988). Folding has been attributed to the accretion of Quesnellia onto the western margin of ancestral North America. The volcanic rocks of the Nicola Group display little to no internal folding, instead they occur as thick, poorly stratified, competent units that have been block faulted (Fig. 2.4; Bailey, 1975, 1988, 1989, 1990; Panteleyev et al., 1996; Logan and Mihalynuk, 2005). Within the Mt. Polley Complex, there is no penetrative deformation other than a weak foliation locally developed in a laminated monzodiorite (Rees et al., 2006).

Middle Jurassic deformation resulted in the folding of the Central Quesnel Belt about a northwesterly-striking axis into a broad syncline of regional extent (Figs. 2.4 and 2.5; Rees, 1987; Bailey, 1990; Panteleyev et al., 1996; Logan and Mihalynuk, 2005). To the west of the Mt. Polley Complex, the sequence of volcanic rocks dip east. To the northeast and to the east of the Mt. Polley Complex, they dip west to southwest (Bailey, 1987). To further assess the effects of regional folding in and around the Mt. Polley area, Logan and Mihalynuk (2005) used scattered exposures of well-bedded sedimentary rocks and water-lain tuff as bedding indicators (Fig. 2.11). They found that all beds are facing upright. However, bedding orientation data were sparse and potentially unreliable in the Mt. Polley Complex. Combining all reliable bedding determinations (Fig. 2.12A and B), Logan and Mihalynuk (2005) defined a shallowly north-northwest-plunging single-phase cylindrical syncline for the regional syncline, with a beta axis of 21°/353°, parallel with the fold axis.

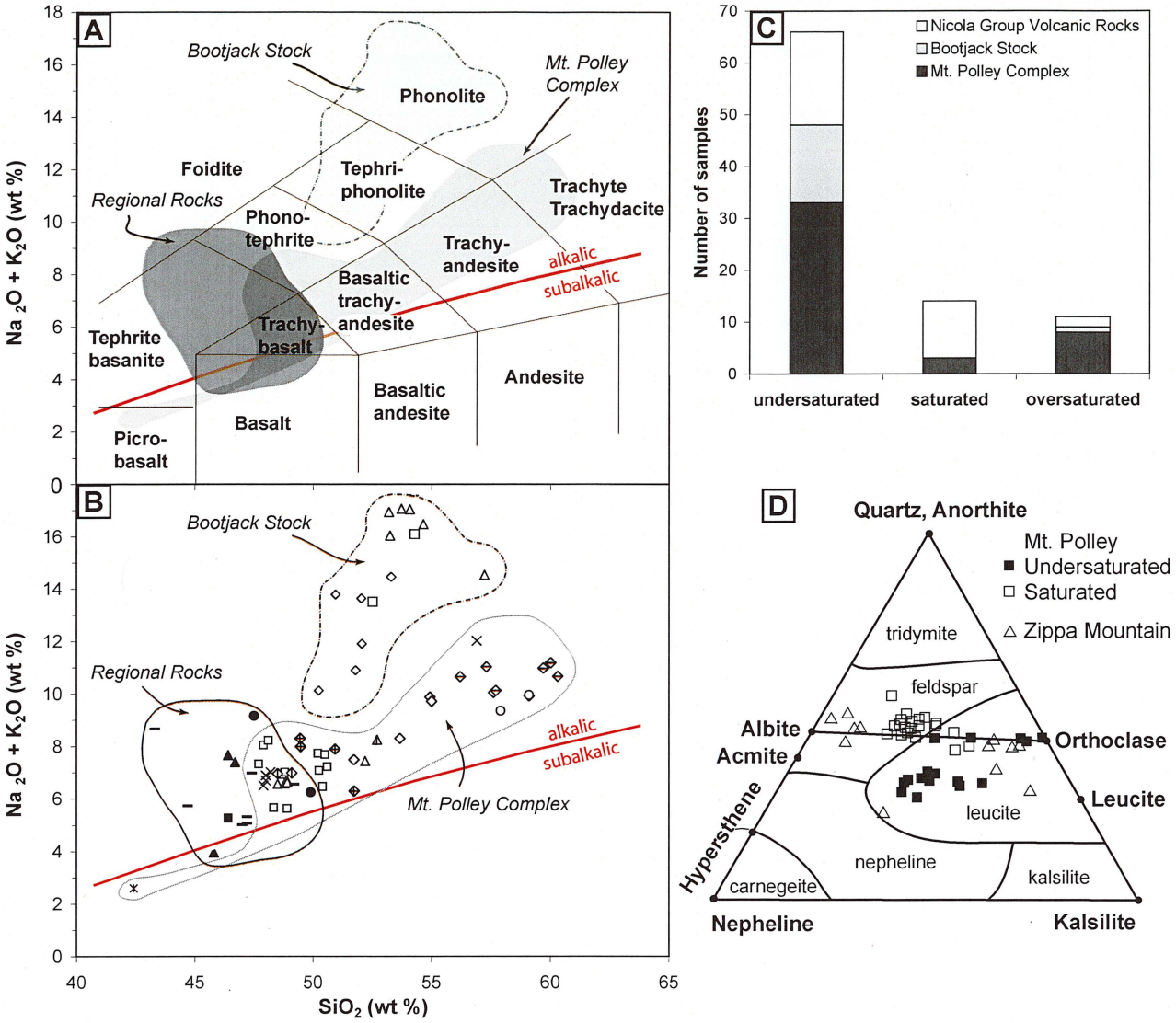

Mt. Polley Complex

- ✳ pyroxenite
- □ diorite
- ⩚ monzodiorite
- △ augite monzodiorite
- ◇ monzonite
- ⧫ hornblende monzonite
- ⧫ augite phyric trachyte
- ⧫ K-feldspar monzonite
- ○ plagioclase porphyry
- × augite porphyry dike

Bootjack Stock

- △ orbicular pseudoleucite
- □ equigranular syenite
- ◇ melasyenite

Nicola Group Volcanics

- ● massive basalt
- ■ hornblende phyric basalt
- – augite phyric basalt
- ▲ augite-KF phyric basalt

Figure 2.10 A) and B) Total alkali-silica (TAS) diagram of LeMaitre (1989) with the alkalic-subalkalic dividing line of Irvine and Baragar (1971) showing the alkalic nature of the Mt. Polley Complex and Bootjack Stock and their composition relative to surrounding Nicola Group values. Data from Fraser (1994) and Bath and Logan (2006). **C)** CIPW classification of igneous rocks from the Mt. Polley Complex, the Bootjack Stock and surrounding Nicola Group Volcanic rocks based on whole rocks analyses. Samples have been grouped by silica content into silica-udnersaturated, silica-saturated and silica-oversatutated. Most rocks can be classified as silica-undersaturated. Data compiled by T. Bissig (2008) from M. Jackson (unpublished data), Logan and Mihalynuk (2005), Bath and Logan (2006) and Logan and Bath (2006). **D)** Quartz-nepheline-kalsilite projections using phase relations for silica-undersaturated and silica-saturated complexes. Silica-undersaturated compositions plot dominantly in the leucite field, silica-saturated compositions plot across the alkali-feldpsar tie line and into the quartz-saturated field. Data from Mt. Polley and Zippa Mountain show both characteristics, with most of the rocks are grouped around the albite-orthoclase tie line, being silica-saturated, although some are silica-undersaturated. Figure from Lang et al. (1994).

Table 2.2 Summary of alteration and mineralization observed in the Central (Bell and Cariboo), West, Southeast, Boundary and Pond Zones.

Ore Zone	Pit	Local geology	Alteration phase	Mineral assemblage	Style	Relationship to mineralization	Mineralization	Comparison with NEZ (Wight Pit)	Ref.
Central Zone	Bell and Cariboo	Abundant monzodiorite and monzonite hydrothermal breccias, minor plagioclase porphyry with lesser intrusion breccia, diorite host rock Cariboo: biotite- grades into actinolite-dominant hydrothermal breccia Bell: actinolite- grades into albite-dominant hydrothermal breccia magnetite breccia is irregularly distributed	Calc-potassic	K-feldspar	Pervasive or fracture controlled	Early	Chalcopyrite in coherent rocks as fracture- or vein-controlled disseminations and hydrothermal cement; rare tetrahedrite, galena, sphalerite and molybdenite; limited oxide minerals include malachite, azurite, magnetite, hematite, and limonite; native Au present as 5 to 30 mm inclusion in chalcopyrite; Bell and Springer pits contain minor bornite, chalcocite, covellite and digenite.	Similarities: no quartz, no molybdenum; minor supergene oxidation Differences: more magnetite, forming a distinct halo; trace bornite; extensive pyrite halo	1, 2, 3, 4, 5, 6, 7, 8, 10
				Pyroxene, actinolite-diopside, chalcopyrite and magnetite, locally garnet -rich, restricted zones of abundant biotite	Vein and breccia cement	Directly associated to mineralization			
			Intermediate calc-silicate	Garnet (andraditic), epidote, albite, K-feldspar, carbonate, chlorite	Replacement, veins, skarn affiliation(?)	Peripheral to mineralization, spatially restricted			
			Propylitic	Albite-epidote-pyrite-calcite-magnetite	Fracture controlled, widespread	Outer halo			
Core Zone									
West Zone	Springer	Monmictic and polymictic hydrothermal (albite dominant) breccias, diorite and plagioclase porphyry (minor intrusion breccia) host rock	Calc-potassic	K-feldspar	Pervasive or fracture controlled	Early		Similarities: highly variable and complex alteration mineralogy, no quartz, no molybdenum, minor supergene oxidation Differences: more magnetite; low amounts of carbonate; mineralization as fine blebs and disseminations or veinlets throughout zone; rare bornite	
				Albite-magnetite-diopside ±actinolite (actinolite lacking and less biotite compared to Central Zone)	Strong, texturally destructive, overprints earlier potassic	Directly associated with highest grades of mineralization			
			Intermediate calc-silicate	Garnet, epidote, albite, K-feldspar, carbonate, chlorite	Veins and vugs within albite breccia	Peripheral to mineralization, spatially restricted			
			Propylitic	Albite-epidote-pyrite	Fracture controlled, widespread	Outer halo			
			Veins	Diopside, calcite, epidote, K-feldspar, sulfide	-	-			
			Retrograde	Calcite, chlorite, sericite, albite, epidote, prehnite, Ca-zeolite	-	-			

Table 2.2 continued

Southeast Zone	Monzonite and hydrothermal breccia developed at contact between Mt. Polley Complex heterogeneous monzonite-diorite with K-feldspar-phyric monzonite and mafic basaltic-andesitic rocks that host the Mt. Polley Complex	Potassic(?) Propylitic	Magnetite, weak K-feldspar, chalcopyrite, albite, epidote Epidote-albite-rich±pyrite	Breccia cement and veins	Direct Possibly associated with a few Au-only zones	Hosted in the cement-poor, clast-supported breccia, including its margins and in basaltic rocks; very high Au/Cu ratios (1 to 4); intermediate between the well defined breccia cement of the NEZ and the more alteration-controlled; disseminated mineralization typical of the Core Zone	Similarities: hydrothermal breccia Differences: weak K-feldspar alteration (compared to all other Mt. Polley Complex deposits); very common pyrite >> chalcopyrite; no bornite; weak calcite alteration; mineralization correlates well with magnetite; Au and Ag closely correlate with chalcopyrite; few Au only zones; sporadic molybdenum	8, 9
Leak Zone	Undifferentiated monzonite rocks with numerous small K-feldspar-phyric dikes and augite-phyric dykes; meter-scale zones of breccia or strongly veined rock	Variable propylitic	Chlorite, epidote, pyroxene, albite, calcite, magnetite, pyrite and locally garnet	Mildly developed	None	Not significant	Similarities: not significant Differences: abundant actinolite; no significant hydrothermal breccia body; no economic Cu-sulfide abundance; no bornite	9
		Calc-silicate?	Local K-feldspar, magnetite, actinolite ± albite, garnet	Moderate to strong, can destroy original rock textures	Very localized only chalcopyrite ± malachite (high grade)			
		Unnamed	Pyrite	Faults/fracture zones	None			
Boundary Zone	Hydrothermal breccia and other monzonite rocks	(Calc?)-potassic	Magnetite-rich; garnet; anomalous carbonate	Narrow pipes of mosaic-like textured breccia, veinlet stock work	Direct	Chalcopyrite and pyrite-bearing breccia cement and veinlet stock work, high Au/Cu ratios (0.5 to 1.8; similar to NEZ), intermediate Ag/Cu ratios (4 to 7; <NEZ, but >Core Zone)	Similarities: mineralization as breccia cement, chalcopyrite-pyrite breccia cement; elevated Ag; similar Cu/Au; anomalous garnet and carbonate alteration Differences: no bornite	9
Pond Zone	Similar to the Southeast Zone; monzodiorite, monzonite and analcite(?)-bearing basalt andesite, recrystallized, laminated limestone or marble	Skarn	Garnet and magnetite with fine chalcopyrite and pyrite	Highly altered intrusions, sulfides are disseminated and in delicate wisps throughout the alteration; veins are rare.	Direct	Significant skarn-related Cu-Au-Ag mineralization	Similarities: Ag mineralization Differences: skarn; no fragmental hydrothermal breccia; no bornite; strong malachite alteration	9

References (Ref.): 1. Hodgson et al. (1976), 2. Bailey and Hodgson (1979) 3. Fraser et al. (1993), 4 Fraser et al. (1994a,b), 5 Fraser et al. (1995), 6. Rees et al. (2004), 7. Ross (2004a), 8. Rees et al. (2005) 9. Rees et al. (2006) 10. Logan and Mihalynuk (2005)

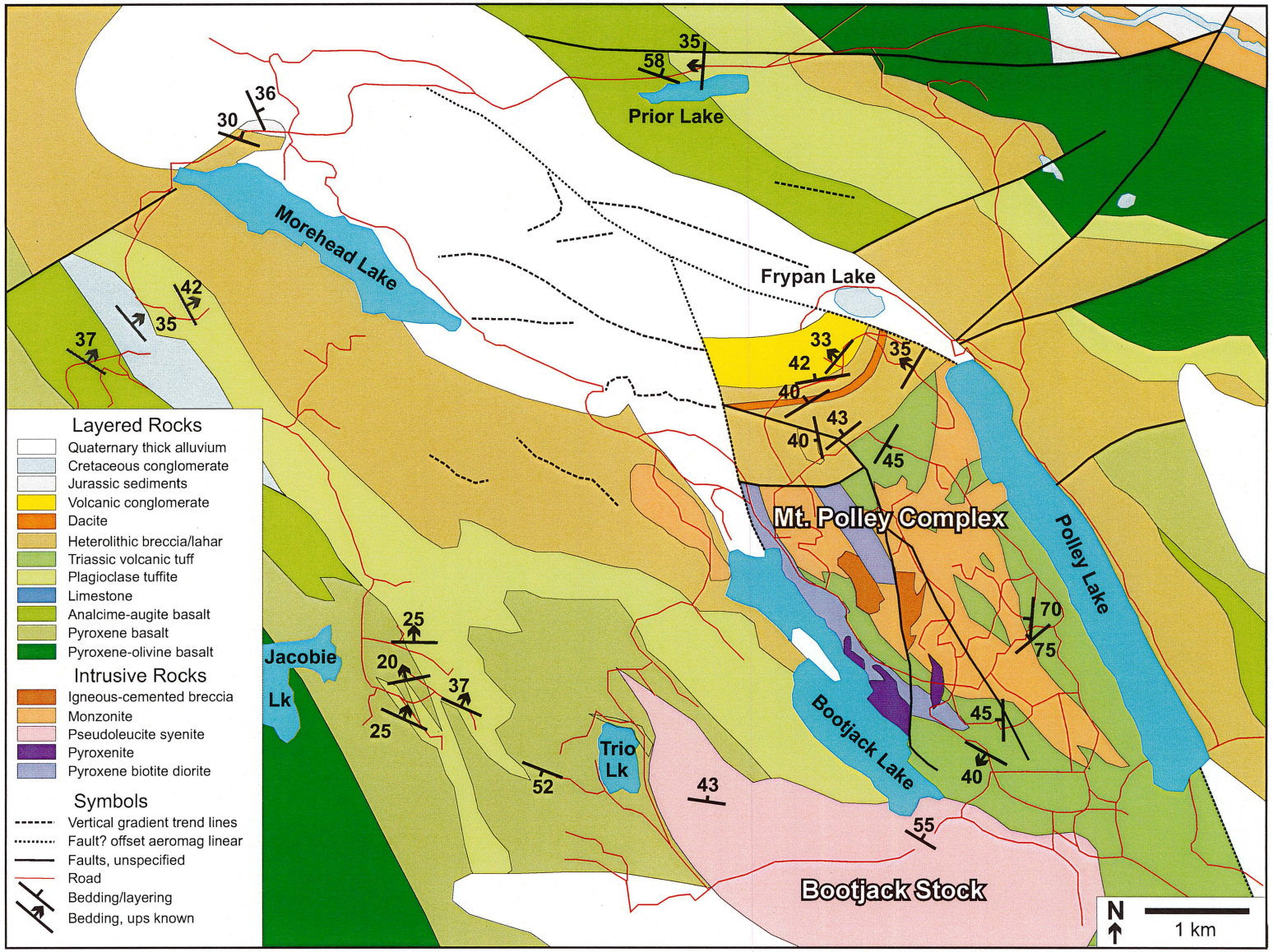

Figure 2.11 Compilation map of the Mt. Polley area. Incorporates unpublished assessment work and published work by Hodgson et al. (1976), Bailey (1990), Panteleyev et al., (1996), Wild (1999) and Shives et al. (2004). Figure courtesy A. Bath (2010), modified from Logan and Mihalynuk (2005).

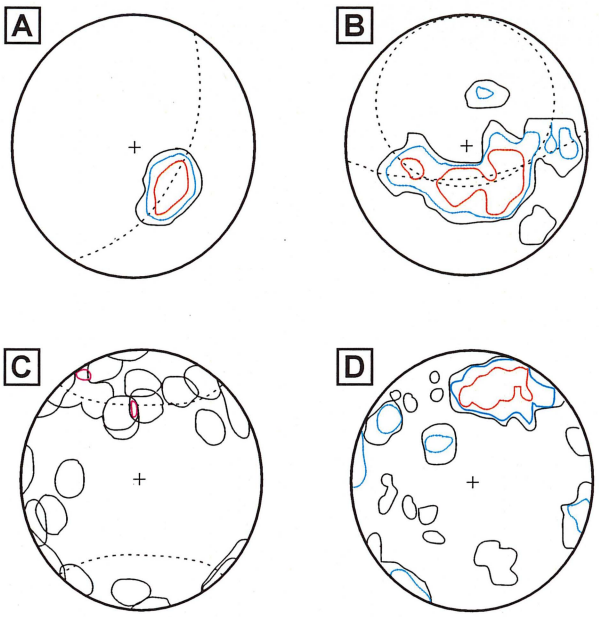

Figure 2.12 Equal area plots from Logan and Mihalnyuk (2005). Data is shown in Fig. 2.11. **A)** Reliable bedding measurements (n=14) from the northern flank of the Mt. Polley Complex. Contours are 8, 16 and 32% of data points per 1% of plot area. **B)** All reliable bedding measurements from the Polley area (n=51). Contours are 2, 4, 8, and 16% of data points per 1% of the plot area. **C)** All veins form the Polley area (n=25). Contours are 4, 8, and 16% of data pointers per 1% area. **D)** All dikes form the Polley area (n=51). Contours are 2, 4, 8, and 16% of data points per 1% area. Figure taken from Logan and Mihalynuk (2005).

Regionally, three periods of faulting have been recognized (Bloodgood, 1987; Bailey, 1988; Bloodgood, 1988; Bailey, 1989, 1990; Panteleyev et al., 1996). The earliest faults are low-angle thrust faults that strike northwest. These are found mainly in the eastern part of the Central Quesnel Belt, and define terrane boundaries. They have been attributed to the obduction of Quesnellia and collision with the Kootenay terrane (Bailey, 1988). The southwest-dipping Eureka thrust is a member of this fault set (Fig. 2.3 and 2.4). The Eureka thrust has truncated the base of the Crooked Amphibolite unit (Slide Mountain terrane) and separates Quesnellia from the Kootenay terrane (Bloodgood, 1988).

The second set of faults strikes dominantly north-easterly to east-north-easterly, has mainly sinistral displacement and are probably high-angle extensional faults that most likely postdate the thrust faults (Fig. 2.4; Bailey, 1990; Panteleyev et al., 1996). Latest movement was likely no later than Cretaceous time and certainly prior to early Tertiary volcanism in the region (Bailey, 1990).

The third fault set is dominantly north-striking with mainly dextral displacement and is related to the major strike-slip faults of the Cordillera (i.e. the Pinchi Fault system; Bailey, 1990). The Chiaz fault (Fig. 2.4) is believed to be part of this fault set. It has dextrally displaced Cretaceous granite by four to seven kilometers and Upper Triassic basalt by at least five kilometers of vertical displacement (west side up; Bailey, 1988; Bailey, 1990).

Structural studies of the Mt. Polley Complex were carried out by Taylor (2004, 2005) and included in Rees et al. (2005), updated in Rees et al. (2006) and by Logan and Mihalnyuk (2005). Faults in the Mt. Polley Complex are generally oriented sub-parallel to regional fault patterns (compare Figs. 2.4 and 2.6A and C). Dominant structures in the mine area include the steep, easterly dipping, north-striking Polley fault in the Core Zone of the Mt. Polley Complex and the north-easterly–trending South Wishbone fault (Fig. 2.6).

Measured faults, shear fractures and non-shear fractures have a wide range of orientations over the Mt. Polley Complex and neighbouring areas, but two sets clearly predominate: a north-striking set (average 359°/78°E) associated with a dextral (to slightly oblique) sense of relative movement (i.e. the Polley fault; Fig. 2.6A) and a northeast to east-northeast-striking set (average 060°/82°SE) with a sinistral (to slightly oblique) sense of movement (i.e. South Wishbone fault, Fig. 2.5A; Rees et al., 2006). Observations in the field show that displacements from both sets of faults were syn-kinematic with mutually cross-cutting relationships and with no particular bias or predictability (Taylor, 2004). These features and the approximately 60° angle between the two sets of faults are consistent with the interpretation that they are a conjugate fault system (Fig. 2.6C; Taylor, 2004). Most of the minor faults associated with both fault sets are anatomising, or are nested networks of slip planes, rather than discrete planar features. The north-easterly-trending fault orientations can wander between 55° and 100°, whereas the north-trending set have relatively more defined planes (Rees et al., 2006).

Vein and dike orientations in the Mt. Polley area were measured by Logan and Mihalnyuk (2005). Most

veins in the Mt. Polley area are steep (Fig. 2.12C) with a mode that dips steeply toward ~150°. A small subset of veins dip moderately to the south-southeast. These data were not unfolded or rotated due to the lack of paleohorizontal control in the Mt. Polley Complex. The average dike orientation is 120°/65° with a smaller population oriented above 310°/85° (Fig. 2.12D).

For the most part, primary textures in the regional rocks have been preserved except where rocks have undergone extensive hydrothermal alteration (Bailey, 1990). Rocks of the Central Quesnel Belt have been metamorphosed predominantly to zeolite facies assemblages (Panteleyev, 1988; Panteleyev and Hancock, 1989; Bailey, 1990; Panteleyev et al., 1996). In the underlying sedimentary rocks, to the east of Mt. Polley, regional metamorphism attained greenschist facies and was associated with thrusting of the terrane during arc amalgamation with ancestral North America (Panteleyev and Hancock, 1989; Bailey, 1990; Gabrielse et al., 1991).

2.7 Metallogeny

Economically, the Late Triassic to Early Jurassic Cu-Au and Cu-Mo porphyry deposits of Quesnellia and Stikinia are an important group of ore deposits in British Columbia (Fig. 1.1; Preto, 1977; McMillan et al., 1995; Logan and Mihalynuk, 2005; Nelson and Colpron, 2007). Porphyry deposits of the Quesnellia and Stikinia Terranes include established producers such as the Highland Valley district (calc-alkalic Cu-Mo; Casselman et al., 1995), Gibraltar (calc-alkalic Cu-Mo; Bysouth et al., 1995), Copper Mountain district (alkalic Cu-Au; Stanley et al., 1995) and Afton-Ajax (alkalic Cu-Au; Ross et al., 1995). The newer mines include Mt. Polley (alkalic Cu-Au; Fraser et al., 1995) and Kemess (calc-alkalic Au-Cu ± Mo; Rebagliati et al., 1995; Duuring et al., 2009). It is anticipated that Galore Creek (alkalic Cu-Au ± Ag; Mihalynuk et al., 1994; Enns et al., 1995; Schwab et al., 2008), Mt. Milligan (alkalic Cu-Au; DeLong et al., 1990; Sketchley et al., 1995), and Red Chris (alkalic Cu-Au; see Figs. 1.1 and 1.4; Newell and Peatfield, 1995) will be the future mines of British Columbia.

Quesnellia and Stikinia contain intrusions of alkalic (shoshonitic) and calc-alkalic character that are associated with porphyry-style mineralization (Mortimer, 1987; Lang et al., 1995b; Nelson and Colpron, 2007). Porphyry-related intrusions were emplaced in Quesnellia and Stikinia between 212 and 176 Ma (Galore Creek to Lorraine, respectively; Godwin et al., 1988; McMillan et al., 1995; Bath, 2010). The most common ages are ca. 205 to 202 Ma, which includes Mt. Polley (Mortensen et al., 1995) and which corresponds to the end of Triassic arc activity (Nelson and Colpron, 2007). Most alkalic porphyry deposits formed either pre- or syn- accretion and display distinctive petrology, alteration and mineralization that indicate a similar tectonic setting for both Quesnellia and Stikinia in the Early Jurassic (McMillan and Panteleyev, 1995; McMillan et al., 1995). Only a few deposits formed in a post-accretion setting (e.g. Lorraine and Mt. Milligan; Jago, 2008; Bath, 2010).

Magmatism and associated porphyry mineralization appears to have migrated eastward across Quesnellia with time, initiating in the west ca 212 Ma with development of calc-alkalic Cu-Mo ± Au deposits (Mortimer, 1987). Calc-alkalic associated mineral occurrences are fewer and more widely spaced than their alkalic counterparts and are located near the western margin of the Nicola Group (Preto, 1977; Mortimer, 1987; Panteleyev et al., 1996; Logan and Mihalynuk, 2005). The loci of magmatism then migrated to the east with submarine to subaerial Na- and K-rich lava flows, co-genetic alkalic intrusions and ca 205 Ma Cu-Au mineralization occupying the central axis of the arc (Mortimer, 1987; Logan and Bath, 2006). Deposition of distal volcaniclastic and younger sedimentary rocks across the terrane followed the cessation of magmatism (Logan and Bath, 2006).

2.7.1 Alteration and mineralization of the Mt. Polley Complex

Previous workers have separated alteration and mineralization features of the Mt. Polley Complex into a Central Zone, mined from the Cariboo and Bell pits, and a West Zone mined from the Springer pit (Figs. 2.6 and 2.8; Fraser, 1994a; Fraser, 1994b; Rees et al., 2005). These zones are separated by the Polley Fault,

but have been referred to together as the "Core Zone", to distinguish them from other, more distal zones, such as the NEZ, Leak Zone, Boundary Zone, Southeast Zone, and Pond Zone (Fig. 1.7; Rees et al., 2005). All known Cu-Au ± Ag ore zones and prospects are located within the Mt. Polley Complex (Rees et al., 2006). The Southeast Zone and the Pond zone are located at the contact between the Mt. Polley Complex and the Nicola Group.

The results of alteration mapping across the Mt. Polley Complex by Imperial Metals geologists are summarized in Figure 2.6A. K-feldspar and albite alteration dominate, with subordinate biotite, actinolite and garnet calc-potassic alteration facies. Secondary calcite is abundant in the NEZ. Potassic alteration is most extensively developed in the northern half of the Mt. Polley Complex, although it is irregular and there does not appear to be a systematic decrease in the intensity of potassic alteration away from the center of the Mt. Polley Complex (Rees et al., 2005). Potassic alteration is noticeably weak to absent south of the Core Zone and in some high-grade ore zones (Rees et al., 2005).

Imperial Metals geologists have used the term "propylitic alteration" wherever secondary chlorite, epidote, albite, calcite and/or pyrite have been observed. These minerals are ubiquitous throughout the Mt. Polley Complex and overlap to a degree with other alteration assemblages (Rees et al., 2005; Rees et al., 2006). As a result, the pattern of propylitization in the Mt. Polley Complex has not been determined. Argillic alteration is absent from Mt. Polley and phyllic alteration is limited to the vicinity of post-breccia veins, fractures and faults in the NEZ (Fraser et al., 1995; Rees et al., 2006; Jackson, 2008).

Deposit-scale studies by Hodgson et al. (1976), Bailey and Hodgson (1979), Fraser (1994a) and Fraser et al. (1995) recognized three concentrically zoned alteration assemblages in the Central Zone (Fig 2.8B). A potassic (biotite-actinolite-K-feldspar + albite) core is surrounded by a discontinuous intermediate calc-potassic zone comprising garnet-epidote-albite-K-feldspar, and an outer propylitic zone of epidote-pyrite-albite-calcite. There is an extensive pyrite zone of undefined width, mapped on the western side of Mt. Polley (Fig. 2.8B; Fraser et al., 1995).

Several ore zones, prospects and Cu showings exist across the Mt. Polley Complex. Table 2.2 summarizes the geology, alteration and mineralization of these zones. Most of the ore in the Mt. Polley Complex is breccia-hosted, with lesser amounts occurring in veins and disseminations. In the Central, West, Southeast and Northeast Zones, hydrothermal-cemented breccias are the main hosts to mineralization (Fraser, 1994a; Fraser et al., 1995; Rees et al., 2006; Jackson, 2008). The Pond Zone is associated with skarn mineralogy and strongly altered intrusive rocks.

2.8 Summary

- The Mt. Polley Cu-Au-Ag deposit is hosted in the Mt. Polley Complex within the Nicola Group, part of the Quesnellia island arc terrane that extends along the eastern margin of the Intermontane Belt of the Canadian Cordillera. Quesnellia formed in response to subduction of the Cache Creek ocean during Late Triassic to Early Jurassic time, and is underlain by the former ocean Slide Mountain terrane and pericratonic Kootenay terrane.
- The Paleozoic rocks of Quesnellia are characterized by fine grained epiclastic sedimentary rocks with both oceanic and arc characteristics, interpreted as basin-fill. This includes the limestone-bearing succession of the Harper Ranch sub-terrane and the basal black phyllite of the Nicola Group.
- The Nicola Group is the principal component of Quesnellia in south-central British Columbia. It is a diverse assemblage of Triassic to Early Jurassic submarine to subaerial volcanic, volcaniclastic, and sedimentary rocks of island arc-marginal basin heritage. The Nicola Group can be divided into four basic units: 1) a basal assemblage of volcano-sedimentary argillitic rocks grading up into siltstone, minor limestone, sandstone and greywacke, 2) a 5.0 to 6.5 km thick sequence of Carnian-Norian submarine, volcanic alkali basaltic flow and breccia rocks, 3) varied volcanic, plutonic breccias and flows and sedimentary rocks, including calc-alkalic and alkalic intrusive centres, that are genetically related to porphyry

Cu-Mo and Cu-Au mineralization, respectively, and 4) a clastic assemblage of Early Jurassic to Middle Jurassic polylithc breccia, dacite tuff and volcaniclastic conglomerate of debatable origin.

- The local geology consists of the nepheline-normative Bootjack Stock and the silica-saturated (quartz free) to silica-undersaturated Mt. Polley Complex. Both of these are alkalic in chemistry and have intruded basalts of the Nicola Group. The Mt. Polley Complex consists of a series of pyroxenite, diorite to syenite, but predominantly variably equigranular to porphyritic monzonite and monzodiorite intrusive rocks and associated breccia bodies. Much of the Mt. Polley Complex consists of breccias which vary considerably in composition; texture and alteration with at least four major genetic classes of breccia are likely present: volcaniclastic, phreatomagmatic, hydrothermal and igneous-cemented breccia.
- Apart from the major structures that define the boundaries of Quesnellia, folding and strike-slip faulting has affected the region around Mt. Polley. Faulting is attributed to subduction-arc tectonics and Cretaceous-Tertiary regional dextral trans-current fault tectonics. The stratigraphic units within the region have a symmetric distribution, having been folded into a broad north-northwest plunging single-phase open syncline.
- The Mt. Polley Complex was emplaced between 209.4 Ma and 195.4 Ma. Based on four samples, mineralization within the Mt. Polley Complex is constrained to a 5 Ma window from approximately 209 to 204 Ma. The age of the spatially related Bootjack Stock can be constrained to be between 202.6 and 201.1 Ma.
- Several ore zones, prospects and Cu-showings exist across the Mt. Polley Complex. Most of the ore is breccia-hosted, with lesser amounts occurring in veins and disseminations. The Pond Zone is a skarn-style of mineralization. Across the Mt. Polley Complex, porphyry-style mineralization is associated dominantly with K-feldspar and albite alteration and subordinate calc-potassic alteration. Propylitic alteration is widespread across the property whereas argillic alteration is absent from Mt. Polley. Secondary calcite is abundant in the NEZ, whereas phyllic alteration is limited to the vicinity of post-breccia veins, fractures and faults in the NEZ.

Chapter 3

Geology of the Northeast Zone

3.1 Introduction

This chapter adds to the previous documentation of ore zones in the Mt. Polley Complex (Fraser, 1995; Fraser et al., 1995; Jackson, 2008) by describing and interpreting the geology of the NEZ. The most salient feature of the NEZ is the ore-hosting breccia complex (Figs. 3.1 and 3.2). Understanding this breccia is important in evaluating its origin(s) and relationship to mineralization and/or igneous activity (Cooke et al., 2006).

This chapter begins with a summary of previous geological work conducted on the NEZ and an overview of the methodology employed in the current study. Included is a description, with examples, of the graphic logging technique employed, and definitions of the breccia nomenclature applied to this thesis. Results of core logging and thin section petrography of coherent and clastic facies are then described. The breccia complex is documented in terms of its clast, matrix and cement characteristics. Interpretations of the intrusive history, NEZ breccia geometry and structural modifications are placed in a paragenetic framework. Fragmentation processes are considered and a genetic interpretation for the breccia complex is presented.

3.2 Previous studies of the NEZ

This section summarizes the findings of previous studies of the geology of the NEZ. A summary of work conducted on the Mt. Polley Complex in general and its other ore zones was presented in Chapter 1 however some reference to the greater Mt. Polley Complex herein is unavoidable.

Following the discovery of Cu-Au-Ag mineralization in the NEZ in 2003, Imperial Metals Corporation conducted geophysical surveys (Shives et al., 2004), an alteration and mineralogy study (Ross, 2004a; 2004b), assessment of the geological environment and conditions of mineralization (Bailey, 2004a; 2004b) and a feasibility study (Gilstrom, 2004) in and around the NEZ.

A number of workers have studied the geology of the NEZ (Logan and Mihalynuk, 2005; Rees et al., 2005; Simpson, 2005; Rees et al., 2006; Jackson, 2008; Tosdal et al., 2008). They found that the NEZ is hosted in a breccia complex and intermediate intrusive rocks, generally of monzodiorite and monzonite composition, but ranging from diorite to possibly syenite compositions. All of these rocks were cut by equigranular to porphyritic monzonite and basalt dikes (Logan and Mihalynuk, 2005; Rees et al., 2005; Rees et al., 2006).

Most authors (Ross, 2004a; Logan and Mihalynuk, 2005; Rees et al., 2005; Simpson, 2005; Rees et al., 2006; Jackson, 2008; Tosdal et al., 2008) interpreted the NEZ breccia complex to contain subsurface hydrothermal breccias, with abundant monzonite clasts that have the same compositions and textures as the intrusive facies. An alternative model was proposed by Bailey (2004a; 2004b), who suggested that the NEZ consisted of highly altered volcaniclastic tuff and breccia, primarily of volcanic origin.

Jackson (2008) conducted a detailed study of the igneous paragenesis, brecciation and alteration history

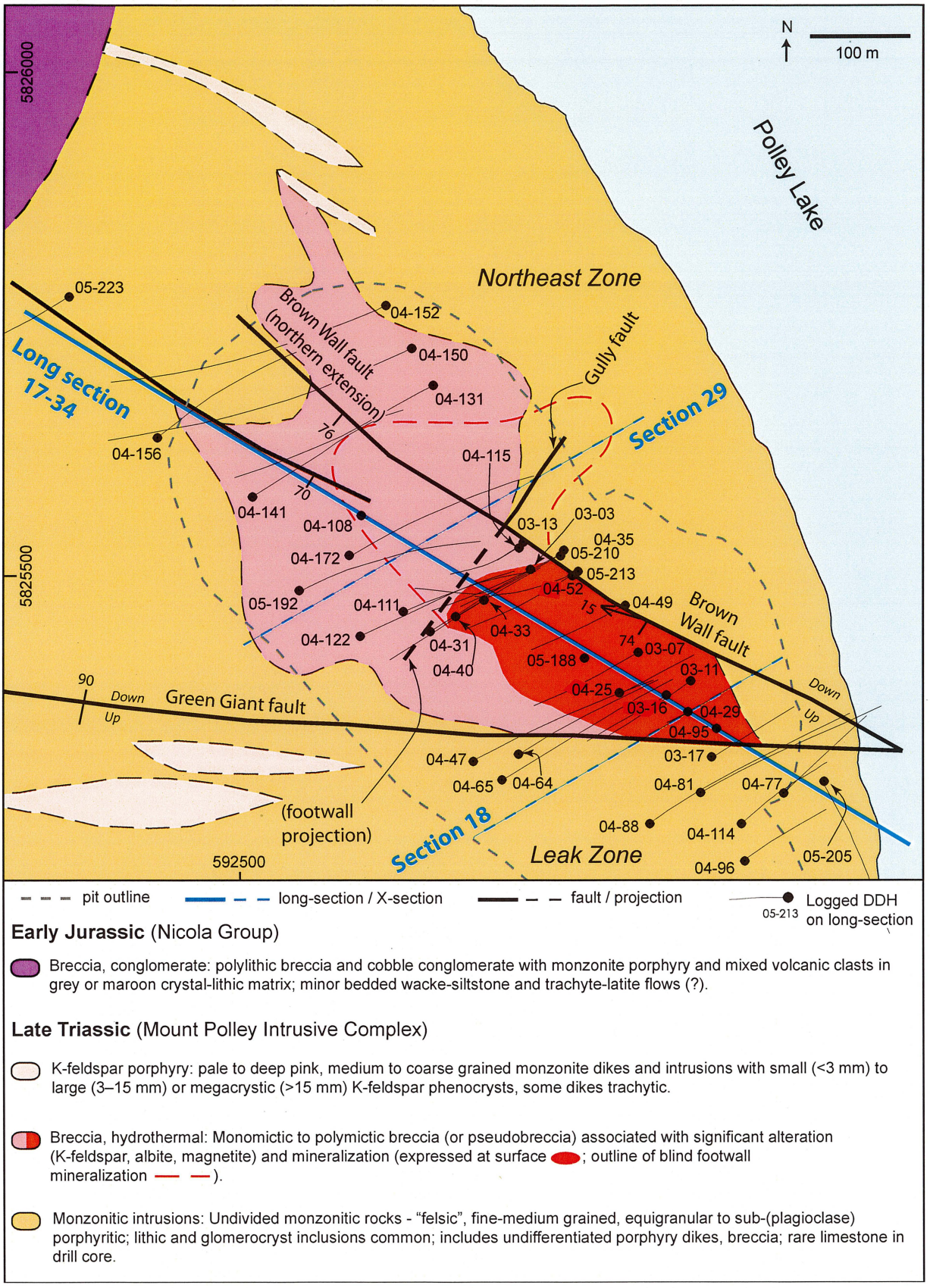

Figure 3.1 Plan view of the Northeast Zone (NEZ) deposit geology. Geology and descriptions taken from Rees et al. (2005) and Rees (2009).

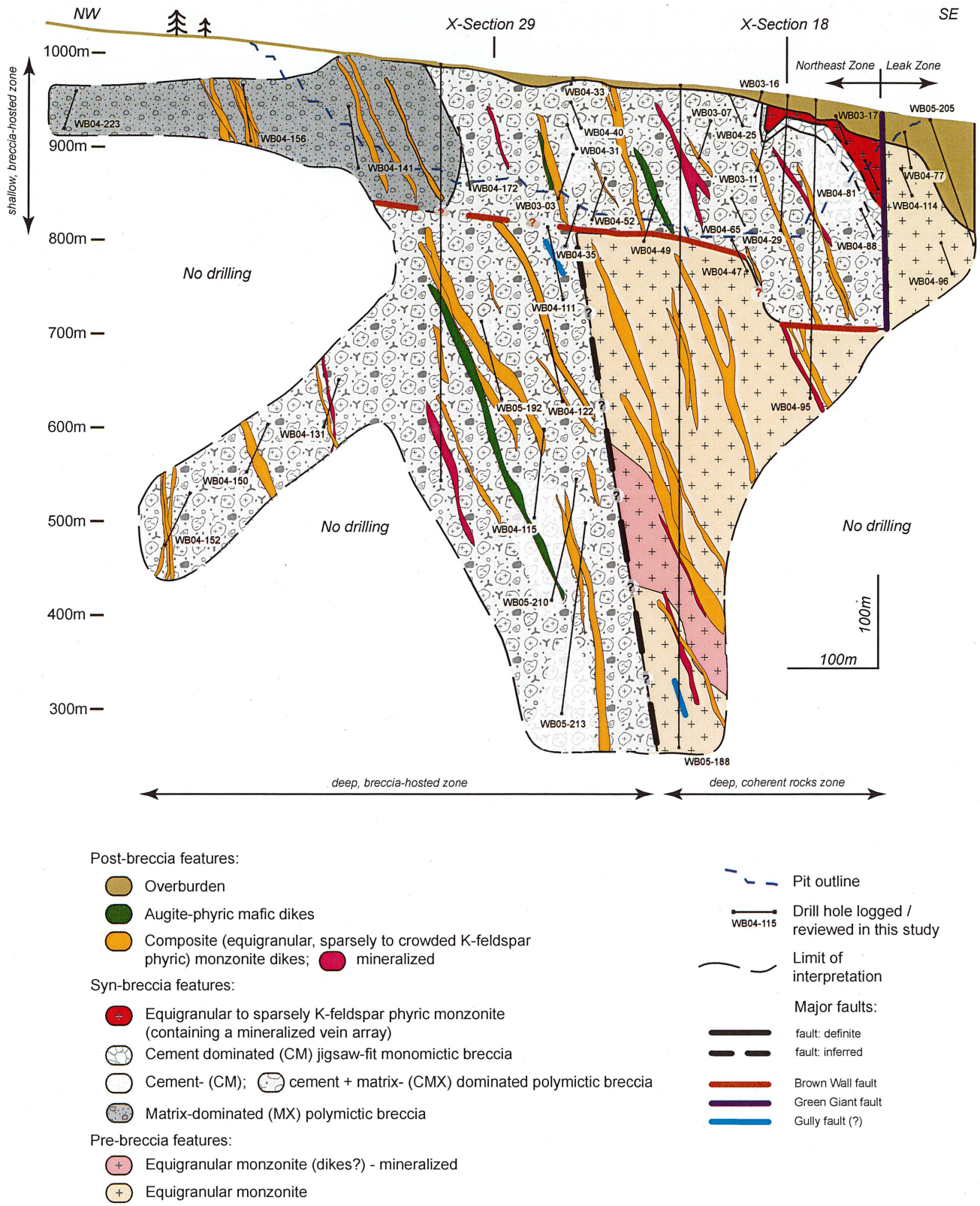

Figure 3.2 Geology of the long-section showing current structural interpretation. Post-breccia intrusions occur as multiple dike-swarms and abudant dikes too small to be shown at this scale. Question marks (?) in faults highlight uncertainties in the fault interpretation.

of the NEZ concurrently with this PhD investigation. Jackson (2008) worked on sections 18 and 29 (Fig. 3.1) and focused mainly on characterizing intrusions and their timing with respect to mineralization and breccia formation. Her detailed breccia descriptions concentrated primarily on the clast types and clast size distribution with less emphasis on the matrix and cement phases (Jackson, 2008). She concluded that the NEZ breccia formed in a single brecciation event triggered by the intrusion of a megacrystic-K-feldspar-phyric porphyry, as originally suggested by Simpson (2005). Variation in the breccia character was attributed to variation in fluid flux, pre-existing rock character and fluidization processes. The permeability established during brecciation was concluded to have exerted the major control over mineralization (Bailey, 2004a; Jackson, 2008).

Limestone does not crop out in the Mt. Polley Complex, but limited intervals of limestone were encountered in the NEZ in two drill holes (256–270 m in WB04-34; 261–300 m WB04-194; Ross, 2004a; Rees et al., 2005). The origin of this limestone is uncertain. The limestone could be equivalent to the Norian limestone that crops out west of Morehead Lake, and which occurs between the top of the basaltic phase of the Nicola successions and the mixed volcaniclastics that are considered stratigraphically equivalent to the base of the Mt. Polley Complex (Rees et al., 2005). The limestone in the NEZ is not underlain by or associated with basaltic rocks (such as in the Pond Zone; Fig. 1.7, Table 2.2). Imperial Metals has interpreted the limestone in the NEZ as slivers of Norian limestone country rock that were separated from their source by Mt. Polley Complex intrusions (Rees et al., 2005).

3.3 Methodology

This section details the core logging methodology employed, as geologic relationships and interpretations of this study were based mainly on drill core observations. The focus of logging was a long-section bisecting the NEZ, trending northwest from mine cross-section 17 to 34. Additional logging of section 18 was conducted in the first field season (Fig. 3.1).

3.3.1 Terminology

This thesis uses non-genetic descriptive terminology to describe the various units logged in the NEZ. A brief definition of these terms is provided below.

All rocks at Mt. Polley can be classified as either coherent or clastic based on their overall texture. Coherent rocks form from the cooling and solidification of magma and have porphyritic, equigranular or aphanitic textures. Clastic rocks form as a result of fragmentation or dissolution processes and are distinguished on the basis of their fragmental character (McPhie et al., 1993).

Breccias are clastic aggregates of sub-rounded to angular clasts, which can be described in terms of clasts, matrix, cement and open space (Davies et al., 2000; Davies, 2002; Simpson et al., 2007). The general term "infill" is used to describe the interstitial material between the clasts and may include any or all of matrix, cement and open space. Matrix (referred to as "rock flour" by many workers, e.g. Sillitoe, 1985; Taylor and Pollard, 1993) is clastic interstitial material <2 mm in diameter and can include small fragments of rock or crystals. Cement is a chemical precipitate, either mineral or crystalline igneous rock (Davies et al., 2000; Davies, 2002; Simpson et al., 2007; Davies et al., 2008a). The term conglomerate is used to describe clastic rocks consisting of dominantly rounded clasts >2 mm (Wentworth, 1922; Bryner, 1968). The terms lobate and globular are used to describe clasts that have delicate irregular edges and/or fluidal shapes.

In this study, breccia clast arrangement has been divided into three categories: jigsaw-fit, rotated and chaotic as in Davies (2002). Jigsaw-fit breccia (or "shatter breccia" - Baker et al., 1986; "crackle breccia" - Taylor and Pollard, 1993; "mosaic breccia" - Laznicka, 1988; Corbett and Leach, 1998) is defined as angular clasts that have undergone limited to no movement. Clasts appear to have only been slightly pulled apart (Sillitoe, 1985) and rounding of clast edges has not taken place. Jigsaw-fit breccia is typically monomictic with limited to no matrix. Rotated clast arrangement is an extension of jigsaw-fit where clasts are still angular to sub-angular and likely to be predominantly still monomictic. In comparison with jigsaw-fit breccia, it is no longer possible

to visually put the clasts exactly "back together" to re-form the precursor unit, but it can be readily inferred. Chaotic clast distribution refers to randomly orientated clasts that have undergone moderate to significant amounts of transportation and considerable attrition (sub-angular to rounded clasts). Chaotic breccias are generally polymictic with abundant matrix.

3.3.2 Breccia description and classification

Davies (2002) conducted an extensive review of breccia terminology and classification from widely used breccia classification schemes including, but not limited to, Baker (1984), Sillitoe (1985), Baker et al. (1986), Laznicka (1988), Taylor and Pollard (1993), and Corbett and Leach (1998). The majority of breccia classification schemes were found to be, at least in part, genetic in nature with no single scheme providing a non-genetic approach with a widely applicable and internally consistent genetic classification (Davies, 2002). Davies et al. (2000), Davies (2002) and Simpson et al. (2007) emphasized that the collection of descriptive data must form the basis for breccia classification as genetic schemes (and interpretations) can change as additional information is gathered. This information is critical in the pursuit of discovering, delineating and mining breccia-hosted deposits. In this study, the descriptive approach of Davies (2002), which is based on the descriptive approach used for volcanic rocks of McPhie et al. (1993), and the genetic approach of Sillitoe (1985) to classifying ore-related breccias has been adopted.

The Mt. Polley breccia has been described and interpreted as part of a four-step process based on a rigorous descriptive framework as detailed in Davies et al. (2000) and Davies (2002): 1 – breccia description; 2 – identification of breccia facies, facies associations and facies organization, 3 – evaluation of genetic origins (i.e. fragmentation, transport, deposition and post-brecciation processes), and 4 – breccia classification. The first step of breccia description includes recording observations of breccia: 1) components (clasts, matrix, cement, open space or vugs), 2) internal organization, 3) grain size, 4) geometry (contact relationships at core scale) and 5) alteration and paragenetic features. This descriptive framework is outlined in detail in Appendix B1.

3.3.3 Graphic logging technique

Core logging was conducted using an amalgamation of three logging and/or mapping techniques. The Anaconda Method was used for mapping altered and mineralized rocks (Einaudi, 1997); graphic logging was conducted as described in *Volcanic Textures* (McPhie et al., 1993) but with modifications for hydrothermal-breccia nomenclature; and the classification of breccias by Davies et al. (2000) and Davies (2002). This study also employed the logging classification codes for clastic and coherent units at Mt. Polley as produced by Imperial Metals in 2006 (Appendix B1). These three techniques were combined to produce a detailed color-coded graphic log that recorded rock type (clastic or coherent) and composition, contact relationships, breccia infill (cement, matrix and open space) and abundance, alteration, veining, paragenetic notes, geochemical anomalies, and sample information (Fig. 3.3).

Prior to logging, breccia clast size divisions, modified from Davies (2002), were chosen: fine (2–4 mm), medium (4–64 mm), coarse (64–160 mm), very coarse (160–256 mm) and mega-clast (>256 mm). A logging scale of 1 cm to 2 m was chosen to facilitate recording detailed breccia characteristics. Strongly anomalous geochemical assay intervals of 2.5 m were recorded on the log sheets to try and match geological characteristics with geochemical anomalies and/or mineralization. Strongly anomalous values for the NEZ were selected as >0.5% Cu, >1% Cu, >0.5 ppm Au, >10 ppm Ag, >50 ppm As, >1000 ppm Pb, >1000 ppm Zn.

Graphic logs generated in this study show the geology in terms of coherent or clastic units, together with their and contact relationships (Figs. 3.3, 3.4). Coherent units were labelled using a graphic code and drawn out beyond the maximum clast size to differentiate them from clastic units. Clastic units were drawn with rounded to angular or globular clast shapes as observed. Graphic codes were also drawn inside clasts to discriminate clast composition (i.e. examples 1 and 2 in Fig. 3.3). The average largest clast size was recorded as the breccia *grain size* (see Fig. 3.4). This was determined by measuring the largest clasts observed in each meter of core and recording the average on the log. Mega-

Figure 3.3 Graphic logging code used for this study. Graphic logging code was modified from that of McPhie et al. (1993) and from Imperial Metals (Appendix B). Chemical anomalies were noted using Imperial Metals' 2.5 m interval geochemical assay data (>0.5 ppm Au, >0.5% Cu, >1% Cu, >10 ppm Ag, >50 ppm As, >1000 ppm Pb, >1000 ppm Zn).

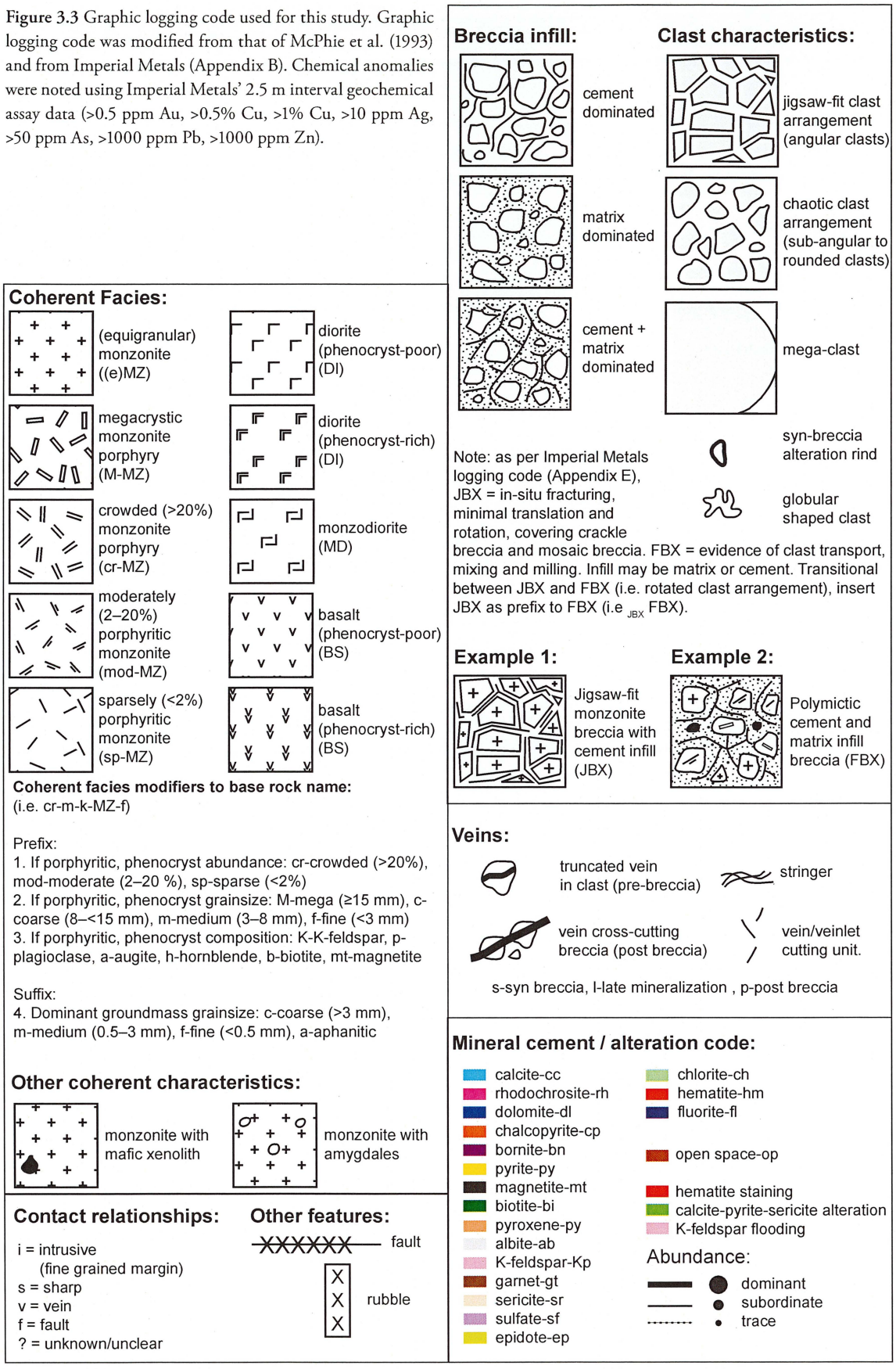

clasts were drawn schematically with the diameter of the clast written in the log (Fig. 3.4). Faults with gouge or cataclasite greater than 10 cm thickness and intervals with rubble-rock were recorded with a hatch and "x", respectively (Figs. 3.3 and 3.4).

It can be difficult to distinguish large mega-clasts and dikes in diamond drill core, in particular where hydrothermal alteration is texturally destructive and has obscured primary features. Clasts in breccias can be up to tens of meters, sometimes >100 m in diameter (Sillitoe, 1985; Baker et al., 1986), therefore identification in drill core requires well-preserved clast boundaries. In this study, the observation of fine-grained margins on the edge of a unit (as denoted by an "*i*" on the log) classified it as a dyke, whereas, when fine-grained margins were not observed, or if truncated phenocrysts were noted at the margin, it was logged as a mega-clast (Figs. 3.3 and 3.4).

Color coded lines and dots of various thickness were used to record the occurrence and intensity of the dominant alteration, breccia cement and vein minerals (Figs. 3.3, 3.4). A letter was added next to the vein if paragenetic interpretation was possible (*s*-syn breccia, *l*-late mineralization or *p*-post mineralization). Where observed, truncated veins were drawn schematically inside clasts. When clear paragenetic relationships were observed, these were sketched with the corresponding mineral color code.

As most information was recorded graphically, written information was minimized. Rock sample location and information was recorded in the *samples, imaging and reasoning* column. A "*s/o*" was added if the sample was collected for scanning only purposes. Graphic logs from this study are provided in electronic Appendix A3.

3.4 Igneous rock types and occurrences

No whole rock geochemistry was undertaken in this study and therefore names of the rock units used in this discussion generally correspond to the nomenclature used by Imperial Metals geologists at the time of logging. Coherent facies names used by the mine at the time of logging were diorite, monzodiorite, equigranular monzonite, porphyritic monzonite, basalt, andesite, augite porphyry and mafic dyke (Appendix B1). Differentiation between the various rock types was hampered by the compositional and textural similarities between units and pervasive K-feldspar hydrothermal alteration (Ross, 2004b; Logan and Mihalynuk, 2005; Jackson, 2008; this study).

Table 3.1 summarizes the characteristics of igneous rock types observed on the long-section in the NEZ. Relative abundance and timing relationships of each rock type, relative to a single brecciation event, are listed in Table 3.1 and displayed schematically in Figure 3.5.

3.4.1 Early intrusions (pre-breccia)

Igneous rocks were assigned a pre-breccia timing if they were observed as a clast in the breccia complex or a xenolith in wall-rock. These igneous rock types include monzonite, crowded to sparsely K-feldspar-phyric monzonite, monzodiorite, diorite, and various mafic rock types (Fig. 3.5).

3.4.1.1 Monzonite

Monzonite is the most abundant igneous rock type and clast component in the NEZ (Fig. 3.6A–I). In hand sample, this facies appears equigranular, but it is infact is a micro-monzonite porphyry with a crystal-crowded texture in thin section (Fig. 3.6A–H; Ross, 2004a; Jackson, 2008; this study). Monzonite can also be aphanitic (Fig. 3.6A) and/or contain rare small (<5 mm) phenocrysts of K-feldspar, plagioclase, augite, hornblende or biotite. In mine terminology they are collectively referred to as equigranular monzonite and for the purposes of this study, the monzonites of equigranular to crystal-crowded to more sparsely porphyritic texture have been grouped as 'monzonite'. Subtle variations in phenocryst size and abundance occur locally and between intrusive units. Logan and Mihalynuk (2005) speculated that the amount of monzonite in the NEZ may have been overestimated due to pervasive potassium metasomatism and hematite alteration.

Petrographic studies of the monzonites have shown that samples are variably altered (Fig. 2.6A–I; Ross, 2004a; Jackson, 2008) with weak to intense

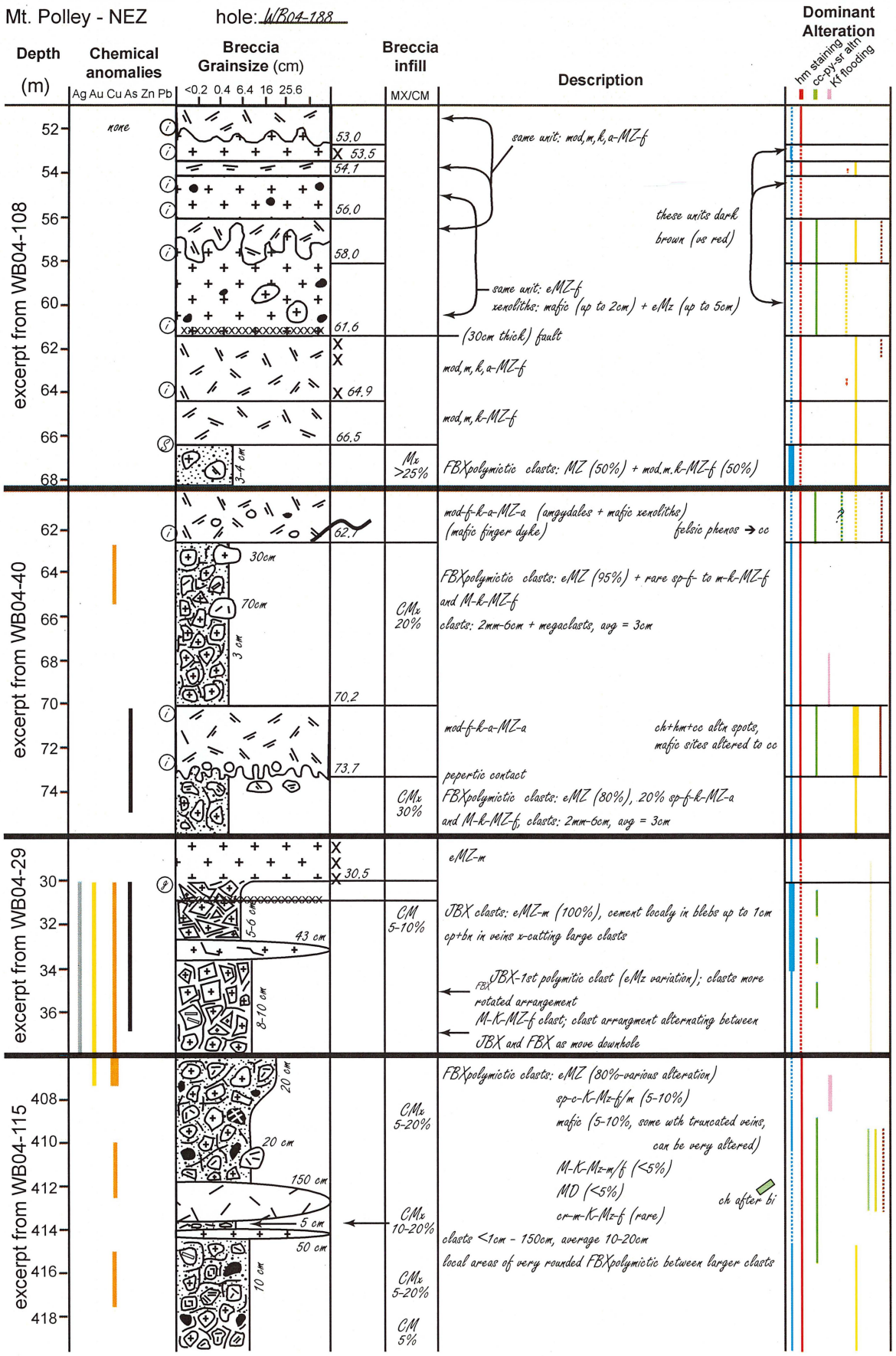

Figure 3.4 Representative graphic logs from selected diamond drill holes. Graphic logging codes summarized in Fig. 3.3.

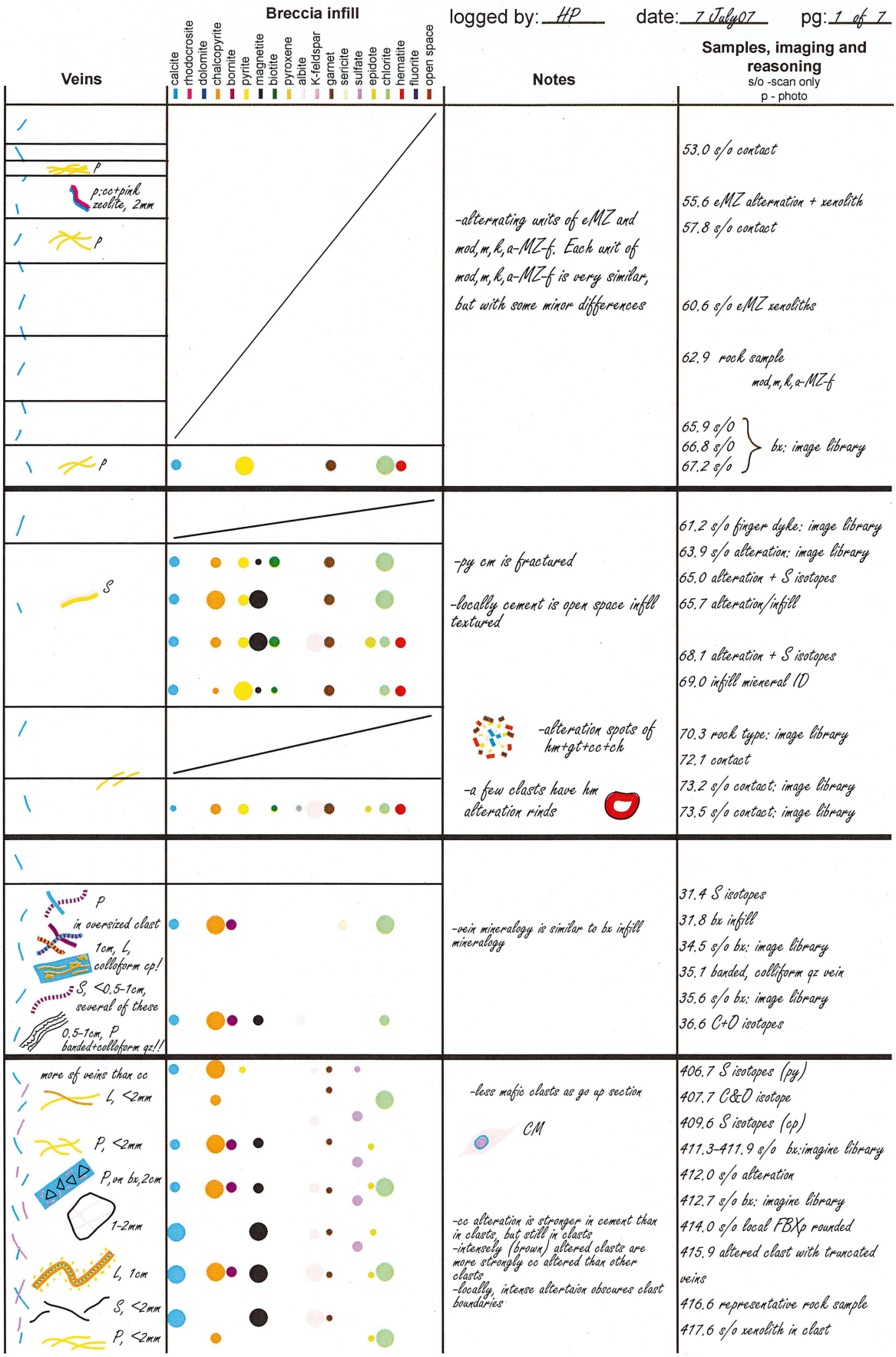

Figure 3.4 continued

Table 3.1 Characteristics and relative abundance of igneous rock types from the NEZ.

Igneous rock type	Sub type	Description	Mode of occurrence	Timing relationship(s)	Relative abundance[1]
Monzonite (Fig. 3.6)	-	Mineralogy: • K-feldspar: aphanitic groundmass to equigranular to fine- to medium-grained crystal crowded, rare >3 mm phenocrysts • plagioclase: 5–20%, ≤1.5 mm, rare >3 mm phenocrysts, euhedral to anhedral • augite: ≤5–15%, ≤1.5 mm, euhedral relict phenocrysts • hornblende: 0–≤3%, ≤0.8 mm, subhedral to anhedral • biotite:0–≤5%, <0.2–0.8 mm, rare >1 mm, euhedral to subhedral • magnetite: 2–10%, ≤0.5 mm, euhedral to subhedral • apatite: <2%, ≤0.5 mm, rarely 0.8 mm, euhedral to subhedral Other: • can be amygdaloidal, irregular shaped, 0.2–10mm, up to 20% locally, filled with chlorite, carbonate ± epidote ± zeolite • xenoliths: up to 2%, 5–35 mm, rounded to sub-angular, monzonite, monzodiorite and finely crystalline "mafic" rock (see below)	clast, coherent xenolith	pre-, and post-brecciation	1
K-feldspar-phyric monzonite porphyry (Fig. 3.7)	Megacrystic[2] K-feldspar-phyric monzonite	Phenocrysts: • K-feldspar: <2–3 0%, 5–>2 cm, euhedral • plagioclase: 10–40%, <0.5–3 mm, euhedral to anhedral • augite ± biotite: <10%, rarely 30%, < 0.5–3 mm, subhedral to anhedral relict crystals • apatite: ≤2%, ≤0.2 mm, euhedral-subhedral • sphene: very rare, ≤0.4 mm, euhedral Groundmass: aphanitic K-feldspar with very fine-grained (<0.1 mm) disseminated magnetite (<2%)	clast (locally globular in shape), coherent (section 18 only; Jackson, 2008)	pre(?), and syn-brecciation	7
	Crystal-crowded[3] K-feldspar-phyric monzonite	Phenocrysts: • K-feldspar: 20–30%, <2 mm–1 cm, euhedral to subhedral, randomly oriented to strongly aligned • plagioclase: 15–20%, <1–3 mm, euhedral to subhedral • augite + biotite ± hornblende: <5–20%, <0.1–1 cm, euhedral to anhedral • magnetite: ≤5%, <0.2–1 mm, subhedral • apatite: ≤2%, <0.2–0.5 mm, euhedral-subhedral Groundmass: aphanitic K-feldspar with very fine-grained (<0.1 mm) disseminated magnetite (<2%). Other xenoliths: <1–2%, 0.2–5 cm, diorite-monzodiorite-monzonite, rounded to subangular	clast, coherent xenolith	pre-, and post-brecciation	3

Table 3.1 Continued

Igneous rock type	Sub type	Description	Mode of occurrence	Timing relationship(s)	Relative abundance[1]
	Moderately[4] K-feldspar-phyric monzonite	Phenocrysts: • K-feldspar: 2–15%, <0.5–10 mm, euhedral to subhedral • plagioclase: 0–20%,<1–2 mm, euhedral to subhedral • augite + biotite ± hornblende: 1–15%, <0.5–4 mm, subhedral to anhedral • magnetite: ≤5%, <0.2–1 mm, subhedral • apatite: ≤2%, <0.2–0.5 mm, euhedral-subhedral Groundmass: aphanitic K-feldspar with very fine-grained (<0.1 mm) disseminated magnetite (<2%). Other: • xenoliths: <2%, mafic (biotite-magnetite-plagioclase ± apatite), isolated mineralized xenolith (WB04-40) • can be amygdaloidal	clast, coherent	pre- and post-brecciation	2i
	Sparsely[5] K-feldspar-phyric monzonite	Phenocrysts: • K-feldspar:1–2%, 3 mm–1 cm, euhedral • Plagioclase: 5–20%, <1–3 mm, euhedral to subhedral • augite ± biotite: 0–≤5%, ≤0.8 mm, subhedral-anhedral • biotite: 0–≤2%, ≤0.8 mm, euhedral-subhedral • magnetite: ≤5%, <0.2–1 mm, subhedral • apatite: ≤2%, <0.2–0.5 mm, euhedral-subhedral Groundmass: aphanitic K-feldspar with very fine-grained (<0.1 mm) disseminated magnetite (<2%) Other: xenoliths: <1%, 3–5 cm, sub-rounded, black, fine-grained mafic (biotite-magnetite-plagioclase ± apatite)	clast (locally globular in shape), coherent	pre- and post-brecciation	2ii
Monzodiorite-diorite (Fig. 3.8)	-	equigranular (fine to medium-grained) to plagioclase ± augite-phyric Phenocrysts: • plagioclase: 5–30%, 0.5–3 mm (rare >1 cm), euhedral - subhedral • K-feldspar: 0–<15%, 0.5–3 mm, euhedral-subhedral • biotite + hornblende: 3–15%, ≤0.5–1 mm (rare 2 mm), • augite: 3–15%, ≤1.5 mm (rare 4 mm), euhedral–subhedral, very rarely rimmed by magnetite • magnetite: ≤2%, <0.2 mm, euhedral-subhedral, can be rimmed with pyrite. • apatite: trace, ≤1 mm, euhedral-subhedral Groundmass: feldspar, very fine-grained (<0.1 mm) disseminated magnetite, calcite blebs (trace, <1 mm), weakly to strongly hematite stained Other: xenoliths: <1%, ≤1 cm, biotite + alkali feldspar with lesser magnetite, medium-grained, two isolated examples of mineralized xenoliths (WB04-31)	clast, coherent xenolith	pre, and post-brecciation	5

Table 3.1 Continued

Igneous rock type	Sub type	Description	Mode of occurrence	Timing relationship(s)	Relative abundance[1]
Mafic (andesite-basalt) (Fig. 3.8)	-	Phenocrysts: • plagioclase: <5–10% (rarely 20%), ≤2 mm, euhedral-subhedral, commonly sericite+calcite altered, can be hematite altered • hornblende + augite: 0–<5%, euhedral-subhedral, • magnetite: ≤2%, micro-phenocrysts and very fine-grained disseminated dusting, subhedral to anhedral, can have pyrite rims/dusting • apatite: trace, <0.5 mm, euhedral-subhedral, Groundmass: plagioclase, trace magnetite, aphanitic/microcrystalline Other: • can be vesicular • amygdales: 0–5%, 1 mm–2 cm, irregular-shaped, gypsum-calcite filled • xenoliths: equigranular monzonite, isolated example containing chalcopyrite flecks	rare clast, xenolith, coherent	pre, post-brecciation	6
Augite-phyric basalt porphyry (Fig. 3.10)	-	Phenocrysts: • augite: 10–30%, <0.5–5 mm, anhedral-euhedral • plagioclase: 0–5%, 0.5–1 mm, euhedral-subhedral, • olivine: 0–7%, 0.5–2 mm, subhedral • hornblende: <2%, <0.8 mm, subhedral, mostly relict • magnetite: <2%, <0.4 mm, subhedral-anhedral Groundmass: plagioclase, trace magnetite, aphanitic-microcrystalline, locally weakly hematite stained	coherent	post-brecciation	4
Mafic (other) (Fig. 3.9)	(various)	i) plagioclase-magnetite-biotite altered xenoliths, up to 3%, <0.5–>4 cm, rounded to angular, common in many coherent facies of the NEZ, uncertain protolith (Figs. 3.6D, F, 3.7H, 3.8A). ii) orthopyroxene-plagioclase-magnetite clasts and xenoliths, rare, interpreted as belonging to the Nicola Group (Fig. 3.9B). iii) hornblende-bearing plagioclase clasts and xenoliths, rare (this study and Jackson, 2008), interpreted as belonging to the Nicola Group (Fig. 3.8I). iv) alkali-feldspar-magnetite-biotite ± pyroxene-bearing altered brown clasts, interpreted monzonite protolith (Fig. 3.9A).	clast, and/or xenolith	pre-brecciation	8

1. 1 = most abundant; 8 = least abundant
2. megacrystic implies at least some phenocrysts were ≥1.5 cm in length
3. crowded = >20% phenocrysts
4. moderately = <20% phenocrysts >2%
5. sparsely = <2% phenocrysts

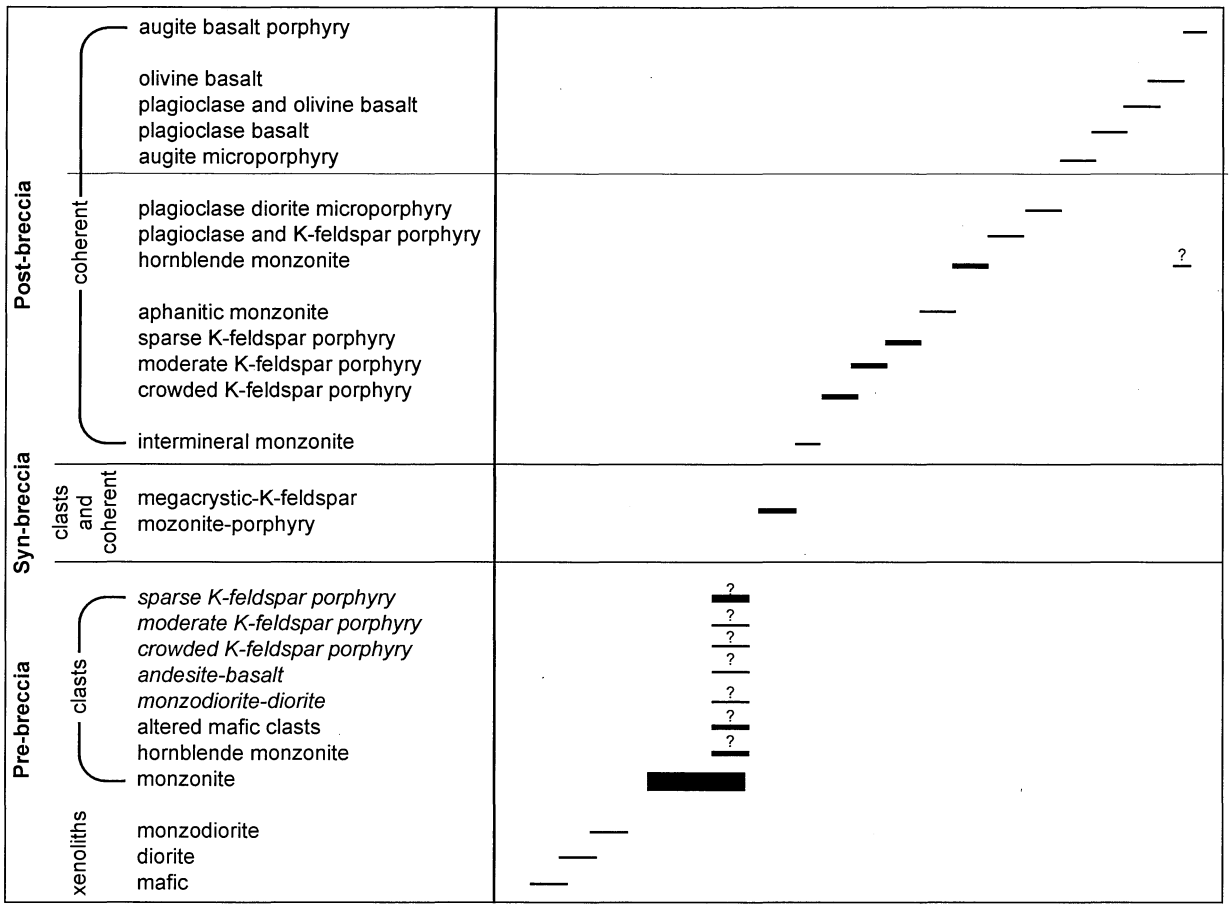

Figure 3.5 Geologic evolution of the NEZ based on cross-cutting relationships, clast and xenolith observations. Modified from Jackson (2008). Question marks (?) indicate uncertainty in timing. Items in italics have been added by this author.

K-metasomatism, hematite staining, calcite and variable illite-muscovite-smectite alteration of feldspars. Plagioclase phenocrysts are commonly rimmed by K-feldspar. Magnetite is rimmed by hematite and less commonly pyrite. Locally, magnetite occurs within augite phenocrysts (Fig. 2.6I) and as rare rims to sphene. When present, biotite was commonly altered to calcite along cleavage planes or rimmed by chlorite (Fig. 3.6H and I, respectively).

3.4.1.2 K-feldspar-phyric monzonite porphyry

The K-feldspar-phyric monzonite porphyry rock type has been divided into four sub-types (Fig. 3.7A–H): 1) crystal-crowded (>20% phenocrysts) K-feldspar-phyric monzonite porphyry; 2) moderately porphyritic (2–20% phenocrysts) K-feldspar-phyric monzonite porphyry; and 3) sparse porphyritic (<2% phenocrysts) K-feldspar-phryic monzonite porphyry. The fourth sub-type, megacrystic K-feldspar-phyric monzonite porphyry shares the general characteristics of the K-feldspar-phyric monzonite porphyry facies but is detailed below in section 2.4.2.

All four sub-types have undergone K-feldspar metasomatism which has obscured groundmass textures. In addition, the presence of fine-grained hematite gives the rock an orange to red-brown color in hand sample and thin section (Fig. 3.7E–H).

K-feldspar-phyric monzonite porphyries commonly have polymodal phenocryst populations with K-feldspar the most visually distinct and coarsest phenocrysts (generally ≥4 mm). Plagioclase, K-feldpsar, augite, biotite and hornblende phenocrysts are generally medium-grained (>0.5 to 3 mm), while magnetite and apatite phenocrysts are fine-grained (<0.5 mm). The aphantic groundmass consists of orange-brown K-feldspar due to moderate to intense hematite staining.

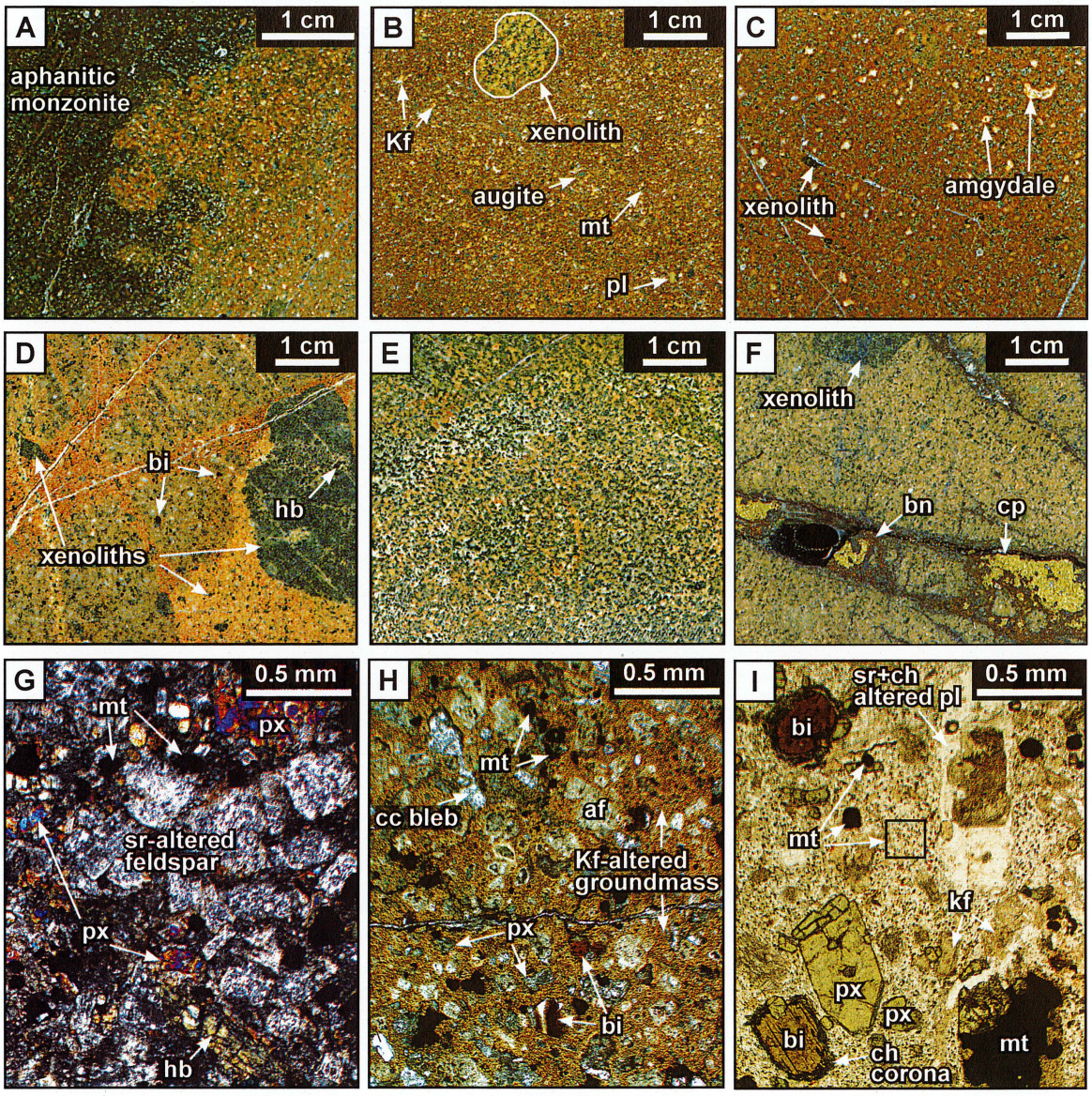

Figure 3.6 Equigranular to microporphyritic (crystal crowded) monzonites of the NEZ. **A)** Aphanitic monzonite cutting "equigranular" monzonite. Red and brown coloring is due to pervasive hematite staining (WB05-141 77.5 m). **B)** Crystal-crowded micromonzonite with equigranular medium grained plagioclase-augite-magnetite-biotite xenolith (WB04-108 49.4 m). **C)** Fine-grained monzonite with calcite- and sulfate-filled amygdales and <5 mm black plagioclase-magnetite-biotite xenoliths; these black xenoliths are commonly found in intrusive units of the NEZ (WB04-141 70.1 m). **D)** Biotite-rich monzonite with common mafic xenolith (as in C) and rare hornblende-bearing mafic xenolith with felsic xenolith. The latter is interpreted as sourced from the Nicola Group volcanics (WB04-108 351.6 m). **E)** Actinolite-magnetite-albite-K-feldspar irregular alteration of monzonite sampled from the Leak Zone (WB04-150 421.8 m; Figs. 2.1 and 2.2). **F)** Fine grained monzonite with larger common mafic xenolith (as in C) and cross-cutting bornite-chalcopyrite ± calcite vein (WB05-188 68.3 m). **G)** Photomicrograph (xpl) showing equigranular nature of some monzonite units. Hornblende, observed in this sample, is a less common mafic mineral in the NEZ (WB04-138 32.2 m). **H)** Photomicrograph (ppl) showing micro-porphyrytic texture of most monzonite units with pervasive hematite stained aphanitic K-feldspar groundmass. Biotite phenocrysts can have calcite alteration along cleavage planes (WB04-108 49.4 m). **I)** Photomicrograph (ppl) of biotite-rich monzonite showing chlorite coronas around biotite, sericite and chlorite altered plagioclase, subhedal magnetite phenocrysts and minute magnetite crystals in groundmass (black square highlight). Magnetite has replaced an augite phenocryst in the lower right-hand corner (WB04-138 499.5 m). Abbreviations: bi-biotite, bn-bornite, cc-calcite, ch-chlorite, cp-chalcopyrite, hb-hornblende, Kf-K-feldspar, mt-magnetite, ppl-plane polarized light, pl-plagioclase, px-pyroxene, sr-sericite, xpl-cross polarized light.

Very fine-grained (<0.1 mm) magnetite crystals are also present throughout the groundmass (Fig. 3.6I; black box). Locally, fine to very fine-grained pyrite occurs as groundmass disseminations or as rims around magnetite grains. More altered examples contain irregular blebs of chlorite ± calcite ± sericite and very fine-grained chlorite ± epidote.

Plagioclase phenocrysts commonly have sericitized cores with orthoclase rims. Mafic mineral sites have commonly been altered to chlorite ± calcite ± sericite ± epidote ± magnetite with blocky to elongate shapes indicating the original minerals may have been augite, biotite or hornblende, respectively (Fig. 3.7E and G). When present, primary biotite is better preserved than hornblende, and commonly occurs as less altered flakes.

3.4.1.3 Monzodiorite-Diorite

Monzodiorite to diorite clasts and xenoliths appear fine to medium equigranular in hand sample but are commonly micro-porphyritic in thin section (i.e. plagioclase micro-porphyry; Fig. 3.8A–D). Pervasive hematite staining of the microcrystalline feldspar groundmass is weak to intense giving the rock a grey-pink to dark brown color respectively. Sericite has commonly replaced feldspar cores and secondary alkali feldspar occurs as rims on plagioclase locally (Fig. 3.8C–D).

3.4.1.4 Mafic (andesite-basalt)

Rare mafic (andesite- basalt) clasts are dark grey-black to grey-brown and typically aphantic to weakly plagioclase-phyric in hand sample (Fig. 3.8G–I). Feldspar phenocrysts are commonly sericite and calcite altered and rarely have alkali-feldspar cores.

3.4.1.5 Other mafic rock types

Other mafic igneous rock types occur as xenoliths and less commonly clasts in the breccia (Table 3.1; Mafic–other). Small black plagioclase-magnetite-biotite altered xenoliths of uncertain origin occur in many NEZ dikes; they can comprise up to 2% of the rock (Figs. 3.6C, D, F, 3.8A). Feldspar-magnetite-biotite ± pyroxene-altered clasts, with a distinctive dark brown color are interpreted to have a monzonitic protolith (Fig. 3.9A). Some of these clasts contain early feldspar and magnetite veins that are truncated at the clast margins. These clasts are interpreted to be equivalent to Jackson's (2008) "altered mafic clasts". Rare pyroxenite and hornblende-bearing clasts and xenoliths are also present (Figs. 3.6D and 3.9B, respectively).

3.4.2 Syn-breccia igneous rocks

The megacrystic K-feldspar-phyric monzonite is interpreted to have been emplaced during the major brecciation event of the NEZ (Figs. 3.5 and3.7A). This rock type has been observed as breccia clasts on the long-section and sections 18 and 29 (Jackson, 2008). This sub-facies shares the general attributes of the K-feldspar-phyric monzonites described above but is defined by the presence of ≥1.5 cm, euhedral K-feldspar phenocrysts, referred to as 'megacrysts', which locally can form irregular glomerocrysts. K-feldspar megacrysts contain inclusions of smaller K-feldspar crystals and rarely sphene inclusions, and have undergone K-feldspar alteration along cleavage planes (Fig. 3.7E). Smaller K-feldspar phenocrysts (<0.3–1.5 mm) are also present in this sub-facies.

Coherent megacrystic K-feldspar-phyric monzonite also occurs as steeply dipping intrusions (4 to >50 m thick) outboard of the breccia in sections 18 and 29 (Jackson, 2008). These intrusions are correlated with the syn-breccia megacrystic K-feldspar-phyric monzonite clasts; however, the textural proof of a co-genetic relationship remains elusive.

3.4.3 Post-breccia igneous rocks

Post-breccia dikes have fine-grained (chilled) margins, are steeply dipping and have cut breccia clasts, cement and matrix. In paragenetic order, post-brecciation rock types include an inter-mineral monzonite, crowded to moderate to sparsely K-feldspar-phyric monzonite, monzonite, diorite-mozodiorite, mafic dikes and augite-± olivine-phyric basalt porphyry (Fig. 3.5). Post-breccia dikes are steeply-dipping, possibly indicating that regional tilting occurred after their emplacement, as suggested by Taylor (2004), or that that they intruded faults that were not vertical.

Post-breccia monzonite occurs as large intrusive bodies of unknown geometry, as isolated dikes and as dike swarms. Dikes have thicknesses that range from <10 cm to >20 m (average 2–6 m). Hundreds of texturally and

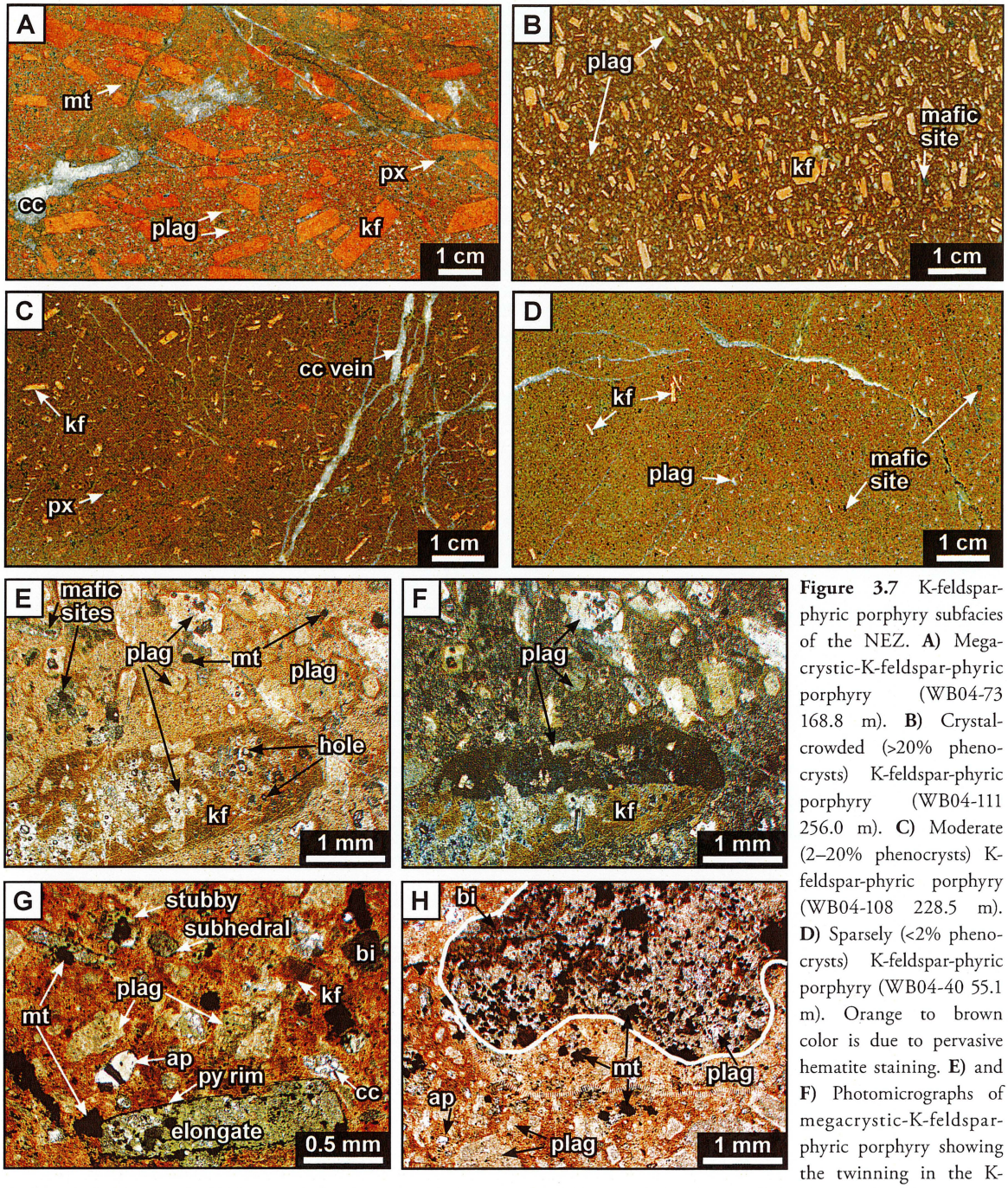

Figure 3.7 K-feldspar-phyric porphyry subfacies of the NEZ. **A)** Megacrystic-K-feldspar-phyric porphyry (WB04-73 168.8 m). **B)** Crystal-crowded (>20% phenocrysts) K-feldspar-phyric porphyry (WB04-111 256.0 m). **C)** Moderate (2–20% phenocrysts) K-feldspar-phyric porphyry (WB04-108 228.5 m). **D)** Sparsely (<2% phenocrysts) K-feldspar-phyric porphyry (WB04-40 55.1 m). Orange to brown color is due to pervasive hematite staining. **E)** and **F)** Photomicrographs of megacrystic-K-feldspar-phyric porphyry showing the twinning in the K-feldspar phenocrysts. Phenocrysts of plagioclase have a brownish outer rim of secondary K-feldspar and a paler core, locally of alkali feldspar. K-feldspar phenocrysts are intensely hematite altered and locally contain larger feldspar crystals. Rounded crystals of magnetite are disseminated in the groundmass (E-ppl, F-xpl, 2.5x, WB03-11 66.8 m). **G)** Photomicrograph showing calcite and chlorite altered mafic sites in stubby, subhedral and elongate shapes indicating augite, biotite and/or hornblende. Locally pyrite has rimmed former magnetite and mafic sites. Calcite blebs are common in some samples (WB05-188 268.8 m). **H)** Photomicrograph of a sparsely K-feldspar-phyric porphyry with common "mafic" xenolith (solid white outline; as in Fig. 3.6C–D) of altered biotite, magnetite, plagioclase ± apatite. An asymmetric reaction rim (hatch line) is present on the lower portion of the xenolith (ppl, 2.5x, WB05-188 268.8 m). Abbreviations: bi-biotite, bn-bornite, cc-calcite, ch-chlorite, cp-chalcopyrite, hb-hornblende, Kf-K-feldspar, mt-magnetite, ppl-plane polarized light, pl-plagioclase, px-pyroxene, sr-sericite, xpl-cross polarized light.

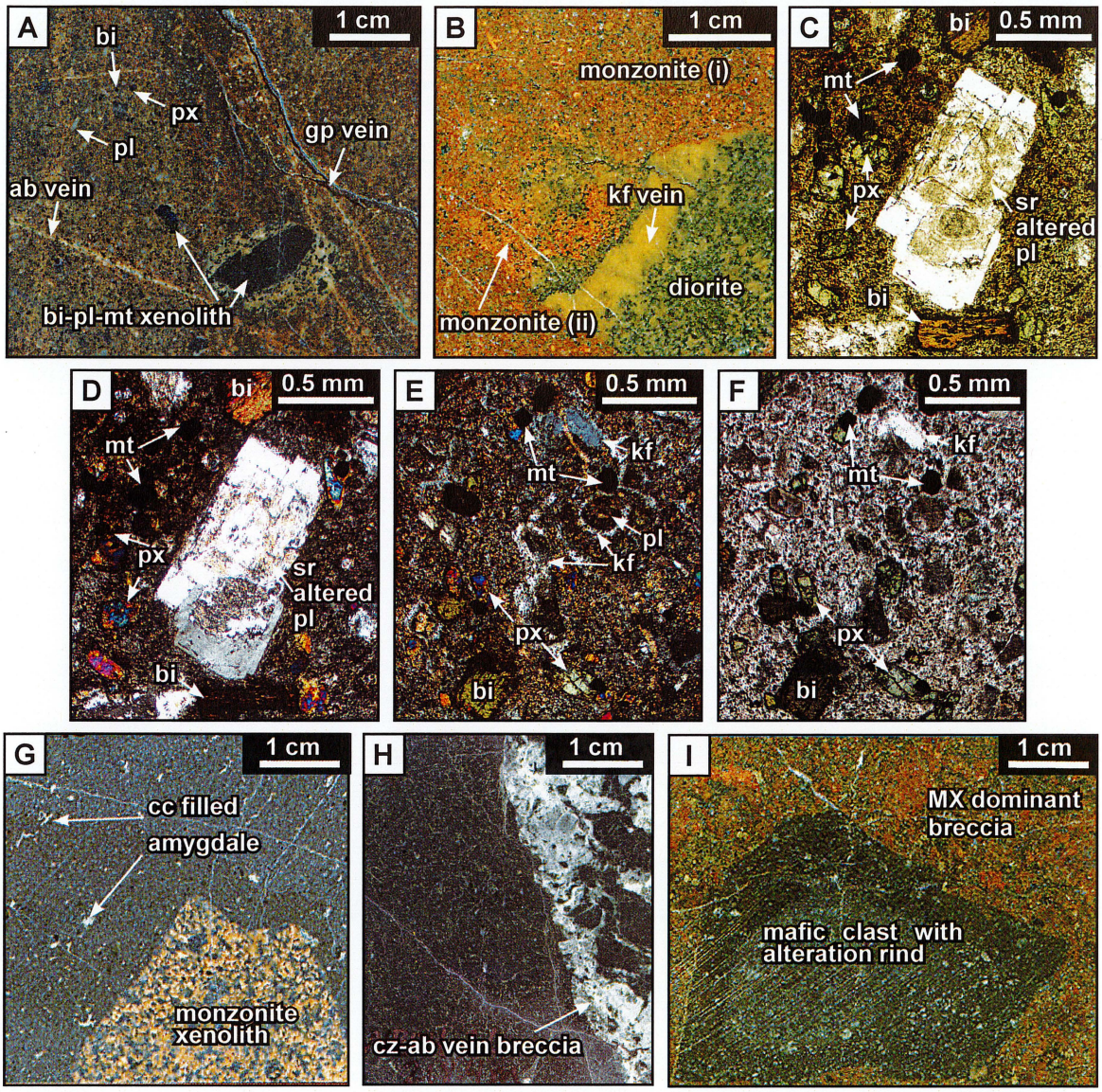

Figure 3.8 Monzodiorite-diorite and andesite-basalt of the NEZ. **A)** Plagioclase-phyric diorite dyke with a commonly observed biotite-magnetite-alkali-feldspar altered mafic xenolith. Albite veins and gypsum veins cut this dyke. Fine-grained hematite alteration has imparted a pink to brown color in hand-sample and pale to intense orange color in thin section (WB04-122 366.6 m). **B)** A variety of monzonites were observed in the NEZ. This example shows monzonite containing a complex xenolith of monzonite and diorite with a truncated K-feldspar vein (WB05-188 266.4 m). **C)** and **D)** Photomicrographs showing plagioclase porphyry. Large plagioclase phenocryst in C is zoned and has been altered by sericite (C-ppl, D-xpl, 5x, WB04-122 366.6 m). **E)** and **F)** Photomicrographs showing K-feldspar alteration rimming plagioclase crystals and bleb of clear secondary K-feldspar in groundmass of diorite. Plagioclase cores have been paritially altered to illite and smectite (E-xpl, F-ppl, 5x, WB04-122 367.1 m). **G)** and **H)** Hand samples of mafic (andesite-basalt) dykes with monzonite xenolith (WB04-152 540.1 m) and cross-cutting clinozoisite + albite vein breccia (WB04-26 218.4 m). **I)** Rare mafic clast in matrix-dominant breccia, showing syn-breccia alteration rind (WB04-108 95.6 m). Abbreviations: ab-albite, bi-biotite, bn-bornite, cc-calcite, ch-chlorite, cp-chalcopyrite, cz-clinozoisite, gp-gypsum, hb-hornblende, Kf-K-feldspar, mt-magnetite, ppl-plane polarized light, pl-plagioclase, px-pyroxene, sr-sericite, xpl-cross polarized light.

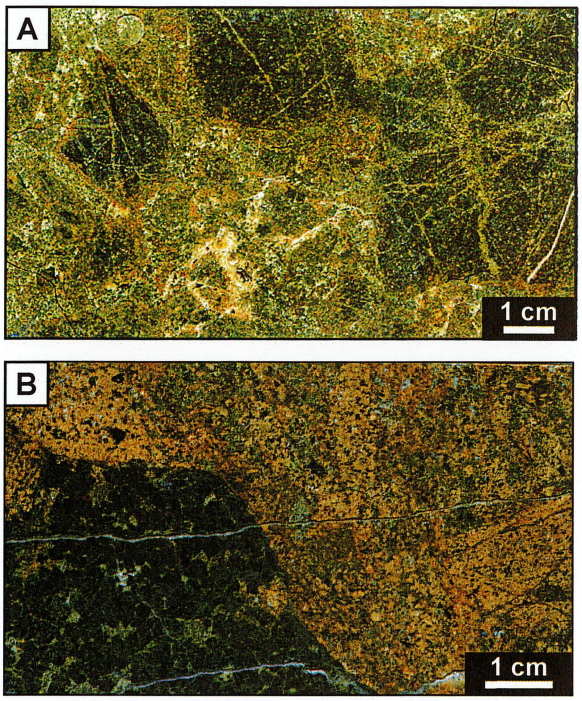

Figure 3.9 Rare mafic igneous rocks of the NEZ observed as clasts in breccia. **A)** Intense alkali-feldspar-magnetite-biotite alteration produces the brown coloration of these clasts of uncertain primary protolith in this matrix-rich and alkali-feldspar-pyroxene-garnet-calcite-chlorite cemented polymictic breccia. These clasts have K-feldspar-hematite stained (syn-breccia) alteration rinds and truncated feldspar veins (WB04-108 391.3 m). **B)** Coarse-grained pyroxene-plagioclase-magnetite clast (lower left corner) in tightly packed polymictic chalcopyrite-feldspar-chlorite ± bornite cemented polymictic breccia. This clast is interpreted to be derived from the Nicola Group volcanics (WB05-122 346.3 m).

compositionally similar monzonite dikes were observed throughout the long-section. Locally, globular clasts of aphanitic monzonite were found in breccia adjacent to monzonite dikes, these clast shapes suggest intrusion into unconsolidated breccia (Jackson, 2008; this study). Some post-breccia monzonite dikes were observed with calcite- ± gypsum-filled amygdales. Larger monzonite bodies up to 40 m thick occur outboard of the breccia body and are cut by post-breccia units (i.e. K-feldspar-phyric monzonite porphyry, monzonite, augite-phyric basalt porphyry).

Crowded to sparsely K-feldspar-phyric monzonite porphyry occur as 1–8 m thick dikes, locally up to 20 m (rarely 26 m) thick and exhibited fine-grained margins against other coherent facies. Alignment of phenocrysts is interpreted to define a flow texture and is most commonly observed in the crystal-crowded sub-facies.

Monzodiorite dikes are <0.5–2 m (rarely 4–5 m) thick and are the second least abundant variety of dike observed from the long-section. Some monzodiorite dikes have calcite- ± gypsum-filled amygdales. Isolated andesite-basalt mafic dikes which are mostly >0.2–5 m thick (isolated 12 m) are the least common dike variety.

3.4.3.1 Augite-phyric basalt porphyry

Augite-(±olivine) phyric basalt is not observed as clasts in the breccia but rather occurs exclusively as steeply-dipping >0.5–8 m thick dikes (rarely <0.2 m in thickness). These dark green to black dikes typically contain fine to coarse augite (± olivine) phenocrsyts in an aphanitic to fine-grained groundmass (Fig. 3.10A–F). The dikes are vertically extensive, have fine-grained (chilled) margins and can be distinguished from the andesite-basalt mafic dikes by the presence of abundant medium to coarse grained equant augite (± olivine) phenocrysts (Fig. 3.10B–F). Cross-cutting relationships between the olivine-bearing and olivine-absent dikes were not observed and they have therefore been grouped into one facies (Table 3.2).Both the groundmass and augite (± hornblende) phenocrysts are weakly to pervasively chlorite ± epidote altered. Some olivine phenocrysts are altered to iddingsite (Ross, 2004a). Locally, olivine phenocrysts contain magnetite-rich melt inclusions. Geochemical analyses have shown that the augite-phyric dikes are enriched in chromium and nickel and may not be genetically related to the NEZ monzonites and diorites (Ross, 2004a). Based on cross-cutting relationships, the augite-phyric basalt dikes are the youngest dikes in the NEZ. They commonly contain fault gouge within or on their margins, which provides evidence for syn- or post-dike faulting.

3.4.4 Igneous rock types–comparison with Jackson (2008)

A detailed description of the coherent facies of the NEZ was provided by Jackson (2008). Table 3.2 summarizes the major coherent facies from Jackson (2008) and compares her findings with this study. While most of the facies are consistent between the two studies, Jackson (2008) used mineralogy and texture to further subdivide the facies into additional sub-facies of post-breccia dikes. Within the monzonitic post-breccia

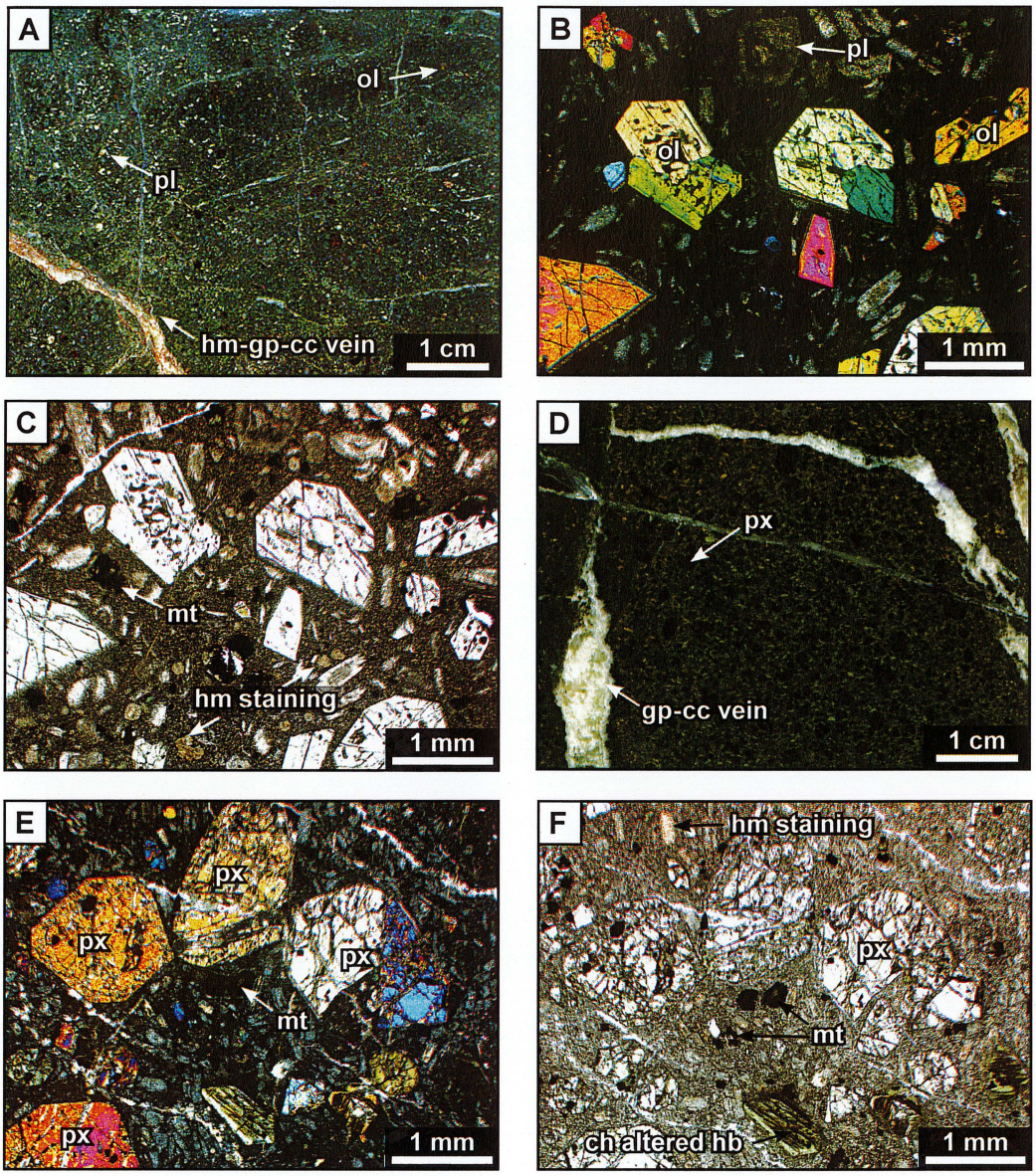

Figure 3.10 Examples of augite-phyric basalt porphyry dykes. **A)** Hand sample of plagioclase-augite-olivine-pyroxene-phyric dike cut by hematite-gypsum-calcite vein and calcite veinlets. (WB05-210 535.6 m) **B)** Photomicrograph (xpl) of sample in A showing olivine phenocrysts can be zoned and contain enclosed pockets of magnetite-rich melt. **C)** Photomicrograph (ppl) of sample in A showing disseminated magnetite and localized hematite staining in microcrystalline plagioclase groundmass. Larger plagioclase crystals in the groundmass can have sericitized cores. **D)** Hand sample of augite-phyric basalt dyke cut by calcite and gypsum vein showing coarse-grained augite phenocrysts (WB05-213-555.2 m). **E)** and **F)** Photomicrographs (xpl and ppl, respectively) of sample in D showing augite phenocrysts, microcrystalline plagioclase groundmass with disseminated magnetite, trace (<2%) chlorite altered amphibole and localized hematite staining of the groundmass. Augite phenocrysts can be zoned and twinned (xpl). Abbreviations: cc-calcite, ch-chlorite, gp-gypsum, hb-hornblende, hm-hematite, mt-magnetite, pl-plagioclase, ppl-plane polarized light, px-pyroxene, ol-olivine, xpl-cross polarized light.

dikes, Jackson (2008) identified trends of decreasing grain size, phenocrysts size and abundance and an increasing proportion of hydrous minerals over time. In the post-breccia mafic dikes, Jackson (2008) recognized increasingly mafic compositions with time.

Table 3.2 Comparison of coherent facies units observed in this study and that of Jackson (2008), with comments regarding temporal trends in the composition and texture of post-breccia dykes. Table modified from Jackson (2008).

Coherent facies (this study)	**Coherent facies (Jackson, 2008)**	**Post-breccia dykes (Jackson, 2008)**	**Trends within post-breccia dykes (Jackson, 2008)**
Monzonite	Equigranular augite-bearing monzonite	Mineralized equigranular augite monzonite Post-mineral equigranular augite monzonite	Decreasing grain size over time
K-feldspar megacrystic porphyry	K-feldspar porphyries	Megacrystic monzonite porphyry	Decreasing phenocrysts size and abundance over time in post-breccia dykes
Crowded K-feldspar monzonite porphyry		Crowded K-feldspar monzonite porphyry	
Moderate K-feldspar monzonite porphyry		Moderate K-feldspar monzonite porphyry	Increasing phenocryst aspect ratio over time in post-breccia dykes
Sparse K-feldspar monzonite porphyry		Sparse K-feldspar monzonite porphyry	
Monzonite (aphanitic)		K-feldspar trachyte porphyry	
Monzonite	K-feldspar and plagioclase porphyry	Post-mineral K-feldspar and plagioclase porphyry	
Monzonite	Hornblende-bearing equigranular monzonite	Hornblende and augite bearing equigranular monzonite	
		Hornblende bearing equigranular monzonite	
		Hornblende and biotite bearing equigranular monzonite	
		Biotite trachyte	
Monzodiorite-diorite	Plagioclase (diorite) microporphyry	Plagoclase (diorite) microporphyry	
Mafic facies (andesite-basalt)	Mafic dykes	Plagioclase-phyric mafic microporphyry	Increasing mafic composition with time in post-breccia dykes
		Plagioclase and augite-phyric mafic microporphyry	
		Augite-phyric mafic microporphyry	
Augite-phyric basalt porphyry	Mafic dykes	Augite and olivine-phyric mafic microporphyry	
		Olivine-phyric mafic microporphyry	
Augite-phyric basalt porphyry	Augite porphyry	Augite porphyry	Exploits faults; commonly contains gouge

3.5 Clastic facies

Many breccias in hydrothermal systems are classified primarily in terms of their "clast" characteristics (i.e. monomictic or polymictic, clast supported e.g. Eichenlaub and Seedorf, 2008). The distinction between matrix and cement is commonly overlooked. with all inter-clast material described as "matrix" (Davies et al., 2000; Simpson et al., 2007). Clast compositions can reflect the original distribution of host rocks and lend insight into transport processes and/or the energetics of the system. However, with a few key exceptions (i.e. juvenile magmatic clasts, accretionary lapilli; Sillitoe, 1985; McPhie et al., 1993; Davies, 2002), clast compositions and shapes generally provide little or no information regarding brecciation processes in subsurface breccia complexes. Conversely, the correct identification of cement and its timing relationships, as well as the presence and abundance of matrix, are key criteria for genetic interpretation of breccias formed in hydrothermal environments (Davies, 2002; Simpson et al., 2007; Davies et al., 2008a; Davies et al., 2008b). In addition, the cement can preserve key evidence for characterizing the hydrothermal fluids involved in the brecciation and ore formation and/or post-brecciation alteration (Simpson et al., 2007; Davies et al., 2008b). All of these features can be important in unraveling the genesis of a breccia-hosted deposit.

Table 3.3 Breccia facies definitions (modified from Davies et al., 2008).

Facies	Infill characteristics
Cement-dominated (CM)	<5% matrix
Cement and matrix (CMX)	5% < matrix <40%
Matrix-dominated (MX)	>40% matrix

An alternative to classifying breccias by clast type and associated clast characteristics is to use a classification scheme based on the infill between the clasts. This type of classification is especially applicable in mine settings where the mineralization is primarily found as breccia cement, such as in the NEZ. However, both the clasts and infill need to be fully described in order to interpret the breccia body.

In this study, the NEZ has been divided into three breccia facies based on infill, as outlined in Table 3.3. Examples are shown in Figure 3.11A–J while Figures 3.2 and 3.12 show the major distribution of CM (cement-dominated), CMX (cement + matrix) and MX (matrix-dominated) breccias facies. Table 3.4 subdivides the three breccia facies into ten sub-facies. Sub-facies were assigned according to the dominant cement(s) within each facies based on mappable hand sample characteristics (CM, CMX, MX breccias) and geometry (MX and CM-vein breccia).

3.5.1 CMX breccia facies

The CMX breccia is the most abundant facies on the long-section, although cement and matrix contents vary throughout the breccia body (Figs. 3.2 and 3.12). This facies has proven to be the most difficult to subdivide due to its highly heterogeneous infill. The CMX facies has been divided into two main sub-facies based on the dominance of sulfide minerals or gangue minerals (CMX1, CMX2; Table 3.4; Fig. 3.11F–H). Clast populations are polymictic to locally monomictic in both sub-facies and similar abundances of matrix and cement were observed (5–40% matrix and 1–15% cement; Table 3.4). Contacts between the sub-facies are most commonly gradational. A third, volumetrically minor sub-facies, CMX3 breccia, has been defined based on geometry. It consists of thin (<0.2 m), discordant, isolated breccia with abundant cement, variable matrix and angular to sub-rounded clasts (Table 3.4). Sub-facies CMX3 breccia have cross-cut the CMX1 and CMX2 subfacies.

Clasts in the CMX breccia consist mostly of variably altered equigranular monzonite wallrock, although crowded to sparsely K-feldspar-phyric monzonite porphyry, megacrystic K-feldspar-phyric monzonite, monzodiorite, and mafic clasts. One isolated clast of marble, inferred to be metasomatized limestone, was also observed (Table 3.4). No clast-within-clast textures or bedding were observed in the CMX facies (Jackson, 2008; this study). Clast shapes are predominantly sub-angular to sub-rounded but can vary greatly in shape. Some well-rounded clasts have been encountered, but were not sufficiently abundant to warrant classification as conglomerate. Angular clasts have been observed in CMX3.

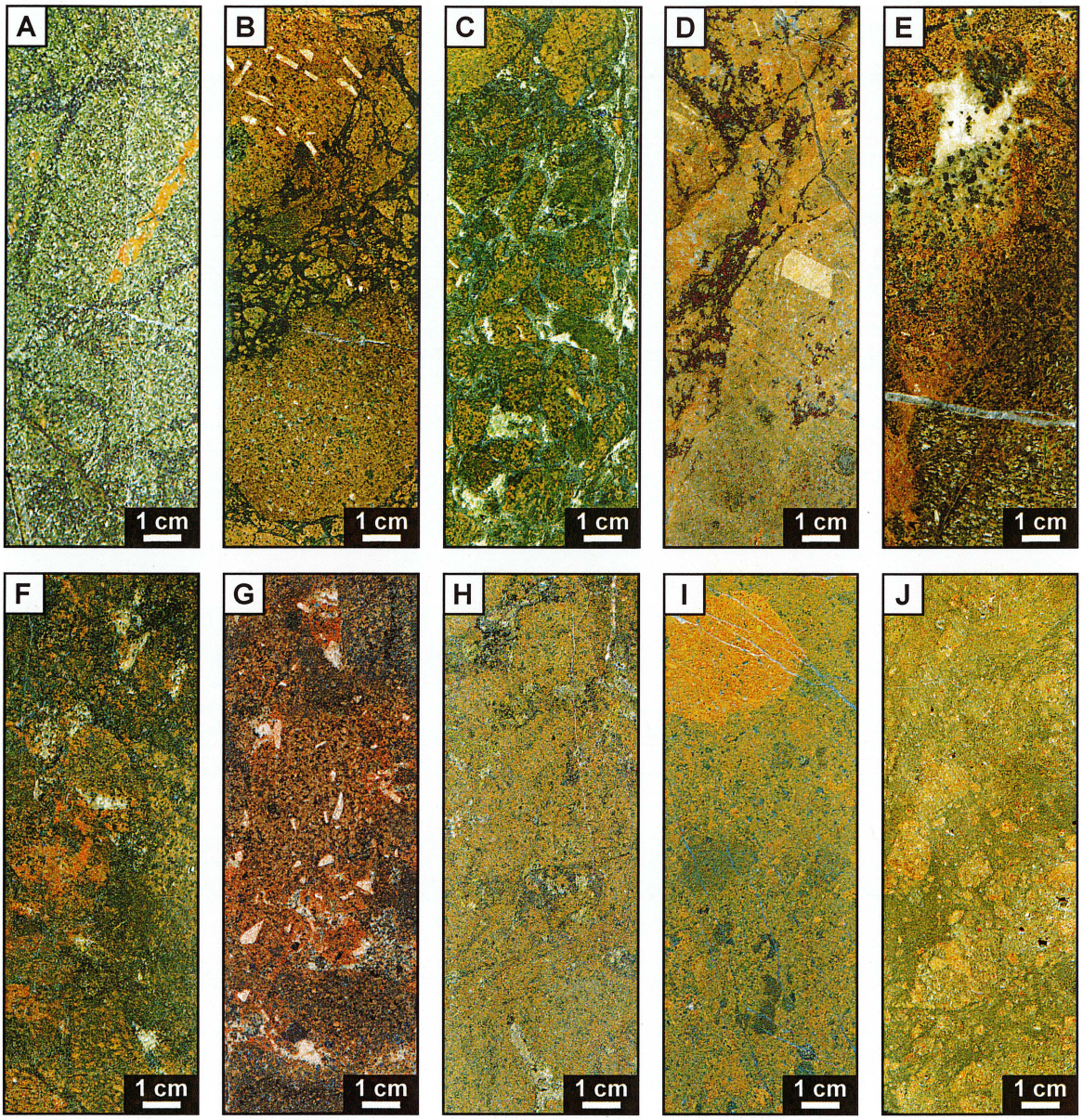

Figure 3.11 Examples of breccia facies from the NEZ and Leak Zone. Textures and cement compositions vary throughout the deposit, but the four main Cu-Fe cements are magnetite, pyrite, chalcopyrite and bornite. **A)** CM facies: magnetite-cemented jigsaw-fit breccia from the Leak Zone. Clasts are angular, have limited displacement and are intensely magnetite-actinolite-altered. One clast contains a truncated orange K-feldspar vein (WB04-77 61.0 m). **B)** CM facies: Polymictic magnetite-cemented rotated breccia (WB05-210 525.6 m). **C)** CM facies: magnetite-pyrite-K-feldspar-calcite-anhydrite-cemented polymicitic breccia with chaotic clast arrangement (WB05-210 424.3 m). **D)** CM facies: K-feldspar altered, bornite-cemented breccia (WB04-122 60.7 m). **E)** CM facies: albite-K-feldspar-magneite-calcite-cemented polymictic breccia. Clast in lower left hand corner has selective-pervasive albite alteration of feldspar crystals (WB05-213 595.7 m). **F)** CMX facies: albite-K-feldspar-magnetite-calcite-chalcopyrite-garnet + matrix cemented polymictic breccia (WB04-108 329.4 m). **G)** CMX facies: polymictic albite-anhydrite-prehnite-magnetite-bornite + matrix cemented breccia (WB04-111 248.8 m). **H)** CMX facies: epidote-magnetite-calcite-chalcopyrite-garnet-hematite + matrix cemented monomictic breccia (WB04-31 82.5 m). **I)** MX facies: polymictic, chaotic clast arrangement, matrix-dominant breccia (WB04-108 79.2 m). **J)** MX facies: monomictic, chaotic clast arrangement, broken K-feldspar crystal and pyrite-matrix dominant breccia. This breccia has been interpreted as a healed fault due to the shear texture in the top portion of the image and its geometry (WB04-108 200.4 m).

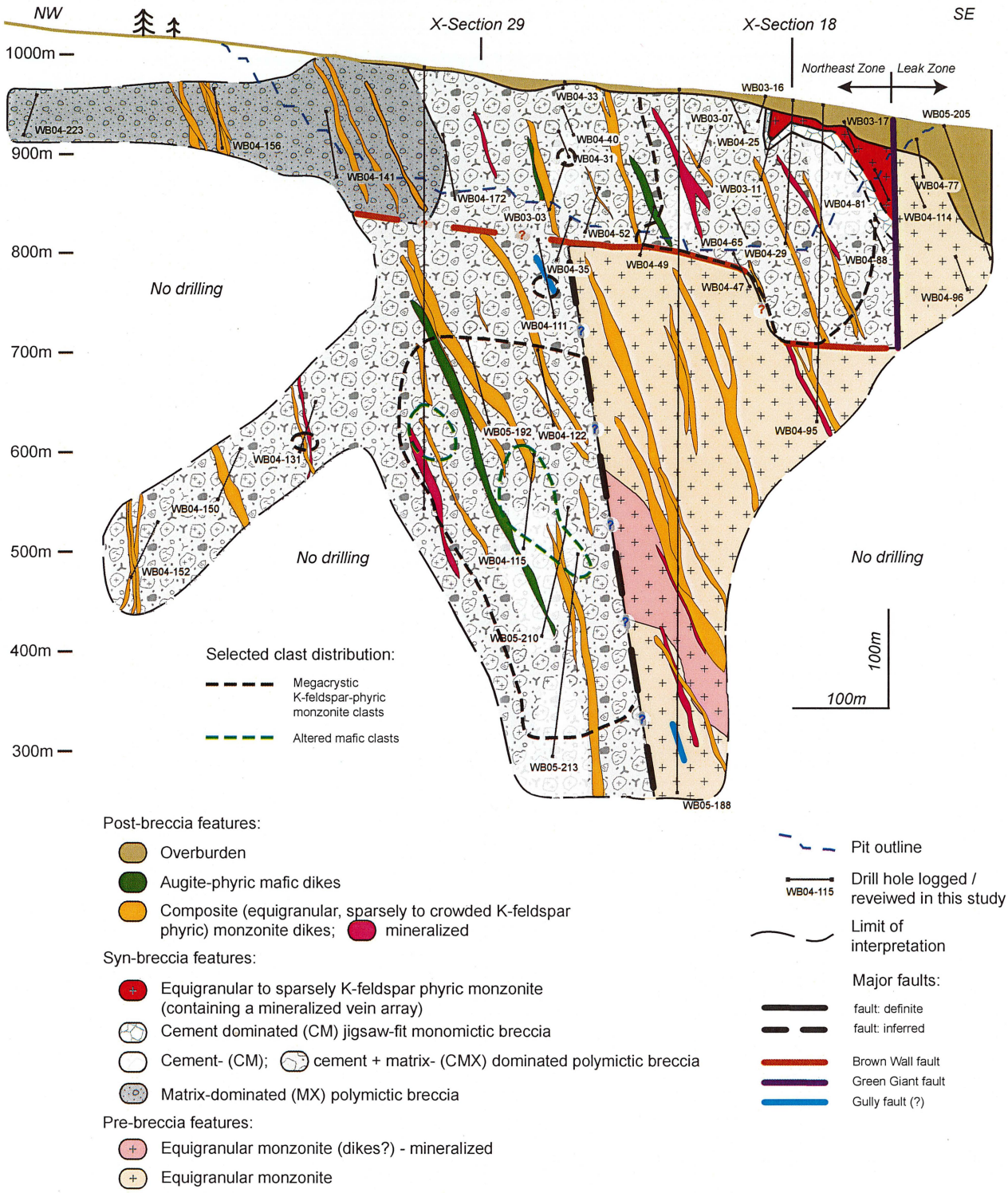

Figure 3.12 Megacrystic-K-feldspar-phyric monzonite porphyry and "altered mafic" clast distribution over geology of the long-section with current structural interpretation and inferred or modeled geologic contacts (faults?, breccia margin?) marked by "?". Post-breccia intrusions are representative of multiple dyke-swarms and abundant intrusions too small to be shown at this scale.

Table 3.4 Summary of breccia facies characteristics from the long-section. Minor and/or accessory cement minerals are not present in all samples.

Facies	Sub-facies name	Dominant cement	Minor/ accessory cement[1]	Internal clast organization	Clast types & abundance	Clast size & shape	Matrix abundance & size	Cement abundance & habit	Open space	Example location	Comments
Cement–dominated breccia (CM)	CM1 chalcopyrite-cemented breccia	cp ± mt, bn, cb, py, gt	ab, bi, kf, bn, ch, sr, cc, gt, ep, mt, hm, py	rotated, occasional jigsaw (hard to determine in areas due to intensely overprinted alteration)	eMz 90–100%, isolated 80% Kmega-mz 0–5% sp-Mz 0–5%, isolated 20%	5–8 cm + megaclasts up to 1m rounded to sub-angular, isolated angular	1–4% mud ± sand sized cement	1–20% massive, open space infill, some coarse euhedral grains, locally symmetric infill	none	WB04-188 50.8–61.05 m WB04-188 20–26 m	includes high grade
	CM2 bornite-cemented breccia	bn, cp ± mt, ab	cb, kf, py, ab, ep, ch, hm, ah, gt, hm	rotated to chaotic, locally jigsaw	eMz 70–95% Kmega-mz 0–10% sp-Mz 0–5% mafic 5–20%	2–10 cm + megaclasts up to 1.2 m rounded to sub-angular, locally angular	0–5% mud ± sand sized cement	5–15% locally 20–30% massive, open space infill, some coarse euhedral grains, locally symmetric infill	none	WB04-122 309.1–330 m WB04-188 95.5–142 m	includes high grade
	CM3 K-feldspar-cemented breccia	mt, kp ± ab, ah, py	ep, ch, ab, cb, cp, py, bi, ah, hm	rotated to chaotic, isolated jigsaw-fit	eMz 40–90%, isolated 100% Kmega-mz 10–60%, isolated <5% sp-Mz 0–50% md/d 40–60%, isolated <5% mafic rare	5–12 cm + megaclasts up to 2 m sub-rounded to sub-angular, isolated angular	0–3% mud ± sand sized cement	10–30% locally up to 40% massive, open space infill, some coarse euhedral grains, locally symmetric infill	none	WB05-213 590–675 m WB05-210 485–49 m	no high grade
	CM4 magnetite-cemented breccia	mt ± py, cb, cp, ab, ch	bn, cp, kp, cb, py, bi, ep, ah, ch, hm	rotated to chaotic, locally jig-saw fit	eMz 70–100% Kmega-mz rare–30% sp-Mz 0–15% md/d 0–rare mafic 0–rare	0.2–20 cm + megaclasts up tp 2 m angular to rounded	0–5% mud ± sand sized cement	20–30% massive, open space fill, some coarse euhedral grains, locally symmetric infill	none	WB05-213 544–559 m WB05-210 517–536 m	includes some high grade

Table 3.4 continued

Facies	Sub-facies name	Dominant cement	Minor/ accessory cement[1]	Internal clast organization	Clast types & abundance		Clast size & shape	Matrix abundance & size	Cement abundance & habit	Open space	Example location	Comments
Cement- and matrix-bearing breccia (CMX)	CMX1 sulfide and matrix breccia	cp ± cb, bn, mt, py, bi, kp	ep, mt, gt, cb, cp, bn, ch, ab, py, kp, bi, ser, do, hm, ah	rotated to chaotic, locally jigsaw in areas	eMz Kmega-mz cr-Mz mod-Mz sp-Mz md/d mafic	85–100%, occassional 40–60% 0–30%, occassional 40–60% rare 0%, isolated 40–60% rare–10%, isolated 40%, 100% 0–5% rare–10%	0.2–30 cm + megaclasts up to 1 m sub-rounded to sub-angular, occassionally angular	5–30% mud and sand - sized cement	1–15% fine grained, massive, occassional open space infill, locally symmetric infill	rare vugs	WB04-111 252.8–255.5 m WB04-31 79–109 m	mostly low to high grade
	CMX2 gangue and matrix breccia	ep / ch / cb / gt ± bi, cb, mt, ab, kf, ah	cp, py, cb, hm, mt, kp, ep, gt, ch, ah	rotated to chaotic	eMz Kmega-mz cr-Mz mod-Mz sp-Mz md/d mafic	70–95%, isolated 40–60% 0–5% 0–20% 0–30%, isolated 40–60% 0–20% 0–5% 0–5%	0.2–30 cm sub-rounded to angular, globular in areas	5–40% mud and sand - sized cement	1–10% fine grained, massive, occasional open space infill	rare vugs	WB0-108 324.3–443.8 m	no high grade
	CMX3 vein breccia	ab, cz, gy/ ah, cc	do, ze, ph, qz, ch, hm, ah	rotated to jigsaw to chaotic	various monzonite + breccia	n/a	0.2 mm–6 cm angular to subangular	<5–10% mud - sand sized	10–50% massive, banded, limited symmetrical infill, can be bladed	isolated	WB04-26 68.1 m WB04-108 6316.1 m WB04-27 177.6 m	rare mineralized clasts, discordant geometry, slightly normal graded mx
Matrix-dominated breccia (MX)	MX1 matrix breccia	n/a	cb, ep, mt, cp, bi, py, kp, ch, hm, kp, gt, py, ab, bn	chaotic, isolated rotated and jigsaw-fit	eMz Kmega-mz sp to mod-Mz mod-Mz md/d mafic	80–100%, isolated 50% 0–10%, isolated 40–80% 0–10% 0–<5% 0–<10% 0–15%	0.2–10 cm, can be up to 15 cm + isolated megaclast up to 1.5 m rounded to sub-angular, globular	15–50% mud and sand-sized	0–10% fine grained, rarely coarse grained, blebs, massive	none	WB04-108 76.5–104.5 m WB03-03 133–143 m	includes isolated pockets of grade and disseminated cp and py
	MX2 healed fault breccia	n/a	py, sr, cc, hm, chl, sf, ab, cz, sr	chaotic	eMz Kmega-mz sp-Mz md/d	90–100% 0–100% 0–100% 0–<5%	0.2–<4 cm, can be up to 10 cm in areas	20–>50% mud to coarse sand-sized, fabric common	5–50% fine grained to coarse grained, blebs, massive	none	WB04-108 200.4 m WB04-95 225.3 m	limited intervals and mineralized clasts, discordant geometry, can have shear fabric

Mineral abbreviations: ab-albite, ah-anhydrite, ak-ankerite, ap-apatite, at-actinolite, bn-bornite, bt-biotite, cb-carbonate, cc-calcite, ch-chlorite, cp-chalcopyrite, cz-clinozoisite, do-dolomite, ep-epidote, gt-garnet, gy-gypsum, hm-hematite, kf-K-feldspar, mt-magnetite, pr-phrenite, px-pyroxene (augite), py-pyrite, qz-quartz, sr-sericite, ze-zeolite (laumontite).

Clast type: eMz-equigranular to crystal-crowded monzonite, Kmega-mz-megacrystic K-feldsapr-phyric monzonite, mafic-various mafic facies, md/d-monzodiorite/diorite, cr-Mz-crowded K-feldspar-phyric monzonite, mod-Mz-moderately K-feldspar-phyric monzonite, sp-Mz-sparsely K-feldspar-phyric monzonite

The CMX1 and CMX2 breccias are massive, poorly sorted and have a chaotic clast arrangement. Clast sizes ranged from 0.2 to 30 cm in CMX1 and CMX2 and from 0.2 to 6 cm in CMX3 breccia, with some megaclasts of approximately 1 m diameter in the former two subfacies. The average largest clast size can vary over tens of meters, rarely meters (see excerpt from log WB04-155, Fig. 3.4), down hole. Clast arrangements in CMX3 breccia vary from jigsaw-fit to rotated to chaotic.

The CMX breccias contain ubiquitous hydrothermal cements and altered matrix, have undergone moderate to intense hydrothermal alteration, and display significant textural variations over short distances. The cement in CMX1 and CMX2 ranges from 1 to ~15 percent (i.e. clast-supported), whereas CMX3 breccia can have >50 percent cement locally (cement + matrix-supported).

Cement textures are commonly massive, although symmetrical bands that have infilled voids are observed locally. When present, individual bands most commonly can be traced inside the former void, rather than rimming the clast. Symmetrically-textured cement is most common in areas with less abundant matrix. Cement mineralogy includes: K-feldspar, magnetite, biotite, actinolite, albite, garnet, bornite, chalcopyrite, pyrite, calcite, epidote, chlorite, anhydrite, hematite, dolomite, phrenite, zeolite and very rare galena and sphalerite. Vein breccias are dominated by calcite, albite and clinozoisite but also contain dolomite, zeolite, prehnite, quartz, chlorite, hematite and anhydrite.

CMX1 and CMX2 breccia contain distinct areas of CM and MX facies (described below). The abundance of matrix is variable in the main breccia body from 5 to 40 percent. Matrix textures are massive throughout the main breccia body (Jackson, 2008 and this study).

3.5.2 CM breccia facies

CM breccia was observed in three settings (Figs. 3.2, 3.12), i) along the upper southeast corner of the breccia at the contact between coherent monzonite and the CMX breccia body, ii) as isolated pods <1 m to >10 m in size in the CMX breccia, and iii) as a <3 m isolated pod of CM breccia in coherent host rock in the Leak Zone (east of the Green Giant fault; WB04-77 60-62 m; Figs. 3.2, 3.11A). CM breccia textures and cement compositions vary throughout the deposit, with some areas exhibiting open space fill textures. The four main sulfide- and oxide-bearing CM sub-facies are chalcopyrite- (CM1; Fig. 3.11C), bornite- (CM2; Fig. 3.11D), K-feldspar- (CM3; Fig. 3.11E) and magnetite-cemented breccia (CM4; Fig. 3.11B; Table 3.4). Contacts between these sub-facies are gradational.

The CM breccia in the upper southeast corner of the deposit and the pod of breccia in the Leak Zone (Fig. 3.2) contain clasts that are dominantly angular to sub-angular, and commonly occur in jigsaw-fit to rotated arrangements (Fig. 3.11A). Conversely, pods of CM breccia in the CMX breccia have angular to sub-angular clasts with a jigsaw-fit arrangement in some areas, and sub-angular to sub-rounded clasts in chaotic clast arrangements in other areas. The CM breccias with angular to sub-angular clasts are dominantly monomictic with clasts of equigranular monzonite. The CM breccias with sub-angular to sub-rounded clasts are polymictic to monomictic. All clast types observed in the CMX breccia are also present in the CM breccia, with the exception of the sparsely-K-feldspar-phyric monzonite (Table 3.4). However, each CM sub-facies has a narrower range of clast compositions than the CMX facies (Table 3.4). The greatest proportion of mafic clasts (5–20%) was observed in the CM2-bornite sub-facies on the long-section. No clast-within-clast textures (Jackson, 2008; this study) or bedding were observed in the CM breccia. Clast sizes ranges from 0.2 mm to 2 m, however most clasts are 2–20 cm in diameter.

The CM breccia infill is similar in composition and texture to that observed in the CMX breccias, with the exception of matrix content (0–5% compared to 5–40%; Table 3.4). The abundance of cement in the CM breccia ranges from 1 to ~30 percent of the breccia (i.e. clast-supported). Several cement minerals are typically present, although areas of dominantly one or two minerals (i.e. magnetite, bornite ± chalcopyrite) are more common in the CM breccia than CMX breccia. The cement textures vary from massive to symmetrical bands infilling voids as explained in the CMX breccia, however, symmetrical banding is more common in the CM facies than the CMX facies.

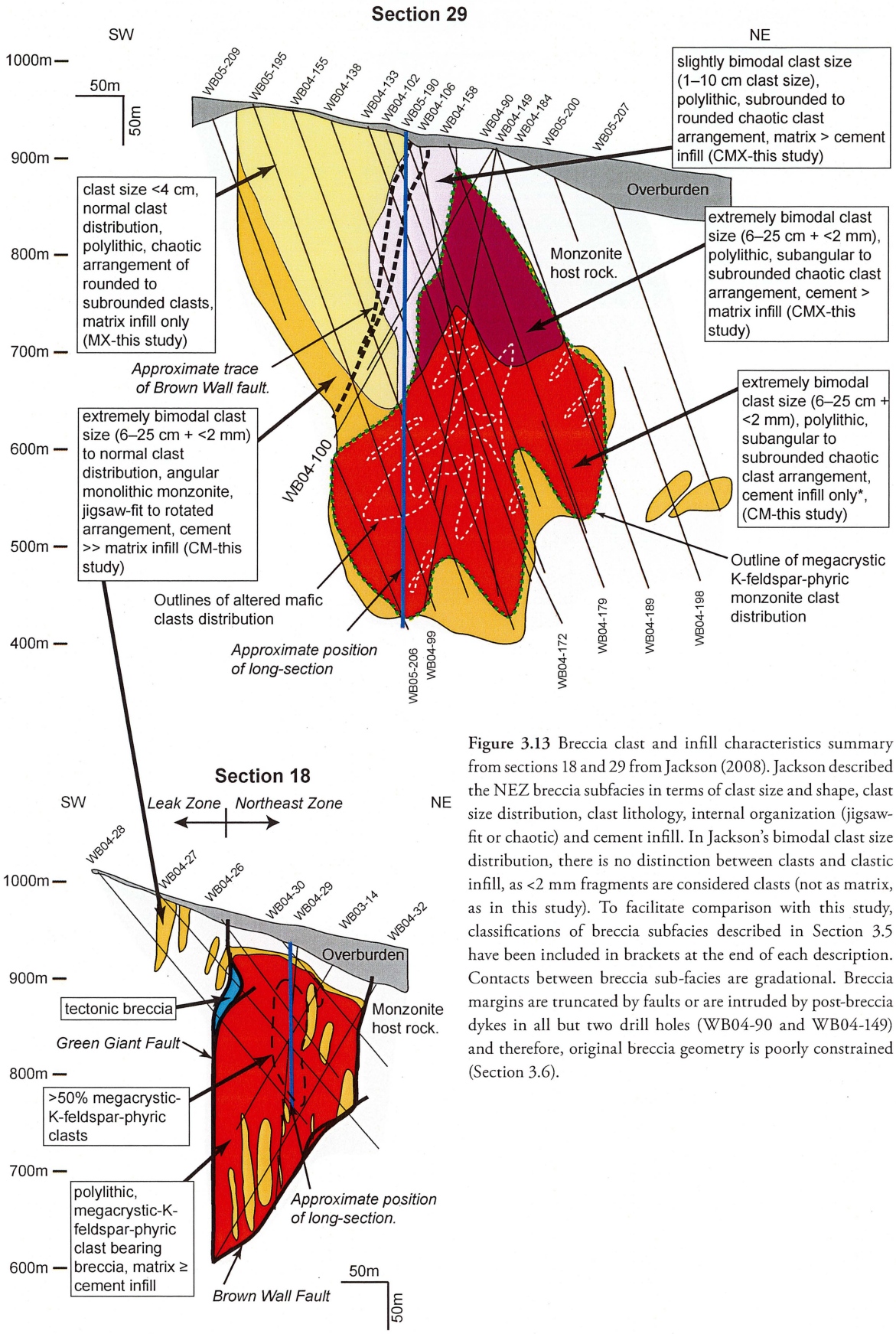

Figure 3.13 Breccia clast and infill characteristics summary from sections 18 and 29 from Jackson (2008). Jackson described the NEZ breccia subfacies in terms of clast size and shape, clast size distribution, clast lithology, internal organization (jigsaw-fit or chaotic) and cement infill. In Jackson's bimodal clast size distribution, there is no distinction between clasts and clastic infill, as <2 mm fragments are considered clasts (not as matrix, as in this study). To facilitate comparison with this study, classifications of breccia subfacies described in Section 3.5 have been included in brackets at the end of each description. Contacts between breccia sub-facies are gradational. Breccia margins are truncated by faults or are intruded by post-breccia dykes in all but two drill holes (WB04-90 and WB04-149) and therefore, original breccia geometry is poorly constrained (Section 3.6).

3.5.3 MX breccia facies

MX breccia has been divided into two sub-facies based on their geometries and textures. The MX1 breccia is a large, poorly constrained breccia body with abundant massive matrix. MX2 breccia occurs as isolated, narrow (generally <1 m) intersections of breccia with a sheared matrix texture. The MX breccias are distinct from CM and CMX breccia in terms of their average largest clast size, and matrix abundances. Clasts generally range from 0.2 mm to 15 cm in the MX breccia (average 5 cm) but isolated mega-clasts (up to 1.5 m) have been observed. Jackson (2008) described this breccia as "fine-grained breccia" (Fig. 3.13). Clast compositions are similar to those of the CMX and CM breccia facies, although overall, the MX breccia has a high percentage of mafic clasts (0–15%), similar to CM2-bornite sub-facies: 5–20%.

The MX1 breccia is observed as a large body in the northern portion of the long-section and in restricted pods with gradational contacts in the CMX breccia (Fig. 3.11I). Infill is massive with <15% of hydrothermal cement dispersed throughout the matrix (Table 3.4). Clasts are chaotically arranged and generally comprise >50 percent of the breccia (i.e. clast-supported), although local sections of MX1 can be matrix-supported. Clast-within-clast textures and surface-derived clasts (e.g. tree trunks) were not observed.

The MX2 is a rare, volumetrically minor sub-facies with thin (<0.2 m), discordant geometry (Fig. 3.11J). MX2 breccia is matrix-rich with abundant small rounded clasts (<4 cm on average), generally in a chaotic arrangement. It contains limited to abundant (1–50%) cement locally (Fig. 3.11J). Some examples exhibit a shear fabric (Fig. 3.11J) and have rare mineralized clasts. The MX2 sub-facies is volumetrically too small to be shown on Figures 3.2 and 3.12.

3.5.4 Clastic facies–comparison with Jackson (2008)

Jackson (2008) recorded breccia clast characteristics from cross-sections 18 and 29 in the southern and northern portions of the NEZ, respectively (Fig. 3.2). Rather than use largest average clast size and infill, as in this study, Jackson (2008) focused on grain size distribution and differences in grain size between different lithologies to lend insight into brecciation processes. Jackson (2008) identified two clast distribution populations; normal (no break in grain size between the largest and smallest clast) and bimodal (two distinct clast size populations). Matrix was not included in Jackson's (2008) assessment; clastic infill <2 mm in size was included in the overall clast size distribution and treated as fine-grained clasts.

Clast observations from sections 18 and 29 are generally consistent with, and complement those from the long-section, despite the difference in Jackson's (2008) approach to breccia classification. Excluding the presence of mega-clasts, the average clast size from Jackson's (2008) study is 6–25 cm, with a discrete zone on the western side of section 29 where the average clast size was <4 cm. This current study observed an average largest clast size of 3–20 cm with an area in the north (MX breccia) where clast size is on average <5 cm. A summary of the clast characteristics from section 18 and 29 are presented in Fig. 3.13.

Infill character was divided by Jackson (2008) into "chemical" infill only (equivalent to this study's CM breccia), chemical infill > clastic infill (CMX equivalent), clastic infill > chemical infill (CMX equivalent), and clastic infill only (MX equivalent). The chemical infill-only breccia (CM equivalent) was most prevalent near the base of the preserved breccia body on section 29 (Fig. 3.13). Clastic infill (MX equivalent) and clastic > chemical infill (CMX equivalent) breccias dominated in the upper portion of the breccia on section 29. These observations correlate well with locations of MX, CMX and pods of CM breccia on the long-section (Fig. 3.12).

A limited volume of igneous-cemented breccia, restricted to the margins of dikes cutting breccia were observed by Jackson (2008), who reported them as unrelated to the main breccia body. In some cases, mafic dikes (augite ± plagioclase ± olivine "basalt") with complex intrusive margins against other units were observed to have formed basalt-cemented breccias with clast size <1 cm. In a few cases these breccias exhibited grading parallel to the dyke margin (Jackson, 2008).

3.5.5 Key clast populations

Two key clast composition populations, altered mafic clasts and megacrystic-K-feldspar-phyric clasts

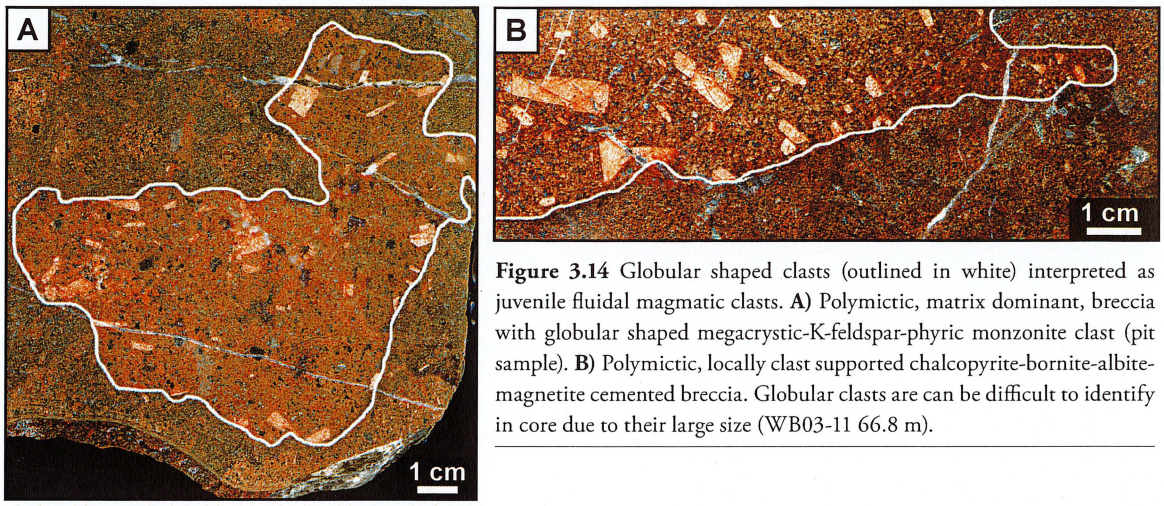

Figure 3.14 Globular shaped clasts (outlined in white) interpreted as juvenile fluidal magmatic clasts. **A)** Polymictic, matrix dominant, breccia with globular shaped megacrystic-K-feldspar-phyric monzonite clast (pit sample). **B)** Polymictic, locally clast supported chalcopyrite-bornite-albite-magnetite cemented breccia. Globular clasts are can be difficult to identify in core due to their large size (WB03-11 66.8 m).

were identified by Jackson (2008). The latter was also highlighted by Rees et al. (2005) and Simpson (2005). The distribution of altered mafic clasts (in amongst other clast types), was observed to define a tabular body, centrally located in the breccia on section 29 (Fig. 3.13). Jackson (2008) interpreted this body of mafic clasts to be representative of a mafic host rock unit. Altered mafic clasts were not identified in section 18.

In this study, altered mafic clasts were identified in a limited area on the long-section, comprising up to 10 percent of the breccia in isolated intervals (Fig 3.12). These clasts are interpreted to be the same as those described by Jackson (2008) on section 29. The location of these clasts on the long-section corresponds to the population location described by Jackson (2008) on section 29 (Fig. 3.13), although Jackson observed up to 90 percent altered mafic clasts in the breccia locally, compared to this study in which altered mafic clasts never comprised more than 20 percent of the breccia.

3.5.5.1 Globular (lobate) shaped clasts

Three populations of globular-shaped clasts were identified in the NEZ: i) monzonite (including aphanitic monzonite; Jackson, 2008 and this study), ii) crowded-K-feldspar- and augite-phyric monzonite and iii) megacrystic-K-feldspar-phyric monzonite (Fig. 3.14). The latter is the second key clast composition identified by Jackson (2008).

Limited examples of monzonite and crowded K-feldspar- and augite-phyric monzonite globular shaped clasts were observed adjacent to cross-cutting coherent units of the same composition. These clasts are interpreted to be blebs separated from the dikes during their intrusion into a poorly consolidated breccia body. These may be genetically related to Jackson's (2008) igneous-cemented breccia.

Significant zones of sub-angular to rounded megacrystic-K-feldspar-phyric monzonite clast-bearing breccia, including some clasts with delicate, globular (lobate) shapes, were observed in the pit and drill core from the NEZ (Fig. 3.12 and 3.13; Rees et al., 2005; Jackson, 2008; this study). Globular-shaped clasts were <10 cm to >1 m in size. Most of the megacrystic-K-feldspar-phyric monzonite clasts were observed in the southern portion of the NEZ, where Jackson (2008) reported sub-angular to sub-rounded and globular-shaped clasts of megacrystic-K-feldspar-phyric monzonite in sections 29 and 18, making up 10 to 20 percent, locally 1 to >90 percent of the breccia (Fig. 3.13). On the long-section, most megacrystic-K-feldspar-phyric monzonite clasts (up to 70% locally) were observed in the deep north portion of the section (drill holes WB05-210 and -213; Fig. 3.12) and in the center of the southern shallow breccia (drill holes WB04-29 and -95; Fig. 3.12). The highest percentage of megacrystic-K-feldspar-phyric clasts was found in the CMX1-chalcopyrite + matrix breccia, but megacrystic-K-feldspar-phyric clasts were also observed in the CM3-K-feldspar breccia, and in isolated areas of the MX1-matrix and MX2-healed fault breccias.

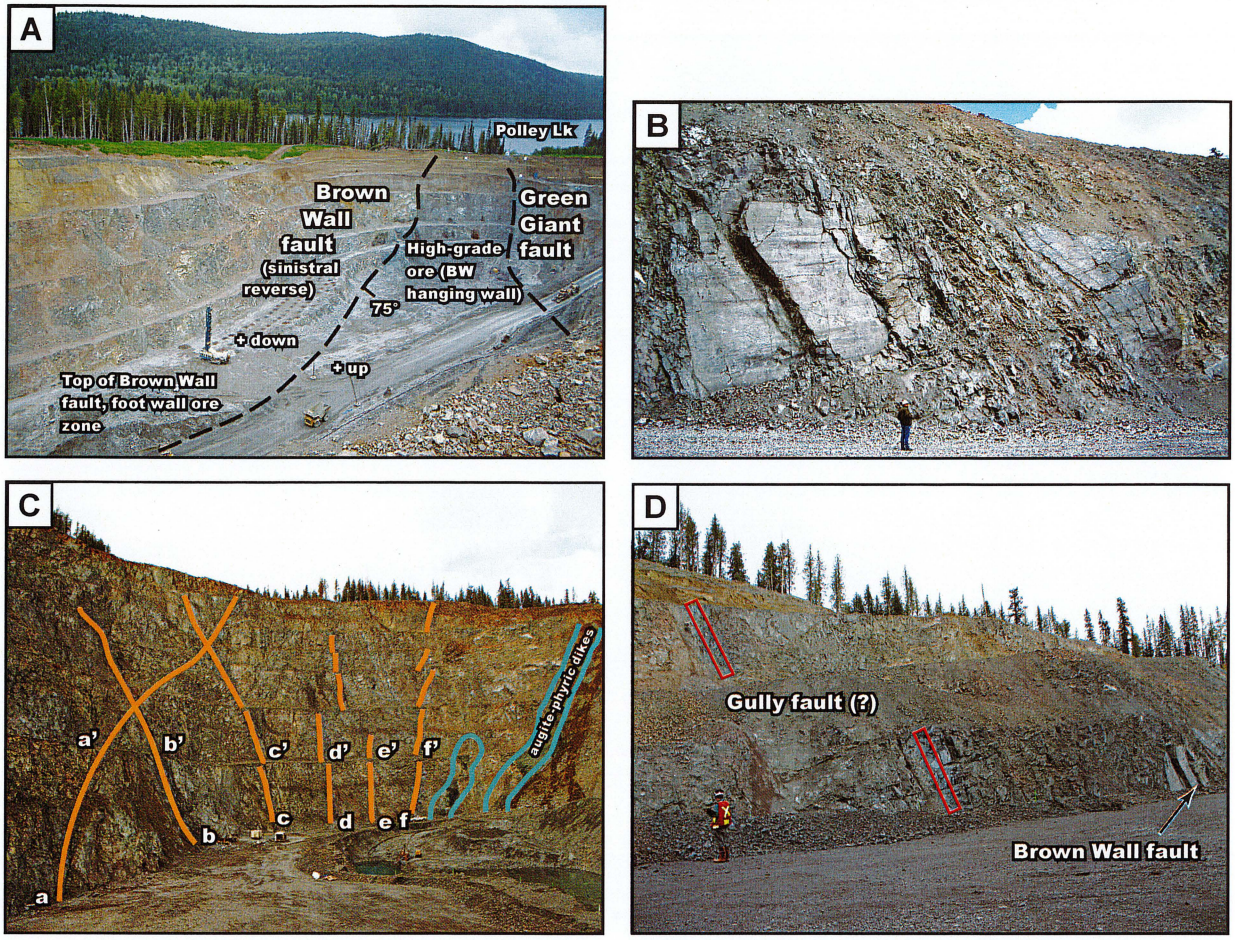

Figure 3.15 Photos of the NEZ showing fault exposures. **A)** Looking east-southeast across the south end of Wight Pit (NEZ). Photo, fault traces and annotation courtesy of Imperial Metals (unknown date). **B)** Looking north-northeast at a portion of the northeast wall of the Wight Pit containing well exposed southern portion of the Brown Wall fault. Note variable dip of the fault plane and near-horizontal slickenslides that indicte strike-slip motion. Photo courtesy of Imperial Metals (September, 2007). **C)** Looking north-northwest at wall of Wight Pit (October, 2007). Highlighted faults (a-f) in this wall were measured to identified a northern extension of the Brown Wall fault in the southern portion of the pit (photo B). A large tension gash was observed in a pit level step that corresponds with fault B and near-horizontal slickenslides were observed in fault d. Fault d was the closest to the modeled Brown Wall fault north extension. **D)** Looking north-northeast at the central portion of the northeast pit wall. A fault (030/78SE, red squares), interpreted as the Gully fault, was observed in the north-eastern wall of the pit at the approximate location, with matching strike and dip, of the projected breccia boundary at depth. However, a similar fault was not evident on the south-western wall of the pit.

3.6 NEZ structure

Two major faults are known to have disrupted the long-section and section 18: the Brown Wall fault (115°/74° SW), which trends sub-parallel to the long-section; and the Green Giant fault (95°/90°), which has cut the southeastern end of the deposit (Figs. 3.1, 3.2, 3.13 and 3.15A–B). R. Tosdal (pers. comm., 2008) speculated that the Brown Wall fault is a splay from the Green Giant fault. A third fault, the Gully fault, has been observed at surface but is unconstrained at depth. It may separate the breccia complex from coherent units on the long-section (Figs. 3.1 and 3.2).

Six faults of unknown displacement were mapped in the northwestern wall of the Wight Pit in order to extend the Brown Wall fault trace (Fig. 3.15C). None of these faults readily matched the dip or the strike of the southern portion of the Brown Wall fault. However, the NEZ is known to contain a plethora of faults with commonly en echelon or anastomosing strikes, which can vary by 20°–30° over 20 m (Taylor, 2004). Subsequent to the fieldwork conducted in this study, Imperial Metals created a three-dimensional ore shell model from all blast hole and drill hole assay data

of the NEZ. A linear break in the ore shells, observed to correlate with the southern portion of the Brown Wall fault, extended into the northern portion of the pit. This linear break has been interpreted by Imperial Metals as the northern extension of the Brown Wall fault, and is shown in Figures 3.1, 3.2, 3.15A and on Figure 3.15C as fault "d".

A fault is inferred to separate breccia and coherent rock on the long-section in the central portion of the deposit (Figs. 3.1, 3.2). Supporting evidence includes the following observations. A fault (030/78SE) was observed in the northeastern wall of the pit (footwall of the Brown Wall fault; Fig. 3.15D). This fault was identified at surface by Imperial Metals as the Gully fault (Rees et al. 2006). The Gully fault is not exposed in the southwestern wall of the pit, the hanging wall to the Brown Wall fault, and so Imperial Metals geologists are skeptical regarding its significance. Two isolated intersections of fault gouge (≥6 m in length) in drill holes WB04-111 (178.6–184.8 m) and WB05-188 (650.3–658.6 m) could be intersections of the Gully fault at depth. Detailed inspection of drill core that intersects the area in question is required to test the hypothesis.

Comparison of the thickness of post-breccia dikes in long-section (narrow) versus cross-section (wide) suggests the post-breccia dikes intruded northeast-trending planes of weakness across the breccia body. This orientation is consistent with the Gully fault as well as one of the two predominate regional structural orientations with a sinistral (to slightly oblique) sense of movement (i.e. South Wishbone fault, Figs 3.4, 3.6A; Rees et al., 2006).

Abundant narrow faults (<0.2–1 m wide) containing gouge and/or cataclasite were observed in drill core and in the open pit. None of these smaller faults have been plotted on the long-section as they cannot be correlated between drill holes. Most of the augite-phyric basalt dikes contain fault gouge and cataclasite (Jackson, 2008 and this study) indicating post-mineralization displacement.

Breccias are commonly localized along fault zones or other structural discontinuities (Baker et al., 1986; Sibson, 1986; Jébrak, 1997). However, the trace of the principal fault need not mimic the geometry of the breccia complex (Mitcham, 1974). Faults may be reactivated subsequent to breccia formation and with differing senses of movement, complicating the understanding of relationships between breccias and faulting (Corbett and Leach, 1998). It is tempting to infer that either the Green Giant fault, Brown Wall fault, Gully fault or some combination thereof localized brecciation; however, no definitive evidence of pre- or syn-breccia fault activity has been identified for any of these structures.

Abundant evidence for post-mineral movement along the Green Giant and Brown Wall faults is available in the open pit (Fig. 3.15A and B). Slickenslides observed on the face of the Brown Wall fault indicate strike-slip motion (Fig. 3.15B) and Imperial Metals have interpreted a dip-slip displacement such that the east side has moved down with respect to west with approximately 100–150 m vertical movement (Rees et al., 2005). The Green Giant fault is an approximately vertical fault zone and Imperial Metals geologists have interpreted sinistral strike-slip movement (Rees et al., 2005). These two faults have disrupted the mineralogical and isotopic zonation patterns within the breccia complex (Chapters 4 and 5) and have produced a wedge of mineralized breccia bounded by unmineralized monzonite in the shallow southern portion of the NEZ. While the estimated amount of displacement is unknown on both faults, it is likely to have been significant (at least several hundred meters) given that the missing portion(s) of the ore body have yet to be identified. Bailey (2004b) noted that the overall structural setting of the NEZ is transpressional, consistent with the regional structural architecture that most likely reflects Cretaceous fault movements.

3.7 Discussion and interpretation

3.7.1 Breccia geometry

Breccia geometry analysis is best carried out at large scales, in outcrop or open pits (Davies, 2002). If this scale of observation is not available or only partly available, such as in the case of the current study, then contact relationships can be inferred from logged breccia characteristics. Contacts between breccia pipes and their host rocks are often abrupt and marked by a narrow (<5

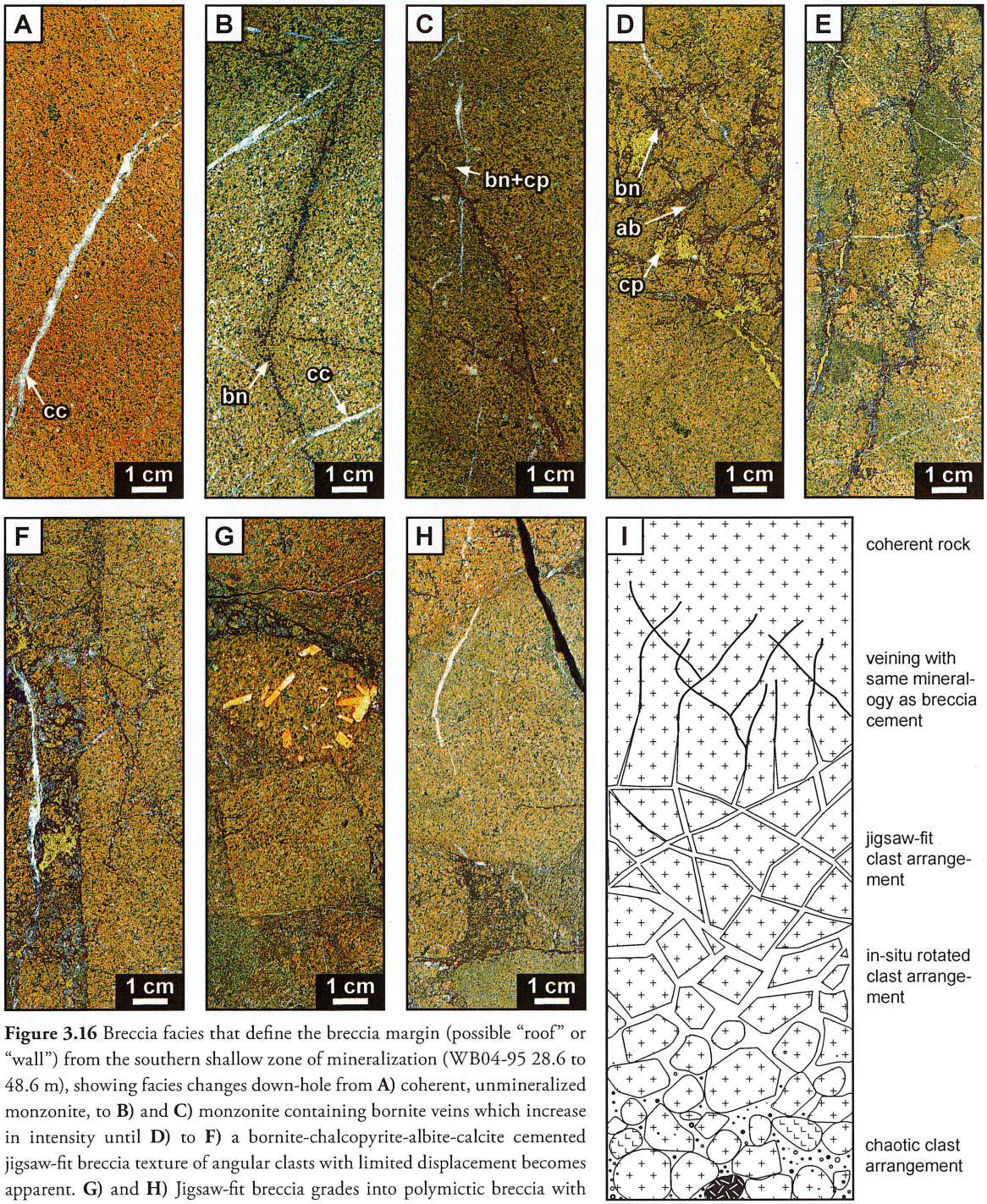

Figure 3.16 Breccia facies that define the breccia margin (possible "roof" or "wall") from the southern shallow zone of mineralization (WB04-95 28.6 to 48.6 m), showing facies changes down-hole from **A)** coherent, unmineralized monzonite, to **B)** and **C)** monzonite containing bornite veins which increase in intensity until **D)** to **F)** a bornite-chalcopyrite-albite-calcite cemented jigsaw-fit breccia texture of angular clasts with limited displacement becomes apparent. **G)** and **H)** Jigsaw-fit breccia grades into polymictic breccia with rounded clasts in a rotated to chaotic arrangement and the same cement mineralogy. **I)** Represetative sketch of breccia facies that define the breccia margin.

m) transition zone of closely spaced fracturing (Sillitoe, 1985). This may comprise veining and/or jigsaw-fit breccia. Fractures may be mineralized or contain fault gouge (Sillitoe, 1985). Alternatively, unfractured host rock may grade into breccia over several meters (Sillitoe, 1985). These contact relationships are termed "breccia margins" herein.

The original breccia geometry of the NEZ is poorly known as faulting and post-breccia dikes obscure most of the primary breccia margins (Jackson, 2008; this

study). The Green Giant and Brown Wall faults (Figs. 3.1, 3.2, 3.13) form a well-defined wedge of breccia in the southern end of the breccia body, but post-mineral displacements mean that these faults are unlikely to be the original breccia margins. In the north end of the pit, breccia margins are poorly constrained and the breccia body remains open at depth.

Original breccia margins have been interpreted to be preserved in a few drill holes on sections 29, 18 and the long-section. A "roof" or "wall" (terminology of Sillitoe, 1985) to the southern portion of the breccia body on the long-section has been interpreted from observations in drill holes WB04-25, WB03-16, WB04-29, WB04-95, WB03-17, and WB04-81 (Fig. 3.16). The northernmost of these drill holes, WB04-25, contains abundant CMX breccia, and no contact with coherent monzonite. At the top of drill holes WB04-29 and WB04-95, coherent monzonite units containing mineralized (>0.5% Cu) veins overlies monomictic jigsaw-fit CM breccia, which in turn overlies polymictic rotated to chaotic CMX breccia (Fig. 3.16). Drill holes WB03-17 and WB04-81 contain equigranular to sparsely K-feldspar-phyric monzonite dikes, cut by abundant bornite and chalcopyrite veins and have high Cu and Ag grades. Collectively, these features are interpreted to be a breccia margin (Fig. 3.16I). These match well with the breccia margin interpreted by Jackson (2008) on section 18. Jackson (2008) noted that where original breccia margins were inferred on sections 29 and 18, a gradation from coherent country rock to a vein-network to jigsaw-fit breccia into rotated, transported and chaotic breccia was observed. Most of the mineralization described by Rees et al. (2005; 2006) as being hosted in monzonite country rock has been interpreted by Jackson (2008) as hosted in crackle breccia, transitional between the chaotic breccia and the monzonite host rock.

Drilling in the NEZ concentrated on the ore-hosting breccia body, with only limited condemnation drilling conducted around the margins of the breccia body (Jackson, 2008). Three-dimensional images produced from drill hole logs show the northern half of the NEZ breccia body as conical, narrowing with depth (Blackwell, 2005; Jackson, 2008). However, the limited drilling, overprinting by post-breccia intrusions and post-brecciation faults, prevent determination of the original geometry of the breccia body (Jackson, 2008; this study). The MX1 breccia occurs as a narrow, vertical sub-pipe to the west of the larger breccia body (Imperial Metals, pers. comm., in Jackson, 2008) on section 18 (Fig. 3.13), and is interpreted to have been truncated by the northern extension of the Brown Wall fault on the long-section (Fig. 3.2). The western margin of the MX1 breccia has not been drilled.

Combining the results from the long-section and the cross-sections, it appears that the cross-sections cut through the entire breccia body and into host rock, whereas the long-section only intersects host rock in the south.

3.7.2 Genetic origins and breccia classification

Davies et al. (2000) and Davies (2002) proposed a genetic classification scheme for breccias, modified from Sillitoe (1985), which included four end-members: magmatic, volcanic, tectonic and hydrothermal. Assignment of a breccia to one of the four end-members is based principally on assessment of the overall fragmentation process (explosive versus non-explosive) and the inferred involvement of water (external or magmatic, i.e "dry"), magma or tectonics in the fragmentation processes (Davies et al., 2000). Both Sillitoe (1985) and Davies et al. (2000) emphasized the common overlap between the four end-members.

The definition of a "magmatic" breccia is taken from the original meaning by Harker (1908; in Sillitoe, 1985) to be fragments set in a crystalline igneous "matrix" (i.e. igneous-cemented breccia). Magmatic breccias include igneous-cemented, auto and explosive (dry) magmatic breccias and can form from a wide variety of processes including, stoping and magma injection into pre-existing broken rock or fault zones (Davies, 2002).

Volcanic breccias include autoclastic, pyroclastic and volcaniclastic breccias (McPhie et al., 1993). There can be overlap between volcanic and sub-volcanic (i.e. hydrothermal) breccias when subsurface breccias breach the surface (e.g. volcanic-hydrothermal breccias; Cooke et al., 2007). Subsurface explosions can vent to the surface in phreatic or phreatomagmatic eruptions, however hydrothermal brecciation need not vent to surface and can form in a range of settings which may or

may not be related to volcanism (Davies et al., 2000).

Tectonic breccias include wear and dilation breccias caused by the brittle failure of rock under tensile, shear or compressive stress (Sibson, 1986; Jébrak, 1997; Davies, 2002). These fault breccias commonly have an internal fabric defined by clast alignment, banding or foliation. Vein breccias can be produced by a combination of tectonic and hydraulic fragmentation, where fault movement promotes fluid movement into dilatant zones with subsequent fluid-driven wall rock implosion (Sibson, 1986; Jébrak, 1997; Davies, 2002).

A hydrothermal breccia is defined as a clastic aggregate generated by interaction of hydrothermal fluid with country rock and/or magma (Davies et al., 2008a). This term encompasses any broken rock formed or cemented by hydrothermal processes. (e.g. gas expansion, corrosion, mineral deposition), regardless of fluid source (meteoric, magmatic-hydrothermal, seawater), fluid phase (liquid, vapour, supercritical fluid) or fluid composition (dilute, saline, hypersaline; Davies et al., 2000). Hydrothermal breccia include phreatomagmatic, phreatic, magmatic-hydrothermal, dissolution and hydraulic breccias (Davies, 2002).

Potential overlaps between magmatic and hydrothermal brecciation are particularly relevant to the NEZ breccia complex. Magmatic-hydrothermal breccias are characterized by both a magmatic and hydrothermal involvement in brecciation. Clasts with delicate irregular edges or globular in shape are significant in that they can form from the injection of a parental magma into an unsolidified rock body (Sillitoe, 1985; Davies et al., 2008). These clasts are produced by quench fragmentation or globules of magma disaggregated from an unsolidified intrusion to produce fluidal-shaped "juvenile-magmatic clasts" (e.g. Fig. 3.14). This unusual clast shape is difficult to preserve during clast comminution but can lend critical insight into the breccia formation process.

Magmatic-hydrothermal breccias are a product of aqueous fluids exsolving from a crystallizing magma chamber (i.e. second boiling; Burnham and Ohmoto, 1980). Hydrothermal fluid causes hydraulic fracturing and can lead to explosive decompression and magmatic-hydrothermal brecciation (Burnham, 1985; Sillitoe, 1985; Corbett and Leach, 1998). This is likely to be the key fragmentation process in mineralized breccia complexes associated with porphyry deposits (Burnham, 1985). Under the classification of Davies et al. (2000), fragmentation due to crystallization and second boiling is classified as "wet" explosive magmatic fragmentation. Although the dominant water involved (at least initially) is magmatic, the exsolved volatiles can mix with external waters in a cycle of exsolution, decompression and fluid mixing (Davies, 2002; Frikken et al., 2005).

3.7.2.1 Interpretations of breccia facies (CM, CMX, MX)

Elucidating the number of breccia bodies and their relative timing of formation with respect to intrusive activity and mineralization are critical in understanding a breccia-hosted ore deposit. The strongest evidence for multiple cross-cutting breccia bodies in a hydrothermal breccia complex is the observation of clast-within-clast textures (Baker et al., 1986; Taylor and Pollard, 1993; Davies, 2002). Of the approximately 16 km of core logged from this study and that of Jackson (2008), no unambiguous examples of clast-within-clast textures were observed in any of the breccia facies. Consequently, the NEZ breccia complex is interpreted to have formed from a single catastrophic brecciation event. This conclusion is in agreement with those of Logan et al. (2007) and Jackson (2008).

3.7.2.1.1 CMX breccia

The CMX breccias contain many of the features that are commonly found in magmatic-hydrothermal breccia, including ubiquitous hydrothermal cements, high-temperature cement and alteration minerals, open space fill textures and variable amounts of matrix (e.g. Sillitoe, 1985). The CMX breccias contain megacrystic-K-feldspar-phyric clasts, most significantly the globular-shaped clasts, interpreted here as juvenile-magmatic clasts. The clasts that are globular-shaped show evidence for limited to no vertical transport as the delicate globular shape cannot be preserved during abrasive transport. These clasts are consistent with formation by explosive magmatic processes. Wispy to globular-shaped clasts may also indicate phreatomagmatic fragmentation processes; however, the relatively low amounts of matrix compared to the MX breccia do not support phreatomagmatic fragmentation (Sillitoe, 1985; Davies

et al., 2000; Davies, 2002).

The CMX breccia also contain sub-angular to sub-rounded clasts of local wall rocks and megacrystic-K-feldspar-phyric monzonite. The polymictic nature, rounding of clasts and presence of matrix are indicative of clasts mixing and abrasion during significant transport. The degree of clast rounding depends on the original rock hardness, internal structure (i.e. bedded vs. massive, how far the clast was transported and the ease with which clasts can break apart to form new angular clasts (Taylor and Pollard, 1993). In this way, a mixture of angular to rounded clasts can be produced. CMX breccias are interpreted to have undergone overall more intense fragmentation, transport and modification than the CM breccias.

The volumetrically minor CMX3 breccia have characteristics of hydraulic fracturing (Sibson, 1986; Jébrak, 1997). This facies is interpreted to be late-stage vein breccias, implying that the system continued to produce conditions suitable for brecciation, albeit on a smaller scale, after the main breccia complex formed. These are likely to be fault-related and form via a very different process to the main breccia.

3.7.2.1.2 CM breccia

CM breccia occur as i) zones of jigsaw-fit to rotated breccia on the margin of the breccia complex, ii) pods of mineralized veining overlying mineralized jigsaw-fit breccia in CMX breccia and iii) pods of sub-angular to sub-rounded clasts in CMX breccia. A common origin for CMX and CM breccia is indicated by the gradational contacts between these two sub-facies. CM breccia with abundant angular clasts and minimal matrix either formed in-situ or underwent limited transport. Abundant angular clasts in a jigsaw-fit arrangement with no appreciable matrix are features consistent with hydraulic brecciation (Sillitoe, 1985; Davies et al., 2008b). The lack of fabric and gouge, and general geometry of the CM breccia favor hydraulic fragmentation over faulting.

3.7.2.1.2 CM breccia

The CM breccia occur as i) zones of jigsaw-fit to rotated breccia on the margin of the breccia complex, ii) pods of mineralized jigsaw-fit breccia underlying mineralized veins in the CMX breccia and iii) pods of sub-angular to sub-rounded breccia in CMX breccia. A common origin for CMX and CM breccia is indicated by the gradational contacts between these two sub-facies. CM breccia with abundant angular clasts and minimal matrix either formed in-situ or underwent limited transport. Abundant angular clasts in a jigsaw-fit arrangement with no appreciable matrix are features consistent with hydraulic brecciation (Sillitoe, 1985; Davies et al., 2008b). The lack of fabric and gouge, and general geometry of the CM breccia favor hydraulic fragmentation over faulting.

Type ii CM breccia pods that contain mineralized veins overtop of mineralized jigsaw-fit breccia in the main breccia complex are surrounded by CMX breccia. These pods are inferred to be fractured mega-clasts that have undergone very limited or no transport. Sillitoe (1985) noted that large blocks inside breccia bodies may be fractured similar the wallrocks of the breccia complex. The CM pods may represent such features, i.e. the "block jostle style" breccia of Taylor and Pollard (1993).

The CM breccia pods of sub-angular to sub-rounded clasts (e.g. Fig. 3.12) are interpreted to have undergone variable amounts of transport. These pods are interpreted to be localized areas of high fluid flux, where matrix was winnowed away. The isolated occurrence of a thin, discordant, unmineralized breccia in the Leak Zone (east of Green Giant fault) is interpreted to be a discrete breccia vein or pipe, separate from the main NEZ breccia complex.

3.7.2.1.3 MX breccia

The body of MX breccia (fine-grained breccia of Jackson, 2008) in the northern portion of the NEZ consists predominantly of rounded to sub-rounded clasts with abundant matrix and an average clast size smaller than CM or CMX breccia. The clast morphology and matrix abundance indicate greater attrition and transport than the CMX breccia. The abundant matrix and rounded clasts are consistent with the fluidization process found in the central portion of breccia pipes associated with porphyry deposits ("mill breccia"; Baker et al., 1986), in pipes associated with phreatic or phreatomagmatic fragmentation processes (Baker et al.,

1986) and volcanic breccias.

A detailed interpretation of the MX breccia is not possible because only a limited portion of it observed in this study. The geometry of the MX breccia has been reported to be a sub-pipe within the large NEZ breccia complex (Blackwell, 2005; Jackson, 2008). Clast in clast textures were not observed in the MX breccia. The MX breccia lacks textural evidence of juvenile-magmatic clasts, surficial (exotic clasts), and sedimentary structures (i.e. bedding), which have been observed in matrix-rich diatremes (e.g. Davies et al., 2008a). The MX breccia is therefore inferred to part of the NEZ breccia complex, and a magmatic-hydrothermal origin is inferred based on correlation with the CMX breccia facies. It is possible that the MX breccia has been juxtaposed against the CMX-CM body by an unidentified fault (Fig. 3.12).

The volumetrically minor sub-facies MX2 breccia is characterized by fine-grained matrix infill with small (average <5 cm) rounded clasts. Some samples have a distinct shear fabric (Fig. 3.11J). This discordant nature and local foliation are consistent with fault processes and the breccias are interpreted to be tectonic breccias associated with faults.

3.8 Summary and conclusions

The igneous rock types of the NEZ are very similar in composition to the rest of the silica-undersaturated to silica-saturated Mt. Polley Complex. Igneous rocks of the NEZ are composed dominantly of monzonite, with lesser K-feldspar-phyric monzonite, monzodiorite, diorite and various mafic facies (Fig. 3.5; Table 3.4). None of the igneous rock types, regardless of timing, were observed to contain modal quartz in this study.

The NEZ breccia complex disrupted the multi-phase monzonitic to dioritic pluton in the northern part of the Mt. Polley Complex. The breccia may have breached the margin of this pluton based on the presence of rafted limestone intersected in drill core and an isolated marble clast in the NEZ breccia complex. Clast compositions reflect wallrock compositions as listed above (Fig. 3.5; Table 3.4).

Magmatic, hydrothermal, hydraulic and tectonic fragmentation processes contributed to the formation of the NEZ breccia complex. The presence of globular (lobate) shaped clasts of megacrystic K-feldspar-phyric porphyry in the breccia complex implies that intrusion of the megacrystic K-feldspar-phyric porphyry triggered brecciation (Logan and Mihalynuk, 2005; Simpson, 2005; Jackson, 2008; this study). Hydrothermal cement and/or altered matrix are ubiquitous throughout the breccia body and the monogenetic NEZ breccia complex contains three main facies: cement-dominated, cement and matrix-bearing; and matrix dominated breccia. CMX is the most abundant breccia facies, with CM breccia located along the breccia margins and in pods of the CMX breccia. MX was primarily located to the northwest of the CM-CMX breccia body. Areas of chaotic CM breccia in CMX breccia suggest complex fluid pathways, possibly where winnowing of matrix occurred. A combination of hydraulic fracturing and explosive magmatic-hydrothermal brecciation formation, followed by clast comminution, matrix generation, hydrothermal cementation and alteration is interpreted to have produced the magmatic-hydrothermal NEZ breccia complex. The considerable textural variation present within the breccia body as a whole supports the interpretation of several processes involved in the formation of the NEZ (Baker et al., 1986). The lack of surficially-derived clasts and sedimentary structures implies that the breccia complex did not breach the surface.

Abundant steeply dipping, sub-vertical, equigranular to porphyritic monzonite and lesser diorite to mafic dikes with fine-grained margins have cross-cut the breccia, as have veins, hydrothermal vein breccias and faults. Post-breccia dikes are interpreted to have exploited regional northeast-trending structural weaknesses. Based on cross-cutting relationships, syn- to post-breccia dikes evolved from K-feldspar megacrystic to crystal-crowded to sparsely porphyritic to equigranular, and they became increasingly mafic and hydrous with time (Jackson, 2008). Jackson (2008) proposed that the K-feldspar megacrysts reflected an extended time at super-solidus temperatures prior to brecciation. The existence of sparsely- to crowded-K-feldspar-phyric monzonite as clasts in the breccia as well as post-breccia dikes suggests that cycles of magmatic crystallization

were repeated, since these units formed both prior to and after brecciation. The presence of amygdales in some post-breccia dikes indicates the system was still episodically vapor-saturated after brecciation.

This chapter has documented the magmatic affinities of the NEZ deposit and shown that the main breccia body is the key host to mineralization. To further our understanding of the formation of the NEZ, a closer look at the breccia cement and alteration is required.

Chapter 4

Mineralization and Alteration of the Northeast Zone

4.1 Introduction

This chapter describes the alteration and mineralization assemblages observed during logging of the long-section through the NEZ. The focus of this chapter is on paragenetic and geochemical relationships, with a particular emphasis on breccia cement. The paragenesis presented herein has built on the results of previous studies of the NEZ, and has employed the following methods: graphic logging; examination of >100 polished thin sections; K-feldspar staining of rock slabs (following the procedure of Bailey, 1960); electron microprobe and Terraspec analyses. This collective data set provides the observational framework that, in conjunction with the isotope and sulfide trace element studies presented in Chapters 5 and 6, forms the basis for the genetic model presented in Chapter 7.

4.2 Short wave infrared spectroscopy

During this study, fine grained white mica and clays were logged in the field as "sericite". Shortwave infrared spectroscopy (SWIR) was then applied to 32 samples to define the mineralogical composition of "sericite". A Terraspec ASD (analytical spectral device) spectroradiometer with RS^3 software (version 4.0.23) was used to collect the spectra. Computer assigned mineral identification, using TSG Professional software (version 5.03.002), was manually checked against a library of spectra and either accepted, re-interpreted or rejected (Appendix C1). The SWIR data suggest that most of the sericite logged from the NEZ is dominantly an illite ± montmorillonite mixture, commonly with calcite (Fig. 4.1).

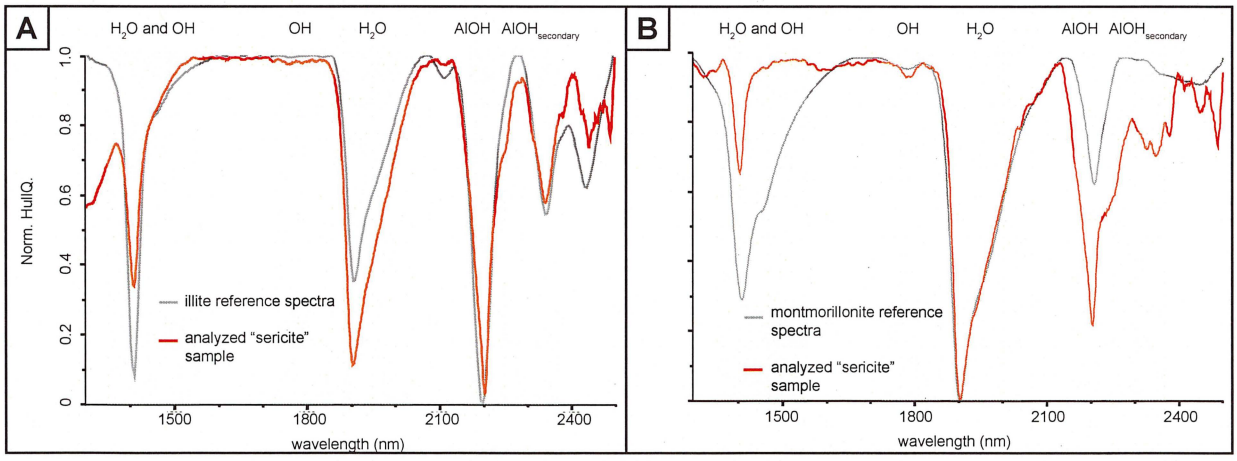

Figure 4.1 Examples of Terraspec spectra for "sericite". **A)** Red line shows representative spectral signature typical of the analysed samples. The "sericite" spectra fits with absorption bands that are characteristic of illite (grey line; Pontual et al., 1997). **B)** Grey spectra show the illite-montmorillonite mixture. The major difference between illlite and montmorillonite spectra is the depth of the 1900 nm H_2O absorption band and pattern of the secondary Al-OH peaks. Shaded areas highlight the principal absorption bands for illite. Reference spectra of illite and montmorillonite were taken from RS^3 (version 4.0.23) software library.

4.3 Previous work

Alteration studies of the Mt. Polley Complex and specifically the NEZ have been conducted previously by Ross (2004a, b, c, d, e), Bailey (2004a, b), Logan and Mihalynuk (2005), Imperial Metals geologists (Rees et al., 2005; Rees et al., 2006), Jackson (2008) and Davidson et al. (in prep). An apatite melt inclusion study was also conducted (Bath et al., 2006). Detailed thin section analyses, augmented by scanning electron microscope (SEM) imaging and mineral identification was conducted by Ross (2004b, e) on samples primarily from the southern half of the NEZ, and from its immediate wall-rocks. The work of Logan and Mihalynuk (2005) examined the regional and local geology of the Mt. Polley Complex. Work by these authors on the NEZ focused on its shallow southern portion. Imperial Metals' interpretations of the NEZ and other mineralized deposits in the Mt. Polley Complex were summarized in comprehensive reports by Rees et al. (2005 and 2006). Jackson (2008) studied cross-sections 18 and 29 through the southern and northern portions of the deposit, respectively (Figs. 3.1 and 3.2). Davidson et al. (in prep.) performed petrography on selected post-breccia veins and vein breccia. The results of previous investigations into the alteration and mineralization of the NEZ are summarized in Tables 4.1 and 4.2; key features are cited throughout the chapter where appropriate.

4.4 Cu-Ag-Au grade distribution and sulfide zonation

For the purposes of the current study, the NEZ long-section has been arbitrarily divided into three zones of alteration and sulfide mineralization, specifically one shallow and two deep zones (Fig. 4.2). The shallow breccia-hosted zone is separated from the deep zones by the Brown Wall fault (Figs. 3.2 and 4.2). The Gully fault separates the deep breccia-hosted mineral zone from variably altered coherent host-rock and pre- and post-breccia dikes that are moderately to weakly mineralized locally (Figs. 3.2 and 4.2). The deep breccia-hosted zone extends to depths >600 m, but is not expressed at surface on the long-section.

Most of the Cu, Ag and Au mineralization in the NEZ (>90% based on visual estimates) occurs as breccia cement. Minor mineralized veins and disseminations occur as a halo to the breccia complex in the monzonite host-rocks; mineralized veins also cross-cut the breccia.

Bornite, chalcopyrite and pyrite are the principal sulfide minerals in the NEZ. These minerals define a zonation pattern at the deposit scale. Bornite- and chalcopyrite-rich cores are surrounded by chalcopyrite-only halos in both the shallow and deep breccia-hosted ore zones (Figs. 4.2 and 4.3). Pyrite is most commonly intergrown with chalcopyrite. While pyrite is not abundant in the NEZ (typically <1%), it is most commonly found peripheral to the chalcopyrite-rich domains (Fig. 4.2). Pyrite and bornite were never observed coexisting in chemical equilibrium in this study or that of Jackson (2008).

Chalcopyrite and bornite are commonly intergrown in the breccia cement at the hand-specimen scale. Bornite and chalcopyrite exsolution textures were noted by Logan and Mihalynuk (2005) and Jackson (2008), indicating co-precipitation. Some bornite grains contain specularite (bladed hematite) laths (Fig. 4.4A and F). Bornite seldom occurs with magnetite. Where it does, bornite is extremely corroded (Jackson, 2008). Bornite cement has filled the void space next to clast walls and chalcopyrite cement has precipitated next to bornite, indicating that bornite preceded chalcopyrite precipitation (Fig. 4.4A). Chalcopyrite occurs as a cement mineral in varying amounts throughout most of the long-section. Rare blebs of chalcopyrite cement were observed in the MX breccia (Fig. 3.2).

Chalcopyrite occurs as an alteration mineral in varying amounts as fine disseminations. It also occurs in rare veins in pre-breccia wall-rock and post-breccia intrusions (Table 4.3). Chalcopyrite has been observed as rims around bornite locally, suggesting a later timing (Fig. 4.4B).

Where chalcopyrite and pyrite co-exist, the pyrite typically occurs as subhedral to euhedral crystals within chalcopyrite, indicating co-precipitation or chalcopyrite overgrowths on earlier-formed pyrite (Fig. 4.4C). Less common examples have been observed of chalcopyrite replacing pyrite (Fig. 4.4D), pyrite

replacing chalcopyrite, and chalcopyrite exsolution lamellae in pyrite (Fig. 4.4E), indicating pyrite formed pre-, syn- and post-chalcopyrite precipitation. Rare veins containing tennantite (± chalcopyrite), galena, or primary chalcocite were observed cutting the breccia. An isolated occurrence has been observed of galena with minor sphalerite and chalcopyrite as a rind around a marble clast in the breccia. Covellite was observed locally as alteration rims around bornite (Fig. 4.4F). Supergene enrichment in the form of malachite, azurite and other secondary Cu-sulfides is limited to the approximately top 20 m of drill holes that contain hypogene Cu-sulfides. Supergene mineralization has not contributed significantly to the economics of the deposit.

Figures 4.5 to 4.7 show Cu, Au and Ag grades, respectively, on the long-section. High-grade Cu (>0.5%) has the greatest spatial extent and is coincident with CM and CMX breccias, although not all CM and CMX breccias carry grade (compare Figures 3.2 and 4.5). In contrast, the MX breccia contains only isolated pockets of mineralization (0.1 to <0.5% Cu), observed as cement or rare mineralized clasts in fault breccia. High-grade Au occurs in the shallow breccia zone, and also at depth around the edges of the high-grade Cu mineralization in the deep breccia zone, hosted by CM and CMX breccias (Fig. 4.6). Most of the Ag is coincident with bornite mineralization and is most abundant in CM and CMX breccia in the shallow breccia zone (compare Figures 4.2 and 4.7). The discontinuous nature of the ore in the NEZ is most likely due to disruption by post-mineralization dikes and faults. Localized intervals of disseminated, rarely veined, chalcopyrite with Cu grades of up to 0.25% (rarely 0.5% Cu) were observed in potassically altered host-rocks at depth below the shallow breccia zone (Fig. 4.5).

Leak Zone

No economic mineralization has been discovered in the Leak Zone (Figs. 4.5 to 4.7). Sparse flecks of chalcopyrite were observed in the intensely magnetite-actinolite-chlorite-K-feldspar altered monzonite host-rocks. Flecks and blebs of chalcopyrite (up to 0.4% Cu) were rarely observed in hematite-altered monzonite dikes. Arsenic anomalies over 1 to 8 m were associated with some fault zones that are ≥1m thick, and/or with equigranular to moderately-feldspar-phyric monzonite dikes. In one case, an As anomaly was coincident with a Au anomaly over a 3 m interval.

4.5 Paragenesis

Evolution of the NEZ hydrothermal system produced a sequence of veins, alteration and hydrothermal breccia that are separated here into five paragenetic stages (Fig. 4.8). These stages have been defined based on the presence and relative abundance of Cu-sulfide minerals, and on their timing relationships with respect to the main hydrothermal brecciation event. Cross-cutting and truncation relationships between veins, clasts and intrusions have been used to constrain the paragenesis following the method of Davies et al. (2008). Timing relationships were determined as follows: pre-breccia mineralization is contained entirely within breccia clasts (e.g. truncated veins) or host-rocks; syn-breccia mineralization occurs as breccia cement and alteration rinds around breccia clasts; post-brecciation features have cross-cut all components of the breccia, and include veins, faults and intrusions. A preliminary version of the NEZ paragenesis was presented in Pass et al. (2007). Sulfide, carbonate, oxide and silicate minerals are the most abundant cement and alteration minerals in the NEZ breccia (Fig. 4.8). Carbonate was found throughout all paragenetic stages, whereas quartz was only identified as a minor component in late-stage vein-breccias. Some breccias and veins are dominated by only a few minerals, while others contain multiple stages of sequential infill. Although the paragenesis is consistent at the deposit scale, breccia infill is inherently varied; consequently, there are local paragenetic reversals or repetitions.

4.5.1 Stage 1: Early (pre-brecciation)

Hydrothermal activity occurred prior to brecciation in the NEZ. Stage 1 produced some moderate to strongly developed pervasive alteration of the monzonite host-rocks, together with minor veins. Early, widespread and pervasive K-metasomatism was associated with hematite dusting ± calcite alteration. Evidence of this event is mostly preserved as reddened and carbonate-altered monzonite clasts within the NEZ breccia. It also occurs as the earliest alteration in the wall-rocks to the breccia complex. Intense and

Table 4.1 Summary of NEZ alteration and mineral assemblages documented by workers prior to 2008.

Alteration phase	Mineral assemblage	Style	Characteristics	Timing relative to mineralization	Mineralization	Reference[1]
K-metasomatism	K-feldspar-fine grained magnetite, rare biotite	Pervasive and texturally destructive, has replaced rims of plagioclase phenocrysts	Locally destroyed mafic minerals, felted crystal texture, magnetite-hematite alteration has imparted red color to the rock	Early (or syn-brecciation), may have had >1 phase or a protracted phase as indicated by fracture (breccia?) infill	Unmineralized	1, 2, 3, 4
	K-feldspar	Veinlets	Overprint groundmass		Unmineralized	
	Fine grained epidote-clinozoisite/prehnite[2]-calcite	Veinlets	Diffuse, green		Fine grained pyrite and chalcopyrite associated with green alteration	
Calc-silicate	(i) Magnetite-garnet-apatite ± albite, overlaps with (ii)	Breccia cement in core of system, locally pervasively altered mafic phenocrysts, thin veinlets on periphery	Garnet compositions are identical to those from Core Zone: pure andradite with minor (10–15%) grossular rims (Fraser, 1994; Ross, 2004b), magnetite interpreted as coeval with garnet, magnetite can be intergrown with apatite and garnet, local alteration of secondary K-feldspar to secondary albite adjacent to magnetite	Early (or syn-brecciation), can occur without significant mineralization (or magnetite)	Not specified	1, 5
	(ii) Sulfide-clinozoisite/prehnite[2]-albite-calcite ± apatite-garnet-diopside, overlaps with (i)	Veins and breccia cement, intense to weak, and diffuse alteration along fractures, finely disseminated chalcopyrite, coarser intergrown clots of chalcopyrite and bornite	Has commonly overprinted (i), sulfides have replaced rims or whole magnetite grains, pale green-blue spots have overprinted mafic phenocrysts and groundmass	Synchornous with majority of Cu-sulfides	Primarily as breccia cement, fine-grained disseminated chalcopyrite, wispy veinlets and coarser grained clots of chalcopyrite and bornite, chalcopyrite and bornite sporadically intergrown with magnetite and lesser pyrite, highest grade developed in magnetite-rich sections of breccia, mineralization also associated-intergrown with clinozoisite-garnet-calcite-apatite and albite, platy calcite occurs with coarse-grained sulfides, bornite commonly occurs as rims chalcopyrite, pyrite is commonly fine grained, minor pyrite encapsulated in chalcopyrite, pyrite generally not abundant, NEZ Cu/Au ratio average: 0.1 to 1.0 (g/t over %), no discrete Au-bearing phases observed	1, 4, 5

Table 4.1 continued

Alteration Phase	Mineral assemblage	Style	Characteristics	Timing relative to mineralization	Mineralization	Reference[1]
Retrograde (transitional from mineralization stage)	Calcite-sericite-albite-chlorite ± clinozoisite[2] ± epidote	Where weak, only mafic phenocrysts replaced to form irregular dark green spots; where intense, texturally destructive fine grained scaly masses were produced, calcite and chlorite replaced garnet and pyroxene, calcite and sericite replaced feldspars, magnetite was partially altered to hematite, sulfides were not affected	Pervasive, widespread throughout the system	Late-stage	Not specified	1
Propylitic	Calcite-chlorite-pyrite, albite ± epidote	Weakly developed, difficult to distinguish from weak pervasive retrograde alteration	Enveloped the breccia, most strongly developed in host-rock monzonite adjacent to northeastern margin of shallow breccia-hosted mineralization	Syn-mineralization (?), peripheral	Unmineralized	1, 3
Post-breccia	Albite-clinozoisite/ prehnite[2]	Local veins and vein breccia	Has cross-cut dikes, crustiform layers observed locally	Post-main stage mineralization	Breccia fragments of mineralization	1, 2
	Calcite-gypsum	Veins	Cross-cut peripheral propylitic zone and breccia, contain celestite and barite		Unmineralized	
	Calcite-zeolites (incldluing stilbite)	Filled open spaces	Fibrous, radiating		Unmineralized	1, 2, 6
Skarn	Garnet-calcite	Observed in a limited (~10 m) interval at the bottom of drill hole WB04-03 (south end of deposit) in contact with recrystallized limestone	Skarn garnets have grossular cores and andraditic cores	Unknown	Unmineralized	1, 3

[1] References: 1) Ross (2004b), 2) Logan and Mihalynuk, (2005), 3) Rees et al. (2005), 4) Rees et al. (2006), 5) Fraser (1994a), 6) Read (1997).

[2] Ross (2004b) expressed some uncertainty in identification of clinozoisite (Ca-Al silicate) and stated that it could be prehnite.

Table 4.2 Alteration-infill and mineralization of the NEZ (sections 18 and 29) from Jackson (2008) and Davidson et al. (in prep), where indicated[1]. Some mineral assemblages have uncertain timing or more than one event, as specified, but have been listed only once.

Classification	Mineral assemblage	Style	Characteristics	Timing	Mineralization
Pre-breccia	Albite-actinolite with magnetite-K-feldspar veins and K-feldspar halos	Texturally destructive	Observed in altered mafic clasts	Pre-mineralization	Unmineralized
	K-feldspar stable hematite-carbonate	Pervasive, widespread	Hematite has preferentially altered feldspars, imparting a red-orange color to the rock, accompanied by clots or blebs of calcite, mafic sites have been altered to chlorite, lateral extent of alteration unknown due to lack of drilling outside mineralized area	Pre- and post-mineralization (observed in clasts, in coherent host rock and in post-breccia dikes, reportedly less intensely altered in post-breccia hornblende-bearing monzonite dikes and absent in mafic dikes)	Unmineralized
	Biotite-magnetite	Texturally destructive	Observed in breccia clasts and in mafic xenoliths hosted by pre-breccia monzonite	Pre-mineralization	Unmineralized
	Chlorite ± biotite (rare)	Selectively pervasive alteration of mafic sites in hematite-carbonate altered host rocks	Chlorite has pseudomorphed augite and hornblende grains	Pre-mineralization	Unmineralized
Syn-breccia	Chlorite	Breccia cement and alteration	Fine grained green to green-brown, mostly observed as abundant infill, most common in peripheral breccia	Peripheral	Unspecified
	Carbonate	Breccia cement and alteration	-	Pre-mineralization or coeval with sulfides	Unspecified
	Biotite	Breccia cement and alteration, has formed distinct 1–2 cm clast rims and uncommonly has overprinted clasts entirely	Alteration presented as dark brown color of rock, overprinted hematite-carbonate alteration, biotite color is dark brown vs. dark green chlorite	Syn-mineralization; predated intense, texturally destructive K-feldspar alteration	Unspecified
	Sulfide	Breccia cement	Magnetite was paragenetically first and has commonly been partially replaced by chalcopyrite and less so by pyrite, magnetite was not observed replacing bornite, chalcopyrite and bornite were coeval, pyrite was less abundant	Syn-mineralization	Divided into four subfacies: chalcopyrite-bornite, chalcopyrite only, chalcopyrite-magnetite, magnetite-pyrite; thin laths of hematite locally occurred in bornite, magnetite was very corroded where bornite and magnetite occurred
	Magnetite	Breccia cement and alteration	Observed as locally dominant cement or monominerallic cement	Pre-mineralization, syn-mineralization, overprinted by K-feldspar and albite-epidote alteration	Unspecified

Table 4.2 continued

Classification	Mineral assemblage	Style	Characteristics	Timing	Mineralization
	K-feldspar	Intense and texturally destructive intervals, breccia cement, clast rims	Located between biotite and albite-epidote alteration on section 29, restricted to core of section 18	Syn-mineralization, possibly also post-breccia, post-dates biotite, bornite post-dates K-feldspar, magnetite overprinted by K-feldspar	Unspecified
	Albite-epidote	Breccia cement	At depth in section 29, not observed in section 18	Overprinted K-feldspar and magnetite alteration	Adjacent to mineralization
	Albite-actinolite	Restricited to the Leak Zone in section 18 as pseudo-breccia texture and a narrow zone within the MBx in Section 29 as breccia cement and replacement of clastic infill: actinolite commonly developed on clast rim with albite replacement of K-feldspar on clast rim and in clast	Spatially restricted to narrow zone in matrix-dominant breccia and west of Green Giant fault on section 18 in the Leak Zone, least volumetrically significant assemblage	Leak Zone alteartion assumed to be pre-mineralization; MBx cement coeval with magnetite alteration	Distal to mineralized zone, can be locally high grade, locally disseminated chalcopyrite in the Leak Zone
Post-breccia	Albite-epidote ± pyrite	Common, albite > epidote, texturally destructive at depth in in section 29, not observed in section 18	Locally, pyrite has replaced magnetite or chalcopyrite	After post-breccia hornblende-bearing monzonite dikes, mafic dykes cut this alteration	Unmineralized
	Chalcopyrite veins	-	Cross-cut breccia and post-breccia monzonite dikes	-	Did not contribute significantly to the metal endowment of the NEZ
	[1]Carbonate (calcite >> dolomite)-albite-chlorite-prehnite ± clays ± quartz ± suflate ± datolite (boro-silicate: $CaB(SiO_4)(OH)$) and calcite-anhydrite-gypsum ± prehnite ± minor barite	Veins and vein breccia	Generally >2 cm in width, can contain significant matrix, calcite can be white or pink (Manganoan calcite)		Microscopic pyrite and chalcopyrite grains observed on margins of clasts in contact with prehnite-albite zones
	Chalcopyrite-albite ± pyrite veins and sulfide replacement	Veins and disseminations, chalcopyrite may have replaced mafic sites	-	-	Did not contribute significantly to the metal endowment of the NEZ
	Sericite-quartz-carbonate	Restricted to immediate vicinity of veins, fractures and small faults, can be texturally destructive	Produced amber colored rock, veins commonly have multiple generations of cementation, can form vein breccia with banded vein fragments clasts	Has post-dated all generations of post-breccia dikes including mafic dikes	Commonly contains finely disseminated pyrite, chalcocite and covellite have replaced bornite and chalcopyrite
	Carbonate (calcite, pink Mn-bearing calcite)-gypsum-clinozoisite-zeolite ± quartz	Veins and vein breccias, carbonate veins can have bladed textures	-	After main stage mineralization	Can have mineralized clasts
	Carbonate (calcite, dolomite, Mn-bearing calcite) ± gypsum	Veins, vein breccia cement and cement of relict open space in main breccia body	Commonly exhibited bladed textures, section 18-ubiquitous; section 29-scarce	After main stage mineralization	Can have mineralized clasts

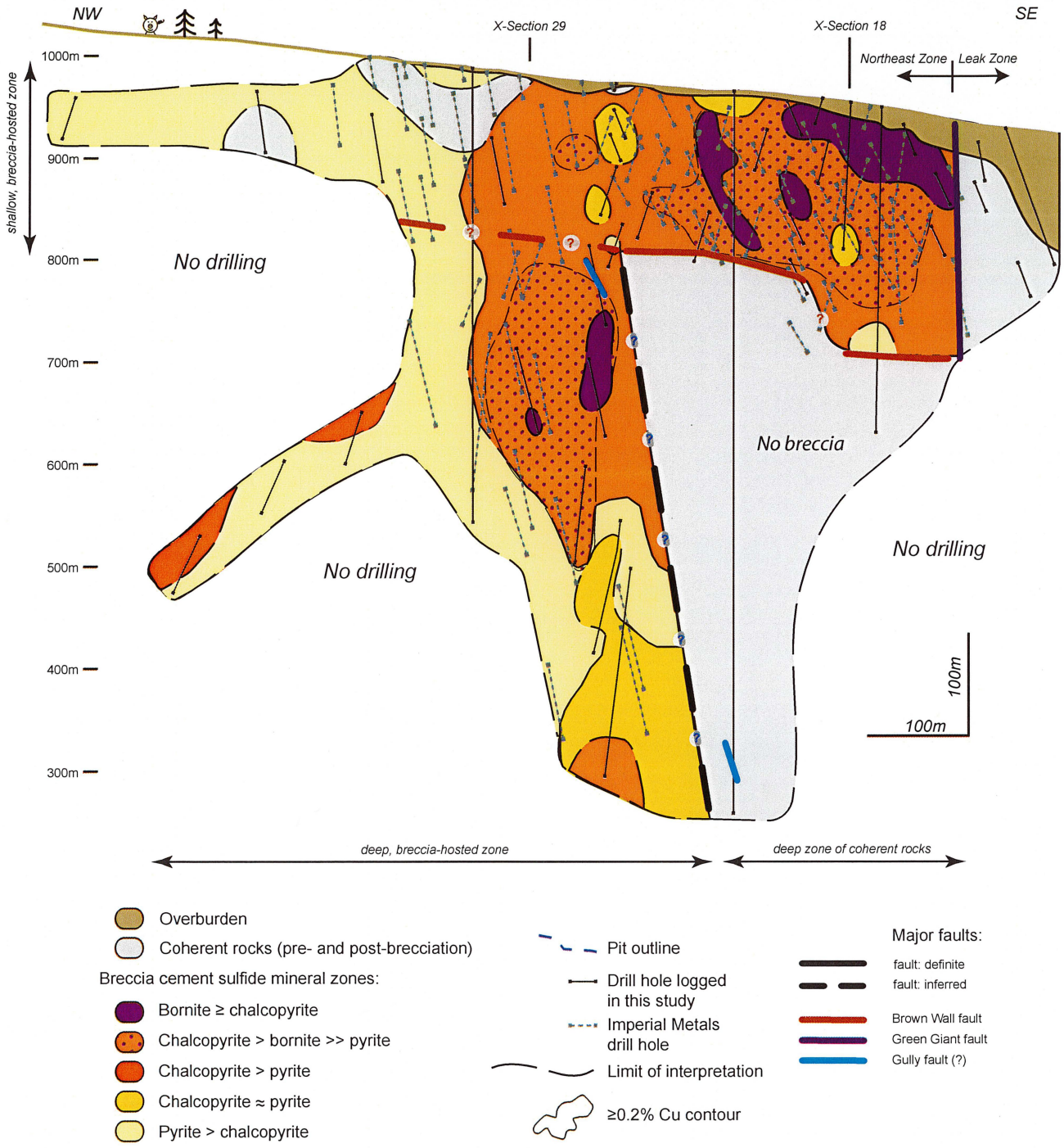

Figure 4.2 Sulfide mineral distribution as breccia cement (stage 2). Chalcopyrite and bornite observations from this study have been augmented by data from Imperial Metals core logs for all drill holes on section. The sulfide mineral zonation pattern from bornite cores, outwards to chalcopyrite- and then pyrite-dominant mineralization was also observed by Rees et al. (2005) on the long-section and by Deyell and Tosdal (2005) on section 18 in the NEZ. The long-section has been divided into three zones: 1) a shallow breccia-hosted zone above the Brown Wall fault, 2) a deep breccia-hosted zone below the Brown Wall fault and north of the inferred location of the Gully fault and 3) host rock in the footwall to the Brown Wall fault and south of the Gully fault.

texturally destructive K-feldspar-magnetite-albite ± epidote alteration of monzonite in the footwall to the Brown Wall fault is interpreted to have formed during stage 1 based on similar alteration assemblages identified in isolated breccia clasts (Fig. 4.9A–E). Jackson (2008) identified a similar pre-breccia alteration assemblage

containing magnetite, albite, actinolite, chlorite and rare biotite.

Stage 1 veins are <0.1 to 0.5 cm thick and include: magnetite-pyroxene-calcite veins (Fig. 4.9E and F), magnetite veins with K-feldspar halos (Fig. 4.9D), K-feldspar, epidote and albite veins in the NEZ and actinolite-albite-magnetite-pyroxene veins in the Leak Zone. These veins generally occur as isolated, irregularly walled veins or as groups of elongate irregular wispy veinlets (Fig. 4.9D). A minor amount of Cu-sulfide mineralization occurred during stage 1 based on observations of rare mineralized clasts and xenoliths. Local areas of disseminated chalcopyrite (± pyrite) occur in intensely potassic-altered monzonite wall-rock in the footwall to the Brown Wall fault (Fig. 4.5), in some cases associated with veins. This mineralization is tentatively correlated with stage 1 hydrothermal activity (Table 4.3).

Leak Zone

The Leak Zone (Figs. 3.2 and 4.2) contains hydrothermal alteration features that distinguish it from the NEZ. Monzonites observed from the Leak Zone lack the characteristic hematite reddening of monzonites in the NEZ. Instead, the Leak Zone monzonites have been intensely magnetite-actinolite-K-feldspar-chlorite-carbonate ± albite ± biotite ± epidote-altered (Fig. 4.9F). The mottled pink-dark green-grey to black alteration is intense and texturally destructive. Lesser veins and patches of pink K-feldspar and magnetite alteration are dispersed throughout these drill holes. Based on the observed mineralogy, Imperial Metals geologists have interpreted the Leak Zone to be an early-formed, deeper and hotter portion of the NEZ hydrothermal system that has been juxtaposed against the shallow breccia zone by the Green Giant fault.

4.5.2 Stage 2: Brecciation and main-stage mineralization

This is the most abundant, widespread and economically important paragenetic stage (Fig. 4.8). Most of the Cu-Ag-Au mineralization in the NEZ precipitated during the cementation of the hydrothermal breccia complex. Sulfides occur as breccia cement and in syn-brecciation veins (Figs. 4.9C and E, 4.10, 4.11).

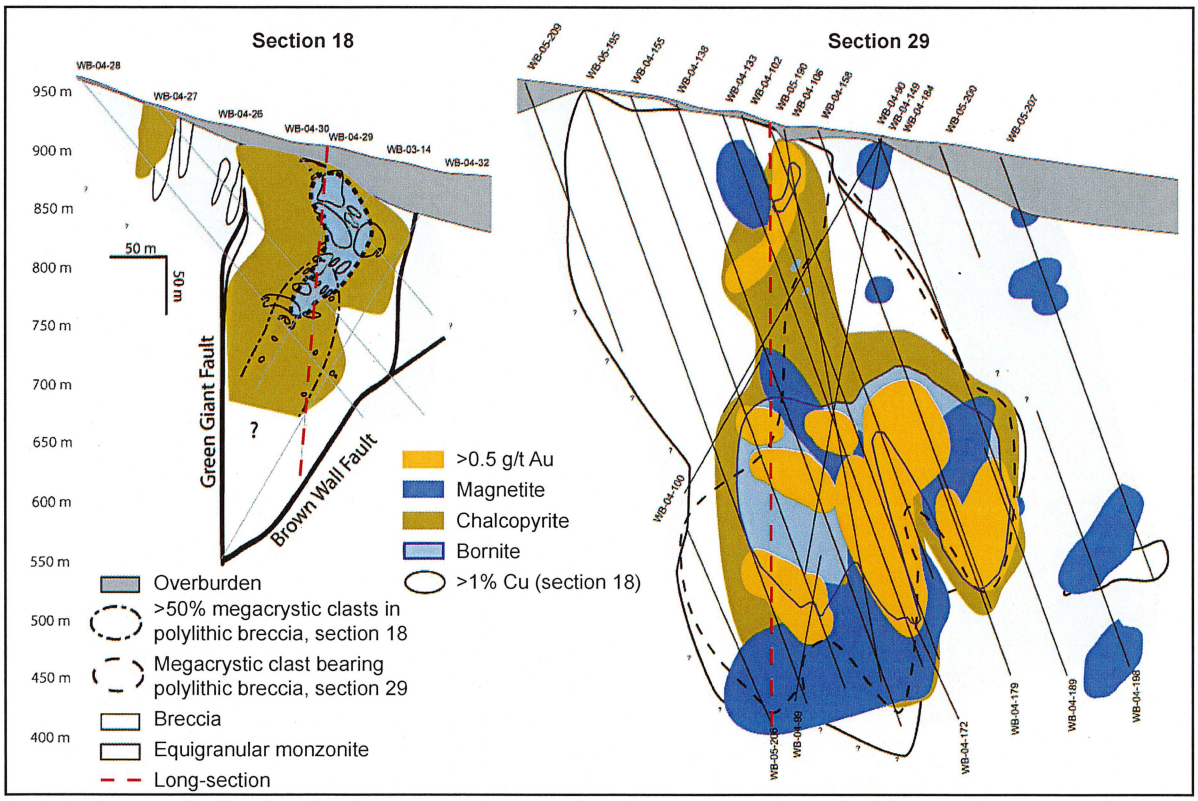

Figure 4.3 NEZ sulfide and magnetite distribution on cross-sections 18 and 29 taken from Jackson (2008). The approximate location of the long-section is shown by the dashed red line.

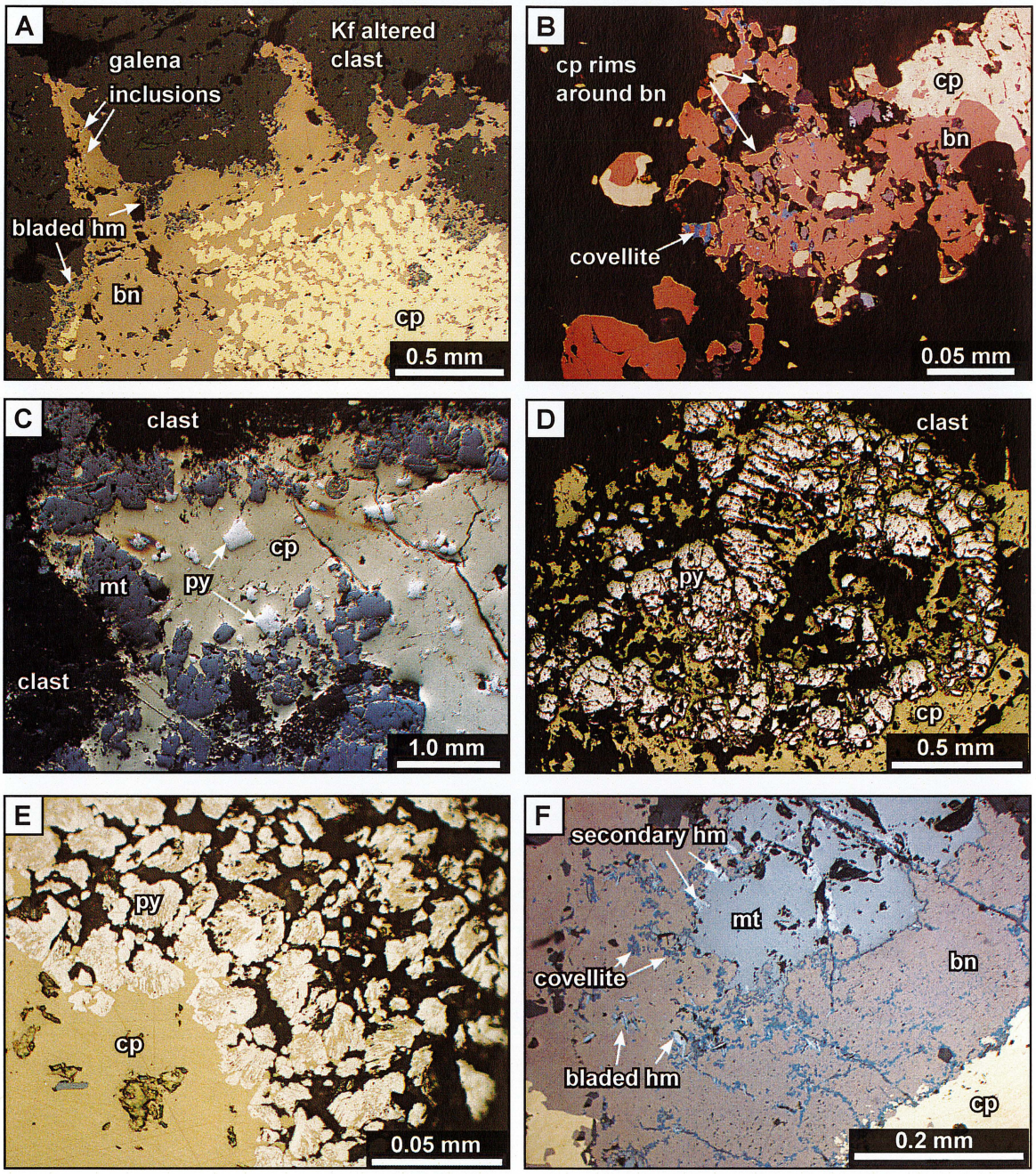

Figure 4.4 Common Cu-Fe cement minerals and their textural relationships. A) Bornite surrounding and intergrown with chalcopyrite. A thin rim of bladed hematite can be seen around the edges of the bornite, as can galena inclusions (WB03-03 120.7 m). B) Reflected light photomicrograph of bornite and chalcopyrite showing chalcopyrite replacement rims around bornite. This texture was found locally (WB04-26 168.0 m). C) Commonly observed open-space cement infill of magnetite, chalcopyrite and pyrite showing paragenetic relationships. Magnetic has been partially replaced by chalcopyrite + pyrite, which are interpreted to be co-genetic. Note the irregular corroded clast margins (WB05-210 424.3 m). D) Chalcopyrite has replaced fractured pyrite grain(s) (WB04-152 515. 1 m). E) Pyrite crystals surrounding chalcopyrite. In this uncommon texture, it is unclear if the pyrite contains exsolution lamellae of chalcopyrite or if chalcopyrite has partially replaced pyrite (WB04-108 304.0 m). F) Bornite contains bladed hematite and is altered to covillite along fracture planes and rims. Secondary hematite alteration is common on magnetite rims throughout the deposit (WB05-188 59.5 m).

The syn-breccia veins are typically <0.1 to <1 cm, rarely >1 cm, in width. They have limited or no alteration selvedges, are straight-walled, fine to coarse grained and have mineralogies consistent with the local breccia cement.

Stage 2 has been subdivided into seven sub-facies based on the predominant cement mineralogy (Table 3.4). Textures and cement compositions vary laterally and vertically throughout the breccia complex.

Cement minerals vary from euhedral crystals (magnetite, clinopyroxene, pyrite, K-feldspar, apatite, garnet, anhydrite) to anhedral blebs (bornite, chalcopyrite, Na-feldspar, K-feldspar, epidote, chlorite, calcite, anhydrite) and highly fractured aggregates (magnetite, pyrite, garnet). These minerals were also observed locally as alteration products in the clasts and matrix. Cement textures ranged from fine (<0.5 mm) to coarse grained (>50 mm), and from symmetrical open-space infill to cryptic fine-grained altered matrix (Figs. 4.10, 4.11). Some domains of breccia cement and syn-breccia veins are monomineralic, while others contain several minerals.

Relative timing relationships have been established from hand sample observations and thin section analyses. Stage 2 evolved from early magnetite ± K-feldspar ± albite ± chlorite to later Cu-Fe-sulfides associated with K-feldspar, albite, biotite, apatite, epidote, calcite, prehnite, actinolite and garnet to late calcite-anhydrite infill (Fig. 4.8). The four main Cu- and/or Fe-bearing cements, in paragenetic order, are magnetite, bornite, chalcopyrite and pyrite (Figs. 3.11 and 4.10).

Two main alteration stages were identified by Ross (2004b) in her study of the southern end of the shallow breccia-hosted zone. These were an early magnetite-garnet-apatite ± albite stage and a younger clinozoisite/prehnite-albite-calcite ± apatite ± garnet stage, the latter being associated with most of the Cu-sulfide mineralization. Both stages were grouped by Ross (2004b) into a calc-silicate alteration assemblage.

Jackson (2008) identified domains of chlorite, biotite, sulfide, magnetite, K-feldspar, albite-epidote and albite-actinolite dominant infill in the NEZ breccia. Carbonate was also identified as a breccia cement by Ross (2004b) and Jackson (2008), in some cases preceding or intergrown with sulfide minerals.

Logan and Mihalnyuk (2005) proposed that Cu-mineralization developed in two stages. Firstly chalcopyrite was deposited within an interconnected network of fracture and veinlets. Then bornite rimmed and replaced the chalcopyrite veinlets. Their bornite veins may be equivalent to stage 3 veins (described below).

Based on observations made during the current study, magnetite formed throughout the main-stage, but was most abundant at its initiation (Fig. 4.8), when it formed monomineralic breccia cement at depth in the deep breccia zone and large (up to 1 cm)

Table 4.3 Examples of intrusive units with low to high grades of Cu and Au.

Intrusive Unit	Mineralization	Occurrence	Grade[1]	Example
Monzonite	cp, or bn (stage 3)	Abundant veins, blebs, lesser disseminations, vein array (breccia halo)	1.069% Cu 0.49 g/t Au 9.9 g/t Ag	WB03-03: 97.5 to 116.3 m WB04-29: 21.34 to 30 m
	cp (stage 1?)	Disseminated, isolated bleb and vein	0.687% Cu 0.3 g/t Au 3.4 g/t Ag	WB05-188: 442.5 to 517.5 m
Sparsely K-feldspar-phyric monzonite	cp (stage 3)	Disseminated ± veins	0.465% Cu 0.06 g/t Au 4.1 g/t Ag	WB04-108: 287.8 to 292.5 m
Moderately K-feldspar-phyric monzonite	cp (stage 3)	Veins	[2]	WB05-108: 225.0 to 227.5 m
Diorite	cp, bn (stage 3)	Veins	[2]	WB05-213 354.9 to 355.6 m
Crowded K-feldspar-phyric monzonite	None identified	-	-	-

[1]Grades reported are the highest reported from drill core intersections contained completely within the intrusive unit.
[2]These units were too thin to obtain assay values completely within the intrusive unit.
Abbreviations: cp-chalcopyrite, bn-bornite, Cu-copper, Au-gold, Ag-silver

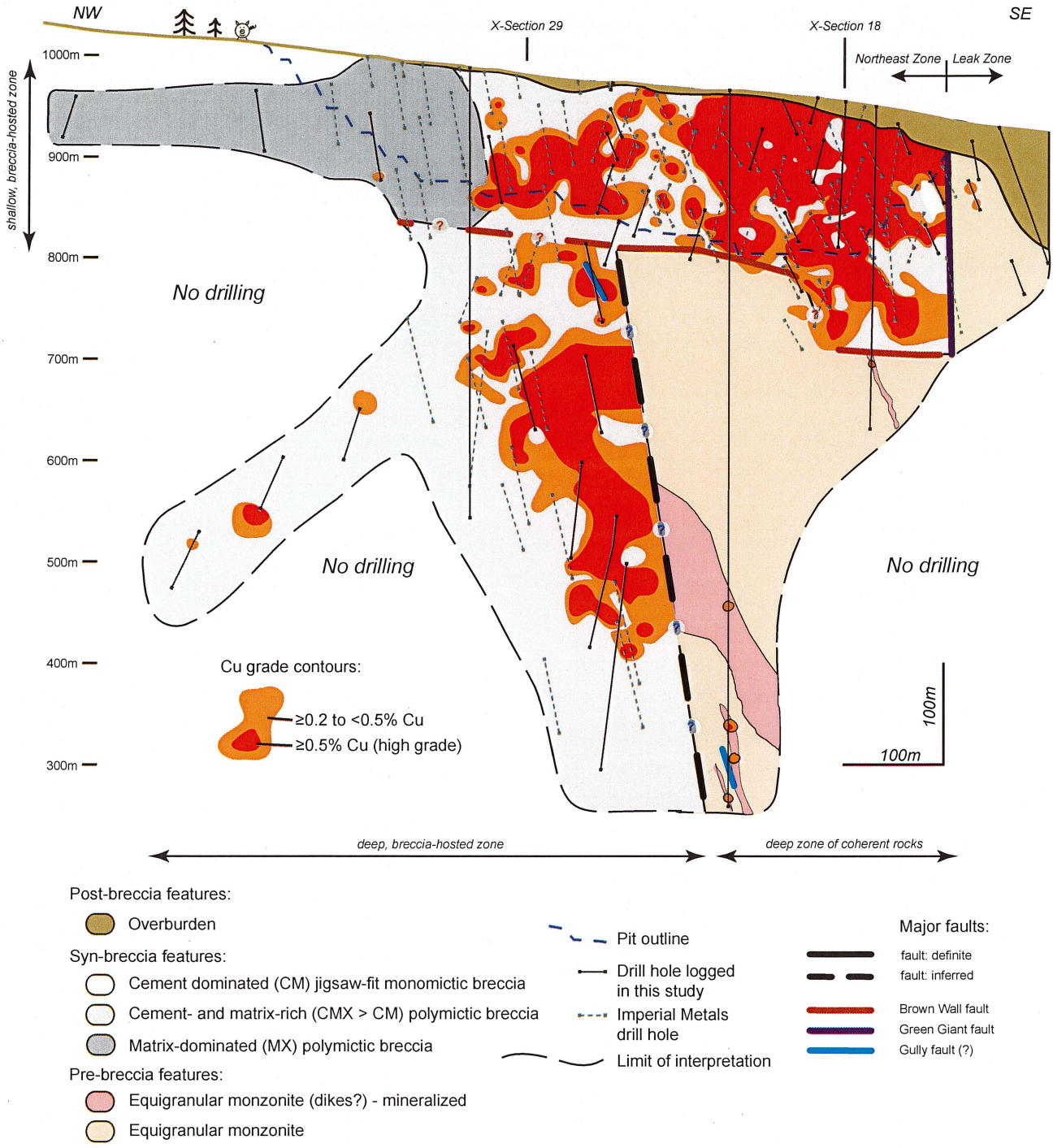

Figure 4.5 Copper grade contours determined from Imperial Metals whole rock assay data taken from all boreholes on section. Contours were produced with Surfer 7.0 (gridding method: minimum curvature with 1.1 and 0.83 x and y spacing, respectively). Also shown is a simplified summary of the main geological elements.

euhedral crystals in veins and multi-mineral infill (Fig. 4.10A to D). Petrographically, magnetite is commonly observed to have been altered to hematite along grain boundaries. Magnetite has also been partially replaced by chalcopyrite or pyrite, which typically forms as rims around magnetite where these minerals occur together (Fig. 4.10B). Rare examples of chalcopyrite pseudeomorphs after magnetite have been observed in stage 2 breccia.

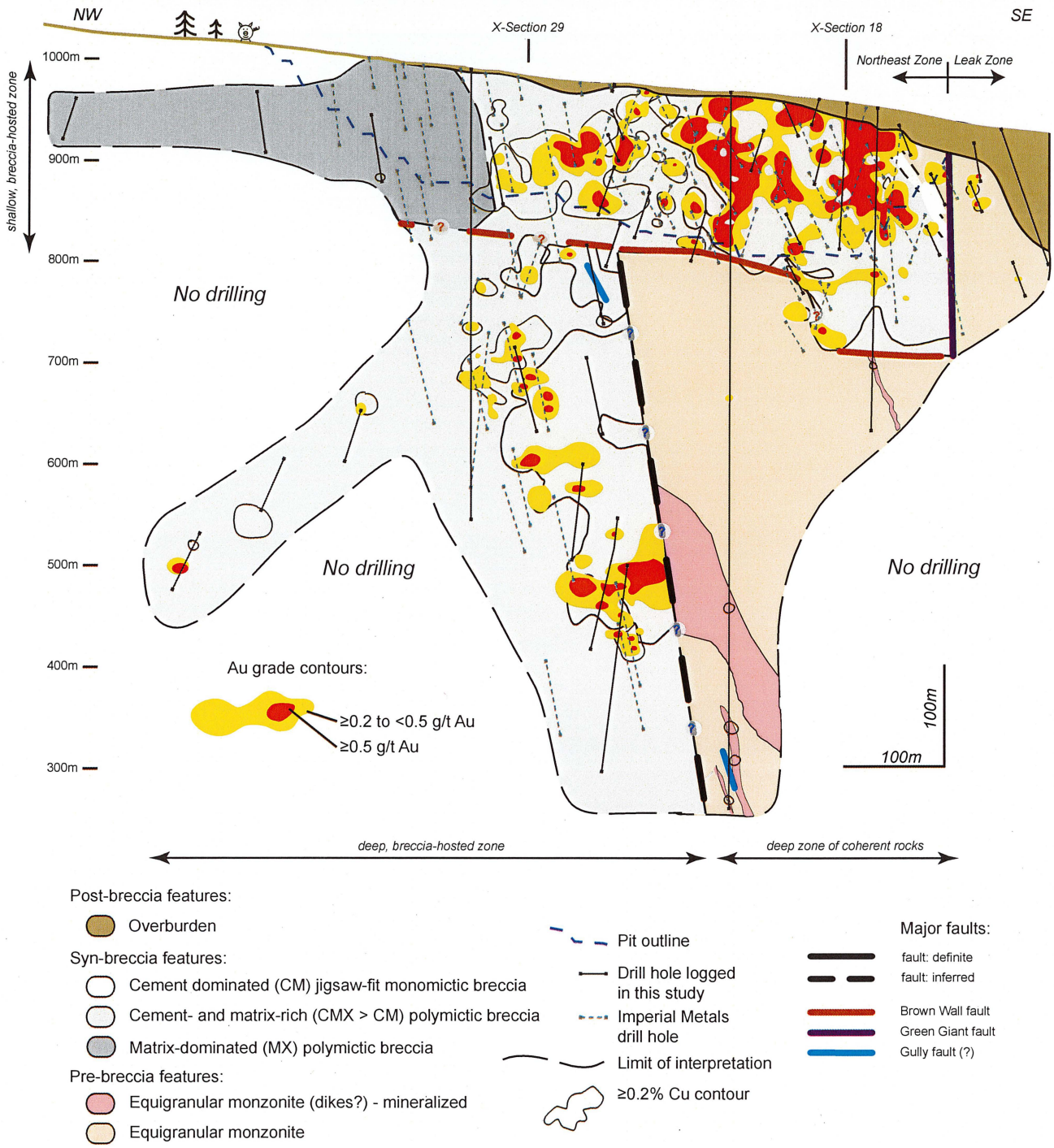

Figure 4.6 Gold grade contours determined from Imperial Metals whole rock assay data taken from all boreholes on section. Contours were produced with Surfer 7.0 (gridding method: minimum curvature with 1.1 and 0.83 x and y spacing, respectively). Also shown is a simplified summary of the main geological elements and the ≥0.2% Cu contour has been outlined in solid black.

Stage 2 chalcopyrite and bornite are typically intergrown with each other, and also with apatite and calcite (Fig. 4.10A, E and F). Chalcopyrite was also observed to be intergrown with clinopyroxene, garnet and feldspar (Figs. 4.9C and 4.10A, G) and in one case galena. Garnet and bornite have not been observed together in this study.

Stage 2 clinopyroxene crystals are light to dark green and euhedral. Garnets are honey- to brown-colored and can be homogenous or zoned (Figs. 4.10G

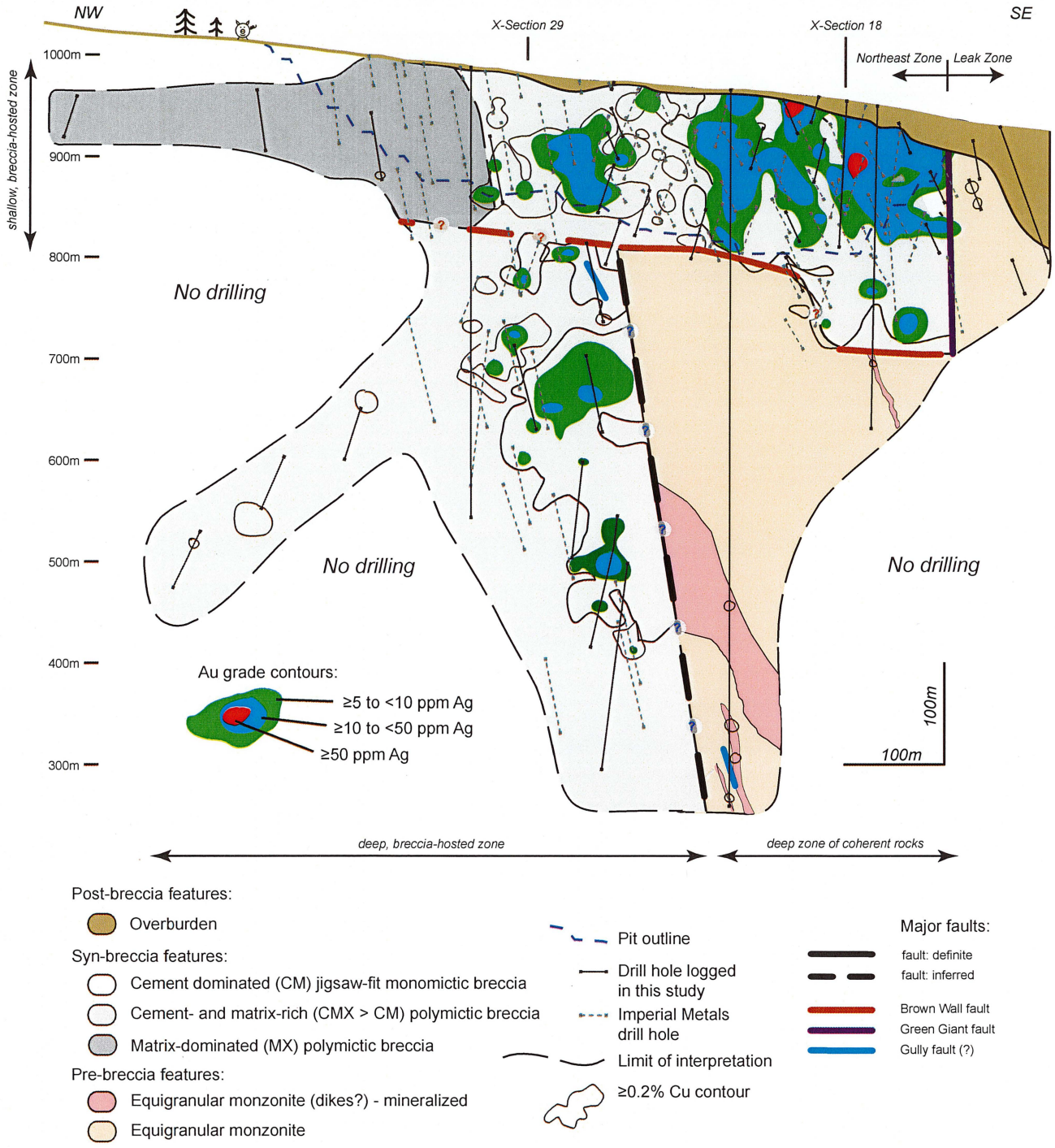

Figure 4.7 Silver grade contours determined from Imperial Metals whole rock assay data taken from all boreholes on section. Contours were produced with Surfer 7.0 (gridding method: minimum curvature with 1.1 and 0.83 x and y spacing, respectively). Also shown is a simplified summary of the main geological elements and the ≥0.2% Cu contour has been outlined in solid black.

and 4.11A–C). Electron microprobe analyses by Ross (2004b), has shown the garnets to be predominantly andraditic.

Feldspar cement most commonly occurs as anhedral blebs (Figs. 4.9E, 4.10C, D and 4.11D–F). Petrographically, mineralogical identification of feldspar blebs was difficult due to hematite ± illite (± muscovite ± montmorillonite) alteration or precipitation in aphanitic masses. Investigation of selected samples using staining and a scanning electron microscope (SEM) with energy

dispersive spectrometry (EDS) identified feldspar compositions of orthoclase, anorthoclase, albite and andesine. In some cases albite was observed to have partially replaced orthoclase.

Calcite, together with elongate tabular crystals or blebs of anhydrite and gypsum, formed late during stage 2 (Fig. 4.12M). Observations from petrographic analyses imply that gypsum has partially replaced anhydrite.

Intense, pervasive, texturally destructive domains of massive, salmon pink-colored K-feldspar (>5 to >50 cm) characterize intervals of intense potassic alteration (Fig. 4.11G). These are believed to be equivalent to Jackson's (2008) "K-feldspar flooding" assemblage. The timing of this intense K-feldspar alteration is uncertain. Some domains have clasts with distinctive K-feldspar alteration rinds and Cu-sulfide breccia cement indicating syn-breccia timing (Fig. 4.11G). Other domains of massive salmon pink-colored K-feldspar alteration are less indicative of their timing. On this basis, intense potassic alteration is interpreted to be part of stage 2, but some may have also developed during stage 3 (late mineralization).

A marble clast with an alteration rind was sampled from the breccia complex at the southern end of the open pit (section 3.5). SEM and EDS analyses have revealed that the dark colored, very fine-grained rind is composed primarily of clinochlore (chlorite) and sphalerite with lesser amounts of pyrite, galena, chalcopyrite and traces of molybdenite (Fig. 4.11H). This base-metal occurrence is assigned to stage 2 based on its mode of occurrence (i.e. clast rind); it is the only observation of sphalerite made during this study.

4.5.3 Stage 3: Late-stage mineralization

Late-stage mineralization (stage 3; Fig. 4.8) is interpreted to have occurred episodically after breccia consolidation. This stage produced Cu-sulfide bearing veins, faults and dikes. It has not been possible to determine paragenetic relationships amongst all stage 3 features due to a lack of cross-cutting relationships.

Assay results from drill core that contains stage 3 mineralization can reach >1 percent Cu, up to 0.5 g/t Au and 1 g/t Ag. Nonetheless, the amount of Cu-mineralization introduced during stage 3 was less than stage 2 (visual estimate of ≤10 volume %, compared to ≥90 volume % of the Cu sulfides in the NEZ; Figs. 4.5 to 4.7).

Stage 3 veins are on average <0.5 to <5 cm wide, but can be >15 cm wide locally. They occur as isolated veins (Fig. 4.12A), as vein networks that have cut breccia clasts (Fig. 4.12B), and as veins that have cross-cut the contacts of post-breccia intrusions (Fig. 4.12A). Sulfide-rich mylonites are a minor but distinctive component of stage 3 (Fig. 4.12C, D). They contain abundant bornite and apatite with lesser chalcopyrite (± K-feldspar ± sulfosalts ± primary chalcocite), commonly with a distinctive foliation (Fig. 4.12C, D).

There are many types of stage 3 veins in the NEZ, but chalcopyrite ± pyrite-bearing veins and albite ± bornite veins are the most common. Some chalcopyrite-albite-calcite veins have albite alteration halos (Fig. 4.12E, F). An isolated example of an albite-galena vein that contains minor chalcopyrite, altered magnetite and calcite has cross-cut the breccia (Fig. 4.12G, H). Numerous barren late-stage carbonate veins have also cut the breccia complex and stage 3 intrusions. Additional garnet is interpreted to have formed during stage 3 because rare garnet veins with epidote alteration halos (<0.4 cm wide) have cross-cut post-breccia intrusions.

Some stage 3 mineralization occurs as chalcopyrite disseminations in post-breccia dikes. Anomalous Cu and Au grades have been identified over limited intervals in some equigranular to sparsely or moderately K-feldspar-phyric monzonite dikes (Table 4.3).

4.5.4 Stage 4: Unmineralized intrusions and veining

Stage 4 veins and intrusions of the NEZ have cross-cut earlier-formed units and contain very limited or no Cu-sulfides, and rare sulfide clasts derived from stage 2 or 3. Stage 4 includes a plethora of barren calcite-, sulfate- (anhydrite, gypsum, minor barite), albite-, clinozoisite- and/or prehnite-bearing veins, vein breccias and dikes (Fig. 4.8). Stage 4 also includes hematite-altered monzonite dikes that have cut the breccia and monzonite pluton of the NEZ and Leak Zone.

Stage 4 veins are typically 1 to 5 mm wide. Minor occurrences of vein breccias are typically <1

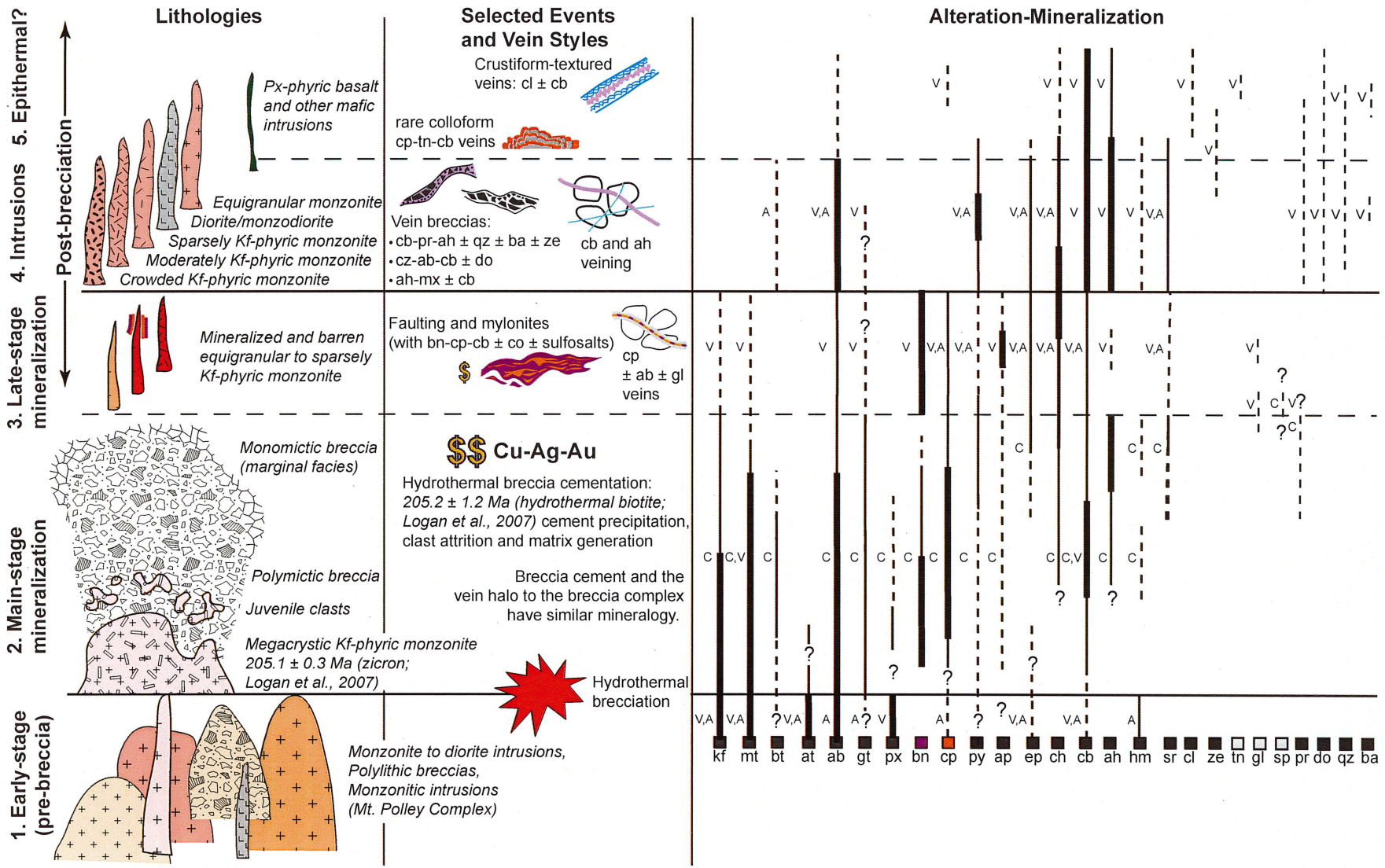

Figure 4.8 Summary of NEZ paragenesis. Questions marks indicate uncertainties regarding the timing and extent of mineral precipitation. Actinolite alteration was observed only in the Leak Zone in this study. Pre-breccia (stage 1) veins were observed as truncated veins in clasts or in the host rocks to the breccia. Syn-mineralization (stage 2) veins have been excluded for clarity, but formed coeval with breccia cement and have the same mineralogy. Stage 3 veins have cut the breccia or occur in post-breccia dikes that have cut the breccia. V-veins, A-alteration observed within coherent units or clasts, C-breccia cement, mx-matrix. Mineral abbreviations: ab-albite, af-alkali feldspar, ah-anhydrite, ap-apatite, at-actinolite, bn-bornite, ba-barite, bt-biotite, cb-carbonate, cc-calcite, cl-chalcedony, ch-chlorite, co-chalcocite, cp-chalcopyrite, do-dolomite, ep-epidote, gl-galena, gt-garnet, hm-hematite, kf-K-feldspar, mt-magnetite, pr-prehnite, px-pyroxene (augite), py-pyrite, qz-quartz, sp-sphalerite, sr-sericite, tn-tennantite, ze-zeolite (laumontite).

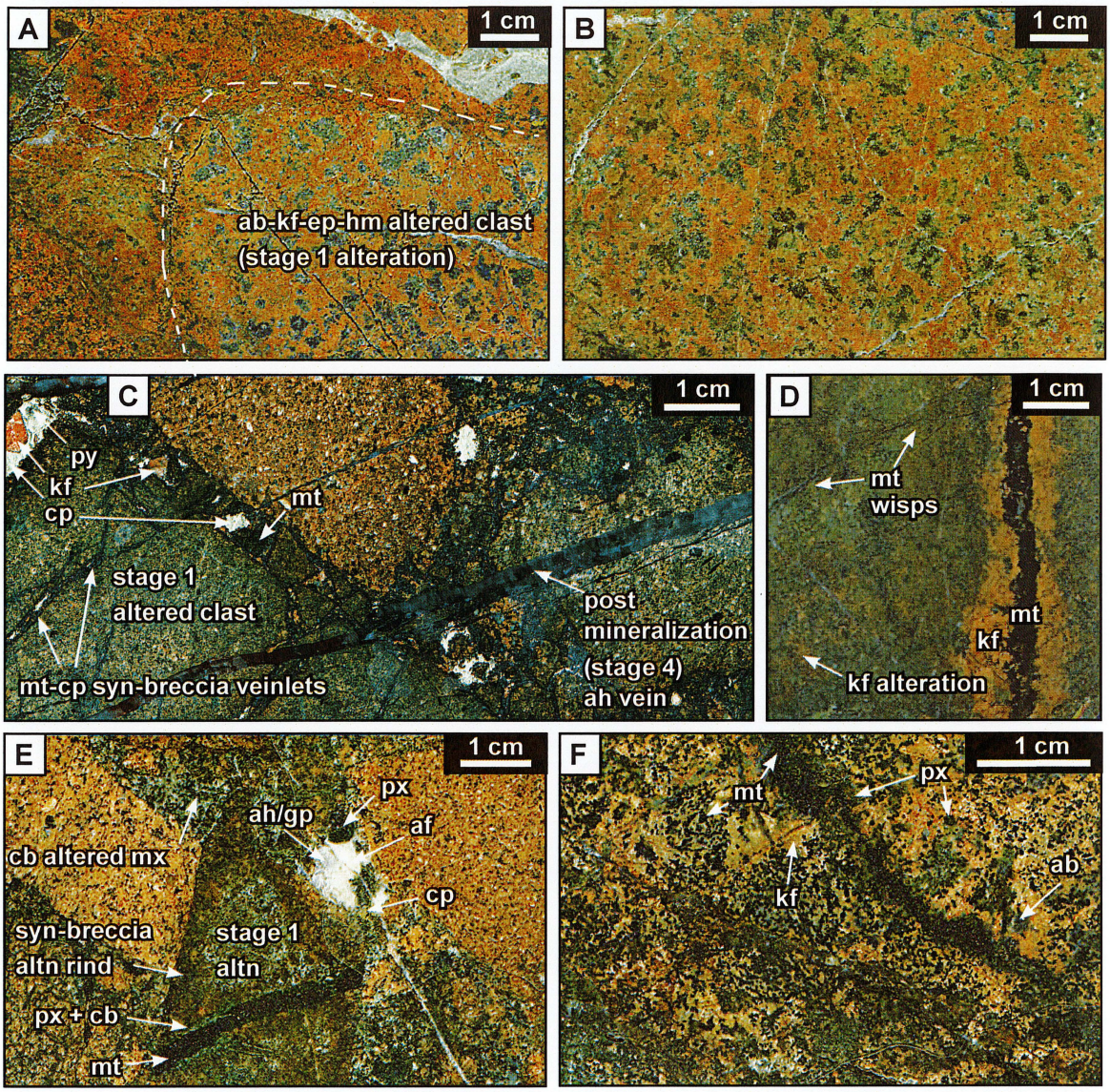

Figure 4.9 Stage 1 alteration (pre-brecciation). **A)** Polymictic CMX breccia with clast of intensely K-feldspar-albite-epidote-altered monzonite (WB04-95 181.6 m). **B)** Intense K-feldspar-clinopyroxene-albite alteration of monzonite host-rock from beneath the zone of shallow breccia-hosted mineralization in the southern end of the NEZ. Alteration is similar to that observed in clast in A (WB05-188 326.4 m). **C)** Three stages of mineralization: Stage 1 intensely K-feldspar-albite altered clast (lower left) containing syn-breccia (stage 2) magnetite-chalcopyrite veinlets. These veins have a similar mineralogy to the stage 2 magnetite-(euhedral)-K-feldspar-chalcopyrite and pyrite-calcite-chlorite cemented polymictic breccias. A stage 4 anhydrite vein has cross-cut the breccia (WB05-213 478.8 m). **D)** Magnetite vein with intense K-feldspar halo and magnetite wisps has cut texturally destructive potassic and albitic altered monzonite from beneath the shallow mineralized zone at the southern end of the NEZ (WB05-188 519.5 m). Alteration is similar to that observed in the lower left clast in C. **E)** Truncated magnetite-clinopyroxene vein with lesser calcite and alkali feldspar in CMX polymictic breccia. Matrix has been altered by carbonate. The center clast exhibits syn-brecciation (stage 2) alteration in the form of a hematite alteration rind (WB05-213 583.7 m). **F)** Strong pervasive K-feldspar-albite-clinopyroxene-magnetite alteration in monzonite(?) host rock (WB05-205 144.5 m, Leak Zone). The veins are similar to the truncated vein in E. Mineral abbreviations: ab-albite, af-alkali feldspar, an-anhydrite, cb-carbonate, cp-chalcopyrite, ep-epidote, gp-gypsum, hm-hematite, kf-K-feldspar, mt-magnetite, mx-matrix, px-clinopyroxene.

to >20 cm wide (Fig. 4.13A–G). Pale to bright pink manganoan calcite-cemented vein breccias (up to 2.1 wt % Mn; Appendix C2; "rhodochrosite" field term), found on the northern periphery of the long-section contain euhedral quartz crystals (Fig. 4.13C, D). This is one of the few known occurrences of quartz at Mt. Polley. Manganoan calcite-filled amygdales have been observed in a hematite-dusted equigranular monzonite

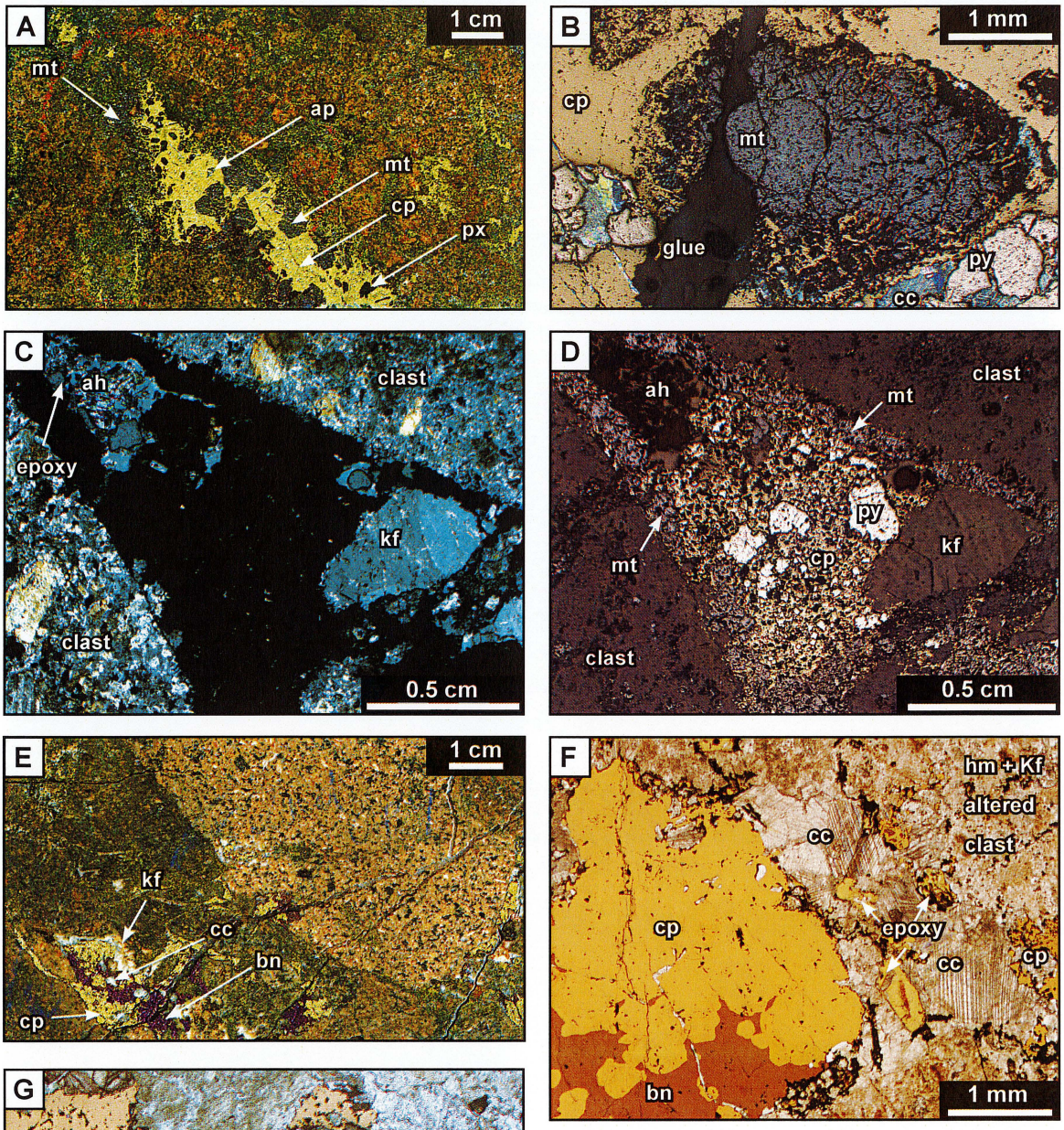

Figure 4.10 Examples of stage 2 breccia cement. **A)** Equigranular monzonite clast-rich breccia with symmetrical open space cement: chalcopyrite (+ bornite + apatite) has overgrown euhedral pyroxene which has overgrown euhedral magnetite (WB05-188 59.5 m). **B)** Chalcopyrite (± pyrite) has partially replaced magnetite cement. (WB04-40 65.0 m). **C)** and **D)** Transmitted (xpl) and reflected light images of breccia cement: chalcopyrite (intergrown with pyrite) with anhydrite and K-feldspar after magnetite (WB05-210 519.3 m). **E)** Polymictic monzonite breccia with open space cement infill: chalcopyrite and bornite intergrown with calcite after K-feldspar (WB04-115 392.3 m). **F)** Reflected and transmitted light image (ppl) of intergrown chalcopyrite and calcite (WB04-115 385.5 m). **G)** Reflected and transmitted light image (ppl) of chalcopyrite, calcite and garnet (WB04-95 65.0 m). Mineral abbreviations: ah-anhydrite, ap-apatite, bn-bornite, cc-calcite, ch-chlorite, cp-chalcopyrite, gt-garnet, hm-hematite, kf-K-feldspar, mt-magnetite, py-pyrite, px-clinopyroxene.

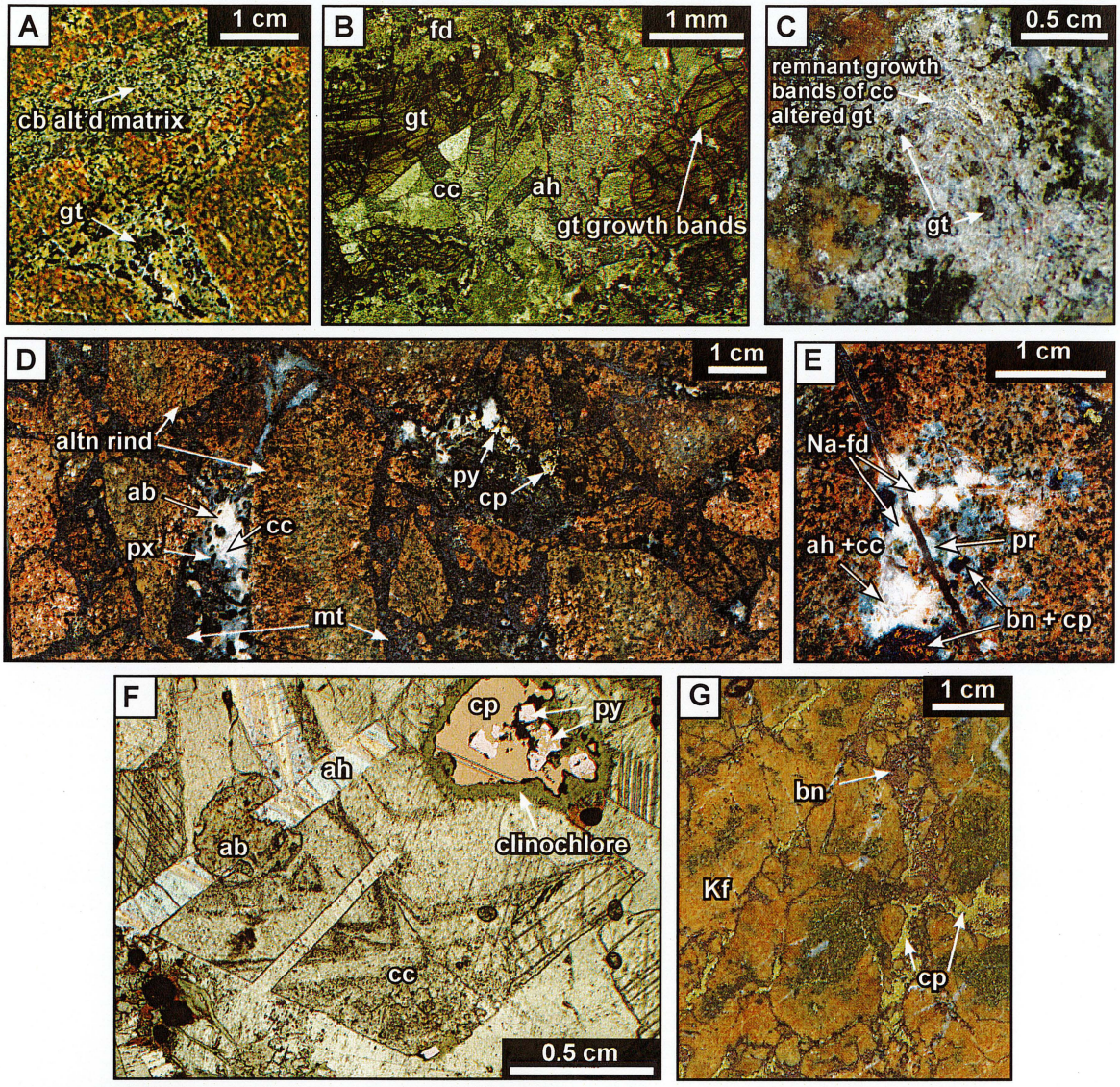

Figure 4.11 Additional examples of stage 2 breccia cement. **A)** Polymictic matrix-dominated breccia with euhedral garnets (WB04-150 459.9 m). **B)** Transmitted light image of breccia cement highlighting zoned garnet (WB04-150 459.9 m-5x magnification). **C)** Carbonate-altered garnet. When preserved, garnet cores have distinctive growth bands. These have been completely replaced by calcite aggregates with magnetite, tridymite, and hematite (WB04-31 82.5 m). **D)** Polymictic magnetite-clinopyroxene-albite-calcite-chalcopyrite-pyrite-cemented breccia. Clasts exhibit albite-epidote alteration with hematite dusted syn-breccia alteration rinds (WB05-210 491.5 m). **E)** Bornite, chalcopyrite, Na-feldspar, prehnite, calcite and anhydrite-cement in a polymictic breccia. Anhydrite crystals are tabular-shaped. (WB04-122 334.1 m). **F)** Combined reflected and transmitted light photomicrograph of primary zoned calcite intergrown with bladed anhydrite and chalcopyrite + pyrite. Albite has paritally replaced anhydrite and calcite. A rim of clinochlore has grown around the chalcopyrite and pyrite, and pyrite alteration has partially replaced some chalcopyrite (WB05-210 491.8 m). **G)** Example of texturally destructive K-feldspar flooding and rare early fine-grained chalcopyrite in clasts (WB03-03 120.9 m). **H)** Reflected and transmitted light image (xpl) of rind on metasomatized limestone clast sampled from the south end of the pit (NEZ DOL). Abbreviations: alt'd-altered, altn-alteration, see Figure 4.8 for mineral abbreviations.

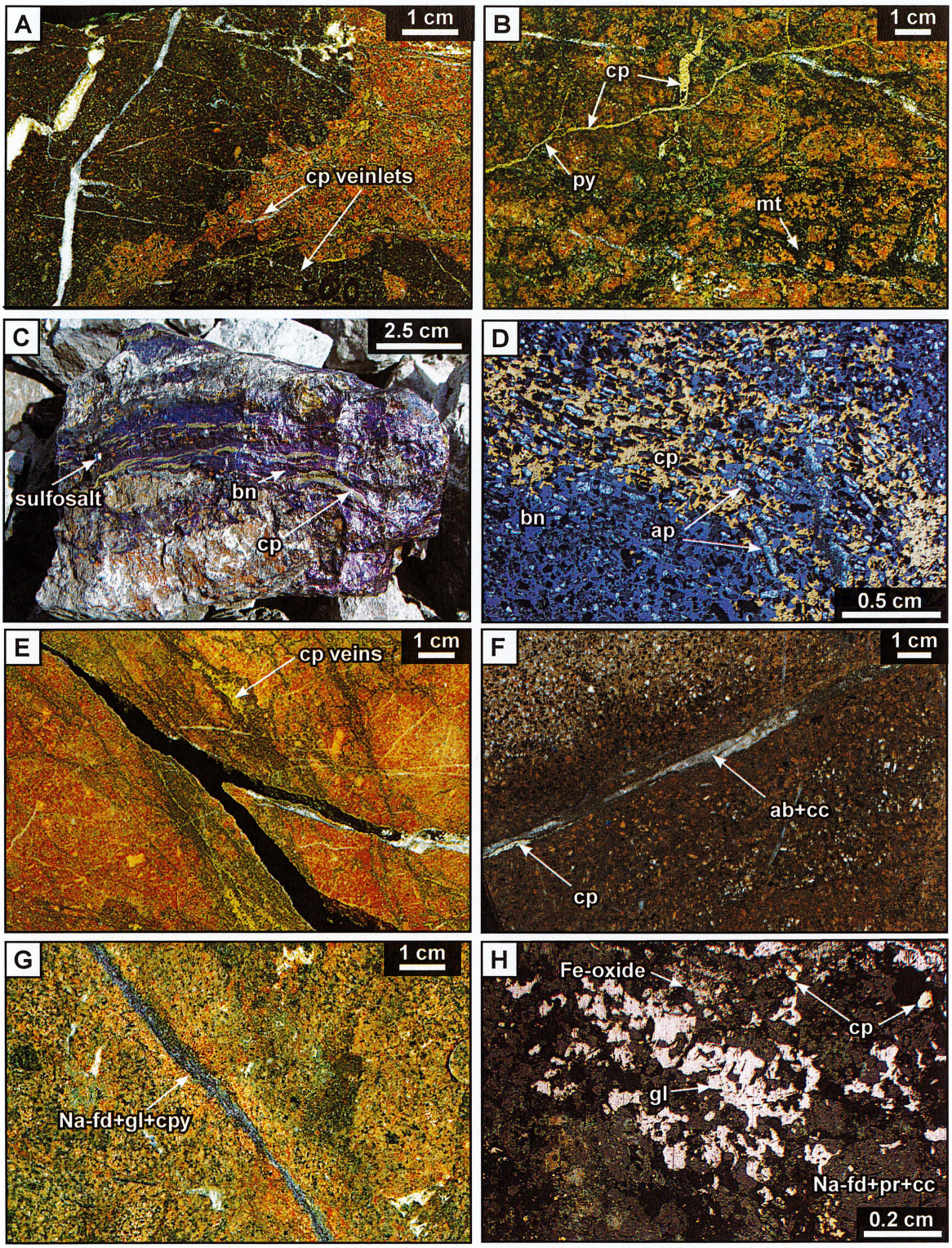

Figure 4.12 Examples of stage 3 post-brecciation mineralization. **A)** Chalcopyrite and calcite veinlets (<1.5 mm) that have cross-cut post-breccia aphanitic and equigranular monzonites. The globular edges of the intrusion and the anastomosing morphology of the veins indicate that the intrusions were semi-ductile during emplacement and vein formation (WB04-29 50.0 m). **B)** Chalcopyrite with minor pyrite vein has cross-cut magnetite-cemented monzonite clast-rich breccia and earlier calcite vein (WB05-213 487.7 m). **C)** Bornite-chalcopyrite mylonite with euhedral sulfosalts (pit sample). **D)** Reflected and transmitted light image of mylonite. Note abundance and alignment of apatite (WB04-12 47.5 m). **E)** Chalcopyrite veining with evidence of shearing in sparsely K-feldpsar-phyric monzonite dike (WB04-108 225.5m). **F)** Chalcopyrite-albite-calcite vein with feldspar halo has cross-cut a post-breccia plagioclase-porphyry dike with selective-pervasive albite alteration (WB05-122 367.1m). **G)** Isolated example of a Na-feldspar-galena-chalcopyrite ± calcite vein with K-feldspar halo has cross-cut polymictic breccia (WB04-111 251.8m). **H)** Reflected light image of vein in F highlighting the occurence of galena. See Fig. 4.8 for mineral abbreviations.

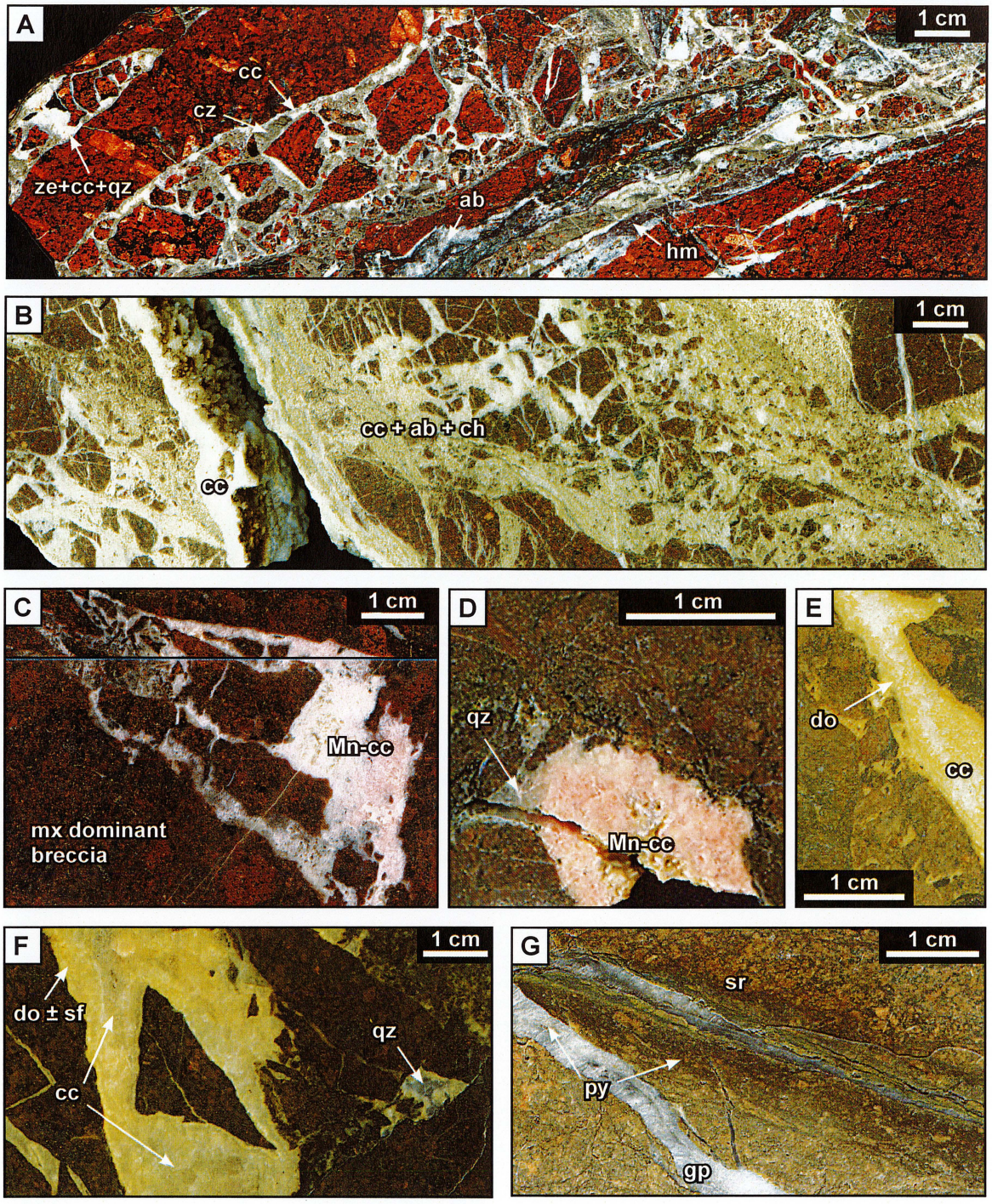

Figure 4.13 Examples of stage 4 veins and vein breccias. **A)** Multiple openings of calcite-albite-clinozoizite-zeolite-hematite vein breccia with traces of quartz has cross-cut polymictic (moderately K-feldpar-phyric monzonite and equigranular monzonite) breccia (WB04-26 68.1 m). **B)** Vein breccia cemented by calcite-albite-chlorite-clays-datolite (boro-silicate) with trace quartz and prehnite vein breccia cut by multiply reactivated calcite vein (WB04-26 221.8 m). **C)** Mangano-calcite cemented vein breccia has cross-cut matrix-dominant stage 2 breccia (WB04-141 126.0 m). **D)** Euhedral quartz forms a partial rim to manganoan calcite infill (WB05-233 188.0 m). **E)** and **F)** Zoned dolomite has overgrown sulfate crystals, followed by sparry calcite infill and late quartz-cemented vein breccia (vein-WB04-108 369.1 m, vein breccia-WB04-108 310.2 m) **G)** Example of phyllic alteration in pyrite vein with sericite alteration halo. This vein is cross-cut by a fibrous gypsum vein (WB05-213 616.5 m). See Fig. 4.8 for mineral abbreviations.

from the same area.

There are abundant pyrite (± sericite) shear veins that have cross-cut the post-breccia monzonite dikes (Fig. 4.13G). These veins are interpreted to be associated with weak phyllic alteration that is commonly located in the center of the dikes.

Several carbonate (calcite ± ankerite ± dolomite) veins and vein breccias have cross-cut the breccia complex and later felsic dikes (Fig. 4.13E, F). Davidson et al. (in prep.) has shown that these vein breccias contain datolite, a boro-silicate ($CaB(SiO_4)(OH)$), together with albite, K-feldspar, prehnite, quartz, anhydrite, gypsum, barite, dolomite, chlorite, clays and abundant calcite. Microscopic pyrite and chalcopyrite grains are associated with the feldspars and prehnite.

4.5.5 Stage 5: Epithermal (?) overprint

A number of calcite-, chalcedony-, and amythest-bearing veins display distinctive banded, colloform and locally bladed carbonate ± anhydrite textures. These veins, which have sericitic alteration halos, have cut the breccia complex and post-breccia dikes, including the augite-phyric basalt dikes (Fig. 4.14A–H). The vein textures and mineralogies are consistent with low-sulfidation epithermal-style features (e.g. White and Hedenquist, 1990; Simmons and Christenson, 1994). Some stage 5 veins contain barite and calcite, which have replaced dolomite locally (Davidson et al., in prep.). A handful of other vein types and an unusual breccia containing clasts with colloform-textured rinds are also inferred to have formed in an epithermal style setting (Fig. 4.14 I–N). All of these stage 5 features, while noteworthy, are too small and rare to be shown on long-section. The exact extent of the distribution of these features is currently unknown. However, epithermal-style veins were also documented in the NEZ by Ross (2004b) and Jackson (2008) as well as in the regional study of Pantelevey et al. (1996) and at Mt. Milligan by LeFort et al (in review).

Colloform textures have been observed in stage 5 chalcopyrite-tennantite-calcite veins (Fig. 4.14K and L). Such textures are rare and are believed to only form at very low temperatures (Ramdohr, 1969).

Stage 5 veins are barren and did not contribute to the Au-Ag endowment of the NEZ, with the exception of the colloform chalcopyrite-tennantite veins, as revealed by selective geochemical assays of stage 5 vein samples (Appendix C3). However, the juxtaposition of porphyry- and epithermal-features implies that significant erosion or unloading took place during the evolution of the hydrothermal system, or that two or more hydrothermal systems were active in the NEZ at different points in time (e.g. Jensen and Barton, 2000; Sillitoe, 2010). This issue will be considered further in Chapter 5.

4.6 Spatial distribution of main-stage cement and alteration minerals

This section describes the spatial distributions of stage 2 K-feldspar, magnetite, biotite, anhydrite-gypsum, garnet, epidote, chlorite and albite breccia cement on the long-section (Fig. 4.15). These observations are compared and contrasted with the silicate cement distributions (i.e. albite-actinolite, albite-epidote, K-feldspar) mapped by Jackson (2008; Fig. 4.16). Jackson (2008)

Figure 4.14 Examples of veins from the NEZ exhibiting epithermal-style textures (stage 5). **A)** Cockade banded quartz-amethyst vein has cross-cut an augite-phyric basalt dike (WB04-27 277.1 m). **B)** Banded, milky chalcedony vein has cross-cut an augite-phyric basalt dike (WB04-27 277.2 m). **C)** Symmetrically banded crustiform quartz vein has cross-cut an equigranular monzonite dike (WB04-108 111.7m). **D)** Asymmetrically banded chalcedony vein with wall-rock fragments has cross-cut an equigranular monzonite dike (WB04-29 130.9 m). **E)** Banded calcite-dolomite vein with bladed chalcedony-calcite core (pit sample 'NEZboil'). **F)** Crustiform texture of chalcedony in E. **G)** Bladed quartz-anhydrite-calcite vein with sericitic halo has cross-cut tennantite vein network (WB03-07 81.0 m). **H)** Transmitted light photomicrograph showing comb quartz texture in bladed vein in G. **I)** Banded crustiform quartz-calcite-dolomite veins with remnant bladed textures have cross-cut local tennantite-chalcopyrite-bornite cemented monomictic breccia (WB03-07 81.0 m). Arrow points at bladed texture. **J)** Polymictic breccia with abudant fine-grained matrix contains monzonite clasts with broken and continuous colloform rinds, broken vein peices and pieces of banded colloform quartz (pit sample 'NEZepi'). **K)** Polymictic breccia with open space infill showing stage 2 chalcopyrite cement (i) and younger banded colloform chalcopyrite-tennantite with microscopic calcite cement (ii) after dogtooth calcite (pit sample NEZ936-11). **L)** Chalcopyrite and tennantite colloform detail in K. **M)** and **N)** Rare examples of graded and laminated matrix in veins that have cross-cut the main breccia body. Veins contain laminated mud- to sand-sized fragments associated with hydrothermal components and epithermal-style veins (WB04-95 219.4 m and WB04-95 255.4 m, respectively).

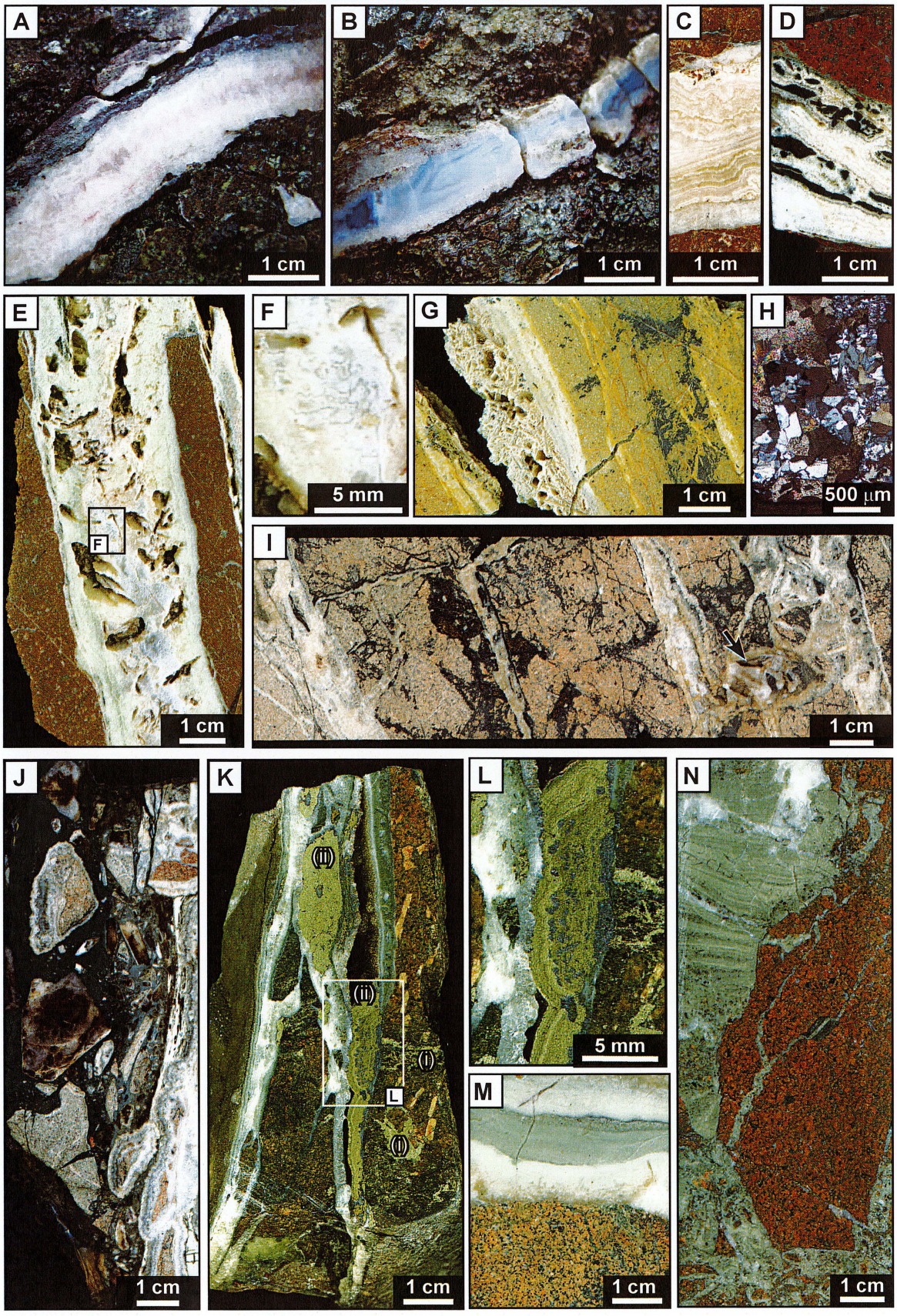
A
1 cm
B
1 cm
C
1 cm
D
1 cm
E
F
1 cm
F
5 mm
G
1 cm
H
500 µm
I
1 cm
J
1 cm
K
(iii)
(ii)
(i)
L
(i)
1 cm
L
5 mm
M
1 cm
N
1 cm

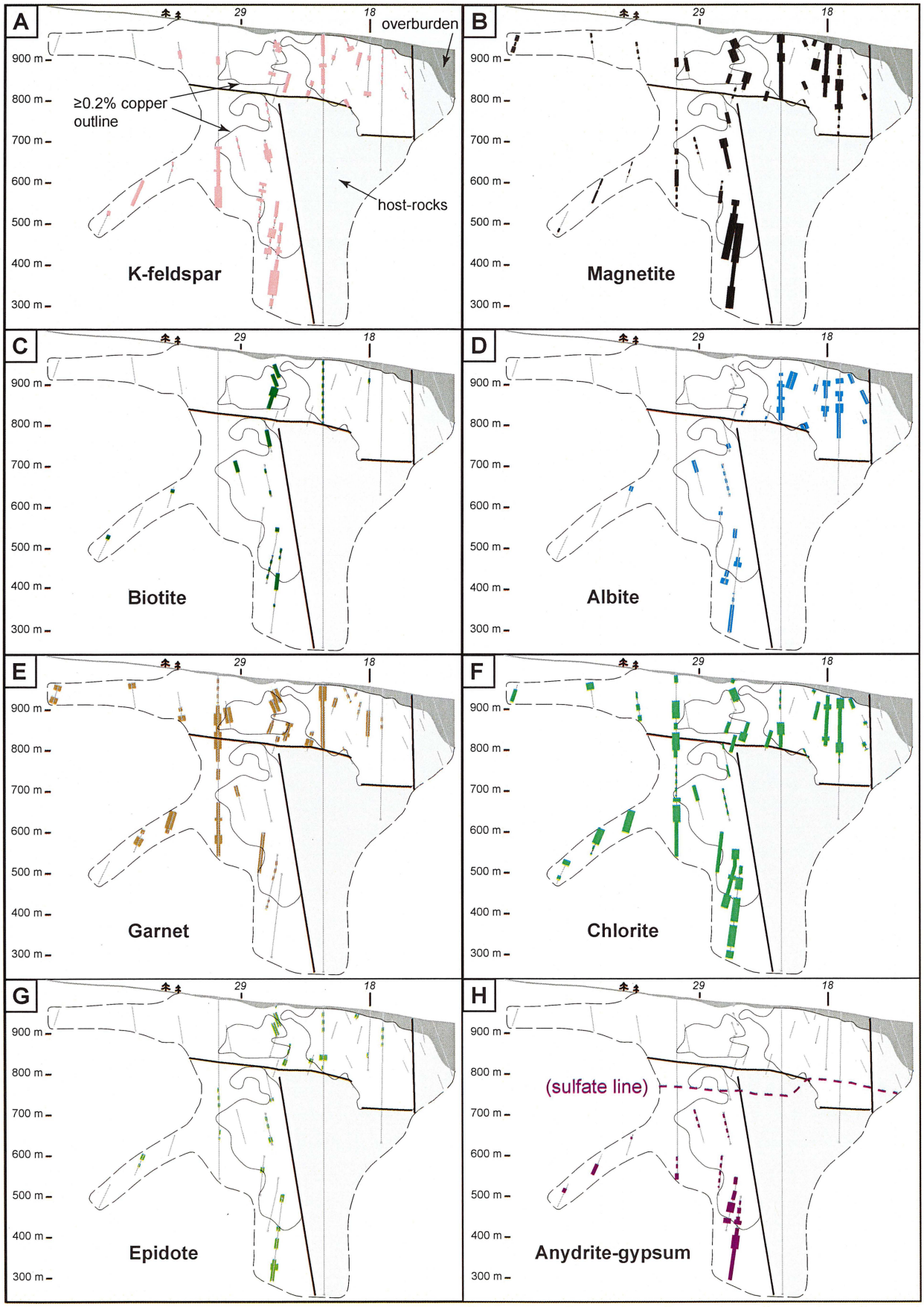
A
29
18
overburden
900 m
800 m
700 m
600 m
500 m
400 m
300 m
≥0.2% copper outline
host-rocks
K-feldspar
B
Magnetite
C
Biotite
D
Albite
E
Garnet
F
Chlorite
G
Epidote
H
(sulfate line)
Anydrite-gypsum

Figure 4.15 (previous page) Spatial distribution of eight main stage (stage 2) breccia cement minerals on a simplified outline of the long-section. See Figure 4.2 for detailed legend of general features. Line thickness indicates relative mineral proportion from minor (thin), to moderate to abundant (thick).

commented that the silicate cements may reflect primary hydrothermal cement and/or post-breccia modification by alteration. They are considered here to be most likely of stage 2 timing.

4.6.1 K-feldspar, magnetite and biotite

The most common cement minerals associated with mineralization on the long-section are K-feldspar and magnetite (Fig. 4.15A and B). Magnetite cement has a wider spatial distribution than K-feldspar, with magnetite found in varying amounts throughout the breccia complex. Magnetite-cemented breccia has been observed in each mineralized center, and well-developed magnetite-chlorite-rich breccia cement (>85% magnetite; Fig. 3.8B) is located slightly below the deep breccia-hosted ore zone and in pockets of the shallow breccia-hosted zone (Fig. 4.15B). Extensive magnetite and chlorite-cemented breccia was also observed at depth on section 29 (Figs. 4.3 and 4.16). K-feldspar-dominated cement forms a tabular zone and pods in cross-section (Fig. 4.15A; Jackson, 2008).

Biotite is more spatially restricted as a cement phase compared to K-feldspar and magnetite on the long-section (compare Figure 4.15C with A and B). Biotite cement is most prevalent in the north side of the shallow ore zone and in the top and bottom of the deep breccia-hosted ore zone (Fig. 4.15C). However, on the long-section, biotite only occurs as the dominant breccia cement at two locations, over intervals of ≤10 cm. In contrast to the long-section, biotite is more widespread on sections 18 and 29 (Fig. 4.16) and is one of the main minerals associated with mineralization, reportedly forming 1–2 cm rims on clasts and in some cases having pervasively altered entire clasts (Jackson, 2008). Ross (2004b) did not report any biotite in her petrographic

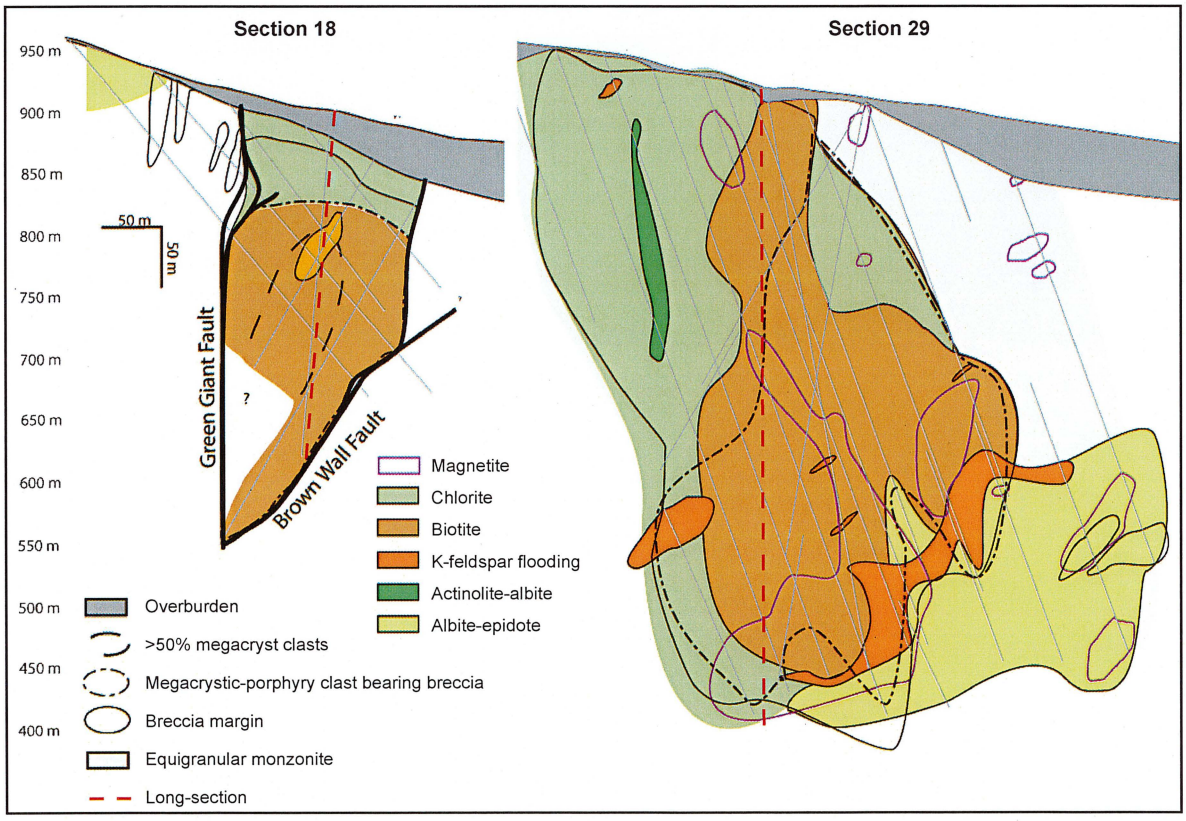

Figure 4.16 NEZ alteration distribution on cross-sections 18 and 29 taken from Jackson (2008). The approximate location of the long-section is shown by the dashed red line.

study of the NEZ, including section 18, and Rees et al. (2005) noted that biotite is rare in the NEZ. Their observations are consistent with the erratic distribution noted in the current study.

4.6.2 Albite

Albite cement is concentrated on the southern side of the shallow and deep breccia-hosted zones (Fig. 4.15D), with the greatest abundances in the shallow mineral zone and at depth in the deep breccia-hosted zone. The latter corresponds well with Jackson's (2008), albite-epidote dominant breccia cement. In the northwestern half of the long-section, albite and garnet rarely occur together (Fig. 4.15). In contrast, zones of these minerals overlap in the southern portion of the shallow zone.

4.6.3 Garnet and epidote

Zones of garnet cement occur with high-grade mineralization in the shallow breccia zone (Fig. 4.15E). However, garnet cement occurs adjacent to the bornite-rich domain in the deep breccia-hosted zone (compare Figs. 4.2 and 4.15E). Garnet is most intensely developed wherever albite is less strongly developed or absent (compare Fig. 4.15 E and D). Garnet cement extends north across the long-section where it is commonly associated with hematite and chlorite cement on the northern periphery of the long-section (i.e. DHH 233, 141, 108, and 131; Figs. 3.2, 4.15E and F). Lesser amounts of garnet cement were observed at the southern end of the shallow zone (Fig. 4.15E). Garnet has been commonly altered by calcite, producing a beige "oatmeal"-like appearance that locally preserves growth banding within altered garnet crystals (Fig. 4.11 A vs C). Garnet was not documented from sections 18 or 29 by Jackson (2008).

Epidote is only a minor breccia cement phase on the long-section, with the exception of the bottom of the deep breccia-hosted zone (Fig. 4.15G). Epidote is less widespread and abundant than garnet cement, but pockets of epidote cement were also observed in the shallow and deep breccia-hosted zones (Fig. 4.15G).

4.6.4 Anhydrite-gypsum

The distribution of sulfate on the long-section defines a "sulfate line" (approximately 740–780 m above sea level elevation, Fig. 4.15H). Above this line, little to no sulfate was observed. Below the line, anhydrite and gypsum occur as cement and in veins, commonly with calcite. The sulfate line is interpreted to be the lowest depths of groundwater permeation and sulfate dissolution, as has been noted from other porphyry Cu deposits (e.g. Rio Blanco, Chile; Frikken et al., 2005; also Sillitoe, 2005; Sillitoe, 2010). Anhydrite cement is most abundant at depth in the deep breccia-hosted zone (Fig. 4.15H), with lesser amounts noted where bornite and chalcopyrite abundances were greatest (compare with Fig. 4.2).

4.6.5 Carbonate, chlorite, hematite and sericite

Carbonate, chlorite, and minor hematite and minor sericite occur as breccia cement in the NEZ. Calcite cement occurs in varying abundance across the long-section. Late-stage calcite veins are ubiquitous, but are particularly abundant near faults. Rare pale pink carbonate (possibly manganoan calcite) cement was observed in the center of the long-section. Chlorite is the most widespread and abundant cement mineral observed from the long-section (Fig. 4.15F). In cross-section, chlorite was observed to be most abundant at shallow levels and peripheral to mineralization (Fig. 4.16; Jackson, 2008).

Domains of oxidized specularite cement are distinct from the widespread and pervasive sub-micron hematite alteration, and best developed in minor quantities on the northern side of the deposit (both shallow and deep zones). Specularite is associated with garnet and chlorite.

A volumetrically minor sericite-bearing breccia cement was observed in the far northern end of the long-section, as well as isolated pockets in the shallow and deep breccia-hosted zones.

4.7 Spatial distribution of alteration assemblages

Breccia cement and alteration minerals in the NEZ define irregular zonation patterns throughout the NEZ (Fig. 4.17). Table 4.4 summarizes the alteration mineral assemblages interpreted from the long-section,

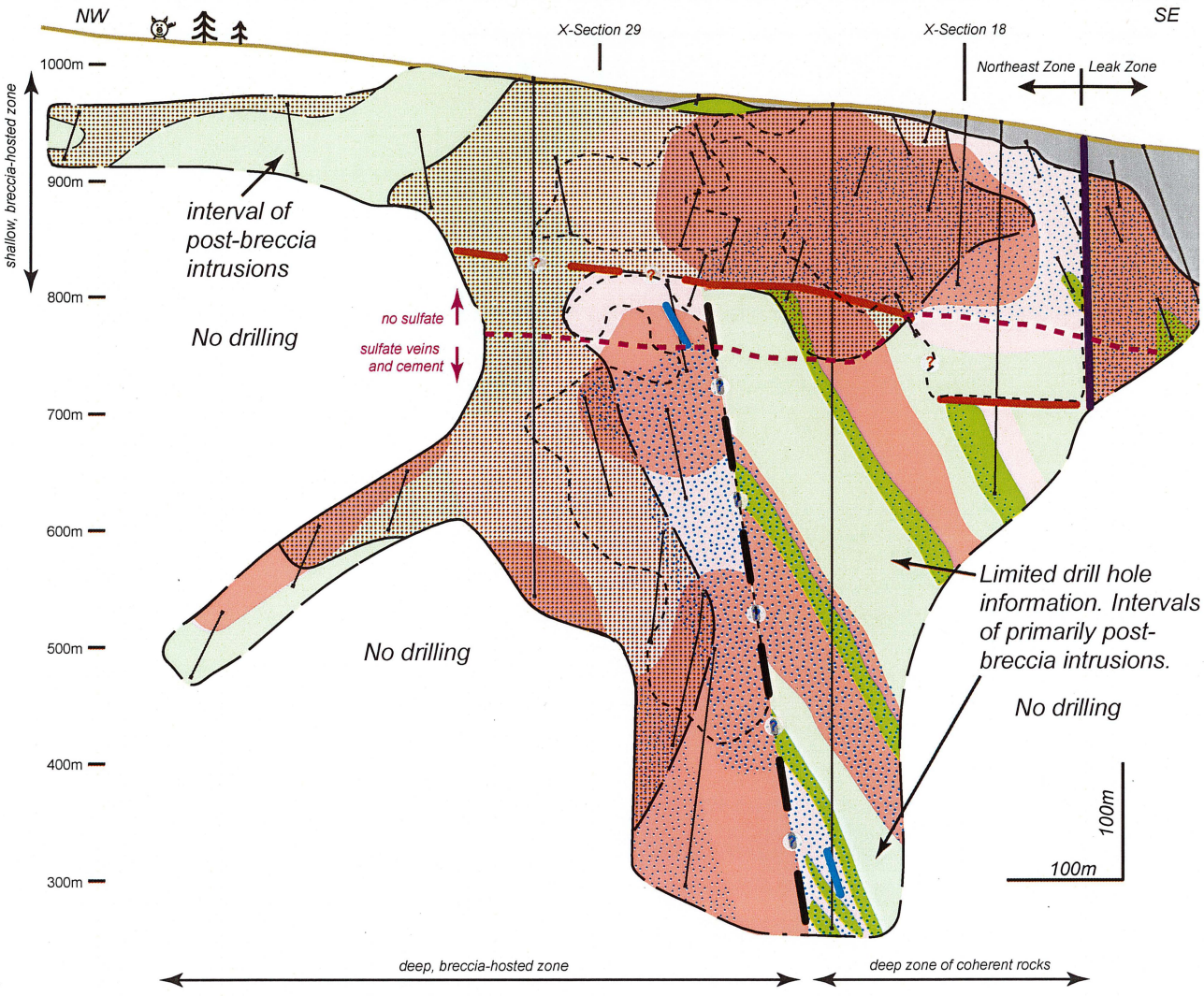

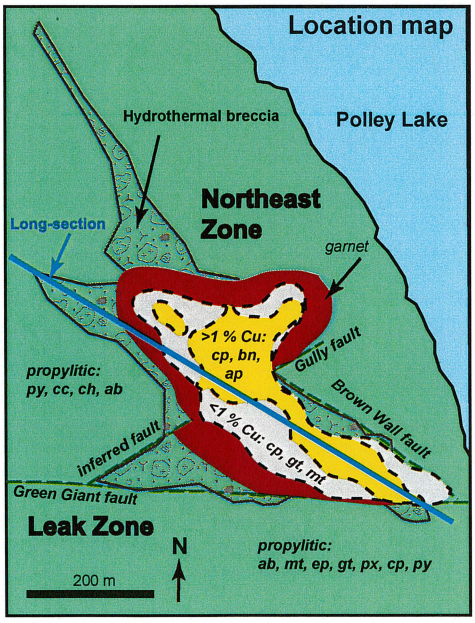

Overburden

Alteration and cement distribution (key minerals):

- Propylitic (chlorite subfacies) (pyrite, chlorite ± hematite* ± sericite)
- Propylitic (epidote-albite subfacies) (epidote, albite, chlorite, pyrite)
- Potassic / Strongly potassic (K-feldspar, magnetite, ± biotite ± chalcopyrite ± bornite ± epidote)
- Sodic (albite)
- Calc-potassic (garnet ± actinolite)
- Sulfate line

- ≥0.2% Cu contour
- WB04-115 — Drill hole logged in this study
- Limit of interpretation

Major faults:

- fault: definite
- fault: inferred
- Brown Wall fault
- Green Giant fault
- Gully fault (?)

Figure 4.17 Summary of alteration and cement distribution on the long-section. Alteration in the deep coherent rocks zone is shown schematically and is interpreted to be lithologically controlled due to abundant post-breccia dikes obscuring contact relationships. Hematite dusting and carbonate alteration are ubiquitous across the section, whereas hematite observed as cement or veins has been included in the propylitic assemblage (chlorite sub-facies*). The ≥0.2% Cu ore shells are outlined. The sulfate line (purple) defines a boundary above which no sulfate was logged, and below which sulfate was observed as veins and breccia cement. Question marks (?) in the faults highlight uncertainty in the fault interpretations. Inset: Map view of NEZ alteration zoning from Imperial Metals (2005, 2006).

Table 4.4. Summary of hydrothermal alteration and breccia cement of NEZ. The spatial distribution of alteration assemblages is shown on Figures 4.15 and 4.17.

Alteration facies (assemblage name)	Diagnostic minerals	Other minerals[1]	Alteration intensity and texture	Timing relative to brecciation[2] (stage #)	T (°C) Lang et al. (1995c)	Spatial association/ location in hydrothermal system	Association with mineralization	Other
K-feldspar-magnetite facies (potassic)	K-feldspar, magnetite, ± biotite,	Chalcopyrite, bornite, carbonate, albite, chlorite, pyrite, garnet, sulfate, sericite, hematite	Weak to intense, can be texturally destructive in host-rocks /cement infill, pervasive, vein, vein halo	Pre (1) Syn (2)	>350°C	Core and adjacent[4]	Moderate to strong	Epidote occurs on the periphery of intense potassic alteration, and in potassic alteration found in host rocks.
Albite facies (sodic)	Albite	Carbonate, chlorite, magnetite, chalcopyrite, bornite, garnet, pyrite, epidote, sulfate, hematite, biotite	Weak to strong / cement infill, selective-pervasive, vein	Pre (1) Syn (2) Post (3, 4, 5)	350–670°C	Core and adjacent	Moderate to strong	
Garnet facies (calc-potassic)	Garnet (actinolite-Leak Zone)	Carbonate, K-feldspar, magnetite, epidote, pyrite, chlorite, albite, chalcopyrite, bornite, biotite, hematite, sericite, sulfate, pyrite	Weak to moderate / cement infill, selective, vein	Pre? (1) Syn (2) Post (3)	400–600°C	Core to peripheral	Weak to strong	
Epidote-albite sub-facies (propylitic)	Epidote, albite,	Chlorite, pyrite, carbonate, magnetite, chalcopyrite, biotite	Weak to moderate / cement infill locally, disseminated to selective to pervasive, locally texturally destroying, vein, vein halo	Pre? (1) Syn (2) Post (3, 4)	<200–300°C	Adjacent-peripheral	None to locally moderate	Commonly intermingled with potassic, mineralized locally up to 0.25% Cu
Chlorite sub-facies (propylitic)	Chlorite, carbonate ± sericite	Pyrite, sulfate, magnetite, hematite, chalcopyrite				Peripheral, overprint, post breccia intrusions	None to weak	
Pyrite-sericite (phyllic)	Pyrite, sericite	Quartz, ± chalcedony ± carbonate	Shear veins and fault-breccia	Post (4, 5?)		Faults	None	
Sulfate-carbonate	Sulfate, carbonate		Veins, vein breccia and faults	Post (4)		Overprint, faults	None	Rare mineralized clasts when observed in breccia

[1] Minor minerals present localy.

[2] Timing relative to brecciation: pre = observed as alteration or truncated vein entirely within breccia clasts; syn = observed as cement to the breccia; post = observed in features that cross-cut breccia cement, matrix and clasts

[3] "core" refers to locations generally within the 0.2% Cu grade ore shell (Fig. 4.5); "adjacent" refers to locations directly neighboring, but outside of the core; "peripheral" refers to areas outside of the adjacent zone, on the edges of the long-section.

their associations with respect to Cu-Au mineralization, and their interpreted timing relative to stage 2 breccia formation. Their spatial distributions are shown on Figures 4.16 and 4.17.

The domains of potassic alteration are defined by the distribution of K-feldspar, magnetite and biotite, which coincide with areas enriched in chalcopyrite and bornite ± epidote in the NEZ and Leak Zone (Figs. 4.2, 4.15, 4.17). Strong, texturally destructive magnetite and K-feldspar ± albite alteration has obscured intrusive boundaries and primary lithologies, as observed in the potassically altered host-rocks below the shallow breccia-hosted zone (Fig. 4.17). Biotite (+ chlorite ± pyrite ± carbonate) alteration has replaced hornblende and augite in some less intensely potassic-altered pre-breccia monzonite intrusions.

Domains of sodic alteration, defined by the distribution of albite, occur on the southeastern side of both the shallow and deep breccia-hosted zones (Fig. 4.17). Within the host-rocks, albite is abundant in some of the potassically-altered monzonite rocks in intervals below the shallow breccia-hosted zone, as well as throughout the Leak Zone.

The spatial distribution of propylitic (chlorite sub-facies) alteration is defined by the distribution of chlorite and pyrite, together with lesser and localized specular hematite and sericite (Fig. 4.17). In the breccia complex, propylitic alteration defines a broad outer halo to the potassic alteration zone (Fig. 4.16), as well as occurring in dikes that have cross-cut monzonite host-rocks and breccia.

A second propylitic assemblage (epidote-albite sub-facies) has affected dikes that have intruded the potassically-altered monzonite host-rocks (Figs. 4.16 and 4.17). This propylitic assemblage is only weakly to moderately texturally destructive. The intermingled domain of potassic and epidote-albite-chlorite alteration below the shallow breccia-hosted zone (Fig. 4.17) is interpreted to be lithologically controlled. Ross (2004b) noted that a similar chlorite-albite-calcite-pyrite ± epidote alteration assemblage defined a broad halo around the main mineralized zone in the southern shallow breccia. Jackson (2008) observed an extensive, texturally destructive albite-epidote ± pyrite alteration assemblage at depth in the northern portion of the deposit (Fig. 4.16). This corresponds well with abundant, texture-preserving albite, epidote and pyrite alteration observed at depth on the long-section (Fig. 4.15).

Although garnet alteration is widespread across the breccia-hosted domains of the NEZ, it is notably absent from the host-rocks and Leak Zone, with the exception of a short interval directly below the Brown Wall fault (Fig. 4.17).

Actinolite alteration was only observed in the Leak Zone during the current study (Fig. 4.17). A narrow vertical zone of actinolite-albite alteration was observed in the matrix-dominant breccia of section 29 by Jackson (2008; Fig. 4.16). These two occurrences do not appear to be related.

Carbonate, chlorite, hematite ± sericite are pervasively developed as alteration minerals across the long-section. They occur in the monzonite host-rocks, breccia clasts and also in dikes that cut the breccia, implying a protracted or repeated history of formation. Chlorite is the most common alteration product of primary mafic minerals. Sub-micron size grains of hematite have partially replaced groundmass and phenocryst feldspars, producing a "reddening" of breccia clasts and post-breccia intrusions (Fig. 3.6). This hematite alteration is most intensely developed around some clast rims and is interpreted to be at least in part a syn-breccia alteration feature. The most abundant population of clasts with strong hematite alteration rinds occurs on the northern margin of the shallow breccia zone, possibly reflecting an overall reduction in intensity of hematite alteration. This "red rock" alteration is less intensely developed in, or absent from isolated post-breccia monzonite dikes. Jackson (2008) noted that some K-feldspar-porphyry dikes had margins that were more intensely altered than their cores.

Feldspar phenocrysts, and less so groundmass, are variably altered to "sericite"-hematite ± calcite (Fig. 3.8). "Sericite" has been identified to be predominantly illite-montmorillonite mixtures, based on analyses using a Terraspec spectroradiometer with RS^3 software. Sericite was also noted in late faults and veins associated with pyrite, and in vein halos to stage 5 epithermal-style vein. Jackson (2008) reported a similar distribution of

sericite-carbonate ± quartz alteration in the immediate vicinity of veins, fractures and small faults in the NEZ. These "phyllic" alteration halos have imparted an amber color to the altered rocks.

4.8 Discussion

The preceding sections have documented the breccia cement, veins and alteration assemblages of the NEZ. In the following discussion, these mineralogical observations are shown to be consistent with the alkalic porphyry model and are used to partially constrain thermal and pH conditions as well as silica contents for the fluids responsible for the NEZ.

4.8.1 Features consistent with the alkalic porphyry model

The following features at the Mt. Polley mine are consistent with the alkalic porphyry model (Jensen and Barton, 2000; Cooke et al., 2007). Albite-dominated and calc-potassic alteration assemblages, which are widespread at Mt. Polley, are more common in alkalic than calc-alkalic porphyry deposits (Lang et al., 1995b). Sodic alteration can form in both deep and shallow parts of alkalic deposits (Lang et al., 1995a; Wilson et al., 2002), as is the case in the NEZ. Calc-potassic alteration assemblages are common in silica-undersaturated porphyry deposits, including the NEZ, but are mostly absent from calc-alkalic deposits (Lang et al., 1995b). Hydrothermal magnetite commonly has a close spatial and temporal relationship to ore, in both alkalic and calc-alkalic systems (Sillitoe, 1979; Lang et al., 1995a; Wilson et al., 2002) and this is true at Mt. Polley. The common presence of epidote in the potassic assemblage of alkalic systems, including the NEZ, differs from the typical potassic assemblage in calc-alkalic deposits in which anhydrite is more common as a major calcium-bearing phase (Lang et al., 1995b; Cooke et al., 2007). Nonetheless, anhydrite is abundant in a few alkalic systems such as Galore Creek (Lang et al., 1995b) and the late stages of infill in the NEZ. Finally, sericitic (phyllic), clay-dominated (argillic) and aluminosilicate-rich (advanced argillic) alteration assemblages, while nearly ubiquitous in calc-alkalic deposits are notably absent or minor in alkalic systems (Lang et al., 1995a; Lang et al., 1995b; Wilson et al., 2003; Cooke et al., 2007) except perhaps in the shallow and late parts of some systems (Jensen and Barton, 2000). Consequently, lithocaps are typically absent in alkalic porphyries compared to calc-alkalic porphyries (Wilson et al., 2002; Fox et al., 2008).

It is not just the temperature and acid conditions in alkalic systems that are different from the calc-alkalic systems, but possibly also the magmatic fluid (Lang et al., 1995a). The close association of the unusual alteration types with alkalic intrusions in a variety of settings strongly suggests that alteration reflects the composition of a magmatic fluid. The development of sodic feldspars with or without calcic minerals such as garnet in the marginal portions of systems indicates higher Na^{+2} and Ca^{+2} activities (Jensen and Barton, 2000). Lang et al. (1995a) have proposed that the high Ca^{+2} and Na^{+2} could be produced from related intrusions, rather than wall rocks or the introduction of non-magmatic fluids such as connate brines or seawater. However, this remains to be tested conclusively. Regardless, it seems very likely that relatively high K^{+} + Ca^{+2} + Na^{+} fluid compositions have precluded argillic and advanced argillic alteration in alkalic systems (Lang et al., 1995a), and this seems to be the case also for the NEZ.

4.8.2 Mineralogy as an indicator of paleo-temperature and pH

Several variables can influence mineral precipitation in hydrothermal systems: concentrations of aqueous species or gases, host-rock compositions, reaction kinetics, duration of hydrothermal activity, degree of equilibrium, permeability, temperature, pressure, total sulfur concentration, redox and acidity (Losada-Calderon and McPhail, 1996; Corbett and Leach, 1998; Cooke et al., 2000). While this invariably results in a complex matrix of factors that can influence mineral deposition, paleo-temperatures and pH conditions can be estimated by comparison of observed mineralogies with known conditions from active geothermal systems, experimental studies and thermodynamic modeling (Figs. 4.18, 4.19, 4.20; Table 4.5; Hemley et al., 1980; Henley and Ellis, 1983; Hedenquist and Houghton, 1987; Reyes, 1990; Spear, 1993; Cooke et al., 1996; Masterman, 2003; Seedorff et al., 2005). The alteration rank scheme of Corbett and Leach (1998) can also be employed to provide approximations of acidity and

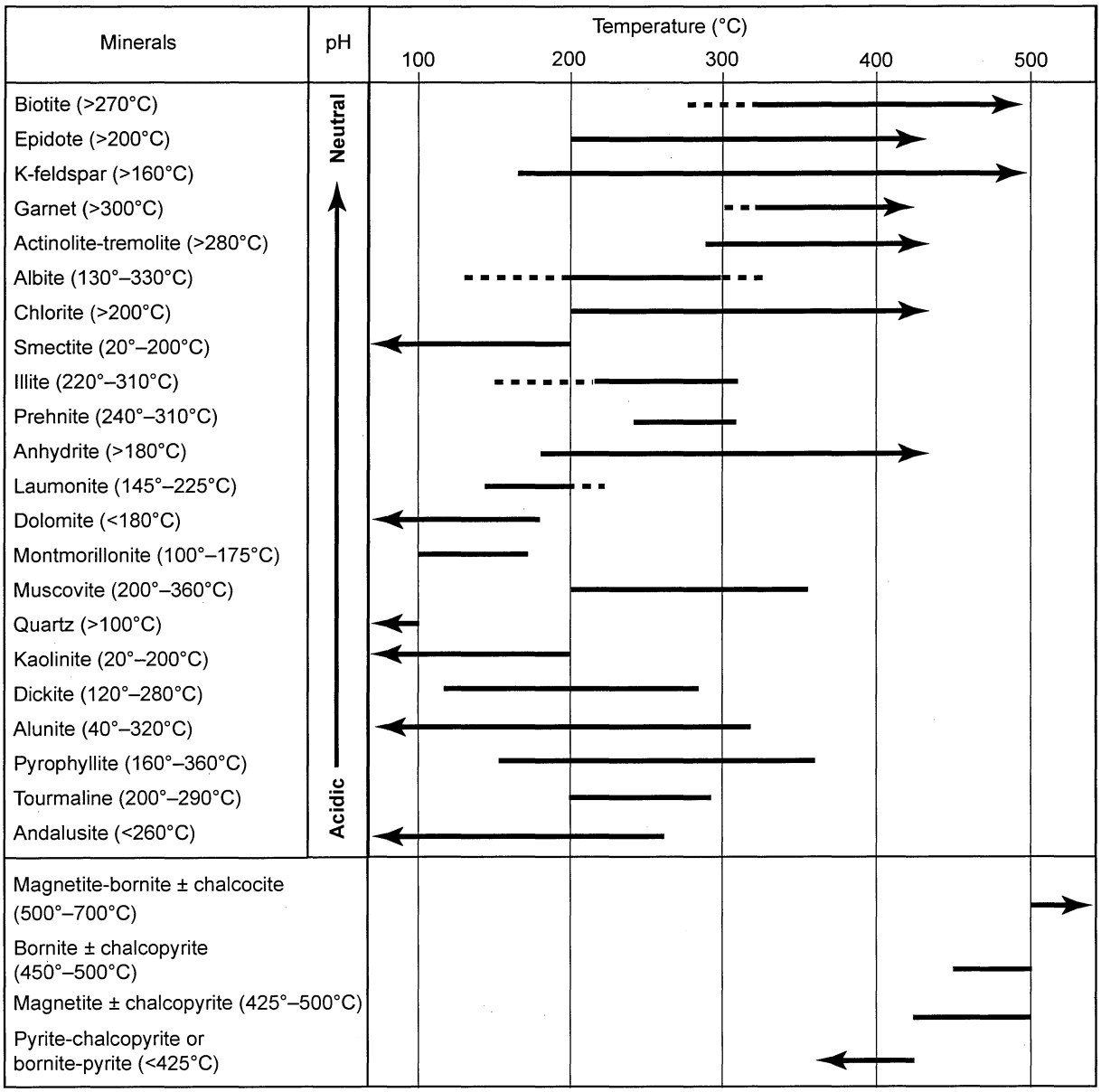

Figure 4.18 Temperature stability ranges of hydrothermal minerals (deduced empirically from active geothermal systems and from experimental modeling; Hemley et al., 1980; Henley and Ellis, 1983; Bird et al., 1984; Hedenquist and Houghton, 1987; Reyes, 1990). Minerals have been arranged by their stability with respect to pH. Sulfide and magnetite formation temperatures are from experimental studies conducted by Simon et al. (2000). Figure modified from Masterman (2003).

temperature (Fig. 4.21). These types of comparisons can provide useful insights into likely fluid conditions, and are necessary where fluid inclusion analyses cannot be used to constrain fluid conditions, as in the current study. This is essential given the lack of suitable host-minerals for fluid inclusions in the NEZ, coupled with the post-mineral deformation effects.

Porphyry-related magmatic hydrothermal systems are active from temperatures above the magmatic solidus (>750° to ~600°C, depending on magmatic composition) down to low temperatures (<200°C, Fig. 4.19; Hemley et al., 1980; Seedorff et al., 2005). For the purpose of this discussion, >600° to ~400°C is classified arbitrarily as high temperature, ~400° to ~300°C as moderate temperature and <300°C as low temperature. This is similar to the terminology of Seedorff and Einaudi (2004). The main alteration assemblages associated with bornite-chalcopyrite ore in the NEZ are potassic, calc-potassic and sodic (K-feldspar, albite, magnetite,

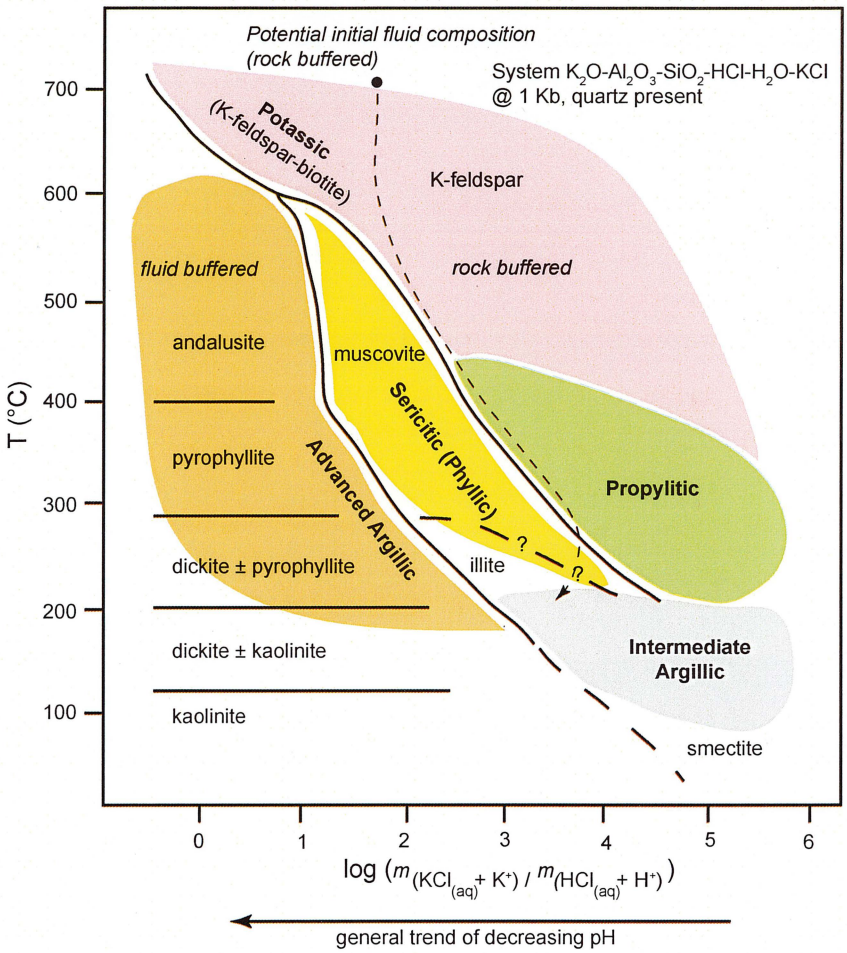

Figure 4.19 Phase diagram for the system K_2O-Al_2O_3-SiO_2-HCl-H_2O-KCl at P_{H_2O}=1 kbar, plotting temperature versus log ($m_{(KCL + K^+)}$/ $m_{(HCl + H^+)}$), showing a possible fluid evolutionary path for the NEZ. Figure modified from Tosdal et al. (2009) after Seedorff et al. (2005).

garnet ± biotite ± pyroxene). Based on the observed mineralogies, they are interpreted to have formed at moderate to high temperatures (i.e. >300°C; Figs. 4.18, 4.19 and 4.21). Similar temperatures of formation may have prevailed during stage 3 veins precipitation (e.g. bornite-chalcopyrite mylonites and chalcopyrite ± albite veins). Minerals consistent with inner and outer propylitic alteration assemblages (epidote-chlorite, illite ± albite ± sulfides; Hedenquist and Houghton, 1987; Corbett and Leach, 1998; Cooke et al., 2007) represent cooler fluid conditions and are interpreted to have formed at temperatures of approximately 300°–280°C and 250°–200°C, respectively (Figs. 4.18, 4.19 and 4.21). Zeolites and many clays (including illite) typically form at temperatures of <300°C (Figs. 4.18 to 4.22, Table 4.5). The presence of minor montmorillonite, illite, and laumontite in Stage 4 and 5 veins, vein breccia and as alteration products of feldspars in post-breccia dikes provide evidence for lower temperature conditions during the waning stages of hydrothermal activity (Figs. 4.18 and 4.21).

Mineralogy can be used to estimate fluid acidities. The associated species $HCl_{(aq)}$ is likely to be the dominant acidic species at moderate to high temperatures (>300°C) in high-salinity fluids (Losada-Calderon and McPhail, 1996). At lower temperatures (and pressures), the strong dissociation of $HCl_{(aq)}$ and other strong acids means that the activity of H^+ best represents acidity in hydrothermal fluids (Losada-Calderon and McPhail, 1996). Therefore, to allow comparison of acidity and temperature controls on alteration mineralogy over the full range of temperatures pertinent to porphyry deposits, $m(HCl_{(aq)} + H^+)$ is used to represent acidity in Figure 4.19. Alteration types such as potassic, propylitic, intermediate argillic, and some sericite, are located primarily on the right hand side of Figure 4.19 and form under near-neutral to alkaline conditions (Table 4.6). Mineral assemblages that form under strongly acidic conditions are advanced argillic, sericitic and high-temperature potassic assemblages,

found primarily on the left-hand side of Figure 4.19. Feldspar- and carbonate-bearing alteration assemblages were stable throughout most of the evolution of the NEZ, consistent with near-neutral pH conditions (Figs. 4.19 and 4.20). Minerals that indicate highly acidic conditions (e.g. andalusite, alunite, pyrophyllite, dickite, kaolinite; Figs. 4.19, 4.20 and 4.21) are lacking from the NEZ. The observed hydrothermal mineralogy of the NEZ plots above the kaolinite-muscovite buffer (Fig. 4.20) and in the chlorite to calc-silicate groups on Figure 21, again consistent with neutral to high (≥7) pH conditions prevailing during much of the history of mineralization and alteration in the NEZ (path A; Fig. 4.21). The only exception is the sericitic (phyllic) alteration assemblage associated with stage 5 veins and areas immediately adjacent to structures, indicating a progression to acidic and lower temperature conditions in the final stages of hydrothermal activity at the NEZ (path B; Fig. 4.21).

4.8.3 Redox conditions during mineralization

The presence and absence of sulfide, oxide, silicate and carbonate minerals can be used to infer the oxygen fugacity (i.e. the redox state) of the fluids that formed the NEZ (Cooke et al., 1996). In addition to pH, Figure 4.20 shows the division between oxidative and reductive environments can be expressed as the line between the predominance of SO_4^{-2}, HSO_4^-, $H_2S_{(aq)}$ and HS^- species, respectively. The widespread occurrence of hematite, magnetite, calcite, anhydrite ± pyrite in the early to late stages of the NEZ is consistent with an oxidized (sulfate-predominant) fluid (Jensen and Barton, 2000, Wilson et al., 2007). The observation of barite in stage 4 vein breccia (Davidson et al., in prep.) from the NEZ are also consistent with an oxidized fluid (Jensen and Barton, 2000). The lower limit of log fO_2 values in Figure 4.19 is defined by stability field of pyrrhotite, which is absent in the NEZ.

4.8.4 Quartz solubility, temperature and pressure

The lack of quartz throughout vast majority of the paragenesis at Mt. Polley is typical of silica-undersaturated porphyry Cu-Au deposits (e.g. the Marian deposit, Philippines; Knittel, 1987; Galore Creek,

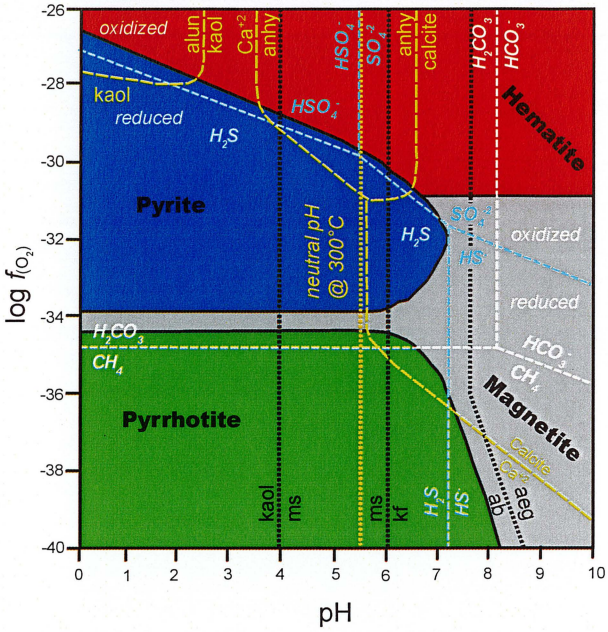

Figure 4.20 pH versus log f_{O_2} diagram at 300°C representing an alkalic system (ΣS = 0.004 molal, ΣC = 0.41 molal, a_{K^+} = 0.00437, $a_{Ca^{+2}}$ = 2.51 x 10^{-5}, 0.5 eq wt % NaCl). Stability fields of Fe-oxides and sulfides, K-feldspar, muscovite, kalinite, alunite, calcite, and anhydrite and the predominance fields of aqueous C- and S-bearing species. Figure modified from Cooke et al. (1996) using thermodynamic data from SUPCRT92 (Johnson et al., 1992). The approximate position of the alkaline buffer ('Ab-Aeg', black dashed line) representing the albite + Fe-phase = aegirine reaction has been taken from Jensen and Barton (2000). Fluids exsolved from alkaline magmas are expected to have an inital compositon near this buffer (Jensen and Barton, 2000). Abbreviations: ab-albite, aeg-aegirine, alun-alunite, anhy-anhydrite, kaol-kaolinte, kf-K-feldspar, ms-muscovite.

Copper Canyon, Rayfield River, Canada; Lang et al., 1995a; Dinkidi deposit, Philippines; Wolfe et al., 1999), but is not easily explained. Quartz solubilities have been modeled over a range of temperature, pressure and pH conditions in order to determine conditions that may explain the lack of quartz vein and breccia cement in the NEZ. The modeling program Geochemist Workbench (TACT, version 7.0.2) was used in conjunction with thermodynamic database UNITHERM using UT2K at 0.5 kbars from 475° to 250°C and 1.0 Kbars from 650° to 250°C (Cleverley and Bastrakov, 2005). Modeling was conducted collaboratively by members of the alkalic research team (this author, Adam Bath, Kevin Byrne, Janina Micko and Wojciech Zukowski).

At an assumed pressure of 0.5 kbar and temperatures of 475° to 250°C, consistent with the

Table 4.5 Alteration types and their implied temperature range and fluid chemistry.

Alteration type	Key minerals	Accessory minerals	Implied temperature (°C)	Fluid Chemistry	Notes / Reference
Potassic					
	Bioite, K-feldspar, magnetite	Epidote, chlorite, muscovite	320°C	Neutral pH, relatively high a^{K+}/a^{H+}	Geothermal; Hendenquist and Houghton (1987)
	-	-	>300°C	≥7	Including skarn; Corbett and Leach (1998b)
	K-feldspar and/or biotite ± magnetite	-	>350°?		Major alteration in alkalic deposits; Lang et al. (1995b, c)
Calc-potassic					
	Garnet, K-feldspar, biotite ± apatite ± anhydrite	-	650°–400°C	-	Major alteration in alkalic deposits; Lang et al. (1995b, c)
Sodic					
	Albite, diopside ± chlorite ± epidote	-	<670° to >350°C	-	Major alteration in alkalic deposits; Lang et al. (1995b, c)
Argillic[1]					
Advanced (high T)			High to low	<4	Corbett and Leach (1998b)
	Pyrohyllite, diaspore, andalusite	Quartz, sulfides, tourmaline, enargite/luzonite	Usually 250°C, but uncertain, andalusite >350°C	Acid pH	High temperature geothermal; Hendenquist and Houghton (1987)
Advanced (low T)			250°–>200°	4–6	Corbett and Leach (1998b)
	Kaolinite alunite	Chalcedony, cristobalite, quartz, pyrite	180°C	Acid pH	Geothermal; Hendenquist and Houghton (1987)
Intermediate	Smectite or interlayered illite smectite (11-14A)	Sulfides, zeolite, quartz, calcite	<200°C	Neutral pH, moderate a^{Ca+}/a^{H+}	Geothermal; Hendenquist and Houghton (1987)
Propylitic					
Inner	Epidote actinolite	Chlorite, illite	300°C	Neutral pH, relateivley high a^{Ca+}/a^{H+}	Geothermal; Hendenquist and Houghton (1987)
			300°–280°C	~5–>7	Corbett and Leach (1998b)
Outer/sub	Epidote	Chlorite, illite, sulfides	250°C	Neutral pH, relateivley high a^{Ca+}/a^{H+}	Geothermal; Hendenquist and Houghton (1987)
			250°–<200°C	~5–>7	Corbett and Leach (1998b)
	Calcite, chlorite, pyrite ± epidote ± albite		300°–<200°C		Major alteration in alkalic deposits; Lang et al. (1995b, c)
Sericitic (phyllic)					
	Sericite (illite) quartz	Sulfides, oxides, kaolinite (minor)	>220°C	Neutral pH, but increasing high a^{K+}, a^{H+}	Geothermal; Hendenquist and Houghton (1987)
			250°–200°C	4–6	Corbett and Leach (1998b)
Silicic[1]					
	Quartz				Seedorf et al. (2005)

[1] Alteration types not generally reported in alkalic porphyry deposits (Lang et al., 1995b, c).

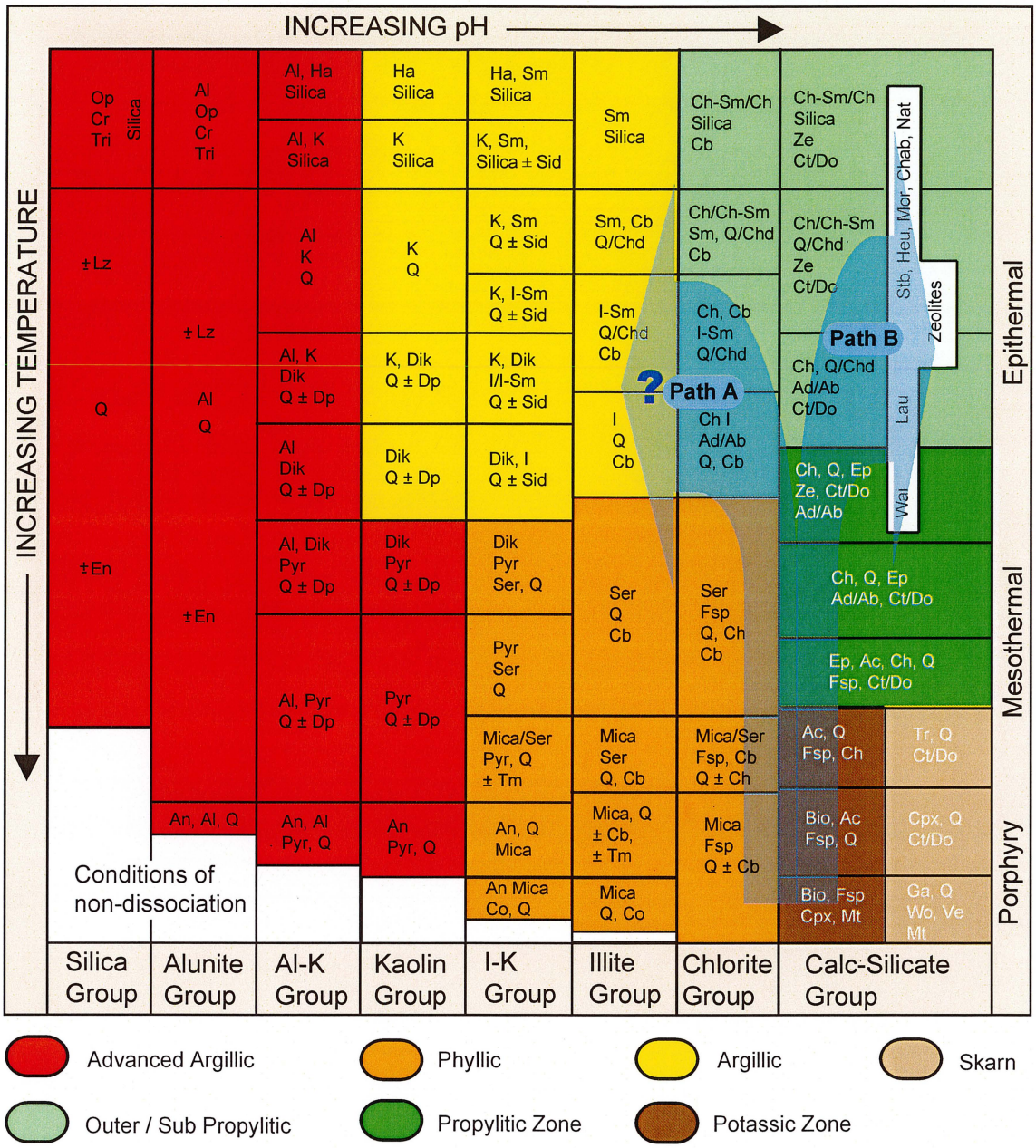

Mineral Abbreviations:

Ab-albite, Ac-actinolite, Ad-adularia, Al-alunite, An-andalusite, Bio-biotite, Cb-carbonate (Ca, Mg, Mn, Fe), Ch-chlorite, Chab-chabazite, Chd-chalcedony, Ch-Sm-chlorite-smectite, Co-corundum, Cpx-clinopyroxene, Cr-cristobalite, Ct-calcite, Do-dolomite, Dik-dickite, Dp-diaspore, En-enargite, Ep-epidote, Fsp-feldspar, Ga-garnet, Ha-halloysite, Heu-heulandite, I-illite, I-Sm-illite-smectite, K-kaolinite, Lau-laumontite, Lz-luzonite, Mt-magnetite, Mor-mordenite, Nat-natrolite, Op-opaline silica, Pyr-pyrophyllite, Q-quartz, Ser-sericite, Sid-siderite, Sm-smectite, Stb-stilbite, Tm-tourmaline, Tr-tremolite, Tri-tridymite, Ve-vesuvianite, Wai-wairakite, Wo-wollastonite, Ze-zeolite.

Figure 4.21 Common alteration mineralogy in hydothermal systems modified from Corbett and Leach (1998b). Approximate temperature and pH ranges: potassic and skarn (high T: >300°C, pH ≥7), propylitic (280°–300°C, pH ~5–>7), outer/sub propylitic (250°–<200°C, pH~5–>7), phyllic (250°–200°C, pH 4–6), argillic (250°–>200°C, pH 4–6), advanced argillic (high to low temperatures, pH <4). Temperature and pH ranges taken from Corbett and Leach (1998b) text. Enargite, luzonite and tourmaline have been added (D. Cooke, pers. comm., 2010). The blue arrows represent possible fluid evolution paths for the NEZ based on observed mineralogy.

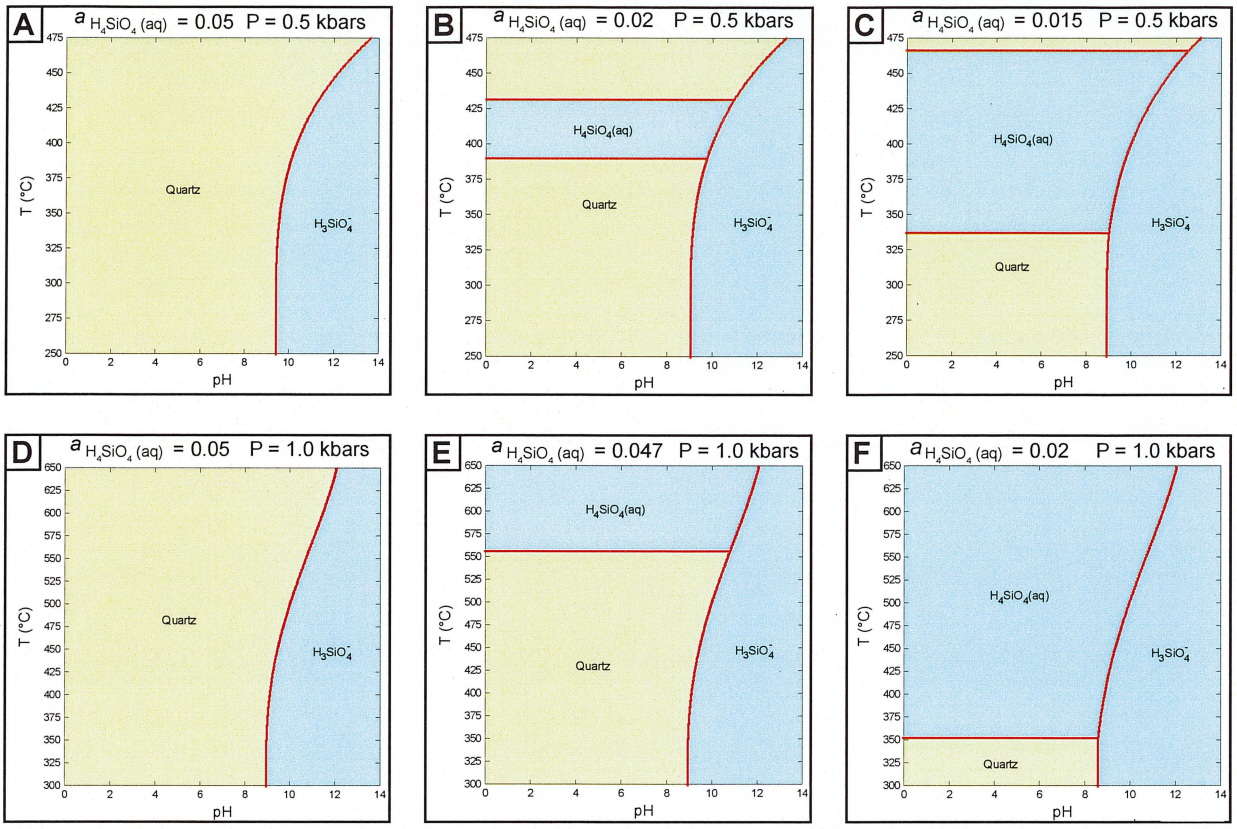

Figure 4.22 Quartz stability and silica predominance fields calculated using Geochemists Workbench (version 7.0.2) for 0.5 and 1.5 kbar confining pressures (a_{H_2O} = 1 for all diagrams). See text for discussion and database references.

temperature range in Figure 4.19, and a silica activity of 0.05, quartz stability is independent of pH up to very alkaline conditions. Only above approximately pH 9.5, is silica soluble (Fig. 4.22A). Increasing silica activity causes the domain of silica solubility to contract to higher pH values. However, if silica activity is decreased to approximately a_{H4SiO4} = 0.02, a silica solubility window opens in the $H_4SiO_{4(aq)}$ predominance field between approximately 430° and 390°C (Fig. 4.22B). This quartz solubility window occurs over a larger temperature range if silica activities can decrease further (e.g. Fig. 4.22C). This suggests that regardless of pH, silica activity must be <0.02 to preclude quartz from precipitating at 0.5 kbars.

Different results were achieved when plots were made at 1.0 kbar (Fig. 4.22D–F). Quartz will precipitate over the typical temperature range for porphyry deposits, up to highly alkaline pH conditions at $a_{H4SiO4} \geq 0.05$ (Fig. 4.22D). At $a_{H4SiO4} \approx 0.047$, quartz is soluble above 550°C (Fig. 4.22E). As silica activity is decreased, silica is soluble at all pH to lower temperatures (Fig. 4.22F); however, at 1.0 kbar, the silica retrograde solubility window is not observed.

This modeling suggests that quartz is most readily precluded from precipitating at strongly alkaline pH (i.e. >9.5). The mineralogical observations discussed in Section 4.8.1 and the fluids exsolved from alkaline magmas (Fig. 4.20; Jenson and Barton, 2000) support a near-neutral to alkaline fluid. It is, therefore unlikely that the ore forming fluids at Mt. Polley were highly alkaline based on the observered mineralogy. Another explanation is required to explain silica-undersaturation of the hydrothermal fluids. This mechanism is discussed in detail in Chapter 5.

The modeling also indicates that if silica activity is driven to <0.02 at 0.5 kbar, or <0.05 at 1.0 kbar, then theoretically, quartz may be precluded from precipitating at acidic as well as alkaline conditions. It remains unclear, however, as to what would allow silica activities

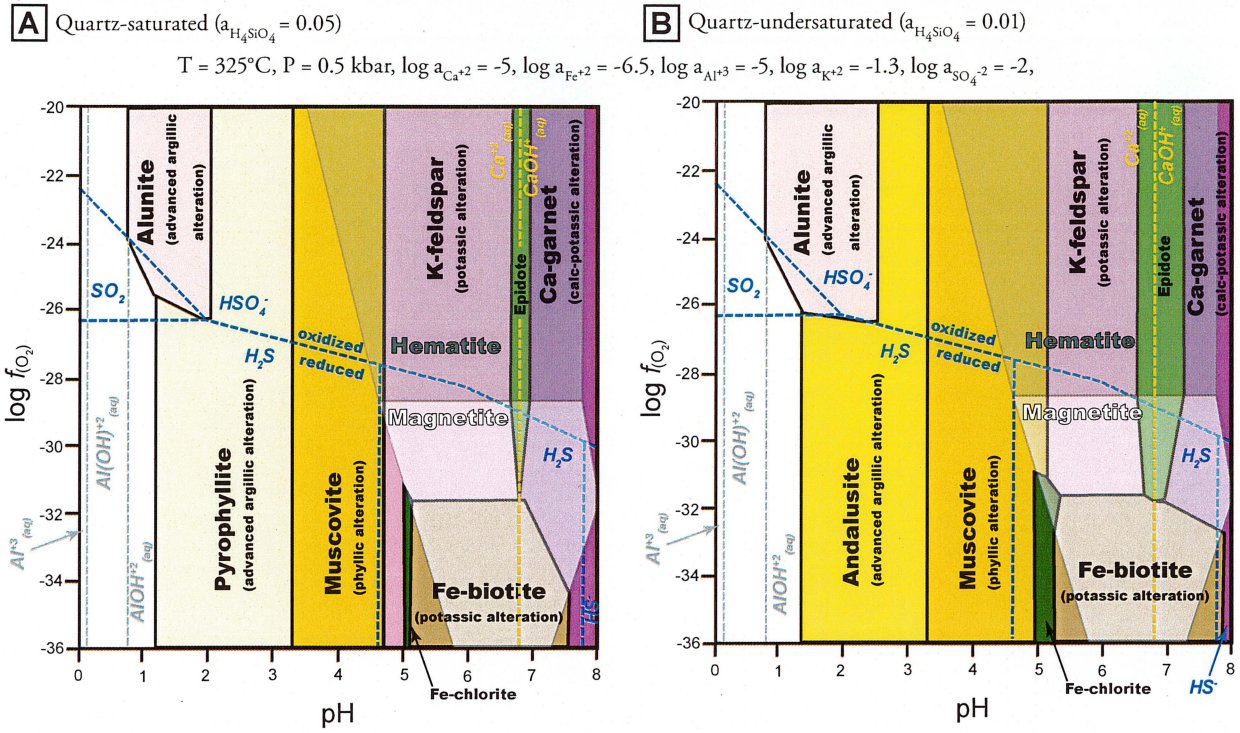

Figure 4.23 Redox and acidity controls on the stability of common alteration minerals in porphyry deposits, highlighting the effects of silica-saturation (A) vs. silica-undersaturation (B). **A)** pH versus log f_{O_2} diagram for quartz-saturated conditions at 325°C. Stability fields of Fe-oxides and Ca-garnet, epidote, K-feldspar, Fe-biotite, Fe-chlorite, muscovite, pyrophyllite-andalusite, alunite and the predominance fields of aqueous S-, Al- and Ca-bearing species. Figure from Braxton et al. (2010) using thermodynamic data from HCH. **B)** Similar conditions as in A) except that quartz is silica-undersaturated (a_{H4SiO4} = 0.01). Comparing A) and B) shows that as silica acitivites are reduced, the muscovite, chlorite, biotite and epidote fields increase, the pyrophyllite field is replaced with andalusite, and the size of the K-feldspar and garnet fields decrease.

to remain so low during alteration of silicate minerals at Mt. Polley, if this were the appropriate scenario for hydrothermal alteration and mineralization. However, acidic conditions are not consistent with the observed mineralogy as detailed in Section 4.82.

Figure 4.23 shows the stability ranges of key alteration minerals at Mt Polley as a function of acidity and redox potential, expressed in terms of log fO_2(g). The diagrams were constructed at the lower end of the estimated temperature and pressure conditions for the NEZ (325°C, 500 bars) as this allows most of the diagnostic mineral phases to be plotted on one diagram. Figure 4.23A shows mineral stabilities for conditions of quartz saturation, whereas Figure 4.23B shows how phase relationships change when the fluid is undersaturated with respect to quartz. The fields of minerals that define calc-potassic and propylitic alteration assemblages are restricted to alkaline pH conditions, and these fields expand with decreasing silica concentration (compare Fig. 4.23A and B). These figures also show the overlap between the hematite field with the upper parts of the K-feldspar field, which illustrates the conditions favourable for the formation of hematite-dusted K-feldspar. Overall, these diagrams confirm that the prevailing conditions of mineralisation at Mt Polley involved near-neutral to alkaline fluids, based on the widespread presence of K-feldspar, garnet, epidote and chlorite alteration, and that oxidising (SO_4^{2-}-predominant) conditions are indicated by the presence of hematite, garnet and epidote. Local excursions to weakly acidic conditions are indicated by domains of phyllic alteration, and transitions to reducing conditions are marked by the development of secondary magnetite, biotite and chlorite. Highly acidic conditions were never achieved at Mt Polley, based on the lack of alunite, pyrophyllite and andalusite (Figs. 4.18, 4.19, 4.21 and 4.23).

4.9 Summary and conclusions

Alteration, cementation, mineralization and veins of the NEZ occurred in five paragenetic stages: pre-breccia (stage 1), brecciation and main-stage mineralization (stage 2), late-stage mineralization (stage 3), unmineralized post-breccia dikes and veins (stage 4) and epithermal-style veins (stage 5; Fig. 4.8).

- During the pre-brecciation stage, early, widespread and pervasive K-metasomatism was associated with hematite dusting ± calcite alteration (Fig. 4.9). Early magnetite ± albite ± pyroxene ± calcite ± epidote veins, some with K-feldspar halos and actinolite-albite-magnetite-pyroxene veins in the Leak Zone also formed at this time.
- Pre-brecciation hydrothermal activity caused moderately to strongly developed pervasive K-feldspar-magnetite-albite ± epidote ± chlorite alteration of the monzonite host-rocks (Fig. 4.9). Minor Cu-sulfide mineralization may have been introduced in this stage.
- Stage 2 is the most important stage economically. Mineralization was associated with widespread brecciation and with Cu-Fe sulfides occurring as cement, alteration and veins (Figs. 4.8). Bornite, chalcopyrite ± pyrite are the dominant sulfides, and mostly occur as breccia cement (Figs. 4.2, 4.3 and 4.4).
- A complicated asymmetrical pattern of potassic (K-feldspar, magnetite ± biotite ± epidote), sodic (albite) and calc-potassic (garnet) alteration formed during stage 2 mineralization. A chlorite sub-facies propylitic alteration assemblage also formed as a halo to the potassic and sodic alteration on the long-section (Figs. 4.10, 4.11, 4.15, 4.16, 4.17).
- The main breccia body was cross-cut by stage 3 veins and sulfide-bearing mylonites associated with monzonitic dikes (Figs. 4.8 and 4.12). Stage 3 locally upgraded Cu, Au and Ag, but did not add a significant amount of new metal to the deposit.
- Barren stage 4 veins, dikes and faults disrupted the mineralized rocks (Figs. 4.8 and 4.13). Numerous pyrite (± sericite ± carbonate) shear veins formed at this time (Figs. 4. 13G). They are associated with weak phyllic alteration that affected the late monzonite dikes.
- Distinctive epithermal-style veins that locally contain bladed textures and are associated with phyllic alteration characterize stage 5 (Figs. 4.8 and 4.14). Their presence implies either that significant erosion or unloading took place during the evolution of the Mt. Polley hydrothermal system or that an epithermal system overprinted the Mt. Polley porphyry deposits some time after 200 Ma. This is discussed further in Chapter 5.
- The NEZ lacks hydrothermal quartz, with the exception of limited stage 4 vein breccia cement and stage 5 chalcedony-amethyst-bearing veins (Figs. 4.13D, 4.14A and B). Secondary carbonates occur throughout the NEZ. These observations are consistent with other silica-undersaturated alkalic deposits (e.g. Galore Creek, Copper Canyon, Rayfield River; Lang et al., 1995a).
- Using the presence and absence of characteristic sulfide, oxide, silicate and carbonate phases, paleo-temperatures of the NEZ indicate high temperatures (i.e. >300°C) and near-neutral to alkaline, oxidized (sulfate-predominant) fluid conditions throughout much of the history of formation of the NEZ (stages 1, 2 and 3) with moderate-temperatures on the periphery of the deposit and in late-stage veins (stages 2, 3 and 4). Evidence for acidic, and lower temperature conditions are preserved in stage 5 (Figs. 4.18 to 4.21).

Chapter 5

Hydrothermal Geochemistry: Stable and Radiogenic Isotopes

5.1 Introduction

Previous studies of silica-undersaturated alkalic porphyry Cu-Au deposits of British Columbia have defined the distribution of alteration and sulfide sequences (e.g. Lang et al., 1995b; Lang et al., 1995c; Jensen and Barton, 2000; Fig. 1.4), but isotopic studies are mostly lacking. The NEZ provides an excellent opportunity to investigate the nature of carbonate minerals found throughout the paragenesis of a porphyry deposit, including the unusual opportunity to investigate carbonates associated with Cu-sulfide ore.

This chapter presents new stable (S, C, O) and radiogenic (Sr, Pb, Nd) isotopic data from hydrothermal minerals of the NEZ. Isotopic results are discussed in the context of constraining the source(s) and nature of ore forming fluid(s), and providing evidence of water-rock interaction and redox changes during ore formation. Processes of silica-undersaturation are speculated upon as part of a new genetic model for Mt. Polley. Analytical methods for all isotopic techniques are listed in Table 5.1.

Table 5.1 Analytical methods for stable (S,C,O) and radiogenic (Pb, Sr) isotope studies.

Isotope	Methodology	Reference	Analytical Uncertainty	Location
$\delta^{34}S_{Sulfide}$	Conventional analyses (hand-drill, 30 mg) as per Robinson and Kusakabe (1975) Laser ablation sulfide isotopic analyses (LA-SI) as per Huston et al. (1995)	CDT (Canon Diablo iron meteorite)	± 0.15 ‰ (conventional)	University of Tasmania (Central Science Laboratory)
$\delta^{34}S_{Sulfate}$	Conventional analyses (hand-drill, 100 mg) as per Yanaglsawa and Sakal (1983)	CDT (Canon Diablo iron meteorite)	± 0.4 ‰	University of Tasmania (Central Science Laboratory)
$\delta^{13}C_{Carbonate}$ and $\delta^{18}O_{Carbonate}$	Conventional analyses (hand-drill, 10 mg), combined procedure developed from McCrea (1950), Craig (1957), Walters et al. (1972) and Swart et al. (1991) used at University of Tasmania. Conventional analyses (micro-drill, <100 to 300 µg) as per Wilson et al. (2009) used at University of British Columbia	$\delta^{13}C$ V-PDB (Vienna Cretaceous Peedee formation beleminte) $\delta^{18}O$ V-SMOW (Vienna standard mean ocean water)	$\delta^{13}C$ ± 0.14 ‰[1] $\delta^{18}O$ ± 0.15 ‰[1]	University of British Columbia (Pacific Center for Isotopic Geochemical Research) and University of Tasmania (Central Science Laboratory)
Sr-Nd-Pb	Acid-cleaned mineral samples and rock chips (5–300 mg) were dissolved (silicates, calcite, sulfides, sulfates) or acid-leached (limestones). Samples solutions split for trace elment analyses by quadrupole-ICPMS (Yu et al., 2001) and Sr-Pb-Nd isotope analysis by MC-ICPMS (Mass et al., 2005). For further details see Appendices D1 and D2.	$^{87}Sr/^{86}Sr$ in SRM987 = 0.71023; $^{143}Nd/^{144}Nd$ in La Jolla = 0.511860; SRM981 Pb (see Woodhead, 2002)	$^{87}Sr/^{86}Sr$ ± 0.00004; $^{143}Nd/^{144}Nd$ ± 0.000020; $^{206,207,208}Pb/^{204}Pb$ ± 0.03%; For further details see Appendices D1 and D2.	University of Tasmania (CODES) and University of Melbourne (School of Earth Sciences)

[1] Average standard deviation of all analyses. See Appendix D4 for specific analysis values.

5.2 Stable isotopes

5.2.1 Sulfur-isotopes

Sulfur-isotope analyses of sulfides and sulfates from Mt. Polley were conducted to assess the spatial variation in sulfide isotopic compositions, establish potential source(s) of S and to comment on the nature of the hydrothermal fluids (Ohmoto and Rye, 1979).

Sulfur-isotopic compositions have been analyzed from 137 samples of chalcopyrite, bornite and pyrite and 22 sulfate samples from the long-section and section 18 of the NEZ (Appendix D3). Sulfur-isotopic analyses involved conventional and laser ablation techniques (Table 5.1). Sulfides from the long-section have $\delta^{34}S_{sulfide}$ values between -7.1 and +1.4 per mil, with most between -3 and -4 per mil (Table 5.2; Appendix D3, Fig. 5.1). These are consistent with values of -7.1 to +0.6 per mil obtained from section 18 by this study and Deyell and Tosdal (2005; Appendix D3). Most of the lowest $\delta^{34}S_{sulfide}$ values were obtained from chalcopyrite (Appendix D3). The $\delta^{34}S_{sulfate}$ values obtained from anhydrite and gypsum were between +6.2 and +9.8 per mil, with two outliers (+13.6 and +14.0 ‰, Fig.5.1C, Appendix D3).

Sulfur-isotopic zoning for main-stage mineralization on the long-section is shown on Figure 5.2. The most negative $\delta^{34}S$ values (-4 to -5 ‰) correspond with areas of moderate to intense K-feldspar-magnetite ± albite ± garnet alteration (compare Figs 5.2 and 4.7). Some low $\delta^{34}S_{sulfide}$ values correspond with bornite-rich zones, whereas others are associated with chalcopyrite–pyrite mineralization (compare Figs 5.2 and 4.2).

Table 5.2 Summary statistics for $\delta^{34}S_{CDT}$ (‰) analyses of sulfides and sulfates from the NEZ. Complete data sets available in Appendix D3.

$\delta^{34}S_{sulfide}$ Long-section					
Stage 2[1]		cp	bn	py	total
	n=	47	9	11	67
	maximum	-0.6	-1.6	1.4	1.4
	minimum	-6.5	-4.2	-5.5	-6.5
	median	-3.4	-3.4	-3.1	-3.4
	average	-3.5	-3.2	-2.5	-3.3
Stage 3		cp	bn	py	total
	n=	19	6	5	30
	maximum	-1.1	-1.1	1.0	1.0
	minimum	-4.0	-4.1	-0.8	-4.1
	median	-2.7	-2.8	-0.5	-2.5
	average	-2.8	-2.7	-0.1	-2.3
Total		cp	bn	py	total
	n=	66	15	16	97
	maximum	-0.6	-1.1	1.4	1.4
	minimum	-6.5	-4.2	-5.5	-6.5
	median	-3.3	-3.2	-1.6	-3.2
	average	-3.3	-3.0	-1.8	-3.0
All NEZ $\delta^{34}S_{sulfide}$ data[2] (this study[3] and Deyell and Tosdal, 2005)					
Total		cp	bn	py	total
	n=	152	26	31	209
	maximum	-0.6	-1.1	1.4	1.4
	minimum	-7.1	-6.4	-7.1	-7.1
	median	-4.1	-3.5	-2.8	-3.9
	average	-4.0	-3.5	-2.6	-3.7
$\delta^{34}S_{sulfate}$ data from NEZ					
	n=	22			
	maximum	14.0			
	minimum	6.3			
	median	8.5			
	average	8.8			

cp-chalcopyrite, bn-bornite, py-pyrite

[1] Includes single early stage cp sample (-0.6 ‰).

[2] Includes six samples from the Leak Zone (Figs. 3.1 and 3.2).

[3] Includes data from the NEZ long-section as well as unpublished data from this study collected from section 18.

5.2.2 Carbon- and oxygen-isotopes

Carbonate veins typically form late in the paragenesis of porphyry deposits in association with propylitic alteration (Gustafson and Hunt, 1975; Ohmoto, 1986; Seedorff et al., 2005). The presence of abundant secondary carbonate, occurring as breccia cement, veins and alteration throughout the paragenetic sequence of the NEZ, provides an unusual opportunity to investigate the isotopic evolution of carbonates in a porphyry deposit during its formational history. Carbon and oxygen isotopic compositions of hydrothermal carbonates from the NEZ and limestones from the Mt. Polley region have been analyzed in order to assess fluid sources, fluid evolution and processes of ore formation (e.g., Ohmoto, 1986; Campbell and Larson, 1998). No previous C- or O-isotopic data have been generated for Mt. Polley.

A total of 61 carbonate samples from main-stage breccia cement and stage 3 and 4 veins were analyzed for their $\delta^{18}O$ and $\delta^{13}C$ isotopic compositions. Three analyses were also completed from samples of a 1 m

diameter marble clast (metasomatized limestone?) that was found in the breccia at the southern end of the NEZ open pit. Nine regional limestone samples were collected from two locations, one ~7 km northeast of the NEZ in the town of Likely (Figs. 1.8 and 2.5), and another ~11 km northwest of the NEZ at the northwest end of Morehead Lake (Fig. 1.8). Microprobe analyses of a subset of the NEZ samples (n=16 samples, 382 point analyses; Appendix C2) showed that the carbonates in the NEZ are calcite. Analyzed samples contain less than 2.1 weight percent Mg, Mn, Fe, Sr, or Ba. All isotopic results for calcite have therefore been determined using the method of Craig (1957). Summary statistics and histograms of C- and O-isotope results are presented in Table 5.3 and Figures 5.3 and 5.4, respectively. The complete $\delta^{13}C$ and $\delta^{18}O$ isotopic dataset is presented in Appendix D4.

Hydrothermal calcite samples have $\delta^{13}C_{(mineral)}$ values from -0.2 to -10.5 per mil (average -3.0 ‰), and $\delta^{18}O_{(mineral)}$ values from +4.0 to +20.9 per mil (average +15.7 ‰; Table 5.3). The marble clast has a similar isotopic composition, with an average $\delta^{13}C$ value of -1.1 per mil and $\delta^{18}O$ value of +16.4 per mil. The regional limestone samples have isotopic compositions that range from -1.3 to +2.7 per mil ($\delta^{13}C$) and +20.6 to +24.0 per mil ($\delta^{18}O$), which are consistent with marine carbonate (Taylor, 1974; Ohmoto, 1986).

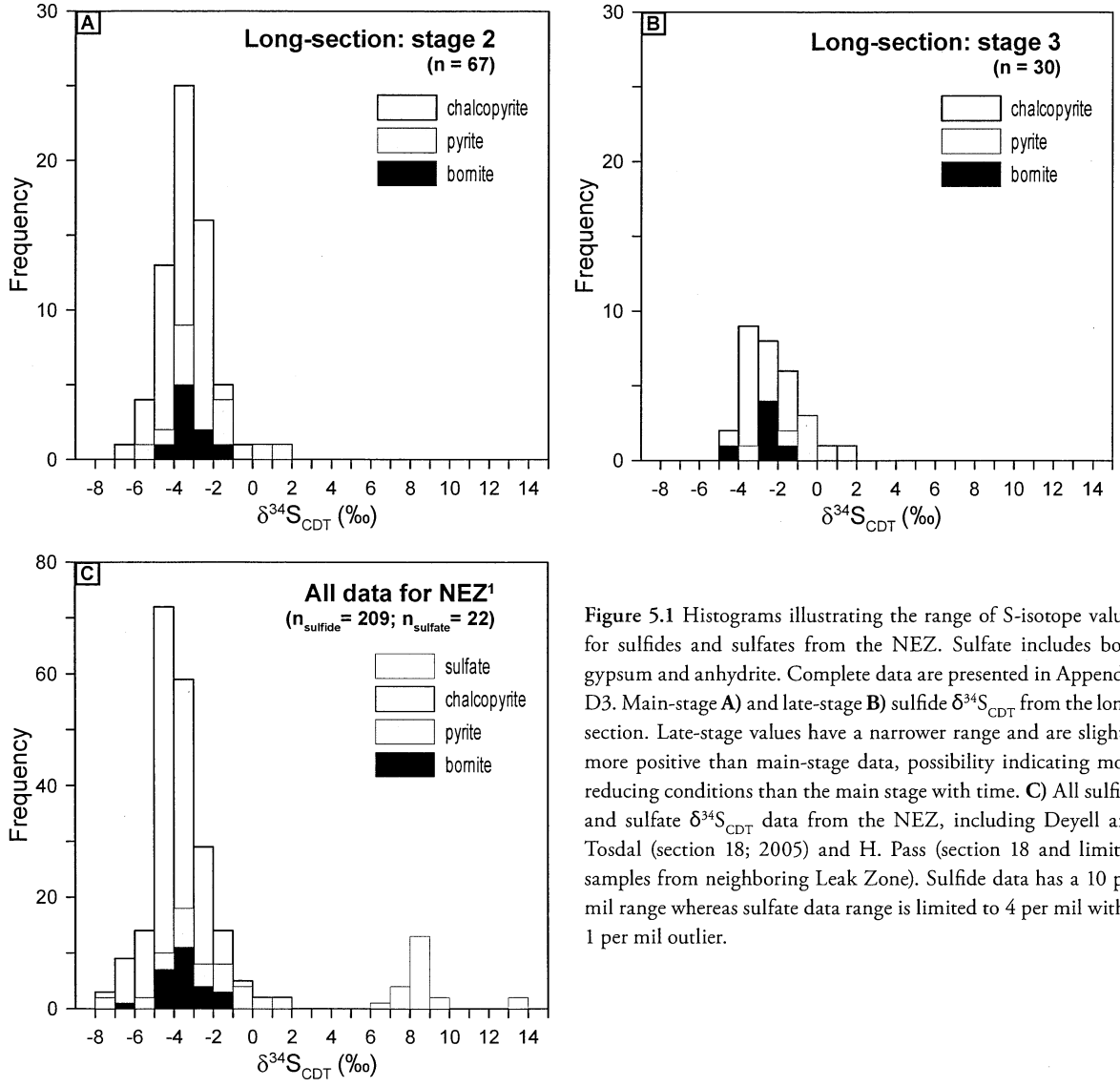

Figure 5.1 Histograms illustrating the range of S-isotope values for sulfides and sulfates from the NEZ. Sulfate includes both gypsum and anhydrite. Complete data are presented in Appendix D3. Main-stage **A)** and late-stage **B)** sulfide $\delta^{34}S_{CDT}$ from the long-section. Late-stage values have a narrower range and are slightly more positive than main-stage data, possibility indicating more reducing conditions than the main stage with time. **C)** All sulfide and sulfate $\delta^{34}S_{CDT}$ data from the NEZ, including Deyell and Tosdal (section 18; 2005) and H. Pass (section 18 and limited samples from neighboring Leak Zone). Sulfide data has a 10 per mil range whereas sulfate data range is limited to 4 per mil with a 1 per mil outlier.

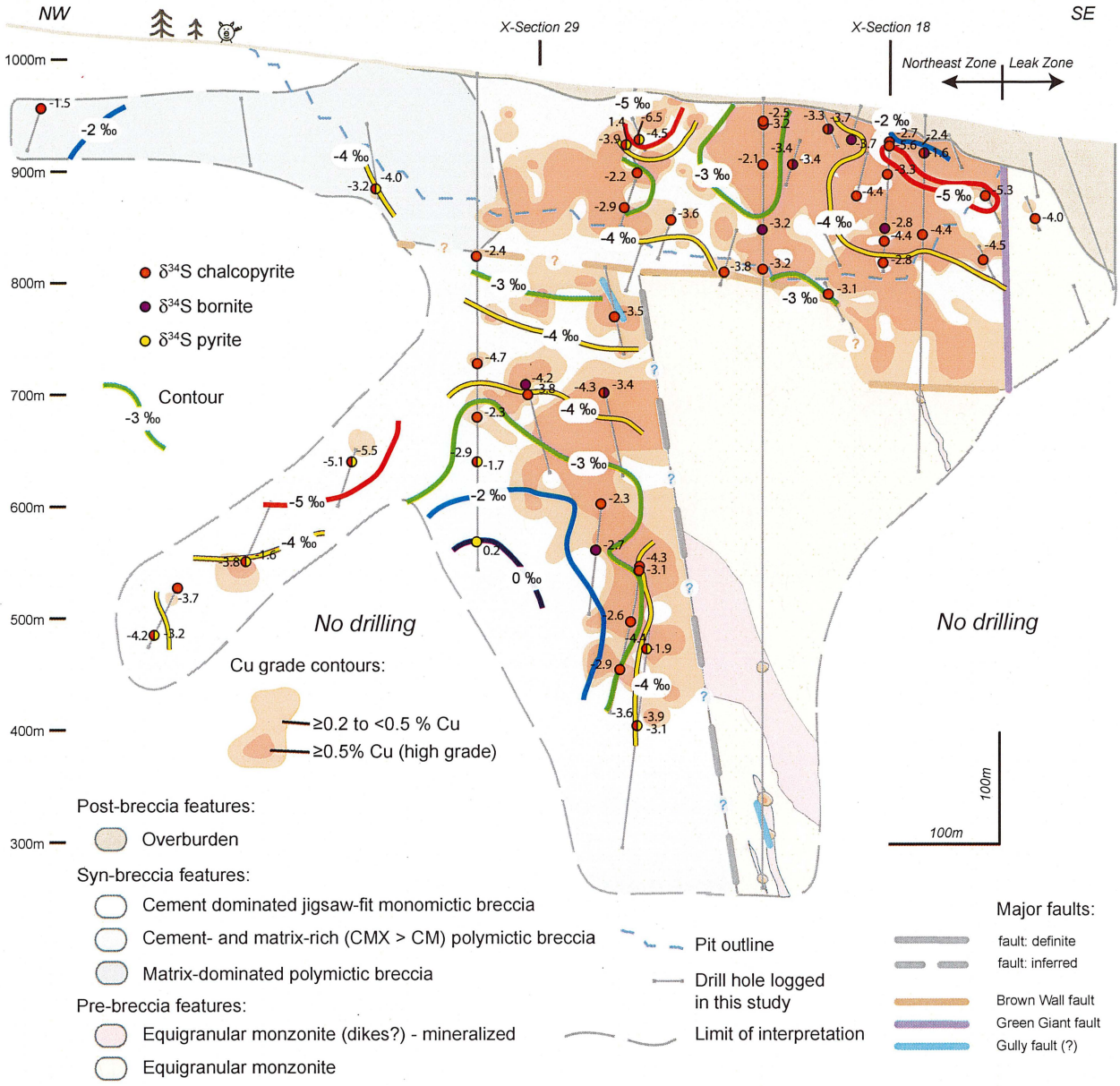

Figure 5.2 Contoured values (n= 44) of $\delta^{34}S_{sulfide}$ (‰) from breccia cement (stage 2) on the long-section, NEZ. Where multiple $\delta^{34}S_{sulfide}$ values were obtained from one sample, the most negative value was selected for contouring to emphasize areas of oxidation. Also shown are Cu-grade contours and a summary of the main geological elements on-section.

Oxygen- and carbon-isotopic zonation patterns for main-stage carbonates are shown on Figures 5.5 and 5.6. The $\delta^{18}O$ isotopic zonation patterns highlight that the lowest $^{18}O_{Carbonate}$ values occur near major faults (Fig. 5.5). The $\delta^{13}C$ isotopic zonation patterns show that the most negative $\delta^{13}C$ values are generally associated with high-grade ore zones, whereas enriched $\delta^{13}C$ values occur on the deposit periphery (compare Figs. 5.6 and 4.5).

5.3 Radiogenic isotopes

Combining Pb-isotope data obtained from sulfides and other Pb-bearing minerals with Rb-Sr and Sm-Nd isotopic data on gangue and ore minerals can provide important constraints on the timing of mineralization and alteration, metal and magma sources, fluid-rock interaction and mixing processes (Richards and Noble, 1998; Tosdal et al., 1999). This section presents new U-Pb and Rb-Sr isotope data for

Table 5.3 Summary statistics for C- and O-isotope mineral data (‰) from the long-section and calculated fluid values at specified temperatures. The full data set is available in Appendix D4. Where duplicate values were available (Appendix D4) for a single mineral phase in an individual sample, the average value was used for these statistics. Where more than one value existed, but represented different phases in a sample, each value was treated as a separate data point.

Stage 2	$\delta^{13}C_{calcite}$	$\delta^{18}O_{calcite}$	$^{13}C\ \Delta$ (550°C)	$\delta^{13}C_{fluid}$ (550°C)	$^{13}C\ \Delta$ (450°C)	$\delta^{13}C_{fluid}$ (450°C)	$^{18}O\ \Delta$ (550°C)	$\delta^{18}O_{fluid}$ (550°C)	$^{18}O\ \Delta$ (450°C)	$\delta^{18}O_{fluid}$ (450°C)
n=	36	36								
maximum	-0.2	20.7	-2.70	2.5	-2.77	2.6	1.21	19.5	2.43	18.3
minimum	-9.6	11.6	-2.70	-6.9	-2.77	-6.8	1.21	10.4	2.43	9.2
median	-2.5	15.0	-2.70	0.2	-2.77	0.3	1.21	13.8	2.43	12.6
average	-2.9	15.3	-2.70	-0.2	-2.77	-0.1	1.21	14.1	2.43	12.9
Stage 3	$\delta^{13}C_{calcite}$	$\delta^{18}O_{calcite}$	$^{13}C\ \Delta$ (400°C)	$\delta^{13}C_{fluid}$ (400°C)	$^{13}C\ \Delta$ (300°C)	$\delta^{13}C_{fluid}$ (300°C)	$^{18}O\ \Delta$ (400°C)	$\delta^{18}O_{fluid}$ (400°C)	$^{18}O\ \Delta$ (300°C)	$\delta^{18}O_{fluid}$ (300°C)
n=	8	8								
maximum	-1.0	16.5	-2.67	1.7	-2.00	1.0	3.24	13.3	5.60	10.9
minimum	-5.0	13.7	-2.67	-2.3	-2.00	-3.0	3.24	10.5	5.60	8.1
median	-1.9	14.8	-2.67	0.8	-2.00	0.1	3.24	11.6	5.60	9.2
average	-2.5	14.9	-2.67	0.2	-2.00	-0.5	3.24	11.7	5.60	9.3
Stage 4	$\delta^{13}C_{calcite}$	$\delta^{18}O_{calcite}$	$^{13}C\ \Delta$ (250°C)	$\delta^{13}C_{fluid}$ (250°C)	$^{13}C\ \Delta$ (200°C)	$\delta^{13}C_{fluid}$ (200°C)	$^{18}O\ \Delta$ (250°C)	$\delta^{18}O_{fluid}$ (250°C)	$^{18}O\ \Delta$ (200°C)	$\delta^{18}O_{fluid}$ (200°C)
n=	17	17								
maximum	-0.9	20.9	-1.30	0.4	-0.19	-0.7	7.27	13.6	9.57	11.3
minimum	-10.5	4.0	-1.30	-9.2	-0.19	-10.3	7.27	-3.3	9.57	-5.6
median	-2.3	17.6	-1.30	-1.0	-0.19	-2.1	7.27	10.3	9.57	8.0
average	-3.3	16.9	-1.30	-2.0	-0.19	-3.1	7.27	9.6	9.57	7.3
Total										
n=	61	61								
maximum	-0.2	20.9	-	2.5 at 550°C	-	2.6 at 450°C	-	19.5 at 550°C	-	18.3 at 450°C
minimum	-10.5	4.0	-	-9.2 at 250°C	-	-10.3 at 200°C	-	-3.3 at 550°C	-	-5.6 at 200°C
median	-2.3	15.3	-	0.2 at 550°C	-	0.1 at 300°C	-	11.6 at 400°C	-	9.2 at 300°C
average	-3.0	15.7	-	-0.7	-	-1.3	-	11.8	-	9.8
Marble clast										
n=	3	3	-	-	-	-	-	-	-	-
maximum	-0.7	16.8	-	-	-	-	-	-	-	-
minimum	-1.5	15.8	-	-	-	-	-	-	-	-
median	-1.1	16.5	-	-	-	-	-	-	-	-
average	-1.1	16.4	-	-	-	-	-	-	-	-
Regional limestone										
n=	9	9								
maximum	2.7	24.0	-	-	-	-	-	-	-	-
minimum	-1.3	20.6	-	-	-	-	-	-	-	-
median	0.6	21.7	-	-	-	-	-	-	-	-
average	1.0	22.0	-	-	-	-	-	-	-	-

ore and gangue minerals from Mt. Polley. The Pb- and Sr-isotope ratios are used here to provide constraints on fluid metal sources for stages 2 and 3 of the Cu-Au mineralization of the NEZ (e.g. Richards and Noble, 1998) and add to the existing Pb-isotope data base for alkalic igneous rock associated Cu-Au mineralization in

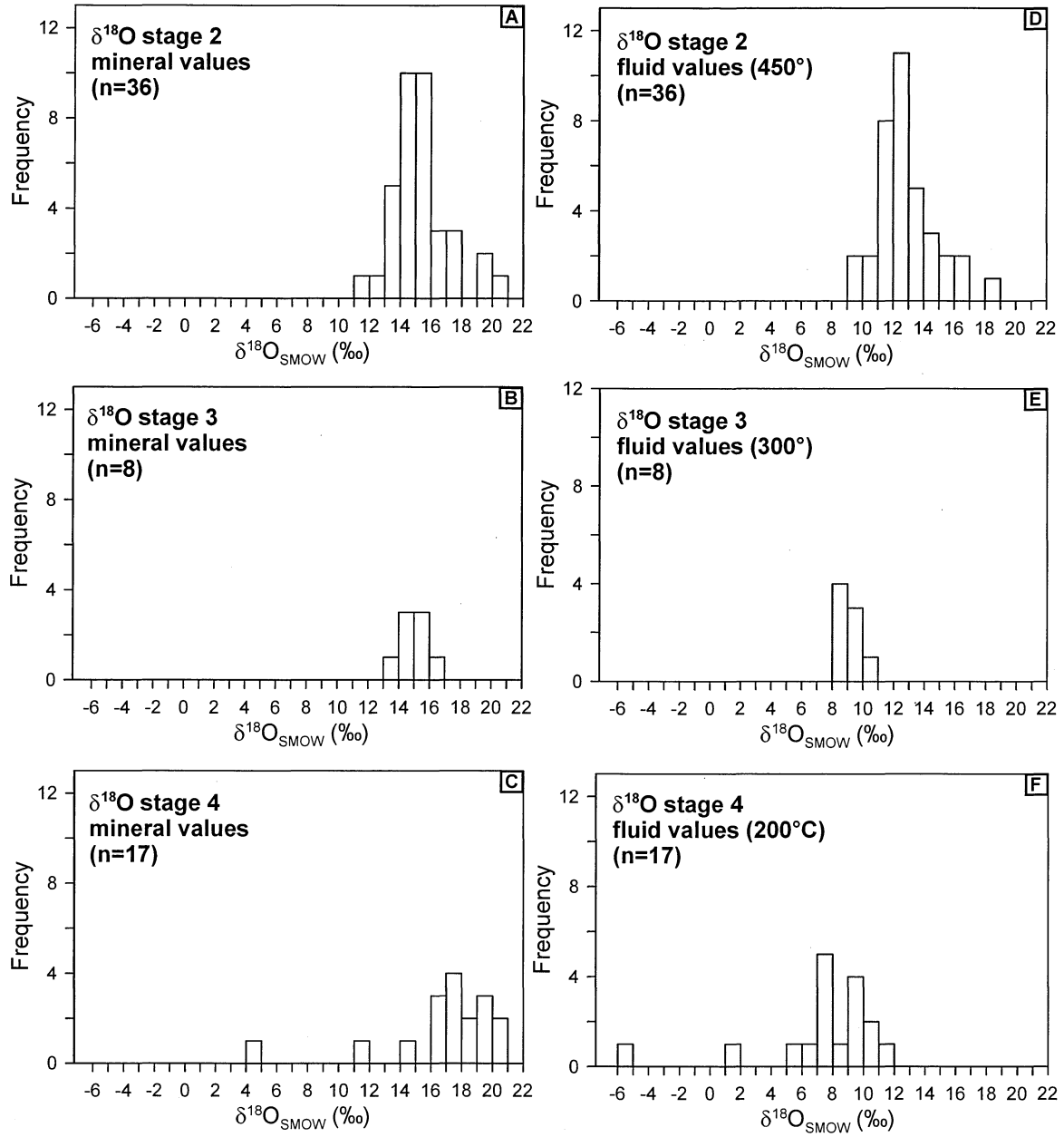

Figure 5.3 Histograms illustrating the range of O-isotope values for carbonate infill and veins from the NEZ. The marble clast samples from the pit have not been included. Mineral values are shown in **A)** stage 2, **B)** stage 3 and **C)** stage 4 and temperature corrected fluid values are shown in **D)** stage 2, **E)** stage 3 and **F)** stage 4. Stage 3 fluid values are slightly more depleted than stage 2 values and are generally consistent with the majority of Stage 4 values, suggesting the possibility of overprinting. Complete data presented in Appendix D4. Note: where duplicate data values were available for a single mineral phase in an individual sample, the average value was used. Where more than one value existed, but represented different phases in a sample, each value was treated as a separate data point.

the Cordillera (Bailey and Archibald, 1990; Mortensen et al., 1995; Tosdal et al., 1999; Logan et al., 2007). Lead- and Sr-isotope data are also provided for two of the regional limestone samples that were subjected to C- and O-isotopic analysis. Neodymium isotope data from Bath (2010) are included for stage 2 gangue apatite to examine the impact, if any, of old, more evolved ε_{Nd} sources on the hydrothermal fluids. The data are listed in Appendices D1 and D2.

5.3.1 Lead-isotopes

A total of 17 samples, including stage 2 breccia cement (chalcopyrite, pyrite, calcite, K-feldspar, garnet and anhydrite), stage 3 galena, stage 4 anhydrite, stage 5

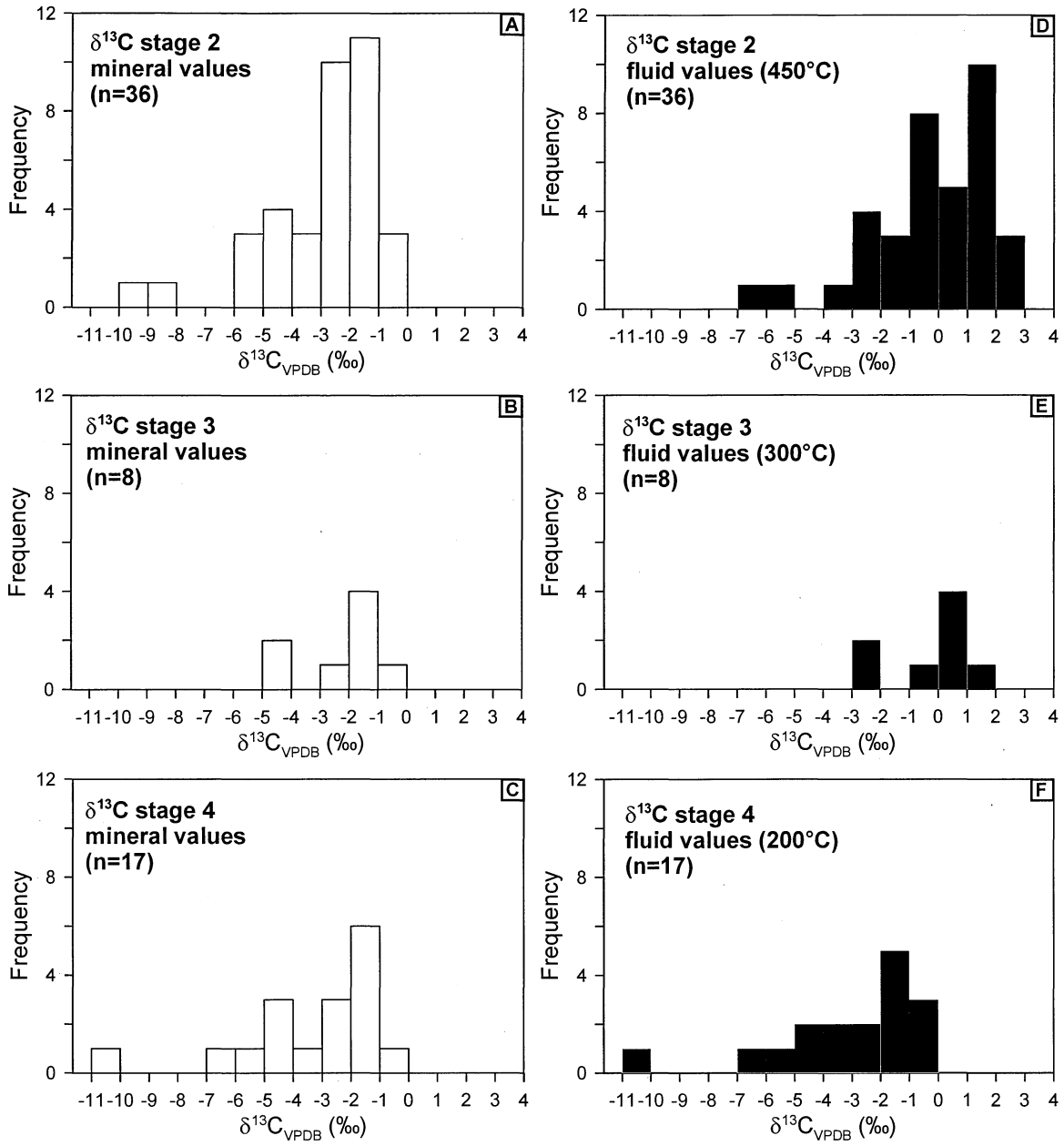

Figure 5.4 Histograms illustrating the range of C-isotope values for carbonate infill and veins from the NEZ. Mineral values are shown in **A)** Stage 2, **B)** Stage 3 and **C)** Stage 4 and temperature corrected fluid values are shown in **D)** Stage 2, **E)** Stage 3 and **F)** Stage 4. The marble clast samples from the pit have not been included. Stage 3 sample sets have a narrower range of data than main stage, but are generally consistent with Stage 2 values. Stage 4 veins have the widest range of values, but values are slightly depleted compared to the Stage 2 and Stage 3. The polynomial distribution of temperature corrected data indicates that more than one population may exist; this may reflect more than one precipitation process. Complete data presented in Appendix D4. Note: where duplicate data values were available for a single mineral phase in an individual sample the average value was used. Where more than one value existed, but represented different phases in a sample, each value was treated as a separate data point.

carbonate, a marble clast and a K-feldspar phenocryst from a juvenile monzonite clast (i.e a clast formed from the injection of magma into an unsolidified rock body; e.g. Chapter 3), were analyzed for their Pb-isotopic compositions. A pseudoleucite phenocryst from the Bootjack Stock syenite (Figs. 2.5 and 2.11) and two samples of limestone from the Mt. Polley region were also analyzed. Results are plotted on Figure 5.7A and B.

Chalcopyrite and pyrite from Mt. Polley have

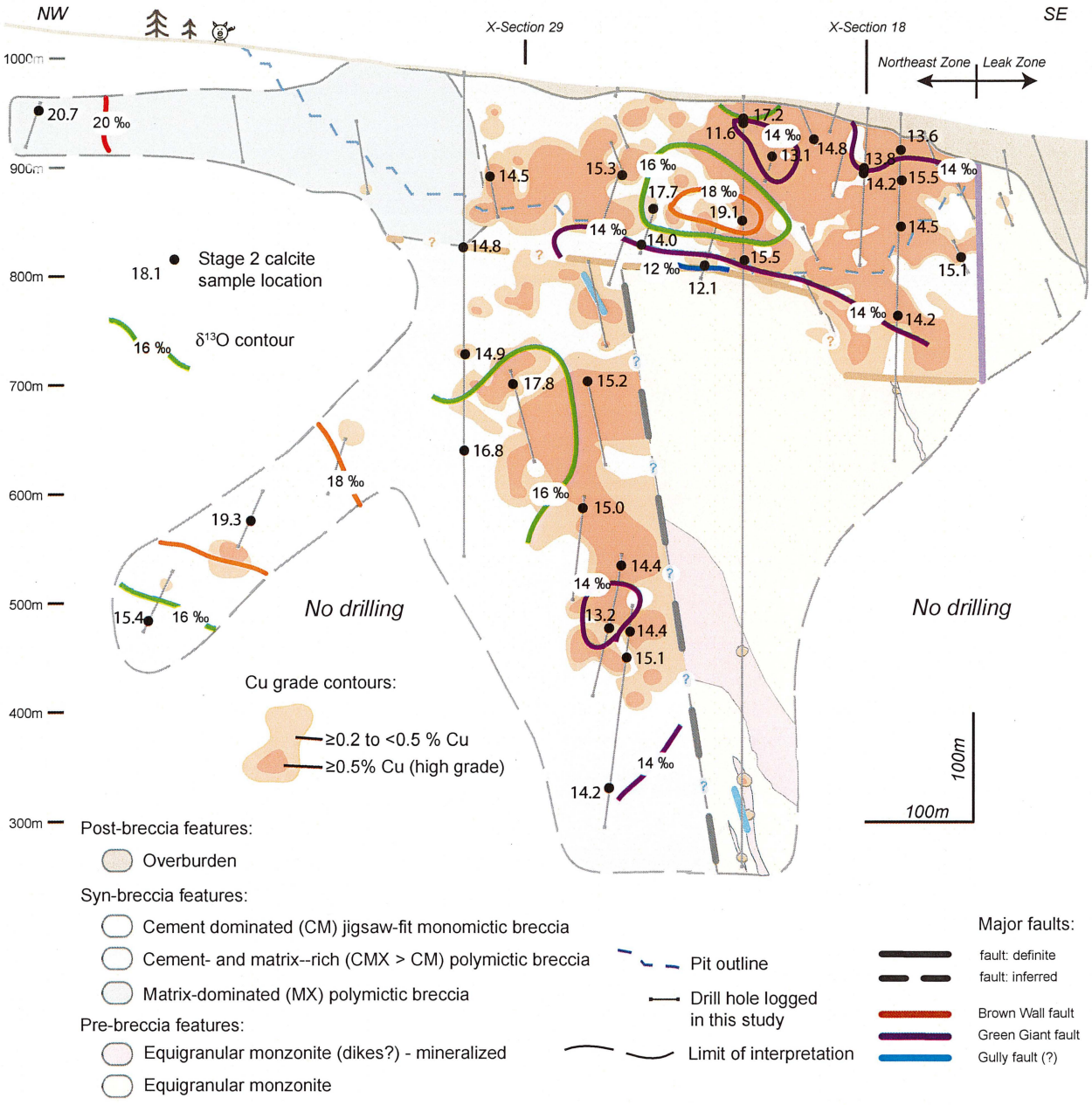

Figure 5.5 Contour diagram of $\delta^{18}O_{SMOW}$ (mineral) values from the stage 2. Where more than one $\delta^{18}O$ value was analyzed per location (duplicate or zoned infill), the most negative or paragenetically earliest value was used for contouring. In general $\delta^{18}O$ values are more positive distal to ore and/or faults.

high Pb and low U and Th concentrations (42 to 604 ppm Pb, 0.18 to 0.34 ppm U and 0.06 to 0.34 ppm Th; Appendix D1). These minerals, together with the stage 3 galena sample, provide the most reliable indications of the original Pb isotopic composition of the mineralizing fluids. The $^{206/204}Pb$ (18.77 to 18.92) $^{207/204}Pb$ (15.56 to 15.59) and $^{208/204}Pb$ ratios (38.22 to 38.32; Fig.5.7) for these samples are considered to be initial ratios, because the samples have very low $^{238}U/^{204}Pb$ and $^{232}Th/^{204}Pb$ values (Appendix D1). The stage 3 galena yielded a model Pb age of 207.8 ± 1.8 Ma, which overlaps with the results of previous U-Pb and Ar-Ar dating (Bailey and Archibald, 1990; Mortensen et al., 1995; Logan et al., 2007). The stage 5 carbonate with bladed textures produced ratios of $^{206/204}Pb$ (18.96 to 19.04) $^{207/204}Pb$ (15.57 to 15.59) and $^{208/204}Pb$ ratios (38.26 to 38.36) at 203 Ma (Fig. 5.7, Appendix D1).

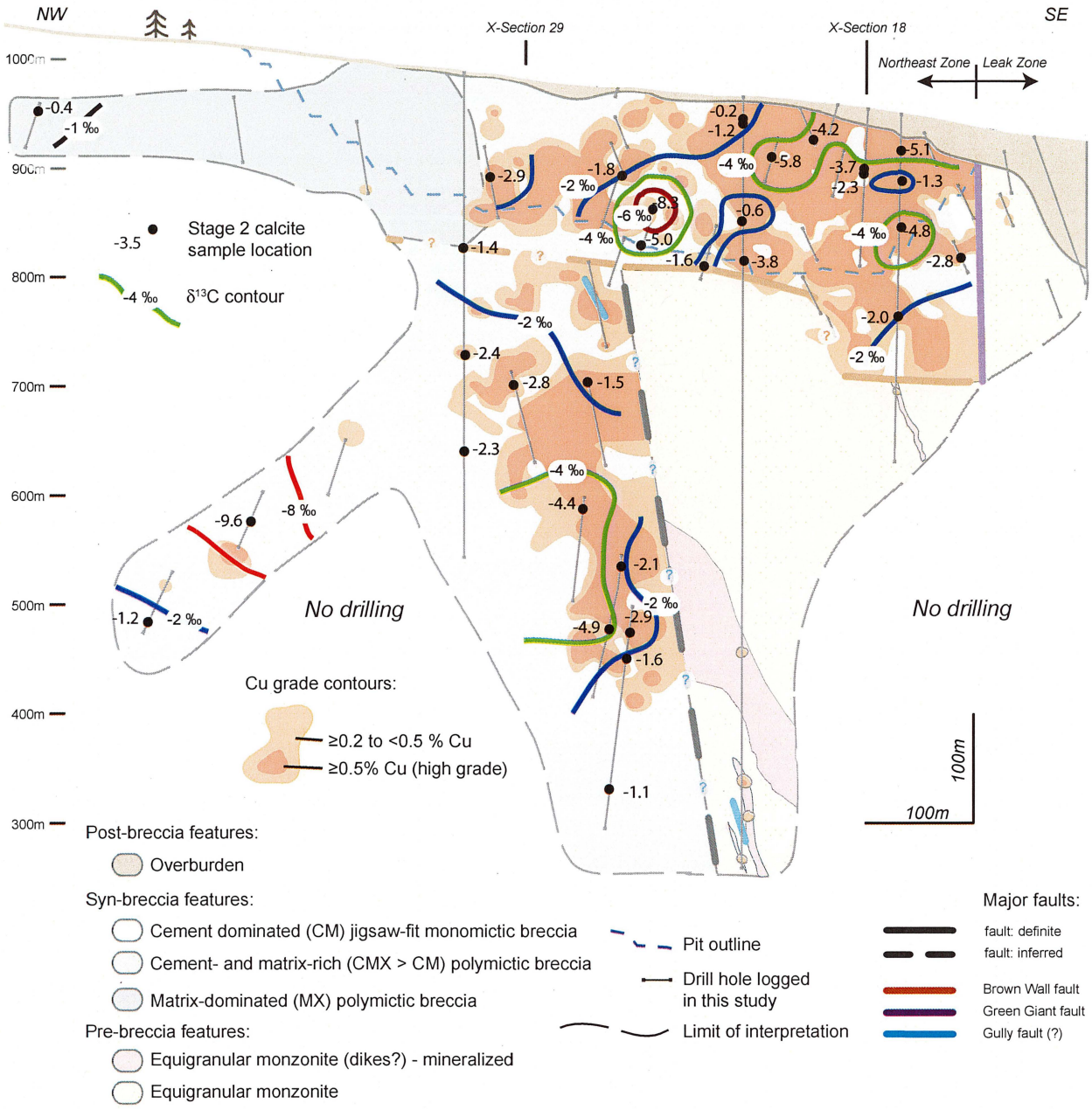

Figure 5.6 Contour diagram of $\delta^{13}C_{PDB}$ (mineral) values from stage 2. Where more than one $\delta^{13}C$ value was analyzed perlocation (duplicate or zoned infill), the most negative or paragenetically earliest value was used for contouring. With the exception of two outlying negative values (-9.6 and -8.3 ‰), the northern deep-level mineralized domain is associated with more negative $\delta^{13}C$ values (-5 to -4 ‰), with values increasing towards zero away from high grade and peripheral to ore. Trends are less distinct in the shallow-level mineralized domain.

Stage 2 K-feldspar contains 4.0 ppm Pb, 0.039 ppm U and 0.035 ppm Th (Appendix D1). Although the Pb content is low, the $^{238}U/^{204}Pb$ and $^{232}Th/^{204}Pb$ values are also low (Appendix D1) and the isotopic data for this sample are considered reliable. Similarly the massive carbonate clast has significantly higher Pb contents relative to U and Th (0.73 to 0.92 ppm Pb, 0.02 ppm U, <0.001 ppm Th), giving low $^{238}U/^{204}Pb$ and $^{232}Th/^{204}Pb$ values (Appendix K). Stage 4 anhydrite has low U/Pb and Th/Pb and an elevated age-corrected $^{206/204}Pb$ of 19.02. (Fig. 5.7, Appendix D1).

Stage 2 garnet has high U/Pb and Th/Pb ratios (Appendix D1) producing initial Pb ratios with large errors. The garnet samples have therefore been rejected. The pseudoleucite phenocryst from the Bootjack syenite

is excluded from further discussion because it has a very high U/Pb ratio (Appendix D1) and contains significant amounts of radiogenic Pb (Fig. 5.7C). Similarly, the regional limestone samples are excluded because they have high U/Pb ratios and radiogenic $^{206/204}Pb$ (Appendix D1).

5.3.2 Strontium- and neodymium-isotopes

Initial Sr ratios have been analyzed from stage 2 breccia cement (pyrite, apatite, calcite, garnet, anhydrite and K-feldspar; n = 13), stage 4 anhydrite (n = 2), a marble clast from the NEZ breccia, a pseudoleucite phenocryst from the Bootjack Stock syenite and two regional limestone samples. The Rb/Sr ratios for these samples are generally low compared to average upper crust (greater than 0.2-0.4; Rollinson, 1993), so that the required age corrections to 203 Ma are small (Appendix D2). One sample of stage 2 apatite was analyzed for $^{143}Nd/^{144}Nd$ (Bath, 2010).

Most of the $^{87}Sr/^{86}Sr_{inital}$ results for stage 2 and 3 minerals range from 0.70331 to 0.70353 (Fig. 5.8; Appendix D2. One analysis of stage 2 garnet yielded a $^{87}Sr/^{86}Sr_{inital}$ value of 0.70371. The Bootjack Stock pseudoleucite and the massive carbonate clast have $^{87}Sr/^{86}Sr_{inital}$ values within the range of the main-stage minerals ($^{87}Sr/^{86}Sr_{inital}$: 0.70342 and 0.70346 to 0.70351, respectively; Appendix D2). Stage 4 anhydrite has higher $^{87}Sr/^{86}Sr_{initial}$ (0.70376 to 0.70377) and higher $^{206}Pb/^{204}Pb$ values than the stage 2 minerals (Appendix D2). The limestone samples have low Rb/Sr values (Appendix D2) and their initial Sr ratios are higher than the veins and breccia cement ($^{87}Sr/^{86}Sr_{inital}$: 0.70622 to 0.70771, respectively; Appendix D2). Variations obtained from replicate analyses of the limestone samples (Appendix D2) probably relate to slight variations in the amount of clay that was leached in each experiment.

Epsilon-Nd results for stage 2 apatite range between +5.9 and +6.5 assuming an age of 200 Ma (Fig. 5.9; Appendix D2). Epsilon-Nd values were calculated using the present-day CHUR (Chondritic Uniform Reservoir; DePaolo and Wasserburg, 1976) reference value of 0.512638 (Skewes and Stern, 1996).

5.4 Discussion

5.4.1 Sulfur-isotopic compositions

Previous S-isotope studies of Australian alkalic porphyry Cu-Au deposits documented systematic S-isotopic zonation patterns around several mineralized complexes (i.e. Cadia district; Harper, 2000; Wilson, 2003; Wilson et al., 2007; and North Parkes; Radclyffe, 1995; Lickfold et al., 2003). Systematic S-isotope zonation patterns have also been documented from alkalic Cu-Au deposits in the Philippines (Wolfe, 2001) and British Columbia (Lorraine, Mt. Polley, Red Chris, Galore Creek, Afton; Deyell and Tosdal, 2005). Deyell and Tosdal (2005) reported 70 $\delta^{34}S$ values of chalcopyrite, pyrite and bornite from section 18 of the NEZ (Fig. 3.1). They identified an isotopic zonation pattern in the breccia complex defined by a core of depleted $\delta^{34}S$ values (-7 ‰) associated with high-grade Cu-Au mineralization, and a change systematically upwards and outwards to higher values (~ -1 ‰) associated with low-grade mineralization. A narrower range of values was observed from the Cariboo pit in the Core Zone of Mt. Polley (-2.3 to +2.4 ‰; average +0.2 ‰; n = 60; Deyell, 2005; Fig. 2.6A; Deyell and Tosdal, 2005).

The range of $\delta^{34}S_{sulfide}$ (-7.1 to +1.4 ‰) and $\delta^{34}S_{sulfate}$ values (+6.3 to +14.0 ‰) from the NEZ is comparable to that obtained from porphyry deposits world-wide ($\delta^{34}S_{sulfide}$ -5 ‰ to +5 ‰; $\delta^{34}S_{sulfate}$ +8 ‰ to +14 ‰ (Ohmoto and Rye, 1979; Ohmoto and Goldhaber, 1997; Wilson et al., 2007). The wide range of negative $\delta^{34}S_{sulfide}$ values and tight grouping of $\delta^{34}S_{sulfate}$ for the NEZ (Fig. 5.1C) are consistent with mineral deposition from an oxidized (sulfate dominant), high-temperature (>400 °C) magmatic-hydrothermal fluid (Ohmoto and Rye, 1979; Rye, 1993; Wilson et al., 2007). This is consistent with observations of anhydrite in the NEZ and also with Bath et al.'s (2006) conclusion of sulfate-saturation observed in melt inclusions from stage 2 apatite in the NEZ.

Temperatures of sulfide precipitation for the NEZ have been calculated using S-isotope geothermometry. Alkalic porphyry Cu deposits typically form at temperatures of 550° to 250°C (Lang et al., 1993; Dunne et al., 1994; Lang et al., 1995a; Ulrich et al., 1999; Wolfe, 2001; Lickfold et al., 2003;

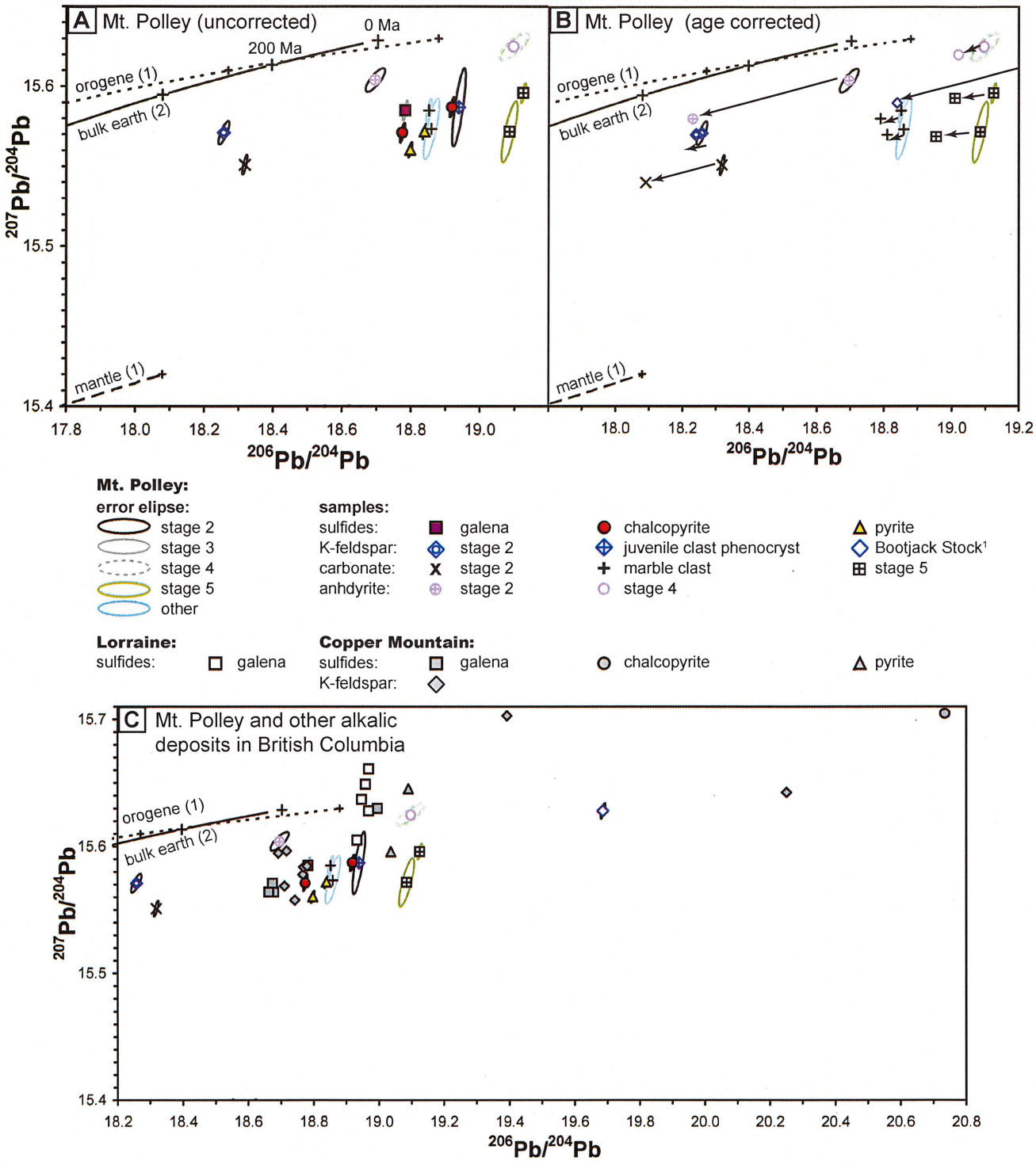

Figure 5.7 Lead-isotopic data from Mt. Polley and other alkalic porphyry deposits. **A)** Uncorrected $^{207}Pb/^{204}Pb$ versus $^{206}Pb/^{204}Pb$ for NEZ hydrothermal minerals and the marble clast. Values plot between the orogene/bulk earth and mantle growth curves. Error ellipses are for 2 sigma. Note error ellipses for sulfides are very small due to high Pb concentration in the samples. **B)** $^{207}Pb/^{204}Pb$ versus $^{206}Pb/^{204}Pb$ for NEZ hydrothermal minerals other than sulfides, showing the shift between uncorrected values (points with error ellipses) to 203 Ma age corrected values (points with no error ellipses). **C)** NEZ values (with error ellipses) compared with other alkalic deposits (no error ellipses) in the Quesnellia terrane (Lorraine and Copper Mountain). Plots were created using Isoplot 3.1 (Ludwig, 2003; normal $^{207}Pb/^{204}Pb$-$^{206}Pb/^{204}Pb$ isochron and 0.8 error correlation). Growth curves are from (1) Zartman and Doe (1981) and (2) Stacey and Kramers (1975).

Wilson et al., 2003; Jago, 2008; Micko et al., 2008). The pyrite–chalcopyrite S-isotope geothermometer of Kajiwra and Krouse (1971) is applicable from 600° to 260°C. The chalcopyrite–bornite geothermometer of Li and Liu (2006) is applicable from 1000° to 0°C. As both geothermometers have potential applications for porphyry systems, they are applied here to 40 sulfide pairs from the NEZ. Sulfide–sulfate pairs were not observed in this study as these minerals precipitated at separate times in the paragenesis. Only six sulfide pairs yielded meaningful results, providing temperature estimates of 253° to 481°C (Appendix D3.4). Either the NEZ sulfides precipitated over a wider temperature range than normal for porphyry deposits, or many of the sulfide pairs are not in isotopic equilibrium. The latter interpretation is favored, as isotopic disequilibrium is common for these sulfides (Reed, 1997).

The increase in $\delta^{34}S_{sulfide}$ isotopic values outwards from oxidized magmatic centers observed at Mt. Polley (Fig. 5.2), and at the alkalic porphyry deposits of the Cadia district (Wilson et al., 2007), are the opposite of what is expected from a cooling magmatic fluid with a constant bulk S-composition (Ohmoto and Rye, 1979). If cooling was the only precipitation mechanism, then $\delta^{34}S_{chalcopyrite}$ values would not change. The observed zonation patterns must therefore reflect other mechanisms. In addition to cooling, changes in the oxidation state (i.e., H_2S/SO_4) and/or the bulk S-composition of the fluid must have occurred during sulfide deposition. Wilson et al. (2007) modelled the effect of changing either the redox state or the bulk S-compositions on $\delta^{34}S_{sulfide}$ values from the Cadia porphyry deposits. They showed that sulfides with distinctly negative $\delta^{34}S_{sulfide}$ values were precipitated from an SO_2-rich magmatic fluid. Specifically, aqueous inorganic sulfate reduction involving the interaction of the fluid with ferrous iron-bearing minerals (e.g., clinopyroxene, magnetite) could have changed the bulk $\delta^{34}S_{fluid}$ value and also resulted in widespread hematite ('red-rock') alteration. Fluid mixing

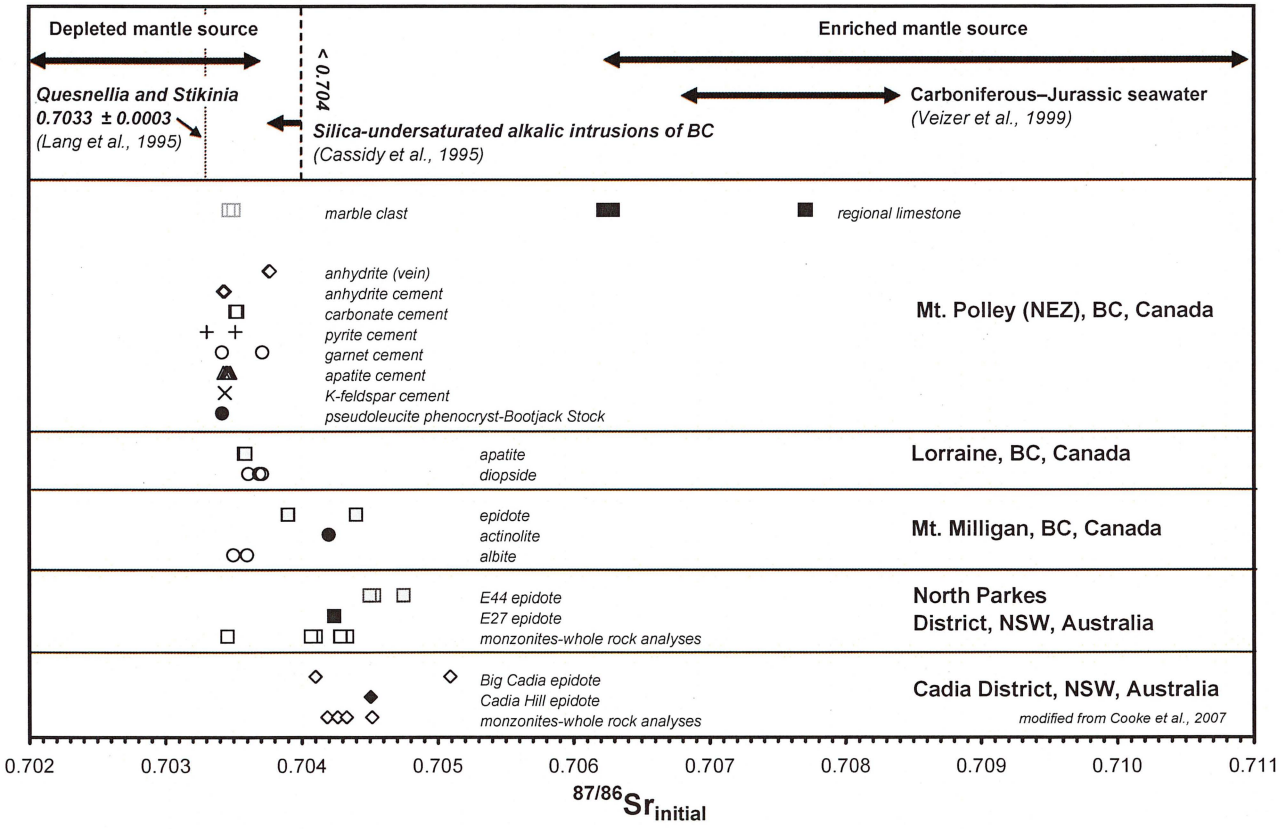

Figure 5.8 Initial $^{87}Sr/^{86}Sr$ isotopic data from Mt. Polley and other alkalic porphyry deposits in British Columbia (BC) and New South Wales (NSW), as well as the Quesnellia and Stikinia terranes (Lang et al., 1995) and Carboniferous to Jurassic seawater (Viezer et al., 1999). Data from Lorraine are from Bath (2010), data from Mt. Milligan are from Jago (2008), data from New South Wales are from Cooke et al. (2007). Mt. Polley apatite and Bootjack Stock data from Bath (2010). Data from Canadian deposits are presented in Appendix D2.

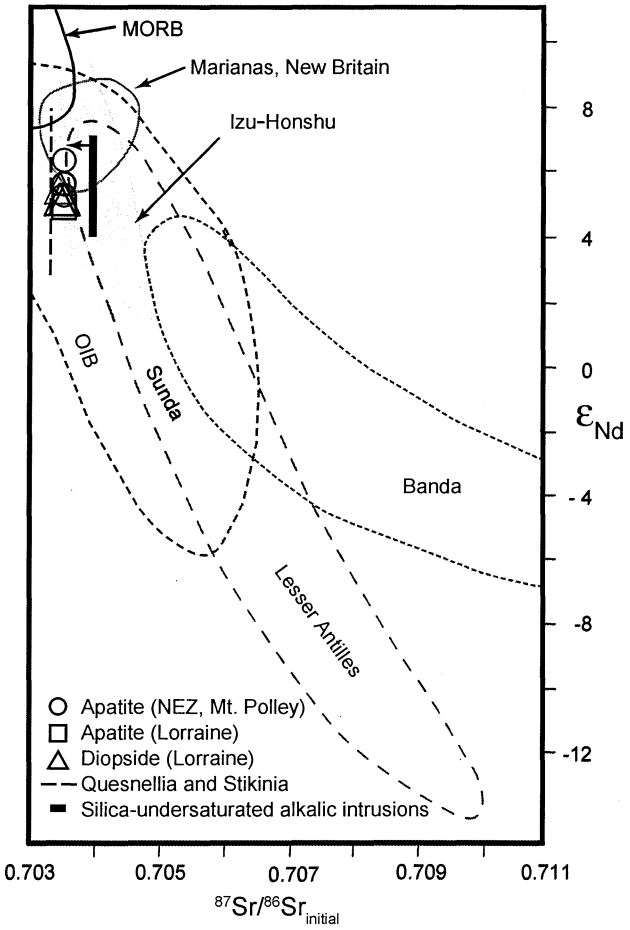

Figure 5.9 Plot of ε_{Nd} vs $^{87}Sr/^{86}Sr_{initial}$ for stage 2 hydrothermal minerals and intrusive rocks related to alkalic porphyry mineralization in British Columbia. Fields after Arculus and Powell (1986). Lorraine apatite and diopside data from Bath (2010). Mesozoic silica-undersaturated alkalic intrusions in British Columbia from Cassidy et al. (ε_{Nd} 4 to 7, $^{87}Sr/^{86}Sr$ <0.704; 1995). Quesnellia and Stikinia saturated and undersaturated alkalic igneous complexes from Lang et al. (ε_{Nd} 2.7 to 7.9, $^{87}Sr/^{86}Sr$ 0.7033 ± 0.0003; 1995a). Figure modified from Cooke et al. (2007).

on the deposit periphery could also change the S-isotope systematics (Wilson et al., 2007). However, the presence of widespread hematite-dusted K-feldspar throughout the NEZ, and epidote on the deposit periphery, support a model of inorganic sulfate reduction during partial alteration of ferrous iron-bearing minerals to hematite.

The $\delta^{34}S_{sulfide}$ isotopic zonation patterns observed on the long-section of the NEZ are not symmetrical compared to those documented from Section 18 (Deyell and Tosdal, 2005). This is most likely due to disruption of isotopic zonation patterns on the long-section by faulting and dike emplacement.

Samples of late-stage chalcopyrite, bornite and pyrite from the NEZ long-section had slightly higher $\delta^{34}S$ values than main-stage sulfides (Table 5.2; compare Figs. 5.1A and B). This may indicate a shift towards less oxidizing conditions or an increased component of water-rock interaction with time.

Overall, the data from the NEZ are generally lower than those obtained from the Core Zone of Mt. Polley (-2.3 to +2.4 ‰; average +0.2 ‰; Fig. 2.6A; Deyell and Tosdal, 2005). This may reflect more oxidizing conditions of mineralization in the NEZ compared to the Core Zone (Fig. 2.6A).

5.4.2 Carbon- and oyxgen-isotopic compositions

Previous whole-rock isotopic studies of hydrothermal systems have shown that a zone of depleted $\delta^{18}O$ can reflect hydrothermal fluid pathways, zones of fluid mixing or water-rock interaction (e.g., Taylor, 1971; Lynch et al., 1990; Taylor and Holk, 2002). The observed decrease of $\delta^{18}O$ values for stage 2 carbonates proximal to major faults in the NEZ (Fig. 5.5) implies either that the faults were fluid conduits during main-stage mineralization, or that the isotopic compositions of carbonates were at least partially reset during post-mineralization faulting. The disruption of metal zoning patterns by the faults (Figs. 4.5, 4.6, 4.7 and 5.5) favors the latter interpretation.

High-grade Cu–Au–Ag mineralization in the NEZ is associated with domains of ^{13}C depletion in stage 2 carbonates (Fig. 5.6). The C-isotopic compositions of carbonates are typically less strongly influenced by isotopic exchange with late-stage hydrothermal fluids than the corresponding O-isotopic compositions (Davidson, 1997). In contrast to the $\delta^{18}O$ isotopic contours, the $\delta^{13}C$ contours do not appear to relate to fluid flow along the major faults (compare Figs. 5.5 and 5.6), which suggests that the $\delta^{13}C$ data may better preserve zoning patterns. The $\delta^{18}O$ and $\delta^{13}C$ zonation patterns suggest that the two largest areas of mineralization in the NEZ may not have been a contiguous body.

5.4.3 Fluid compositions

The isotopic compositions of fluids that precipitated calcite can been calculated using the

calcite-H_2O equilibrium equation from Friedman and O'Neil (1977; after O'Neil et al., 1969) for $\delta^{18}O$, and calcite-CO_2 from Ohmoto and Rye (1979; after Bottinga, 1969) for $\delta^{13}C$, provided that an independent temperature estimate is available. Porphyry deposits are formed by hydrothermal fluids typically in the range of 600° to 300°C (Burnham and Ohmoto, 1980), with lower temperatures typical of late-stage hydrothermal activity. No primary fluid inclusions were observed at Mt. Polley, and so alteration mineralogy (Chapter 4) and S-isotope pairs provide the only temperature constraints for mineralization (481° to 253°C). For the purposes of C–O-isotopic modeling calculations, the following temperatures have been assumed: 550° to 450°C (stage 2), 400° to 300°C (stage 3) and 250° to 200°C (stage 4; Figs. 5.3D, E, F; 5.4D, E, F, 5.10 and Fig. 5.11). These conservative temperature estimates are required because it is not possible to constrain temperatures of formation from fluid inclusion analyses due to a lack of suitable material for analysis. Based on the assumed temperature ranges and the measured isotopic compositions of calcite (Table 5.3), the ranges of fluid compositions are estimated to be -6.9 to +2.6 ($\delta^{13}C$) and +9.2 to +19.5 ($\delta^{18}O$) for stage 2, -3.0 to +1.7 ($\delta^{13}C$) and +8.1 to +13.3 ($\delta^{18}O$) for stage 3, and -10.3 to +0.4 ($\delta^{13}C$) and -5.6 to +13.6 ($\delta^{18}O$) for stage 4. These results partially overlap with magmatic $^{18}O_{fluid}$ values, and mostly do not overlap with magmatic $\delta^{13}C_{fluid}$ values (Fig. 5.11A), implying that more than one source of C and O was involved in mineralization at Mt. Polley.

Many of the calculated fluid $\delta^{18}O_{fluid}$ values are extremely heavy (>10 ‰; Figs. 5.10 and 5.11B–C). Such heavy $\delta^{18}O_{fluid}$ values are rarely seen in hydrothermal ore deposits apart from sediment-hosted massive sulfide deposits (e.g., Large et al., 2001). These heavy values may be a product of a low-T basinal brine, an incorrect choice of calculation of fluid values for stage 2 (temperature estimates >300°C generally have little effect on $\delta^{18}O$; see Fig. 5.11B and C), a shift caused by sulfate substitution into carbonate (i.e. Davidson et al., in prep) or the possibility of $\delta^{18}O$ resetting by a lower temperature overprint. The latter two options are considered to be the most likely.

The vertical spread in $\delta^{13}C$ data may suggest that redox changes, either the oxidation of CH_4 or the reduction of CO_2, played an important role in the NEZ (Fig. 5.11B, C). If the CO_2 reservoir had a typical magmatic $\delta^{13}C$ value of -5 to -6 per mil, then all of the $\delta^{13}C_{Carbonate}$ values greater than -5 per mil (i.e., most of the data) could reflect reduction of CO_2 to CH_4 somewhere in the system (Ohmoto, 1972). However, reduction of CO_2 would require a significant quantity of reductant to be available at the site of precipitation, which is inconsistent with the presence of widespread hematite alteration through the mineralized intrusive complex and the lack of pyrrhotite, graphite or other significant reductants. Another mechanism is required to explain the high $\delta^{13}C$ values.

The $\delta^{13}C_{calcite}$ and $\delta^{18}O_{calcite}$ data from the NEZ do not plot on simple cooling curves for calcite precipitated from a mantle-derived magmatic-hydrothermal fluid (Fig. 5.11A). The anomalously high $\delta^{13}C_{calcite}$ values suggest that the mineralizing fluid must have interacted with a $\delta^{13}C$-enriched source in order to shift $\delta^{13}C$ values by up to approximately +5 per mil (Fig. 5. 11A). This enrichment could have been caused by interaction with a C-bearing sedimentary source. Such interaction could have occurred if mineralizing fluids interacted with lenses of limestone in the Nicola Group volcanics near the site of mineralization. Alternatively, the Mt. Polley igneous complex may have undergone partial isotopic exchange, either by fluid-rock interaction or by magmatic assimilation, with the volcanic arc and carbonate platform succession of the Harper Ranch sub-terrane, units that underlie the Nicola Group (Monger, 1977). Another possibility is the formation of a CO_2-enriched melt due to flat slab subduction of a carbonate-covered oceanic plateau of the Cache Creek ocean beneath Quesnellia (e.g. Cloos, 1993; McInnes and Cameron, 1994; Mihalynuk et al., 1994; Gutscher et al., 2000; Mungall, 2002; Stern, 2002; Johnston and Borel, 2007; Marín-Cerón et al., 2010).

5.4.4 Calcite precipitation processes

Calcite cannot precipitate simply by cooling of a hydrothermal fluid because calcite has retrograde solubility (Reed and Spycher, 1985; Zheng and Hoefs, 1993). Calcite deposition can be achieved either by boiling, which combines cooling with CO_2 degassing and pH increase, fluid mixing between CO_2-rich and Ca-rich hydrothermal fluids, water-rock interaction or

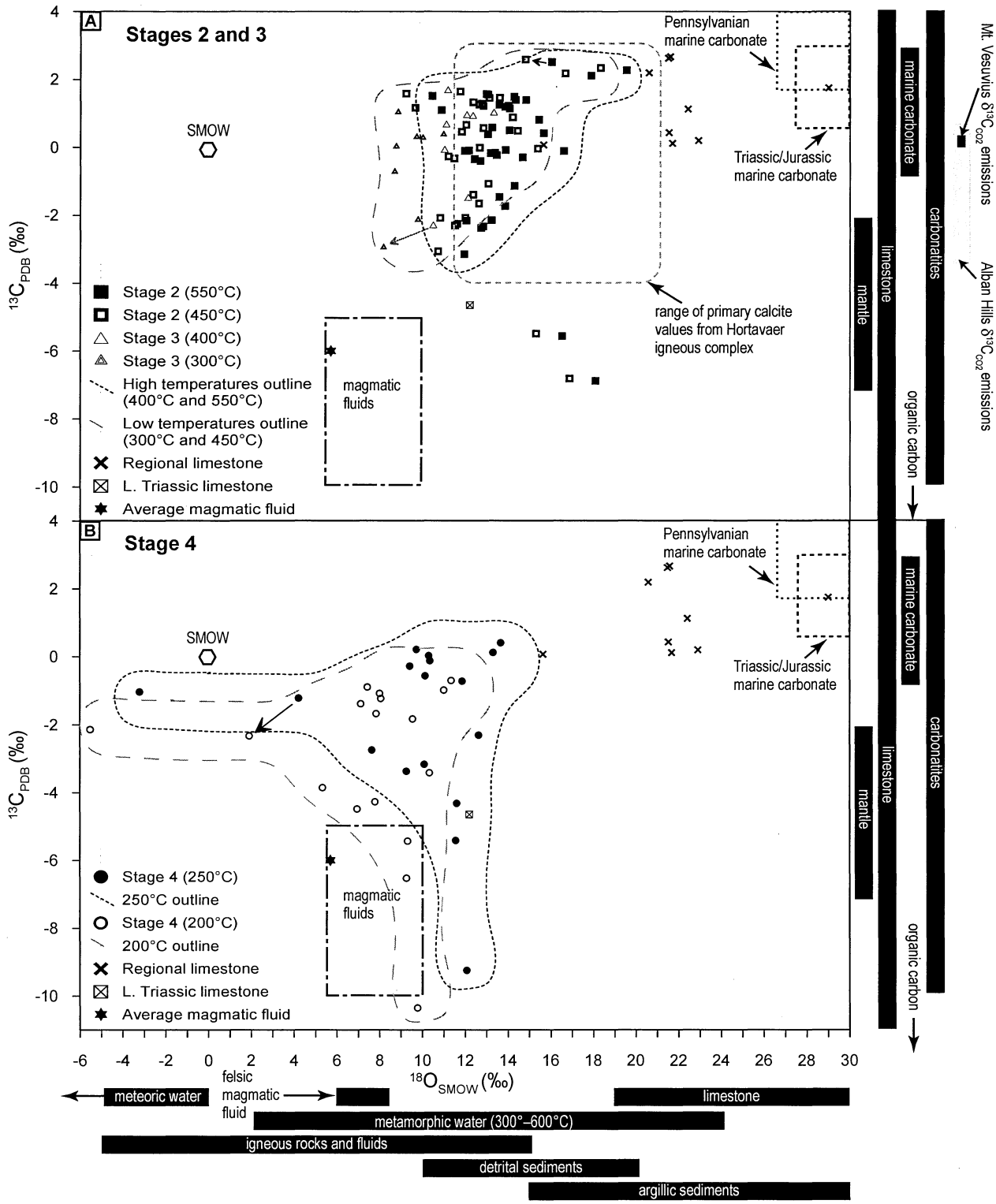

Figure 5.10 Fluid $\delta^{13}C_{PDB}$ vs $\delta^{18}O_{SMOW}$ plot of isotopic analyses for NEZ carbonates (see legend for estimated fluid temperatures) and common large reservoirs that are important in hydrothermal systems, including an average magmatic fluid value (★). **A)** Filled symbols for stage 2 (550°C) and stage 3 (400°C) fluid values, and open symbols for stage 2 (450°C) and stage 3 (300°C) values at specified temperatures. Arrows show how temperature corrections shift data points (black = stage 2, grey = stage 3). Also shown are isotopic values of volcanic emissions from Mt. Vesuvius (Italy; Chiodini et al., 2001) and Alban Hills (Italy; Chiodini and Frondini, 2001), and primary calcite data from the Hortavaer igneous complex (Norway). **B)** Filled (250°C) and open (200°C) symbols of fluids responsible for stage 4 veins. The black arrow shows how temperature corrections shift data points. Fields are from Taylor (1974) and Hoefs (1987) as compiled in Rollinson (1993), Ohmoto (1986), Campbell and Larson (1998), and Veizer et al. (1999).

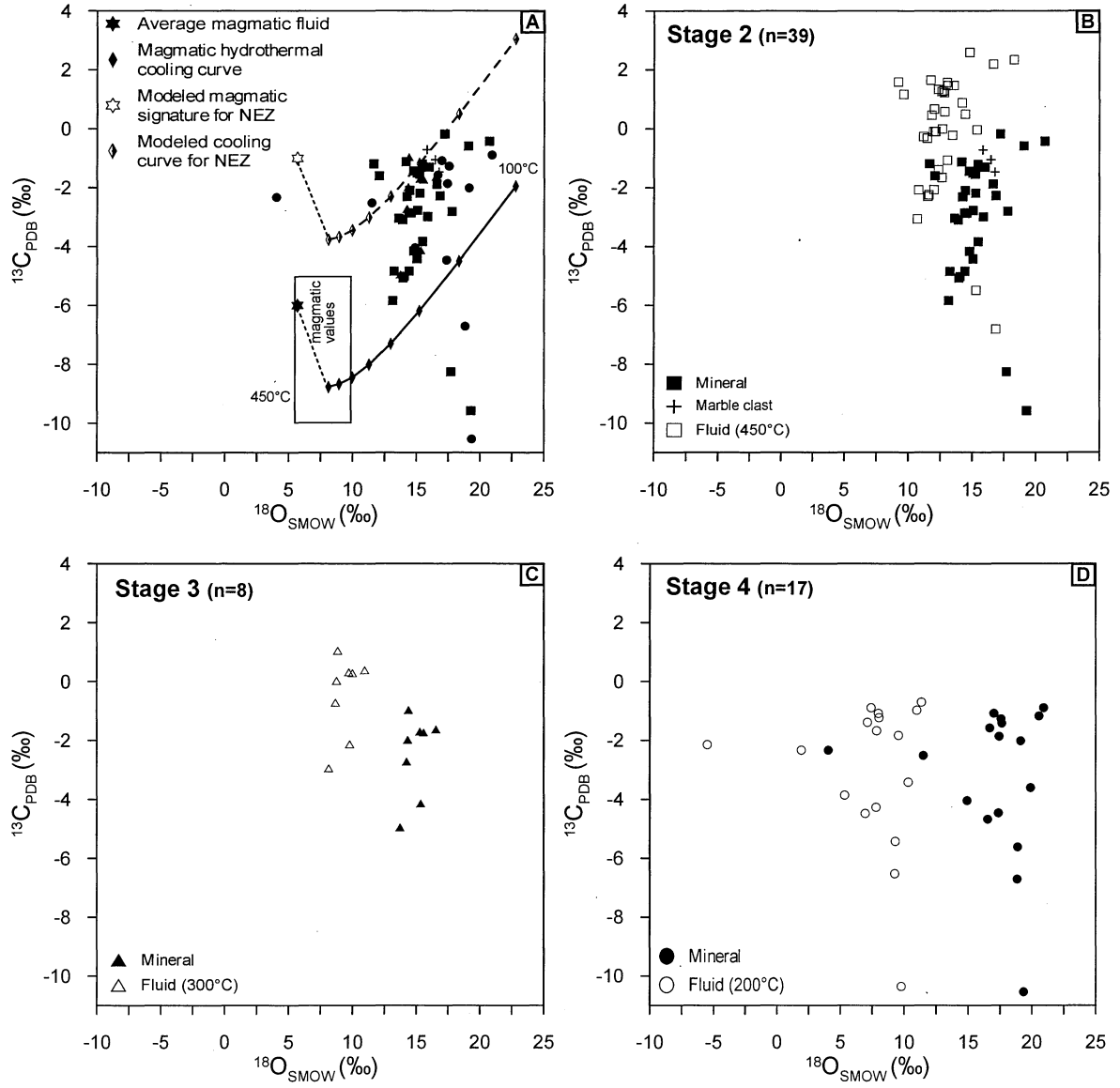

Figure 5.11 Plots of $\delta^{13}C_{PDB}$ vs $\delta^{18}O_{SMOW}$ data from the NEZ. **A)** Overall the $\delta^{13}C_{mineral}$ values are enriched and are not consistent with simple precipitation from a typical magmatic fluid (✱) as values would be expected to cluster around the magmatic equilibrium fractionation cooling curve (solid black line in A). The range of magmatic values determined from the isotopic study of carbonatites, kimberlites, diamonds and primary magmatic water are outlined in the elongate thin black line box ($\delta^{18}O$ +5.5 to +10 ‰, $\delta^{13}C$ -5 to -10 ‰; Ohmoto, 1986, Taylor, 1974, Taylor, 1997). Simple fractionation modeling of $\delta^{13}C$ presents a "what-if" scenario to approximate a $\delta^{13}C$ isotopic value of the magmatic fluid (✡) responsible for the values observed in the data set, assuming C-source has the dominant vertical shift effect on fluid values. The $\delta^{13}C$ value was increased by +5 per mil to capture most of the data (black dashed line in A). **B)** Stage 2 mineral and fluid values (450°C). Correction to this higher temperature shifts values to more enriched $\delta^{13}C$ with little effect on $\delta^{18}O$. **C)** Stage 3 mineral and fluids values (300°C). Temperature corrections shifts values to more enriched $\delta^{13}C$ and more depleted $\delta^{18}O$. **D)** Stage 4 mineral and fluid values (200°C). This stage shows the largest range of values. Temperature correction shifts values to more depleted $\delta^{18}O$ with a limited effect on $\delta^{13}C$. The majority of stage 2 and 3 carbonate samples are intergrown with chalcopyrite and/or bornite. The effect of different temperatures on fluid values is illustrated in Figure 5.10. Temperature corrections have been made using the calcite-H_2O equilibrium equation from Friedman and O'Neil (1977; after O'Neil et al., 1969) for $\delta^{18}O$ and calcite-CO_2 from Ohmoto and Rye (1979; after Bottinga, 1969) for $\delta^{13}C$.

heating (Holland and Malinin, 1979; Reed and Spycher, 1985; Zheng and Hoefs, 1993).

Boiling is known to drive C- and O-isotopes towards heavier values (Zheng, 1990), consistent with the Mt. Polley C- and O-isotope data set. Boiling may therefore have caused carbonate precipitation process in the NEZ. Bladed carbonates are considered to be a favorable indicator of boiling in epithermal systems, based on observations of their occurrences from boiling zones in modern geothermal systems (Simmons and Christenson, 1994). Bladed calcite occurs in stage 5 veins from the NEZ, providing empirical evidence for post-brecciation boiling at Mt. Polley. The presence of bladed stage 2 anhydrite crystals may be evidence for boiling during main-stage mineralization. Bladed anhydrite has been documented from young porphyry-related epithermal deposits where boiling is known to have occurred (e.g., Acupan, Philippines–Cooke and Bloom, 1990; Cooke and McPhail, 2001; Lihir, PNG–Carman, 1994, 2003), and bladed barite is common in some boiling epithermal systems (e.g., Emperor, Fiji–Begg et al., 1997), adding support to this hypothesis.

Under oxidizing (carbonate-stable) conditions, the fractionation of ^{13}C is redox-independent but strongly pH-dependent. Specifically, it is controlled by isotopic exchange between aqueous carbonate species (i.e., H_2CO_3, HCO_3^- (Ohmoto, 1972). The paucity of clay minerals (e.g., illite, kaolinite, pyrophyllite) and the abundance of secondary garnet, K-feldspar, pyroxene, actinolite and calcite in the NEZ imply that pH conditions in the NEZ were near-neutral to alkaline. Chemical reactions involving the aqueous carbonate system (H_2CO_3, HCO_3^-, CO_3^{2-}) may therefore have strongly affected the ^{13}C compositions of carbonates in the NEZ.

Enriched $\delta^{18}O_{fluid}$ values calculated for calcite from stages 2 and 3 discount the possibility of mixing with meteoric water or seawater as important mechanisms for calcite precipitation, because meteoric water typically has negative $\delta^{18}O$ values and seawater has a value of 0 per mil (Campbell and Larson, 1998). Mixing with either water type would therefore cause ^{18}O depletion. The $\delta^{18}O$ data from stage 4 calcite is, however, permissive of a component of mixing with an ^{18}O-depleted fluid such as meteoric water or seawater (Fig. 5.10). Bailey (2004a) proposed that abundant albite alteration in and around Mt. Polley could have been produced by seawater penetrating into the magmatic complex. While seawater involvement cannot be ruled out for stage 4, the C-, O- and S-isotopic data from stages 2 and 3 do not provide any support for Bailey's (2004a) hypothesis.

Very few processes can enrich $\delta^{18}O_{calcite}$ values as observed in the NEZ other than by Rayleigh fractionation during open system degassing or limestone–fluid interaction. Rayleigh fractionation during open system degassing could occur in a system where CO_2 concentrations exceed H_2O. Under such conditions, significant ^{16}O–^{18}O fractionation may occur between H_2O and CO_2, with ^{18}O preferentially incorporated into CO_2 (Richet et al., 1977; Reed, 1997). There is little or no evidence for carbonic fluids in the NEZ other than the weak, pervasive carbonate alteration. In contrast, there is abundant evidence for hydrous fluid involvement throughout the NEZ paragenesis, with secondary hydrous minerals abundant in the veins, altered rocks and breccias. Water-rock interaction therefore remains as the most likely process to account for the measured $\delta^{18}O_{calcite}$ values in the NEZ.

5.4.5 Carbon-oxygen isotopic modeling

Because water-rock interaction can strongly influence the isotopic compositions of secondary carbonate minerals (Sverjensky, 1981; Shelton, 1983; Kitto, 1994), the effects of water-rock interaction have been modelled to test whether it can explain the array of C- and O-isotopic data obtained from the NEZ, using the techniques of Sverjensky (1981) and Shelton (1983). Provided that two isotopic end-member compositions can be identified, mixing lines can be plotted on a $\delta^{18}O$ vs $\delta^{13}C$ plot. The shapes of the mixing lines will vary both as a function of temperature and the mole fraction of H_2CO_3 in the fluid (e.g., Fig. 5.12), and can be used to interpret the extent of mixing in a closed or open system, the temperature of isotopic exchange, and the CO_2 concentration of the mineralizing fluid (Sverjensky, 1981; Shelton, 1983; Kitto, 1994).

Two end-member components have been used here to model water-rock interaction: a magmatic-hydrothermal fluid with an assumed composition of $\delta^{13}C_{fluid} = -6$ per mil and $\delta^{18}O_{fluid} = +5.7$ per mil; and a Late

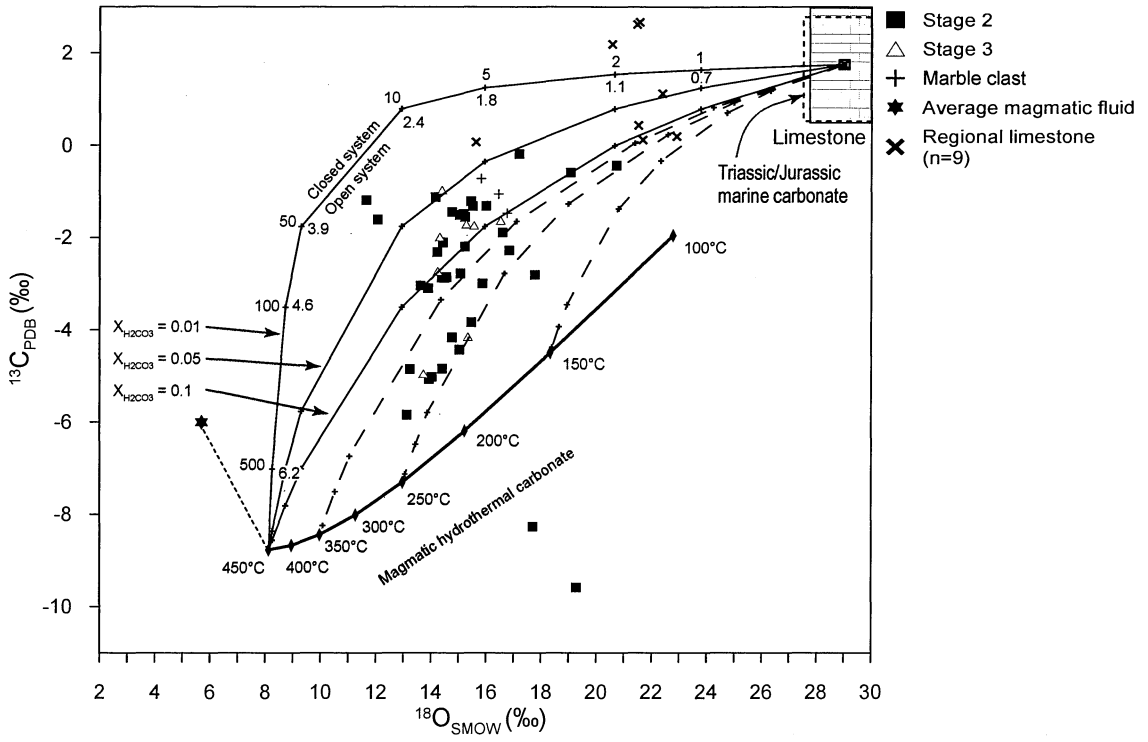

Figure 5.12 Modeling of magmatic fluid and limestone interaction. $\delta^{13}C_{PDB}$ vs $\delta^{18}O_{SMOW}$ plot for NEZ stage 2 and stage 3 carbonates (mineral values). Superimposed on this diagram are an average magmatic fluid ( ), values for regional limestone sampled near Mt. Polley, the carbonate equilibrium cooling curve for magmatic fluid (solid, thick black line), isothermal mixing curves for specified $X_{H_2CO_3}$ (thin, solid black lines) for open and closed systems and mixing curves at $X_{H_2CO_3}$ = 0.1 (dashed, thin black lines) for specified temperatures, based on Shelton (1983) after Sverjensky (1981). Average Late Triassic limestone value (from Viezer et al., 1999) was used as the original starting material as interbedded limestone stratigraphically underlies the host rocks to Mt. Polley. Calculated curves from 450° to 150°C for fluid-rock interaction encompass the field of isotopic data and provide a viable option to explain the shift to lighter $\delta^{13}C$ isotopic values for stages 2 and 3.

Triassic marine carbonate ($\delta^{13}C$ +1.8 ‰ and $\delta^{18}O$ +29.0 ‰; Veizer et al., 1999; Fig. 5.12). The Triassic carbonate has been used as a proxy for unaltered limestone, which could not be obtained from the Mt. Polley Complex. H_2CO_3 is assumed to have been the dominant C-bearing species, and $\delta^{13}C_{H2CO3} \approx \delta^{13}C_{CO2} \approx \delta^{13}C_{fluid}$ (e.g., Ohmoto, 1986). Calculations were completed for magmatic fluid with H_2CO_3 mole fractions (X) from 0.1 to 0.01 molal (as in Kitto, 1994) using the equations of Shelton (1983; after Sverjensky, 1981), and $\Delta^{13}C_{calcite\text{-}CO2}$ and $\Delta^{18}O_{calcite\text{-}H_2O}$ values were calculated at the temperatures shown in Figure 5.12.

Three mixing lines were calculated that illustrate the isotopic compositions of carbonate produced by interaction of magmatic-hydrothermal fluid with marine carbonate under conditions of increasing $X_{H_2CO_3}$ (0.01, 0.05 and 0.1) at 450°C (Figure 5.12). Another three mixing lines at constant $X_{H_2CO_3}$ (=0.1) model decreasing temperatures effects (350°C, 250°C and 100°C).

Figure 5.12 shows how varying $X_{H_2CO_3}$ during water-rock interaction at a constant temperature primarily causes an increase in $\delta^{13}C_{calcite}$ values relative to the hydrothermal fluid, whereas decreasing temperature causes $\delta^{18}O_{calcite}$ values to increase markedly relative to $\delta^{13}C_{calcite}$. Hydrothermal carbonates that precipitated directly from the magmatic fluid at a range of temperatures without significant isotopic (and in this case water-rock) interaction would plot on the magmatic hydrothermal carbonate cooling curve (Fig. 5.12).

The modeling results show that fluid-rock (or melt-rock) interaction between magmatic-hydrothermal fluids and limestone could explain the elevated $\delta^{13}C$ values of carbonate gangue from the NEZ if enough limestone was available. A decrease in temperature could explain the eleavated $\delta^{18}O_{calcite}$. The array of isotopic data for stage 2 and 3 carbonate samples plots between the

end-member fluid and rock compositions (Fig. 5.12). The regional limestone samples from the Mt. Polley area are depleted in ^{18}O relative to average Triassic limestone, possibly due to low temperature alteration (Fig. 5.12).

The amount of limestone that the Mt. Polley magmas and/or mineralizing fluids may have interacted with is unknown, and therefore a mass balance calculation has not been done. Intervals of limestone have been observed as xenoliths in the Mt. Polley Complex (Rees et al., 2005), however, only three spatially restricted exposures of limestone are known to occur close to the NEZ, in addition to the marble clast. The limestone xenoliths are believed to be equivalent in stratigraphic age and position to the Norian regional limestone units of the Nicola Group (LS–Likely and LS–Morehead; Fig. 2.3; C. Rees, pers. comm.).

5.4.6 Lead-isotopic compositions

The Pb-isotopic compositions of stage 2 pyrite and chalcopyrite are similar to stage 3 galena (Fig. 5.7). Stage 2 and 4 anhydrite samples are more radiogenic than the stage 2 and 3 sulfides (Fig. 5.7). The heterogeneous data set implies that either i) the Pb-isotopic composition of the mineralizing fluids changed with time, or ii) that there was more than one source of Pb. The NEZ samples plot above the mantle growth curve of Zartman and Doe (1981) and below the bulk Earth growth curve of Stacey and Kramer (1975) or orogene growth curve of Zartman and Doe (1981) on Figure 5.7. This implies that Pb in the NEZ was derived from a mixture of mantle and crustal sources. The large marble clast from the NEZ breccia has low U/Pb and Th/Pb, and similar initial Pb ratios to the stage 2 and 3 sulfide signature. If this clast was originally Triassic limestone, then it has been isotopically reset by the hydrothermal system.

Figure 5.7C compares NEZ Pb-isotopic data with data from other alkalic deposits from the Quesnellia terrane: Lorraine (180.3 ± 3 Ma; Bath, 2007) and Copper Mountain (204 ± 6 Ma to 200.3 ± 2.1 Ma, Fig. 1.4; Mortensen et al., 1995). The NEZ data overlap with Copper Mountain, suggesting similar Pb sources and/or processes. The Lorraine data are notably more radiogenic than Mt. Polley and Copper Mountain. This may relate at least in part to Lorraine forming ~20 Ma after Mt. Polley, when tectonic amalgamation of the Quesnellia Arc to the North American craton occurred (Nokleberg et al., 2000), possibly allowing for more crustal Pb input into that system.

The clustering of the British Columbia alkalic deposits isotopic Pb data around 0 Ma (Fig. 5.7), instead of the age of formation (~205 Ma; Mortensen et al., 1995; Logan et al., 2007) indicates that the Pb was extracted from a high U-reservoir at some point in its evolution, compared to the orogene or bulk Earth models of Zartman and Doe (1981) or Stacey and Kramers (1975), respectively. Comparing this data set to that of the modern geologic environments of Zartman and Doe (1981), the NEZ data plot within the mature arc field. This Pb-isotopic composition is typical of arcs built on continental-derived crust or subduction of pelitic sediments and assimilation into slab melts (Zartman and Doe, 1981).

The stage 5 carbonate vein plots to the right of the stage 2 and 3 sulfides, and lies on a normal, time-integrated growth curve (Fig. 5.7), implying that the stage 5 veins are up to ~100 million years younger than stage 2 and 3 sulfides (R. Tosdal; pers. comm., 2009; Appendix D1). The bladed textures and presence of chalcedony in the stage 5 vein are consistent with epithermal conditions. The combination of epithermal textures, minerals and significantly evolved Pb isotopic compositions implies that telescoping of an epithermal environment into the NEZ occurred ~100 m.y. after breccia formation. Fraser (1994) noted that a thermal event in the Cretaceous appears to have reset some thermally-sensitive geochronologic data, providing support for a late hydrothermal event at Mt. Polley.

5.4.7 Strontium- and neodymium-isotopic compositions

Strontium- and Nd-isotopes can help to provide insights into the source(s) of alkali elements (i.e. calcium, barium, sodium and potassium) and rare earth elements, which can be important elements in ore fluids (Richards and Noble, 1998). The NEZ gangue minerals have low initial Sr ratios, consistent with a predominance of mantle-derived Sr and by inference, calcium (e.g., Kelser et al., 1975; Sillitoe, 1987; Fig. 5.8). All of the initial Sr ratios for the NEZ gangue minerals are higher than the average value estimated for the Quesnellia and Stikinia

terranes (Lang et al., 1995a) and lower than gangue minerals from Lorraine and Mt Milligan (Jago, 2008; Bath, 2010; Fig. 5.8) and from the alkalic porphyry deposits of New South Wales (Cooke et al., 2007). This implies that the NEZ gangue minerals contain a predominance of mantle-derived Sr, with a minor component of crustal contamination. The amount of crustal contamination was less than for the other alkalic porphyry deposits shown on Fig. 5.8.

Initial Sr ratios for the NEZ gangue minerals are mostly well constrained between 0.70331 and 70353. One sample of stage 2 garnet and a stage 3 anhydrite sample have slightly higher initial Sr ratios, possibly indicating a greater component of crustally-derived Sr (Fig. 5.8, Appendix D2). The marble clast from the NEZ breccia has comparable initial Sr ratios to the NEZ gangue, implying isotopic resetting of the limestone protolith. The regional limestone samples contain more radiogenic Sr than the NEZ gangue minerals, but one sample has a low initial Sr ratio (<0.7065) compared to Phanerozoic marine limestones (~0.7067 to 0.709; Veizer et al., 1999), implying that it has been altered.

The proportions of mantle-derived and crustally-derived Sr have been estimated for the NEZ gangue minerals (Appendix D2). The initial Sr ratio estimated for the Quesnellia and Stikinia terranes (0.7033; Lang et al., 1995a) is assumed to be the most primitive composition possible for Mt. Polley (i.e. 100% magmatic). Seawater, either at the time of mineralization (~205 Ma, Mortensen et al., 1995; Logan et al., 2007; initial strontium = 0.70775, Veizer et al., 1999), or during the initiation of the Quesnellia arc (320-285 Ma, Nokleberg et al., 2000; Nokleberg et al., 2005; initial strontium = 0.70824, Veizer et al., 1999) can be taken as the crustal end member (i.e. 100% seawater-derived Sr). The hydrothermal mineral compositions from the NEZ fall between these end-members, and can give an indication as to the amount of crustal interaction by the fluids. The calculations show that magmatically derived Sr in the NEZ minerals comprised between 99.9 percent (pyrite) and 89.4 percent (anhydrite) of the total Sr (Appendix D2). Overall, the NEZ minerals show a strong mantle-derived initial Sr signature, with evidence for a limited contribution of crustal Sr. This is consistent with the O- and C-isotope data that suggest fluids interacted with a heavy C (and possibly O) source. This is also supported by a study of alkalic plutons in the Quesnellia and Stikinia terranes (Averill, Mt. Polley, Whiterocks Mountain, Zippa Mountain), in which low initial Sr values (<0.704) were found and U–Pb ages on xenocrystic zircons indicate a minor older crustal component must have been contributed to some of these plutons (Cassidy et al., 1995). It remains a conundrum that there is currently little Sr isotope evidence for a large scale interaction with limestone yet the modelling of the C- and O-isotope data suggest water-rock ratios of 2 to 4 with a source enriched in Sr and depleted in $\delta^{13}C$ relative to the igneous rocks. Field data is required to resolve this but the hypothesized limestone and precursor igneous rocks are currently not exposed at Mt. Polley. Melt inclusion studies may provide useful information in future studies of this problem.

Figure 5.9 compares the initial ratios of $^{143}Nd/^{144}Nd$, expressed as ε_{Nd}, and initial Sr ratios, for Mt. Polley apatite to selected modern oceanic magmatic provinces, and to Triassic–Jurassic alkalic systems from British Columbia. On this diagram, crustal rocks will have negative ε_{Nd} values while mantle-derived rocks will have positive ε_{Nd} values (Arculus and Powell, 1986; Rollinson, 1993). Apatite from the NEZ has ε_{Nd} values consistent with a depleted mantle source, as do the other rocks from British Columbia, and the apatite and diopside from Lorraine (Bath, 2010). It is important to note that of the radiogenic isotopes, Nd is the least sensitive to crustal contamination and small amounts of recycled crust mixed with large amounts of mantle component become isotopically invisible (Taylor et al., 1980; Rollinson, 1993), and so this diagram cannot be used to identify small degrees of crustal contamination.

5.4.8 Implications for generation of silica-undersaturated magmas

Silica-undersaturated alkalic igneous rocks are among the least understood igneous associations (Coulson et al., 1999) and several mechanisms have been proposed for their formation. Mixing between different primary magmas with similar potassium compositions, produced from a heterogeneous mantle source, created highly variable primary melts during a single, volumetrically small eruption in a study of scoria from the Roman Comagmatic Province (Italy;

Kamenetsky et al., 1995). Melt inclusion compositions in the scoria were K-enriched and silica-depleted with 2–5 weight percent K_2O, 0.9–1.5 weight percent Na_2O and 45–50 weight percent SiO_2 (Kamenetsky et al., 1995). Partial melting of moderately alkali-rich quartz eclogite to produce monzonites characterized by high Na_2O + K_2O (near 10 wt% total) with moderate SiO_2 contents of (53 to 63 wt%) was proposed by Miller (1978). Miller's (1978) study focused on alkali-rich monzonitic plutons in California, USA, which form part of the alkalic belt that stretches from British Columbia to southern California. Most monzonitic rocks from his study were slightly saturated in silica, but one pluton included both silica-undersaturated and silica-saturated units, similar to the Mt. Polley Complex.

Limestone assimilation has been shown experimentally to affect the petrologic evolution of basaltic magmas to produce silica-undersaturated rocks (Iacano-Marziano and Gaillard, 2006; Iacono-Marziano et al., 2007, 2008; Iacono-Marziano et al., 2009). Experimental studies used natural hydrated basalts from Stromboli volcano and were compared with natural samples from Alban Hills, Italy, a site of extensive undersaturated intrusions. Results showed that calcite and dolomite addition to a basaltic magma promoted the crystallization of Ca-rich clinopyroxene at the expense of other magmatic phases (e.g. olivine and plagioclase). As a consequence of massive clinopyroxene crystallization, the residual melt became strongly silica-depleted and nepheline normative.

The Late Triassic, silica-undersaturated Zippa Mountain pluton (Lueck and Russell, 1994; Fig. 1.14) in the Stikinia terrane of British Columbia exhibits evidence for carbonate assimilation (Coulson et al., 1999; Coulson et al., 2007). Zippa Mountain also shows the most complete range of features characteristic of the silica-undersaturated alkalic igneous complexes in British Columbia (Lang et al., 1995a; Coulson et al., 1999). Zippa Mountain is zoned from clinopyroxenite at its margins to a core of megacrystic K-feldspar-syenite. Zippa Mountain rocks contain 45 to 60 weight percent SiO_2, and are subalkalic to strongly alkalic (Coulson et al., 1999). The pluton intruded metamorphosed Palaeozoic carbonate units. The accessory calcite that is present in the syenite may be a primary feature, but Coulson et al. (1999) argued that evidence exists within the pluton that the calcite could have resulted from the assimilation of the country rock (i.e. observation of marble xenoliths with reaction rims). These authors concluded that generation of peralkaline syenitic rocks of Zippa Mountain required interaction with carbonate country-rock, in addition to fractional crystallization and crystal sorting. Furthermore, the interaction between magma and carbonate forced a larger than typical magmatic zonation, from alkalic and silica-undersaturated syenitic magmas to peralkaline compositions (Coulson et al., 1999). The processes inferred for Zippa Mountain may also have occurred in the magma chamber that sourced the Mt. Polley Complex and Bootjack Stock. If this hypothesis is correct, then Zippa Mountain exhibits the characteristics of a magma chamber that has undergone carbonate assimilation, and Mt. Polley represents the higher-level intrusions, breccias and mineralization that could emanate from that type of a modified, silica-undersaturated magma chamber.

Carbonate assimilation by a shallow magma chamber or a CO_2-enriched melt from subducted carbonate could explain the enriched $\delta^{13}C$ isotopic values observed in the NEZ. Increasing the CO_2 content of the melt by carbonate assimilation could have been the trigger for widespread magmatic-hydrothermal brecciation and, in combination with crystal fractionation, could also account for the silica-undersaturated nature of the Mt. Polley intrusive rocks. Decarbonation is known to produce significant shifts in $\delta^{13}C$ (Brown et al., 1985). The enriched $\delta^{13}C_{fluid}$ values calculated from this study (-4 to +2.5 ‰) are similar to $\delta^{13}C$ values of gases emitted from vents in the Alban Hills volcanic region (-3.5 to +0.9 ‰; Chiodini and Frondini, 2001) and Mount Vesuvius (+0.06 to +0.34 ‰; Chiodini et al., 2001; Fig. 4.10), both located in Italy. Isotopic analyses of the very high volumes of CO_2 emitted from the Alban Hills and Mount Vesuvius provide evidence for a predominance of CO_2 derived from decarbonation of sedimentary carbonate beneath these volcanic regions (Chiodini and Frondini, 2001; Iacono-Marziano et al., 2008; Iacono-Marziano et al., 2009). Carbon- and O-isotope values of primary calcite from the monzonitic silica-saturated to syenitic silica-undersaturated Hortavaer igneous complex in Norway

are also similar to this study ($\delta^{13}C$: -3.97 to +2.94 ‰; and $\delta^{18}O$: +11.51 to +21.15 ‰; Barnes et al., 2005; Fig. 4.10). Based on mineralogical, isotopic and igneous composition data, Barnes et al. (2005) argued for a carbonate assimilation model at Hortavaer. Although the effects of country rock assimilation are typically most obvious along the margins of intrusions, the work of Iacono-Marziano et al. (2007 and 2008) has shown that as little as 2–3 weight percent carbonate assimilation can affect the magmatic system dramatically.

Magmatic carbonate assimilation liberates large quantities of CO_2, which could potentially cause magmatic-hydrothermal brecciation. Mafic to intermediate magmas that are associated with extensive hydrothermal activity, including magmatic-hydrothermal breccia formation, typically contain between 2 and 4 weight percent water (Burnham, 1985; Burnham, 1997). These magmas also have low CO_2 solubilities (0.075 to 0.25 wt% at 100 MPa to 300 MPa, up to 0.4 wt% at crustal pressures; Kamenetsky et al., 2007; Ganino et al., 2008; Iacono-Marziano et al., 2009). Due to its low solubility in the melt, CO_2 partitions strongly into the fluid phase, adding significantly to the CO_2 partial pressure (Iacono-Marziano et al., 2007; Iacono-Marziano et al., 2009). High gas concentrations are not sustainable in the shallow crust, and so the gas will segregate and be expelled from the magma, generating active hydrothermal systems at shallow depths (Burnham, 1985; Iacono-Marziano et al., 2007; Menand and Phillips, 2007). For example, Iacono-Marziano et al. (2008) suggested that 9 weight percent carbonate assimilation would liberate a CO_2-rich fluid (90% CO_2 + 10% H_2O), thereby increasing the volume of the magma by 20 percent (200 MPa, 1150°C). Critical to the carbonate assimilation model of Barnes et al. (2005) for the Hortavaer igneous complex was the requirement of an open-system such that CO_2 could escape after reaching critical saturation, and thus allow carbonate devolatization to occur over an extended period. The repeated brecciation events that occurred in the Mt. Polley Complex could be such an escape mechanism. This open-system behavior would promote Rayleigh isotopic fractionation and could help to explain the enriched $\delta^{18}O_{calcite}$ values from the NEZ.

There will be a depth control on the amount of CO_2 generated by carbonate assimilation, as the solubility of CO_2 in melts and water is directly proportional to confining pressures and temperatures (Holland and Malinin, 1979). Adding CO_2 to hydrothermal fluids has the potential to promote aqueous phase separation at greater depth and higher temperatures (e.g., Hedenquist and Henley, 1984), which may have also contributed to brecciation in the NEZ.

If carbonate assimilation contributed to silica-undersaturated magmatism and the formation of the magmatic-hydrothermal breccia of the NEZ, then this might be expected to be apparent in the Sr-isotope dataset. But hydrothermal carbonate from the NEZ and the marble clast have low initial Sr ratios (Fig. 5.8). This would seem to preclude the incorporation of crustal Sr in the evolution of Mt. Polley. However, there are examples of crustal contamination that are not reflected in Sr isotope data sets. A study of the late Archean Nuk gneisses by Taylor et al. (1980) revealed two sources of Pb (mantle and old crust); however, the corresponding Sr-isotopic compositions were found to be low, even in the most crustally contaminated rocks. Taylor et al. (1980) concluded that this indicates that Pb contamination was most likely related to a fluid phase, whereas Sr was of magmatic derivation. In the case of the NEZ, there appears to be evidence for mixing of Pb, C and O sources, but only limited evidence for multiple Sr sources as shown above, similar to the findings of Taylor et al. (1980).

Shifts in the Sr-isotopic signature resulting from different amounts of carbonate assimilation are relatively small for most Italian volcanoes where carbonate assimilation has been inferred to occur (Iacono-Marziano et al., 2008 and references therein). Specifically, the initial Sr ratio has only increased by ~0.00025 during the addition of 8–9 weight percent calcite to the magma. Although it is noted that initial starting compositions for the Italian volcanoes (0.7067) are much higher than those of Mt. Polley (0.7033), the absolute shift in the initial Sr ratios would be similar (Fig. 5.8).

If carbonate assimilation has played a part in the genesis of the Mt. Polley Complex, then this may have implications for parental magma composition(s). While the term "assimilation" has been used to describe the

incorporation of carbonate into a magma, the carbonate is not chemically assimilated (i.e. it does not melt), rather it decomposes via thermal reaction(s) as outlined below.

(1) Limestone: $CaCO_3$ + heat ⇨ $CaO + CO_2$ (Gilchrist, 1989)

(2) Dolomite: $2CaMg(CO_3)_2$ + heat ⇨ $CaCO_3 + 2MgO + CaO + 3CO_2$ (Engler et al., 1988)

Limestone decomposition begins at 750° to ~700°C (Malik et al., 1985; Kantiranis et al., 2005) with a theoretical decomposition temperature of 848°C (Appendix D5; Gilchrist, 1989). Dolomite decomposition initiates at lower temperatures (700° to 550°C; Engler et al., 1988; Gunasekaran and Anbalagan, 2007). Using these values for limestone or dolomite (or a mixed carbonate) decomposition implies that the parental magma must have been intermediate to mafic in composition, based on the solidus and liquidus temperatures of various types of magmas (Appendix D5; Roberston and Wyllie, 1971; Lambert and Wyllie, 1972; Mysen and Boettcher, 1975). However, it is important to realize that during the breakdown of an impure limestone containing SiO_2 or clay minerals, a variety of silicate minerals form at the expense of dolomite or calcite, each involving the release of CO_2 (Ganino et al., 2008). Therefore, complete assimilation of pure carbonate is not the only process that can increase P_{CO2}.

Additional work is required to prove whether carbonate assimilation was a factor in the formation of the Mt. Polley Complex and other silica-undersaturated alkalic porphyry systems. If this model is correct, the obvious exploration implication is that such systems may form in arc terranes built on a carbonate-bearing substrate, or where carbonate platforms are subducted (e.g. Cloos, 1993; McInnes and Cameron, 1994; Gutscher et al., 2000; Shives et al., 2004; Marín-Cerón et al., 2010).

5.5 Summary and conclusions

Stable isotope studies have provided a number of constraints on fluid sources, composition and physiochemical conditions for the NEZ. The wide range of negative $\delta^{34}S_{sulfide}$ values and tight grouping of $\delta^{34}S_{sulfate}$ for the NEZ are consistent with mineral precipitation from an oxidized (sulfate-predominant), high- temperature (>400°C) magmatic-hydrothermal fluid. Based on conservative temperature ranges for porphyry deposits and the measured isotopic compositions of calcite from the NEZ, the estimated ranges of fluid compositions are -6.9 to +2.6 ($\delta^{13}C$) and +9.2 to +19.5 ($\delta^{18}O$) for stage 2, -3.0 to +1.7 ($\delta^{13}C$) and +8.1 to +13.3 ($\delta^{18}O$) for stage 3, and -10.3 to +0.4 ($\delta^{13}C$) and -5.6 to +13.6 ($\delta^{18}O$) for stage 4. These results partially overlap with magmatic $\delta^{18}O_{fluid}$ values, and mostly do not overlap with magmatic $\delta^{13}C_{fluid}$ values, implying that more than one source of C and O were involved in mineralization at Mt. Polley. The heavy $\delta^{18}O$ values suggest a shift caused by sulfate substitution into carbonate or the possibility of $\delta^{18}O$ resetting by a lower temperature overprint. The anomalously high $\delta^{13}C_{calcite}$ values suggest that the mineralizing fluid must have interacted with a ^{13}C-enriched source. The modeling results show that fluid-rock interaction between magmatic-hydrothermal fluids and limestone could explain the elevated $\delta^{13}C$ values of carbonate gangue from the NEZ. However, only limited limestone is known at the site of precipitation. Alternatively, the silica-undersaturated magma compositions, widespread magmatic-hydrothermal brecciation, high $\delta^{13}C$ values and quartz-free hydrothermal infill, may have been caused by carbonate assimilation in the magma chamber that fed the Mt. Polley Complex–Bootjack Stock.

Overall, the NEZ minerals show depleted mantle Sr and Nd signatures, with evidence for a limited contribution of crustal Sr. This is consistent with the O- and C-isotope data that suggest fluids interacted with a heavy C (and possibly O) source. The possibility of Sr leaching prior to magmatic-hydrothermal interaction cannot be ruled out.

Lead in the NEZ was derived from a mixture of mantle and crustal sources. The Pb-isotopic composition of the NEZ is typical of island arcs built on continental-derived crust or subduction of pelitic sediments and assimilation into slab melts (Zartman and Doe, 1981). The modeled Pb age of stage 3 galena (207.8 ± 1.8 Ma) overlaps with the results of previous geochronlogical data that indicate mineralization occurred between 209 and 204 Ma in the Mt. Polley Complex (Bailey and

Archibald, 1990; Mortensen et al., 1995; Logan et al., 2007). Limited isotopic Pb data from a bladed carbonate and chalcedony vein indicates that telescoping of an epithermal environment occurred in a younger event approximately 100 m.y. after porphyry formation.

Redox and pH changes and water-rock interaction are concluded to have been important processes of ore formation and hydrothermal alteration in the NEZ. High-grade Cu–Au–Ag mineralization in the NEZ is associated with domains of $\delta^{13}C$ and $\delta^{34}S_{sulfide}$ depletion in stage 2 carbonates and sulfides, respectively. Apparent disruptions of the $\delta^{34}S_{sulfide}$, $\delta^{18}O$ and $\delta^{13}C$ zonation patterns (Figs. 5.2, 5.5 and 5.6) suggest that the two largest areas of mineralization in the NEZ may not have been a contiguous body. The presence of widespread hematite-dusted K-feldspar throughout the NEZ, epidote on the deposit periphery, and $\delta^{34}S_{sulfide}$ zonation patterns support a model of inorganic sulfate reduction, in addition to cooling, to promote Cu-sulfide precipitation at temperatures between ~480° and 250°C.

Several processes may have contributed to the precipitation of calcite throughout the formation of the NEZ, including boiling, CO_2 degassing, pH increase, and water-rock interaction. All of these mechanisms are consistent with the Mt. Polley dataset and therefore are likely to have operated at specific times during the hydrothermal evolution of the NEZ. Enriched $\delta^{18}O_{fluid}$ values calculated for calcite from stages 2 and 3 discount the possibility of mixing with meteoric water or seawater as important mechanisms for calcite precipitation. However, the $\delta^{18}O$ data from stage 4 calcite is permissive of a component of mixing with an ^{18}O-depleted fluid such as meteoric water or seawater.

Chapter 6

Hydrothermal Geochemistry: Sulfide Mineral Chemistry

6.1 Introduction

This chapter documents the results of laser-ablation inductively coupled plasma mass-spectrometry (LA-ICP-MS), a micro-analytical technique that can be used to establish in-situ sulfide mineral compositions. These data are used to provide insights into the evolution of hydrothermal fluids and depositional processes associated with the NEZ. The objective of this work has been to characterize variations in the trace element compositions of pyrite, chalcopyrite and bornite at Mt. Polley. A secondary objective was to evaluate whether systematic changes in the trace element geochemistry of sulfide minerals occurred outboard of the NEZ and in turn, whether this could be used as an exploration vector. Limited sample availability from locations distal to ore (Fig. 6.1) have restricted the outcome of the secondary objective. Preliminary results of this study were reported in Pass et al. (2009).

6.2 Previous work

Only limited research has previously been conducted that characterized the major and trace element compositions of sulfides at Mt. Polley. Ross (2004) used scanning electron microscopy to identify abundant minute inclusions (up to ~10 μm, but usually <5 μm) of two types of galena in five chalcopyrite and bornite samples. Ross (2004) found that a Pb-S-Se phase was more abundant as inclusions than the Pb-S-Se-Ag phase in the Cu-Fe sulfides. She also identified pure galena (no Se-peak), an Ag-S-Se mineral and an Ag-bearing selenium-telluride mineral as inclusions in and/or attached to Cu sulfides. Despite the NEZ Au endowment, no Au peaks (or visible Au) were identified in Ross' (2004) study.

Whole rock Cu:Au ratios from the Central and West Zones of Mt. Polley (Figs. 2.6 and 2.8) were investigated by Fraser (1994). Copper and Au assay values were found to be closely correlated, but visible Au was never observed in hand specimen. Native Au was noted in the form of 5–40 μm inclusions in chalcopyrite. The Au was interpreted to have been introduced during calc-silicate alteration in the core of the deposit, and constant Cu:Au ratios suggested that chalcopyrite and Au probably co-precipitated from the same fluid (Fraser, 1994). The Central and West Zones were found to contain only trace amounts of bornite and pyrite was found to have an antithetic spatial relationship with copper and Au.

Platinum group elements were identified from Mt. Polley drill core samples by Thompson et al. (2001; Appendix E1). These include two samples of chalcopyrite-pyrite and one sample of chalcopyrite-pyrite-bornite collected from the Cariboo-Bell and Springer pits (Fig. 2.6A) that were crushed and analyzed for heavy mineral concentrates. The host mineralogy and substitution behavior of the PGEs was not investigated.

6.3 Methods

Twenty-one breccia samples containing stage 2 sulfide cement were selected from the NEZ long-section for in-situ LA-ICPMS analysis at the University of Tasmania (Fig. 6.1). Where possible, samples were

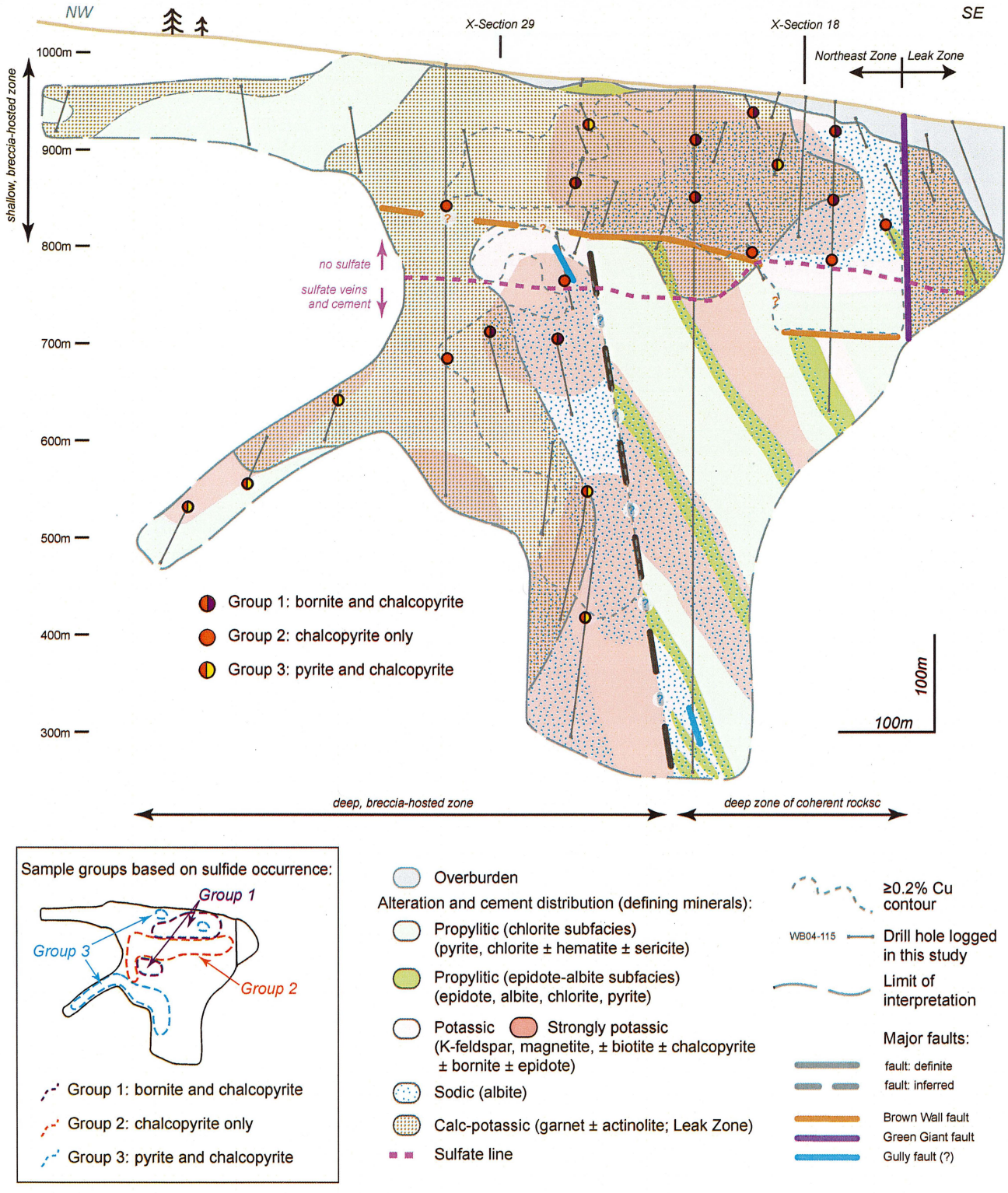

Figure 6.1 Sample locations of stage 2 sulfide breccia cement used for LA-ICP-MS trace element analyses (n = 21). Sample locations are overlain onto the alteration and cement distribution from the long-section. Also shown are the ≥0.2% Cu ore shells. Inset shows the location of sample groups. Samples were assigned to one of three groups based on sulfide occurrence: group 1-bornite and chalcopyrite both present; group 2-chalcopyrite only; and group 3-pyrite and chalcopyrite present.

selected that contained several sulfides, in order to maximize the number of individual sulfide minerals analyzed per sample. In total, 8 bornite, 21 chalcopyrite and 6 pyrite grains were analyzed (Table 6.1). A 213 nm New Wave UP213 solid state Nd-YAG laser microprobe coupled with an Agilent 4500 quadrupole mass spectrometer was used to ablate polished 2.5 cm diameter circular resin mounts made from each of the 21 samples selected. Mounts were cleaned in an ultrasonic bath of distilled water followed by an ultrasonic bath in acetone, for 5 minutes each prior to analyses. The following methodology is modified from the detailed descriptions in Large et al. (2007), Large et al. (2009), Danyushevsky et al. (2003) and Danyushevsky et al. (in press).

Table 6.1 Sulfide sample list with analytical methods per sample. All samples contain stage 2 sulfide breccia cement.

DDH	Depth (m)	Mineral[1]	Analyses				Group[2]
			Microprobe	LA-ICP-MS line analyses	LA-ICP-MS spot analyses	LA-ICP-MS map	
WB03-03	120.7	cp, bn	cp, bn	cp: line x 5 bn: line x 5	bn: spot x 5 (rim & core) cp: spot x 3 (rim & core)	map (bn + cp)	1
WB03-11	83.5	cp	-	cp: line x 5	py: spot x 4	-	3
WB04-25	37.0	cp, bn	-	cp: line x 5 bn: line x 5	-	-	1
WB04-40	68.1	cp, py	cp, py	cp: line x 5 py: line x 4	cp: spot x 4 py: spot x 3 (rim & core)	-	3
WB04-47	284.5	cp	-	cp: line x 5	-	-	2
WB04-88	203.3	cp	-	cp: line x 5	-	-	2
WB04-95	35.9	cp, bn	cp, bn	cp: line x 5 bn: line x 5	bn: spot x 5 (rim & core) cp: spot x 5 (rim & core)	-	1
WB04-95	107.1	cp, bn	-	cp: line x 5 bn: line x 5	-	-	1
WB04-95	168.6	cp	cp	cp: line x 5	cp: spot x 3 (rim & core)	-	2
WB04-108	148.8	cp	-	cp: line x 5	-	-	2
WB04-108	304.0	cp	-	cp: line x 5	-	-	2
WB04-111	224.5	cp, py	cp,	cp: line x 5	cp: spot x 5 (rim & core)	-	2
WB04-122	311.5	bn, cp	cp, bn	cp: line x 5 bn: line x 5	bn: spot 5 (rim & core) cp: spot 5 (rim & core)	-	1
WB04-131	376.2	cp, py	-	cp: line x 5 py: line x 5	-	-	3
WB04-150	485.8	cp, py	-	cp: line x 6 py: line x 3	py: spot 4 (rim & core)	-	3
WB04-152	515.1	cp, py	-	cp: line x 5 py: line x 3	-	-	3
WB04-188	59.5	cp, bn	cp, bn	cp: line x 5 bn: line x 5	bn: spot 5 (rim & core) cp: spot 5 (rim & core)	-	1
WB04-188	118.2	bn, cp	cp, bn	cp: line x 5 bn: line x 5	bn: spot 5 (rim & core) cp: spot 5 (rim & core)	-	1
WB04-192	312.0	bn, cp	-	cp: line x 5 bn: line x 5	-	-	1
WB04-210	424.3	cp, py	cp, py	cp: line x 5 py: line x 5	cp: spot 5 (rim & core) py: spot 5 (rim & core)	map (cp + py)	3
WB04-213	563.8	cp, py	cp, py	cp: line x 5 py: line x 5	cp: spot 5 (rim & core) py: spot 5 (rim & core)	map (py)	3

[1] cp-chalcopyrite, bn-bornite, py-pyrite

[2] Group 1 samples contain bornite and chalcopyrite; group 2 chalcopyrite only; group 3 pyrite and chalcopyrite

Analyses were performed in spot (n = 118) and line (n = 170) modes. Most spot analyses were carried out using a laser beam of 40 μm, a repetition rate of 5 Hz and laser energy ~6 J/cm^2. Some analyses of fine-grained material were carried out using a laser beam of 30 μm. Spot analysis time was 90 seconds, including a 30 second pre-ablation background measurement. Line analyses were carried out using a 25 μm laser beam to obtain good resolution. Line mode pre-ablation was conducted at 25 μm/s, 5 Hz repetition rate, with analyses conducted at 3 μm/s and 10 Hz repetition. Data were collected in time-resolved mode.

All analyses were quantified using a STDGL2b2 primary standard (Danyushevsky et al., 2003; Danyushevsky et al., in press) run twice every 1.5–2 hours, following the procedure of Longerich et al. (1996). Iron was chosen as the internal standard as it was shown to have stoichiometric concentrations in all three minerals studied (see Section 6.4.2) and it is both homogeneous and abundant in STDGL2b2 (Danyushevsky et al., in press). Results were compiled and concentrations calculated using macros written in-house for Microsoft Excel. The data were plotted as a line graph of counts per second versus time (hereafter referred to as time-resolved element profiles) and the integration times for the background and signal were selected for each analysis (Fig. 6.2A, Appendix E2).

For most elements, 1 sigma standard deviation is <6 percent (but rarely better than 5%; Large et al., 2009), however, Pt and Au are more variable (~15%). Selenium and Tl have a standard deviation of ~10 percent, whereas the standard deviation for and Zn and Cd can be up to 50 percent (Danyushevsky et al., 2003; Danyushevsky et al., in press). Average detection limits for each block of data run between a set of standards are listed in Appendix E3.

A separate batch of analyses was conducted for PGEs on a subset of the samples analyzed for trace element compositions. Ten samples containing bornite, chalcopyrite, and pyrite from the NEZ were analyzed for Ni, Cu^{63}, Cu^{65}, Ru^{99}, Ru^{101}, Rh, Pd^{105}, Pd^{106}, Cd, W, Re, Os, Ir, Pt and Au. This limited set of elements was selected in order to minimize PGE detection limits. The spot analysis method was modified as follows for these analyses. In addition to the STDGL2b2 primary standard, the primary standard PGENi5 (Wolhlgemuth-Ueberwasser et al., 2007) and pure copper metal were run twice every 1.5 hours. Pure Cu metal was analyzed to correct for argide interferences ($Cu^{65}Ar^{40}$; $Cu^{63}Ar^{40}$) on Pd^{105} and Rh^{103}. Palladium (Pd^{106}) was corrected for isobaric interference from Cd^{106}. The laser conditions used to ablate rims and cores of grains were: spot size 110 μm, at 10 Hz, and a laser energy of ~6 J/cm^2.

Two pyrite grains and part of a chalcopyrite-bornite bleb shown to contain Pd and Pt from spot analyses were selected for qualitative element mapping using LA-ICP-MS (Table 6.1) based on the methodology of Large et al. (2009). Parallel lines were ablated across the samples to produce multi-element maps. Lines were pre-ablated prior to data acquisition to reduce surficial contamination. For pyrite mapping, a 25 μm laser beam (10 Hz, ~5 J/cm^2) was rastered across the sample at 25 μm/s in a series of lines at 25 μm spacing. A 15 μm laser beam and spacing was used for mapping of the chalcopyrite and bornite. Every data point recorded in the mass spectrometer forms a separate pixel in the map. The data was smoothed with a 3 point median filter to remove anomalous spikes. The primary sulfide standard(s) were measured before and after each image (Danyushevsky et al., in press) in order to assess drift. Images analyzed over more than 2.5 hours were corrected for drift. A gas background was measured before each image and subtracted from each subsequent line analysis.

Two sets of images were collected for each sample. The objective of the first image set was to map Pd concentrations. Due to the overall low PGE abundances, coupled with the technique detection limits, only Pd of the PGEs was found in high enough concentrations to map. Detection limits for Pd maps are estimated to have been 0.400 ppm compared to <0.05 ppm for spot analysis). Laser mounts were then re-polished and a second set of maps was produced, showing a total of 25 major and trace elements. A neighboring location to the Pd-bearing chalcopyrite spot analyses in sample WB03-03 120.7 m, which included bornite and chalcopyrite, was mapped for the second image set in order to optimize the analyses of these two minerals.

To determine whether any of the major elements in each of pyrite, chalcopyrite and bornite occurred

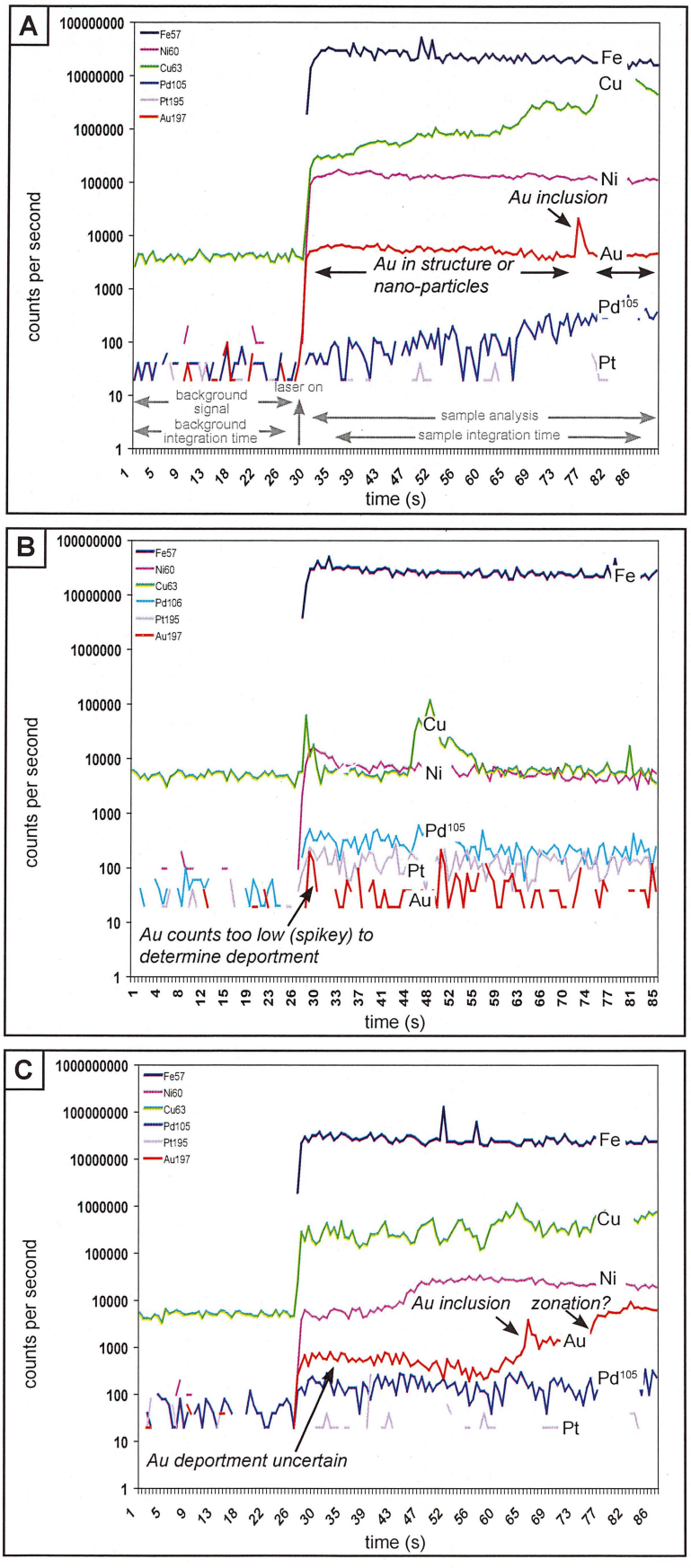

Figure 6.2 LA-ICP-MS time-resolved element profiles of pyrite spot analyses showing selected element patterns. Comparing the Au patterns in A), B) and C) illustrates the challenges in interpreting whether Au occurs in the pyrite structure or as homogeneously disseminated nano-particles. Interpretation of micro- to meso-scale inclusions can be done with confidence when concentrations are well above background. Gold (2.88 ppm) in **A)** has been interpreted as occurring both within the structure or as homogeneously distributed nano-particles (flat red line above 1000 counts per second) and as a micro-inclusion. Gold was reported as 0.02 ppm in **B)**, but the counts per second are too low to intepret gold deportment. The element profile in **C)** (0.86 ppm Au) is similar to that in A, but some uncertainty exists as to the Au deportment, especially where there are <1000 counts per second. Gold may also be zoned in this example. Assessment of more than one analyses per sample is required to make confident deportment interpretations. A) sample WB04-40 68.1 m, data file # MY09A28. B) sample WB05-213 536.9 m, data file # MY09A57. C) sample WB05-210 424.3 m, data file # MY09A53, Table 6.4 and Appendix E1.

in stoichiometric concentrations, electron microprobe analyses were undertaken on a subset of samples selected for LA-ICP-MS analyses (Table 6.1). This was required to facilitate LA-ICP-MS data reduction, which requires that the concentration of an internal standard be known in order to quantify the LA-ICPMS data (Danyushevsky et al., in press). Ten samples (6 bornite grains, 11 chalcopyrite grains, 5 pyrite grains) were analyzed using a Cameca SX100 electron microprobe in the Central Science Laboratory (CSL) at the University of Tasmania. Detection limits and analytical uncertainties are listed in Appendix E4.

In addition to the core samples selected for in-situ LA-ICP-MS study, two samples of Cu-sulfide flotation concentrate were collected for chemical characterization. The Cu-sulfide flotation concentrate samples (~90% derived from the NEZ), were collected from the mill on two separate days (Nov. 18 and 19, 2007). The samples were analyzed by Genalysis Laboratory Services Pty Ltd in Western Australia for 34 major and trace elements including Au, Ag and PGEs, plus loss on ignition (LOI). Platinum group elements and Au were analyzed by fire assay Ni sulfide collection ICP-MS. Silver was analyzed by four-acid digest ICP-MS. A complete list of individual element analytical techniques and detection limits is listed in Appendix E5.

Table 6.2 Summary of the major element compositions of pyrite, chalcopyrite and bornite by electron microprobe analyses. Values in weight percent (wt %). Full data set available in Appendix E4. Percent difference = (maximum result - minimum result) / average result) * 100.

	S	Fe	Cu
Detection limit (average)	0.0738	0.0619	0.0778
Standard deviation (average)	0.525	0.576	0.445
Pyrite			
summary for 5 grains = 11 spots:			
maximum	53.9	47.0	0.0475
minimum	52.8	45.3	0.0015
average	53.6	46.5	0.0253
percent difference (%)	2.0	3.7	182
stoichiometric concentration:	53.5	46.5	n/a
Chalcopyrite			
summary for 11 grains = 45 spots:			
maximum	35.4	30.3	34.5
minimum	34.9	29.6	34.0
average	35.2	29.9	34.2
percent difference (%)	1.4	2.1	1.4
stoichiometric concentration:	34.9	30.5	34.6
Bornite			
summary for 6 grains = 21 spots:			
maximum	26.5	11.4	62.7
minimum	25.7	11.0	61.9
average	26.1	11.1	62.3
percent difference (%)	3.1	3.6	1.4
stoichiometric concentration:	25.6	11.1	63.3

6.4 Results

6.4.1 NEZ Cu-sulfide concentrate

A composite NEZ Cu-sulfide concentrate sample was analyzed five times. Analyzes detected up to 236 ppb Pd, 96 ppb Pt, 19 ppb Rh, 1 ppb Ru, 8.8 ppm Au and 140 ppm Ag. Osmium, Rh and Ir were below detection limits. Complete results are presented in Appendix E5.

6.4.2 Sulfide major element chemistry

Electron microprobe results are summarized in Table 6.2 and the full data set is presented in Appendix E4. They show that both Fe and S are present within 4 percent of ideal stoichiometric values in the analyzed pyrite, chalcopyrite and bornite grains. Copper concentrations in chalcopyrite and bornite are within 1.5 percent of ideal stoichiometric values. Because trace element analysis by LA-ICP-MS rarely produces precision better than 5 percent (Danyushevsky et al., in press), variations of this magnitude in the internal standard are within analytical precision for quantifying the LA-ICP-MS data.

6.4.3 Sulfide trace element chemistry

LA-ICP-MS analyses produce large amounts of data with a unique detection limit calculated for every element of each analysis (Danyushevsky et al., in press). Detection limits will vary and the range produced will overlap to some extent with the range of concentrations that are above their unique detection limit. For the purpose of evaluating a large amount of data by graphical and statistical methods, it was at times necessary to assign half the detection limit value (i.e. 0.5 x detection limit) to analyses that were below their individual detection

limit (i.e. when calculating median concentrations; Table 6.3). Where this has been done is explicitly stated in data tables and figures in the current study. Table 6.3 also reports the number of analyses above individual detection limits for each element. When plotting maps of the spatial distribution of elements in sulfide minerals (Section 6.4.3.3), a value of zero was assigned to analyses that were below their calculated detection limit. This was done to avoid providing a misleading appearance of element occurrences. The following results and discussion of element concentrations and deportment in sulfide grains is based entirely on results above detection limits unless otherwise stated.

Unlike transmission electron microscope analyses, the LA-ICP-MS technique cannot distinguish between an element present in solid solution in the mineral structure and as homogeneously distributed nano-particles (Large et al., 2009). However, if the element particles are of sufficient size (i.e. in the micro-, rather than nano-size range), then they can be identified as inclusions (Large et al., 2009). This size dependency presents a challenge for LA-ICP-MS users when assessing element deportment (e.g. Fig. 6.2).

For an element distributed homogeneously, either as nano-particles or in the crystal structure, the analytical error (precision) is an expression of the analytical noise, usually <10 percent (Gilbert et al., 2005). For an inhomogeneous sample, the analytical error expresses sample variability, i.e. the occurrence of elements as inclusions, and can be used to aid in element deportment interpretation. However, for elements close to or below the detection limit the analytical error is very high, creating "spikey" time-resolved profiles in which element deportment cannot be determined (Fig. 6.2). The "spikey" signal is due mainly to very low count rates in the sample, and also to a higher signal to noise ratio (Gilbert et al., 2005).

Time-resolved element profiles, element maps and precision values each have their own strengths in determining element deportment within the limits of LA-ICP-MS analyses. These three techniques have all been used in this study.

On the basis of sulfide occurrence, samples were assigned one of three groups:

- Group 1 – both bornite and chalcopyrite present
- Group 2 – chalcopyrite only
- Group 3 – pyrite and chalcopyrite present

For the purposes of the following discussion, elements are grouped into lithophile (Mg, Al, Ca, Ti, V, Cr, Mn, Zr, Ba, La, W, Th and U), siderophile (Co, Ni, Mo, PGEs, and Au) and chalcophile (Cu, Zn, As, Se, Ag, Cd, Sn, Sb, Te, He, Tl, Pb and Bi) categories.

A summary of all bornite, chalcopyrite and pyrite LA-ICP-MS data is given in Figure 6.3; Figure 6.4 shows results for chalcopyrite only from each group. The full data set, detection limits and accompanying precision data are presented in Appendix E3. Summary statistics for siderophile and chalcophile data are presented in Table 6.3. The PGE study results are presented separately in Table 6.4 with the full data set in Appendix E1. Table 6.5 presents a summary of element deportment and associations as observed in each sulfide mineral and as detailed below.

6.4.3.1 Lithophile elements

Most of the lithophile element concentrations that were recorded above detection limits were highly erratic and variable in all sulfides (Appendix E3). The exceptions were Mn and Ti in pyrite, which were mostly above detection limits (maximum 1230 ppm and 52.2 ppm respectively; Appendix E3). Chromium, W, Zr, Th and U had no more than one analysis above detection in any of the three sulfides analyzed (Appendix E3). The most abundant and widespread lithophile elements were Mg, Al, Mn and Ca, with the first three the most spatially widespread.

Lithophile element concentrations above detection limits (including Ti and Mn), are generally interpreted to be due to the presence of silicate, oxide, carbonate or sulfate mineral inclusions in the analyzed sulfides. Some of the manganese is interpreted to occur within the pyrite structure or as nano-particles as indicated by analytical precision and time-resolved element profiles.

Multi-element maps of sulfide compositions (Figs. 6.5 to 6.6) show that the majority of the lithophile elements are concentrated in the K-feldspar, anhydrite or calcite cement intergrown or surrounding the sulfide

Table 6.3 Summary of siderophile and chalcophile trace element chemistry of bornite, chalcopyrite and pyrite by LA-ICP-MS analyses. The full data set is available in Appendix E3.1. Detection limits and analytical precisions are listed in Appendices E3.2 and E3.3, respectively. Chalcopyrite data was synthesized for the entire data set, and also split into the three groups based on coexisting sulfides (see text for explanation). Values in ppm. Analyses below data set detection limits were assigned a 0.5 x detection limit value for purposes of calculating average, median, and standard deviation.

	All bornite analyses (group 1)						All chalcopyrite analyses (groups 1–3)						All pyrite analyses (group 3)					
Element	**#[1] of individual analyses**	**# of results >DL[1]$_{dataset}$**	**Max[1]**	**Avg[1]**	**Median**	**Std Dev[1]**	**# of individual analyses**	**# of results >DL$_{dataset}$**	**Max[1]**	**Avg[1]**	**Median**	**Std Dev[1]**	**# of individual analyses**	**# of results >DL$_{dataset}$**	**Max[1]**	**Avg[1]**	**Median**	**Std Dev[1]**
Co^{59}	67	7	46.0	2.84	1.42	5.85	158	30	45300	290	1.11	3590	61	61	2450	511	330	469
Ni^{60}	67	1	11.9	5.12	5.52	3.73	158	2	651	8.35	3.96	51.4	61	61	2210	293	123	425
Mo^{95}	67	2	33.3	2.69	1.46	4.10	158	9	32.2	1.65	1.07	2.84	61	22	54.2	2.95	0.53	8.43
Pt^{195}	51	0	0.490	0.244	0.205	0.130	106	3	0.830	0.240	0.190	0.179	46	4	0.438	0.062	0.060	0.074
Au^{197}	67	3	[2]0.986	0.069	0.040	0.117	158	12	1.29	0.062	0.040	0.115	61	59	[2]483	8.50	0.36	61.3
Cu^{65}	67	67	689000	586000	591000	64700	158	158	428000	336000	330000	19100	61	59	9280	2190	1240	2260
Zn^{66}	67	8	227	13.7	6.03	31.7	158	51	30100	2150	6.26	5480	61	61	38000	7520	2870	8700
As^{75}	67	1	15.3	7.15	5.48	4.30	158	4	47.8	7.22	5.39	5.00	61	47	1360	80.0	21.2	188
Se^{77}	67	67	1770	311	295	200	158	158	3310	403	259	418	61	61	728	276	253	151
Ag^{107}	67	67	4120	913	815	500	158	158	[2]2120	134	50.6	248	61	60	248	40.9	28.3	49.7
Cd^{111}	67	0	26.0	11.5	14.8	8.16	158	52	1580	53.4	11.7	173	61	56	3220	150	31.8	429
Sn^{118}	67	7	26.5	1.27	0.730	3.34	158	34	20.5	1.12	0.54	2.33	61	41	7.44	1.42	0.34	1.94
Sb^{121}	67	1	10.0	0.690	0.690	1.18	158	54	6.95	0.901	0.550	1.09	61	40	29.8	3.15	0.46	4.94
Te^{125}	67	29	353	22.0	2.82	63.1	158	83	[2]2920	25.5	1.71	232	61	57	137	7.08	4.02	17.2
Tl^{205}	27	0	0.085	0.056	0.048	0.019	83	1	0.185	0.067	0.065	0.044	31	27	0.774	0.102	0.040	0.152
Pb^{208}	67	67	2920	106	14.0	379	158	158	18800	1260	135	2610	61	61	1910	147	82.5	260
Bi^{209}	67	67	327	75.8	58.3	62.1	158	138	45.1	4.24	1.52	7.28	61	57	32.4	5.66	4.04	7.38

Table 6.3 continued

	Chalcopyrite analyses (group 1)						Chalcopyrite analyses (group 2)						Chalcopyrite analyses (group 3)					
Element	**# of individual analyses**	**# of results >DL[1]$_{dataset}$**	**Max[1]**	**Avg[1]**	**Median**	**Std Dev[1]**	**# of individual analyses**	**# of results >DL$_{dataset}$**	**Max[1]**	**Avg[1]**	**Median**	**Std Dev[1]**	**# of individual analyses**	**# of results >DL$_{dataset}$**	**Max[1]**	**Avg[1]**	**Median**	**Std Dev[1]**
Co^{59}	65	16	45300	699	1.11	5570	33	2	5.22	1.88	0.68	2.03	60	12	95.0	4.69	1.00	12.9
Ni^{60}	65	1	651	13.8	3.96	79.8	33	0	10.3	4.28	2.62	3.38	60	1	15.2	4.66	4.03	3.84
Mo^{95}	65	1	3.60	1.68	1.34	1.18	33	1	13.8	1.37	0.93	2.29	60	7	32.2	1.78	0.99	4.10
Pt^{195}	47	2	0.830	0.259	0.170	0.203	23	0	0.205	0.136	0.140	0.070	36	1	0.660	0.283	0.205	0.166
Au^{197}	65	3	1.29	0.069	0.040	0.164	33	2	0.424	0.051	0.030	0.068	60	7	0.255	0.061	0.035	0.058
Cu^{65}	65	65	377000	335000	331000	15100	33	33	399000	343000	331000	25100	60	60	428000	333000	329000	18400
Zn^{66}	65	1	17.1	5.64	3.95	4.46	33	2	242	14.9	6.01	40.5	60	48	30100	5640	1860	7710
As^{75}	65	1	11.9	5.81	4.50	2.85	33	0	12.3	8.14	10.0	3.46	60	3	47.8	8.25	6.42	6.85
Se^{77}	65	65	3310	526	323	556	33	33	1340	430	388	347	60	60	656	256	218	142
Ag^{107}	65	65	[2]2120	112	36.5	293	33	33	1070	187	124	239	60	60	958	129	50.6	188
Cd^{111}	65	0	16.7	8.18	11.2	5.76	33	3	111	11.4	4.46	20.1	60	49	1580	125	61.3	265
Sn^{118}	65	3	20.5	0.773	0.485	2.47	33	1	0.775	0.496	0.450	0.198	60	30	12.0	1.83	0.69	2.60
Sb^{121}	65	14	3.69	0.588	0.479	0.564	33	1	0.765	0.471	0.415	0.198	60	39	6.95	1.48	0.87	1.49
Te^{125}	65	39	[2]2920	54.9	2.31	359	33	18	185	9.80	1.65	31.6	60	26	16.9	2.40	1.61	2.38
Tl^{205}	36	0	0.080	0.042	0.045	0.029	18	0	0.185	0.104	0.080	0.051	29	1	0.125	0.074	0.065	0.035
Pb^{208}	65	65	18800	2250	732	3450	33	33	8040	1360	375	2170	60	60	2310	133	33.2	398
Bi^{209}	65	64	13.6	2.52	1.54	2.48	33	33	45.1	13.2	9.10	11.5	60	44	8.64	1.20	0.48	1.92

[1] #- number, DL-detection limit, max-maximum, avg-average, std dev-standard deviation; [2] maximum value is an extreme isolated outlier

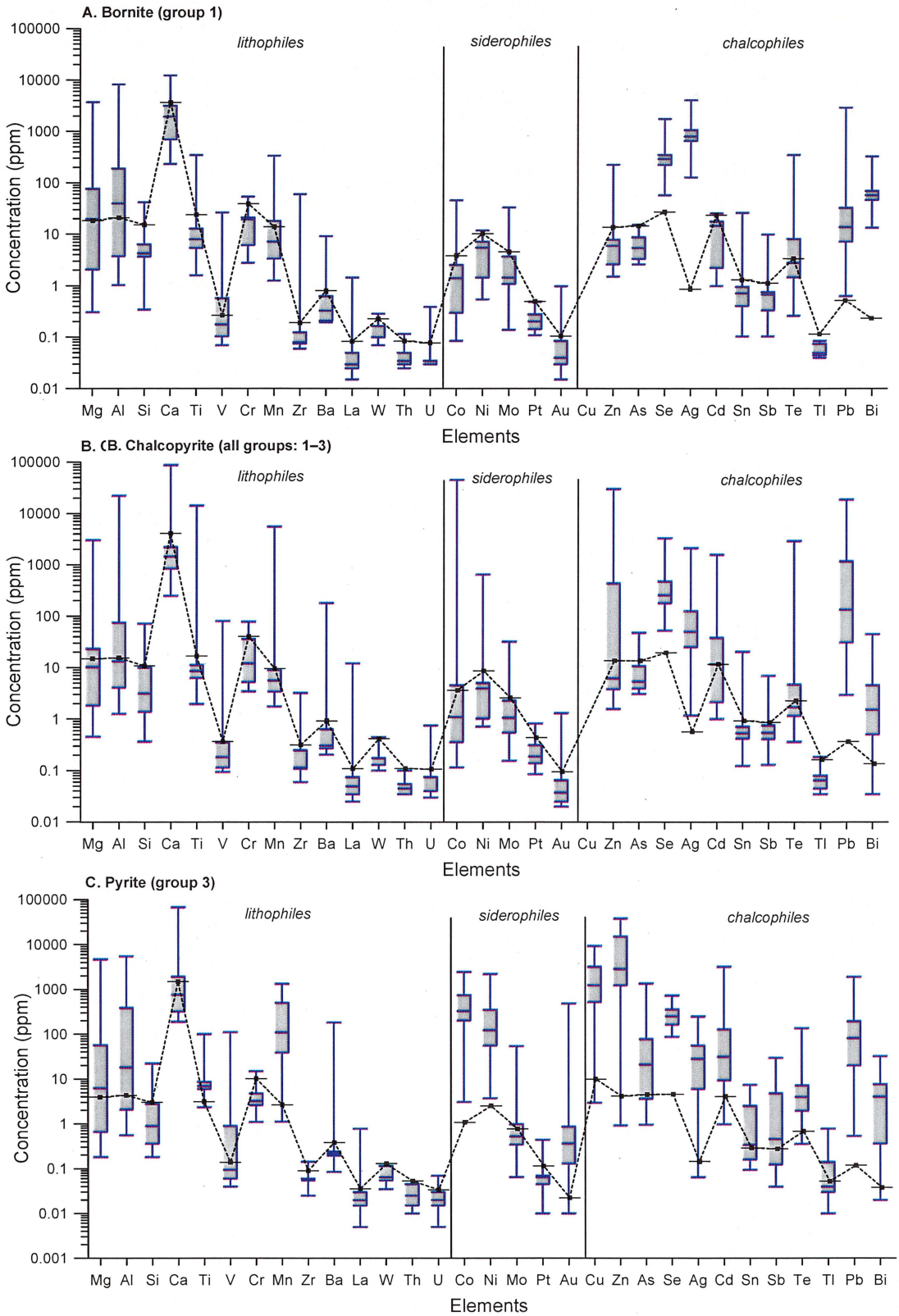

Figure 6.3 Box and whisker plots of all elements analyzed for bornite, chalcopyrite and pyrite. Whiskers (blue) define the maximum and minimum values, the box (grey, blue edge) defines the 25th and 75th percentiles, and the line in the center of the box is the median. For data less than detection, half of the individual detection limit has been used. The average detection limit for each element (black dashed line) has also been graphed. Ranges shown below the *average* detection limit (black dashed line) for each element reflect the range in *individual* analysis detection limits, and in some cases may be lower than the average detection limit shown. See Table 6.3 for number of individual analyses conducted for each element and the number of results reported above individual detection limits.

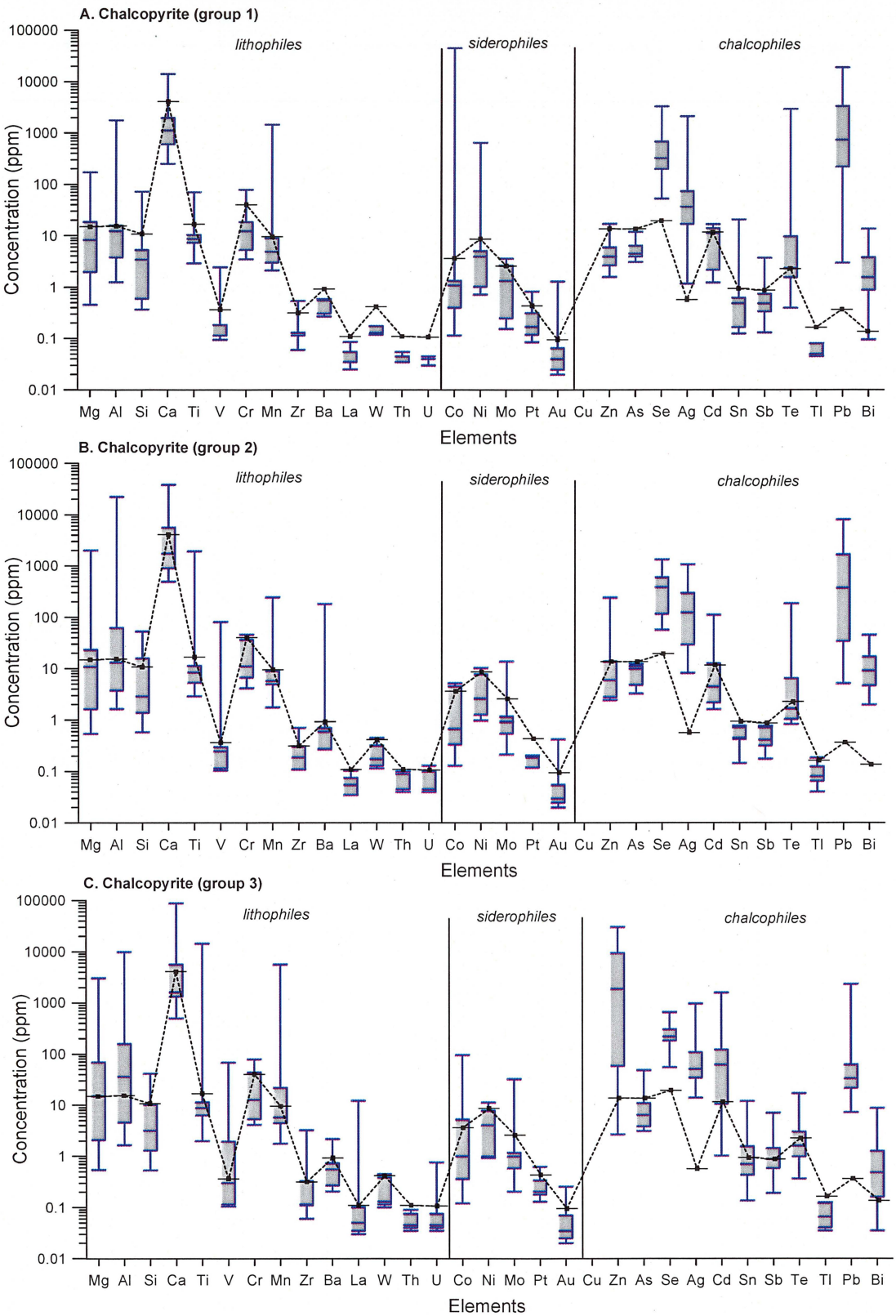

Figure 6.4 Box and whisker plots of all elements analyzed for chalcopyrite from the three groups (see text for explanation). Whiskers (blue) define the maximum and minimum values, the box (grey, blue edge) defines the 25th and 75th percentiles, and the line in the center of the box is the median. For data less than detection, half of the individual detection limit has been used. The average detection limit for each element (black dashed line) has also been graphed. Ranges shown below the *average* detection limit (black dashed line) for each element reflect the range in *individual* analysis detection limits, and in some cases may be lower than the average detection limit shown. See Table 6.3 for number of individual analyses conducted for each element and the number of results reported above individual detection limits.

Table 6.4 Summary of PGE results from pyrite, chalcopyrite and bornite by LA-ICP-MS analyses. All values in ppm. Bold values highlight PGE (plus Au and Ag) concentrations above detection limits. Full data set available in Appendix E1. Silver concentrations have been added from Appendix E3.1. For brevity the average detection limits for each element are listed here in the table header; however, individual analysis detection limits listed in the data columns may be lower than the average.

Data file	DDH	Depth	Mineral[1]	Ru^{99}	Ru^{101}	Rh^{103}	Pd^{105}	Pd^{106}	Ag^{107}	Re^{185}	Os^{189}	Ir^{193}	Pt^{195}	Au^{197}
		average DL[2]	chalopyrite	0.050	0.030	0.040	0.039	0.039	0.35	0.005	0.024	0.006	0.016	0.010
		average DL	bornite	0.060	0.030	0.040	0.042	0.050	0.39	0.006	0.025	0.006	0.018	0.012
		average DL	pyrite	0.030	0.010	0.020	0.018	0.018	0.13	0.003	0.009	0.003	0.0083	0.005
MY09A23	WB03-03	120.7	b	<0.055	<0.030	<0.041	<0.045	<0.041	**1340**	<0.005	<0.024	<0.006	<0.017	<0.012
MY09A24	WB03-03	120.7	b	<0.055	<0.030	<0.041	<0.045	<0.041	**1310**	<0.005	<0.024	<0.006	<0.017	<0.012
MY09A25	WB03-03	120.7	c	<0.053	<0.026	<0.038	<0.041	**0.057**	**2120**	<0.005	<0.023	<0.006	<0.016	<0.010
MY09A26	WB03-03	120.7	c	<0.053	<0.026	<0.038	<0.041	<0.038	**343**	<0.005	<0.023	<0.006	<0.016	<0.010
MY09A27	WB04-40	68.1	p	<0.028	<0.013	<0.019	<0.020	<0.017	**4.68**	<0.002	<0.009	<0.003	<0.008	**2.26**
MY09A28	WB04-40	68.1	p	<0.028	<0.013	<0.019	<0.020	<0.017	**4.36**	<0.002	<0.009	<0.003	<0.008	**2.86**
MY09A29	WB04-40	68.1	c	<0.053	<0.026	<0.038	<0.041	<0.038	**61.3**	<0.005	<0.023	<0.006	<0.016	**0.02**
MY09A30	WB04-95	35.9b	b	<0.055	<0.030	<0.041	<0.045	<0.041	**787**	<0.005	<0.024	<0.006	<0.017	<0.012
MY09A31	WB04-95	35.9b	c	<0.053	<0.026	<0.038	<0.041	<0.038	**69.3**	<0.005	<0.023	<0.006	<0.016	**0.011**
MY09A32	WB04-95	168.6	c	<0.053	<0.026	<0.038	<0.041	<0.038	**152**	<0.005	<0.023	<0.006	<0.016	<0.010
MY09A33	WB04-95	168.6	c	<0.053	<0.026	<0.038	<0.041	<0.038	**127**	<0.005	<0.023	<0.006	<0.016	**0.011**
MY09A42	WB04-111	224.5	c	<0.053	<0.026	<0.038	<0.041	<0.038	**29.3**	<0.005	<0.023	<0.006	<0.016	**0.65**
MY09A43	WB04-111	224.5	c	<0.053	<0.026	<0.038	<0.041	<0.038	**8.20**	<0.005	<0.023	<0.006	<0.016	**0.04**
MY09A44	WB04-122	311.5	c	<0.053	<0.026	<0.038	<0.041	<0.038	**44.6**	<0.005	<0.023	<0.006	<0.016	<0.010
MY09A45	WB04-122	311.5	b	<0.055	<0.030	<0.041	<0.045	<0.041	**628**	<0.005	<0.024	<0.006	<0.017	<0.012
MY09A46	WB04-122	311.5	b	<0.055	<0.030	<0.041	<0.045	<0.041	**643**	<0.005	<0.024	<0.006	<0.017	<0.012
MY09A47	WB04-188	59.5	b	<0.055	<0.030	<0.041	<0.045	<0.041	**645**	<0.005	<0.024	<0.006	<0.017	**0.21**
MY09A48	WB04-188	59.5	c	<0.053	<0.026	<0.038	<0.041	<0.038	**280**	<0.005	<0.023	<0.006	<0.016	<0.010
MY09A49	WB04-188	118.2	c	<0.053	<0.026	<0.038	<0.041	<0.038	**32.7**	<0.005	<0.023	<0.006	<0.016	**0.012**
MY09A50	WB04-188	118.2	b	<0.055	<0.030	<0.041	<0.045	<0.041	**572**	<0.005	<0.024	<0.006	<0.017	<0.012
MY09A51	WB04-188	118.2	b	<0.055	<0.030	<0.041	<0.045	<0.041	**700**	<0.005	<0.024	<0.006	<0.017	<0.012
MY09A52	WB04-210	424.3	p	<0.028	<0.013	<0.019	**0.15**	**0.13**	-[3]	<0.002	<0.009	<0.003	<0.008	**1.38**
MY09A53	WB04-210	424.3	p	<0.028	<0.013	<0.019	**0.090**	**0.046**	-	<0.002	<0.009	<0.003	<0.008	**0.68**
MY09A54	WB04-210	424.3	p	<0.028	<0.013	<0.019	**0.59**	**0.54**	**6.06**	<0.002	<0.009	<0.003	<0.008	**0.83**
MY09A55	WB04-210	424.3	p	<0.028	<0.013	<0.019	**1.1**	**1.1**	**0.16**	<0.002	<0.009	<0.003	<0.008	**0.99**
MY09A56	WB04-210	424.3	c	<0.053	<0.026	<0.038	<0.041	<0.038	**40.9**	<0.005	<0.023	<0.006	<0.016	**0.034**
MY09A57	WB04-213	563.8	p	<0.028	<0.013	<0.019	**0.16**	**0.17**	**20.9**	<0.002	<0.009	<0.003	**0.088**	**0.015**
MY09A58	WB04-213	563.8	p	<0.028	<0.013	<0.019	**0.035**	**0.071**	**0.74**	**0.02**	<0.009	<0.003	**0.011**	**0.38**
MY09A59	WB04-213	563.8	c	<0.028	<0.013	<0.019	<0.020	**0.062**	**703**	**0.0048**	<0.009	<0.003	**0.012**	<0.004

[1] Mineral: b-bornite, c-chalcopyrite, p-pyrite; [2] DL-detection limit; [3] "-" not measured

Table 6.5 Element deportment and associations. Interpretations are from time-resolved element profiles, multi-element maps and analytical precision values.

	All analyses above DL[1]	**Crystal structure or nano-particles**	**Inclusions**	**Not detected (≤ 1 analyses > DL)**
Bornite (group 1)				
Lithophile	none	none	Mg, Al, Ti, V, Mn, limited Si, Ca, rare Zr, Ba, La, Th and U	Cr, W
Siderophile	none		limited Co and rare Ni, Mo, Au	Pd[2], Pt
Chalcophile	Cu, Se, Ag, Pb, Bi	Ag, Bi, Se, Te?[3]	Pb, Ag, Te, limited Zn, Sn, very rare Bi, Se	As, Cd, Tl, Sb
Observed element associations	-	Ag-Bi ± Se	Ag-Te ± Se Pb ± Se rare Bi-Pb very rare Ag-Te-Au inclusions Co-Ni-Mn-Mg-Al Sn-Al-Mn-Mg	-
Chalcopyrite (groups 1–3)				
Lithophile	none	none	Mg, Al, Ti, V, Mn, limited to rare Si, Ca, Zr, Ba, La, U (all three groups)	Cr, W, Th (all three groups)
Siderophile	none	none	limited Co, rare Mo, Au, isolated Pd, Pt (applies to all three groups)	Ni (all three groups)
Chalcophile	Cu, Se, Ag, Pb (all three groups)	Cu, Ag? (all three groups)	abundant Pb, Te, Bi, rare As (all three groups)	Tl (all three groups)
		Group 1: Group 2: Se? Group 3: Se? Ag? Bi?	Group 1: isolated Zn, Se, Ag, limited Sb, Group 2: limited Zn, Se?, Ag, Cd Group 3: abundant Zn, Se?, Ag, Cd, Sb	Group 1: Cd Group 2: isolated Sn, Sb Group 3: isolated Sn
Observed element associations	-	-	Pb-Se ± Te ± Bi Pb-Ag-Bi-Se-Te Ag-Te ± Au Ag-Se-Te Zn-Cd ± Sn (sphalerite) Pt-Te ± Ag, Te-Pt ± Ag Co-Al-Mn-Mg ± V-Zn-Ca Zn-Si-Mg-Mn-Al-Fe-Ti	-
Pyrite (group 3)				
Lithophile	Mn[4]	Mn?	Mg, Al, Si ± Ca, V in some but not all samples, abundant Ti	Cr, Zr, W, Th, U
Siderophile	Co, Ni[4], Au[4]	Co, Ni, Au	Co, Au, limited Mo, rare Pd, Pt	none
Chalcophile	Pb, Se, Cu[4], Zn[4], Ag[4], Te[4], Bi[4]	Se, Zn, Cd?, Ag? Pb? Te?	abundant Pb, Cu, Zn, Ag, As, Bi, Sn, Sb, Se, Te, Cd	none
Observed element associations	-	Ni-Co	Pb-Ag ± Bi (galena), large, abundant, zoned Cu-Ag, zoned Au-Ag ± Te Au-As (rare) Au (rare) Bi-Te? Ag-Te Au-Ag Zn-Cd ± Sn (sphalerite)	-

[1]DL-detection limit; [2]observed in time-resolved element profiles, but below analytical detection limit; [3]"?" indicates the element may occur in the crystal structure or as evenly distributed nano-particles, but it was not possible to confidently resolve; [4]Only ≤3 analyses less than detection limit.

minerals. Some inclusions that contain these elements occur within the sulfides, especially in pyrite (Fig. 6.7). Titanium defines similar patterns to Si and Ca in Figure 6.7, suggesting that titanite occurs as inclusions in chalcopyrite in this sample. Titanium inclusions define similar patterns to Mg, Al, Si, K and Mn in Figures 6.5 and 6.6 suggesting that Ti may occur as rutile inclusions in K-feldspar.

6.4.3.2 Siderophile elements

Co, Ni, Mo

Overall, more than half of all analyses of Co and Ni in bornite and chalcopyrite were below detection limits (Table 6.3, Fig. 6.8A). Median concentrations were <6 ppm for both elements. A few Co and rare Ni inclusions were identified in bornite and chalcopyrite (Figs. 6.6 and 6.8).

All analyses of Co and Ni in pyrite (n = 61; Fig. 6.3A) were above detection limits and these elements are interpreted to occur primarily within the pyrite structure (Figs. 6.7 and 6.9A). Median Co and Ni concentrations in pyrite are 330 ppm and 123 ppm, respectively. Multi-element maps (Figs. 6.5 and 6.7) are in agreement with time-resolved profiles and precision data, showing rare Co and Ni inclusions in chalcopyrite and bornite and zonation within pyrite.

Molybdenum was detected above detection limits in approximately one-third of the pyrite analyses, up to a maximum concentration of 54.2 ppm (Table 6.3). This is interpreted to be caused by small molybdenite inclusions. Multi-element maps suggest that Mo may occur in low concentrations in K-feldspar either within the mineral structure or as minor inclusions (Figs. 6.5 and 6.7). Molybdenum was rarely detected in bornite and chalcopyrite.

Au

LA-ICP-MS analyses from this study have shown that Au in the NEZ sulfides is hosted primarily in pyrite, with 59 out of 61 analyses returning values between 0.011–4.32 ppm Au (plus one outlier of 483.2 ppm) and a median of 0.36 ppm Au (Table 6.3). In contrast, Au was most commonly near or below detection limits in chalcopyrite. Only 12 out of 158 chalcopyrite analyses returned Au concentrations above detection limits; results ranged from 0.050–1.29 ppm Au. In bornite, Au was detected above detection limits in three out of 67 analyses (0.13, 0.15, 0.99 ppm Au; Figs. 6.3 and 6.8B, C, D, Tables 6.3, Appendices E1 and E3). A total of 40 of the 67 bornite analyses were line analyses, which have the potential to average out the Au concentrations provided by small isolated inclusions; however, inspection of time-resolved profiles showed that, with only rare exceptions, Au was at background levels in the bornite samples that returned results below detection limits (Appendix E6). Figures 6.9 to 6.12 show Au concentrations in pyrite, chalcopyrite and bornite with reflected light photomicrographs showing locations of selected analyses.

Gold occurs as micro-nuggets, primarily within pyrite, but also in some chalcopyrite grains. Only rare Au inclusions were detected in bornite. Mapping and time-resolved element profiles have shown that Au also occurs homogenously distributed at low concentrations throughout pyrite, either as nano-particles or dissolved in the pyrite structure (Figs. 6.2A, 6.5, 6.7).

A textural comparison of pyrite grains that contained <1 ppm Au with those that have >1 ppm Au has shown that, while some pyrite grains contain distinct inclusion-rich cores, others contain few large inclusions and others are inclusion-free (compare Figs. 6.9 and 6.10). No unique texture was identified that could distinguish >1 ppm Au in these samples and no visible gold was observed in this study.

PGEs

Palladium (up to 1.13 ppm) and Pt (up to 0.830 ppm) were identified in a few group 3 pyrite and chalcopyrite grains, and also in some and group 1 chalcopyrite grains (Tables 6.3, 6.4, Figs. 6.10, 6.11, Appendices E1 and E2). Palladium concentrations in pyrite were found to be 1–2 orders of magnitude greater than in chalcopyrite. Palladium was observed in two bornite grains as isolated inclusions, however, time averaged results were below detection limits (Table 6.4, Fig. 6.12). Ruthenium, Rh, Os and Ir were not detected.

Palladium and Pt were identified as micro-inclusions primarily in pyrite (Figs. 6.5, 6.7, 6.13). Due to higher detection limits, maps of chalcopyrite did not

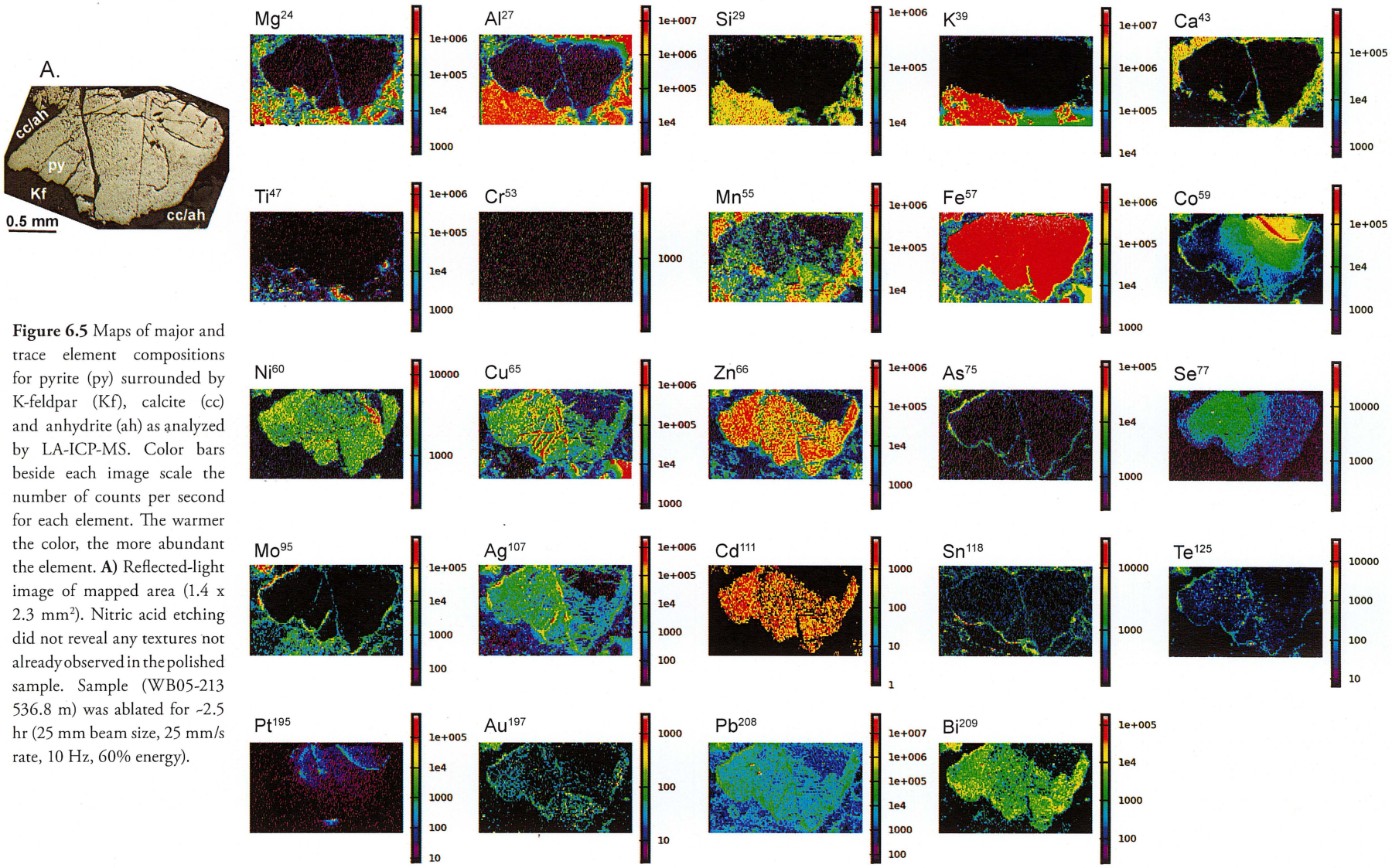

Figure 6.5 Maps of major and trace element compositions for pyrite (py) surrounded by K-feldpar (Kf), calcite (cc) and anhydrite (ah) as analyzed by LA-ICP-MS. Color bars beside each image scale the number of counts per second for each element. The warmer the color, the more abundant the element. **A)** Reflected-light image of mapped area (1.4 x 2.3 mm^2). Nitric acid etching did not reveal any textures not already observed in the polished sample. Sample (WB05-213 536.8 m) was ablated for ~2.5 hr (25 mm beam size, 25 mm/s rate, 10 Hz, 60% energy).

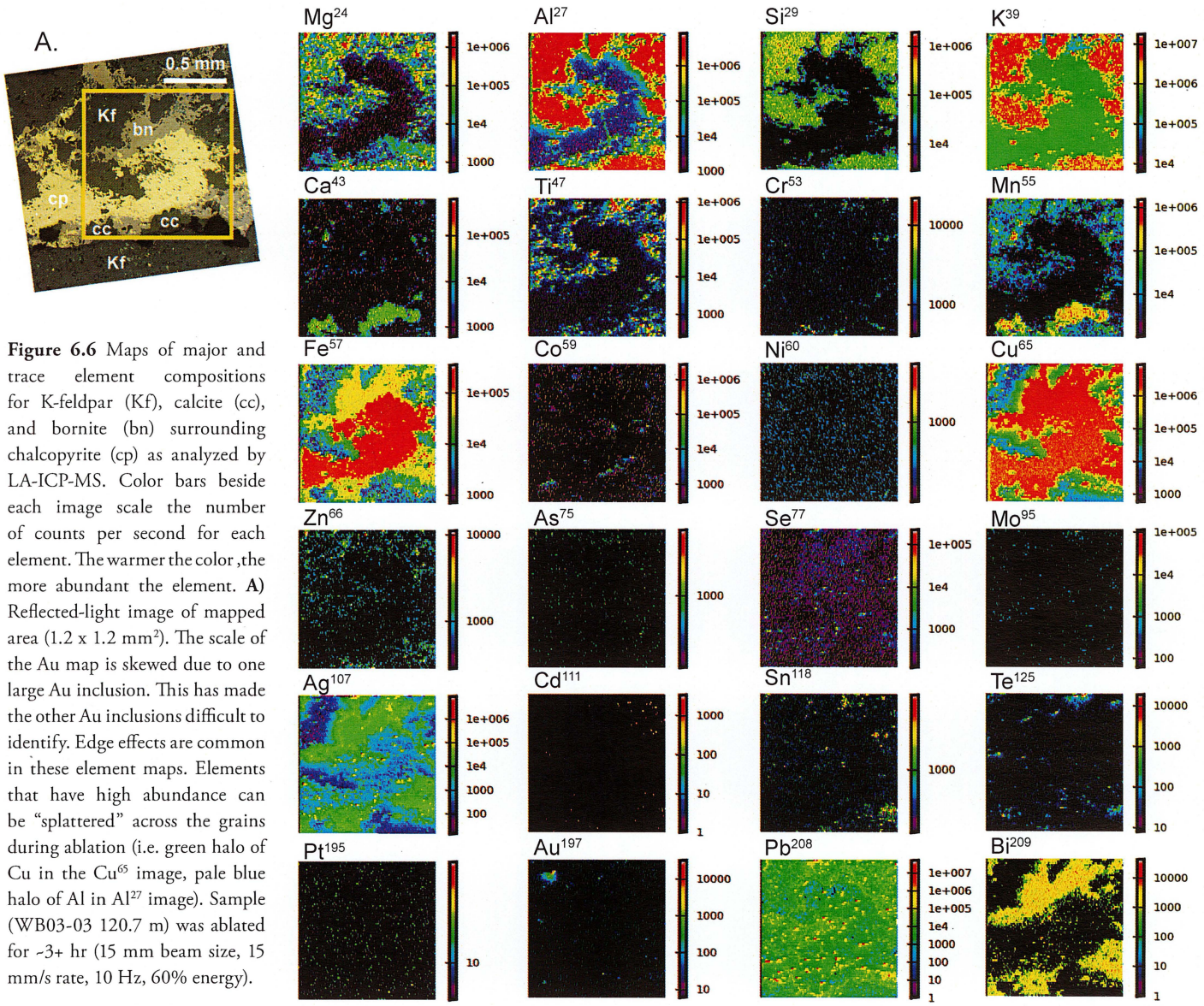

Figure 6.6 Maps of major and trace element compositions for K-feldpar (Kf), calcite (cc), and bornite (bn) surrounding chalcopyrite (cp) as analyzed by LA-ICP-MS. Color bars beside each image scale the number of counts per second for each element. The warmer the color ,the more abundant the element. **A)** Reflected-light image of mapped area (1.2 x 1.2 mm^2). The scale of the Au map is skewed due to one large Au inclusion. This has made the other Au inclusions difficult to identify. Edge effects are common in these element maps. Elements that have high abundance can be "splattered" across the grains during ablation (i.e. green halo of Cu in the Cu^{65} image, pale blue halo of Al in Al^{27} image). Sample (WB03-03 120.7 m) was ablated for ~3+ hr (15 mm beam size, 15 mm/s rate, 10 Hz, 60% energy).

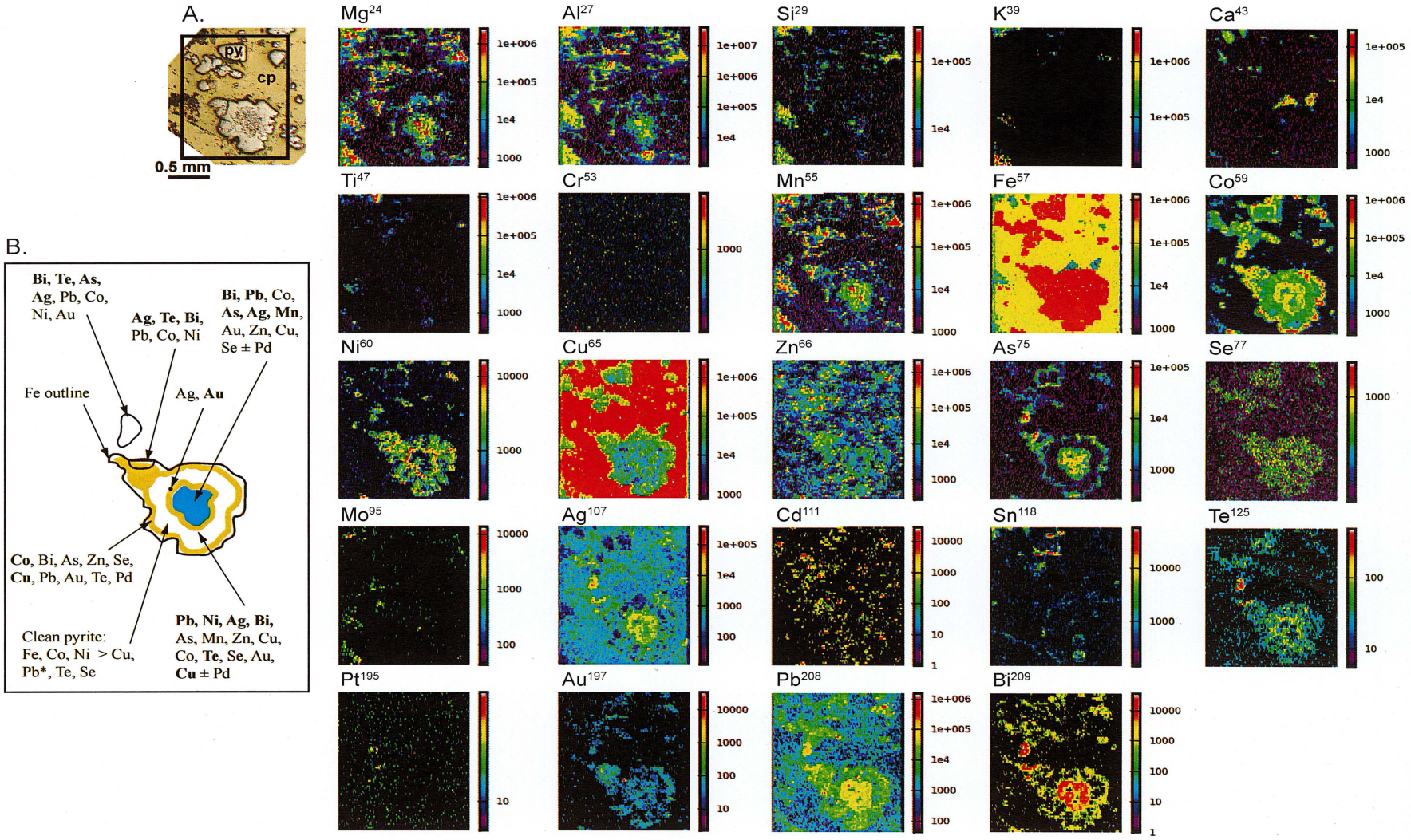

Figure 6.7 Maps of major and trace element compositions for pyrite (py) surrounded by chalcopyrite (cp) as analyzed by LA-ICP-MS. Color bars beside each image scale the number of counts per second for each element. The warmer the color, the more abundant the element. Color intensities (red to black) cannot be compared between different elements unless the scales are the same. **A)** Reflected-light image of mapped area (0.9 x 1.1 mm^2). Sample (WB05-210 424.3 m) was ablated for ~2.5 hr (15 mm beam size, 15 mm/s rate, 10 Hz, 60% energy). **B)** Sketch of zoned pyrite grain showing element associations. Bold font indicate elements that are abundant. There is some uncertainty as to Pd associations due to repolishing of the pyrite grain between separate mapping runs. Lead* patterns can be smeared in these maps (S. Gilbert, pers. com., 2009).

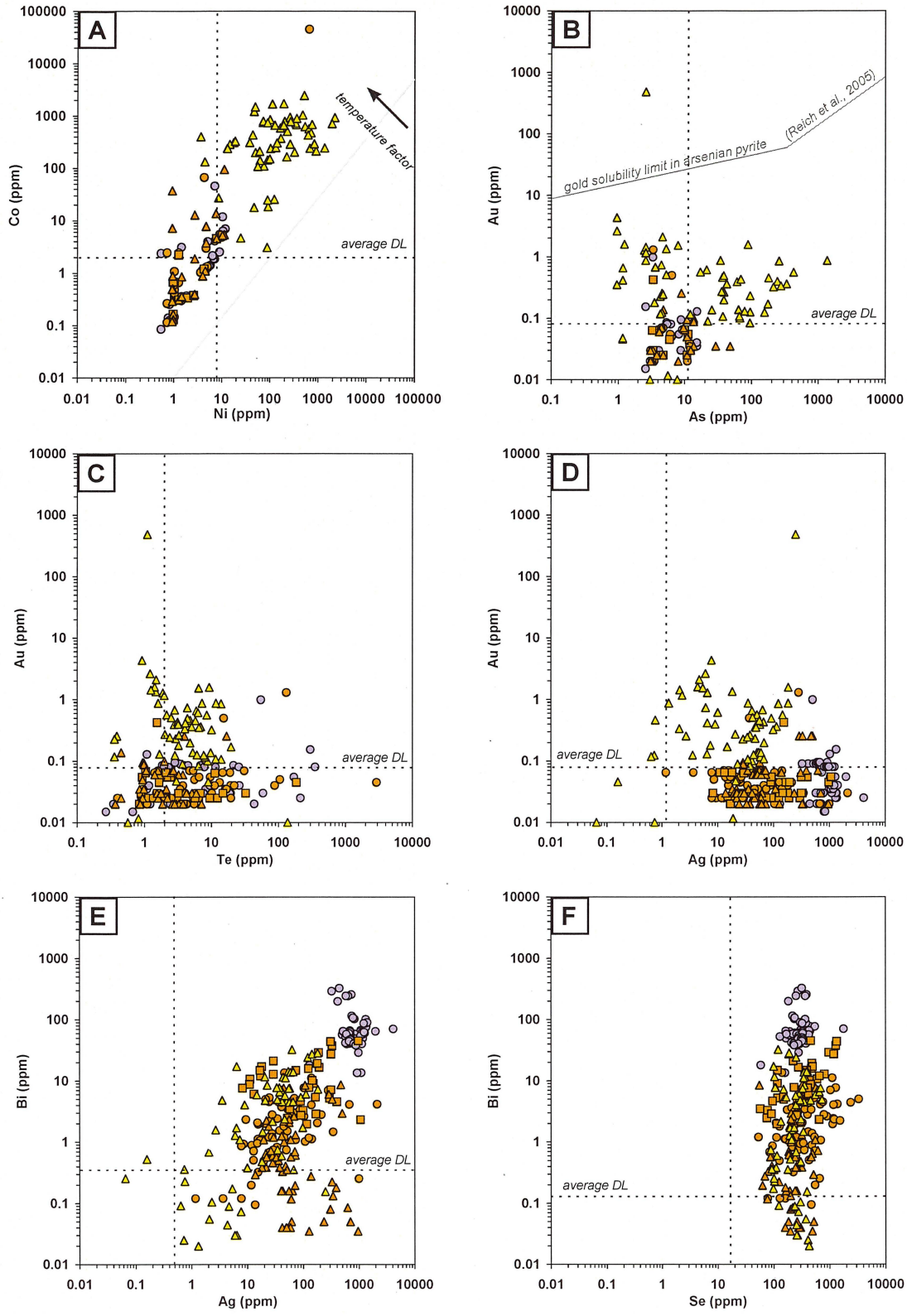
A
Co (ppm)
Ni (ppm)
temperature factor
average DL
B
Au (ppm)
As (ppm)
gold solubility limit in arsenian pyrite
(Reich et al., 2005)
average DL
C
Au (ppm)
Te (ppm)
average DL
D
Au (ppm)
Ag (ppm)
average DL
E
Bi (ppm)
Ag (ppm)
average DL
F
Bi (ppm)
Se (ppm)
average DL

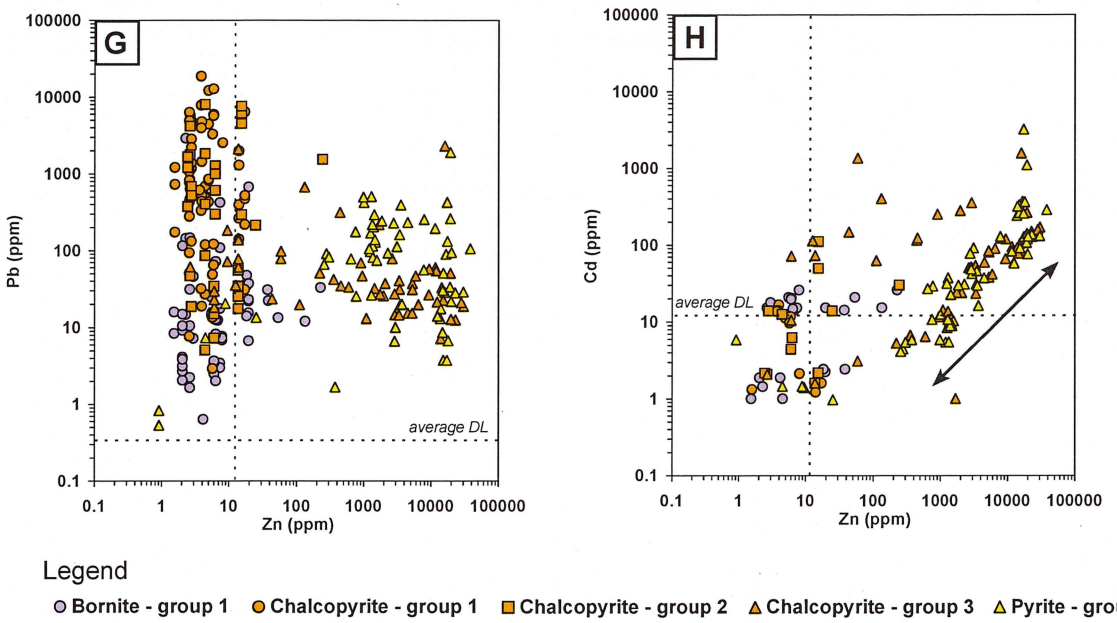

Figure 6.8 Bivariant plots showing selected element relationships from LA-ICP-MS analyses of bornite, chalcopyrite and pyrite collected from the NEZ long-section. Where a value was less than the specific detection limit, half of the specific detection limit was used. Average detection limits (dashed lines) were calculated for all minerals for a given element. **A)** Co and Ni are found primarily in pyrite. **B), C) and D)** Au is primarily found in pyrite and is associated with As, Te and Ag, although Ag appears to have the most data points at high concentrations. Time-resolved element profiles are the most reliable tool for interpreting Au associations. The Au solubility line as a function of As in arsenian pyrite from Carlin-type and epithermal-type gold deposits from Reich et al. (2005) is plotted in B) and suggests that the Au-bearing fluids were not saturated with Au. **E)** Bismuth and Ag occur in the bornite structure or as evenly disstributed nano-particles, whereas these elements appear as inclusions in chalcopyrite and pyrite. **F)** Selenium occurs in all three minerals between 100 and 1000 ppm. **G)** Lead is found above detection in all three minerals, although the highest concentrations are in group 2 chalcopyrite. Zn occurs primarily in group 3 pyrite and chalcopyrite. **H)** Cadmium and Zn have a linear relationship in most pyrite samples, suggesting abundant sphalerite inclusions.

indicate any Pd, even though spot analyses detected isolated Pd inclusions (compare Fig. 6.12C and Table 6.4). Palladium occurs in growth bands, as discrete isolated micro-inclusions (Fig. 6.13A) and may also occur homogeneously distributed at low concentration throughout the pyrite crystal structure (Fig. 6.13B), however results are inconclusive.

6.4.3.3 Chalcophile elements

Ag, Bi, Se

Elevated concentrations of Ag were detected in bornite (median 815 ppm, maximum 4120 ppm) with lesser amounts in chalcopyrite and pyrite (chalcopyrite: median 50.6 ppm, maximum 2120 ppm; pyrite: median 28.3 ppm, maximum 249 ppm; Fig. 6.3A and 6.8E; compare Figs. 6.10 to 6.12, Table 6.3, Appendix E3). A similar pattern is defined by Bi, with the highest concentrations detected in bornite, followed by chalcopyrite and pyrite (Table 6.3 and Appendix E3). Bismuth concentrations within the chalcopyrite groups vary. Group 2 chalcopyrites are more enriched in Bi, followed by group 1 and then group 3 (Fig. 6.4). Multi-element mapping and time-resolved profiles clearly show that Ag and Bi are homogenously distributed in bornite (Figs. 6.6 and 6.12C and D) and occur as inclusions in chalcopyrite and pyrite (Figs. 6.6, 6.9C, 6.11C and D). Analytical precision data indicate Ag may also occur in the pyrite and chalcopyrite structure or as nano-particles in some samples (Appendix E3).

Compared to other elements analyzed, Se concentrations are relatively consistent in all three minerals (median 253–295 ppm; Fig. 6.3 and 6.8F; Table 6.3), however the predominant mode of deportment varies between the minerals. The high concentrations (>100 ppm) and low precision values (<10%) indicate that Se either occurs in the bornite structure or as

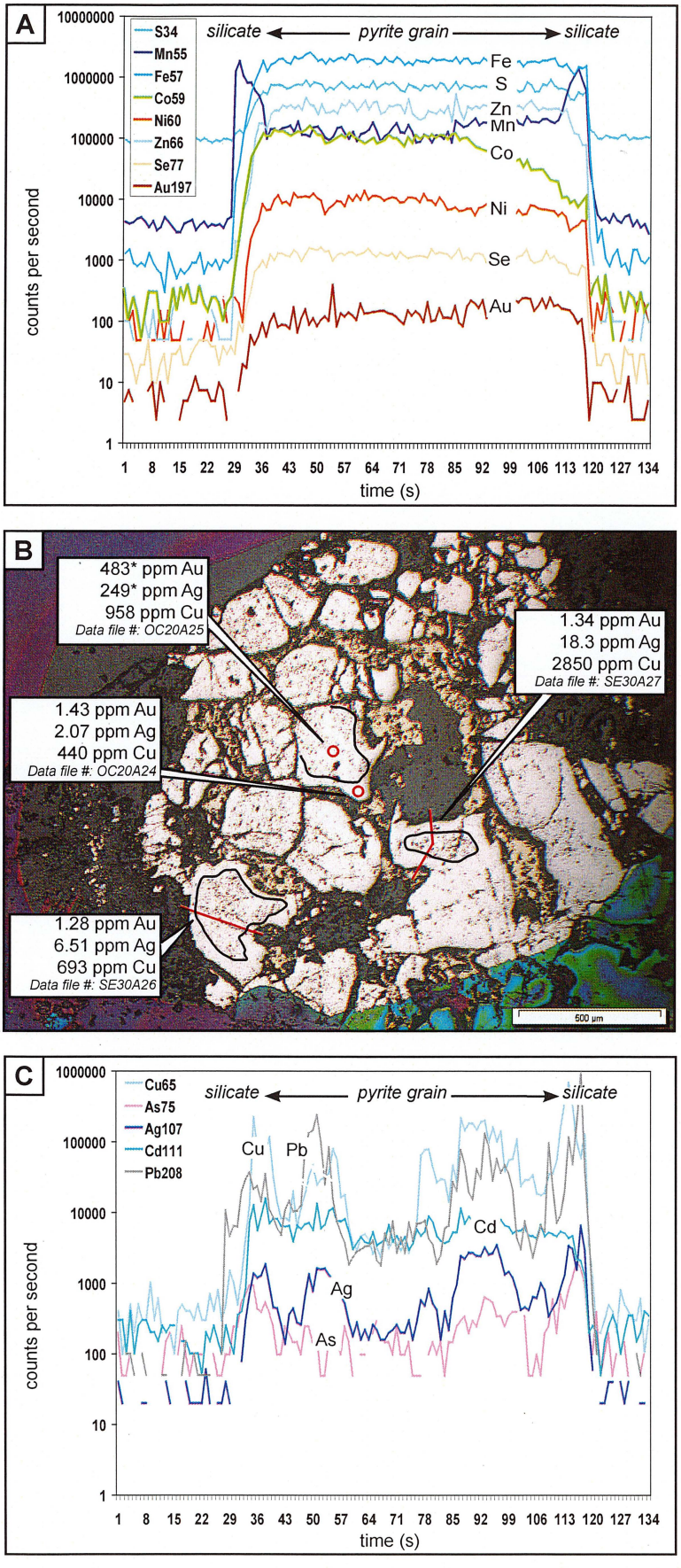

Figure 6.9 A) Selected time-resolved element profiles from pyrite LA-ICP-MS line analyses. These elements are interpreted to occur either in the pyrite structure or as evenly distributed nano-particles. Grain is in lower left hand corner of B), sample WB04-40 68.1 m, data file SE30A26. Reflected light photo **B)** of Au-enriched (>1 ppm) pyrite showing results for spot and line analyses (red circles and lines). Values with an "*" are an isolated example of very high Au and Ag concentrations in pyrite due to a single large inclusion of Au-Ag, likely electrum. The other values are typical of Au-enriched analyses. Note spot and line analyses include inclusion-rich cores (outlined in black) and thin, clean pyrite rims. Data file numbers correspond to those listed in Appendix E3.1 and E3.3. **C)** Time-resolved LA-ICP-MS line analysis profiles for selected elements interpreted as inclusions. Inclusions appear to be zoned. Grain is in lower left hand corner in B (same analyses as in A), sample WB04-40 68.1 m, data file SE30A26.

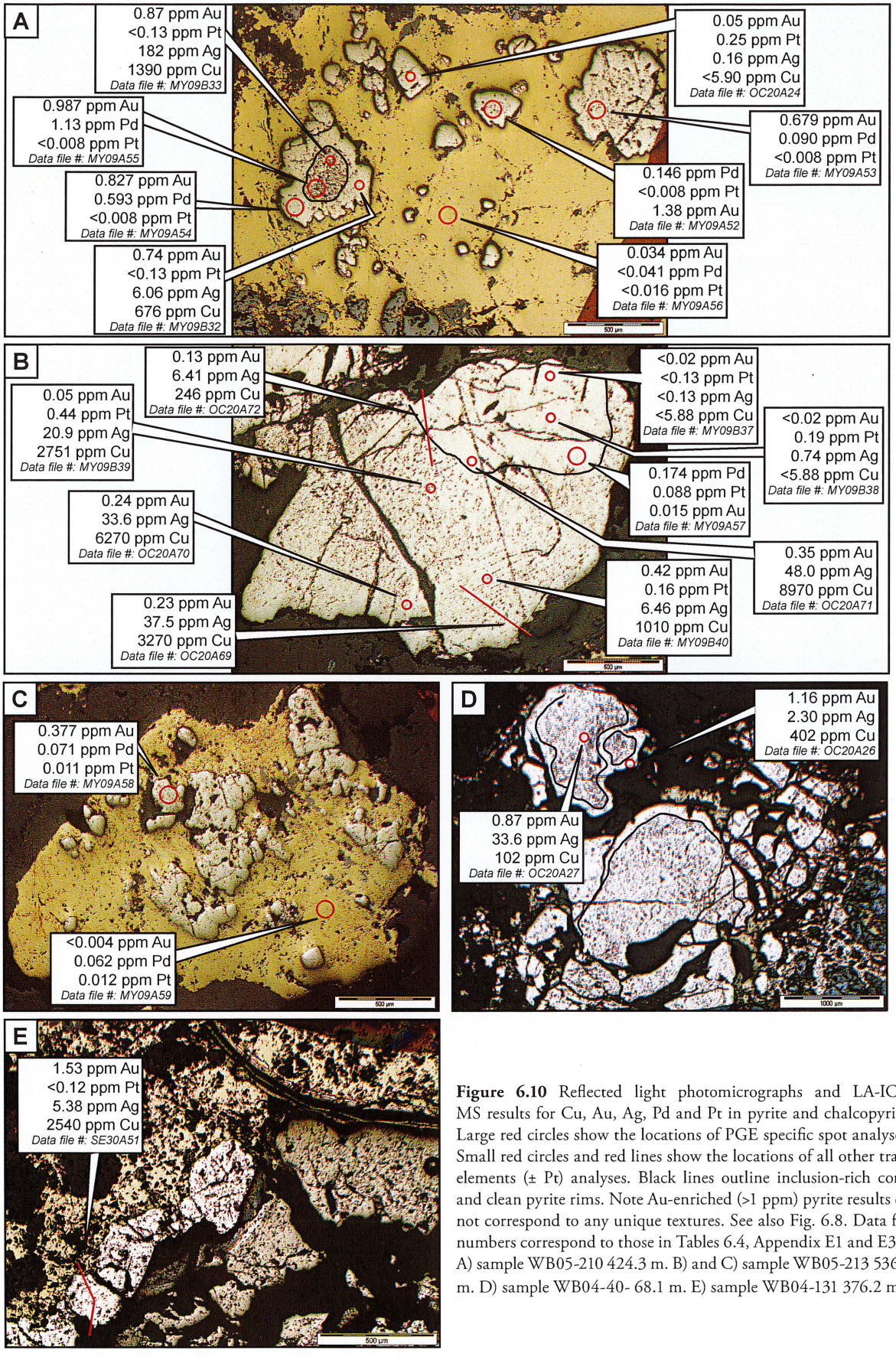

Figure 6.10 Reflected light photomicrographs and LA-ICP-MS results for Cu, Au, Ag, Pd and Pt in pyrite and chalcopyrite. Large red circles show the locations of PGE specific spot analyses. Small red circles and red lines show the locations of all other trace elements (± Pt) analyses. Black lines outline inclusion-rich cores and clean pyrite rims. Note Au-enriched (>1 ppm) pyrite results do not correspond to any unique textures. See also Fig. 6.8. Data file numbers correspond to those in Tables 6.4, Appendix E1 and E3.1. A) sample WB05-210 424.3 m. B) and C) sample WB05-213 536.8 m. D) sample WB04-40- 68.1 m. E) sample WB04-131 376.2 m.

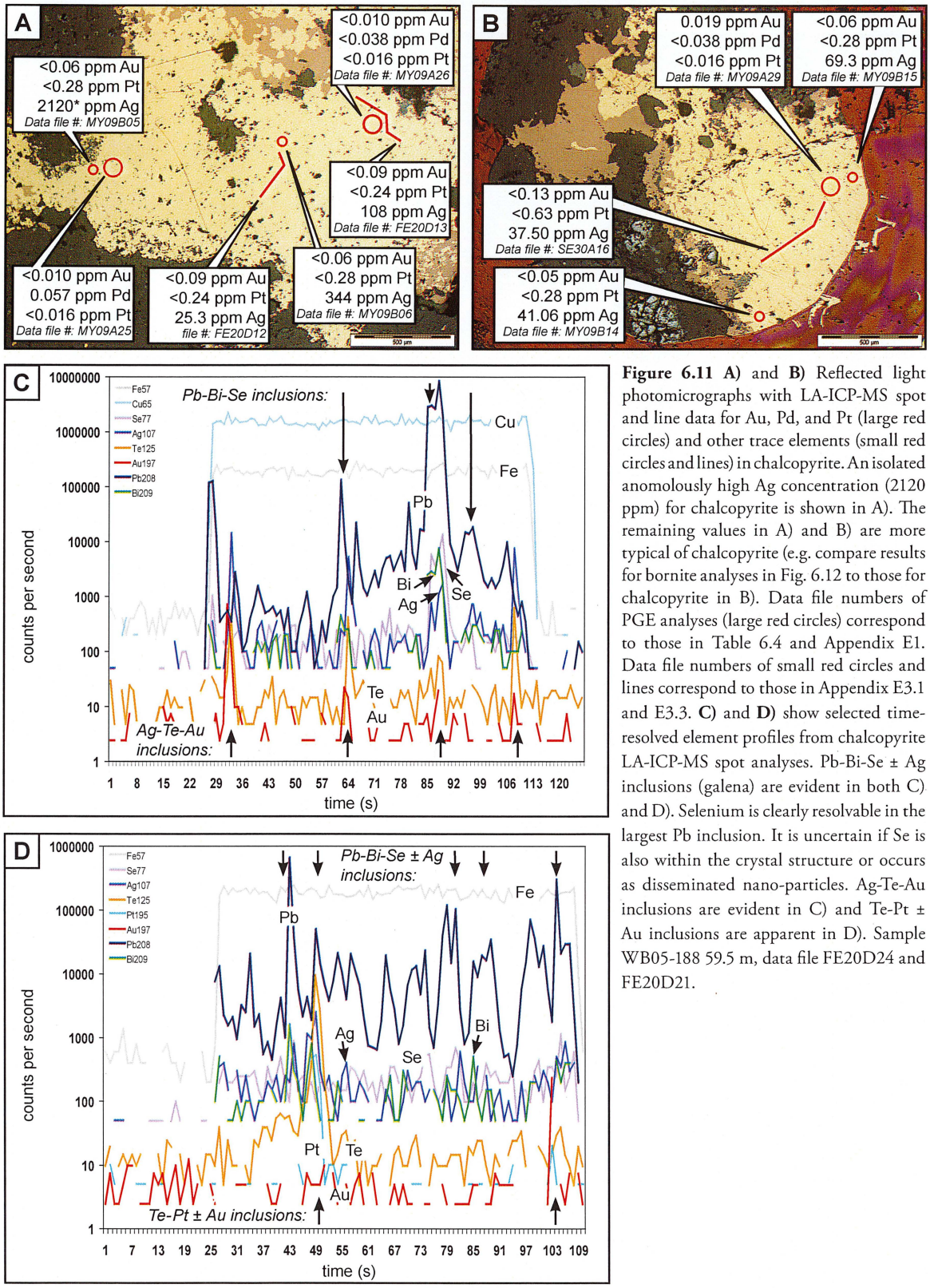

Figure 6.11 A) and **B)** Reflected light photomicrographs with LA-ICP-MS spot and line data for Au, Pd, and Pt (large red circles) and other trace elements (small red circles and lines) in chalcopyrite. An isolated anomolously high Ag concentration (2120 ppm) for chalcopyrite is shown in A). The remaining values in A) and B) are more typical of chalcopyrite (e.g. compare results for bornite analyses in Fig. 6.12 to those for chalcopyrite in B). Data file numbers of PGE analyses (large red circles) correspond to those in Table 6.4 and Appendix E1. Data file numbers of small red circles and lines correspond to those in Appendix E3.1 and E3.3. **C)** and **D)** show selected time-resolved element profiles from chalcopyrite LA-ICP-MS spot analyses. Pb-Bi-Se ± Ag inclusions (galena) are evident in both C) and D). Selenium is clearly resolvable in the largest Pb inclusion. It is uncertain if Se is also within the crystal structure or occurs as disseminated nano-particles. Ag-Te-Au inclusions are evident in C) and Te-Pt ± Au inclusions are apparent in D). Sample WB05-188 59.5 m, data file FE20D24 and FE20D21.

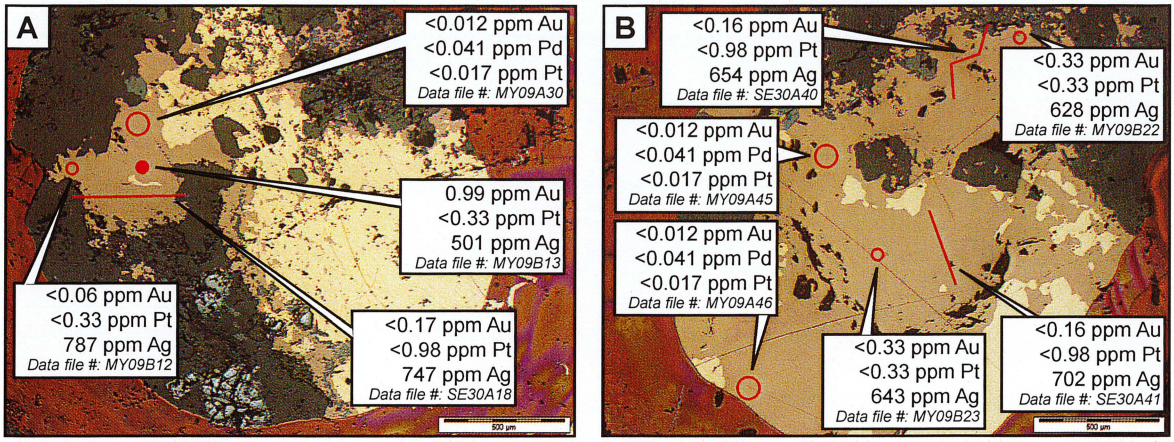

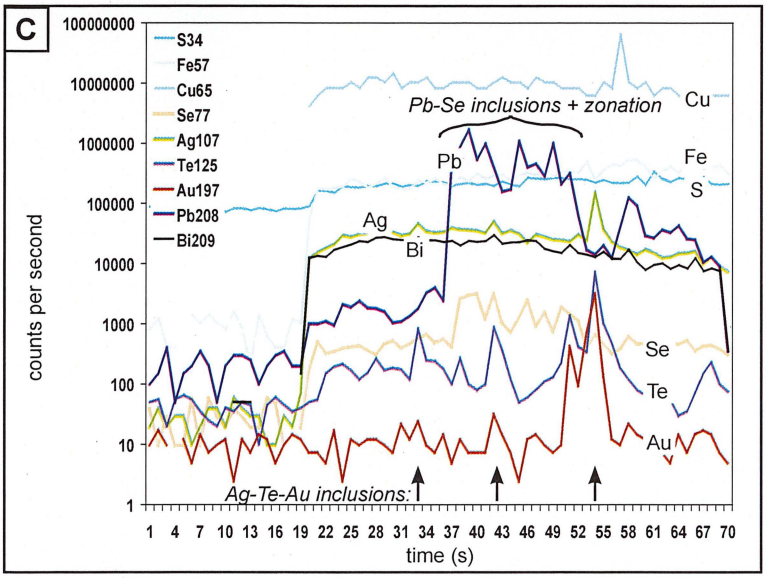

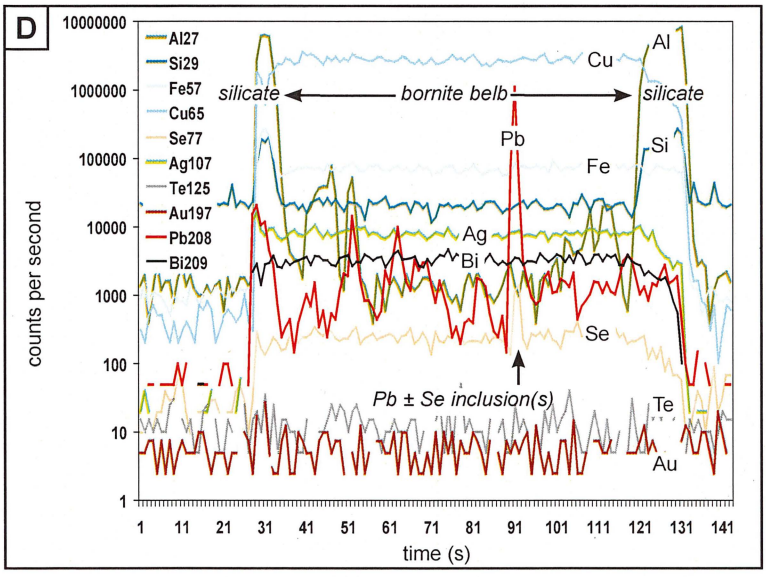

Figure 6.12 A) and **B)** Reflected light photomicrographs showing LA-ICP-MS results for Au, Pd and Pt spot analyses (large red circles) and other trace elements (small red circles and lines). LA-ICP-MS time-resolved profiles of bornite showing selected element patterns (C and D). **C)** Bornite spot analyses from the solid red spot in A). Cu, Fe, S, Ag, and Bi are interpreted to occur within the bornite crystal structure. It is uncertain if Se also occurs within the bornite structure. Se-bearing galena (see E below) inclusions are evident, as are very rare Ag-Te-Au inclusions. Sample WB04-95 35.9 m, data file MY09B13. **D)** Bornite line analyses illustrating large galena inclusions (zoned?). Selenium is resolvable in the largest galena (Pb) inclusion. Aluminum-bearing inclusions are evident within the bornite bleb. Copper, Fe, Ag, Bi and Se are interpreted to occur within the bornite structure. Tellurium and Au are at background levels within the bornite bleb. Silicon and Al are enriched in the silicate phase on either side of the bornite bleb. Sample WB04-122 311.5 m, data file SE30A39, analyses location not shown in B). Data file numbers of large red circle (PGE) analyses correspond to those in Tables 6.4 and Appendix E1. Data file numbers of small red circles and lines correspond to those in Appendix E3.1 and E3.3.

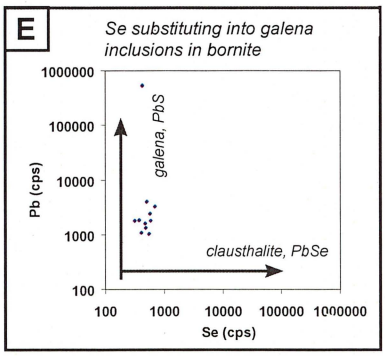

homogeneously distributed nano-particles. (Fig. 6.8F, Appendix E3). Selenium occurs primarily as inclusions in group 1 chalcopyrite. Selenium deportment is difficult to determine in group 2. Selenium counts in time-resolved profiles were near the limit for confidently identifying micro-inclusions. Precision values from spot analyses within one grain suggest Se occurs both as inclusions and is homogeneously distributed. Group 3 chalcopyrite has Se-bearing inclusions and also appears to have Se in the structure or Se-bearing nano-particles, based on mapping results and precision values (Fig. 6.7, Appendix E3). Selenium occurs in the structure or as Se-bearing nano-particles in pyrite.

Pb

Lead concentrations in sulfides can vary by up to three orders of magnitude within individual samples and also between sample locations. Overall, the values range from 0.535 to 18,800 ppm (Fig. 6.8G, Table 6.3, Appendix E3). Lead is abundant in all three minerals as micro- to macro-scale inclusions, and occurs primarily as galena (Figs. 6.6, 6.9, 6.11, 6.12). Where lead concentrations are significantly higher for one analysis compared to other analyses in a given sample, this is typically due to abundant and/or large galena inclusions. Lead concentrations (as inclusions) decrease from group 1 chalcopyrite (mean 732 ppm) to group 2 (mean 375 ppm) to group 3 (mean 33.2 ppm, Fig. 6.4, Appendix E3). LA-ICP-MS maps of Pb in pyrite (Figs. 6.5 and 6.7) and precision data suggest that Pb also occurs in the pyrite structure or as homogeneously distributed nano-particles, in addition to coarser galena inclusions, however the abundance of Pb inclusions (Figs. 6.5 and 6.7) qualifies the confidence of this interpretation.

Zn, Cd, Sn, Sb

Concentrations of Zn, Cd and to a lesser extent Sn and Sb showed marked variations between the three sulfide groups (Figs. 6.3, 6.4 and 6.14, Table 6.5). Concentrations are generally highest in group 3 pyrite and chalcopyrite, with Zn the highest, followed by Cd (pyrite: median Zn 2870 ppm, median Cd 31.8 ppm; chalcopyrite: median Zn 18560 ppm, median Cd 61.3 ppm; Fig. 6.8G and H, Table 6.3). Group 2 chalcopyrite has intermediate Zn, Cd and Sn values, when results were above detection limits. No Cd or Sb were measured above detection limits in bornite (group 1) and the lowest concentrations of Zn and Sn were observed in approximately half of the bornite (group 1) samples where these elements appear to occur as isolated mineral inclusions (Figs. 6.3 and 6.4, Table 6.3, Appendix E3). While there are abundant inclusions, Zn and Cd may also occur in the pyrite structure or as homogeneously distributed nano-particles in some samples as suggested by time-resolved profiles and precision data (Fig. 6.9A).

As, Te, Tl

Arsenic occurs as inclusions in most pyrite samples; concentrations are variable, but are low overall (median 21.2 ppm; Table 6.3). Only four chalcopyrite analyses detected As. No As was detected in bornite, with the exception of one analyses (Table 6.3, Figs. 6.3 and 6.4).

Tellurium occurs in mineral inclusions within bornite. Concentrations of Te are erratic, with only half of the analyses above the detection limit (median 2.02 ppm, maximum 353 ppm; Table 6.3; Fig. 6.3). Tellurium-bearing inclusions in chalcopyrite are present locally. In general, Te concentrations are higher in group 1 chalcopyrite and lower in group 3 chalcopyrite (Fig. 6.4). Low concentrations of Te (median 4.02 ppm; Table 6.3) were detected in most of the analyzed pyrite grains, where Te is interpreted to occur as inclusions (Fig. 6.5; Table 6.3). However, mapping and some precision data suggest low levels of homogenously distributed Te in pyrite, which may be located in the crystal structure or disseminated as nano-particles (Fig. 6.7).

With the exception of one analysis, Tl was not detected in bornite or chalcopyrite (Table 6.3). Low concentrations of Tl (<0.774 ppm) were detected in some pyrite grains.

Cu

Abundant Cu inclusions occur in pyrite, with concentrations up to 9,280 ppm (Table 6.3). LA-ICP-MS mapping has shown that Cu is also present in low concentrations either in the pyrite structure or disseminated as nano-particles (Figs. 6.5 and 6.7). The analytical precision data support the interpretation of abundant micro-scale inclusions.

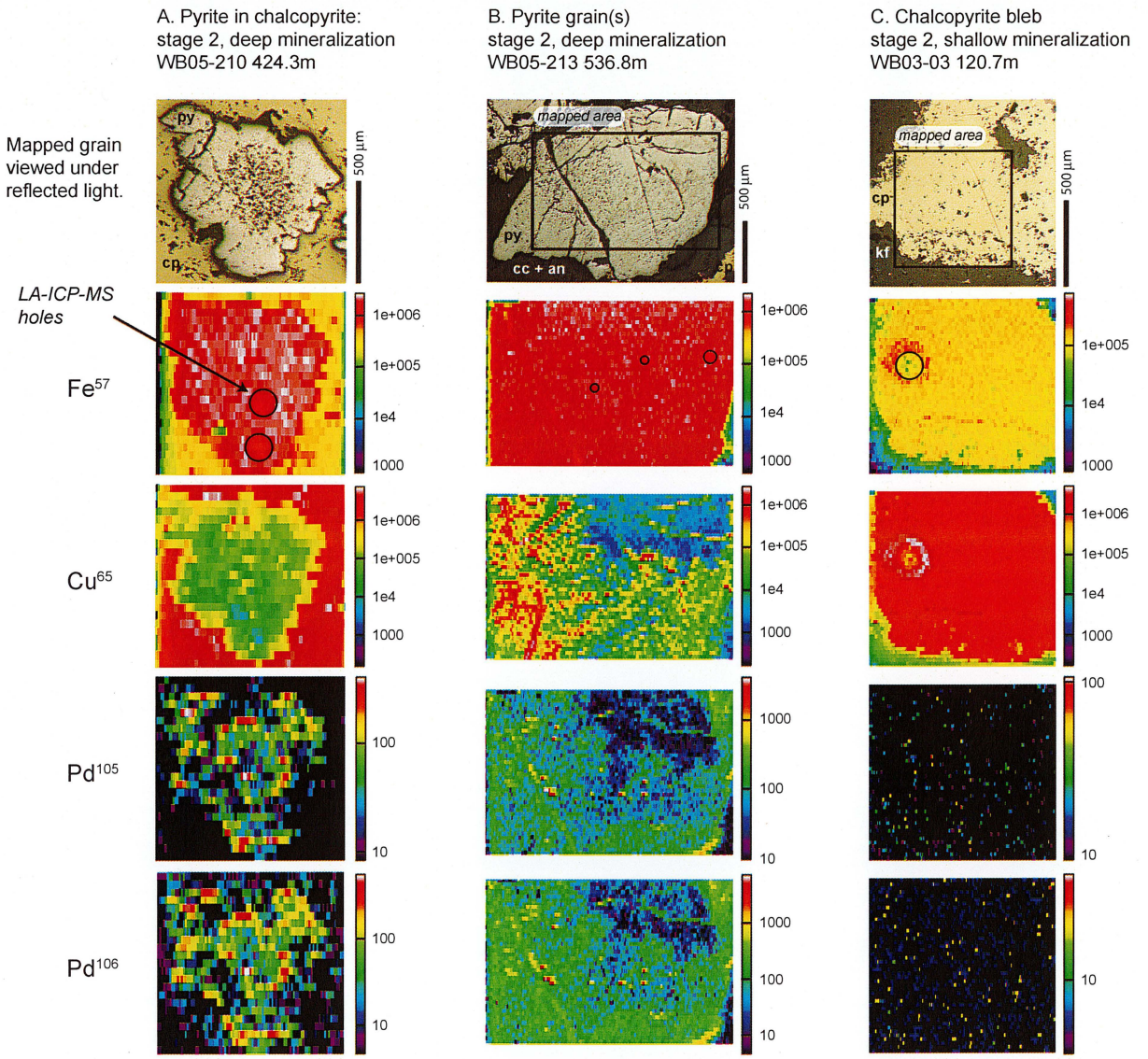

Figure 6.13 Maps of iron (Fe), copper (Cu) and palladium (Pd^{105} and ^{106}) in pyrite and chalcopyrite from LA-ICP-MS analyses. **A)** Iron and Cu show edge effects in this pyrite grain. Palladium maps are noisy (green) but Pd micro-inclusions (red) are evident in the inclusion-rich core and in the inclusion-free rims of the grain. A ring void of Pd is observed between these populations. **B)** Element patterns are not annular in this pyrite grain. Palladium inclusions are in the inclusion-rich central portion of the grain(s). Because the Pd^{105} and Pd^{106} scans correlate, the low level Pd (green) may either be Pd in the pyrite structure, or Pd as homogeneously distributed nano-particles; however, results are inconclusive. **C)** Chalcopyrite maps for Pd^{105} and Pd^{106} are noise only; they are the same magnitude as the gas background due to the higher detection limits for the mapping technique (approximately 0.4 ppm), even though spot analyses detected 0.06 ppm Pd. The Pd^{105} images have been corrected for Ar^{40}-Cu^{65} interferences; Pd^{106} images have been corrected for Cd^{106} interferences. In each map, the pixel height is determined by the beam size. A 25 µm beam was used to produce the pyrite maps and a 15 µm beam was used for the chalcopyrite map. Mineral abbreviations: py-pyrite, cp-chalcopyrite, cc-calcite, an-anhydrite, kf-K-feldspar.

6.4.3.4 Chemical element mapping results

LA-ICP-MS chemical multi-element mapping allows evaluation of element patterns within an individual mineral grain more easily than spot or line analyses (e.g. Figs. 6.5 to 6.7), although detection limits are generally higher. The following discussion focuses on spatial patterns best identified from 2D multi-element mapping at the grain scale and demonstrates the complex paragenesis of pyrite and the more homogeneous nature of chalcopyrite and bornite in the NEZ.

Examples of concentric growth zone patterns defined by pyrite trace element compositions are

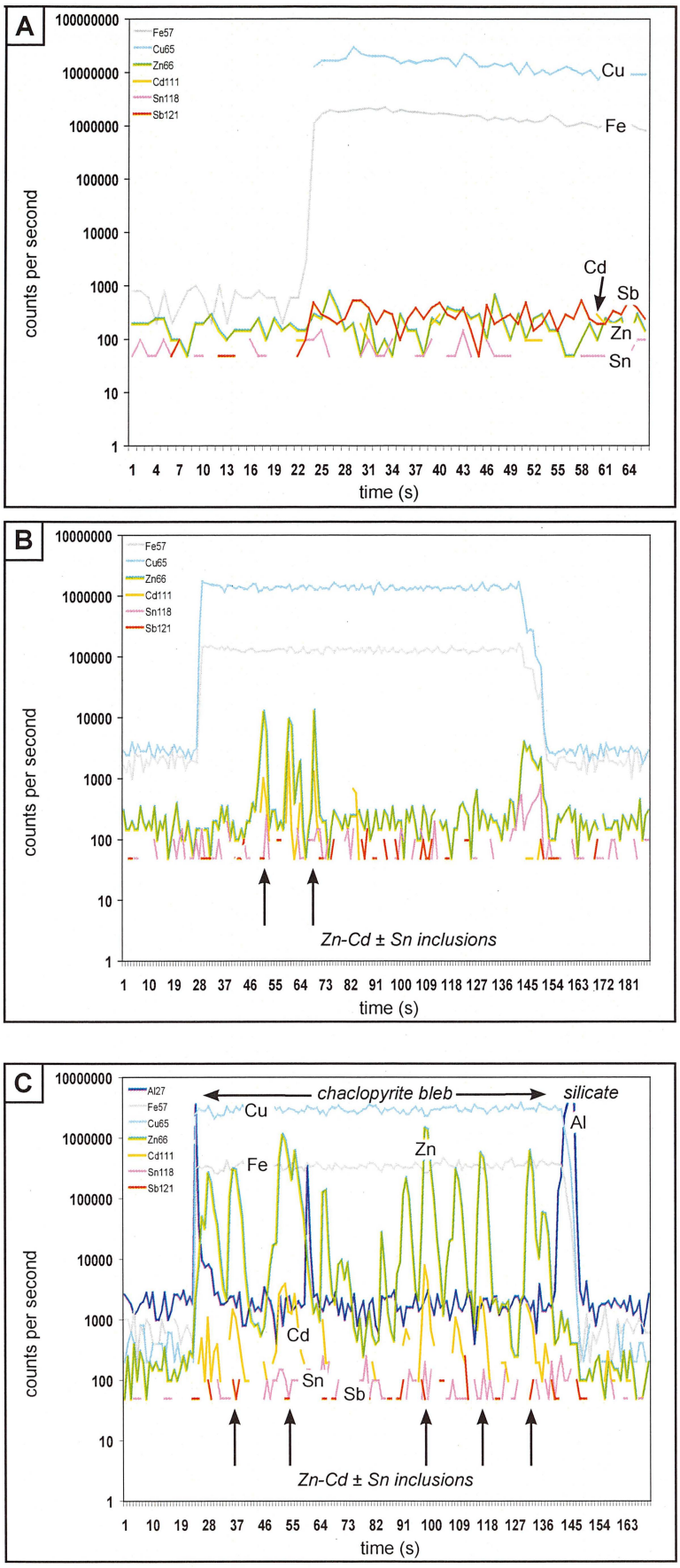

Figure 6.14 LA-ICP-MS time-resolved element profiles showing Zn, Cd, Sn and Sb element patterns for the three chalcopyrite groups as described in the text. **A)** A typical element profile for group 1 chalcopyrite in which Zn, Cd and Sn are at background levels with background levels (or limited inclusions, Appendix E3.1) of Sb. **B)** Group 2 chalcopyrite in which some samples have Zn, Cd ± Sn inclusions and Sb was not detected. **C)** Group 3 chalcopyrite where there are abundant Zn, Cd ± Sn (and Sb, not shown in this example) inclusions. A) sample WB03-03 120.7 m, data file number OC20A08, spot analysis, B) sample WB04-108 304.0 m, data file number JN04A61, line analyses, C) sample WB05-213 586.3 m, data file number OC20A86, line analysis, Tables 6.3 and Appendix E3.1.

shown in Figures 6.7 and 6.13A. The Mg, Al, Mn ± Si inclusion-rich pyrite cores are also relatively enriched in Co, As, Ag, Pb Bi ± Pd. An inner ring, surrounding the core, is composed of similar elements, but also with pronounced relative Ni ± Te enrichment. A domain of relative trace element depletion separates an outer ring from the inner ring; only low levels of Co, Ni, Cu, Te Se ± Pb and a distinct absence of As are observed in this depleted domain. The outer ring is relatively enriched in Co. Low levels of Co, Cu, Zn, Se, Te, Au, Pb ± Ag and Bi are evident throughout most of the pyrite grain, either substituted in the pyrite structure or occurring as abundant, evenly distributed nano-particles. Abundant Zn- and Cd-bearing inclusions are evident in pyrite (and chalcopyrite) as are lesser inclusions of Pb and an isolated Au-Ag inclusion.

Based on the images shown in Figures 6.7 and 6.13, a detailed paragenesis for stage 2 pyrite, from core to outer rim, is listed below. Note that color bars in multi-element maps (i.e. Fig. 6.7) cannot be used to compare concentrations between different elements as the scales are relative to each individual element's highest and lowest concentration. However, within one element map, where an element occurs in more than one location, the highest concentration for that element is **bold** and marked by (***), an intermediate concentration for that element is marked by (**) and (*) is a lower concentration. An example is shown in Figure 6.7B.

Core: **As** (***), **Bi** (***), Co (**), **Ag** (**), **Pb** (**), **Zn** (*), Te (*), Au, Se, Cu, ± Pd and Mg, Al, Mn, Si inclusions

Inner ring: **Ni** (***), **Bi** (***), Co (**), **Te** (**), **Pb** (**), As (*), **Cd** (*), ± Pd, Cu, Au, Se

Depleted zone: Co (*), Ni (*), Te (*), Pb (*), Se, Cu

Outer ring: **Co** (***), Ni (**), Bi (**), **Zn** (*), As (*), Ag (*), **Cd** (*), Te (*), Pb (*), Pd, Se, Au

At least two stages of pyrite growth are apparent in Figure 6.5 and 6.13B. An area in the upper right corner of the pyrite grain (Figs. 6.5 and 6.13B) is enriched in Fe, Co and Ni ± Pt. The remainder of the grain has a more homogeneous distribution of Ni, Cu, Zn, Ag, Cd, Pb and Bi ± Pd, although a thin outer rim enriched in Co, As, Mo, Te, Au ± Ag and Sn is evident. These asymmetrical patterns for Co, Se and Pt distribution have been confirmed by mapping the same grain twice (Appendix E7).

Chalcopyrite and bornite have relatively homogeneous compositions compared to the mapped pyrite samples (compare Figs. 6.7, 6.5 and 6.13 to Fig. 6.6). In Figure 6.6, the Cu-Fe sulfides can readily be distinguished based on their elevated Ag and Bi contents. No appreciable amounts of Co, As, Ni or Mo were detected in bornite or chalcopyrite.

6.5 Discussion

6.5.1 Element deportment and associations

Trace elements can occur as stoichiometric and non-stoichiometric substitutions for elements in a crystal structure (i.e. Fe, Cu, S in sulfides) and as nano- to micro-sized mineral inclusions within the host mineral (Huston et al., 1995). Many sulfide minerals undergo changes in the solid state to relatively low temperatures, forming intergrowth textures produced by exsolution or unmixing of elements (Craig and Vaughan, 1990). Pyrite is one of the minerals that is most likely to retain evidence of its original depositional conditions, whereas chalcopyrite readily changes composition during cooling (Barton and Skinner, 1979). Bornite also undergoes exsolution during cooling from high temperatures to surface conditions where only the composition Cu_5FeS_4 is stable. During the exsolution process, all excess Fe or Cu, as well as the contents of minor metals dissolved at high temperatures, are exsolved as metal and/or sulfides (Makovivky, 2006).

Only limited work has been published on trace elements in bornite, other than the occurrence and deportment of Au. Silver and Bi were detected in bornite, as well as an abundance of exsolved phases, notably chalcopyrite (Cu), pyrrhotite, cobalt pentlandite (Co, Ni), carrollite (Co, Ni), wittichemite (Bi), galena (Pb), mawsonite (Sn), Ag, and electrum (Au, Ag), by Cook and Ciobanu (2001) at the Ocna de fier-Dognecea skarn deposit. These minerals were interpreted as high-T exsolution from an impurity-rich precursor. Bornite from three southwestern North America porphyry deposits

Table 6.6 Ionization potential of manganese, siderophile, and chalcophile elements considered in this study. Values taken from Railsback (2003).

Element	Ionic charge	Ionic radius (Å)	Ionic potential	Possible subsitution
Elements in sulfide structure				
Fe	+ 2	0.76	2.6	n/a
Fe	+ 3	0.64	4.7	n/a
Cu	+ 1	0.96	1.0	n/a
Cu[1]	+ 2	0.69	2.9	Fe^{+2}?
S	- 1	0.53	-1.9	n/a
S	- 2	1.84	-1.1	n/a
Siderophile elements + Mn				
Mn	+ 2	0.8	2.5	Fe^{+2}
Mn	+ 3	0.64	4.7	Fe^{+3}
Mn	+ 4	0.53	7.5	x[2]
Co	+ 2	0.74	2.7	Fe^{+2}
Co	+ 3	0.63	4.8	Fe^{+3}
Ni	+ 2	0.72	2.8	Fe^{+2}
Ni	+ 3	0.73	4.1	x
Mo	+ 4	0.68	5.9	x
Mo	+ 6	0.62	9.7	x
Pt	+ 2	0.96	2.1	x
Pd	+ 2	0.86	2.3	x (Fe^{+2}?)
Au	+ 1	1.37	0.7	Cu^{+1}?
Au	+ 3	0.85	3.5	x
Chalcophile elements				
Zn	+ 2	0.74	2.7	Fe^{+2}
As	- 3	2.22	-1.4	x (S^{-2}?)
As	+ 5	0.47	10.6	x
As	+ 3	0.69	4.3	x (Fe^{+3}?)
Se	+ 6	0.42	14.3	x
Se	+ 4	0.5	8.0	x
Se	- 2	1.98	-1.0	S^{-2}
Ag	+ 1	1.26	0.8	Cu^{+1}
Cd	+ 2	0.97	2.1	x
Sn	+ 4	0.71	5.6	x
Sn	+ 2	1.12	1.8	x
Sb	+ 5	0.62	8.1	x
Sb	- 3	2.45	1.2	S^{-2}
Sb	+ 3	0.9	3.3	x
Te	+ 6	0.56	10.7	x
Te	- 2	2.21	-0.9	S^{-2}
Te	+ 4	0.89	4.5	Fe^{+3}
Tl	+ 1	1.4	0.7	Cu^{+1}?
Tl	+ 3	0.95	3.2	x
Pb	+ 2	1.2	1.7	x
Pb	+ 4	0.84	4.8	Fe^{+3}
Bi	+ 3	1.2	2.5	Fe^{+2}
Bi	+ 5	0.74	6.8	x
Bi	- 2	-	-	-[3]
Bi	- 3	-	-	-[3]

[1] Cu^{+2} is not found experimentally in chalcopyrite or bornite (Goh et al., 2006).

[2] An "x" indicates subsitition based on ionic potential is unlikely.

[3] The only bismuthide minerals are of Pd, Ag, Pt, Au and Pb.

(Ajo, Misson and Bisbee) were found to contain high values of Au (~4 ppm) and Ag (>250 ppm) together with elevated Tl, Se and Te. However, element deportment was not mentioned (Titley and Ruiz, 2005). Simon et al. (1997) reported that Se can be accommodated in the bornite structure.

The trace element contents of chalcopyrite are highly variable (Titley and Ruiz, 2005). While only trace amounts of Te, Ag, Au, Pt, Pd and Sb have been reported from chalcopyrite, it is can contain significant quantities of Zn and Sn, and also Co, Ni, Ag, Mn which can substitute for Cu and/or Fe. Selenium and As can substitute for S in the chalcopyrite structure (Craig and Vaughan, 1990; Huston et al., 1995; Cook and Ciobanu, 2001; Taseska et al., 2008). In addition to these trace element substitutions, Huston et al. (1995) observed Pb-, Bi-, Zn(?)- and Ba-bearing inclusions in chalcopyrite from unmetamorphosed and weakly metamorphosed VHMS deposits.

Pyrite can contain an abundance of trace elements (Craig and Vaughan, 1990; Huston et al., 1995; Large et al., 2007; Deditius et al., 2009b). Nickel, Co and Mn are known to occur as major solid solution stoichiometric substitutions for Fe, whereas Se and Te can substitute in significant concentrations for S (Craig and Vaughan, 1990; Huston et al., 1995). Arsenic, Tl, Au, Sb, Bi and possibly Mo occur as non-stoichiometric substitutions in pyrite (Craig and Vaughan, 1990; Huston et al., 1995; Large et al., 2007). Gold is known to occur in the pyrite lattice at concentrations of up to 110 ppm (Cook and Chryssoulis, 1990; Scaini et al., 1998) as well as micro- to nano-scale inclusions (Arif and Baker, 2004; Reich et al., 2005). Huston et al. (1995) found that Cu, Zn, Pb, Ba, Bi, Ag and Sb occurred mainly as inclusions in pyrite from unmetamorphosed and weakly metamorphosed VHMS deposits.

The concept of ionic potential (IP = ionic charge ÷ ionic radius) was used by Railsback (2003) to group ions with similar ionic potential, in part to help explain trace element substitution behavior. Table 6.6 lists the elements analyzed in this study, their ionic charge(s) as commonly found in geology, their radii and ionic potential. While trace element substitution in sulfide minerals is complicated, ionic potential can be used as a first order approximation to assist in determining

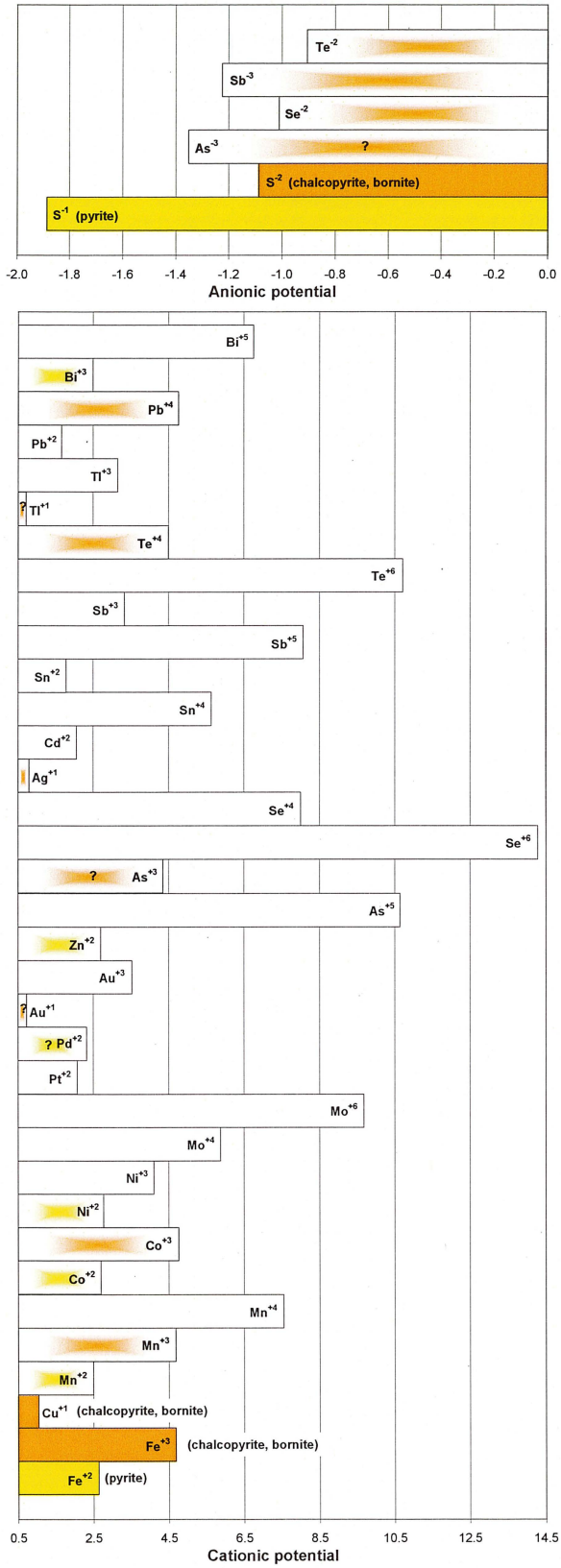

Figure 6.15 Graphic representation of ionic potentials from Table 6.6. Ions are color-coded by mineral: orange (chalcopyrite and bornite) and yellow (pyrite). Solid colors are ions in the three sulfides. Shaded colors represent possible element substitutions based on similar ionic potential value for the matching solid color.

possible trace element substitutions. The ionic charges of Fe and S in pyrite are +2 and -1, respectively. Experiments conducted by Goh et al. (2006) and Pearce et al. (2006) have shown that the oxidation states of Cu and Fe are +1 and +3, respectively, and S is -2, in both chalcopyrite and bornite.

Ions of Ag^{+1}, Se^{-2} and possibly Te^{-2} are likely to substitute into the bornite structure because their ionic potentials are close to those of Cu^{+1}(Ag), and S^{-2} (Se, Te; Table 6.6, Figure 6.15). Similarly, these ions could occur as stoichiometric substitutions in chalcopyrite; although it is clear from concentration values (Table 6.3, Appendix E3) that Ag^{+1} preferentially substitutes into bornite over chalcopyrite, at least in the NEZ. The occurrence of $Ag^{+1}$and Se^{-2} in the structure of bornite and chalcopyrite is generally consistent with observations in this study. However, Te was found to occur as inclusions in all three sulfide minerals in this study. This may have been caused by exsolution or unmixing of Te during cooling.

Based on the ionic potential of bismuth (Bi^{+3}), pyrite would be predicted to be enriched in this element. But in the NEZ, Bi is most abundant in bornite, not pyrite. Precision values, time-resolved element profiles and element mapping indicate that Bi occurs in the bornite structure or as evenly distributed nano-particles. Given that Ag and Pb are also elevated in bornite, submicroscopic inclusions of Ag-Pb-bismuthides are also postulated to occur disseminated throughout bornite.

Stoichiometric substitutions of Co^{+2}, Ni^{+2} and Mn^{+2} for Fe^{+2} in pyrite are well established (Craig and Vaughan, 1990; Huston et al., 1995). These substitutions, which were also observed in the current study, are consistent with the similar ionic potentials of these elements (Table 6.6, Figure 6.15).

The ionic potentials of As^{+5}, Cd^{+2}, Sn^{+2}, Sn^{+4}, Pb^{+2}, Pt^{+2}, $Au^{+3} \pm Pd^{+2}$, $\pm Au^{+1}$ are dissimilar to those of Fe^{+2} and Cu^{+1} supports the observation of these minerals primarily as inclusions in the NEZ Fe ± Cu sulfides. The ionic potentials of Au^{+1} and Pd^{+2} are similar, but not very close to that of Cu^{+1} (see Fig. 6.15) and this could explain why Au and Pd occur both as inclusions and possibly as stoichiometric substitutions within pyrite. Although non-stoichiometric substitutions are known to occur (e.g. As, Au, Tl; Huston et al., 1995), these cannot

be evaluated by simply comparing ionic potential.

In addition to the primary exsolution of mineral inclusions during cooling, as mentioned above, Huston et al. (1995) and Large et al. (2007) attributed the presence of inclusions in pyrite to "cleaning" or "purifying", during hydrothermal or metamorphic recrystalization. This effect is particularly evident for elements that occur mainly as inclusions or as non-stoichiometric substitutions, but did not appear to effect stoichiometrically substituted elements (Huston et al., 1995). Large et al. (2007) asserted that Au, Cu, Pb and Zn (amongst others) are loosely held elements in the pyrite structure or occur as submicroscopic mineral inclusions. These elements may be easily liberated from pyrite via recrystallization and locally redistributed during post-depositional processes as discrete microscopic sulfide phases (Large et al., 2007). The observation of Zn primarily as inclusions in pyrite, chalcopyrite ± bornite from the NEZ is not consistent with the simple assumption that ionic potential controls substitution behavior, because the ionic potential of Zn^{+2} is similar to that of Fe^{+2}. It may be that Zn was redistributed within NEZ sulfides by post-mineralization processes. This could also account for the abundance of galena inclusions in all three sulfide minerals, which are also variably enriched in Ag, Bi, Se and Te throughout the NEZ and sphalerite (Zn, Cd ± Sn ± Sb) inclusions observed in chalcopyrite and pyrite.

Gold in the NEZ sulfides is associated with Te and Ag ± Bi, Pb, and Se. Arsenic is associated with Au, Te ± Ag. Solitary Au inclusions are rare (Table 6.5). Figure 6.8B–D show that there is no dominant correlation between Au and As, Te or Ag, although Au-Ag appear to have the highest Au concentrations, including one outlier of >100 ppm Au.

The results of multi-element mapping of PGEs in pyrite from the NEZ (Figs. 6.5 to 6.7 and 6.13) shows that Pd-Te-Ni-Bi-Co ± Au ± As and Pt-Bi-Te ± As are the common PGE element associations in pyrite. These results suggest that sub-microscopic Pd-telluride or Pd-bismuthide minerals occur in pyrite (Figs. 6.7 and 6.13). The former is consistent with observations from other alkalic deposits in British Columbia (Nixon and Laflamme, 2002; Nixon et al., 2004). In order to confirm these element associations, additional line analyses or mapping, with only selected elements (i.e Pd with Pt, Te, Pb, Bi, Sb, As, Se) to maintain low detection limits, would be required. The occurrence of Pd as inclusions and in solid solution in pyrite is consistent with the findings of Nixon et al. (2004) who noted that pyrite may be significantly enriched in PGEs relative to other sulfides in some alkalic deposits of British Columbia. However, Nixon (2004) found that bornite and chalcopyrite were the preferred hosts for PGEs in the Afton alkalic porphyry deposit.

LA-ICP-MS analyses of pyrite from the NEZ have highlighted complex element zonation patterns within individual sulfide grains (e.g. Figs. 6.6 and 6.7). Detailed investigations typically reveal considerable heterogeneity (e.g. Campbell and Larson, 1998), which implies that hydrothermal processes can change rapidly and may represent cyclic changes in chemical conditions and/or fluid composition during precipitation. Deditius et al. (2009a) studied the trace elements in pyrite from high-sulfidation Au-Ag deposits and concluded that the element zonation observed most likely reflected changes in the fluid composition rather than substitution possibilities in the pyrite. This may also be the case in the NEZ.

6.5.2 Deposit-scale metal zonation

Metal zonation occurs at the deposit-scale in the NEZ. Results of LA-ICP-MS analyses show that the zonation patterns of several elements are consistent with the macro-scale zonation patterns (Figs. 4.5 to 4.7). Figures 6.16 to 6.21 show the relative concentrations of selected elements (Pb, Bi, Ag, Te, Se, Co, Ni, Zn, Cd, Au, Pt, As) detected in sulfides across the long-section. Spatial patterns are best defined in the deep breccia-hosted ore zone (Figs. 6.16 to 6.21). Lead, Ag and Bi are most abundant in sulfides from the ore zones (groups 1 and 2 bornite and chalcopyrite), with Bi and Ag preferentially occurring in bornite and Pb in chalcopyrite (Figs. 6.16A, B and 6.22B). Zinc and Cd are most abundant in group 3 pyrite and chalcopyrite on the edge or outboard of the deep breccia-hosted ore zone (Fig. 6.17A and B). Cobalt, Ni, Au and As are found primarily in pyrite outboard of the deep breccia-hosted ore zone (Figs. 6.18 and 6.19). Tellurium and Se occur in sulfides throughout the deposit, but their abundances and mineral affinities are erratic (Fig. 6.20). Platinum

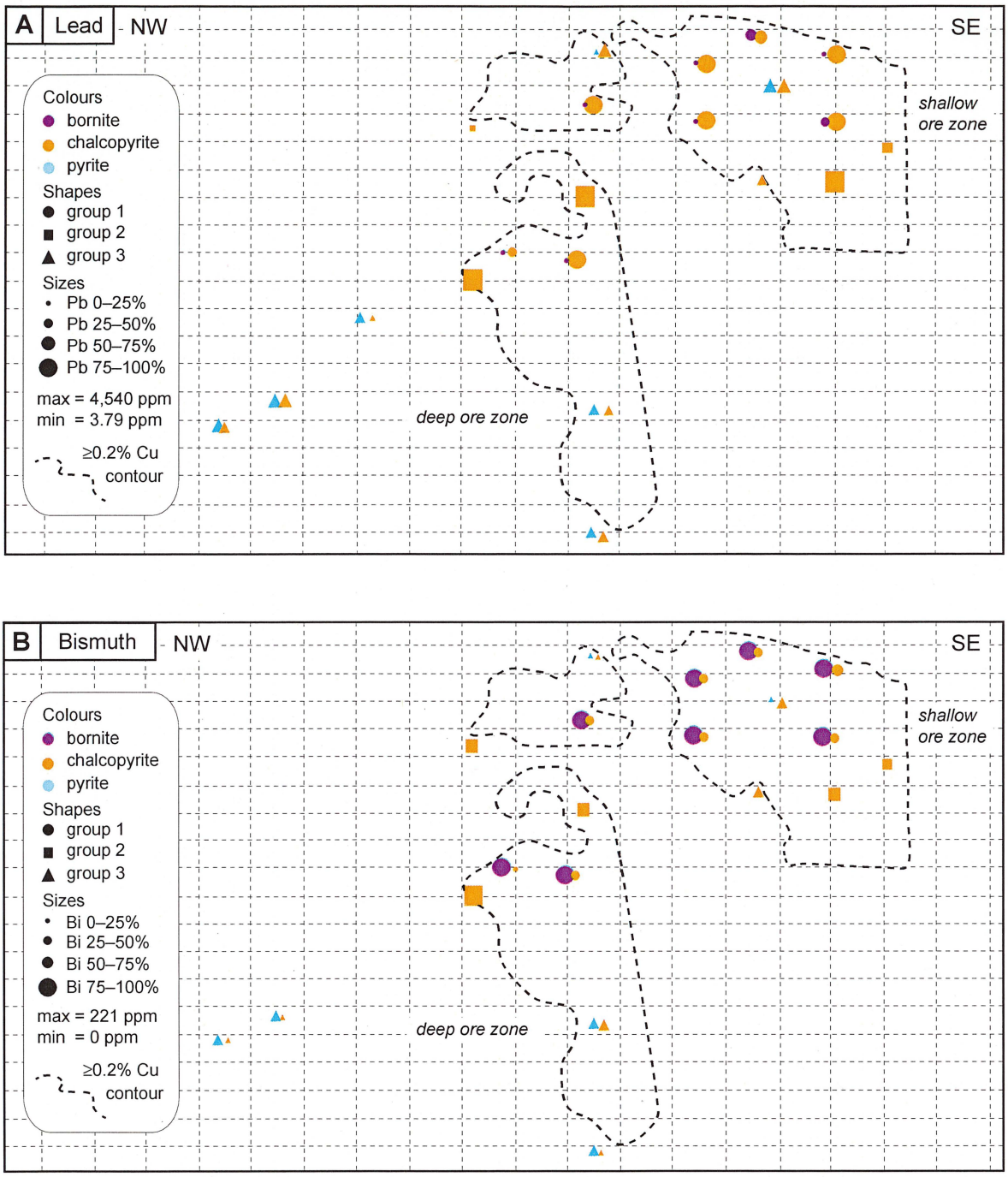

Figure 6.16 NEZ long-section showing the spatial distribution and relative abundance maps of **A)** Pb and **B)** Bi in bornite, chalcopyrite and pyrite as determined from LA-ICP-MS analyses. For both maps colors indicate mineral species, shape indicates group number, and abundance, expressed as percentage of the data, is indicated by relative size. Median values for each sample are plotted. The full data set is provided in Appendix E3.1, summarized in Table 6.3. Where a data value was less than the detection limit, a value of zero was given to emphasize only real data. Maps were produced using ioGAS (version 3.2). Bismuth and Pb are found in varying abundance throughout the deposit in pyrite, chalcopyrite and bornite. The highest Bi concentrations are found in bornite (group 1) and group 2 chalcopyrite. Lesser amounts are found in group 1 chalcopyrite and pyrite (group 3). Chalcopyrite (group 3) has the least amount of Bi. Lead is predominantly found in chalcopyrite of groups 1 and 2. Group 1: bornite and chalcopyrite present, Group 2: chalcopyrite only, Group 3: pyrite and chalcopyrite present.

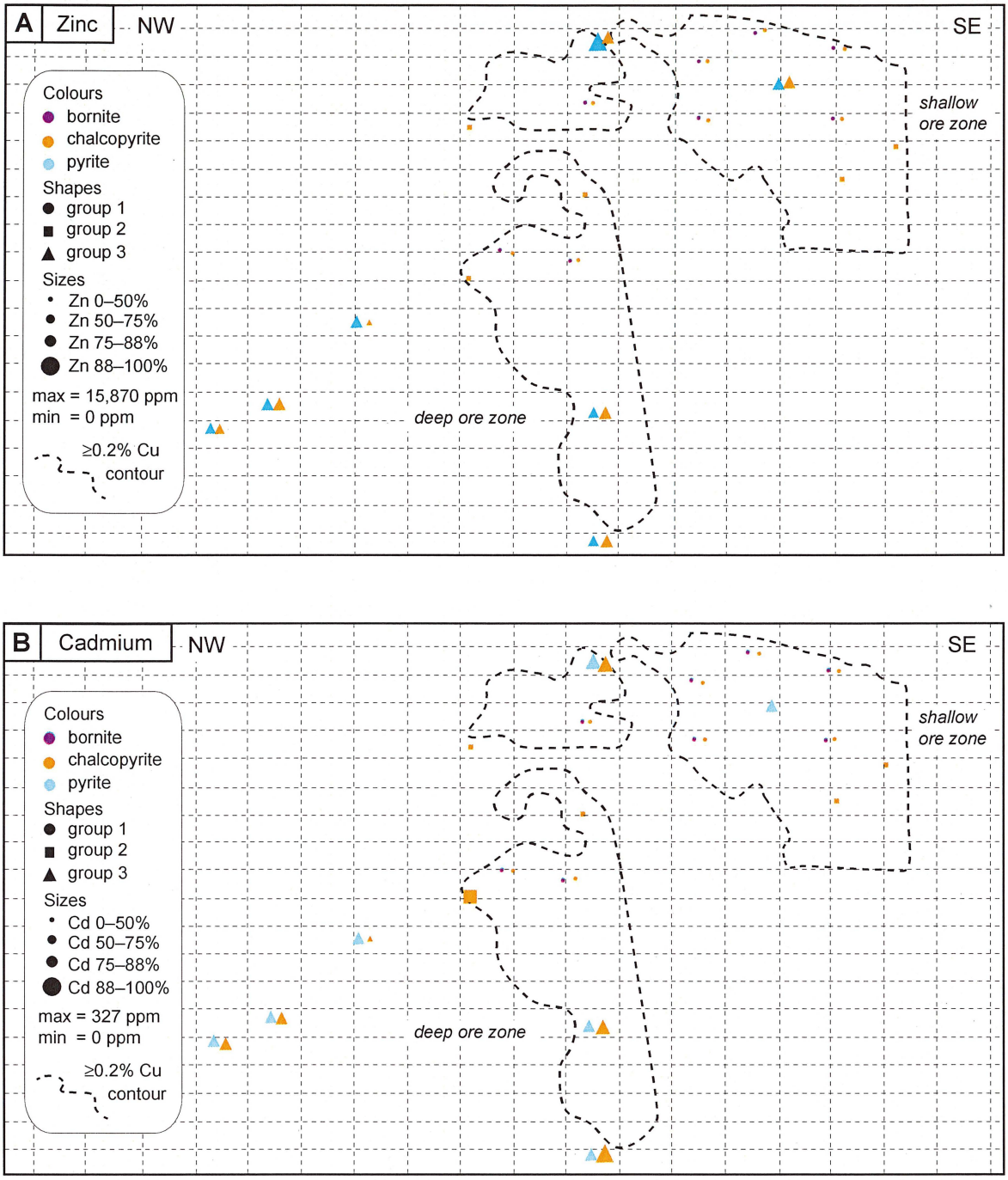

Figure 6.17 NEZ long-section showing the spatial distribution and relative abundance maps of **A)** Zn and **B)** Cd in bornite, chalcopyrite and pyrite as determined from LA-ICP-MS analyses. For both maps colors indicate mineral species, shape indicates group number, and abundance, expressed as percentage of the data, is indicated by relative size. Median values for each sample are plotted. The full data set is provided in Appendix E3.1, summarized in Table 6.3. Where a data value was less than the detection limit, a value of zero was given to emphasize only real data. Maps were produced using ioGAS (version 3.2). Bismuth and Pb are found in varying abundance throughout the deposit in pyrite, chalcopyrite and bornite. Zinc and Cd have similar spatial patterns and are found in locations where pyrite and chalcopyrite occur together (group 3), primarily on the edge or outboard of the ore zones. Group 1: bornite and chalcopyrite present, Group 2: chalcopyrite only, Group 3: pyrite and chalcopyrite present.

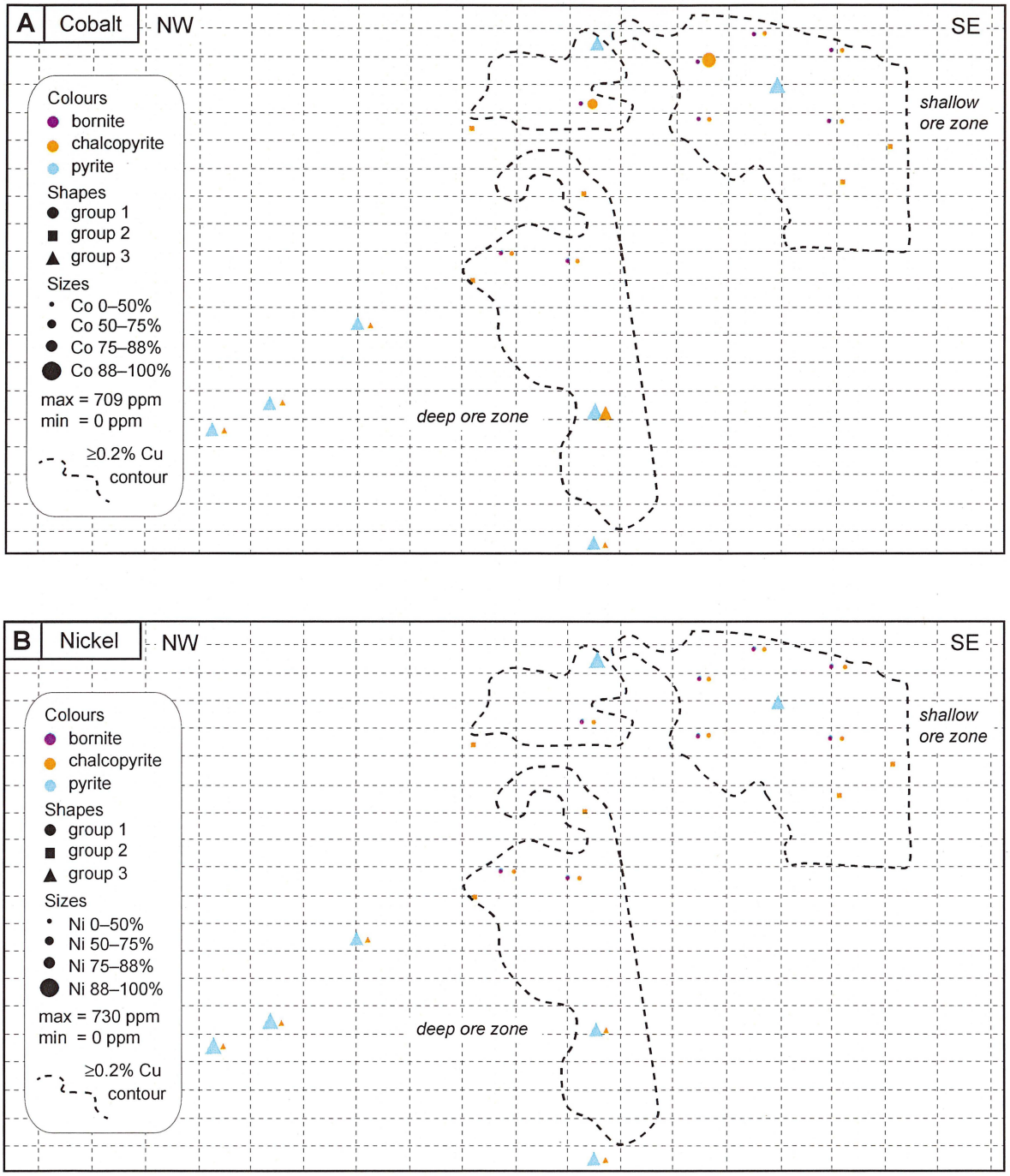

Figure 6.18 NEZ long-section showing the spatial distribution and relative abundance maps of **A)** Co and **B)** Ni in bornite, chalcopyrite and pyrite as determined from LA-ICP-MS analyses. For both maps colors indicate mineral species, shape indicates group number, and abundance, expressed as percentage of the data, is indicated by relative size. Median values for each sample are plotted. The full data set is provided in Appendix E3.1, summarized in Table 6.3. Where a data value was less than the detection limit, a value of zero was given to emphasize only real data. Maps were produced using ioGAS (version 3.2). Cobalt and Ni are most abundant in pyrite (group 3), where pyrite is located outside of the deep ore zone and in pockets in the shallow ore zone. Group 1: bornite and chalcopyrite present, Group 2: chalcopyrite only, Group 3: pyrite and chalcopyrite present.

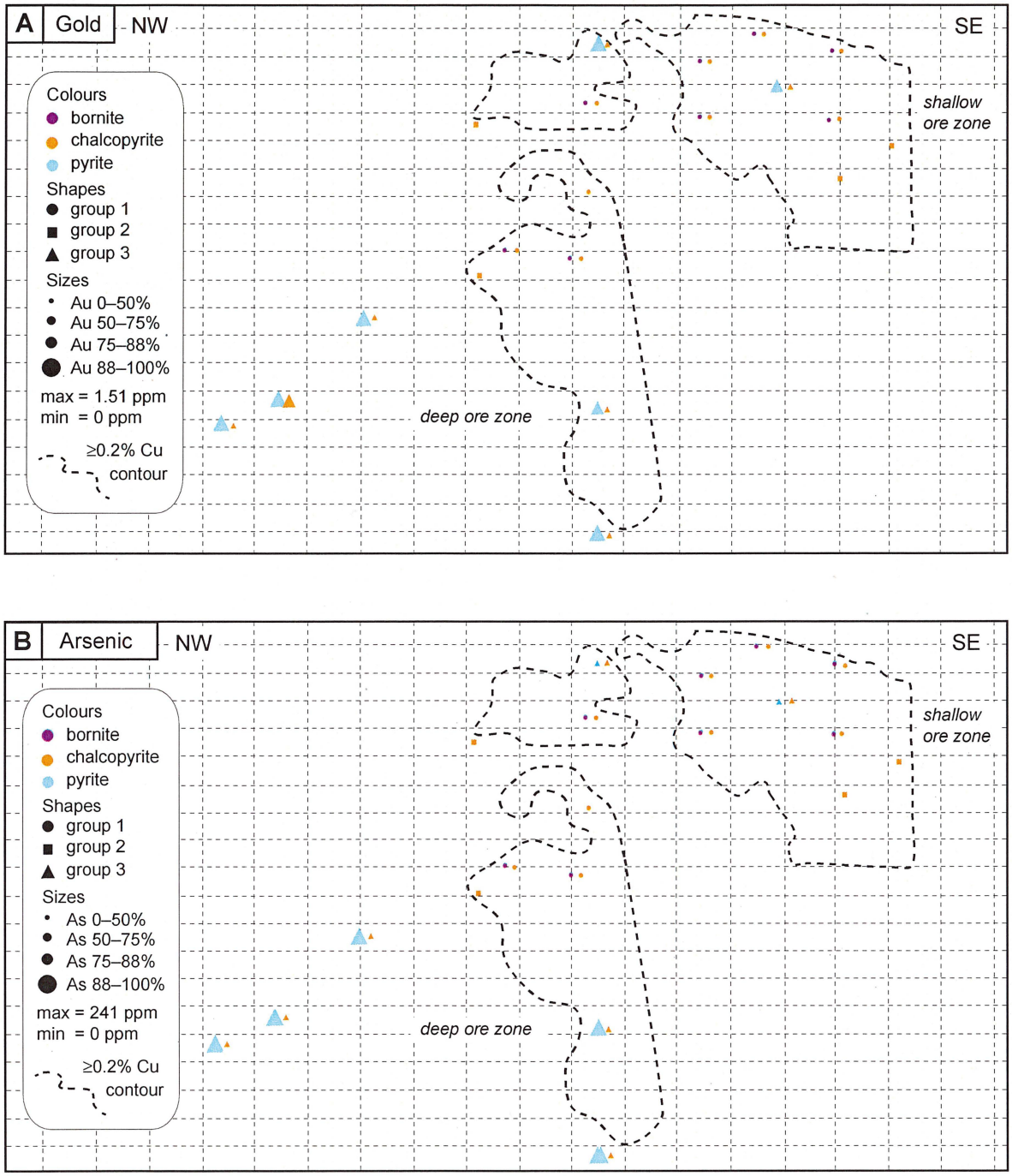

Figure 6.19 NEZ long-section showing the spatial distribution and relative abundance maps of **A)** Au and **B)** As in bornite, chalcopyrite and pyrite as determined from LA-ICP-MS analyses. For both maps colors indicate mineral species, shape indicates group number, and abundance, expressed as percentage of the data, is indicated by relative size. Median values for each sample are plotted. The full data set is provided in Appendix E3.1, summarized in Table 6.3. Where a data value was less than the detection limit, a value of zero was given to emphasize only real data. Maps were produced using ioGAS (version 3.2). All pyrite (group 3) samples contain Au. Pyrite is primarily found on the edges of the deep ore zone and in pockets in the shallow ore zone. While overall As concentrations are low, As can be found in pyrite predominantly located outside of the deep ore zone. Group 1: bornite and chalcopyrite present, Group 2: chalcopyrite only, Group 3: pyrite and chalcopyrite present.

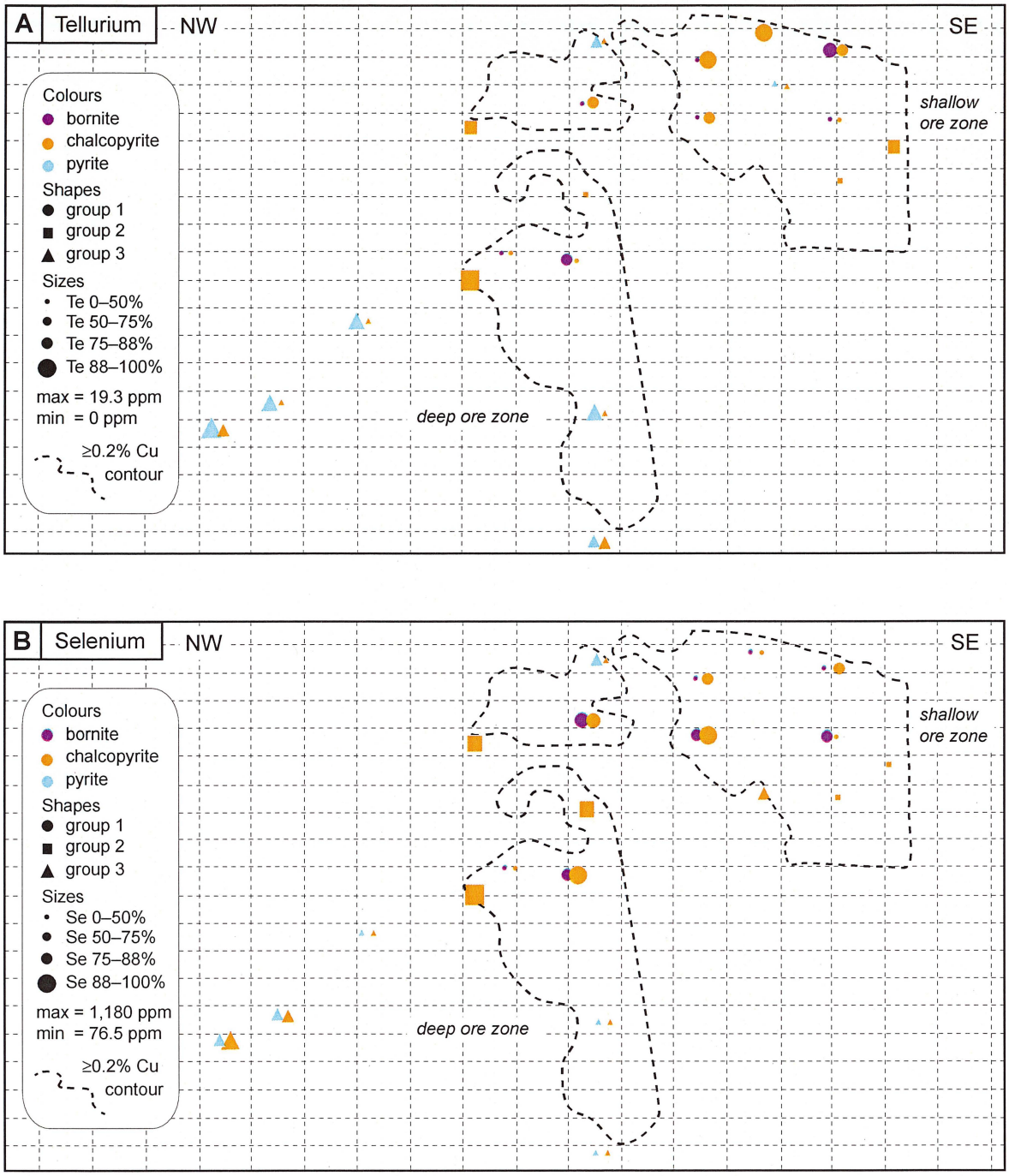

Figure 6.20 NEZ long-section showing the spatial distribution and relative abundance maps of **A)** Te and **B)** Se in bornite, chalcopyrite and pyrite as determined from LA-ICP-MS analyses. For both maps colors indicate mineral species, shape indicates group number, and abundance, expressed as percentage of the data, is indicated by relative size. Median values for each sample are plotted. The full data set is provided in Appendix E3.1, summarized in Table 6.3. Where a data value was less than the detection limit, a value of zero was given to emphasize only real data. Maps were produced using ioGAS (version 3.2). Tellurium and Se can be found across the deposit but abundance and mineral affinity are erratic. Group 1: bornite and chalcopyrite present, Group 2: chalcopyrite only, Group 3: pyrite and chalcopyrite present.

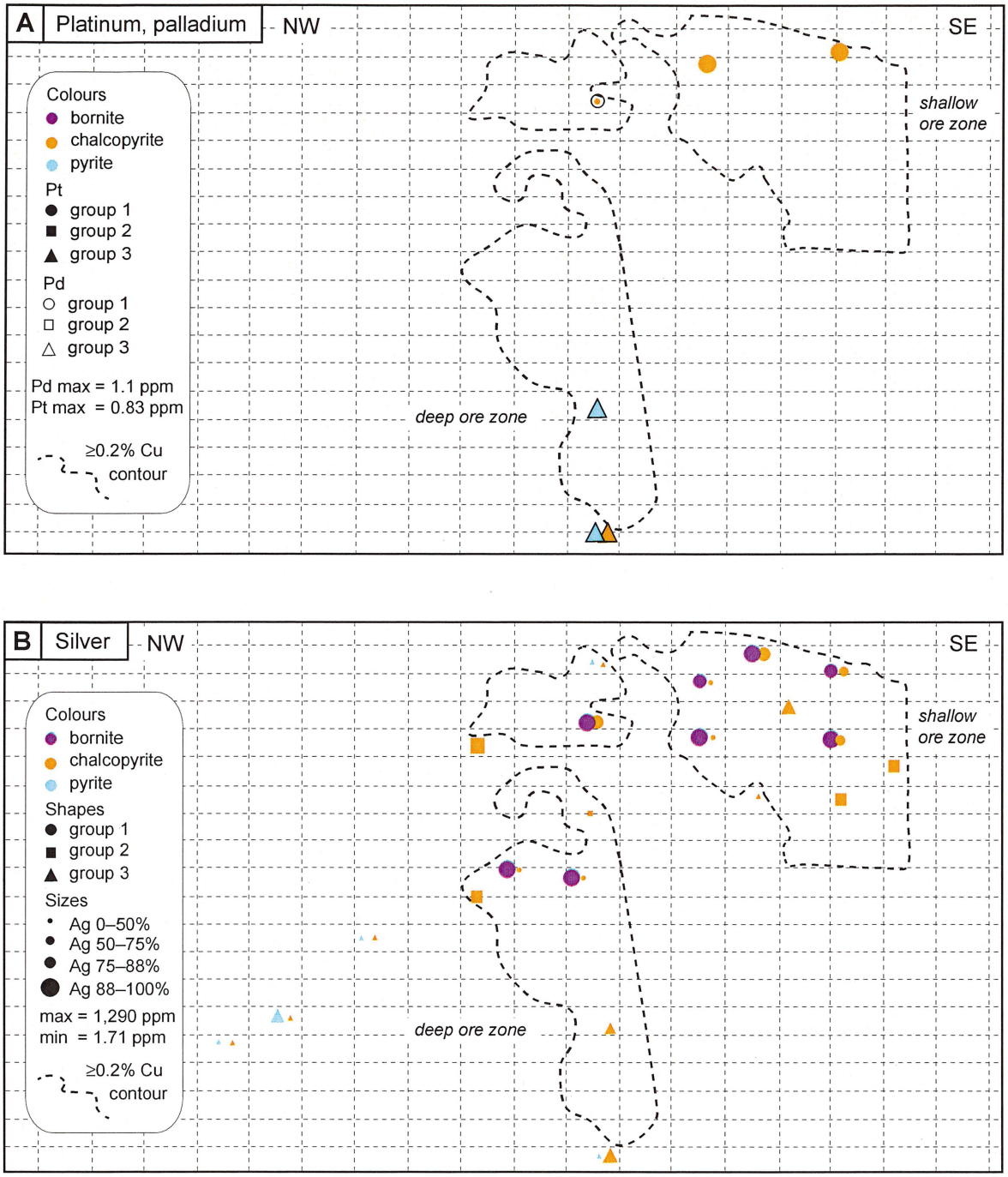

Figure 6.21 NEZ long-section showing the spatial distribution and relative abundance maps of **A)** Pt and Pd and **B)** Ag in bornite, chalcopyrite and pyrite as determined from LA-ICP-MS analyses. Note not all sample locations were analyszed for Pd. For both maps colors indicate mineral species, shape indicates group number, and abundance, expressed as percentage of the data for Ag, is indicated by relative size. For the Pt and Pd maps a solid filled shape indicates the mineral group number for Pt, a black outlined shaped indicates the mineral group number for Pd. Median values for each sample are plotted. The full data set is provided in Appendices E1 and E3.1, summarized in Tables 6.3 and 6.4. Where a data value was less than the detection limit, a value of zero was given to emphasize only real data. Maps were produced using ioGAS (version 3.2). Limited samples contain Pd and Pt were in the shallow and deep breccia-hosted domain. The highest concentrations occured in pyrite. Silver is most abundant in bornite ± chalcopyrite associated with high-grade ore in the shallow and deep breccia-hosted zones. Group 1: bornite and chalcopyrite present, Group 2: chalcopyrite only, Group 3: pyrite and chalcopyrite present.

and Pd were identified in limited samples within the shallow and deep ore zones, as well as just outside the deep breccia-hosted ore zone (Fig. 6.21A).

Metal zonation patterns in porphyry deposits have been described by many workers (e.g. Emmons, 1927; Sillitoe, 1988; Jones, 1992). Within an idealized gold-enriched porphyry system, from the center of the system outwards, there may be: 1) a barren (or subeconomic) core, 2) a Mo zone, 3) bornite, 4) chalcopyrite, 5) pyrite halo, 6) Pb-Zn-Ag and 7) distal Au-As-Hg-Sb-Te (epithermal; Jones, 1992; Cooke et al., 1998). Gold typically occurs: 1) in the center of the system, where it is associated with highest Cu grades, 2) within an "intermediate zone" that lies outside of the Cu zone, commonly associated with Pb-Zn-Ag, and largely coincident with the pyrite halo and 3) in some cases in distal locations, several kilometers away from the porphyry center (Emmons, 1927; Jones, 1992). Although these generalized zoning relationships appear to pertain to many porphyry deposits, each individual deposit can display unique uncommon variations.

Metals in the NEZ are zoned, similar to other to other porphyry deposits (Fig. 1.6). Based on the results of LA-ICP-MS analyses of sulfides from the NEZ, trace element enrichments and depletions in sulfides appear to also define broad zonation patterns in the NEZ, although the patterns are asymmetric. As can be seen in Figures 6.16 to 6.21, spatial patterns are clearer for the deep breccia-hosted ore zone than for the shallow ore zone. A summary of the sulfide metal zonation found in and around the deep breccia-hosted ore zone of the NEZ is provided in Fig. 6.22, where it is compared to the classic zonation pattern of Emmons (1927).

The NEZ has a core where sulfides are enriched in Fe, Cu and Bi (Figs. 4.5, 6.16B and 6.22). Zinc and Au occur on the edges of the Cu-rich center in the deep breccia-hosted ore zone (Figs. 4.6, 6.17A and 6.22). These patterns are similar to the model of Emmons (1927). Notable differences include the abundance of Ag and Pb with little to no Au in the sulfides from the core of the deep breccia-hosted ore zone (Figs. 4.6, 4.7 and 6.16A, 6.19A, 6.21B) and therefore the NEZ zonation from sulfides is most comparable to the second "intermediate zone" Au domain listed above, as the gold lies outside of the main bornite-bearing Cu zone, but

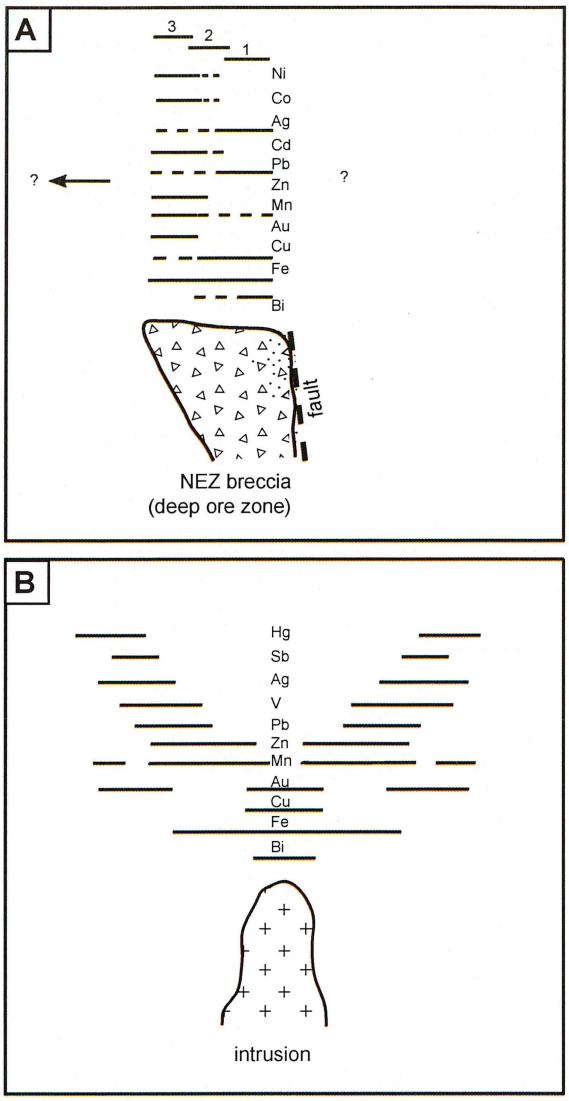

Figure 6.22 A) Metal zoning in the lower NEZ ore zone based on elements enriched in bornite, chalcopyrite and pyrite as detected by LA-ICP-MS. Numbers (1–3) correspond to the approximate zones for each mineral group. Group 1: bornite and chalcopyrite present, Group 2: chalcopyrite only, Group 3: pyrite and chalcopyrite present. **B)** Classical hypogene metal zoning in porphyry deposits from Jones (1992) after Emmons (1927). Two Au zones are shown, central and peripheral. The peripheral Au zone overlaps with Zn (± Pb) zones, as in the NEZ. Note Hg and V were not included in NEZ LA-ICP-MS analyses and Cd, Co and Ni have been added to A).

lacks the Pb. However, this result is not consistant with Au zonation patterns from assay data (Fig. 4.6) that correlate with bornite (Fig. 4.2), in the shallow breccia-hosted domain.

6.5.3 Au in porphyry deposits

Sillitoe (1979) defined Au-rich porphyry deposits as those containing >0.4 g/t. Kirkham and Sinclair (1955) included Cu in the definition and defined Au-rich porphyries as those with Au (g/t):Cu (wt %) ratios greater than 1:1. More recently, Kesler et al. (2002) defined Au-rich deposits as those having a Cu:Au atomic ratio of less than 40,000. Table 6.7 lists resources and Cu:Au atomic ratios for each of the currently active and past-producing zones of Mt. Polley. While Cu and Au concentrations vary across the Mt. Polley Complex, as a whole, values are 0.290 g/t Au, 0.340 weight percent Cu and the atomic Cu:Au ratio is 36,338. Therefore Mt. Polley can only be classified as an Au-rich deposit using the definition of Kesler et al. (2002). Specifically, the NEZ cannot be classified as a high-Au deposit by any classification, but instead is classified as a porphyry Cu-Au deposit.

Table 6.7 Proven and probable reserves for the ore zones of Mt. Polley together with calculated Cu:Au atomic ratios.

Mt. Polley producing zones	Proven and probable reserves (tonnes ore)	Cu (wt %)	Au (g/t)	Atomic Cu:Au
Currently producing zones[1]				
NEZ	785,362	0.730	0.209	108,256
Springer	39,233,777	0.336	0.270	38,570
Pond	1,372,216	0.476	0.270	54,641
Southeast	1,752,306	0.274	0.513	16,554
C2	3,006,923	0.295	0.446	20,500
Mt. Polley	46,150,584	0.340	0.290	36,338
Past-producing zones[2]				
Cariboo + Bell	27,700,000	0.330	0.560	18,264

[1] Data for currently producing zones are from the Imperial Metals Corp. news release of March 30, 2009 (www.imperialmetals.com/s/News'-2009).

[2] Data from Graham (2003).

A close correlation between hypogene Au and Cu grades in potassic alteration zones of a number of porphyry copper deposits has been well documented (Sillitoe, 1979; Seward, 1984; Sillitoe, 1988; Jones, 1992). Within this potassic domain, bornite is reported as the preferred gold host. Examples include Granisle (Cuddy and Kesler, 1982), North Parkes (House, 1994), Ridgeway (Wilson, 2003), and Batu Hijau (Arif and Baker, 2004). Studies of Au solubilities in sulfide minerals by Cygan and Candela (1995), Gammons and Williams-Jones (1997), Simon et al. (1999; 2000) and Kesler et al. (2002) support field observations that bornite is the preferred host for Au in many porphyry Cu-Au deposits.

The NEZ differs from other ore zones in the Mt. Polley Complex in its high bornite content, and possibly from most other porphyry Cu-Au deposits in its Au and Ag deportment. In the Central Zone of the Mt. Polley Complex (Fig. 2.6), only trace amounts of bornite were observed and fine native Au inclusions were associated with chalcopyrite and magnetite (Hodgson et al., 1976; Fraser, 1994). Compared to the Central Zone, Bailey (2004) attributed the NEZ Cu- and Au-enrichment to the presence of bornite in addition to chalcopyrite. However, mineral specific, micro-scale LA-ICP-MS data from this study show that in the 21 samples analyzed from across the long-section, gold in the NEZ is preferentially hosted in pyrite within chalcopyrite ± chalcopyrite, not bornite. Despite the large difference in scale from the LA-ICP-MS data, bulk mine assay data of 2.5 m intervals, including all sulfides present as well as sulfide distribution observations on the long-section, may support the LA-ICP-MS conclusions, at least in the deep breccia-hosted domain. Figures 4.17 and 6.23 show that the ≥0.2% Cu ore shells are within the potassic alteration assemblage on the long-section and in areas dominated by Cu-Fe sulfides, similar to most porphyry Cu-Au deposits. However, Cu and Au are only weakly correlated compared to Cu and Ag (Fig. 6.24A and B). Figure 6.23 also shows that within the deep breccia-hosted domain, Au is most abundant along the edge of the ≥0.2% Cu ore shell and is not coincident with areas that are dominantly bornite-rich. Additionally, Figure 6.25 shows that elevated Ag assay data are coincident with areas enriched in bornite on the long-section. These observations are consistent with the LA-ICP-MS results from this study that bornite is enriched in Ag and lacks Au while and pyrite ± chalcopyrite are enriched in Au.

However, in comparing Figures 6.19A and 6.23 there is a disconnect in the LA-ICP-MS and assay data sets in the shallow breccia-hosted zone. High-grade Au domains in the shallow breccia-hosted zone are coincident with areas of enriched bornite and chalcopyrite cement. This infers that Au is hosted in a non-sulfide phase,

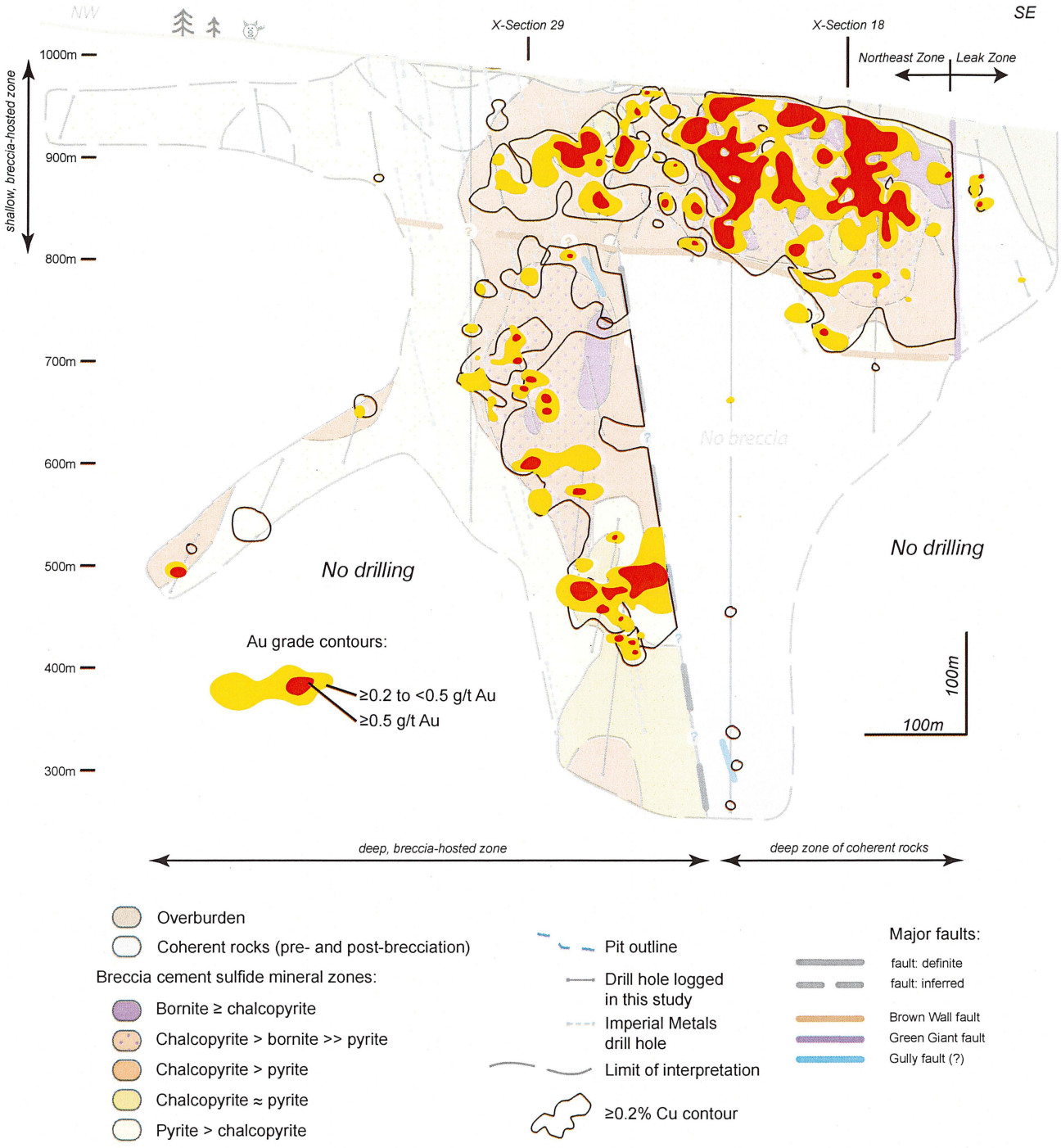

Figure 6.23 Gold grade contours determined from Imperial Metals whole rock assay data taken from all boreholes on section overlain on the sulfide mineral distribution of stage 2 breccia cement. The ≥0.2% Cu contour has been outlined in solid black. Gold enrichment is located on the margins of the the deep, breccia-hosted ore zone and in the shallow breccia-hosted ore zone.

possibly minute electrum grains or a silicate phase in the shallow breccia-hosted zone.

Much of the Au in porphyry Cu deposits is inferred to be precipitated with Cu from chloride-rich fluids of magmatic origin (Sillitoe, 1988). Chloride complexing of Au ($AuCl_2^-$) is favored in solutions of high-temperature (>300°C), high-salinity, and very low reduced sulfur concentrations or in fluids of

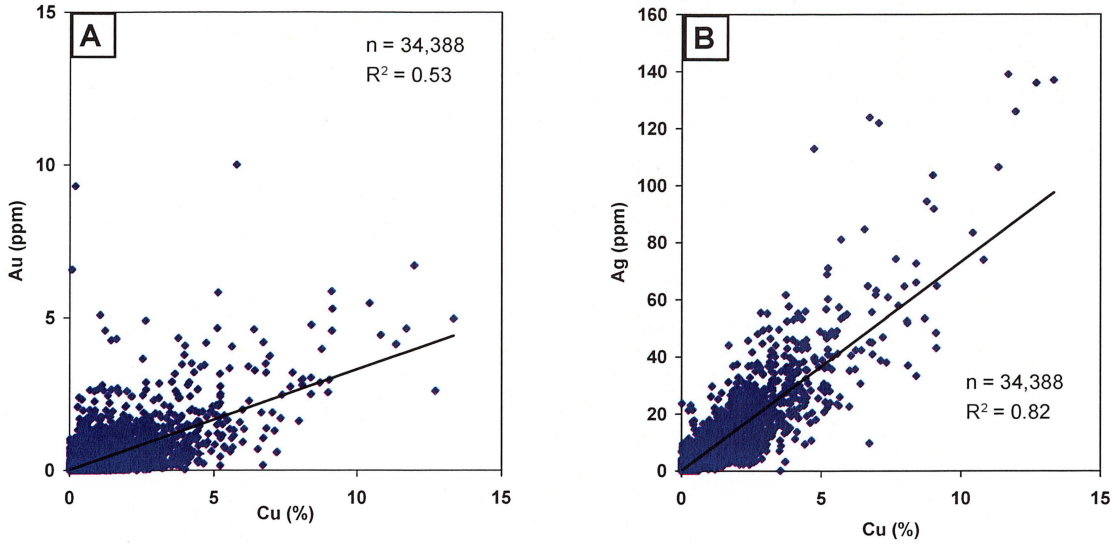

Figure 6.24 Bivariant plots showing **A)** Cu:Au and **B)** Cu:Ag ratios for the NEZ. Data taken from Imperial Metals Corporation whole rock data from the NEZ up to and including 2005. There is good correlation between Ag and Cu assays B), however, Au and Cu are only weakly correlated A). The weak correlation is interpreted to be at least in part due to the occurrence of Au in pyrite on the outer edges of the deep ore zone and in pockets of the shallow ore zone.

elevated oxidation potential (Seward, 1984), similar to conditions interpreted for the NEZ. Simon et al (1999) showed that bornite can contain one order of magnitude more Au in solid solution than chalcopyrite or the intermediate solid solution (ISS; the high-temperature form of chalcopyrite; Simon et al., 1999). Furthermore, they found that the amount of Au that can occur in bornite and chalcopyrite/ISS decreased with decreasing temperature, from 1280–8212 ppm Au in bornite at 600°C to 13–80 ppm Au in bornite at 400°C (Simon et al., 1999). Gold chloride complexes are destabilized below 300°C, which may define the outer edge of the intermediate Au zone that lies between the Cu and Pb-Zn zones of Jones (1992). Below 300°C, the transport of Au as $Au(HS)_2^-$ is favored in solutions of high α_{H2S} or α_{HS^-} and of neutral to alkaline pH (Seward, 1984) as bisulfide becomes a more efficient complexing ligand for Au than chloride (Huston and Large, 1989). Experiments by Seward (1973) have also shown that at temperatures from 300° to 160°C and in the presence of a pyrite-pyrrhotite redox buffer, gold is also soluble as thio complexes at acid (pH = 4) to alkaline (pH = 9.5) conditions. Maximum solubilities were obtained at neutral pH. Gold may be deposited from these cooler fluids by any mechanism that destabilizes the bisulfide or thio complex, including boiling, pH, temperature, pressure, redox and total sulfur concentration changes (Seward, 1973; Huston and Large, 1989; Cooke and Simmons, 2000). Lower temperature conditions can result in Au being deposited in association with chalcopyrite and pyrite, although in lower abundances than with bornite (Scaini et al., 1998; Simon et al., 2000). Experimental studies conducted at 25°C and 90°C have shown that more Au will precipitate with pyrite in near-neutral conditions (pH = 6) than at acidic conditions (pH = 3; Scaini et al., 1998). Such conditions may occur on the edges of porphyry deposits where assemblages are rock buffered (Seedorff et al., 2005).

Gold in Au-enriched porphyry Cu deposits may be susceptible to remobilization and distribution late in the cooling history (Mutschler et al., 1991; Jones, 1992). If the deposit has been affected by late-stage, lower temperature phyllic alteration, the presence of H_2S in the fluids may cause Au to dissolved and then to redeposit on the surfaces of all sulfide minerals, including pyrite, thus erasing the apparent Au-bornite association seen in unmodified porphyry deposits (Scaini et al., 1998; Simon et al., 1999). In this scenario, Au could be particularly abundant in chalcopyrite-pyrite-bearing phyllic alteration (Kesler et al., 2002). An alternate interpretation is that Au in these types of deposits is primarily introduced during phyllic-stage alteration (e.g. Hedenquist et al., 1998). The NEZ lacks the textural

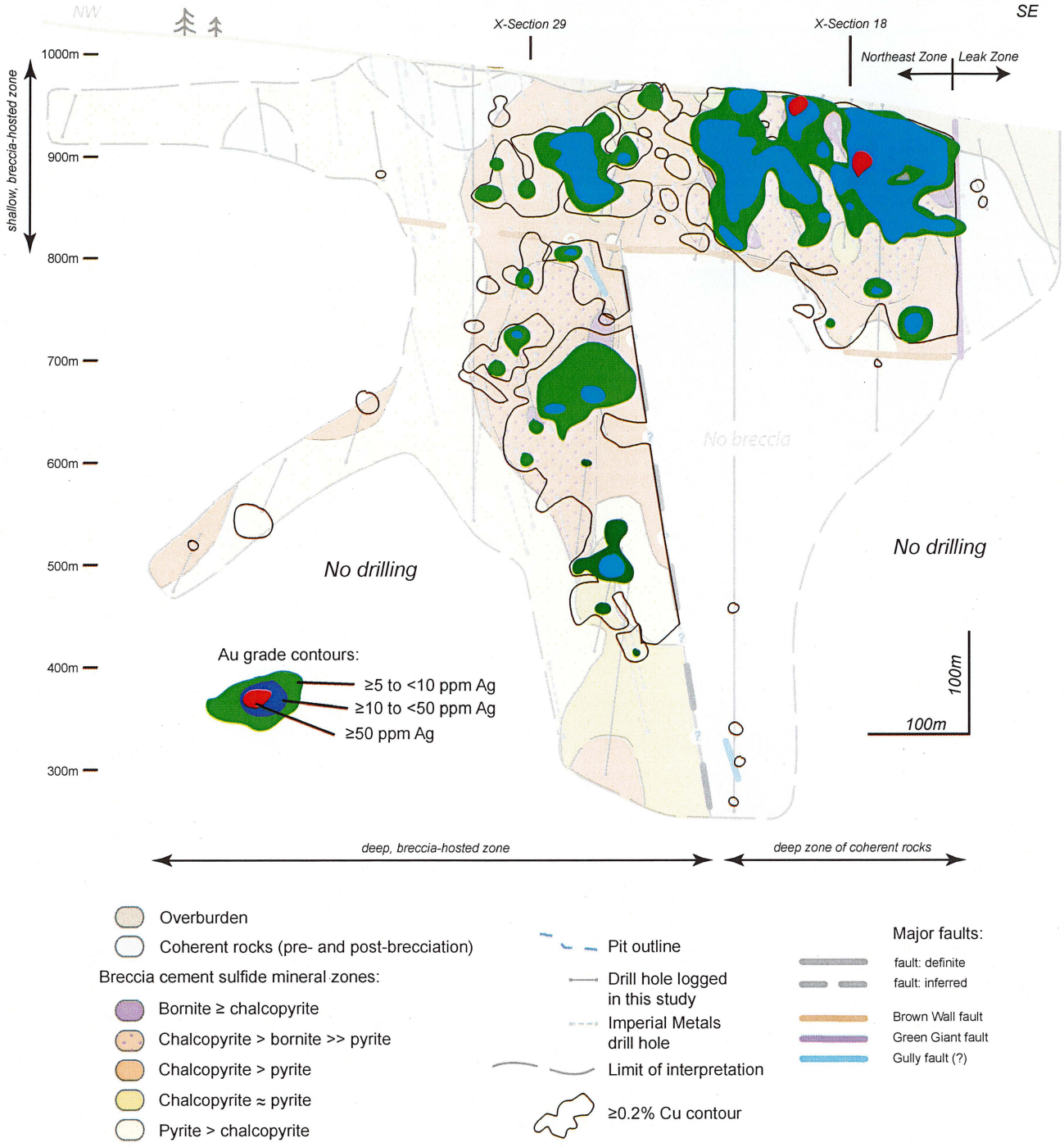

Figure 6.25 Silver grade contours determined from Imperial Metals whole rock assay data taken from all boreholes on section overlain on the sulfide mineral distribution of stage 2 breccia cement. The ≥0.2% Cu contour has been outlined in solid black. Silver enrichment is coincident with areas of bornite enrichment in the deep and shallow breccia-hosted ore zones.

evidence for remobilization of Au, as the bornite-cement breccia is largely unaltered, with only thin rims of chalcopyrite and covellite observed locally. Pyrite was not observed overprinting bornite. Additionally, phyllic alteration is restricted to faults and post-breccia veins and therefore the remobilization of Au from bornite to pyrite is not favored for the NEZ.

Although the distribution of Au in many porphyry Cu deposits has been addressed using bulk assays, Kesler et al. (2002) noted that little information

is available on the gold content of specific metal sulfides and oxides that make up the ore assemblages. While additional work is needed to confirm the conclusions of the current study, if indeed they are correct and Au is associated with pyrite ± chalcopyrite outside of the bornite core, it could suggest that Au was still mobile during bornite precipitation. Gold may have remained in solution as a chloride or thio complex due to highly oxidized and/or near neutral pH fluids conditions until a change in physiochemical conditions away from the core of the system prompted Au precipitation. Gold precipitation at lower temperatures (i.e. ~300°C) would not be accommodated in bornite and instead would precipitate with pyrite ± chalcopyrite (Scaini et al., 1998).

6.5.4 PGEs in porphyry deposits

The NEZ concentrate has high concentrations of Pd for a porphyry deposit, with up to 236 ppb Pd and 96 ppb Pt (Appendix E4), where crustal levels of Pd and Pt are 0.4–2.8 ppb and 0.4 ppb, respectively (Taylor and McLennan, 1985; Wedepohl, 1995). Assays of up to 15 ppb Pd and Pt in concentrate are considered to be normal, whereas values of >1900–130 ppb Pd are considered high in porphyry Cu deposits (Tarkian and Stribrny, 1999). PGE analyses from NEZ concentrate are consistent with those from Thompson et al.'s (2001) work on the Central and West Zones of Mt. Polley, and also for other alkalic porphyry Cu-Au deposits in which elevated concentrations of PGEs, particularly Pd and Pt have been reported (i.e. Afton, Copper Mountain, Galore Creek, Mt. Milligan; Mutschler et al., 1985; Thompson et al., 2001; Nixon, 2004). Similar PGE enrichment has been noted from several porphyry Cu deposits globally, including the Skouries alkalic porphyry deposit in Greece (Eliopoulos and Economou-Eliopoulos, 1991; Economou-Eliopoulos, 2005), Santo Tomas II porphyry Cu-Au deposit in the Phillipines (Piestrzynski et al., 1994) and and the Aksug Cu-Mo deposit in Russia (Berzina et al., 2005). In these porphyry deposits, Pd and Pt are the most abundant PGEs, with only trace amounts of Ir, Os, Ru and Rh (Tarkian and Stribrny, 1999).

It is not well understood why porphyry deposits contain significant amounts of PGEs, but experiments have shown that a typical porphyry system has the capacity to transport significant amounts of Pd, enough to form mid-sized PGE deposits, if sources allow (Xiong and Wood, 2000). The presence of Pd and Pt in mineralized alkalic porphyry deposits is consistent with the genetic models for alkalic arc magmas (Thompson et al., 2001). These models suggest that the magmas are derived from an enriched mantle source region, possibly following collision and the cessation of subduction. Tarkian and Stribrny's (1999) review of PGEs in porphyry deposits identified a trend that suggests Au-rich island arc porphyry Cu deposits (such as Mt. Polley) may contain more Pd (and Pt) than continental margin associated deposits. The oxidized nature of the alkalic arc magma plays a key role by inhibiting sulfide fractionation, allowing precious metals to be available for transport to the porphyry environment (Thompson et al., 2001). The solubilities of the PGE elements are very high as chloride complexes in oxidized magmatic fluids that are exceptionally rich in chloride (Gammons et al., 1992). A high magmatic oxidation state may provide a strong control on Pd mineralization, but Pd distribution in Cu-porphyry systems will also potentially be affected by the evolution of the magmatic-hydrothermal system (Economou-Eliopoulos and Eliopoulos, 2000).

Although the primary product from Mt. Polley is Cu (with Au and Ag credits), Pd is not currently recovered during mine processing. Palladium contents of several hundred ppb in the mine concentrate could be considered to be an encouraging economic factor for a Pd by-product (Economou-Eliopoulos and Eliopoulos, 2000). However, based on this study, it appears that Pd (± Pt) is hosted primarily in pyrite at Mt. Polley. Pyrite-hosted PGEs in alkalic porphyry deposits may not be recovered by smelters when the pyrite is excluded from the concentrate.

6.5 Conclusions

The use of LA-ICP-MS spot, line and mapping techniques has permitted a detailed study of trace element deportment in bornite, chalcopyrite and pyrite from the NEZ. Each of these sulfide minerals has exhibited unique trace element signatures. Sulfides were placed in three groups to facilitate interpretation: group 1 (bornite and chalcopyrite), group 2 (chalcopyrite only)

and group 3 (pyrite and chalcopyrite). These groups correspond spatially to the high-grade core of the NEZ (group 1), an intermediate mineralized domain (group 2) and to the outer edge of sampling (group 3) of the deep ore zone (Fig. 6.1). The following conclusions can be made:

- Bornite is enriched in Ag, Bi, and Se. These elements have substituted into the bornite structure, or are evenly disseminated as nano-particles. Bornite also contains abundant macro- to micro-inclusions of Se ± Bi-bearing galena, with lesser amounts of Ag-Te ± Se-bearing inclusions and a few Co- and Ni- bearing silicate inclusions. Only a limited number of microscopic Au inclusions, and isolated Pd-, Pt- and Mo-bearing inclusions were identified in bornite. Concentrations of these elements were mostly below detection limits. Ruthenium, Rh, Os, Ir, As, Cd, Tl, Sb, Cr and W were not detected in bornite.
- Definitive stoichiometric substitutions of trace elements into chalcopyrite of the NEZ were not confirmed by the current study. A distinct spatial zonation was identified, based on trace elements contained in chalcopyrite from groups 1, 2 and 3. Lead concentrations are caused by galena inclusions in chalcopyrite, and decrease from group 1 to group 3. Conversely, Zn concentrations, which relate to sphalerite inclusions, increased from group 1 in the core of the deposit to group 3 on the edges of the deposit. Group 1 chalcopyrite contained isolated Zn-Se-Ag-bearing inclusions, but Cd was not detected. Group 2 chalcopyrite contained limited Zn-Ag-Cd-bearing inclusions with limited Sn and Sb. Group 3 contained abundant Zn-Ag-Cd-Sb-bearing inclusions. While Se concentrations are elevated in chalcopyrite from all three groups, a general decrease is observed from group 1, associated with the high-grade core of the deposit, to group 3, associated with the outer margins of the deep breccia-hosted zone. Gold is more abundant than Pd which is more abundance than Pt in chalcopyrite. These elements were detected as limited or isolated inclusions in chalcopyrite, but concentrations were mostly below detection limits. Ruthenium, Rh, Os, Ir, Ni, Tl, Sb, Cr, W and Th were not detected in chalcopyrite.
- Pyrite from the NEZ is enriched in Cu, Zn, Co, Ni, Se, Au and Te. These elements have substituted into the pyrite structure or evenly disseminated as nano-particles. Pyrite contains abundant micro-inclusions of chalcopyrite, galena, sphalerite, electrum and tellurides, resulting in locally elevated concentrations of Pb, Cu, Co, Zn, Ag, Au Bi, As, Sb, Sn, Se, Te and Cd. Gold-, Pd- and Pt-bearing inclusions were primarily detected in pyrite. Gold contents were found to be 1–3 orders of magnitude higher in pyrite than in chalcopyrite. Gold displays variable associations with Ag, Te and As. The primary association of Au ± Pd with pyrite in this study may have important metallurgical implications given that the ore-processing circuits at most copper mines are designed to exclude pyrite from concentrates.

Chapter 7

Synthesis and Genetic Model

1.1 Introduction

This thesis aimed to document the geology of the alkalic, breccia-hosted porphyry Cu-Au-Ag deposit of the NEZ, to use geochemical methods to constrain fluid compositions and sources, and to propose a genetic model for mineralization. The preceding chapters provided insights into the magmatic and hydrothermal evolution of the NEZ. This chapter synthesizes these results into a new genetic model for Mt. Polley, and comments on its implications for silica-undersaturated porphyry deposits elsewhere. The chapter concludes with a brief summary of exploration implications and recommendations for future research.

7.2 Geological evolution of the NEZ and the Mt. Polley Complex

7.2.1 Tectonic setting, volcanism and plutonism

The Mt. Polley Complex is one of several alkalic plutons associated with Cu-Au mineralized centers in the Quesnellia-Stikina oceanic island arc (Fig. 1.4). Inception of the arc began with the subduction of the Cache Creek oceanic plate in the Devonian to Pennsylvanian (Figs. 2.2 and 7.1A; Mortimer, 1987; Bailey, 1990; Mihalynuk et al., 1994; Monger and Nokleberg, 1996; Nokleberg et al., 2000; Nokleberg et al., 2005). The arc arguably formed above the axial or flanking portions of displaced passive pericratonic strata of the Yukon-Tanana and Kootenay terranes, which had previously rifted from the North American cratonal margin (Mortimer, 1987; Bailey, 1990; Mihalynuk et al., 1994; Monger and Nokleberg, 1996; Nokleberg et al., 2000; Nokleberg et al., 2005). The Triassic to Jurassic volcanic rocks evolved compositionally with time, from basaltic to intermediate silica-saturated, to shoshonitic silica-undersaturated compositions (Logan and Bath, 2006). Monzonites, monzodiorites, diorites and syenites of the Mt. Polley Complex are interpreted to have intruded the Nicola Group volcanics at shallow-crustal levels late in the evolution of the Quesnellia arc (Figs. 2.3, 7.1B and 7.2A and B; Panteleyev et al., 1996). Pre-accretionary porphyry deposits, including Mt. Polley and the co-magmatic alkaline volcanic rocks, are interpreted to have formed during the culmination of arc magmatism prior to accretion of Quesnellia to ancestral North America (Fig. 7.1B; McMillan et al., 1995).

7.2.2 Previous genetic models

Some previous workers proposed that Cu-Au mineralization at Mt. Polley occurred inside a dissected volcano (e.g. Bailey and Hodgson, 1979; Bailey, 2004a; Bailey, 2004b), but the lack of volcanic detritus and the predominance of monzonite clasts in the breccias discount this model. Instead, most workers proposed that mineralization occurred in subvolcanic magmatic-hydrothermal breccia complexes associated with the Mt. Polley monzonites (e.g. Hodgson et al., 1976; Fraser et al., 1995; Ross, 2004; Logan and Mihalynuk, 2005; Simpson, 2005; Rees et al., 2006; Jackson, 2008). Key supporting evidence is the recognition of juvenile-magmatic clasts in the NEZ (Fig. 3.14) and Central Zone (Bell pit; Logan and Mihalynuk, 2005; Simpson, 2005; Jackson, 2008). The results of the current study support a magmatic-hydrothermal model for brecciation and mineralization in the Mt. Polley Complex.

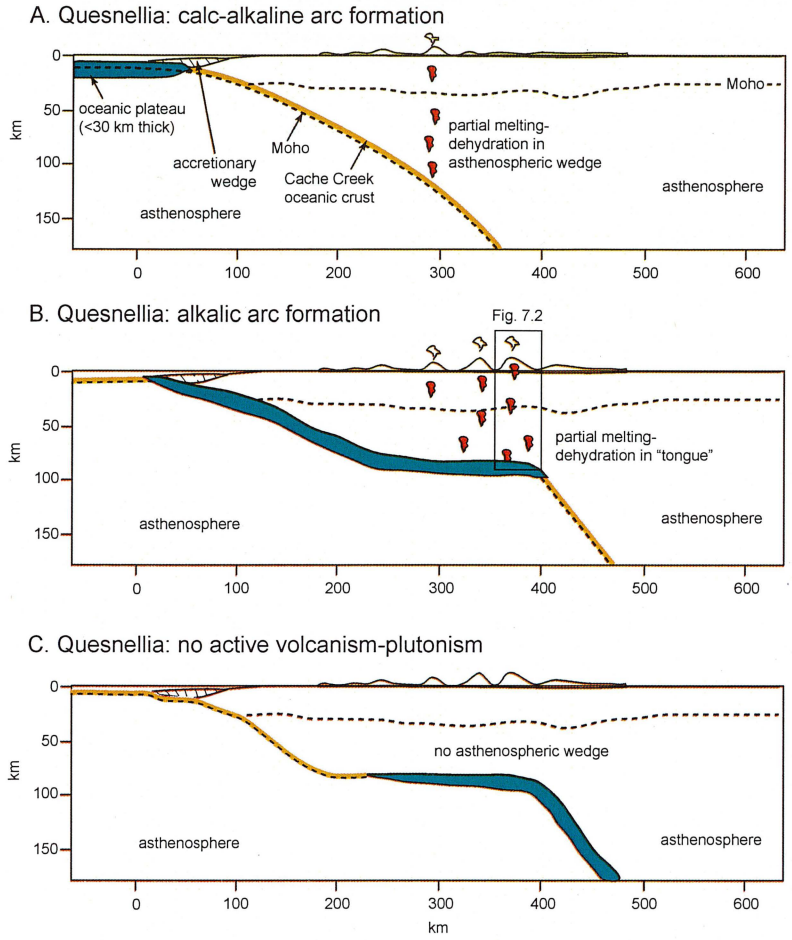

Figure 7.1 Three-stage evolution showing transition from steep to flat subduction style due to subduction of buoyant, over-thickened oceanic crust (e.g. oceanic plateau), with impact on magmatic arcs. **A)** Steep or normal subduction (≥ 30° dip), with calc-alkalic arc produced by slab dehydration and partial melting in overlying asthenospheric wedge. **B)** Early-stage magmatic flat subduction; oceanic slab crosses 700°C geotherm at ~80 km depth allows alkalic arc to develop. Partial melting continues in narrow intervening tongue of asthenospheric material. **C)** Prolonged (amagmatic) flat subduction; asthenospheric tongue has cooled and retreated, consequently partial melting can no longer occur; oceanic slab is cooler than 600°C, volcanism-plutonism ceases. Figure modified from Gutscher et al. (2000).

7.2.3 Early-stage (pre-breccia)

The monzonite that hosts the NEZ breccia complex preserves evidence for hydrothermal activity that occurred prior to brecciation (Fig. 7.2B). The earliest-formed and most widespread alteration assemblages in the NEZ resulted from intense pervasive K- and Fe-metasomatism ± calcite alteration of the host rocks (Fig. 4.8). Stage 1 veins and high-temperature (>350°C) potassic and sodic alteration occurred beneath the shallow breccia-hosted zone, and calc-potassic (actinolite) alteration occurred in the Leak Zone (Figs. 3.1 and 4.17). Either stockwork development was minimal at this time, or any early-formed stockwork is poorly exposed by the current extent of drilling. Little to no Cu-sulfide deposition occurred during the early stage.

7.2.4 Brecciation and main-stage mineralization

The NEZ breccia complex formed in response to magmatic-hydrothermal phenomena, based on the textural, mineralogical and geochemical features outlined in Chapters 3 to 6 (e.g. Fig. 4.8). Intrusion of a hydrous, megacrystic K-feldspar-phyric-monzonite porphyry led to magmatic-hydrothermal brecciation (Fig. 7.2C). Fluids released from the intrusion triggered brecciation of the wallrocks and the crystallizing intrusion when hydrostatic pressure exceeded both lithostatic load and the tensile strength of the monzonite wallrock during second boiling, causing catastrophic brittle failure (Burnham and Ohmoto, 1980; Burnham, 1985). The megacrystic texture suggests an extended time at super-solidus temperatures prior to brecciation (Jackson, 2008).

Clast comminution, matrix generation and hydrothermal cementation-alteration followed

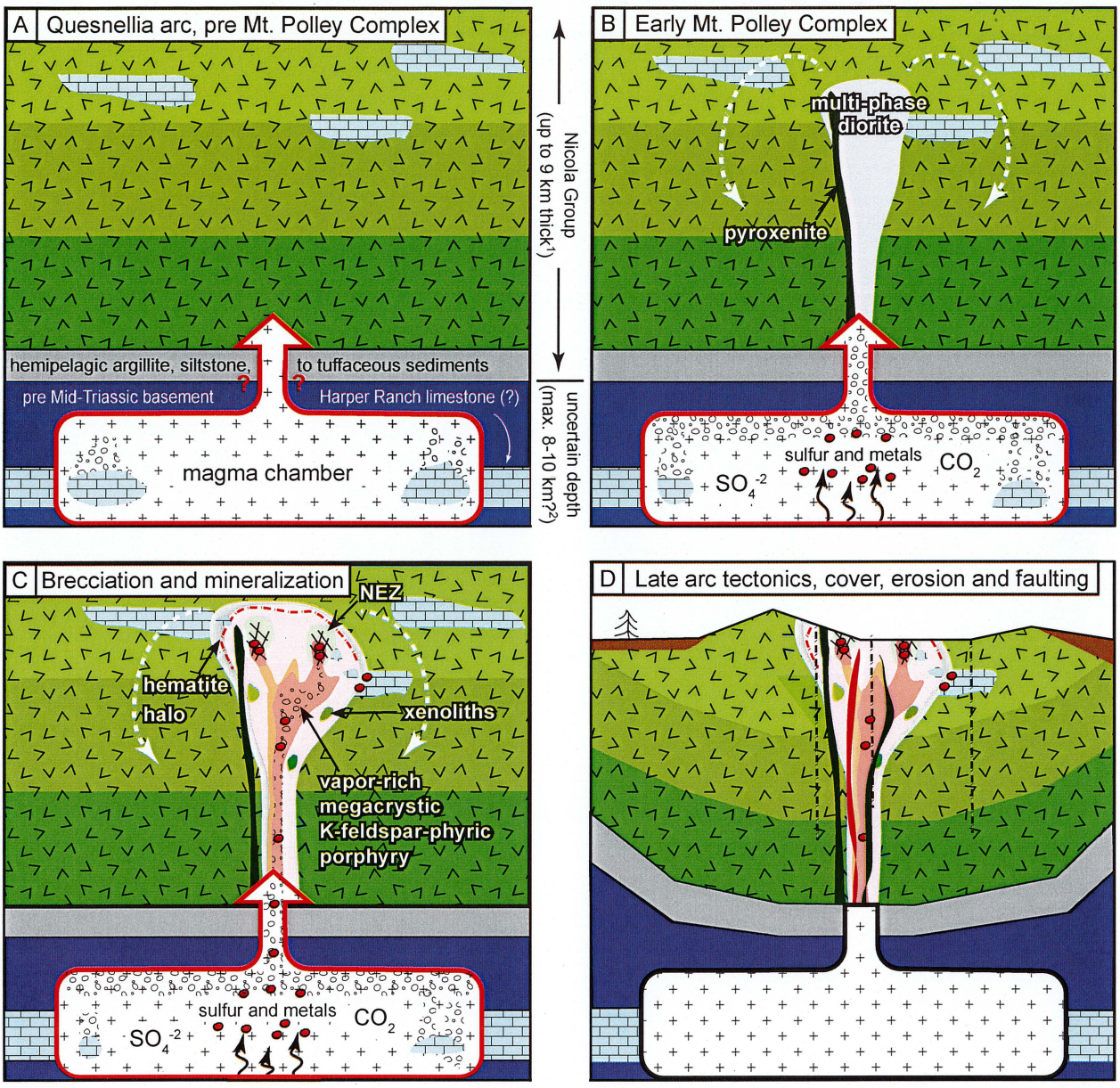

Figure 7.2 Conceptual genetic model for the Mt. Polley Complex, modified from Imperial Metals (2005, 2008). **A)** Pre-Mt. Polley Complex: basaltic to intermediate volcanic rocks intercalated with limestone lenses of the Nicola Group (Quesnel Arc) overlie a sedimentary carbonate-bearing substrate. Depth of magma chamber is uncertain and has been placed at an estimated maximum depth as in Iacono-Marziano et al. (2009). **B)** Early Mt. Polley Complex: intrusion of pyroxenite and multiple diorite bodies of the Mt. Polley Complex. Hydrothermal circulation is established with fluids from the intrusions interacting with regional wallrock, including limestone. In the magma chamber, carbonate assimilation produces a CO_2 vapor-rich melt. The CO_2 partial pressure within the magma chamber increases. **C)** The Mt. Polley Complex is composed of silica-undersaturated to silica-saturated dioritic to monzonitic (± porphyry) intrusions with widespread hematite dusting and carbonate alteration. Nicola Group xenoliths have been entrained in the Mt. Polley Complex. Magmatic-hydrothermal brecciation is triggered by intrusion of a silica-undersaturated megacrystic K-feldspar-phyric monzonite. Breccia cementation follows with cores of potassic ± calc-potassic alteration surrounded by propylitic alteration halos. Sulfide mineralization is deposited as breccia cement as a result of inorganic sulfate reduction and cooling during water-rock interaction. **D)** Post-brecciation intrusions cut the Mt. Polley Complex and a cover sequence was deposited. Obduction of Quesnellia onto the margin of ancestral North America and orogenesis during the latest stages of arc evolution caused the Mt. Polley Complex to be uplifted, folded and faulted. Erosion removed a significant portion of the Mt. Polley Complex.

[1]Maximum thickness of Nicola Group from Panteleyev et al. (1996). [2]Magma chamber adapted from Iacono-Marziano et al. (2009).

immediately after brecciation, as hydrothermal fluids, clasts and matrix migrated through the breccia complex. Hydrothermal cement and/or altered matrix filled pore spaces throughout the breccia body as it consolidated. CMX breccia was the most abundant breccia facies formed. CM breccia was identified along some breccia margins and in pods of the CMX breccia. MX breccia was observed primarily to the northwest of the CM-CMX breccia body. These spatial variations in the abundances of cement and matrix are inferred to relate at least in part to fluidization processes (e.g., Jackson, 2008). Irregular domains of chaotic CM breccia in CMX breccia (Figs. 3.2 and 3.12) suggest complex fluid pathways, possibly where winnowing of matrix occurred. The lack of surficially-derived clasts or sedimentary structures implies that the breccia complex did not breach the surface. The lack of breccia clast-in-clast textures implies that the NEZ was a monogenetic breccia pipe.

Hydrous, CO_2-enriched fluids caused mineralization and alteration during and after brecciation. The CO_2 concentrations could not have been too high otherwise calc-silicate phases such as garnet, pyroxene and clinozoisite-epidote would have been destabilized and only calcite or other carbonates would be observed (e.g. Cooke et al., 1996). This suggests that brecciation in the NEZ was primarily steam-driven, although a small to moderate dissolved CO_2 component could have significantly affected brecciation by promoting boiling and/or magmatic-hydrothermal brecciation (e.g. Hedenquist and Henley, 1985; Iacono-Marziano et al., 2007; Iacono-Marziano et al., 2009).

The potassic, sodic and calc-potassic assemblages of the NEZ are inferred to have formed during brecciation, coeval with and after the emplacement and disaggregation of the megacrystic K-feldspar porphyry (Figs. 3.12, 3.13 and 4.8). Alteration assemblages within the breccia body are zoned vertically and laterally, but their distributions are a product of protracted and/or repeated fluid flow. High-temperature (>300°C) fluids, enriched in Cu, Ag, Au, Pd, Pt, PO_4^{-2}, SO_4^{-2} and undersaturated in silica are interpreted to have migrated upwards through the deep breccia-hosted domain, probably along a brecciated structural conduit (Figs. 3.12 and 4.3). The magnetite-, K-feldspar- ± biotite-rich potassic and sodic alteration zones are interpreted to be the highest-temperature portion of the NEZ breccia complex as currently exposed, and are believed to lie proximal to the fluid source (Fig. 7.3). These alteration assemblages coincide with the deepest observed occurrence of megacrystic K-feldspar porphyry clasts (Figs. 3.12, 3.13 and 7.3). As hydrothermal fluids flooded the breccia body, sulfide and oxide minerals were precipitated in a zoned fashion, from magnetite-dominant cement associated with intense potassic and sodic alteration in the deep breccia-hosted zone upwards to bornite ± specularite-chalcopyrite (+ calc-potassic alteration in the shallow breccia-hosted zone), and outwards to chalcopyrite ± pyrite cemented breccia (calc-potassic altered domain) (Figs. 4.2, 4.17 and 7.3). Fluids are interpreted to have continued to migrate outwards and upwards, producing a peripheral propylitic ± garnet assemblage at near-neutral to alkaline pH (Figs. 4.19, 4.21 and 7.3).

Magmatic-hydrothermal processes also occurred in the Core Zone of the Mt. Polley Complex (Fig. 2.6), based the observation of igneous-cemented breccia and juvenile-magmatic clasts (e.g. Fraser, 1995 and Logan and Mihalynuk, 2005). Rees et al. (2006) highlighted that it is currently not possible to constrain the relative timing of NEZ brecciation and mineralization relative to the Core Zone or other areas of breccia in the Mt. Polley Complex (Fig. 2.6). Geochronologic data provide evidence that the Mt. Polley Complex was formed between 209.4 and 195.4 Ma, with mineralization constrained to a 5 m.y. window between 209 and 204 Ma (Fig. 2.9). These data are not sufficiently precise to resolve the relative timing between brecciation events in the different mineralized zones (Fig. 2.9). The most obvious links between the ore bodies are the observations of juvenile-magmatic clasts of megacrystic K-feldspar-phyric monzonite in the Wight pit (NEZ) and Bell pit (Core Zone; Logan et al., 2007), and the common monzonite wallrocks. In the absence of unequivocal data, similar but distinctive alteration and mineralization between the Core Zone, the NEZ and other zones within the Mt. Polley Complex suggests genetically related, but separate mineralized breccia complexes that may have formed anytime within the 209 and 204 Ma window.

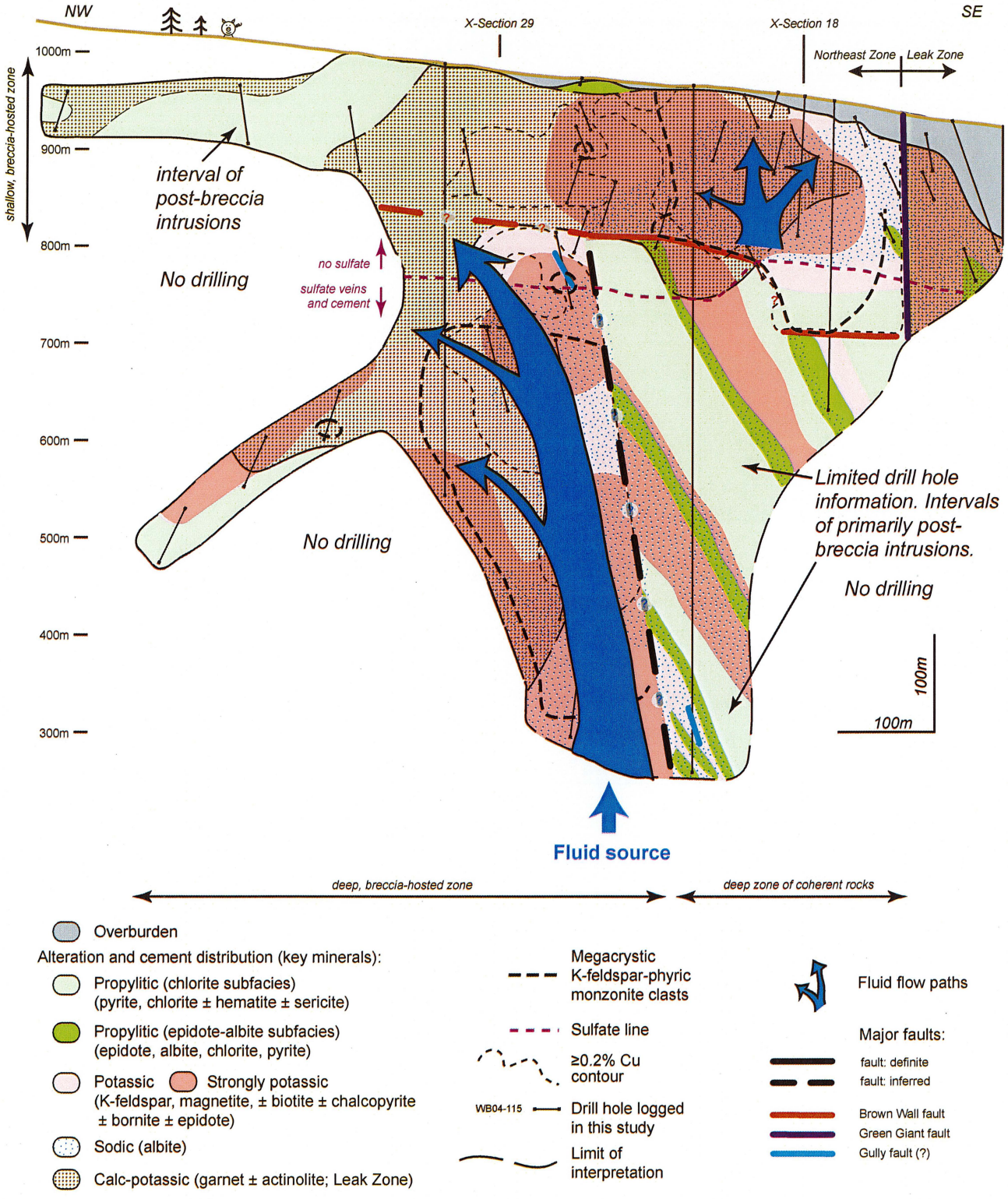

Figure 7.3 Magmatic-hydrothermal fluid flow paths during brecciation. High temperature (>300°C) fluids are interpreted to have migrated upwards through the deep breccia-hosted domain. The magnetite-, K-feldspar- ± biotite-rich potassic and sodic alteration zones are interpreted to be the highest-temperature portion of the NEZ breccia complex as currently exposed, and are believed to lie proximal to the fluid source. These alteration assemblages coincide with the deepest observed occurrence of megacrystic K-feldspar porphyry clasts (heavy dashed black line). Fluids are interpreted to have continued to migrate outwards and upwards, producing a peripheral propylitic ± garnet assemblage at near-neutral to alkaline pH. The shallow breccia-hosted domain has been truncated by faults and therefore only a partial fluid path is estimated.

7.2.4.1 Metal and fluid sources

The $\delta^{34}S_{sulfide}$ isotopic compositions of main and late-stage chalcopyrite, pyrite and bornite from the NEZ range from -7.1 to +1.4 per mil, with most between -3 and -4 per mil. Sulfur isotopic compositions of anhydrite and gypsum are between +6.2 and +9.8 per mil, with two outliers of +13.6 and +14.0 per mil (Fig. 5.1). These values, together with the presence of hematite, are consistent with an oxidized (SO_4^{-2} dominant), high-temperature (>400°C) magmatic-hydrothermal fluid (Figs. 4.19 and 4.20). Limited sulfide geothermometry indicates temperatures of ~ 480° to ~ 250°C (Appendix D).

The $\delta^{34}S$ values of main-stage sulfides define zonation patterns across the deposit, from low $\delta^{34}S$ values in the mineralized core outwards to higher $\delta^{34}S$ values on the deposit periphery (Fig. 5.2). These patterns cannot be achieved by cooling alone (e.g., Wilson et al., 2007). Inorganic sulfate reduction during hematite alteration is considered to have been a fundamental process for the generation of H_2S required for Cu-Fe sulfide deposition in the NEZ.

Hydrothermal calcite occurs throughout the NEZ paragenesis (Fig. 4.8). The $\delta^{13}C$ values range from -0.2 to -10.5 per mil (average -3.0 ‰), and $\delta^{18}O$ values from +4.0 to +20.9 per mil (average +15.4 ‰), and are not consistent with simple precipitation from a typical magmatically-derived hydrothermal fluid (Figs. 5.3, 5.4 and 5.11). Water-rock interaction, boiling and/or Rayleigh fractionation are required to account for the enriched $\delta^{18}O$ values. Enriched $\delta^{13}C$ values suggest the involvement of a heavy carbon source such as limestone. Isotopic modeling has demonstrated that water-rock interaction between hydrothermal fluids and limestone best explains the array of $\delta^{13}C$ and $\delta^{18}O$ data from Mt. Polley (Fig. 5.12).

Lead-isotopic data suggest mixing of mantle and crustal sources during mineralization. Main-stage chalcopyrite, pyrite and late-stage galena yielded $^{206/204}Pb$ values of 18.77-18.92, $^{207/204}Pb$ of 15.56-15.59, and $^{208/204}Pb$ of 38.22-38.32 (Fig. 5.7). Strontium-isotopic data (0.70331 to 0.70371; Fig. 5.8) provide evidence of a strongly depleted mantle source of Sr with minor crustal input. Epsilon Nd values for main-stage apatite range between +5.9 and +6.5, also indicating a depleted mantle source (Fig. 5.9).

The stable and radiogenic isotopic data and alteration mineralogy at Mt. Polley imply that the Mt. Polley Complex interacted with a limited amount of crustal, $\delta^{13}C$-enriched material prior to mineralization. This interaction was insufficient to shift initial Sr ratios to significantly higher values. A possible $\delta^{13}C$-enriched source is the carbonate platform of the Harper Ranch sub-terrane that underlies the Nicola Group (Monger, 1977), or possibly marble of the pericratonic Yukon-Tanana-Kootenay terranes (Figs. 7.2C and 7.4; McMillan et al., 1995; Nokleberg et al., 2000). In this model, as magmas ascended through the sedimentary substrate, they assimilated a component of wallrock carbonate (Fig. 7.2A and B). That assimilation caused CO_2 saturation of the magmas, and drove them to silica-undersaturated compositions through pyroxene crystallization (Iacono-Marziano et al., 2007, 2008). Carbon-dioxide exsolution probably helped to drive magmatic-hydrothermal brecciation in the Mt. Polley Complex (Fig. 7.2C). High-grade Cu-Au-Ag mineralization was intimately associated with brecciation, producing high-temperature breccia cement and alteration features including K-feldspar-magnetite-garnet-biotite-actinolite-augite-apatite-albite and Cu-Fe-sulfides (Figs. 4.5, 4.6, 4.7, 4.17 and 4.21). Inorganic sulfate reduction produced widespread hematite dusting and generated H_2S, essential for the processes of copper-iron sulfide deposition.

Another potential source of enriched $\delta^{13}C$ could be a CO_2-enriched melt produced during flat slab subduction (i.e. Gutscher et al., 2000; Fig. 7.1), possibly a carbonate-covered oceanic plateau ± seamounts and sediments of the Cache Creek ocean subducted beneath the Quesnellia terrane at the end of the Triassic (Fig. 7.4; Johnston and Borel, 2007). Buoyancy analysis has shown that oceanic plateaus must be >30 km thick to jam subduction zones and that seamounts and carbonate platforms can therefore be subducted (Cloos, 1993; Gutscher et al., 1999), potentially transporting carbonate deep into subduction zones (Fig. 7.2B; Blundy et al., 2010; Marín-Cerón et al., 2010). While the specified details of the CO_2-enrichment process remain unclear, it is well established that sediments, as well as the down-

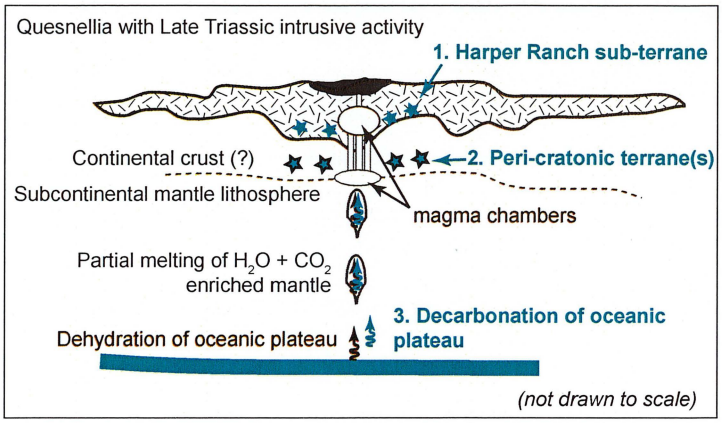

Figure 7.4 Schematic section through the upper 150 km of a subduction zone, showing the principal crustal and upper mantle components and their interactions, modified from Stern (2002). Possible carbonate sources for the Mt. Polley Complex are highlighted in blue: 1. The Harper Ranch-Okanagan sub-terrane, part of the lower Quesnellia Devonian to Permian stratigraphy. It contains carbonate platform successions, preserved as limestone bodies up to 1 km long (Monger and Berg, 1987). 2. The Yukon-Tanana-Kootenay pericratonic terranes are dominated by clastic successions of mafic to felsic volcanic rocks, coeval granitic plutons, and local marble (McMillan et al., 1995; Nokleberg et al., 2000). 3) Decarbonation of oceanic plateau during subduction (Stern, 2002, Marin-Ceron et al., 2010).

going slab, control the chemistry of subduction related magmatism (Stern, 2002) and therefore decarbonation of subducted carbonate from the Cache Creek terrane may have influenced magma chemistry.

7.2.4.2 Sulfide Chemistry

Gold contents were found to be 1–3 orders of magnitude higher in pyrite than in chalcopyrite in the NEZ (Table 6.3, Figs. 6.3, 6.4 and 6.8). Gold, Pd- and Pt-bearing inclusions were primarily detected in pyrite on the fringes of the deep breccia-hosted zone (Figs. 6.19A and 6.21A). Gold was not detected in bornite (Figs. 6.8 and 6.12). In the shallow breccia-hosted zone, assay data show that high gold grades are associated with areas rich in bornite and chalcopyrite (Fig. 6.23), implying that another phase, possibly minute electrum grains, hosts gold in this area.

7.2.5 Post brecciation mineralization and intrusive activity

Multiple stages of alteration and mineralization are common in alkalic porphyry deposits (Lang et al., 1995), and this was certainly the case for the NEZ (Fig. 4.8). Magmatic and hydrothermal activity continued episodically for some time after breccia consolidation based on late-stage dikes and veins that cross-cut the breccia complex. The dikes that intruded the breccia complex evolved with time from K-feldspar megacrystic to crystal-crowded to sparsely porphyritic to equigranular, and also became increasingly mafic and hydrous (Fig. 3.5, Table 3.2; Jackson, 2008). The absence of alteration halos around some of these dikes suggests that hydrothermal fluids were either less abundant or not present during the waning stages of magmatic activity. Late-stage mineralization occurred shortly after the main-stage, based on a model Pb age of 207.8 ± 1.8 Ma from stage 3 galena.

Minor in-situ hydraulic and tectonic fragmentation produced stage 4 vein breccias, probably during post-stage faulting (Fig. 4.8). The vein breccias (Fig. 4.13), together with amygdales that occur in some post-breccia dikes, suggest that the hydrothermal system was still (at least episodically) vapor-saturated during post-brecciation magmatism and hydrothermal activity.

Potassic alteration occurred intermittently after breccia cementation, with the last potassic alteration event associated with stage 3 bornite-chalcopyrite ± K-feldspar-bearing mylonites and sulfide veins. Calc-potassic alteration was associated with some stage 3 and 4 veins. Sodic alteration occurred throughout the evolution of the NEZ, but was particularly well-developed during stages 3 and 4. Conversely, weak phyllic alteration was associated with some stage 4 veins.

Stage 3 and 4 fluids were oxidized and near-neutral to alkaline, but $\delta^{34}S_{sulfide}$ isotopic compositions indicate that late-stage fluids were less oxidizing than the main-stage fluids (Fig. 5.1). The $\delta^{18}O$ isotopic data from barren calcite veins indicate a component of meteoric or seawater input during the waning stages of hydrothermal activity (Fig. 5.3 and 5.4), possibly entrained along major faults (Fig. 5.5). Fluid conditions were no longer exclusively silica-undersaturated as evidenced by minor quartz precipitation during stage 4.

7.2.6 Epithermal overprint and post-brecciation faulting

Significant erosion occurred after stage 4. Lead isotope data from stage 5 veins indicate that at ~100 m.y. after Mt. Polley formed, primarily barren, low sulfidation epithermal-style calcite-anhydrite-chalcedony veins overprinted the NEZ. Restricted phyllic alteration accompanied epithermal-style vein emplacement.

Deformation, possibly accompanied by bulk rotation of the Mt. Polley Complex caused disruption of the NEZ in the Cretaceous or Tertiary (Fig. 7.2D; Bailey, 2004b; Taylor, 2004; Rees, 2008). Significant post-mineral fault movement separated the shallow breccia-hosted zone from the parent breccia body, creating a down-faulted panel. The relative timing of this deformation with respect to epithermal-style veining is unknown.

7.3 Exploration Implications

Several features observed in the Mt. Polley Complex may be useful for helping to vector towards mineralized ore zones in alkalic porphyry deposits:

- Ore grades within the NEZ breccia are in part a function of the permeability and porosity of the breccia. Mineralization in the NEZ is associated with CMX and CM breccia facies (matrix <40% and matrix <5% of the infill, respectively). MX breccia facies (matrix >40% of breccia infill) was not favorable for extensive mineralization, but indicates proximity to the CMX facies. Exploration in breccia complexes should focus on locating domains where matrix is likely to be less abundant, such as on the roof of the breccia.
- Magnetite-K-feldspar-albite-biotite (± garnet) alteration has the closest association with the NEZ ore zones, while propylitic alteration (chlorite-calcite ± pyrite ± epidote ± albite) formed a halo to ore. Garnet (including carbonate-altered garnet, sometimes referred to as "oatmeal texture"), "red rock" hematite and carbonate alteration were found in, as well as >450 m laterally from the ore zones and may be significant in terms of increasing the target footprint. However, the NEZ lacks a significant halo of pyrite alteration compared to most calc-alkalic deposits, showing that the outer sulfide halo to an alkalic porphyry deposit may only consist of minor disseminated chalcopyrite and pyrite. Additionally, zonal patterns of alteration and mineralization may be disrupted by significant younger faults and intrusions in ancient terranes that have a significant history of post-mineral deformation, such as Quesnellia.
- The NEZ ore body has been disrupted significantly by several faults. Unraveling the history of fault movements could help to locate dismembered sections of the ore body and would assist in unraveling the original geometry of the breccia complex.
- The $\delta^{34}S_{sulfide}$ isotope values become increasingly negative towards the centre of the ore zone, providing a vector to ore, but the patterns in the NEZ are likely to have been disrupted by late-stage intrusions and faulting. Elevated $\delta^{18}O_{carbonate}$ (>16 ‰) and $\delta^{13}C_{carbonate}$ (>-4 ‰) isotope values also indicate proximity to ore zones in the NEZ, although the O-isotopic patterns may have been disturbed by carbonate recrystallization during late-stage faulting and so should be used with caution and in conjunction with other vectors.
- While porphyry deposits may be found in clusters, alteration and mineralization can vary considerably within an alkalic intrusive complex, particularly in and between ore zones (e.g. NEZ versus Core Zone versus Pond Zone; Fig. 2.6). Variability should be anticipated and flexible exploration criteria employed (e.g., Rees et al., 2006).
- Regions or terranes underlain by sedimentary terranes that include significant carbonate packages may be favorable for the formation of alkalic porphyry and epithermal deposits.

7.4 Future Research

Many unresolved questions remain with regards to metal source enrichment, igneous petrogenesis and how the magmatic, structural and hydrothermal

evolution dictates alkalic deposit formation (Jensen and Barton, 2000). Recommendations for research to further our understanding of alkalic deposits include:

- Detailed SEM and electron microprobe analyses of high gold grade samples may reveal the repository for gold in the bornite-rich ore zones at Mt. Polley. LA-ICP-MS trace element studies of non-sulfide minerals may also provide an answer to this conundrum.
- Detailed mapping and logging of the root zones of the megacrystic K-feldspar-phyric monzonite may provide further genetic information on breccia formation, when deeper exposures of the breccia complex are exposed. This study will best be achieved if Imperial Metals Corporation conducts underground mining in the NEZ.
- Due to the lack of quartz, only a few fluid inclusion studies have been conducted on silica-undersaturated porphyry deposits. A fluid inclusion study using garnet, as has been conducted at Galore Creek (Dunne et al., 1994), may give more insights into fluid compositions, temperatures and the depth of breccia formation at Mt. Polley. However, the significant fault disruptions reduce the chances of finding suitable fluid inclusions. If they can be found, they could provide useful insights into the abundance of CO_2, depths of mineralization and brecciation, and could help to constrain the chemistry of the mineralizing fluids.
- Detailed geochemical and isotopic studies of clinopyroxene and plagioclase in the Mt. Polley Complex rocks may help to test the hypothesis that carbonate assimilation played a role in the formation of the silica-undersaturated intrusive complex
- In Stern's (2002) review of subduction zones, the questions of, "What happens to subducted carbonates?" and "What fraction of this returns to the surface as carbon dioxide?" are listed amongst the top ten areas of future research questions. It appears there are a growing number of studies associated with alkalic, barren and mineralized, silica-undersaturated systems that call upon the idea of carbonate assimilation. Several pieces of the puzzle are present; however, the process to put them all together remains unresolved.

References

Allen, D. G., Panteleyev, A., and Armstrong, A. T., 1976, Galore Creek, *in* Brown, A. S., ed., Porphyry Deposits Of The Canadian Cordillera, Canadian Institute of Mining and Metallurgy Special Volume 15: Ste. Anne de Bellevue, Paper 41, p. 402-414.

Arculus, R. J., and Powell, R., 1986, Source component mixing in the regions of arc magma generation: Journal of Geophysical Research, v. 91, p. 5913-5926.

Arif, J., and Baker, T., 2004, Gold paragenesis and chemistry at Batu Hijau, Indonesia: implications for gold-rich porphyry copper deposits: Mineralium Deposita, v. 39, p. 523-535

Bailes, R. J., 1977, The Cariboo-Bell Alkaline stock, British Columbia: Unpublished M.Sc. thesis, University of Manitoba, 47 p.

Bailey, D. G., 1975, Geology of the Morehead Lake Area, South-Central British Columbia (93A/12), *in* Carter, N. C., ed., Geological Fieldwork 1975: Victoria, BC, B.C. Dept. Mines Petroleum Resources, p. 59-63.

Bailey, D. G., 1976, Geology of the Morehead Lake area, central British Columbia, Preliminary Map No. 20: Map with notes, British Columbia Ministry of Energy, Mines and Petroleum Resources.

Bailey, D. G., 1978, The geology of the Morehead Lake area, south-central British Columbia: Unpublished PhD thesis, Queen's University, 198 p.

Bailey, D. G., 1987, Geology of the Hydraulic Map area (NTS93A/12), Preliminary Map No. 67: Scale 1:50,000, British Columbia Ministry of Energy, Mines and Petroleum Resources.

Bailey, D. G., 1988, Geology of the Central Quesnel Belt, Hydraulic, South Central British Columbia, Geological Fieldwork 1987, Paper 1988-1, British Columbia Ministry of Energy, Mines and Petroleum Resources, p. 147-153.

Bailey, D. G., 1989, Geology of the Central Quesnel Belt, Swift River, South-Central British Columbia (93B/16, 93A/12, 93G/1), Geological Fieldwork 1988, Paper 1989-1: Victoria, Ministry of Energy, Mines and Petroleum Resources, p. 167-172.

Bailey, D. G., 1990, Geology of the Central Quesnal Belt, British Columbia (Parts of NTS 93A, 93B, and 93H), Ministry of Energy, Mines and Petroleum Resources, Open File 1990-31, 13 p.

Bailey, D. G., 2004a, Mt. Polley Copper-Gold Deposits, Geology and Chemistry, Notes of Visit, October 12-15, 2004, Bailey Geological Consultants (Canada) Ltd.: North Vancouver, BC, *prepared for* Imperial Metals Corporation, internal company report, 9 p.

Bailey, D. G., 2004b, Mt. Polley Copper-Gold Deposits, South Central British Columbia, August 1, 2004, Bailey Geological Consultants (Canada) Ltd.: North Vancouver, BC, *prepared for* Imperial Metals Corporation, internal company report, 5 p.

Bailey, D. G., and Archibald, D. A., 1990, Age of the Bootjack Stock, Quesnel terrane, South-Central British Columbia, Geological Fieldwork 1989, Paper 1990-1, BC Minisitry of Energy, Mines and Petroleum, p. 79-82.

Bailey, D. G., and Hodgson, C. J., 1979, Transported Altered Wall Rock in Laharic Breccias at the

Cariboo-Bell Cu-Au Porphyry Deposit, British Columbia: Economic Geology, v. 74, p. 125-153.

Bailey, D. K., and Hampton, C. M., 1990, Volatiles in alklaline magmatism: Lithos, v. 26, p. 157-165.

Bailey, E. H., and Stevens, R. E., 1960, Selective Staining of K-feldspar and Plagioclase on Rock Slabs and Thin Sections: The American Mineralologist, v. 45, p. 1020-1025.

Baker, E. M., 1984, A Classification of gold-bearing breccia pipes with reference to exploration: 7th Australian Geological Convention, p. 48-49.

Baker, E. M., Kirwin, D. J., and Taylor, R. G., 1986, Hydrothermal breccia pipes: Townsville, Australia, James Cook University of North Queensland, Geology Department, EGRU Contribution 12, 45 p.

Baker, T., Ash, C. H., and Thompson, J. F. H., 1997, Geological Setting and Characteristics of the Red Chris Porphyry Copper-gold deposit, Northwestern British Columbia: Exploration and Mining Geology, v. 6, p. 297-316.

Baker, T., and Thompson, J. F. H., 1998, Fluid evolution at the Red Chris porphyry Cu-Au deposit, Northwest British Columbia: Abstracts with Programs - Geological Society of America, v. 30, p. 367.

Barnes, C. G., Prestvik, T., Sundvoll, B., and Surratt, D., 2005, Pervasive assimilation of carbonate and silicate rocks in the Hortavaer igneous complex, north-central Norway: Lithos, v. 80, p. 179-199.

Barr, D. A., Fox, P. E., Northcote, K. E., and Preto, V. A., 1976, The Alkaline Suite Porphyry Deposits - A Summary, *in* Brown, A. S., ed., Porphyry Deposits Of The Canadian Cordillera, CIM Special Volume 15: Ste. Anne de Bellevue, Harpell's Press Cooperative, p. 359-367.

Barrie, C. T., 1993, Petrochemistry of shoshonitic rocks associated with porphyry copper-gold deposits of central Quesnellia, British Columbia, Canada: Journal of Geochemical Exploration, v. 48, p. 225-258.

Barton, P. B., and Skinner, B. J., 1979, Sulfide mineral stabilities, *in* Barnes, H. L., ed., Geochemistry of Hydrothermal Ore Deposits: New York, Wiley-Interscience, p. 278-403.

Bath, A., 2007, Net textured Cu-Fe sulfides associated with apatite in biotite-clinopyroxene form the Lorraine deposit, BC: magmatic or porphyry mineralization?, Shallow- and Deep-Level Alkalic Mineral Deposits: Developing an Integrated Exploration Model, Year 2 - Porphyry Module Update to Project Sponsors, p. 2.1-2.5.

Bath, A., 2010, Geology, Geochronology and Alteration of the Lorraine Alkalic Porphyry Cu-Au Deposit, British Columbia, Canada: Unpublished PhD thesis, University of Tasmania, 288 p.

Bath, A. B., and Logan, J. M., 2006, Petrography and Geochemistry of the Late Triassic Bootjack Stock (NTS 093A/12), South-Central British Columbia, Geological Fieldwork 2005, Paper 2006-1, B.C. Ministry of Energy and Mines, British Columbia Geological Survey, p. 5-20.

Bath, A. B., Logan, J. M., and Kamenetsky, V. S., 2006, Apatite in Cu-sulfide ore from the Mount Polley alkalic porphyry, BC Canada: Geochimica et Cosmochimica Acta, v. 70, p. A40-A40.

BCMINFILE, 2010, Galore Creek (Central Zone), British Columbia Geological Survery, http://minfile.gov.bc.ca/report.aspx?f=PDF&r=Minfile_Detail.rpt&minfilno=104G++090, 5 p.

Beane, R. E., and Titley, S. R., 1981, Porphyry Copper Deposits, Part II. Hydrothermal Alteration and Mineralization, *in* Skinner, B. J., ed., Economic Geology 75th Anniversary Volume: El Paso, Economic Geology Publishing Company, p. 235-269.

Begg, G. C., Loucks, R. R., Gray, D. R., Foster, D. A., Kent, A. J. R., and Cooke, D. R., 1997, Magmas, fluids, and tectonics; the Emperor story: Abstracts - Geological Society of Australia, v. 44, p. 9.

Berzina, A. N., Sotnikov, V. I., Economou-Eliopoulos, M., and Eliopoulos, D. G., 2005, Factors controlling palladium and gold contents in the Aksug porphyry Cu-Mo deposit (Russia): Mineral Deposit Research: Meeting the Global Challenge, Eighth Biennial SGA Meeting, Beijing, China, 18-21 August 2005, v.1, p. 353-356.

Bishop, S. T., Heah, T. S., Stanley, C. R., and Lang, J. R., 1995, Alkalic Intrusion hosted copper-gold

mineralization at the Loraine deposit, north-central British Columbia, *in* Schroter, T. G., ed., Porphyry Deposits of the Northwestern Cordillera of North America, CIM Special Volume 46: Sainte-Anne-de-Bellevue, Quebec, Harpell's Press Cooperative, p. 623-629.

Blackwell, J., 2005, Wishbone Rock Classification and Model, *prepared for* Imperial Metals Corporation, internal company report, 20 p.

Blackwell, J., and Stubley, T., 2005, Surficial Geology of the Mount Polley Property, *in* Rees, C., Bjornson, L., Blackwell, J., Ferreira, L., McAndless, P., Rees, C., Robertson, S., Roste, G., Stubly, T., and Taylor, C., eds., Geological Report on the Mount Polley Property and Summary of Exploration in 2003-2004, Imperial Metals Corporation, internal company report, p. 115-120.

Bloodgood, M. A., 1987, Geology of the Triassic Black Phyllite in the Eureka Peak Area Central British Columbia (93A/7), Geological Fieldwork 1986, Paper 1987-1, B.C. Ministry of Energy, Mines and Petroleum Resources, p. 135-141.

Bloodgood, M. A., 1988, Geology of the Quesnel Terrane in the Spanish Lake Area, Central British Columbia, Geological Fieldwork 1987, Paper 1988-1, B.C. Ministry of Energy, Mines and Petroleum Resources, p. 139-145.

Blundy, J., Cashman, K. V., Rust, A., and Witham, F., 2010, A case for CO2-rich arc magmas: Earth and Planetary Science Letters, v. 290, p. 289-301.

Bottinga, Y., 1969, Calculated fractionation factors for carbon and hydrogen isotope exchange in the system calcite-carbon dioxide-graphite-methane-hydrogen-water vapor: Geochimica et Cosochimica Acta, v. 33, p. 49-64.

Braxton, D., Cooke, D., Harris, A., Tosdal, R., Waters, P., and Wurst, A., 2010, Keystone Conference Workshop: Metallogeny of Porphyry Cu-Au Deposits, SEG 2010 Conference, 33 p.

Brown, P. E., Bowman, J. R., and Kelly, W. C., 1985, Petrologic and stable isotope constraints on the source and evolution of skarn-forming fluids at Pine Creek, California: Economic Geology, v. 80, p. 72-95.

Bryner, L., 1968, Proposed terminology for hydrothermal breccias and conglomerates: Economic Geology, v. 63, p. 692.

Burnham, C. W., 1985, Energy Release in Subvolcanic Environments: Implications for Breccia Formation: Economic Geology, v. 80, p. 1515-1522.

Burnham, C. W., 1997, Magmas and Hydrothermal Fluids, *in* Barnes, H. L., ed., Geochemistry of Hydrothermal Ore Deposits, Chapter 3: New York, John Wiley and Sons, Inc., 65 p.

Burnham, C. W., and Ohmoto, H., 1980, Late-Stage Processes of Felsic Magmatism, *in* Ishihara, S., and Takenouchi, S., eds., Granitic Magmatism and Related Mineralization Special Issue 8: Japan, Society of Mining Geologists, p. 1-11.

Byrne, K., Tosdal, R., and Chamberlain, C., 2008, Magmatic-hydrothermal evolution and zonation of a breccia-centered Cu-Au alkalic porphyry: Southwest Zone, Galore Creek, Shallow- and Deep-Level Alkalic Mineral Deposits: Developing an Integrated Exploration Model, Year 3 - Porphyry Module Final Update to Sponsors, *prepared for* MDRU, University of British Columbia and CODES, University of Tasmania, p. 3.1-3.21.

Bysouth, G. D., Campbell, K. V., Barker, G. E., and Gagnier, G. K., 1995, Tonalite-trondhjemite fractionation of peralumnious magma and the formation of syntectonic porphyry copper mineralization, Gibraltar Mine, central British Columbia, *in* Schroeter, T. G., ed., Porphyry Deposits of the Northwestern Cordillera of North America, CIM Special Volume 46: Quebec, Harpell's Press Cooperative, p. 201-213.

Campbell, A. R., and Larson, P. B., 1998, Chapter 8 Introduction to Stable Isotope Applications in Hydrothermal Systems, *in* Richards, J. P., and Larson, P. B., eds., Techniques in Hydrothermal Ore Deposits Geology, 10. Reviews in Economic Geology, Society of Economic Geologists, Inc., p. 173-193.

Carman, G. D., 1994, Genesis of the Ladolam Gold Deposit, Lihir Island, Papua New Guinea, Monash University, unpublished PhD thesis, 382 p.

Carman, G. D., 2003, Geology, Mineralization, and Hydrothermal Evolution of the Ladolam Gold Deposit, Lihir Island, Papua New Guinea, *in* Simmons, S. F., and Graham, I. G., eds., Volcanic, Geothermal, and Ore-Forming Fluids: Rulers and Witnesses of Processes within the Earth, Special Publication 10: Boulder, Colorado, Society of Economic Geologists, Inc., p. 247-279.

Casselman, M. J., McMillan, W. J., and Mewman, K. M., 1995, Highland Valley porphyry copper deposits near Kamloops, British Columbia: A review and update with emphasis on the Valley deposit, *in* Schroeter, T. G., ed., Porphyry Deposits of the Northwestern Cordillera of North America, CIM Special Volume 46: Quebec, Harpell's Press Cooperative, p. 161-191.

Cassidy, K. F., Lueck, B. A., and Russell, K. J., 1995, Geochemical Characteristics and Tectonic Significance of Mesozoic Silica-Undersaturated Alkalic Intrusions in the Cordillera of British Columbia: GAC/MAC annual meeting Victoria, May 17-19, v.20, p. A-115.

Chamberlain, C. M., Bath, A. B., Blackwell, J., Cooke, D. R., Henry, A. D., Jackson, M., Jago, C. P., Micko, J., Pass, H. E., Simpson, K. A., Tosdal, R. M., and Zukowski, W., 2007a, Towards an integrated model for alkalic porphyry and epithermal deposits in BC: Association for Mineral Exploration British Columbia Mineral Exploration Roundup Programs with Abstracts Vancouver, BC, p. 21.

Chamberlain, C. M., Jackson, M., Jago, C. P., Pass, H. E., Simpson, K. A., Cooke, D. R., and Tosdal, R. M., 2007b, Toward an Integrated Model for Alkalic Porphyry Copper Deposits in British Columbia (NTS 093A, N; 104G), *in* BC Ministry of Energy and Mines, Geological Fieldwork 2007, Paper 2007-1: Victoria, Crown Publications, p. 259-274.

Chiodini, G., and Frondini, F., 2001, Carbon dioxide degassing from the Albani Hills volcanic region, Central Italy: Chemical Geology, v. 177, p. 67-83.

Chiodini, G., Marini, L., and Russo, M., 2001, Geochemical evidence for the existence of high-temperature hydrothermal brines at Vesuvio volcano, Italy: Geochemica et Cosmochimica Acta, v. 65, p. 2129-2147.

Cleverley, J. S., and Bastrakov, E. N., 2005, K2GWB: Utility for generating thermodynamic data files for The Geochemist's Workbench® at 0-1000°C and 1-5000 bar from UT2K and the UNITHERM database: Computers and Geosciences, v. 31, p. 756-767.

Cloos, M., 1993, Lithospheric buoyancy and collisional orogenesis: subduction of oceanic plateaus, continental margins, island arcs, spreading ridges, and seamounts: Geological Society of America Bulletin, v. 105, p. 715-737.

Cook, N. J., and Chryssoulis, S. L., 1990, Concentrations of invisible gold in the common sulfides: The Canadian Mineralogist, v. 28, p. 1-16.

Cook, N. J., and Ciobanu, C. L., 2001, Paragenesis of Cu-Fe ores form Ocna de Fier-Dognecea (Romania), typifying fluid plume mineralization in a proximal skarn setting: Mineralogical Journal, v. 65, p. 351-371.

Cooke, D., Tosdal, D., Chamberlain, C., Deyell, C., Bath, A., Jackson, M., Jago, P., Pass, H., Micko, J., Henriques, F., Logan, J., and Simpson, K., 2006, Year 1 - Porphyry Module Update to Project Supports: Vancouver, BC, *prepared for* MDRU-University of British Columbia and CODES-University of Tasmania, 23 p.

Cooke, D. R., and Bloom, M. S., 1990, Epithermal and subjacent porphyry mineralization, Acupan, Baguio District, Philippines: a fluid-inclusion and paragenetic study: Journal of Geochemical Exploration, v. 35, p. 297-340.

Cooke, D. R., Bull, S. W., Large, R. R., and McGoldrick, P. J., 2000, The Importance of Oxidized Brines for the Formation of Australian Proterozoic Stratiform Sediment-Hosted Pb-Zn (Sedex) Deposits Economic Geology, v. 95, p. 1-18.

Cooke, D. R., Heithersay, P. S., Wolfe, R., and Calderon, A. L., 1998, Australian and western Pacific porphyry Cu-Au deposits: AGSO Journal of Australian Geology & Geophysics, v. 17, p. 97-104.

Cooke, D. R., and McPhail, D. C., 2001, Epithermal Au-Ag-Te Mineralization, Acupan, Baguio District, Philippines: Numerical Simulations of Mineral Deposition: Economic Geology, v. 96, p. 109-131.

Cooke, D. R., McPhail, D. C., and Bloom, M. S., 1996, Epithermal Gold Mineralization, Acupan, Baguio District, Philippines: geology, Mineralization, Alteration, and the Thermochemical Environment of Ore Deposition: Economic Geology, v. 91, p. 243-272.

Cooke, D. R., and Simmons, S. F., 2000, Chapter 6 Characteristics of Genesis of Epithermal Gold Deposits, *in* Hagemann, S. G., and Brown, P. E., eds., Reviews in Economic Geology, 13: Boulder, CO, Society of Economic Geologists, p. 221-244.

Cooke, D. R., Wilson, A. J., House, M. J., Wolfe, R. C., Walshe, J. L., Lickfold, V., and Crawford, A. J., 2007, Alkalic porphyry Au-Cu and associated mineral deposits of the Ordovician to Early Silurian Macquarie Arc, NSW: Australian Journal of Earth Science, v. 54, p. 445-463.

Corbett, G. J., and Leach, T. M., 1998a, Chapter 3 Structure of Magmatic Ore Systems, Southwest Pacific Rim Gold-Copper Systems: Structure, Alteration and Mineralization, Special Publication No.6, Society of Economic Geologists, p. 11-30.

Corbett, G. J., and Leach, T. M., 1998b, Chapter 4 Controls on Hydrothermal Alteration and Mineralization, Southwest Pacific Rim Gold-Copper Systems: Structure, Alteration and Mineralization, Special Publication No.6, Society of Economic Geologists, p. 69-81.

Coulson, I. M., Russell, J. K., and Dipple, G. M., 1999, Origins of the Zippa Mountain pluton: a Late Triassic, arc-derived, ultrapotassic magma from the Canadian Cordillera: Canadian Journal of Earth Sciences, v. 36, p. 1415-1434.

Coulson, I. M., Westphal, M., Anderson, R. G., and Kyser, T. K., 2007, Concommitant skarn and syenitic magma evolution at the margins of the Zippa Mountain pluton: Mineralogy and Petrology, v. 90, p. 199-221.

Cox, K. G., Bell, J. D., and Pankurst, R. J., 1981, The Interpretation of Igneous Rocks: London, George Allen and Unwin Ltd., 464 p.

Craig, H., 1957, Isotopic standards of carbon and oxygen and corrective factors for mass spectrographic analysis of carbon dioxide: Geochimica et Cosochimica Acta, v. 12, p. 133-149.

Craig, J. R., and Vaughan, D. J., 1990, Compositional and textural variations of the major iron and base-metal sulphide minerals, *in* Gray, P. M. J., Powyer, G. J., Castle, J. F., Vaughan, D. J., and Warner, N. A., eds., Sulphide Deposits-their origin and processing: London, England, The Institution of Mining and Metallurgy, p. 1-16.

Cuddy, A. S., and Kesler, S. E., 1982, Gold in the Granisle and Bell Copper porphyry copper deposits, British Columbia, *in* Levinson, A. A., ed., Precious Metals in the Northern Cordillera, Special Publication Number 10: Chicago, USA, The Association of Exploration Geochemists, p. 139–156.

Cygan, G. L., and Candela, P. A., 1995, Chapter 6 Preliminary Study of Gold Partitioning Among Pyrrhotite, Pyrite, Magnetite, and Chalcopyrite in Gold-Saturated Chloride Solutions at 600° to 700°C, 140 MPa (1400 bars), *in* Thompson, J. F. H., ed., Magmas, Fluids and Ore Deposits, Mineralogical Association of Canada Short Course Series, Shourt Course Volume 23: Victoria, BC, p. 129-137.

Danielson, V., 2005, Imperial reopens Mount Polley, The Northern Miner: Vancouver, BC, Vol. 91, No. 34, October, p. 14-20.

Danyushevsky, L., Robinson, P., Brian, W., McGoldrick, P., Large, R., and Gilbert, S., 2003, LA-ICPMS of sulphides: Evaluation of an XRF glass disc standard for analysis of different sulphide matrixes: 2003 Goldschmidt Conference, Japan: Geochimica Et Cosmochimica Acta, v. 67, p. A73 Suppl.

Danyushevsky, L. V., Robinson, P., Gilbert, S., Norman, M., Large, R., McGoldrick, P., and Shelley, J. M. G., in press, A technique for routine quantitative multi-element analysis of sulphide minerals by laser ablation ICP-MS: Geochemistry: Exploration, Environment, Analysis.

Davidson, G., 1997, Carbon/Oxygen Isotopes - their principles and uses in the exploration and understanding of fossil hydrothermal systems, *in* Center for Ore Deposit Research, ed., Exploration Geochemistry and Hydrothermal Geochemistry Part 2, Master of Economic Geology Course Work Manual 12, Fourth ed.: Hobart, CODES - University of Tasmania, p. 327-357.

Davidson, G. J., Cooke, D., and Wilson, A., in prep., Cracking the sulfate isotopic determination problem in ancient hydrothermal systems: a pilot assessment of the use of the carbonate-associated sulfate (CAS) method: Geology.

Davies, A. G. S., 2002, Geology and Genesis of the Kelian Gold Deposit, East Kalimantan, Indonesia: Unpublished PhD thesis, University of Tasmania, 404 p.

Davies, A. G. S., Cooke, D. R., and Gemmell, J. B., 2000, Breccias associated with epithermal and porphyry systems - towards a systematic approach to their description and interpretation: Gold in 2000. Poster session extended abstracts, Lake Tahoe, Nevada, p. 98-103.

Davies, A. G. S., Cooke, D. R., Gemmell, J. B., and Simpson, K. A., 2008a, Diatreme Breccias at the Kelian Gold Mine, Kalimantan, Indonesia: Precursors to Epithermal Gold Mineralization: Economic Geology, v. 103, p. 689-716.

Davies, A. G. S., Cooke, D. R., Gemmell, J. B., Van-Leeuwen, T., Cesare, P., and Hartshorn, G., 2008b, Hydrothermal Breccias and Veins at the Kelian Gold Mine, Kalimantan, Indonesia: Genesis of a Large Epithermal Gold Deposit: Economic Geology, v. 103, p. 717-757.

Deditius, A. P., Utsunomiya, S., Ewing, R. C., Chryssoulis, S. L., Venter, D., and Kesler, S. E., 2009a, Decoupled geochemical behaviour of As and Cu in hydrothermal systems: Geology, v. 37, p. 707-710.

Deditius, A. P., Utsunomiya, S., Reich, M., Kesler, S. E., Ewing, R. C., and Walshe, J. L., 2009b, Behaviour of trace elements in pyrite in ore deposits, *in* Fu, B., and Gleeson, S. A., eds., Smart Science for Exploration and Mining, Proceedings of the 10th Biennial SGA Meeting of The Society for Geology Applied to Mineral Deposits, 2: Townsville, Australia, Economic Geology Research Unit, James Cook University, p. 710-712.

Delong, R. C., 1996, Geology, Alteration, mineralization and metal zonation of the Mt. Millligan porphyry copper-gold deposit, unpublished MSc thesis, University of British Columbia, 250 p.

DeLong, R. C., Godwin, C. I., Harris, M. W., and Caira, N. M., 1990, Geology and Alteration at the Mount Milligan Gold-Copper Porphyry Deposit, Central British Columbia, Geological Fieldwork 1990, Paper 1991-1, p. 199 - 205.

DePaolo, D. J., and Wasserburg, G. J., 1976, Nd isotopic variations and petrogenetic models: Geophysical Research Letters, v. 3, p. 249-252.

Devine, F., and Baxter, P., 2007, Report on the 2006 Airborne Radiometric, Geological Mapping, Geochemical Soil Sampling and Diamond Drilling Program. Lorraine-Jajay Property, Omineca Mining Division, BC, *prepared for* Teck Cominco Ltd., 58 p.

Deyell, C. L., 2005, Sulphur isotope zonation at the Mt. Polley alkalic porphyry Cu-Au deposit, British Columbia, Canada: Mineral Deposit Research: Meeting the Global Challenge, Proceedings of the 8th Biennial SGA Meeting, Beijing, China, v.1, p. 373-376.

Deyell, C. L., and Tosdal, R. M., 2005, Alkalic Cu-Au Deposits of British Columbia: Sulphur Isotope Zonation as a Guide to Mineral Exploration, Geological Fieldwork 2004, Paper 2005-1: Victoria, BC, British Columbia Geological Survey Branch, p. 191-208.

Dominguez, S., Malavieille, J., and Lallemand, S. E., 2000, Deformation of accretionary wedges in response to seamount subduction; insights from sandbox experiments: Tectonics, v. 19, p. 182-196.

Dunne, K. P. E., Lang, J. R., and Thompson, J. F. H., 1994, Fluid inclusion studies of zoned hydrothermal garnet at the Galore Creek Cu-Au porphyry deposit, northwestern British Columbia: Program with Abstracts - Geological Association of Canada; Mineralogical Association of Canada: Joint Annual Meeting, v.10, p. 31.

Duuring, P., Rowins, S. M., McKinley, B. S. M., Dickinson, J. M., Diakow, L. J., Kim, Y.-S., and Creaser, R. A., 2009, Magmatic and structural controls on porphyry-style Cu-Au-Mo mineralization at Kemess South, Toodoggone District of British Columbia, Canada: Mineralium Deposita, v. 44, p. 435-462.

Economou-Eliopoulos, M., 2005, Chapter 10: Platinum-Group Element Potential of Porphyry Deposits, *in* Mungall, J. E., ed., Exploration for Deposits of Platinum-Group Elements, Short Course Series Volume 35: Oulu, Finland, Mineralogical Association of Canada, p. 203-246.

Economou-Eliopoulos, M., and Eliopoulos, D. G., 2000, Palladium, platinum and gold concentration in porphyry copper systems of Greece and their genetic significance Ore Geology Reviews, v. 16, p. 59-70.

Eichenlaub, A. B., and Seedorf, E., 2008, Exploration of genetic links between breccia pipes and porphyry copper deposits in a Laramide hydrothermal system, Sombrero Butte, Pinal County, Arizona, USA, *in* Spencer, J. E., and Titley, S. R., eds., Ore and Orogenesis: Circum-Pacific tectonics, geologic evolution, and ore deposits: Tuscon, Arizona Geological Society Digest 22, p. 591-599.

Einaudi, M. T., 1997, Mapping Altered and Mineralized Rocks and introduction to The "Anaconda Method", Standford University, 16 p.

Eliopoulos, D. G., and Economou-Eliopoulos, M., 1991, Platinum-Group Element and Gold Contents in the Skouries Porphyry Copper Deposit, Chalkidiki Peninsula, Northern Greece: Economic Geology, v. 86, p. 740-749.

Emmons, W. H., 1927, Relations of metalliferous lode systems to igneous intrusives: Transactions of the American Institute of Mining, Metallurgical and Petroleum Engineers, Incorporated, v. 75, p. 797-815.

Engler, P., Santana, M. W., Mittleman, M. L., and Balazs, D., 1988, Non-isothermal in situ XRD analysis of dolomite decomposition: The Rigaku Journal, v. 5, p. 3-8.

Enns, S. G., Thompson, J. F. H., Stanley, C. R., and Yarrow, E. W., 1995, The Galore Creek porphyry copper-gold deposits, northwestern British Columbia, *in* Schroeter, T. G., ed., Porphyry Deposits of the Northwestern Cordillera of North America, CIM Special Volulme 46: Quebec, Harpell's Press Cooperative, p. 630-644.

Fox, N., Harris, A. C., Cooke, D. R., and Collett, D., 2008, Contrasting mineralisation and alteration styles and a possible alkalic lithocap at the Cadia East porphyry Au-Cu deposit, NSW, Australia, Proceedings of the 33rd International Geological Congress, Oslo, Norway, 6 - 14 August 2008.

Fox, P. E., 1975, Alkaline rocks and related mineral deposits of the Quesnel Trough, British Columbia, Symposium on Intrusive Rocks and Related Mineralization of the Canadian Cordilleran: Program with abstracts, Geological Association of Canada, Cordilleran Section, p. 12.

Fox, P. E., and Cameron, R. S., 1991, A model for alkaline copper-gold porphyry deposits: Program with Abstracts - Geological Association of Canada; Mineralogical Association of Canada: Joint Annual Meeting, Vancouver, BC, Canada, v.16, p. 39.

Fraser, T. M., 1994a, Geology, alteration and origin of hydrothermal breccias at the Mount Polley alkalic copper-gold porphyry deposit, south-central British Columbia: Unpublished M.Sc. thesis, University of British Columbia, 259 p.

Fraser, T. M., 1994b, Hydrothermal Breccias and Associated Alteration of the Mount Polley Copper-Gold Deposit (93 A/12), Geological Fieldwork 1993, Paper 1994-1, p. 259-267.

Fraser, T. M., Godwin, C. I., Thompson, J. F. H., and Stanley, C. R., 1993, Geology and Alteration of the Mount Polley Alkalic Porphyry Copper-Gold Deposit, British Columbia (93A/12), *in* British Columbia Geological Survey Branch, ed., Geological Fieldwork 1992, Paper 1993-1: Victoria, BC, p. 295-300.

Fraser, T. M., Stanley, C. R., Nikic, Z. T., Pesalj, R., and Gorc, D., 1995, The Mount Polley alkalic porphyry copper-gold deposit, south-central British Columbia, *in* Schroeter, T. G., ed., Porphyry

Deposits of the Northwestern Cordillera of North America, CIM Special Volume 46: Sainte-Anne-de-Bellevue, Quebec, Harpell's Press Cooperative, paper 44, p. 609-622.

Friedman, I., and O'Neil, J. R., 1977, Compilation of stable isotope fractionation factors of geochemical interest, *in* Fleischer, M., ed., Data of Geochemistry, 6th ed., Prof. Paper 440-55: Washington, DC, Government Printing Office, 49 p.

Frikken, P. H., Cooke, D. R., Walshe, J. L., Archibald, D., Skarmeta, J., L.Serrano, and Vargas, R., 2005, Mineralogical and Isotopic Zonation in the Sur-Sur Tourmaline Breccia, Rip Blanco-Los Bronces Cu-Mo Deposit, Chile: Implications for Ore Genesis: Economic Geology, v. 100, p. 935-961.

Gabrielse, H., Monger, J. W. H., Wheeler, J. O., and Yorath, C. J., 1991, Chapter 2 Tectonic Framework. Part A. Morphological belts, tectonic assemblages, and terranes, *in* Gabrielse, H., and Yorath, C. J., eds., Geology of Canada, 4, Geological Survey of Canada, p. 15-28.

Gammons, C. H., Bloom, M. S., and Yu, Y., 1992, Experimental investigation of the hydrothermal geochemistry of platinum and palladium: I. Solubility of platinum adn palladium sulfide minerals in $NaCl/H_2SO_4$ solutions at 300°C: Geochimica et Cosmochimica Acta, v. 56, p. 3881-3894.

Gammons, C. H., and Williams-Jones, A. E., 1997, Chemical Mobility of Gold in the Porphyry-Epithermal Environment: Economic Geology, v. 92, p. 45-59.

Ganino, C., Arndt, N. T., Zhou, M., Gaillard, F., and Chauvel, C., 2008, Interaction of magma with sedimentary wall rock and magnetite ore genesis in the Panzhihua mafic intrusion, SW China: Mineralium Deposita, v. 43, p. 677-694.

Garnett, J. A., 1978, Geology and mineral occurences of the southern Hogem Batholith, B.C. Ministry of Energy, Mines and Petroleum Resources Bulletin 70, 75 p.

Gilbert, S., Danyushevsky, L., and Norman, M., 2005, Laser Ablation ICPMS Methodology, Sulfide microanalysis to enhance exploration success (Industry project C201, 2002). What controls trace-metal values in hydrothermal sulfides. The LA-ICPMS prespective. (ARC Linkage project 2003-2004): Hobart, CODES, University of Tasmania, p. 2.1-2.9.

Gilchrist, J. D., 1989, Extraction Metallurgy: Oxford, Pergamon Press, 145 p.

Gillstrom, G., 2004, 43-101 Technical Report, Mount Polley Mine, 2004 Feasibility Study, August 1, 2004: Vancouver, BC, *prepared for* Imperial Metals Corporation, 145 p.

Godwin, C. I., Gabites, J. E., and Andrew, A., 1988, Leadtable: A Galena Lead Isotope Data Base for the Canadian Cordillera, with a guide to its use by explorationists, A contribution to the Canada/British Columbia Mineral Development Agreement, 1985 - 1900, Mineral Resources Division, Geological Survey Branch, 187 p.

Goh, S. W., Bucklye, A. N., Lamb, R. N., Rosenberg, R. A., and Moran, D., 2006, The oxidation states of copper and iron in mineral sulfides, and the oxides formed on initial exposure to chalcopyrite and bornite to air: Geochemica et Cosmochimica Acta, v. 70, p. 2210-2228.

Graham, R., 2003, Imperial Metals on the mend, High-grade zone found at Mount Polley, The Northern Miner, October 17-23, v. 39, no. 35.

Gunasekaran, S., and Anbalagan, G., 2007, Thermal decomposition of natural dolomite: Bulletin of Material Science, v. 30, p. 339-344.

Gustafson, L. B., and Hunt, J. P., 1975, The porphyry copper deposit at El Salvador, Chile: Economic Geology, v. 70, p. 857-912.

Gutscher, M.-A., Maury, R., Eissen, J.-P., and Bourdon, E., 2000, Can slab melting be caused by flat subduction?: Geology, v. 28, p. 535-538.

Gutscher, M.-A., Olivet, J.-L., Aslanian, D., Eissen, J.-P., and Mauryd, R., 1999, The "lost Inca Plateau": cause of flat subduction beneath Peru?: Earth and Planetary Science Letters, v. 171, p. 335-341.

Harker, A., 1908, The geology of the small isles of Inverness-shire (Rhum, Canna, Eigg, Muck, etc.), Scotland Geological Survery Memoir, 210 p.

Harper, B. L., 2000, Hydrothermal alteration at the Ridgeway porphyry gold-copper deposit, NSW: Unpublished B.Sc. Honours thesis, University of Tasmaina, 130 p.

Harris, A. C., and Golding, S. D., 2002, New evidence of magmatic-fluid related to phyllic alteration: implications for the genesis of porphyry Cu deposits: Geology, v. 30, p. 335-338.

Hedenquist, J. W., A. Arribas, J., and Reynolds, T. J., 1998, Evolution of an Intrusion-Centered Hydrothermal System: Far Southeast-Lepanto Porphyry and Epithermal Cu-Au Deposits, Philippines: Economic Geology, v. 93, p. 373-404.

Hedenquist, J. W., and Henley, R. W., 1985, Hydrothermal Eruptions in the Waiotapu Geothermal System, New Zealand: Their Origin, Associated Breccias, and Relation to Precious Metal Mineralization: Economic Geology, v. 80, p. 1640-1668.

Hedenquist, J. W., and Houghton, B. F., 1987, Epithermal gold mineralization and its volcanic environments: Sydney, University of Sydney, Earth Resources Foundation, 422 p.

Heithersay, P. S., and Walshe, J. L., 1995, Endeavour 26 North: A porphyry copper-gold deposit in the late Ordovician, shoshonitic Goonumbla volcanic complex, New South Wales, Australia: Economic Geology, v. 90, p. 1506-1532.

Hemley, J. J., Montoya, J. W., Marinenkoa, J. W., and Luce, R. W., 1980, Equilibria in the System Al_2O_3-SiO_2-H_2O and Some General Implications for Alteration/Mineralization Processes: Economic Geology, v. 75, p. 210-228.

Henley, R. W., and Ellis, A. J., 1983, Geothermal systems ancient and modern; a geochemical review: Earth-Science Reviews, v. 19, p. 1-50.

Hodgson, C. J., Bailey, R. J., and Verzosa, R. S., 1976, Cariboo-Bell, *in* Brown, A. S., ed., Porphyry Deposits Of The Canadian Cordillera, CIM Special Volume 15: Ste. Anne de Bellevue, Harpell's Press Cooperative, p. 388-396.

Hoefs, J., 1987, Stable Isotope geochemistry: Berlin, Springer-Verlag.

Holland, H. D., and Malinin, S. D., 1979, The solubility and occurrence of non-ore minerals *in* Barnes, H. L., ed., Geochemistry of Hydrothermal Ore Deposits: New York, John Wiley and Sons, p. 461-508.

Holliday, J., McMillan, C., and Tedder, I., 1999, Discovery of the Cadia Ridgeway gold-copper deposit: New generation gold mines - case histories of discovery: Perth, Australian Mineral Foundation, p. 101-107.

Holliday, J. R., Wilson, A. J., Blevin, P. L., Tedder, I. J., Dunham, P. D., and Pfitzner, M., 2002, Porphyry gold-copper mineralization in the Cadia district, eastern Lachlan Ford Belt, New South Wales, and it's relationship to shoshonitic magmatism: Mineralium Deposita, v. 37, p. 100-116.

House, M. J., 1994, Gold distribution at the E26 porphyry copper-gold deposit, Goonumbla, NSW, upublished MSc thesis, University of Tasmania, 126 p.

Huston, D. L., and Large, R. R., 1989, A chemical model of the distribution of gold and in volcanogenic massive sulfide deposits: Ore Geology Reviews, v. 4, p. 171-200.

Huston, D. L., Sie, S. H., Suter, G. F., Cooke, D. R., and Both, R. A., 1995, Trace Elements in Sulfide Minerals from Eastern Australian Volcanic-Hosted Massive Sulfide Deposits: Part I. Proton Microprobe Analyses of Pyrite, Chalcopyrite, and Sphalerite, and Part II. Selenium Levels in Pyrite: Comparison with δ^{34} Values and Implications for the Source of Sulfur in Volcanogenic Hydrothermal Systems: Economic Geology, v. 90, p. 1167-1196.

Iacano-Marziano, G., and Gaillard, F., 2006, Limetone Assimilation: a Dominant non-Magmatic Source of Volcanic CO_2: EOS Transactions. AGU, Joint Assembly Supplement, Abstract, p. V34A-04.

Iacono-Marziano, G., Gaillard, F., and Pichavant, M., 2007, Limestone assimilation and the origin of CO_2 emissions at the Alban Hills (Central Italy): Constraints from experimental petrology: Journal of Volcanology and Geothermal Research, v. 166, p. 91-105.

Iacono-Marziano, G., Gaillard, F., and Pichavant, M., 2008, Limestone assimilation by basaltic magmas: an experimental re-assessment and application to Italian volcanoes: Contributions to Mineral Petrology, v. 155, p. 719-738.

Iacono-Marziano, G., Gaillard, F., Scaillet, B., Pichavant, M., and Chiodini, G., 2009, Role of non-mantle CO_2 in the dynamics of volcano degassing: The Mount Vesuvius example: Geology, v. 37, p. 319-322.

Imperial Metals Corporation, 2007, "Imperial Reports 2006 Production and Updated Mount Polley Reserve" (Fri. March 2, 2007 News Release): Vancouver, BC.

Imperial Metals Corporation, 2009a, Imperial Metals Annual Information Form, For the year ended December 31, 2008: Vancouver, BC, http://www.imperialmetals.com/i/pdf/Imperial.AIF.2009.march30.pdf.

Imperial Metals Corporation, 2009b, Imperial Updates Mineral Reserve and Mineral Resource Estimates for Mount Polley and Huckleberry, www.imperialmetals.com/s/News-2009, marketwire media release, 30 March 2009.

Imperial Metals Corporation, 2010, Annual Information Form for the year ended December, 31 2009, http://www.imperialmetals.com/i/pdf/2010_AIF.pdf, p. 68.

Irvine, T. N., and Baragar, W. R. A., 1971, A guide to the chemical classification of the common volcanic rocks: Canadian Journal of Earth Sciences, v. 8, p. 523-548.

Jackson, M., Tosdal, D., Chamberlain, C., Pass, H., and Bath, A., 2007a, Brecciation, Mineralization, and Igneous Rocks of the Northeast zone, Mount Polley Mine, BC: Association for Mineral Exploration British Columbia Mineral Exploration Roundup Programs with Abstracts Vancouver, BC, p. 23.

Jackson, M., Tosdal, R., and Chamberlain, C. C., 2007b, Igneous rocks related to brecciation and mineralization in the Mount Polley alkalic Cu-Au porphyry system, British Columbia: Ores and Orogenesis - Program with Abstracts, Tucson, Arizona, p. 166.

Jackson, M., Tosdal, R. M., Chamberlain, C. M., Simpson, K., and McAndless, P., 2007c, Breccia architecture as a control on ore distribution, Mount Polley mine, British Columbia: Breccias - An EGRU 25th Birthday Symposium, Townsville, Australia, EGRU Contribution 65, p. 12.

Jackson, M. L., 2008, Evolution of the Northeast Zone Breccia Body, Mount Polley Mine, British Columbia: Unpublished M.Sc. thesis, University of British Columbia, 238 p.

Jago, C. P., 2008, Metal- and alteration-zoning, and hydrothermal flow paths at the moderately-tilted, silica-saturated Mt. Milligan Cu-Au alkalic porphyry deposit, unpublished MSc thesis, University of British Columbia, 227 p.

Jago, C. P., and Tosdal, R., 2008, The Early Jurassic Mt. Milligan (British Columbia): an example of the younger silica-saturated alkalic porphyry Cu-Au deposit, Shallow- and Deep-Level Alkalic Mineral Deposits: Developing an Integrated Exploration Model, Year 3 - Porphyry Module Final Update to Sponsors, *prepared for* MDRU-University of British Columbia and CODES-University of Tasmania, p. 5.1 - 5.10.

Jébrak, M., 1997, Hydrothermal breccias in vein-type ore deposits: A review of mechanisms, morphology and size distribution: Ore Geology Reviews, v. 12, p. 111-134.

Jensen, E., 2003, Magmatic and Hydrothermal Evolution of the Cripple Creek Gold Deposit, Colorado, and Comparisons with Regional and Global Magmatic-Hydrothermal Systems Associated with Alkaline Magmatism: Unpublished PhD thesis, University of Arizona, 846 p.

Jensen, E. P., and Barton, M. D., 2000, Chapter 8 Gold Deposits Related to Alkaline Magmatism *in* Hagemann, S. G., and Brown, P. E., eds., Gold in 2000, Reviews in Economic Geology, 13: Chelsea, MI, Society of Economic Geologists Inc., p. 279-314.

Johnson, J. W., Oelkers, E. H., and Helgeson, H. C., 1992, SUPCRT92: A software package for calculating the standard molal thermodynamic properties of minerals, gases, aqueous species and

reactions from 1 to 5000 bars and 0° to 1000°C Computers and Geosciences, v. 18, p. 899-947.

Johnston, S. T., and Borel, G. D., 2007, The odyssey of the Cache Creek terrane, Canadian Cordillera: Implications for accretionary orogens, tectonic setting of Panthalassa, the Pacific superwell, and break-up of Pangea: Earth and Planetary Science Letters, v. 253, p. 415-428.

Jones, B. K., 1992, Application of metal zoning to gold exploration in porphyry copper systems: Journal of Geochemical Exploration, v. 43, p. 127 - 155.

Jones, G. J., 1985, The Goonumbla porphyry copper deposits, New South Wales: Economic Geology, p. 591 – 613.

Kajiwra, Y., and Krouse, H. R., 1971, Sulfur isotope partitioning in metallic sulfide systems: Canadian Journal of Earth Science, v. 8, p. 1397-1408.

Kamenetsky, V., Métrich, N., and Cioni, R., 1995, Potassic primary melts of Vulsini (Roman Provine): evidence from mineralogy and melt inclusions: Contributions to Mineral Petrology, v. 120, p. 186-196.

Kamenetsky, V. S., Pompilio, M., Métrich, N., Sobolev, A. V., Kuzmin, D. V., and Thomas, R., 2007, Arrival of extremely volatile-rich high-Mg magmas changes explosivity of Mount Etna: Geology, v. 35, p. 255-258.

Kantiranis, N., Filippidis, A., Tsirambides, A., and Christaras, B., 2005, Thermal decomposition study of crystalline limestone using P-wave velocity Construction and Building Materials.

Kelser, S. E., Jones, L. M., and Walker, R. L., 1975, Intrusive Rocks Associated with Porphyry Copper Mineralization in Island Arc Areas: Economic Geology, v. 70, p. 515-526.

Kesler, S. E., Chryssoulis, S. L., and Simon, G., 2002, Gold in porphyry copper deposits: its abundance and fate: Ore Geology Reviews, v. 21, p. 103-124.

Kirkham, R. V., and Sinclair, W. D., 1955, Porphyry copper, gold, molybdenum, tungsten, tin, silver, *in* Eckstrand, O. R., Sinclair, W. D., and Thorpe, R. I., eds., Geology of Canadian Mineral Deposit Types, 8: Geology of Canada, Geological Survey of Canada, p. 421-446.

Kitto, P. A., 1994, Structural and Geochemical Controls on Mineralisation at Renison, Tasmania: Unpublished PhD thesis, University of Tasmania, 180 p.

Knittel, U., 1987, The Cordon syenite complex; an undersaturated potassic igneous center in the Philippine island arc: Neues Jahrbuch fuer Mineralogie, v. 157, p. 57-80.

Lambert, I. B., and Wyllie, P. J., 1972, Melting of gabbro (quartz eclogite) with excess water to 35 kilobars, with geological applications: Journal of Geology, v. 80, p. 693-708.

Lang, J. R., 1992, Mount Milligan Geochemistry, *prepared for* MDRU Porphyry Cu-Au Project, Year 1, p. 2-49.

Lang, J. R., Stanley, C. R., and Thompson, J. F. H., 1993, A Subdivision of Alkalic Porphyry Cu-Au Deposits Into Silica-Saturated and Silica-Undersaturated Subtypes, Copper-Gold Porphyry Systems of British Columbia, Annual Technical Report, Year 2, Mineral Deposits Research Unit, p. 15-27.

Lang, J. R., Lueck, B., Mortensen, J. K., Russell, J. K., Stanely, C. R., and Thompson, J. F. H., 1995a, Triassic-Jurassic silica-undersaturated and silica-saturated alkalic intrusions in the Cordillera of British Columbia: Implications for arc magmatism: Geology, v. 23, p. 451-454.

Lang, J. R., Stanley, C. R., and Thompson, J. F. H., 1995b, Porphyry Copper-Gold Deposits Related to Alkalic Igneous Rocks in the Triassic-Jurassic Arc Terranes of British Columbia, *in* Pierce, F. W., and Bolm, J. G., eds., Porphyry Copper Deposits of the American Cordillera, Arizona Geological Society, Digest 20 p. 219-236.

Lang, J. R., Stanley, C. R., Thompson, J. F. H., and Dunne, K. P. E., 1995c, Na-K-Ca Magmatic-Hydrothermal Alteration in Alkalic Porphyry Cu-Au Deposits, British Columbia, *in* Thompson, J. F. H., ed., Magmas, Fluids and Ore Deposits, Mineralogical Association of Canada Short Course Series, Short Course Volume 23: Victoria, BC, p. 339-366.

Lang, J. R., and McClaren, M., 2003, Hydrothermal alteration, mineralization and exploration potential of the Mars alkalic copper-gold-molybdenum porphyry occurence, Laberge map area (105E/7), Yukon, Yukon Exploration and Geology 2003, p. 261-1269.

Large, R. R., Bull, S. W., Winefield, P.R., 2001, Carbon and Oxygen Isotope Halo in Carbonates Related to the McArthur River (HYC) Zn-Pb-Ag Deposit, North Australia: Implications for Sedimentation, Ore Genesis, and Mineral Exploration: Economic Geology, v. 96, p. 1567-1593.

Large, R. R., Danyushevsky, L. V., Hollit, C., Maslennikov, V. V., Meffre, S., Gilbert, S., Bull, S., Scott, R., Emsbo, P., Thomas, H., Singh, B., and Foster, J., 2009, Gold and Trace Element Zonation in Pyrite using a Laser Imaging Technique: Implications for the Timing of Gold in Orogenic and Carlin-Style Sediment-Hosted Deposits: Economic Geology, v. 104, p. 635-668.

Large, R. R., Maslennikov, V. V., Robert, R., Danyushevsky, L. V., and Chang, Z., 2007, Multistage Sedimentary and Metamorphic Origin of Pyrite and Gold in the Giant Sukhoi Log Deposit, Lena Gold Province, Russia: Economic Geology, v. 102, p. 1232-1267.

Laznicka, P., 1988, Breccias and coarse fragmentites. Petrology, Environments, Associations, Ores: Amsterdam, Elsevier, 832 p.

LeFort, D., Hanley, J., Guillong, M., in review, Epithermal Au-Pd mineralization associated with an alkalic porphyry Cu-Au deposit, Mt. Milligan, Quesnel Terrane, British Columbia, Canada: Economic Geology.

LeMaitre, R. W., Bateman, P., Dudek, A., Keller, J., Lameyre, J., Bas, M. J. L., Sabine, P. A., R.Schmid, Sørensen, H., Streckeisen, A., Woolley, A. R., and Zanettin, B., 1989, Igneous Rocks: A Classification and Glossary of Terms: Recommendations of the International Union of Geological Sciences Subcommission on the Systematics of Igneous Rocks: London, Blackwell Scientific Publications, 236 p.

Li, Y. B., and Liu, J. M., 2006, Calculation of sulfur isotope fractionation in sulfides: Geochimica et Cosmochimica Acta, v. 70, p. 1789 - 1795.

Lickfold, V., Cooke, D. R., Crawford, A. J., and Fanning, C. M., 2007, Shoshonitic magmatism and the formation of the Northparkes porphyry Cu–Au deposits, New South Wales: Australian Journal of Earth Sciences, v. 54, p. 279-306.

Lickfold, V., Cooke, D. R., Smith, S. G., and Ullrich, T. D., 2003, Endeavour Copper-Gold Porphyry Deposits, Northparkes, New South Wales: Intrusive History and Fluid Evolution: Economic Geology, v. 98, p. 1607-1636.

Logan, J. M., 2004, Alkaline Magmatism and Porphyry Cu-Au Deposits at Galore Creek, Northwestern British Columbia, Geological Fieldwork 2004, Paper 2005-1, B.C. Ministry of Energy and Mines, p. 237-248.

Logan, J. M., and Bath, A. B., 2006, Geochemistry of Nicola Group Basalt from the Central Quesnel Trough at the Latitude of Mount Polley (NTS 093A/5, 6, 11, 12), Central British Columbia, *in* British Columbia Ministry of Engergy Mines and Petroleum Resources, ed., Geological Fieldwork 2005, Paper 2006-1: Victoria, p. 83-98.

Logan, J. M., and Koyanagi, V. M., 1989, Preliminary Geology and Mineral Deposits of the Galore Creek Area, North-western British Columbia (104G/7W), Geological Fieldwork 1988, Paper 1989-1, B.C. Ministry of Energy, Mines and Petroleum Resources, p. 269-284.

Logan, J. M., Loyanagi, V. M., and Rhys, D. A., 1989, Geology and Mineral Occurences of the Galore Creek Area (104A and B), BC: BC Ministry of Engery, Mines and Petroleum Resources, Open File 1989-8.

Logan, J. M., and Mihalynuk, M. G., 2005, Regional Geology and Setting of the Cariboo, Bell. Springer and Northeast Porphyry Cu-Au Zones at Mount Polley, South-Central British Columbia, Geological Fieldwork 2004, Paper 2005-1, B.C. Ministry of Energy and Mines, p. 249-270.

Logan, J. M., Mihalynuk, M. G., Ullrich, T., and Freidman, R. M., 2007, U-Pb Ages of Intrusive

Rocks and $^{40}Ar/^{39}Ar$ Plateau Ages of Copper-Gold-Silver Mineralization Associated with Alkaline Intrusive Centres at Mount Polley and the Iron Mask Batholith, Southern and Central British Columbia, Geological Fieldwork 2006, Paper 2007-1, B.C. Ministry of Energy and Mines, p. 93-116.

Longerich, H. P., Jackson, S. E., and Gunther, D., 1996, Laser ablation inductively couple plasma mass spectrometric transient signal data acquisition and analyte concentration calculation: Journal of Analytical Atomic Spectrometry, v. 11, p. 899-904.

Losada-Calderon, A. J., and McPhail, D. C., 1996, Chapter 8 Porphyry and high-sulfidation epithermal mineralization in the Nevados del Famatina mining district, Argentina, *in* Camus, F., Sillitoe, R. M., and Petersen, R., eds., Andean copper deposits; new discoveries, mineralization, styles and metallogeny, Special Publication, vol. 5: Littleton, CO, Society of Economic Geologists, p. 91-118.

Lowell, J. D., and Guilbert, J. M., 1970, Lateral and Vertical Alteration-Mineralization Zoning in Porphyry Ore Deposits Economic Geology, v. 65, p. 373-408.

Ludwig, K. R., 2003, User's Manual for Isoplot 3.00, A Geochronological Toolkit for Microsoft Excel, Berkeley Geochronological Center, Special Publication No.4, 71 p.

Lueck, B. A., and Russell, J. K., 1994, Silica-Undersaturated, Zoned, Alkaline Intrusions within the British Columbia Cordillera, *in* British Columbia Geological Survey Branch, ed., Geological Fieldwork 1993, Paper 1994-1: Victoria, BC, p. 311-315.

Lynch, J. V. G., Longstaffe, F. J., and Nesbit, B. E., 1990, Stable isotopic and fluid inclusion indications of large-scale hydrothermal paleoflow, boiling, and fluid mixing in the Keno Hill Ag-Pb-Zn district, Yukon Territory, Canada: Geochemica et Cosmochimica Acta, v. 54, p. 1045-1059.

Maas, R., Kamenetsky, M. B., Sobolev, A. V., Kamenetsky, V. S., and Sobolev, N. V., 2005, Sr-Nd-Pb isotopic evidence for a mantle origin of alkali chlorides and carbonates in the Udachnaya kimberlite, Siberia: Geology, v. 35, p. 549-552.

MacDonald, G. A., and Katsura, T., 1964, Chemical composition of Hawaiian lavas: Journal of Petrology, v. 5, p. 82-133.

Makovivky, E., 2006, Crystal Structures of Sulfides and other Chalcogenides, *in* Vaughan, D. J., ed., Reviews in Mineralogy and Geochemistry: Sulfide Mineralogy and Geochemistry, 61: Chantilly, Virgina, The Mineralogical Society of America, p. 7-125.

Malik, W. U., Gupta, D. R., Masood, I., and Gupta, R. S., 1985, Kinetic study of thermal decomposition of calcium carbonate in teh presence of K_2CO_3 and $BaCO_3$: Journal of Materials Science Letters, v. 4, p. 532-536.

Marín-Cerón, M. I., Moriguti, T., Makishima, A., and Nakamura, E., 2010, Slab decarbonation and CO_2 recycling in the Southwestern Colombian volcanic arc: Geochemica et Cosmochimica Acta, v. 74, p. 1101-1121.

Masterman, G., 2003, Geology of the Rosario Cu-Mo-Ag Mine, Collahusai, Chile, University of Tasmania, Unpublished PhD thesis, 253 p.

McCrea, J. M., 1950, On the isotopic chemistry of carbonates and paleotemperature scale: Journal of Chemical Physics, v. 18, p. 849-857.

McInnes, B. I. A., and Cameron, E. M., 1994, Carbonated, alkaline hybridizing melts from a sub-arc environment: Mantle wedge samples from the Tabar-Lihir-Tanga-Feni arc, Papua New Guinea: Earth and Planetary Science Letters, v. 122, p. 125-141.

McMillan, W. J., and Panteleyev, A., 1995, Porphyry copper deposits of the Canadian Cordillera, *in* Pierce, F. W., and Bolm, J. G., eds., Bootprints along the Cordillera; Porphyry copper deposits from Alaska to Chile, 20. Porphyry copper deposits of the American Cordillera: Tucson, AZ, United States, Arizona Geological Society, p. 203-218.

McMillan, W. J., Thompson, J. F. H., Hart, C. J. R., and Johnston, S. T., 1995, Regional geological and tectonic setting of porphyry deposits in British

Columbia and Yukon Territory, *in* Schroter, T. G., ed., Porphyry Deposits of the Northwestern Cordillera of North America, CIM Special Volume 46: Sainte-Anne-de-Bellevue, Quebec, Harpell's Press Cooperative, p. 40-57.

McPhie, J. C., Allen, R., and Doyle, M., 1993, Volcanic textures, a guide to the interpretation of textures in volcanic rocks: Hobart, Centre for Ore Deposit Research, University of Tasmania, 198 p.

Meffre, S., Large, R. R., Scott, R., Woodhead, J., Chang, Z., Gilbert, S. E., Danyushevsky, L. V., Maslennikov, V., and Hergt, J. M., 2008, Age and pyrite Pb-isotopic composition of the giant Sukhoi Log sediment-hosted gold deposit, Russia: Geochimica et Cosmochimica Acta v. 72, p. 2377-2391.

Menand, T., and Phillips, J. C., 2007, Gas segregation in dykes and sills: Journal of Volcanology and Geothermal Research, v. 159, p. 393-408.

Micko, J., 2007, Lithological distribution, hydrothermal alteration and mineralization at the Central Zone, Galore Creek alkalic Cu-Au porphyry deposit, NW British Columbia, Shallow- and Deep-Level Alkalic Mineral Deposits: Developing an Integrated Exploration Model, Year 2 - Porphyry Module Update to Project Sponsors, *prepared for* MDRU-University of British Columbia and CODES-University of Tasmania, p. 3.1-3.10.

Micko, J., Tosdal, R., Simpson, K., Chamberlain, C., and Schwab, D., 2008, Controls and Hydrothermal Zonation of Central Zone Mineralization at the Galore Creek Alkalic Cu-Au Porphyry Deposit, northwestern British Columbia, Shallow- and Deep-Level Alkalic Mineral Deposits: Developing an Integrated Exploration Model, Year 3 - Porphyry Module Final Update to Sponsors, *prepared for* MDRU-University of British Columbia and CODES-University of Tasmania, p. 2.1-2.27.

Mihalynuk, M. G., 1999, Geology and Mineral Resources of the Tagish Lake Area (NTS 104M/8,9,10E15 and 104N/12W) Northwestern British Columbia, Bulletin 105: Victoria, British Columbia Ministry of Energy and Mines, 202 p.

Mihalynuk, M. G., Nelson, J., and Diakow, L. J., 1994, Cache Creek terrane entrapment: oroclinal paradox within the Canadian Cordillera: Tectonics, v. 13, p. 575-595.

Miller, C. F., 1978, Monzonitic Plutons, California, and a Model for Generation of Alkali-Rich, Near Silica-Saturated Magmas: Contributions to Mineralogy and Petrology, v. 67, p. 349-355.

Mitcham, T. W., 1974, Origin of Breccia Pipes: Economic Geology, v. 69, p. 412-413.

Monger, J. W. H., 1977a, Upper Paleozoic rocks of the northwestern British Columbia, Paper 77-1A, Geological Survey of Canada, 255-262 p.

Monger, J. W. H., 1977b, Upper Paleozoic rocks of the western Canadian Cordillera and their bearing on Cordilleran evolution: Canadian Journal of Earth Sciences, v. 14, p. 1832-1859.

Monger, J. W. H., and Berg, H. C., 1987, Lithotectonic terrane map of Western Canada and southeastern Alaska, Miscellaneous Field Studies Map: U. S. Geological Survey, Map MF-1874-B plus 12 p.

Monger, J. W. H., and Nokelberg, W. J., 1996, Evolution of the northern North American Cordillera; generation, fragmentation, displacement and accretion of successive North American plate margin arcs, *in* Coyner, A. R., and Fahey, P. L., eds., Geology and ore deposits of the American Cordillera: Geological Society of Nevada Symposium Proceedings: Reno/Sparks, Nevada, Geological Society of Nevada, p. 1133-1152.

Monger, J. W. H., Wheeler, J. O., Tipper, H. W., Gabrielse, H., Hanns, T., Struik, L. C., Campbell, R. B., Dodds, C., Gehrels, G. E., and O'Brien, J., 1991, Part B. Cordilleran Terrranes, Upper Devonian to Middle Jurassic Assemblages, Chapter 8, *in* Gabriesse, H., and Yorath, C. I., eds., Geology of the Cordilleran Orogen in Canada, Geology of Canada, Number 4, Geological Survey of Canada, p. 281-327.

Mortensen, J. K., Ghosh, D. K., and F.Ferri, 1995, U-Pb geochronology of intrusive rocks associated with copper-gold porphyry deposits in the Canadian Cordillera, *in* Schroter, T. G., ed., Porphyry Deposits of the Northwestern Cordillera of North

America, CIM Special Volume 46: Sainte-Anne-de-Bellevue, Quebec, Harpell's Press Cooperative, p. 142-158, paper 7.

Mortimer, N., 1987, The Nicola Group: Late Triassic and Early Jurassic Subduction-related Volcanism in British Columbia: Canadian Journal of Earth Science, v. 24, p. 2521-2536.

Mortimer, N., van-der-Heyden, P., Armstrong, R. L., and Harakal, L. J., 1990, U-Pb and K-Ar Dates Related to the Timing of Magmatism and Deformation in the Cache Creek Terrane and Quesnellia, Southern British Columbia: Canadian Journal of Earth Science, v. 27, p. 117-123.

Morton, R. L., 1976, Alkalic volcanism and copper deposits of the Horsefly Area, British Columbia: Unpublished PhD thesis, Carleton University, 196 p.

Müller, D., and Groves, D. I., 1993, Direct and indirect associations between potassic igneous rocks, shoshonites and gold-copper deposits: Ore Geology Reviews, v. 8, p. 383-406.

Mungall, J., 2002, Roasting the mantle: Slab melting and the genesis of major Au and Au-rich Cu deposits: Geology, v. 30, p. 915-918.

Mutschler, F. E., Griffin, M. E., Stevens, D. S., and Shannon, S. S. Jr., 1985, Precious metal deposits related to alkaline rocks in the North American Cordilleran - an interpretive review: Transactions of the Geological Society of South Africa, v. 88, p. 355-377.

Mutschler, F. E., Mooney, T. C., and Johnson, D. C., 1991, Precious metal deposits related to alkaline igneous rocks - A space-time trip through the Cordillera: Mining engineering, v. 43, p. 304 - 309.

Mysen, B. O., and Boettcher, A. L., 1975, Melting of a hydrous mantle; II, Geochemistry of crystals and liquids formed by anatexis of mantle peridotite at high pressures and high temperatures as a function of controlled activities of water, hydrogen, and carbon dioxide: Journal of Petrology, v. 16, p. 549-593.

Nelson, J., and Colpron, M., 2007, Tectonics and Metallogeny of the British Columbia, Yukon and Alaskan Cordillera, 1.8 GA to the Present: Mineral Deposits of Canada, v. A Synthesis of Major Deposit-Types, District Metallogeny, the Evolution of Geological Provinces, and Exploration Methods: Geological Association of Canada, Mineral Deposits Division, p. 755-791.

Nelson, J., and Mihalynuk, M., 1993, Cache Creek ocean: Closure or enclosure?: Geology, v. 21, p. 173-176.

Nelson, J. L., and Bellefontaine, K. A., 1996, The Geology and Mineral Deposits of North-Central Quesnellia; Tezzeron Lake to Discovery Creek, Central British Columbia: Ministry of Employment and Investment, Energy and Minerals Divison, Geologial Survery Branch, Bulletin 99, p.1-112.

Newell, J. M., and Peatfield, G. R., 1995, The Red-Chris porphyry copper-gold deposit, northwestern British Columbia, *in* Schroeter, T. G., ed., Porphyry Deposits of the Northwestern Cordillera of North America, CIM Special Volume 46: Quebec, Harpell's Press Cooperative, p. 674-687.

Nixon, G., Cabri, L., Laflamme, G., Sylvester, P., and Turbeett, M., 2004, Platinum-Group Elements in Alkaline Cu-Au Porphyries., Geofile 2004-6, 2008, British Columbia Ministry of Energy and Mines.

Nixon, G. T., 2004, Platinum-Group-Elements in the Afton Cu-Au Porphyry Deposit, Southern British Columbia, *in* British Columbia Ministry of Engergy and Mines, Geological Fieldwork 2003, Paper 2004-1: Victoria, p. 263-289.

Nixon, G. T., and Laflamme, J. H. G., 2002, Cu-PGE Mineralization in Alkaline Plutonic Complexes, Geofile 2002-2, B.C. Ministry of Energy and Mines.

Nixon, G. T., and Peatfield, G. R., 2003, Geological setting of the Lorraine Cu-Au porphyry deposit, Duckling Creek Syenite Complex, North-central British Columbia: BC Ministry of Mines and Energy, Open File Report 2003-4, 24 p.

Nokleberg, W. J., Bundtzen, T. K., Eremin, R. A., Ratkin, V. V., Dawson, K. M., Shpikerman, V. I., Goryachev, N. A., Byalobzhesky, S. G., Frolov, Y. F., Khanchuk, A. I., Koch, R. D., Monger, J. W.

H., Pozdeev, A. I., Rozenblum, I. S., Rodionov, S. M., Parfenov, L. M., Scotese, C. R., and Sidorov, A. A., 2005, Metallogenesis and Tectonics of the Russian Far East, Alaska, and the Canadian Cordillera: Menlo Park, U.S. Geological Survey, Professional Paper 1697, 429 p.

Nokleberg, W. J., Parfenov, L. M., Monger, J. W. H., Norton, I. O., Khanchuk, A. I., Stone, D. B., Scotese, C. R., Scholl, D. W., and Fujita, K., 2000, Phanerozoic Tectonic Evolution of the Circum-North Pacific: Menlo Park, U.S. Geological Survey, Professional Paper 1626, 133 p.

O'Neil, J. R., Clayton, R. N., and Mayeda, T. K., 1969, Oxygen isotope fractionation in divalent metal carbonates: Journal of Chemical Physics, v. 51, p. 5547-5558.

Ohmoto, H., 1972, Systematics of Sulfur and Carbon Isotopes in Hydrothermal Ore Deposits: Economic Geology, v. 67, p. 551-578.

Ohmoto, H., 1986, Stable Isotope Geochemistry of Ore-deposits, Reviews in Mineralogy, 16: Washington, DC, Mineralogical Society of America, p. 491-559.

Ohmoto, H., and Goldhaber, M. B., 1997, Sulfur and Carbon Isotopes, *in* Barnes, H. L., ed., Geochemistry of Hydrothermal Ore Deposits: USA, John Wiley and Sons, p. 517-600.

Ohmoto, H., and Rye, R. O., 1979, Isotopes of sulfur and carbon, *in* Barnes, H. L., ed., Geochemistry of Hydrothermal Ore Deposits.: New York, John Wiley and Sons, p. 509-567.

Orchard, M. J., 1995, Report on conodonts and other microfossils from Quesnel Lake (93A, 93B and 93H), Geological Survery of Canada.

Ossandon, C. G., Freraut, C. R., Gustafson, L. B., Lindsay, D. D., and Zentilli, M., 2001, Geology of the Chuquicamata Mine: A Progress Report: Economic Geology, v. 96, p. 249-270.

Panteleyev, A., 1987, Quesnel Gold Belt - Alkalic Volcanic Terrane Between Horsefly and Quesnel Lakes (93A/6) Geological Fieldwork, 1986, Paper 1987-1, British Columbia Ministry of Energy, Mines and Resources, p. 125-133.

Panteleyev, A., 1988, Quesnel Mineral Belt-The Central Volcanic Axis Between Horsefly and Quesnel Lakes (93A/05E, 06W), Geological Fieldwork, 1987, Paper 1988-1, British Columbia Ministry of Energy, Mines and Resources, p. 131-137.

Panteleyev, A., Bailey, D. G., Bloodgood, M. A., and Hancock, K. D., 1996, Geology and Mineral Deposits of the Quesnel River - Horsefly Map Area, Central Quesnel Trough, British Columbia NTS MAP SHEETS 91A/5, 6, 7, 11, 12, 13; 93B/9, 16; 93G/1; 93H/4, GSC Bulletin 97: Victoria, 156 p.

Panteleyev, A., and Hancock, K. D., 1989, Quesnel Mineral Belt: Summary of the Geology of the Beaver Creek - Horsefly River Map Area, Geological Fieldwork, 1988, Paper 1989-1, British Columbia Ministry of Energy, Mines and Resources, p. 159-166.

Pass, H., Cooke, D., Ferreira, L., Rees, C., Simpson, K., and Chamberlain, C., 2008, Geochemistry, alteration and mineralization of Long-section 17-34, Northeast Zone, Mt. Polley breccia-hosted alkalic Cu-Au porphyry deposit, Shallow- and Deep-Level Alkalic Mineral Deposits: Developing an Integrated Exploration Model, Year 3 - Porphyry Module Final Update to Project Sponsors: Vancouver, BC, *prepared for* MDRU-University of British Columbia, CODES-University of Tasmania, p. 5.1-5.34.

Pass, H. E., Cooke, D. R., Chamberlain, C. C., and Simpson, K. A., 2007a, Infill paragenesis and hydrothermal alteration in the North East Zone of the Mt. Polley magmatic-hydrothermal breccia complex, British Columbia: Association for Mineral Exploration British Columbia Mineral Exploration Roundup Programs with Abstracts Vancouver, BC, p. 22.

Pass, H. E., Cooke, D. R., Chamberlain, C. C., and Simpson, K. A., 2007b, Infill paragenesis and hydrothermal alteration in the North East Zone of the Mt. Polley magmatic-hydrothermal breccia complex, British Columbia, Canada: 9th Biennial SGA Meeting, Mineral Exploration and Research: Digging Deeper Conference, Dublin, Ireland v.1, p. 423-426.

Pass, H. E., Cooke, D. R., Chamberlain, C. C., Simpson, K. A., Rees, C., and Ferreira, L., 2007c, Zonation and infill of breccia-hosted mineralization within an alkalic porphyry Cu-Au deposit, Mount Polley, BC, Canada: Ores and Orogenesis - Program with Abstracts, Tucson, Arizona, p. 176.

Pass, H. E., Danyushevsky, L. V., Gilbert, S., and Cooke, D. R., 2009, LA-ICPMS analyses of PGEs in pyrite and Cu-sulfides from Mt. Polley alkalic Cu-Au porphyry deposit, Canada: Smart Science for Mineral Exploration and Mining, Townsville, Australia, v.Proceedings of the 10th Biennial SGA Meeting of The Society for Geology Applied to Mineral Deposits, p. 738-740.

Pearce, C. I., Pattrick, R. A. D., Vaughan, D. J., Henderson, C. M. B., and van der Laan, G., 2006, Copper oxidation state in chalcopyrite: Mixed Cu d^9 and d^{10} characteristics: Geochemica et Cosmochimica Acta, v. 70, p. 4635 - 4642.

Piestrzynski, A., Schmidt, S. T., and Franco, H., 1994, Pd-minerals in the Sto. Tomas II, porphyry copper deposit, Tuba Benguet, Phillipines: Mineralogica Polonica, v. 25, p. 21-31.

Preto, V. A., 1975, Geology of the Nicola Group South of Allison Lake (92H/10E), *in* Carter, N. C., ed., Geological Fieldwork 1975: Victoria, BC, B.C. Dept. of Mines Petroleum Resources, p. 55 - 58.

Preto, V. A., 1977, The Nicola Group: Mesozoic Volcanism Related to Rifting in Southern Bitish Columbia, The Geological Association of Canada, Special Paper Number 16, p. 40-57.

Radclyffe, D., 1995, Regional scale propylitic alteration in the Northparkes mineral field, University of Tasmania, unpublished BSc (Hons) thesis, 118 p.

Railsback, L. B., 2003, An earth scientist's periodic table of the elements and their ions: Geology, v. 31, p. 737-740.

Ramdohr, P., 1969, The ore minerals and their intergrowths Oxford, Pergamon Press, 1174 p.

Read, P. B., 1997, Surface geology of the area east of the Cariboo Pit, Mount Polley Mine, *prepared by* Geotex Consultants Ltd., unpublished report for Mount Polley Mining Corporation - Imperial Metals Corporation, December, 1997.

Read, P. B., and Okulitch, A. V., 1977, The Triassic Unconformity of Southcentral British Columbia: Canadian Journal of Earth Sciences, v. 14, p. 606-638.

Rebagliati, C. M., 1988, Mt. Milligan property assessment report, Omineca mining division NTS 93/1, latitude 55°08' N, longitude 124°04' W, *prepared for* United Lincoln Resources, Inc.

Rebagliati, C. M., Bowen, B. K., Copeland, D. J., and Niosi, S. W. A., 1995, Kemess South and Kemess North porphyry gold-copper deposits, norhtern British Columbia, *in* Schroeter, T. G., ed., Porphyry Deposits of the Northwestern Cordillera of North America, CIM Special Volume 46: Quebec, Harpell's Press Cooperative, p. 377-396.

Redmond, P. B., Einaudi, M. T., Inan, E. E., Landtwing, M. R., and Heinrich, C. A., 2004, Copper deposition by fluid cooling in intrusion-centered systems: New insights from the Bingham porphyry ore deposit, Utah: Geology, v. 32, p. 217-220.

Reed, M. H., 1997, Chapter 7 - Hydrothermal Alteration and its Relationship to Ore Fluid Composition, *in* Barnes, H. L., ed., Geochemistry of Hydrothermal Ore Deposits: New York, John Wiley and Sons, Inc, p. 303-366.

Reed, M. H., and Spycher, N. F., 1985, Boiling, cooling and oxidation in epithermal system: A numerical modelling approach, *in* Berger, B. R., and Bethke, P. M., eds., Geology and Geochemistry of Epithermal Deposits, Vol. 2: Chelsea, MI, Society of Economic Geologists, p. 249-272.

Rees, C., 1987, The Intermontane Omineca Boundary in the Quesnel Lake Area, East-central British Columbia: Tectonic Implications Based on Geology, Structure and Paleomagnetism, Unpublished PhD thesis, Carelton University, 421 p.

Rees, C., 2008, Alkalic Project Sponsor's Meeting, Mount Polley, powerpoint presentation, September, Imperial Metals Corporation, 86 slides.

Rees, C., 2009, Map 2 Geology of the Mount Polley Complex, 1:15385, Imperial Metals Corporation, March 2009.

Rees, C., Bjornson, L., Blackwell, J., Ferreira, L., McAndless, P., Rees, C., Robertson, S., Roste, G., Stubly, T., and Taylor, C., 2005, Geological Report on the Mount Polley Property and Summary of Exploration in 2003-2004: Vancouver, BC, *prepared for* Imperial Metals Corporation, internal company report, 163 p.

Rees, C., Ferreira, L., with, Bjornson, L., Blackwell, J., Roste, G., Stubly, T., and Taylor, C., 2006, Geological Report on the Mount Polley Property and Summary of 2005 Exploration Vancouver, BC, *prepared for* Imperial Metals Corporation, internal company report, 157 p.

Reich, M., Kelser, S. E., Utsunomiya, S., Palenik, C. S., Chryssoulis, S. L., and Ewing, R. C., 2005, Solubility of gold in arsenian pyrite: Geochemica et Cosmochimica Acta, v. 69, p. 2781 - 2796.

Reyes, A. G., 1990, Petrology of Philippine geothermal systems and the application of alteration mineralogy to their assessment: Journal of Volcanology and Geothermal Research, v. 43, p. 279-309.

Richards, J. P., 1995, Chapter 17 Alkalic-type Epithermal Gold Deposits - A Review, *in* Thompson, J. F. H., ed., Magmas, Fluids and Ore Deposits, Mineralogical Association of Canada Short Course Series, Short Course Volume 23: Victoria, BC, p. 367-400.

Richards, J. P., 2003, Tectono-Magmatic Precursors for Porphyry Cu-(Mo-Au) Deposit Formation: Economic Geology, v. 98, p. 1515-1533.

Richards, J. P., and Noble, S. R., 1998, Application of Radiogenic Isotope Systems to the Timing and Origin of Hydrothermal Processes, *in* Larson, P. B., and Richards, J. P., eds., Techniques in hydrothermal ore deposits geology, 10: Boulder, Society of Economic Geologists, Inc., p. 195-233.

Richet, P., Bottinga, Y., and Javoy, M., 1977, A review of hydrogen, carbon, nitrogen, oxygen, sulphur, and chlorine stable isotope fractionation amoung gaseous molecules: Annual Review Earth and Planetary Science, v. 5, p. 65-110.

Roberston, J. K., and Wyllie, P. J., 1971, Experimental studies on rocks from the Deboullie Stock, northern Maine, including melting relations in water deficient environment: Journal of Geology, v. 79, p. 549-571.

Rollinson, H., 1993, Using geochemical data: evaluation, presentation, interpretation: London, UK, Longman Group UK Limited, 352 p.

Ross, K. V., 2004a, Alteration Study of the Bell Zone, Mount Polley Mine, British Columbia, Panterra Geoservices Inc.: Surrey, BC, *prepared for* Imperial Metals Corporation, internal company report, 69 p.

Ross, K. V., 2004b, Alteration Study of the Northeast Zone, Mount Polley Mine, British Columbia, Panterra Geoservices Inc.: Surrey, BC, *prepared for* Imperial Metals Corporation, internal company report, 108 p.

Ross, K. V., 2004c, Alteration Study of the Springer Zone, Mount Polley Mine, British Columbia, Panterra Geoservices Inc.: Surrey, BC, *prepared for* Imperial Metals Corporation, internal company report, 33 p.

Ross, K. V., 2004d, Petrographic Studies of the Northeast, Nordic, and Leak Zones, Mount Polley Mine, British Columbia, Panterra Geoservices Inc.: Surrey, BC, *prepared for* Imperial Metals Corporation, internal company report, 46 p.

Ross, K. V., 2004e, Petrographic Study of Thirteen Samples From the Northeast Zone, Mount Polley, British Columbia, Panterra Geoservices Inc.: Panterra Geoservices Inc., *prepared for* Imperial Metals Corporation, internal company report, 32 p.

Ross, K. V., Godwin, C. I., Bond, L., and Dawson, K. M., 1995, Geology, alteration and mineralization of the Ajax East and Ajax West copper-gold alkalic porphyry deposits, southern Iron Mask batholith, Kamloops, British Columbia, *in* Schroeter, T. G., ed., Porphyry Deposits of the Northwestern Cordillera of North America, CIM Special Volume 46: Quebec, Harpell's Press Cooperative, p. 565- 580.

Rye, R. O., 1993, The Evolution of Magmatic Fluids in the Epithermal Environment: The Stable Isotope Perspective: Economic Geology, v. 88, p. 733-753.

Scaini, H. J., Bancroft, G. M., and Knipe, S. W., 1998, Reactions of aqueous Au^{+1} sulfide species with pyrite as a function of pH and temperature: American Mineralogist, v. 83, p. 316-322.

Schroeter, T., Pardy, J., and Cathro, M., 2004, Significant British Columbia Porphyry Cu-Au Reources, BC Ministry of Energy and Mines, Geofile 2004-11, p. 1-2.

Schroeter, T. G., 1995, Porphyry Deposits of the Northwestern Cordillera of North America, CIM Special Volume 46: Quebec, Canada, Harpell's Press Cooperative, p. 888.

Schwab, D. L., Petsel, S., Otto, B. R., Morris, S. K., Workman, E. E., and Tosdal, R. M., 2008, Overview of the Late Triassic Galore Creek copper-gold-silver porphyry system, northwestern British Columbia, Canada, *in* Spencer, J. E., and Titley, S. R., eds., Ores and Orogenesis: Circum-Pacific tectonics, geologic evolution, and ore deposits, Digest 22: Tuscon, Arizona Geological Society, p. 471-484.

Seedorff, E., Dilles, J. H., John M. Proffett, J., Einaudi, M. T., Zurcher, L., Stavast, W. J. A., Johnson, D. A., and Barton, M. D., 2005, Porphyry Deposits: Characteristics and Origin of Hypogene Features, *in* Hedenquist, J. W., Thompson, J. F. H., Goldfarb, R. J., and Richards, J. P., eds., Economic Geology, 100th Anniversary Volume 1905-2005: Littleton, Colorado, Society of Economic Geologists, Inc., p. 251-298.

Seedorff, E., and Einaudi, M. T., 2004, Henderson Porphyry Molybdenum System, Colorado: II. Decoupling of Introduction and Deposition of Metals during Geochemical Evolution of Hydrothermal Fluids: Economic Geology, v. 99, p. 39-72.

Seward, T. M., 1973, Thio complexes of gold and the transport of gold in hydrothermal ore solutions: Geochemica et Cosmochimica Acta, v. 37, p. 379-399.

Seward, T. M., 1984, The transport and deposition of gold in hydrothermal systems, *in* Forster, R. P., ed., Gold -82: The geology, geochemistry and genesis of gold deposits, Geological Soceity of Zimbabwe Special Publication No. 1: Rotterdam, A.A. Balkema, p. 165-181.

Shelton, K. L., 1983, Composition and origin of ore-forming fluids in a carbonate-hosted porphyry copper and skarn deposit; a fluid inclusion and stable isotope study of Mines Gaspe, Quebec: Economic Geology, v. 78, p. 387-421.

Shives, R. B. K., Carson, J. M., Ford, K. L., Holman, P. B., and Cathro, M., 2004, Mount Polley 2003 multisensor geophysical survey, Associated Mining Consultants Ltd., *prepared for* Imperial Metals Corporation, internal company report, 79 p.

Sibson, R., 1986, Brecciation Processes in Fault Zones - Inferences From Earthquake Rupturing: Pure and applied geophysics, v. 124, p. 159-175.

Sillitoe, R. H., 1979, Some thoughts on gold-rich porphyry copper deposits: Mineralium Deposita, v. 14, p. 161-174.

Sillitoe, R. H., 1985, Ore-Related Breccias in Volcanoplutonic Arcs: Economic Geology, v. 80, p. 1467-1514.

Sillitoe, R. H., 1987, Copper, gold and subduction: a trans-Pacific perspective, Pacific Rim Congress 87, The Australasian Institute of Mining and Metallurgy Conference Proceedings: Gold Coast, p. 399-403.

Sillitoe, R. H., 1988, Gold and Silver Deposits in Porphyry Systems: Bulk mineable precious metal deposits of the Western United States; symposium proceedings, Reno, NV, USA, April 6-8, 1987, p. 233 - 257.

Sillitoe, R. H., 1997, Characteristics and controls of the largest porphyry copper-gold and epithermal gold deposits in the circum-Pacific region: Australian Journal of Earth Sciences, v. 44, p. 373-388.

Sillitoe, R. H., 2000, Gold-Rich Porphyry Deposits: Descriptive and Genetic Models and Their Role in Exploration and Discovery, *in* Hagemann, S. G., and Brown, P. E., eds., Gold in 2000, 13, Society of Economic Geologists, p. 315-345.

Sillitoe, R. H., 2002, Some Metallogenic features of gold and copper deposits related to alkaline rocks and consequences for exploration: Mineralium Deposita, v. 37, p. 4-13.

Sillitoe, R. H., 2005, Supergene oxidized and enriched porphyry copper and related deposits, *in* Hedenquist, J. W., Thompson, J. F. H., Goldfarb, R. J., and Richards, J. P., eds., Economic Geology; one hundredth anniversary volume, 1905-2005: Littleton, CO, Society of Economic Geologists, p. 723-768.

Sillitoe, R. H., 2010, Porphyry Copper Systems: Economic Geology, v. 105, p. 3-41.

Simmons, S. F., and Christenson, B. W., 1994, Origins of Calcite in a Boiling Geothermal System: American Journal of Science, v. 294, p. 361-400.

Simon, G., Kesler, S. E., and Essene, E. J., 1997, Phase relations amoung selenides, sulfides, tellurides and oxides: II. Applications to selenide-bearing ore deposits: Economic Geology, v. 92, p. 468-484.

Simon, G., Kesler, S. E., and Essene, E. J., 1999, Experimental Partitioning of Gold Between Bornite and Chalcopyrite in Porphyry Copper-Gold Deposits: GAC-MAC Joint Annual Meeting, Sudbury, Canada, Abstract Volume 24, p. 116.

Simon, G., Kesler, S. E., Essene, E. J., and Chryssoulis, S. L., 2000, Gold in Porphyry Copper Deposits: Experimental Determination of the Distribution of Gold in the Cu-Fe-S System at 400° to 700°C: Economic Geology, v. 95, p. 259-270.

Simpson, K., 2005, Report to Imperial Metals re site visit by K. Simpson, Northeast Zone, Mt. Polley Porphyry System: Vancouver, BC, *prepared for* Imperial Metals Corporation, internal company report, 5 p.

Simpson, K. A., Davies, A. G. S., Cooke, D. R., and Gemmell, J. B., 2007, Description before interpretation: a suggested framework for consistent description of subsurface fragmental rocks: Breccia Symposium, Townsville, Australia, June, EGRU Contribution 65, p. 27.

Sinclair, W. D., 2007, Porphyry Deposits, *in* Goodfellow, W. D., ed., Mineral Deposits of Canada: A Synthesis of Major Deposit-Types, District Metallogency, the Evolution of Geological Provinces, and Exploration Methods: Geological Association of Canada, Mineral Deposits Division, Special Publication No.5, p. 223-243.

Sketchley, D. A., Rebagliati, C. M., and DeLong, C., 1995, Geology, alteration and zoning patterns of the Mt. Milligan copper-gold deposits, *in* Schroeter, T. G., ed., Porphyry Deposits of the Northwestern Cordillera of North America, CIM Special Volume 46: Quebec, Canada, Harpell's Press Cooperative, p. 650-665.

Skewes, A. M., and Stern, C. R., 1996, Late Miocene mineralized breccia in the Andes of central Chile:Sr adn Nd isotopic evidence for multiple magmatic sources, *in* Camus, F., Sillitoe, R. H., and Peterson, R., eds., Andean copper deposits: new discoveries, mineralisation, styles and metallogeny, Society of Economic Geologists Special Publication no. 5, p. 119-130.

Smith, I. E. m., 1994, The monzonite alkaline association: Program with Abstracts - Geological Assocition of Canada, v. 19, p. A105.

Spear, F. S., 1993, Metamorphic phase equilibria and pressure-temperature-time paths: Chelsea, Michigan, Mineralogical Society of America, Monograph, 799 p.

Stacey, J. S., and Kramers, J. D., 1975, Approximation of Terrestrial Lead Isotope Evolution by a Two-Stage Model: Earth and Planetary Science Letters, v. 26, p. 207-221.

Stanley, C. R., Holbek, P. M., Huyck, H. L. O., Lang, J. R., Preto, V. A. G., Blower, S. J., and Bottaro, J. C., 1995, Geology of the Copper Mountain alkalic copper-gold porphyry deposits, Princeton, British Columbia, *in* Schroeter, T. G., ed., Porphyry Deposits of the Northwestern Cordillera of North America, CIM Special Volume 46: Montreal, Canada, Canadian Institute of Mining, Metallurgy adn Petroleum, p. 537-564.

Stern, R. J., 2002, Subduction Zones: Reviews of Geophysics, v. 40, p. 3-1 to 3-8.

Streckeisen, A., 1976, To each plutonic rock its proper name: Earth Science Review, v. 13, p. 1-33.

Struik, L. C., 1986, Imbricated terranes of the Cariboo gold belt with correlations and implications for tectonics in southeastern British Columbia: Canadian Journal of Earth Sciences, v. 23, p. 1047-1061.

Sverjensky, D. A., 1981, Isotopic alteration of carbonate host rocks as a function of water to rock ratio; an example from the Upper Mississippi Valley zinc-lead district: Economic Geology, v. 76, p. 154-157.

Swart, P. K., Burns, S. J., and Leder, J. J., 1991, Fractionation of the stable isotopes of oxygen and carbon in carbon dioxide during the reaction of calcite with phosphoric acid as a function of temperature and technique: Chemical Geology; Isotope Geoscience Section, v. 86, p. 89-96.

Tarkian, M., and Stribrny, B., 1999, Platinum-group elements in porphyry copper deposits: a reconnaissance study: Mineralogy and Petrology, v. 65, p. 161-183.

Taseska, M., Makreski, P., Stibilj, V., Jacimovic, R., Stafilov, T., and Jovanovski, G., 2008, Determination of Trace Elements in Chalcopyrite ($CuFeS_2$) By k_o-Instrumental Neutron Activation Analysis After Matrix Elements Removal: Macedonian Journal of Chemistry and Chemical Engineering, v. 27, p. 141-147.

Taylor, B. E., and Holk, G. J., 2002, Stable Isotope Applications in the Exploration for Volcanic-Associated Massive Sulphide Deposits: a Preliminary Summary, *in* Galley, A., Bailes, A., Hannington, M. D., Holk, G. J., Katsube, J., Paquette, F., Paradis, S., Santaguida, F., and Taylor, B. E., eds., Database for Camiro project 94E07: Interrelationships between subvolcanic intrusions, large-scale alteration zones and VMS deposits, Open File 4431, Natural Resources Canada, p. 41-46.

Taylor, C., 2004, Structural Geology of the Wishbone Deposit, Mount Polley Porphyry Copper-Gold Deposit, British Columbia, Geological Report on the Mount Polley Property and Summary of Exploration in 2003-2004, Imerial Metals Corporation, internal company report, 14 p.

Taylor, C., 2005, Mount Polley 2005 Exploration Model (memo), Imperial Metals Corporation, internal company report, 6 p.

Taylor, H. P., 1971, Oxygen isotope evidence for large-scale interaction between meteoric ground waters and Tertiary granodiorite intrusions, Western Cascade range, Oregon: Journal of Geophysical Research, v. 76, p. 7855-7874.

Taylor, H. P., 1974, The Application of Oxygen and Hydrogen Isotope Studies to Problems of Hydrothermal Alteration and Ore Deposition: Economic Geology, v. 69, p. 843-883.

Taylor, H. P., 1979, Oxygen and hydrogen isotope relationships in hydrothermal mineral deposits, *in* Barnes, H. L., ed., Geochemistry of Hydrothermal Ore Deposits: New York, J. Wiley and Sons, p. 236-277.

Taylor, P. N., Moorbath, S., Goodwin, R., and Petrykowski, A. C., 1980, Crustal contamination as an indicator of the extent of early Archean continental crust: Pb isotopic evidence from the late Archean gneisses of west Greenland: Geochemica et Cosmochimica Acta, v. 44, p. 1437-1453.

Taylor, R. G., and Pollard, P. J., 1993, Mineralized breccia systems: methods of recognition and interpretation: Townsville, Australia, James Cook University of North Queensland, Geology Department, Contribution 46, 31 p.

Taylor, S. R., and McLennan, S. M., 1985, The continental crust; its composition and evolution: Boston, Blackwell Scientific Publishing.

Tedder I. J., Holliday, J., and S., H., 2001, Discovery and evaluation drilling of the Cadia Far East gold – copper deposit: New Generation Gold Deposits 2001 Conference Proceedings, Perth, p. 171 – 184.

Thompson, J. F. H., Lang, J. R., and Stanley, C. R., 2001, Platinum Group Elements in Alkaline Porphyry Deposits, British Columbia: Exploration and Mining in British Columbia - 2001, p. 57-64.

Titley, S. R., and Beane, R. E., 1981, Porphyry Copper Deposits; Part 1. Geologic Settings, Petrology, and Tectogenesis, *in* Skinner, B. J., ed., 75th Anniversary Volume: El Paso, Society of Economic Geologists, p. 214-234.

Titley, S. R., and Ruiz, J., 2005, Genetic implications of some trace elements in chalcopyrite, Geological Society of America, 2005 annual meeting, Abstracts with Programs vol. 37, no. 7: Salt Lake

City, UT, USA, Geological Society of America, p. 314-315.

Tosdal, R. M., Jackson, M., Pass, H. E., Rees, C., Simpson, K. A., Cooke, D. R., Chamberlain, C. M., and Ferreira, L., 2008, Hydrothermal Breccia in the Mount Polley Alkalic Porphyry Copper-Gold Deposit, British Columbia (NTS 093A/12), Geoscience BC Summary of Activities 2007, Report 2008-1, Geoscience BC, p. 105-114.

Tosdal, R. M., Wooden, J. L., and Bouse, R. M., 1999, Pb Isotopes, Ore Deposits, and Metallogenic Terranes, *in* Lambert, D. D., and Ruiz, J., eds., Review in Economic Geology, 12: Boulder, Society of Economic Geologists, Inc., p. 1-28.

Townsend, A. T., Yu, Z., McGoldrick, P., and Hutton, J. A., 1998, Precise lead isotope ratios in Australian galena samples by high resolution inductively coupled plasma mass spectrometry: Journal of Analytical Atomic Spectrometry, v. 13, p. 809-813.

Ulrich, T., Günther, D., and Heinrich, C. A., 1999, Gold concentrations of magmatic brines and the metal budget of porphyry copper deposits: Nature, v. 399, p. 676-679.

Veizer, J., Ala, D., Azmy, K., Bruckschen, P., Buhl, D., Bruhn, F., Carden, G. A. F., Diener, A., Ebneth, S., Godderis, Y., Jasper, T., Korte, C., Pawellek, F., Podlaha, O. G., and Strauss, H., 1999, $^{87}Sr/^{86}Sr$, $\delta^{13}C$ and $\delta^{18}O$ evolution of Phanerozoic seawater: Chemical Geology, v. 161, p. 59-88.

Walters, L. J., Claypool, G. E., and Choquette, P. W., 1972, Reaction rates and ^{18}O variation for the carbonate-phosphoric acid preparation method: Geochimica et Cosochimica Acta, v. 36, p. 129-140.

Wedepohl, K. H., 1995, The composition of the continental crust.: Geochemica et Cosmochimica Acta, v. 59, p. 1217-1232.

Wentworth, C. K., 1922, A scale of grade and class terms for clastic sediments: Journal of Geology, v. 30, p. 377-392.

Wernicke, B. P., and Klepacki, D. W., 1988, Escape hypothesis for the Stikine Block: Geology, v. 16, p. 461-464.

Wheeler, J. O., and McFeely, P., 1991, Tectonic assemblage map of the Canadian Cordillera and adjacent parts of the United States of America--Carte des assemblages tectoniques de la Cordillere canadienne et des parties adjacentes des Etats-Unis d'Amerique, Geological Survey of Canada, "A" Series Map, Report: 1712A, 1 sheet.

White, N. C., and Hedenquist, J. W., 1990, Epithermal environments and styles of mineralization: variations and their causes, and guidelines for exploration: Journal of Geochemical Exploration, v. 36, p. 445-474.

Wilkinson, W. J., Stevenson, R. W., and Garnett, J. A., 1976, Lorraine, *in* Brown, A. S., ed., Porphyry Deposits Of The Canadian Cordillera, CIM Special Volume 15, p. 397-401.

Wilson, A., Cooke, D. R., and Thompson, J. F. H., 2002, Alkalic and high-K calc-alkalic porphyry Au-Cu deposits: A summary, *in* Cooke, D. R., and Pongratz, J., eds., Giant Ore Deposits: Characteristics, Genesis and Exploration, CODES Special Publication 4, p. 51-55.

Wilson A.J., Cooke D.R., Stein H.J., Fanning, C. M., Holliday, J. R., and Tedder, I. J., 2007, U-Pb and Re-Os geochronologic evidence for two alkalic porphyry ore-forming events in the Cadia district: Economic Geology, v. 102, p. 3-26.

Wilson, A. J., 2003, The geology, genesis and exploration context of the Cadia gold-copper porphyry deposits, New South Wales, Australia: Unpublished PhD thesis, University of Tasmania, 335 p.

Wilson, A. J., Cooke, D. R., Harper, B. J., and Deyell, C. L., 2007, Sulfur isotopic zonation in the Cadia district, southeastern Australia: exploration significance and implications for the genesis of alkalic porphyry gold-copper deposits: Mineralium Deposita, v. 42, p. 465-487.

Wilson, A. J., Cooke, D. R., and Harper, B. L., 2003, The Ridgeway Gold-Copper Deposit: A High-Grade Alkalic Porphyry Deposit in the Lachlan Fold Belt, New South Wales, Australia: Economic Geology, v. 98, p. 1637-1666.

Wilson, A. J., Cooke, D. R., and Richards, T., 2004, Veins, pegmatites and breccias: examples from the alkalic Cadia Quarry gold-copper porphyry

deposit, NSW, Australia, *in* Cooke, D. R., Deyell, C., and Pongratz, J., eds., 24 ct Au Workshop, CODES Special Publication 5: University of Tasmania, Center for Ore Deposit Research, p. 45-55.

Wilson, S. A., Dipple, G. M., Power, I. M., Thom, J. M., Anderson, R. G., Raudsepp, M., Gabites, J. E., and Southam, G., 2009, Carbon Dioxide Fixation within Mine Wastes of Ultramafic-Hosted Ore Deposits: Examples from the Clinton Creek and Cassiar Chrysotile Deposits, Cananda: Economic Geology, v. 104, p. 95-112.

Wolfe, R. C., 1994, The geology, paragenesis and alteration geochemistry of the Endeavour 48 Cu-Au porphyry, Goonumbla N.S.W., University of Tasmania, Unpublished BSc (Hons) thesis, 76 p.

Wolfe, R. C., 2001, Geology of the Didipio Region and Paragenesis of the Dinkidi Cu-Au Porphyry Deposit: Unpublished PhD thesis, University of Tasmania, 201 p.

Wolfe, R. C., Cooke, D. R., and Joyce, P., 1999, Geology, mineralisation and genesis of the alkaline Dinkidi Cu-Au porphyry, North Luzon, Philippines: Australasian Institute of Mining and Metallurgy, v. 4, p. 509-516.

Wolhlgemuth-Ueberwasser, C. C., Ballhaus, C., Berndt, J., Paliulionyte, V., and Meisel, T., 2007, Synthesis of PGE sulphide standards for laser ablation inductively coupled plasma mass spectrometry: Contributions to Mineralogy and Petrology, v. 154, p. 607-617.

Woodhead, J., 2002, A simple method for obtaining hightly accurate Pb isotope data by MC-ICP-MS: Journal of Analytical Atomic Spectrometry, v. 17, p. 1381-1385.

Woodhead, J., Hergt, J., Meffre, S., Large, R. R., Danyushevsky, L., and Gilbert, S., accepted, In situ Pb-isotope analysis of pyrite by laser ablation (multi-collector and quadrapole) ICPMS: Chemical Geology.

Xiong, Y., and Wood, S. A., 2000, Experimental quantification of hydrothermal solubility of platinum-group elements with special reference to porphyry copper environments: Mineralogy and Petrology, v. 68, p. 1-28.

Zartman, R. E., and Doe, B. R., 1981, Plumbtectonics - The Model: Tectonophysics, v. 75, p. 135-162.

Zheng, Y.-F., 1990, Carbon-oxygen isotopic covariation in hydrothermal calcite during degassing of CO_2: Mineralium Deposita, v. 25, p. 246-250.

Zheng, Y. F., and Hoefs, J., 1993, Carbon and oxygen isotopic covariations in hydrothermal calcites Theoretical modeling on mixing processes and application to Pb-Zn deposits in the Harz Mountains, Germany: Mineralium Deposita, v. 28, p. 79-89.

Appendices

Appendix A1

Detailed legend to Figure 1.1, map of Canada

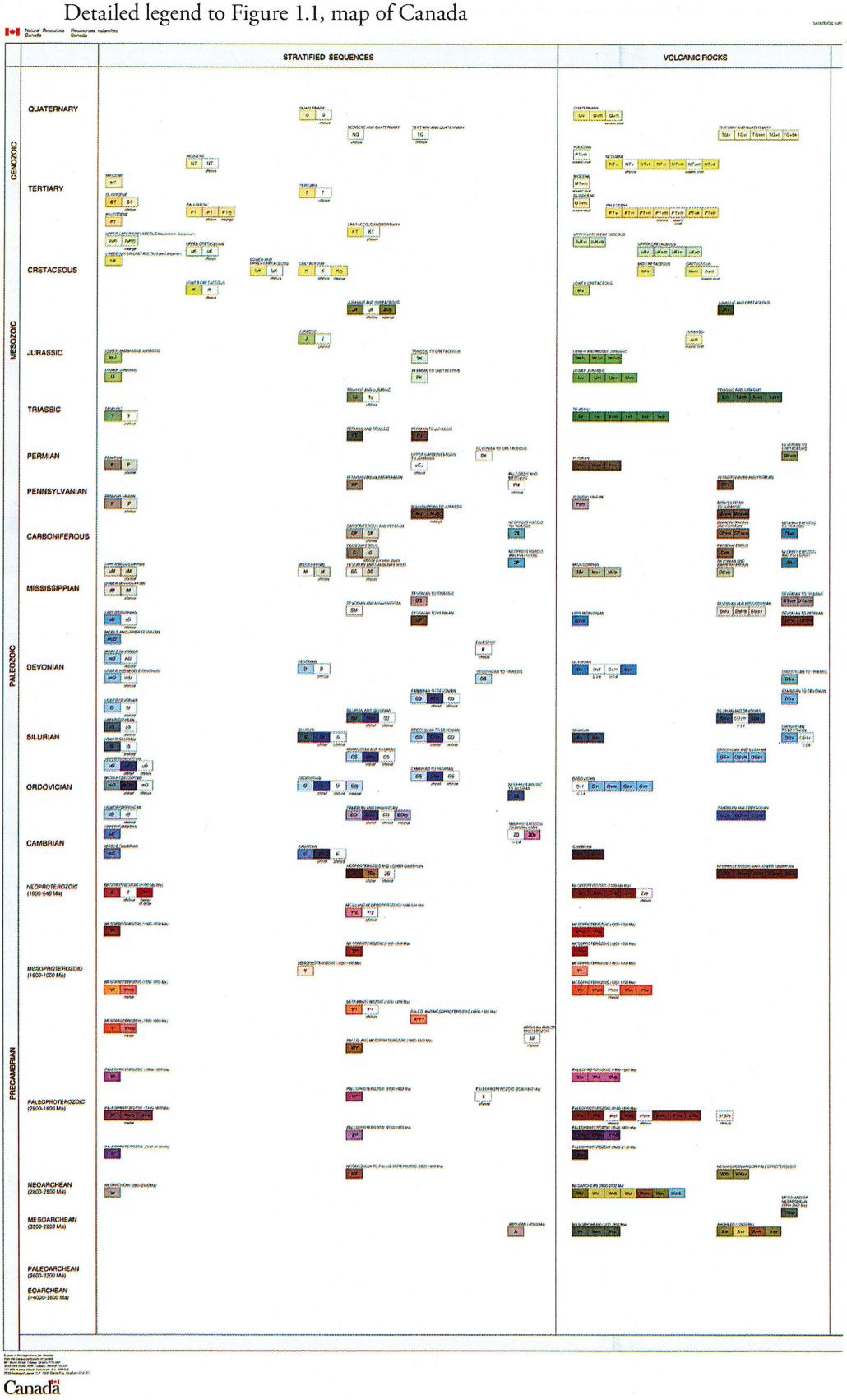

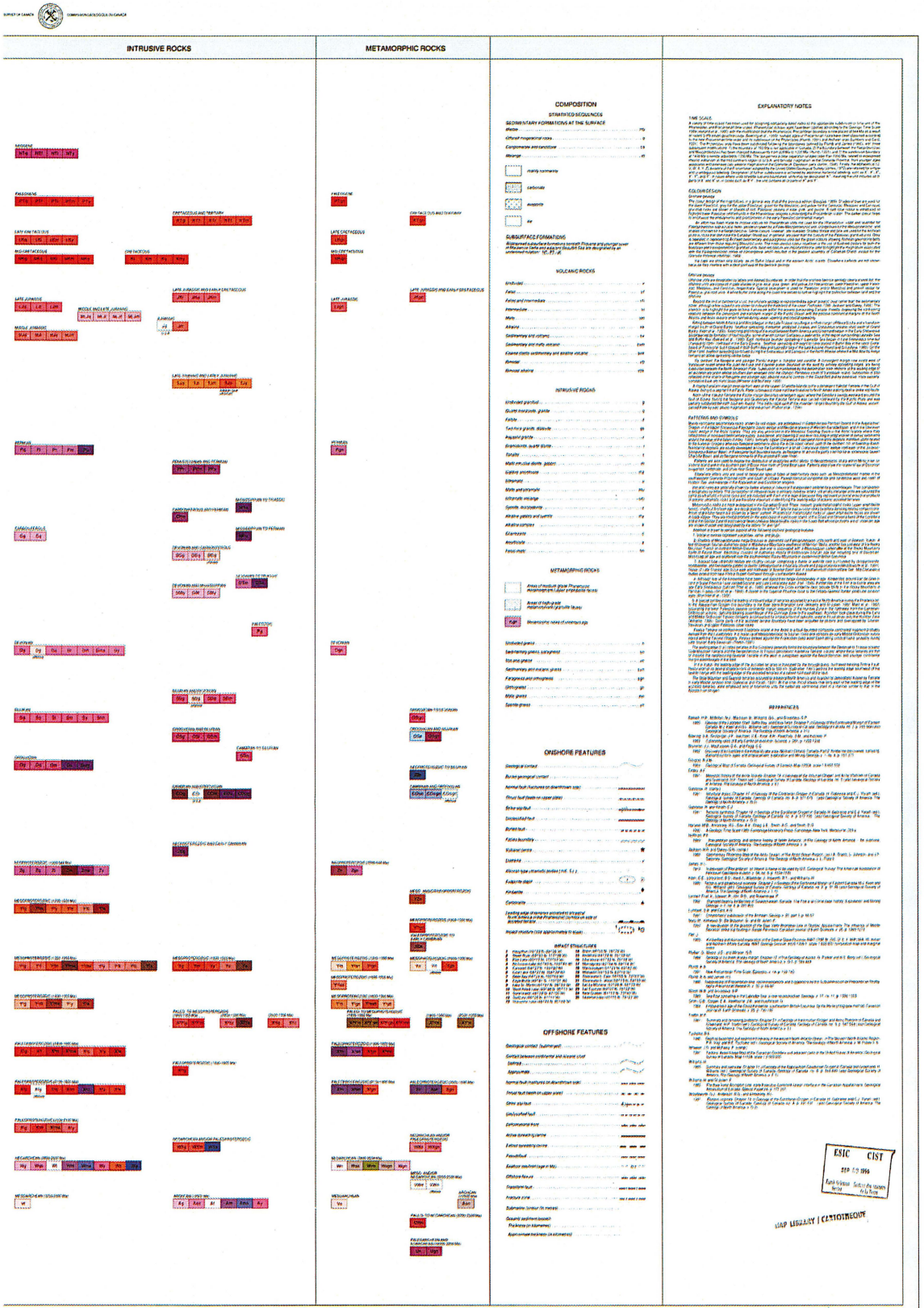
INTRUSIVE ROCKS
METAMORPHIC ROCKS
COMPOSITION
STRATIFIED SEQUENCES
SEDIMENTARY FORMATIONS AT THE SURFACE
SUBSURFACE FORMATIONS
VOLCANIC ROCKS
INTRUSIVE ROCKS
METAMORPHIC ROCKS
ONSHORE FEATURES
IMPACT STRUCTURES
OFFSHORE FEATURES
EXPLANATORY NOTES
REFERENCES
ESIC CIST
SEP 13 1996
MAP LIBRARY / CARTOTHÈQUE
NOT TO BE TAKEN FROM LIBRARY
NE PAS SORTIR DE LA BIBLIOTHÈQUE
1860A
THIS LEGEND ACCOMPANIES MAP 1860A

Appendix A2

Appendix A2.1 Selected alkalic porphyry deposits (from Tosdal et al., 2008).

Deposit	Location	Age	Mineralization Style	Grade and tonnage data	References
Ridgeway	Macquarie Arc (Molong Belt), NSW, Australia	Late Ordovician (~456–454 Ma)	Intrusion-centered, volcanic hosted, quartz-carbonate-sulfide stockwork	77 Mt @ 1.87 g/t Au, 0.63% Cu	Holliday et al. (1999); Harper (2000); Holliday et al. (2002); Wilson (2003); Wilson et al. (2003); Wilson et al. (2007a, b)
Cadia Quarry	Macquarie Arc (Molong Belt), NSW, Australia	Late Ordovician (~443–441 Ma)	Intrusion-hosted, sheeted quartz-carbonate-sulfide veins, breccias, and pegmatites	40 Mt @ 0.40 g/t Au, 0.2% Cu	Holliday et al. (2002); Wilson (2003); Wilson et al. (2004); Wilson et al. (2007a, b)
Cadia Hill	Macquarie Arc (Molong Belt), NSW, Australia	Late Ordovician (~443–441 Ma)	Intrusion-hosted, sheeted quartz-carbonate-sulfide veins	352 Mt @ 0.63 g/t Au, 0.16% Cu	Holliday et al. (2002); Wilson (2003); Wilson et al. (2007a, b)
Cadia East	Macquarie Arc (Molong Belt), NSW, Australia	Late Ordovician (~443–441 Ma)	Intrusion-centered, volcanic hosted, quartz-carbonate-sulfide sheeted veins	830 Mt @ 0.69 g/t Au, 0.35% Cu	Tedder et al. (2001); Holliday et al. (2002); Wilson (2003); Wilson et al. (2007a, b)
Northparkes (E22)	Macquarie Arc (Junee-Narromine Belt, NSW, Australia	Late Ordovician (~444–437 Ma)	Intrusion-centered, volcanic hosted, quartz-carbonate-sulfide stockwork	18.6 Mt @ 0.61 g/t Au, 0.71% Cu	Jones (1985); Heithersay and Walshe (1995); Lickfold et al. (2003); Lickfold et al. (2007)
Northparkes (E26)	Macquarie Arc (Junnee-Narromine Belt, NSW, Australia	Late Ordovician (~444–437 Ma)	Intrusion-centered, volcanic hosted, quartz-carbonate-sulfide stockwork	65.3 Mt @ 0.39 g/t Au, 1.37% Cu	Jones (1985); Heithersay and Walshe (1995); Lickfold et al. (2003); Lickfold et al. (2007)
Northparkes (E27)	Macquarie Arc (Junnee-Narromine Belt, NSW, Australia	Late Ordovician (~444–437 Ma)	Intrusion-centered, volcanic hosted, quartz-carbonate-sulfide stockwork	14.4 Mt @ 0.73 g/t Au, 0.71% Cu	Wolfe (1994); Lickfold et al. (2003); Lickfold et al. (2007)
Northparkes (E48)	Macquarie Arc (Junnee-Narromine Belt, NSW, Australia	Late Ordovician (~444–437 Ma)	Intrusion-centered, volcanic hosted, quartz-carbonate-sulfide stockwork	33.4 Mt @ 0.59 g/t Au, 1.04% Cu	Jones (1985); Heithersay and Walshe (1995); Lickfold et al. (2003); Lickfold et al. (2007)
Mt. Polley (Northeast Zone)	Quesnellia Terrane, Intermontane Belt, south central British Columbia, Canada	Late Triassic (205 Ma)	Breccia-hosted, lesser veins cross-cutting breccia an veins extending into surrounding host rock, minor intrusion hosted	55.6 Mt @ 0.30 g/t Au, 0.66 g/t Ag, 0.36% Cu	Mortensen et al. (1995); Bailey and Archibald (1990); Logan et al. (2007); Logan (unpublished data; 2009); Imperial Metals (2007); Jackson et al. (2008); Pass et al. (2008)

Appendix A2.1 continued

Deposit	Location	Age	Mineralization Style	Grade and tonnage data	References
Galore Creek (Central Zone)	Stikinia Terrane, Intermontane Belt, northwest British Columbia, Canada	Late Triassic to Early Jurassic (~210–197 Ma)	Intrusion-centered, disseminated in volcanic and sedimentary rocks, locally breccia-hosted, rarely veined	Measured and indicated: 785.7 Mt @ 0.29 g/t Au, 4.87 g/t Ag, 0.52% Cu Total inferred: 522.5 Mt @ 0.29 g/t Au, 4.79 g/t Ag, 0.35% Cu	Enns et al. (1995); Lang et al. (1995); Mortensen et al. (1995); Logan and Koyanagi (1989); Logan et al. (1989); Logan (2004); Micko et al. (2008)
Galore Creek (Southwest Zone)	Stikinia Terrane, Intermontane Belt, northwest British Columbia, Canada	Late Triassic (~201–210 Ma)	Breccia-centered, intrusion-hosted, biotite-K-feldspar-magnetite-sulfide cement, veins and alteration	69 Mt @ 0.69 g/t Au, 0.42% Cu	Allen et al. (1976); Enns et al. (1995); Lang et al. (1995); Mortensen et al. (1995); Logan (2004); Byrne et al. (2008)
Mt Milligan	Quesnellia Terrane, Intermontane Belt, north central British Columbia, Canada	Early Jurassic	Intrusion hosted and stratigraphic control in volcanic host sequence; disseminated replacement and sulfide veinlets, quartz-K-feldspar-chalcopyrite veins near intrusive contacts	Measured and indicated: 417.1 Mt @ 0.41 g/t Au, 0.21% Cu	Rebagliati (1988); Sketchly et al. (1995); Delong (1996); Jago (2008); Jago and Tosdal (2008)
Lorraine	Quesnellia Terrane, Intermontane Belt, British Columbia, Canada	Early middle Jurassic (~181–180 Ma)	Intrusion-hosted, fine disseminated sulfides, selective replacement of ferromagnesium minerals by sulfides. K-metasomatism(?) of host rocks	32 Mt @ 0.26 g/t Au, 0.66% Cu	Wilkinson et al. (1976); Bishop et al. (1995); Nixon and Peatfield (2003); Devine and Baxter (2007); Bath and Cooke (2008)
Dinkidi	Cagayan Valley Basin, Northern Luzon, Philippines	Miocene	Intrusion-hosted alkalic porphyry system associated with silica-undersaturated calc-potassic and silica-saturated potassic stockworks in a zoned alkalic intrusive complex	110 Mt @ 1.2 g/t Au, 0.5% Cu	Wolfe (2001)

Abbreviations: NSW-New South Wales, Au-gold, Cu-copper

Appendix A2.2 Summary of district scale geologic setting for selected alkalic porphyry deposits in British Columbia (from Tosdal et al., 2008).

Deposit	Host rocks	Intrusive rocks	Age of intrusive rocks	Structural control on the intrusive complexes
Mt. Polley (Northeast Zone)	Nicola Group (middle to late Triassic to early Jurassic); three basic assemblages i) fine-grained sedimentary rocks, ii) submarine pyroxene- ± olivine- ± plagioclase-phyric alkali basaltic volcanics, analcite bearing, silica-saturated and -undersaturated, overlain by lenses of limestone, tuffs and debris flow breccias (Mortimer, 1987; Rees et al., 2002)	Bootjack stock ~2 km south of the Mt. Polley Complex. It is believed to be coeval with the Mt. Polley Complex but this is as yet unproven. Intrusive facies include spare pseudoleucite melasyenite, orbicular pseudoleucite syenite and equigranular coarse to medium grained syenite (Bath and Logan, 2006)	Bootjack Stock: 200.7 ± 2.8 to 203.1 ± 2.0 Ma (Mortensen et al., 1995; Bailey and Archibald, 1990).	Northwest trending fault structures may have controlled location of plutons (Bailey, 1978)
Galore Creek	Stuhini Group (middle to upper Triassic); subalkaline hornblende and plagioclase-phyric basaltic andesite, subalkaline to alkaline augite-phyric basalt with accompanying volcaniclastic rocks, and pseudoleucite-bearing shoshonitic volcanic and volcaniclastic rocks (Logan and Koyanagi, 1994; Enns, 1995)	Galore Creek alkalic syenite suite; these intrusive units are characterized by feldspathoid-bearing minerals and common megacrystic orthoclase-phyric porphyries (Logan and Koyanagi, 1994; Enns, 1995)	The Galore Creek alkalic suite was emplaced between 210 ± 1 Ma to 197.2 ± 1.2 Ma (Upper Triassic to Lower Jurassic age; Enns et al., 1995; Mortensen et al., 1995)	not known
Mt Milligan	The Witch Lake succession of the Triassic Takla Group, consisting of a moderately northeast-dipping, alternating coherent- and clastic sequence that includes porphyritic clinopyroxene basaltic-trachyandesites. Coherent rocks are lavas and/or shallow intrusions	The composite MBX stock has at least three plagioclase-phyric phases, ranging from normative quartz monzonite to monzodiorite, and plot within the alkaline and shoshonitic fields (Lang, 1992; Barrie, 1993). Textural variations include: 1) plagioclase-phyric, 2) crowded plagioclase-phyric, 3) flow-aligned plagioclase, 4) medium-grained equigranular, 5) xenolithic monzonite containing monzonitic and biotite-magnetite hornsfels xenoliths. The monzodiorite Rainbow Dike protrudes outward from the southeastern to eastern margin of the MBX stock	U-Pb ages: 189 ± 3.3 Ma from the Heidi Lake stock, 183 ± 3 Ma from the North Slope stock, and 182.5 ± 4.3 Ma from the Southern Star stock (Mortensen et al., 1995); titanite form the MBX stocks (DDH 90-616) dated at 186.9 ± 0.5 Ma (Richard Friedman, 2008, written communication cited in Tosdal et al., 2008)	Not obvious due to post-mineral deformation
Lorraine (Lower Main Zone)	Duckling Creek Syenite Complex (early middle Jurassic) of the Hogem Batholith (Late Triassic to Cretaceous). The Duckling Creek Syenite Complex consists of biotite pyroxenite, diorite, monzonites, syenites, K-feldspar megacrystic syenites (Nixon and Peatfield, 2003) and fine-grained K-feldspar rock	Intrusive rocks of the Duckling Creek Syenite Complex range from silica-saturated to silica-undersaturated (Nixon and Peatfield, 2003). Intrusive rocks within the Lorraine area of the Duckling Creek Syenite Complex appear to be components of a dyke swarm (Sillitoe, 2007). The causative intrusion has not been identified	The Duckling Creek Syenite Complex was emplaced between 180.23 ± 0.28 Ma and 176.8 ± 0.3 Ma (P. Baxter, written communication, 2008; F. Devine, written communication, 2007 as cited in Tosdal et al., 2008)	Phase I syenitic and biotite pyroxenite have northwesterly trending contacts parallel to the regional trend of the Duckling Creek Syenite Complex and Hogem Batholith (Garnett, 1978; Nixon and Peatfield, 2003). Late phase 2 and 3 dykes trend north-northeast and west-northwest and are sub-parallel to late dextral and sinistral fault sets, respectively

Appendix A2.3 Summary of deposit scale geologic setting for selected alkalic porphyry deposits in British Columbia (from Tosdal et al., 2008).

Deposit	Host rocks / wall rocks to ore deposits	Gross composition of host intrusive rocks	Geometry of intrusive bodies	Geometry of the mineralized center	Mineralization age constraints	Nature of post-mineralization deformation
Mt. Polley (Northeast Zone)	Mt. Polley Complex: alkalic intrusive complex comprising primarily fine-grained porphyritic diorite and monzonite, plagioclase porphyry and syenite dykes with abundant screens of metavolcanic rocks and hydrothermal breccias (Logan and Mihalynuk, 2005)	Equigranular to porphyritic monzonite to diorite to syenite	Stocks to single and composite pencil dikes, trending approximately northeast-southwest and dipping ~15°	150 m by 500 m northwest trending, steeply dipping breccia body	205.1 ± 0.3 Ma U-Pb zircon, megacrystic K-feldspar syenite (suspected to be the causative intrusion to the Northeast Zone breccia); 205.2 ± 1.2 Ar-Ar hydrothermal biotite alteration (biotite associated with chalcopyrite; interpreted to be the age of mineralization of the Northeast Zone), Logan et al., 2007	Extensive faulting (poorly constrained); possible regional bulk rotation and tilting ~15° (Taylor, 2004)
Galore Creek (Central Zone)	Supercrustal country rocks of the Stuhini Group including augite-phyric basalts, reworked volcanogenic sedimentary rocks, orthoclase-phyric andesites	Orthoclase (and pseudoleucite) phyric, silica-undersaturated syenites and monzonite dikes	Polyphase sheeted dikes trending broadly northwest-southeast, dipping 64 to 45 ° west	All three east-west oriented ore sheets are located in the North Gold Lens, Central Replacement Zone and South Gold Lens are roughly wedge to ellipsoid-shaped with the lower extension dipping 60 –45 ° west	An orthoclase megacrystic syenite intrusion that is late- to post-mineral returned U-Pb zircon age of 205 ± 2.3 Ma	See structural controls on the intrusive complex
Galore Creek (Southwest Zone)	Megacrystic orthoclase-phyric syenite and monzonite dikes and matrix-bearing, poorly sorted, polylithic breccia	Silica-saturated syenites, monzonite, monzodiorite and diorite dikes	Polyphase composite dikes trending broadly north, dipping west	The main ore body has a semi-ellipsoidal shape, is east-trending and dips 60–45° south	201.3 ± 1.1 Ma Ar-Ar hydrothermal vein biotite. Hosted in brecciated intrusive rocks, mineralization is distinctly younger than the Central Zone	Reverse fault locally truncates mineralization and juxtapose alteration assemblages; compressional regime
Mt Milligan	MBX stock, Rainbow monzonite stock, and augite-phyric volcaniclastic and tuffaceous rocks	Equigranular to crowded porphyry of monzonitic composition	Elliptical stock with sill/dike emanating from margin	A northwest striking ellipsoid intrusive body, with a principle axis ratio of ~2:1, and a diameter of ~400 m	Post-dates intrusion of MBX stock and Rainbow dike; U-Pb rutile age of 182.5 ± 4 Ma form the Rainbow Dike apophysis of the MBX stock (Nelson and Bellefontaine, 1996)	Tilted ~45° northeast and cut by normal separation faults
Lorraine	Biotite pyroxenite, fine-grained K-feldspar biotite rock and syenitic to monzonitic rocks	Silica-saturated to -undersaturated syenite, monzonite, biotite pyroxenite	Dike swarm complex that trends east-southeast and dips moderately southwards. Late phase 2 and 3 intrusives trend north-northeast and west-northwest (within the Lower Main Zone) and dip sub-vertically	Panel of mineralization that dips moderately southwards	Pre-mineralization phase I syenite 180.23 ± 0.28 and post-mineralization phase 2 monzonite 180.0 ± 2.3 Ma. Coarse apatite from apatite-enriched mineralized biotite pyroxenite 180.3 ± 3 Ma	West-northwest-trending steeply dipping sinistral faults and north-northeast-trending steeply dipping faults that predominantly show relative dextral movement

Appendix A2.4 Mineralization and alteration of selected alkalic porphyry deposits (from Tosdal et al., 2008).

Deposit	Mineralization			Alteration			References
Ridgeway	**Early**: qz-mt-bn-cp-or-py-(at) veins	**Transitional**: qz-cp-or-(ch) veins	**Peripheral**: ep-ch-py-cc-qz-ph-ze-(cp)-(bn) **Late**: qz-py-sr-cc-(ch)-(cp)-(fl)	**Deep:** (at)-bi-or-ab-qz-mt	**Shallow:** ab-ch-qz-py-cc	**Peripheral**: ch-ab-hm-mt-ep; **Late**: sr-py alteration halos around late stage faults	Harper (2000); Wilson (2003); Wilson et al. (2003); Wilson et al. (2007a)
Cadia Quarry	**Early:** ab flooding with bn-cp-ep stringers; mt stringers and qz-mt ± cp veinlets	**Transitional:** sheeted qz-sulfide ± cc veins	**Peripheral:** ep-cc veins **Late:** qz-cc-base metal sulfide veins	**Early stage:** mt-ab	**Main stage:** bi-or (mt destructive)	**Peripheral:** ch-cc-ab-hm-ep ± at alteartion **Late stage:** qz-sr-py-rt-ch halos around veins and faults	Holliday et al. (2002); Wilson (2003); Wilson et al. (2004); Wilson et al. (2007a, b)
Cadia Hill	**Early:** mt-bi-ch-cp-or-qz, mt-qz-ch-cp-py-pr, or-qz-bi-cp-mt, qz-mt-or-cc-cp-bn veins	**Transitional:** qz-cc-cp-bn, bn-cp-ch-ep-ab and or-qz-bi-cc-cp-py veins	**Peripheral:** ph-cc-ep veins **Late:** ch-bi-py, ep-cc-cp, il-ms-cc-py-qz-sp-gl-cp veins	**Early:** ab, or-bi-ap, also minor cp and mt locally	**Transitional:** or-epi-ab and minor qz-cc or bi locally (primary mt destroyed)	**Peripheral:** hm-ch-ep **Late:** il-ms-py-qz-cc	Wilson (2003); Wilson et al. (2007a)
Cadia East	**Early:** mt-at-cp-py, qz-mt-cp-py-or, or-qz-bn-cp-mt and qz-mt-cp-cc-bn veins	**Transitional:** qz-cc-cp-bn, and bi-sp-py-qz veins	**Peripheral:** ph-cc-ep veins **Late:** il-ms-cc-py-qz-sp-gl-cp veins	**Early:** ab, or-bi- ap, also minor cp and mt locally	**Transitional:** or-ap-bi (primary mt destroyed)	**Peripheral:** hm-ch-ep **Late:** il-ms-py-qz-cc	Wilson (2003); Wilson et al. (2007a)
Northparkes (E22, E26, E27, E48)	**Early:** mt and Kf-qz-bi-mt-Cu-sulfides-ah viens	**Main:** qz-Kf-ah-cb-fl-Cu-sulifdes veins	**Late:** qz-sr-cb-cp-py-sp-gl-fl veins	**Pre-mineral:** sr-ab alteration **Early:** bi-mt alteration of QMP; peripheral ep-hm alteration	**Main stage:** or-qz, followed by sr-ah-hm	**Late:** phyllic alteration	Lickfold (2002); Lickfold et al. (2003)
Mt. Polley (Northeast Zone)	**Pre-breccia:** disseminations and blebs of cp (± py?) in rare clasts and xenloiths. Spatially restricted cp disseminations and rare veins in host rocks (timing uncertain)	**Syn-breccia veins and cement:** bn centers located within zones of abundant cp, adjacent zones contain lesser cp and py	**Post-breccia:** veins: cp ± ab ± bn; mylonitic bn. Cp veins; colloform cp-tn-cc veins Intrusions: limited and localized disseminated and rarely veined cp	**Potassic:** Kf-mt-cc (at-Leak Zone) ± bi ± sulfate ± cp ± bn **Sodic:** ab-Kf **Calc-potassic:** gt (found across the deposit in all assemblages)	**Adjacent:** **Inner propylitic:** ep-ab-ch-py-cc (± gt)	**Shallow/peripheral:** **Outer propylitic:** py-ch-cc ± hm ± sr ± ze (± gt) **Late:** sr-py-cc; sulfate-cc **Peripheral:** rh-qz	Lang et al. (1995); Jackson et al. (2008); Pass et al. (2008)

Appendix A2.4 continued

Deposit	Mineralization			Alteration			References
Galore Creek (Central Zone)	**Early (Main mineralization event: d**isseminated; occurs throughout the Central Zone with focus on the North Gold Lens and South Gold Lens: bn+cp ± Kf ± bi ± hm ± ah	**Transitional (minor):** Bbreccia-hosted; restricted to the Central Replacement Zone; latest hydrothermal cement in gt, di, bi, and mt-cemented breccia: cp-py+ah	**Transitional to late (minor):** breccia-hosted; restriticted to the South Gold Lens; again latest hydrotehrmal cement in di + mt + ah ± ch cemented breccia; bn + cp	**Deep:** Calcic alteration (gt-di-mt-bi-ah-or) overprinting potassic alteration (Kf-bi-hm-ah-ap)	-	**Peripheral:** ep ± ch ± cc-sd ± ah ± py **Late:** Locally fault-bounded sodic alteration observed: ab ± sr ± hm ± ah ± cb ± py	Enns et al. (1995); Loagn and Koyanagi (1989); Logan et al. (1989) and (1995); Micko (2007); Micko et al. (2008)
Galore Creek (Southwest Zone)	**Early:** Pervasive disseminated mt-bt	**Main stage:** Hydrothermal breccia, zones from core of cp-(bn) to cp>py into py>cp; replacement ± cement	**Peripheral:** ep-ch-gt-py ± (cp) alteration and veins and ah-cp veinlets **Late:** qz-Fe-carbonate ± (py) viens	**Deep:** Phlogopite-mt ± Kf ± (rt)	**Gradational from the core:** ferroan di-mt-(sphene) ± phlogopite ± (ferro-actinolite) ± ab	**Peripheral:** ch-mt, grandite-sp-py, Kf-ah ± cb **Late:** Structurally controlled qz-Fe-carboante-hm ± (py) veins	Enns et al. (1995); Lang et al. (1995); Byrne et al. (2008)
Mt Milligan	**Early:** qz-pr-mt-cp-(py) veinlets	**Transitional:** py-cc-(mt)-(cp) veins	**Peripheral:** py-ep-ab-at-cc-ch **Late:** dl-ak-sr-qz-py-en-tn-(cp)	**Deep:** bi-or-mt-qz	**Shallow:** ab-at/uralite-ch-(ep)-(cc)	**Peripheral:** ep-ch-at/uralite-cc-(ab) **Late:** dl-sr ch-(Kf)-(ab)-py-hm alteration halos around late-stge faults	Rebagliati (1988); Sketchly et al. (1995); Delong (1996); Jago (2008); Jago and Tosdal (2008)
Lorraine (Lower Main Zone)	**Early:** mt-px-ab-cp (patches, veins), bi-Kf veins; foliation defined by alignment of ferromagnesian minerals	**Transitional:** disseminated mt-cp-bn-cc-py; core of bn-cp to cp>py to cp<py; selective replacement of bi by Cu-Fe sulfides and mt	**Peripheral:** disseminated py>cp-ch-il/ms and cz **Late:** cp-py-qz veins	**Deep:** Kf metasomatism (positive correlation between Cu and Kf); ab patches; titanite ± mt ± cz-ep ± gt; Ca-rich plagioclase absent; localized coarse Kf veins ± coarse bi	**Shallow:** Selective replacement of plagioclase with il-ms and cz; remnants of Ca-rich plagioclase preserved; localized selective replacement of bi by ch in py>cp zones	**Peripheral:** il-ms-cz selective replacement of plagioclase; Ca-rich plagioclase preserved **Late:** sr-cb ± py alteration halos around late-stage faults; ep-hm-py; mt-px-Kf-cp polymictic breccia; qz veins with cp + py	Wilkinson et al. (1976); Nixon and Peatfield (2003); Bath and Cooke (2008)

Appendix A2.4 continued

Deposit	Mineralization			Alteration			References
Dinkidi	**Calc-potassic stage:** perthite-at and at-perthite-bn-ap veins, bn-or vein-dykes, layered perthite-di pegmatite	**Potassic stage:** qz-at-Kf-mt-cb-sulfide veins and breccias	**Late stage:** ze veins and breccias (laumonite, stilbite, chabazite, clinoptilolite)	**Early:** mt-bi alteration	**Main stage:** or-at-suflide alteration (qz alteration associated with the potassic vein stage)	**High Level:** advanced argillic alteration (kaolinite-pyrophyllite-quartz) on Dinkidi ridge	Wolfe (2001)

Abbreviations: ab-albite, at-actinolite, ah-anhydrite, ak-ankerite, ap-apatite, bi-biotite, bn-bornite, cb-carbonate, cc-calcite, ch-chlorite, cp-chalcopyrite, cz-clinozoisite, di-diopside, dl-dolomite, en-enargite, ep-epidote, fl-fluorite, gl-galena, gt-garnet, hm-hematite, il-illite, Kf-K-feldspar, mt-magnetite, ms-muscovite, or-orthocase, ph-prehnite, py-pyrite, px-pyroxene, QMP-quartz monzonite porphyry, qz-quartz, rh-rhodochrosite, rt-rutile, sr-sercite, tn-tennantite, ze-seolite

Appendix A2.5 Fluid chemistry of selected alkalic porphyry deposits (from Tosdal et al., 2008).

Deposit	Temperature	Salinity	Pressure / depth	Sulfur isotopes	Comments	References
Ridgeway	Average 450° to 440°C	63 to 53 eq. wt. % NaCl + KCl	Unrealistic minimum P_t estimate of 3.4 kbars from fluid inclusions (approximately 13.6 km depth at lithostatic pressure)	**Sulfides** (n = 43): −5.7 to +9.2‰, with most between -4 and -1‰ **Sulfates:** no data available	Fluid inclusions appear to have undergone post-entrapment modification (halite homogenising inclusions). Salinity estimates are valid, but P and T_h estimates are dubious	Harper (2000); Wilson (2003); Wilson et al. (2003); Wilson et al. (2007a)
Cadia Quarry	490° to 415°C	61 to 53 eq. wt. % NaCl + KCl	3.6–3.2 kbars (same problem as Ridgeway)	No data available	-	Holliday et al. (2002); Wilson (2003); Wilson et al. (2004); Wilson et al. (2007a, b)
Cadia Hill	490° to 415°C	61 to 53 eq. wt. % NaCl + KCl	3.6–3.2 kbars (same problem as Ridgeway)	**Sulfides** (n = 28): -9.8 to +9.1‰, with most between -6 and -2‰ **Sulfates:** no data available	-	Wilson (2003); Wilson et al. (2007a)
Cadia East	490° to 415°C	61 to 53 eq. wt. % NaCl + KCl	3.6–3.2 kbars (same problem as Ridgeway)	**Sulfides** (n = 41): -5.4 to -1.0‰ **Sulfates:** no data available	-	Wilson (2003); Wilson et al. (2007a)
Northparkes (E22, E26, E27, E48)	Early stage: >550° to 460°C; Late stage: 400° to 350°C	Early stage: 60 to 55 eq. wt % NaCl + KCl; Late stage: ~40 eq. wt % NaCl + KCl	Early stage: 450 to ~300 bars (~1.7–1.0 km depth assuming lithostatic load); Late stage: 200 to ~150 bars (similar depths assuming hydrostatic load)	**Sulfides** (n = 53): -19.7 to -0.7‰ **Sulfates (n = 5):** +4.4 to +21.8‰	Late-stage sericite at E26 and E48 has O/D isotopic compositions indicative of magmatic-hydrothermal fluids	Wolfe (1994); Heithersay and Walshe (1995); Lickfold (2002); Harris and Golding (2002); Lickfold et al. (2003)
Mt. Polley (Northeast Zone)	481° to 255°C (based on py-cp and cp-bn sulfur isotope thermometers)	No data available	No data available. Interpreted as shallow by Rees et al. (2005)	**Sulfides** (n = 210): -7.1 to +1.4‰, with most between -2 and -5‰ **Sulfates** (n = 22): +6.2 to +14.0‰, with most between +7.3 and +9.8‰	Stage 5: Epithermal overprint(?) contains bacterial associated $\delta^{34}S$ values (n=4): -53.9 to -36.7‰	Rees et al. (2006); Pass et al. (2008)
Galore Creek (Central Zone)	Primary fluid inclusions in garnet (Micko et al., 2008): 561.2° to 545.5°C and 465.8° to 464.7°C	Estimated at: 12-10 eq. Wt. % NaCl + KCl	Not yet determined	**Sulfides** (n = 106): -17.2 to -3.4‰ **Sulfates** (n = 7): +11.0 to +9.21‰	Fluid inclusions study at Galore Creek restricted to garnets of the Central Replacement Zone and the North Gold Lens. They are representative of the main calcic event in the early main alteration stage of the Central Zone. Initial results are locally limited. An extensive study has been initiated.	Dunne et al. (1994); Deyell and Tosdal (2005); Micko (2007); Micko et al. (2008)

Appendix A2.5 continued

Deposit	Temperature	Salinity	Pressure / depth	Sulfur isotopes	Comments	References
Galore Creek (Southwest Zone)	Average 220° to 175°C (n=7)	22 to 20 wt % NaCl + KCl	Likley to be CO_2-rich inclusions; some vapour in vapour inclusions = ~1 kbar	No data available	Provisional results of fluid inclusions analysis from late, volumetrically minor, quartz veins	Byrne et al. (2008)
Mt Milligan	455° to 340°C	<16 wt % NaCl eq.	Uncertain, few py-cpy geothermometer results agree with pressure corrected fluid inclusions T_H at ~1.2 kbar (~3.5km depth)	**Sulfides** (n = 116): -4.8 to +0.4‰, with most between -2.5 and 0‰ **Sulfates:** no data available	Fluid inclusions are 2 phase liquid-vapour homogenize to liquid, show supercritical behavior in the deep core, fluid is CO_2-bearing	Jago (2008)
Lorraine	Biotite-apatite thermometer. Coarse patches of apatite and biotite with sulfide inclusions: 632° to 515°C	Secondary inclusions only. Timing uncertain. No daughter halite crystals in secondary inclusions (i.e. <23 wt % NaCl)	No data available	**Sulfides** (n = 43): -16.6 to 0‰ **Sulfates** (n = 7): no data available	-	Deyell and Tosdal (2005); Bath and Cooke (2008)
Dinkidi	>600° to ~200°C	>68 to 13 wt % NaCl; also up to 1.1 wt % Cu and 8.3 wt % Fe (PIXE data)	1260 to 820 bar, 4.5 to 2.9 Km depth (lithostatic load)	**Sulfides** (n = 57): -4.2 to -0.2‰ **Sulfates** (n = 7): no data available	-	Wolfe (2001)

Abbreviations: eq.-equivalent, bn-bornite, cp-chalcopyrite, py-pyrite, wt-weight

Appendix A3.1

Appendix A3.1 Drill holes logged in this study with meterage.

Diamond Drill Hole #	Depth logged (m)	Total meters (m)
Section 18		
WB04-26	18.3–227.7	209
WB04-27	3.05–355.7	353
WB04-32	41.45–386.2	345
WB04-73	3.7–306.2	303
Long-section		
WB03-03	84.5–147.6	55
WB03-07	45.0–87.2	42
WB03-11	46.0–87.6	42
WB03-13	3.66–53	49
WB03-16	15.2–31.9	17
WB03-17	39.6–68.5	29
WB04-25	9.2–53.8	45
WB04-29[1]	21.3–151.0	150
WB04-31	76.9–119.9	43
WB04-33	3.3–13.8	12
WB04-35	144.0–196.1	52
WB04-40	39.2–79.7	38
WB04-47	266.4–313.0	47
WB04-49	125.7–182.5	57
WB04-64	191.2–226.1	35
WB04-52	114.3–165.6	51
WB04-77	49.4–69.7	20
WB04-81	102.5–134.3	32
WB04-88	198.6–218.9	20
WB04-95	27.6–322.2	294
WB04-96	186.1–229.5	43
WB04-108	0–443.8	444
WB04-111	176.2–262.4	83
WB04-114	94.1–136.4	42
WB04-115	368.4–418.9	42
WB04-122	309.1–392.3	80
WB04-131	359.7–425.2	66
WB04-141	64.3–138.1	74
WB04-150	420.9–496.0	75
WB04-152	514.5–589.1	75
WB04-156	55.1–121.0	66
WB04-172	93.6–123.9	30
WB05-192	308.3–330.8	23
WB05-188	6.1–709.3	708
WB05-205	143.3–152.6	9
WB05-210	409.0–566.0	133
WB05-213	453.9–675.2	115
WB05-223	73.4–126.6	53
WB07-239	2.2–400.4	398
	total	4898

Appendix A3.1 continued

[1] tie with section 18.

Appendix B1

Appenidx B1.1 Descriptive framework for breccia nomenclature and classification (based on the approach to volcanic rocks of McPhie et al., 1993; modified after Davies et al., 2000). Taken from Davies, 2002.

Descriptive names for breccias

Ideal combination:

5 +	4 +	3 +	2 +	1
Alteration	**Internal Organisation**	**Components A+B+C**	**Grain size**	**Geometry**

Minimum combination: ***4 + 3 + 2***

2 + 4 + 3	eg. medium-grained jigsaw-fit quartz-cemented andesite breccia
2 + 4 + 3 + 1	eg. coarse-grained massive, matrix-supported, rock-flour matrix polymict breccia pipe
5 + 4 + 3 + 2 + 1	eg. kaolinite-altered, monomict clast-supported fine-grained breccia dyke

1) Geometry

- eg. Pipe, cone, dyke, vein, irregular, tabular
- Contacts – sharp, gradational, faulted, irregular, planar, concordant, discordant

2) Grain size (clast)

- Mud (<1/16 mm)
- Sand (1/16 - 2 mm)
- Breccia / conglomerate
  - Fine-grained (2 - 4 mm)
  - Medium-grained (4 - 64 mm)
  - Coarse-grained (64 - 256 mm)
  - Very coarse-grained (>256 mm)

3) Components

a) Clasts

- Monomict or polymict
- Lithology/type – lithic (type), vein, breccia, juvenile magmatic, accretionary lapilli, pseudoclastic; mineralised, altered
- Morphology – angular, sub-angular, sub-round, round, faceted, tabular, equant

b) Matrix

- Rock flour, crystal fragments, lithic fragments, vein fragments
- Texture – banded, laminated, massive
- Grain size

c) Cement

- Ore and gangue mineralogy, and grain size
- Texture – e.g. cockade, massive, drusy,bladed, banded
- Crystalline igneous rock (not clastic)

d) Open space or vugs

4) Internal Organisation (outcrop scale features)

- Clast abundance – clast/matrix/cement supported
- Clast distribution – jigsaw-fit, in-situ rotated, chaotic
- Massive (non-graded) or graded
- Stratified or unstratified

5) Alteration

- Clasts/matrix/cement and paragenesis/texturally destructive

Appenidx B1.2 Imperial Metals Corporation 2007 logging codes for coherent rocks at Mt. Polley.

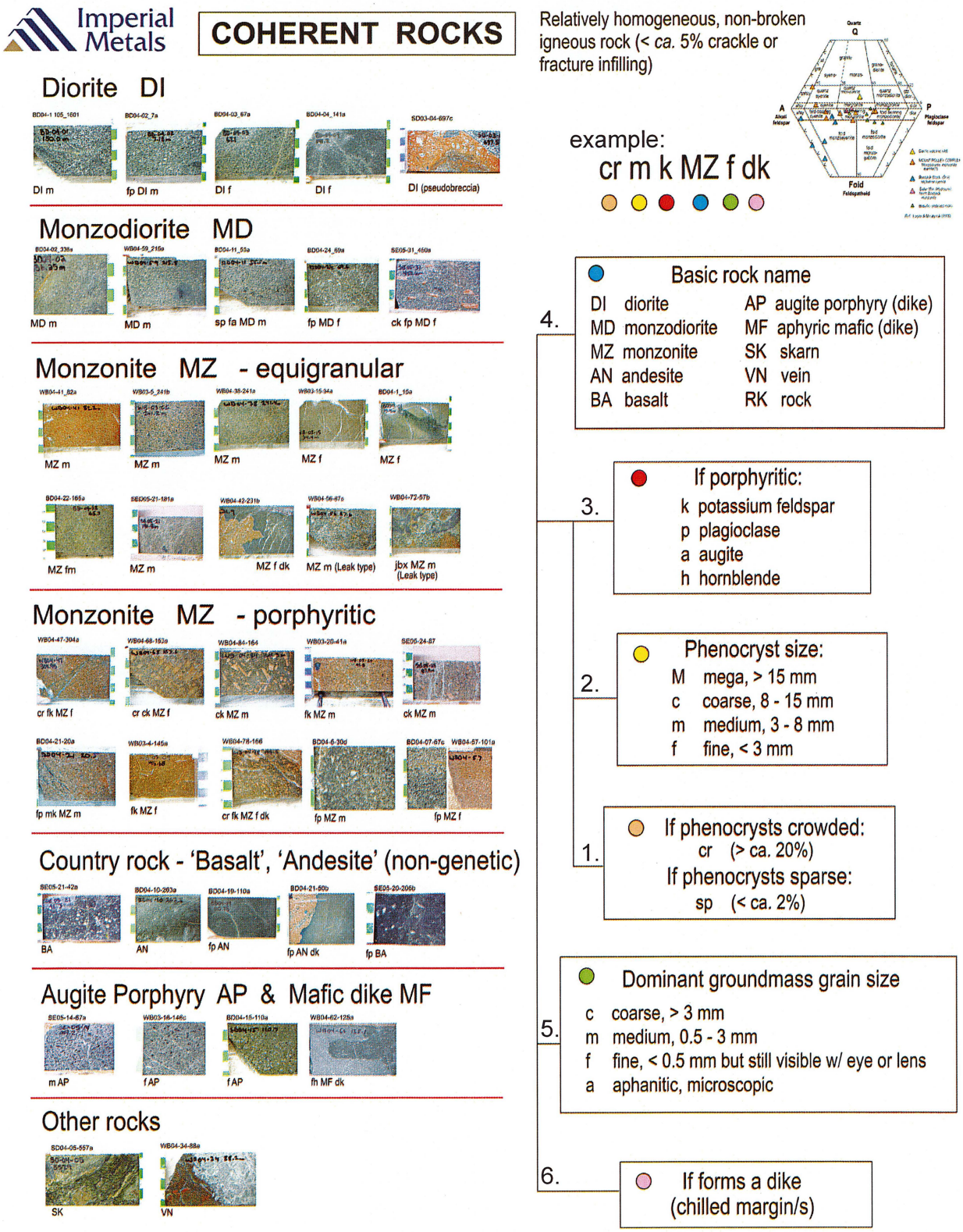

Appendix B1.3 Imperial Metals Corporation 2007 logging codes for clastic or broken rocks at Mt. Polley.

Imperial Metals

CLASTIC ROCKS

1. Fragmental type breccia FBX

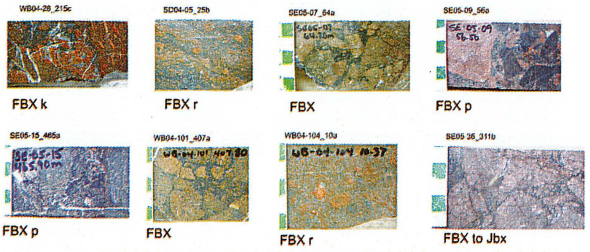

Evidence of clast transport, mixing, milling.
Matrix may be rock particles or mineral cement.

FBX * ←

k	Kf-phyric clasts (NEZ, SEZ)
r	smaller, round & dispersed fragments
m	sulfide/mineralized clasts
p	polymictic clasts
s	sedimentary/volcanogenic matrix

Add more as necessary

2. Jigsaw type breccia JBX

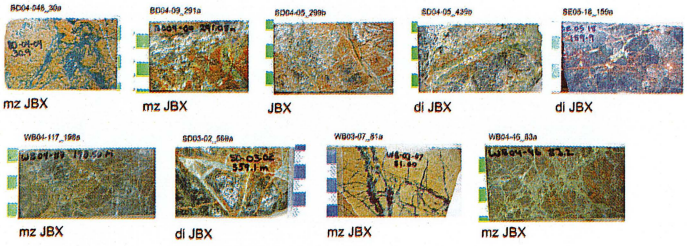

In situ fracturing, minimal translation & rotation.
Jbx should cover crackle breccia, mosaic breccia.
Note: Alteration may mask fracture control.

Precursor rock (basic) → mz JBX

Transitional type: Insert 'jbx' immediately before rock name, e.g. ck jbx MZ m, jbx FBX

3. Igneous breccia IBX

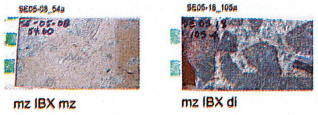

Cement is igneous 'melt'.

Cement, i.e. intrusion → mz IBX di ← Inclusion rock, if monomictic

4. Breccia - undefined BX

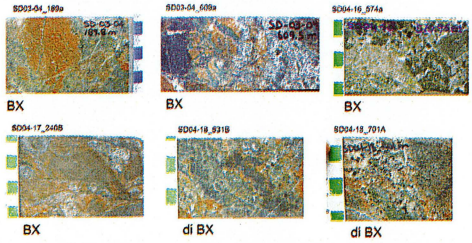

Matrix is strong hydrothermal alteration, breccia type unknown.

Uncertain if alteration follows matrix (FBX), fractures (JBX), or igneous 'veins' (IBX).

Basic rock, if known → di BX

5. Fault FLT, Tectonic breccia (healed fault) TBX

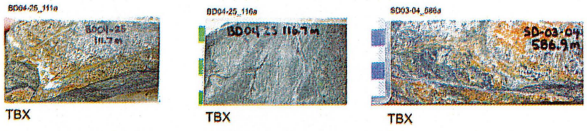

(Healed fault)
fbx TBX

Precursor rock (basic) → mz FLT

gg Gouge (precursor unknown)

6. OTHER (including volcaniclastic)

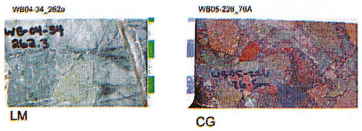

SD sandstone	CG conglomerate
SL siltstone	LM limestone

Appendix F

Appendix F H. Pass Rock Catalogue, 2010.

UTas #	Field Number	Composition	Rock Name	Ore mineral 1	Ore mineral 2	Ore mineral 3	Drill Hole	Depth (m)	Hand specimen	Powder
166323	WB03-03_92	felsic	monzonite	cpy			WB03-03	92.0	R	
166324	WB03-03_118.5	felsic	breccia	cpy	bn		WB03-03	118.5	R	
166325	WB03-03_120.7	felsic	breccia	cpy	bn		WB03-03	120.7	R	
166326	WB03-03_123.3	felsic	breccia	cpy			WB03-03	123.3	R	
166327	WB03-03_129.9	felsic	breccia	cpy			WB03-03	129.9	R	
166328	WB03-03_130.2	felsic	monzonite	cpy			WB03-03	130.2	R	
166329	WB03-03_133.3	felsic	breccia	cpy			WB03-03	133.3	R	
166330	WB03-07_58.3	felsic	breccia	cpy	bn		WB03-07	58.3	R	PD
166331	WB03-07_78.8	felsic	monzonite	cpy			WB03-07	78.8	R	
166332	WB03-07_82	felsic	monzonite	cpy	bn	tn	WB03-07	82.0	R	
166333	WB03-11_54.4	felsic	breccia	cpy	bn		WB03-11	54.4	R	
166334	WB03-11_64.5	felsic	breccia	cpy	bn		WB03-11	64.5	R	
166335	WB03-11_66.8	felsic	breccia	cpy			WB03-11	66.8	R	
166336	WB03-11_83.5	felsic	breccia	cpy			WB03-11	83.5	R	PD
166337	WB03-16_21.4	felsic	breccia				WB03-16	21.4	R	
166338	WB03-16_24.7	felsic	breccia	cpy			WB03-16	24.7	R	
166339	WB03-16_31.6	felsic	breccia	cpy	bn		WB03-16	31.6	R	PD
166340	WB03-17_42.3	felsic	monzonite	cpy			WB03-17	42.3	R	
166341	WB03-17_47.3	felsic	monzonite	cpy	bn		WB03-17	47.3	R	PD
166342	WB03-17_52.8	felsic	monzonite	cpy			WB03-17	52.8	R	
166343	WB03-17_66	felsic	monzonite	cpy	bn		WB03-17	66.0	R	
166344	WB04-25_29.91	felsic	mylonite	cpy	bn		WB04-25	29.9	R	
166345	WB04-25_31.65	felsic	breccia	cpy			WB04-25	31.7	R	
166346	WB04-25_32.5	felsic	mylonite	cpy	bn		WB04-25	32.1	R	
166347	WB04-25_37	felsic	breccia	cpy	bn		WB04-25	37.0	R	PD
166348	WB04-26_30.4	felsic	diorite				WB04-26	30.4	R	
166349	WB04-26_37.3	felsic	breccia	cpy			WB04-26	37.3	R	PD
166350	WB04-26_43.2	mafic	Breccia				WB04-26	43.2	R	PD
166351	WB04-26_53.3	felsic	breccia	cpy			WB04-26	53.3	R	
166352	WB04-26_54	felsic	breccia	cpy			WB04-26	54.0	R	PD
166353	WB04-26_58.8	felsic	breccia				WB04-26	58.8	R	
166354	WB04-26_59.4	felsic	breccia	cpy			WB04-26	59.4	R	
166355	WB04-26_60.2	felsic	monzonite				WB04-26	60.2	R	
166356	WB04-26_61.6	felsic	monzonite	cpy			WB04-26	61.6	R	
166357	WB04-26_68.1	felsic	monzonite	cpy			WB04-26	68.1	R	
166358	WB04-26_70.6	felsic	breccia	cpy			WB04-26	70.6	R	
166359	WB04-26_70.6b	felsic	breccia	cpy			WB04-26	71.7	R	
166360	WB04-26_79.7	felsic	breccia	cpy			WB04-26	79.7	R	PD
166361	WB04-26_94.5	felsic	monzonite				WB04-26	94.5	R	
166362	WB04-26_97.5	felsic	monzonite				WB04-26	97.5	R	

Thin Section	Polished block	Northing	Easting	Azimuth	Dip	Other preps	Other Comments
1TS		5495.92	2729.91	240	-60		
		5495.92	2729.91	240	-60		
1TS	PB	5495.92	2729.91	240	-60	polished slab, S isotopes, LAICPMS, thin section is doublesize, thick section off glass in box #1	
1TS		5495.92	2729.91	240	-60		
1TS		5495.92	2729.91	240	-60	thick section on glass in with thinnies	
	PB	5495.92	2729.91	240	-60	polished slab,	late veins
1TS		5495.92	2729.91	240	-60		
		5414.34	2837.32	240	-60	S isotope	
		5414.34	2837.32	240	-60		
1TS		5414.34	2837.32	240	-60	C-O isotopes, S-istopes	phyllic alteration, stage 5 veins
1TS		5385.63	2889.25	240	-60		
		5385.63	2889.25	240	-60		possible JV clast
1TS		5385.63	2889.25	240	-60		JV clast
1TS	PB	5385.63	2889.25	240	-60	LAICPMS mount	
1TS		5370.63	2864	240	-60		
		5370.63	2864	240	-60		
		5370.63	2864	240	-60		cb cement
		5310.06	2910.33	60	-50		
1TS		5310.06	2910.33	60	-50	S isorope	stage 3 vein
1TS		5310.06	2910.33	60	-50		stage 4 vein
		5310.06	2910.33	60	-50		stage 3 vein
		5373.6	2818.8	60	-50	thick section off glass in box #1	stage 3 vein
		5373.6	2818.8	60	-50		
1TS	PB	5373.6	2818.8	60	-50		mylonite, stage 3 vein
	PB	5373.6	2818.8	60	-50	LAICPMS, S isotope	
1TS		5306.4	2805	60	-50		stage 4 vein bx, section18
		5306.4	2805	60	-50	S-isotope	section 18
1TS		5306.4	2805	60	-50	C-O isotope	section 18
		5306.4	2805	60	-50	S-isotope	section 18
		5306.4	2805	60	-50	S-isotope	section 18
1TS		5306.4	2805	60	-50		stage 4 veining, section 18
1TS		5306.4	2805	60	-50	LAICPMS mount, thick section (off glass in paper box #1)	section 18
		5306.4	2805	60	-50		section 18, cb cement, megacrystic Kf-phyric porphyry
		5306.4	2805	60	-50		section 18, megacrystic Kf-phyric porphyry
		5306.4	2805	60	-50		stage 4 vein bx, section 18
1TS		5306.4	2805	60	-50	thick section off glass in paper box #1	good paragensis, section 18
		5306.4	2805	60	-50		cb cement, section 18
		5306.4	2805	60	-50	S-isotope	section 18
		5306.4	2805	60	-50		intrusive contact, section 18
		5306.4	2805	60	-50		section 18, megacrystic Kf-phyric porphyry

Appendix F continued

UTas #	Field Number	Composition	Rock Name	Ore mineral 1	Ore mineral 2	Ore mineral 3	Drill Hole	Depth (m)	Hand specimen	Powder
166323	WB03-03_92	felsic	monzonite	cpy			WB03-03	92.0	R	
166324	WB03-03_118.5	felsic	breccia	cpy	bn		WB03-03	118.5	R	
166325	WB03-03_120.7	felsic	breccia	cpy	bn		WB03-03	120.7	R	
166326	WB03-03_123.3	felsic	breccia	cpy			WB03-03	123.3	R	
166327	WB03-03_129.9	felsic	breccia	cpy			WB03-03	129.9	R	
166328	WB03-03_130.2	felsic	monzonite	cpy			WB03-03	130.2	R	
166329	WB03-03_133.3	felsic	breccia	cpy			WB03-03	133.3	R	
166330	WB03-07_58.3	felsic	breccia	cpy	bn		WB03-07	58.3	R	PD
166331	WB03-07_78.8	felsic	monzonite	cpy			WB03-07	78.8	R	
166332	WB03-07_82	felsic	monzonite	cpy	bn	tn	WB03-07	82.0	R	
166333	WB03-11_54.4	felsic	breccia	cpy	bn		WB03-11	54.4	R	
166334	WB03-11_64.5	felsic	breccia	cpy	bn		WB03-11	64.5	R	
166335	WB03-11_66.8	felsic	breccia	cpy			WB03-11	66.8	R	
166336	WB03-11_83.5	felsic	breccia	cpy			WB03-11	83.5	R	PD
166337	WB03-16_21.4	felsic	breccia				WB03-16	21.4	R	
166338	WB03-16_24.7	felsic	breccia	cpy			WB03-16	24.7	R	
166339	WB03-16_31.6	felsic	breccia	cpy	bn		WB03-16	31.6	R	PD
166340	WB03-17_42.3	felsic	monzonite	cpy			WB03-17	42.3	R	
166341	WB03-17_47.3	felsic	monzonite	cpy	bn		WB03-17	47.3	R	PD
166342	WB03-17_52.8	felsic	monzonite	cpy			WB03-17	52.8	R	
166343	WB03-17_66	felsic	monzonite	cpy	bn		WB03-17	66.0	R	
166344	WB04-25_29.91	felsic	mylonite	cpy	bn		WB04-25	29.9	R	
166345	WB04-25_31.65	felsic	breccia	cpy			WB04-25	31.7	R	
166346	WB04-25_32.5	felsic	mylonite	cpy	bn		WB04-25	32.1	R	
166347	WB04-25_37	felsic	breccia	cpy	bn		WB04-25	37.0	R	PD
166348	WB04-26_30.4	felsic	diorite				WB04-26	30.4	R	
166349	WB04-26_37.3	felsic	breccia	cpy			WB04-26	37.3	R	PD
166350	WB04-26_43.2	mafic	Breccia				WB04-26	43.2	R	PD
166351	WB04-26_53.3	felsic	breccia	cpy			WB04-26	53.3	R	
166352	WB04-26_54	felsic	breccia	cpy			WB04-26	54.0	R	PD
166353	WB04-26_58.8	felsic	breccia				WB04-26	58.8	R	
166354	WB04-26_59.4	felsic	breccia	cpy			WB04-26	59.4	R	
166355	WB04-26_60.2	felsic	monzonite				WB04-26	60.2	R	
166356	WB04-26_61.6	felsic	monzonite	cpy			WB04-26	61.6	R	
166357	WB04-26_68.1	felsic	monzonite	cpy			WB04-26	68.1	R	
166358	WB04-26_70.6	felsic	breccia	cpy			WB04-26	70.6	R	
166359	WB04-26_70.6b	felsic	breccia	cpy			WB04-26	71.7	R	
166360	WB04-26_79.7	felsic	breccia	cpy			WB04-26	79.7	R	PD
166361	WB04-26_94.5	felsic	monzonite				WB04-26	94.5	R	
166362	WB04-26_97.5	felsic	monzonite				WB04-26	97.5	R	

Thin Section	Polished block	Northing	Easting	Azimuth	Dip	Other preps	Other Comments
1TS		5495.92	2729.91	240	-60		
		5495.92	2729.91	240	-60		
1TS	PB	5495.92	2729.91	240	-60	polished slab, S isotopes, LAICPMS, thin section is doublesize, thick section off glass in box #1	
1TS		5495.92	2729.91	240	-60		
1TS		5495.92	2729.91	240	-60	thick section on glass in with thinnies	
	PB	5495.92	2729.91	240	-60	polished slab,	late veins
1TS		5495.92	2729.91	240	-60		
		5414.34	2837.32	240	-60	S isotope	
		5414.34	2837.32	240	-60		
1TS		5414.34	2837.32	240	-60	C-O isotopes, S-istopes	phyllic alteration, stage 5 veins
1TS		5385.63	2889.25	240	-60		
		5385.63	2889.25	240	-60		possible JV clast
1TS		5385.63	2889.25	240	-60		JV clast
1TS	PB	5385.63	2889.25	240	-60	LAICPMS mount	
1TS		5370.63	2864	240	-60		
		5370.63	2864	240	-60		
		5370.63	2864	240	-60		cb cement
		5310.06	2910.33	60	-50		
1TS		5310.06	2910.33	60	-50	S isorope	stage 3 vein
1TS		5310.06	2910.33	60	-50		stage 4 vein
		5310.06	2910.33	60	-50		stage 3 vein
		5373.6	2818.8	60	-50	thick section off glass in box #1	stage 3 vein
		5373.6	2818.8	60	-50		
1TS	PB	5373.6	2818.8	60	-50		mylonite, stage 3 vein
	PB	5373.6	2818.8	60	-50	LAICPMS, S isotope	
1TS		5306.4	2805	60	-50		stage 4 vein bx, section18
		5306.4	2805	60	-50	S-isotope	section 18
1TS		5306.4	2805	60	-50	C-O isotope	section 18
		5306.4	2805	60	-50	S-isotope	section 18
		5306.4	2805	60	-50	S-isotope	section 18
1TS		5306.4	2805	60	-50		stage 4 veining, section 18
1TS		5306.4	2805	60	-50	LAICPMS mount, thick section (off glass in paper box #1)	section 18
		5306.4	2805	60	-50		section 18, cb cement, megacrystic Kf-phyric porphyry
		5306.4	2805	60	-50		section 18, megacrystic Kf-phyric porphyry
		5306.4	2805	60	-50		stage 4 vein bx, section 18
1TS		5306.4	2805	60	-50	thick section off glass in paper box #1	good paragensis, section 18
		5306.4	2805	60	-50		cb cement, section 18
		5306.4	2805	60	-50	S-isotope	section 18
		5306.4	2805	60	-50		intrusive contact, section 18
		5306.4	2805	60	-50		section 18, megacrystic Kf-phyric porphyry

Appendix F continued

UTas #	Field Number	Composition	Rock Name	Ore mineral 1	Ore mineral 2	Ore mineral 3	Drill Hole	Depth (m)	Hand specimen	Powder
166363	WB04-26_145	felsic	breccia	cpy			WB04-26	145.0	R	
166364	WB04-26_146	felsic	breccia	cpy	bn		WB04-26	146.0	R	
166365	WB04-26_153.9	felsic	breccia	cpy			WB04-26	153.9	R	
166366	WB04-26_156.8	felsic	breccia	cpy			WB04-26	156.8	R	
166367	WB04-26_162.9	felsic	breccia	cpy			WB04-26	162.9	R	PD
166368	WB04-26_168	felsic	breccia	cpy	bn		WB04-26	168.0	R	
166369	WB04-26_170.7	felsic	breccia	cpy			WB04-26	170.7	R	PD
166370	WB04-26_172.2	felsic	mylonite	cpy	bn		WB04-26	172.2	R	
166371	WB04-26_175.2	felsic	monzonite				WB04-26	175.2	R	
166372	WB04-26_179.7	felsic	breccia	cpy			WB04-26	178.7	R	
166373	WB04-26_201.5	felsic	monzonite	cpy			WB04-26	201.5	R	
166374	WB04-26_212.8	felsic	breccia	cpy			WB04-26	212.8	R	
166375	WB04-26_218.4	mafic	mafic				WB04-26	218.4	R	
166376	WB04-26_221.6	felsic	monzonite				WB04-26	221.6	R	PD
166377	WB04-26_228.6	felsic	monzonite				WB04-26	228.6	R	
166378	WB04-27_6.6	felsic	monzonite				WB04-27	6.6	R	
166379	WB04-27_12.2	felsic	breccia				WB04-27	12.2	R	
166380	WB04-27_22.1	felsic	breccia				WB04-27	22.1	R	PD
166381	WB04-27_26	felsic	breccia				WB04-27	26.0	R	
166382	WB04-27_37.8	felsic	diorite				WB04-27	37.8	R	
166383	WB04-27_44.3	felsic	diorite				WB04-27	44.3	R	
166384	WB04-27_47	felsic	breccia				WB04-27	47.0	R	
166385	WB04-27_71.1	felsic	monzonite				WB04-27	71.1	R	
166386	WB04-27_76.7	felsic	monzonite				WB04-27	76.7	R	
166387	WB04-27_100.3	felsic	monzonite				WB04-27	100.3	R	
166388	WB04-27_105.6	felsic	diorite				WB04-27	105.6	R	
166389	WB04-27_125.4	felsic	breccia				WB04-27	125.4	R	
166390	WB04-27_146.3	felsic	breccia	cpy			WB04-27	146.0-146.3	R	
166391	WB04-27_148.6	felsic	breccia				WB04-27	148.6	R	
166392	WB04-27_151.1	felsic	breccia				WB04-27	151.1	R	
166393	WB04-27_159	felsic	breccia	cpy			WB04-27	159.0	R	
166394	WB04-27_173.7	felsic	breccia				WB04-27	173.7	R	
166395	WB04-27_177.6	felsic	breccia				WB04-27	177.6	R	
166396	WB04-27_198.8	felsic	diorite				WB04-27	198.8	R	
166397	WB04-27_205.2	felsic	diorite	cpy			WB04-27	205.2	R	PD
166398	WB04-27_208.4	felsic	breccia	cpy			WB04-27	208.4	R	
166399	WB04-27_213.2	felsic	breccia	cpy			WB04-27	213.2	R	
166400	WB04-27_213.2b	felsic	breccia				WB04-27	213.2	R	

Thin Section	Polished block	Northing	Easting	Azimuth	Dip	Other preps	Other Comments
		5306.4	2805	60	-50		section 18
		5306.4	2805	60	-50	S-isotope, Thicksection of glass in paper box #1	cb cement, section 18
1TS		5306.4	2805	60	-50		section 18
		5306.4	2805	60	-50		section 18
		5306.4	2805	60	-50	thicksection off glass in paper box #1	section 18
1TS		5306.4	2805	60	-50	C-O isotope	cb cement, section 18
		5306.4	2805	60	-50	S-isotope, thicksection off glass in paper box #1	section 18
1TS		5306.4	2805	60	-50	S-isotope, thicksection off glas in paper box #1, LAICPMS mount	section 18
		5306.4	2805	60	-50		section 18
		5306.4	2805	60	-50		section 18
		5306.4	2805	60	-50		section 18
		5306.4	2805	60	-50		cb cement, section 18
1TS		5306.4	2805	60	-50		section 18
1TS		5306.4	2805	60	-50		stage 4 veins, section 18
		5306.4	2805	60	-50		section 18
		5278.3	2757.9	56.4	-50		albite, garnet altn, section 18
1TS		5278.3	2757.9	56.4	-50	S isotope, thicksection off glass in paper box #1	section 18
1TS		5278.3	2757.9	56.4	-50	S isotope, C-O isotope, thicksection off glass in paper box #1	stage 4 vein
		5278.3	2757.9	56.4	-50	S isotope, thicksection off glass in paper box #1	section 18
1TS		5278.3	2757.9	56.4	-50		section 18
		5278.3	2757.9	56.4	-50	S isotope, thicksection off glass in paper box #1	
		5278.3	2757.9	56.4	-50		
		5278.3	2757.9	56.4	-50		
		5278.3	2757.9	56.4	-50		
		5278.3	2757.9	56.4	-50		
1TS		5278.3	2757.9	56.4	-50		stage 4 vein
1TS		5278.3	2757.9	56.4	-50		healed fault
1TS	PB	5278.3	2757.9	56.4	-50	LASI thick section off glass in paper box #1, LAICPMS mount	
		5278.3	2757.9	56.4	-50		
		5278.3	2757.9	56.4	-50		
		5278.3	2757.9	56.4	-50		
		5278.3	2757.9	56.4	-50		stage 4 vein
		5278.3	2757.9	56.4	-50		stage 4 vein breccia
		5278.3	2757.9	56.4	-50		
		5278.3	2757.9	56.4	-50	S isoptope	
		5278.3	2757.9	56.4	-50		stage 4 vein breccia
	PB	5278.3	2757.9	56.4	-50	S-isotope, LASI thick section off glass in paper box #1, LAICPMS mount	
		5278.3	2757.9	56.4	-50		

Appendix F continued

UTas #	Field Number	Composition	Rock Name	Ore mineral 1	Ore mineral 2	Ore mineral 3	Drill Hole	Depth (m)	Hand specimen	Powder
166401	WB04-27_228.4	felsic	breccia	cpy			WB04-27	228.4	R	
166402	WB04-27_233.3	felsic	breccia	cpy	bn		WB04-27	233.3	R	
166403	WB04-27_244.3	felsic	monzonite	cpy			WB04-27	244.3		PD
166404	WB04-27_248.9	felsic	monzonite				WB04-27	248.9	R	
166405	WB04-27_274.9	felsic	breccia	cpy			WB04-27	274.9	R	PD
166406	WB04-27_284.2	felsic	breccia	cpy			WB04-27	284.2	R	PD
166407	WB04-27_287	felsic	breccia	cpy			WB04-27	287.0	R	PD
166408	WB04-27_288.7	felsic	breccia	cpy	bn		WB04-27	288.7	R	
166409	WB04-27_294.4	felsic	breccia	cpy			WB04-27	294.4	R	
166410	WB04-27_297.7	felsic	breccia	cpy			WB04-27	297.7	R	PD
166411	WB04-27_298.9	felsic	breccia	cpy			WB04-27	298.9	R	PD
166412	WB04-27_299.5	felsic	breccia	cpy			WB04-27	299.5	R	
166413	WB04-27_305.2	felsic	breccia				WB04-27	305.2	R	
166414	WB04-27_311.1	felsic	monzonite				WB04-27	311.1	R	
166415	WB04-27_319.8	felsic	monzonite				WB04-27	319.8	R	
166416	WB04-27_321.4	felsic	diorite				WB04-27	321.4	R	PD
166417	WB04-27_335.4	felsic	diorite				WB04-27	335.4	R	PD
166418	WB04-27_353.5	felsic	diorite				WB04-27	353.5	R	PD
166419	WB04-29_25.2	felsic	monzonite	cpy			WB04-29	25.2	R	
166420	WB04-29_31.4	felsic	breccia	cpy			WB04-29	31.4	R	
166421	WB04-29_31.8	felsic	breccia	cpy			WB04-29	31.8	R	
166422	WB04-29_33	felsic	monzonite	cpy	tn		WB04-29	33.0	R	PD
166423	WB04-29_35.1	felsic	breccia	cpy			WB04-29	35.1	R	
166424	WB04-29_36.6	felsic	breccia	cpy	bn		WB04-29	36.6	R	
166425	WB04-29_46.7	felsic	breccia	cpy			WB04-29	46.7	R	
166426	WB04-29_50	felsic	monzonite	cpy			WB04-29	50.0	R	
166427	WB04-29_58.6	felsic	breccia	cpy			WB04-29	58.6	R	
166428	WB04-29_63.8	felsic	breccia	cpy			WB04-29	63.8	R	
166429	WB04-29_103.4	felsic	breccia	cpy			WB04-29	103.4	R	
166430	WB04-29_108	felsic	breccia	cpy			WB04-29	108.0	R	
166431	WB04-29_111	felsic	breccia	bn			WB04-29	111.0	R	PD
166432	WB04-29_115.7	felsic	breccia	cpy			WB04-29	115.7	R	
166433	WB04-29_116.9	felsic	mylonite	cpy	bn		WB04-29	116.9	R	
166434	WB04-29_125.1	felsic	breccia	cpy	bn		WB04-29	125.1	R	
166435	WB04-29_130.9	felsic	monzonite				WB04-29	130.9	R	
166436	WB04-29_137.5	felsic	breccia	cpy			WB04-29	137.5	R	
166437	WB04-29_139.4	felsic	monzonite				WB04-29	139.4	R	

Thin Section	Polished block	Northing	Easting	Azimuth	Dip	Other preps	Other Comments
		5278.3	2757.9	56.4	-50		stage 4 vein
		5278.3	2757.9	56.4	-50S-isotope, LASI thick section off glass in paper box #1		
		5278.3	2757.9	56.4	-50S-isotope,		
		5278.3	2757.9	56.4	-50		
		5278.3	2757.9	56.4	-50S-isotope,		
		5278.3	2757.9	56.4	-50C-O isotope, S-isotope		
		5278.3	2757.9	56.4	-50S-isotope (sulfate)		
1TS		5278.3	2757.9	56.4	-50		
		5278.3	2757.9	56.4	-50		
		5278.3	2757.9	56.4	-50S isotope (sulfide+ sulfate)		
1TS		5278.3	2757.9	56.4	-50S-isotope (sulfate)		
		5278.3	2757.9	56.4	-50S-isotope (sulfate)		
		5278.3	2757.9	56.4	-50		stage 4 vein bx
		5278.3	2757.9	56.4	-50S-isotope (sulfate)		
		5278.3	2757.9	56.4	-50		
		5278.3	2757.9	56.4	-50S-isotope (sulfate)		
1TS		5278.3	2757.9	56.4	-50C-O isotope, S-isotope (sulfate)		
		5278.3	2757.9	56.4	-50S-isotope (sulfate)		
1TS		5354.5	2886.2	246	-85		phyllic alteration
		5354.5	2886.2	246	-85		
		5354.5	2886.2	246	-85S-isotope		
1TS		5354.5	2886.2	246	-85C-O isotope, S-isotope , LAICPMS mount from thick section - in paper box #1		stage 5 colloform cpy-tn veins, phyllic alteration
1TS		5354.5	2886.2	246	-85		stage 5 vein with chalcedony, phllyic alteration
		5354.5	2886.2	246	-85cb cement		
		5354.5	2886.2	246	-85		
	PB	5354.5	2886.2	246	-85S-isotope, LAICPMS mount, thick section off glass in paper box #1		stage 3 cpy veins cut coherent contact
		5354.5	2886.2	246	-85S-isotope, thick section off glass in paper box #1		
		5354.5	2886.2	246	-85S-isotope, thick section on glass in wood box #1		
1TS		5354.5	2886.2	246	-85		
		5354.5	2886.2	246	-85		
		5354.5	2886.2	246	-85S-isotope		
		5354.5	2886.2	246	-85		
		5354.5	2886.2	246	-85S isotope, thick section off glass in paper box #1, LAICPMS mount		late sulfide mylonite
		5354.5	2886.2	246	-85cb cement		
1TS		5354.5	2886.2	246	-85LAICPMS mount, epi-vein characterization		stage 5 chalcedony vein
		5354.5	2886.2	246	-85C-O isotope, thick sections off glass in paper box #1		
1TS		5354.5	2886.2	246	-85		

Appendix F continued

UTas #	Field Number	Composition	Rock Name	Ore mineral 1	Ore mineral 2	Ore mineral 3	Drill Hole	Depth (m)	Hand specimen	Powder
166438	WB04-29_146	felsic	monzonite	cpy			WB04-29	146.0	R	
166439	WB04-29_148.8	felsic	breccia	cpy			WB04-29	148.8	R	
166440	WB04-31_79.3	felsic	monzonite				WB04-31	79.3	R	
166441	WB04-31_80.65	felsic	breccia	cpy			WB04-31	80.7	R	PD
166442	WB04-31_82.5	felsic	breccia	cpy			WB04-31	82.5	R	
166443	WB04-31_84.6	felsic	breccia	cpy			WB04-31	84.6	R	
166444	WB04-31_98.9	felsic	mylonite				WB04-31	98.9	R	
166445	WB04-31_111.8	felsic	breccia	cpy			WB04-31	111.8	R	
166446	WB04-31_114.5	felsic	breccia	cpy			WB04-31	114.5	R	
166447	WB04-31_114.8	felsic	breccia	cpy	bn		WB04-31	114.8	R	
166448	WB04-32_48.8	felsic	diorite				WB04-32	48.8	R	
166449	WB04-32_60.3	felsic	breccia				WB04-32	60.3	R	
166450	WB04-32_71.1	felsic	breccia	cpy			WB04-32	71.1	R	
166451	WB04-32_111.6	felsic	diorite	cpy			WB04-32	111.6	R	
166452	WB04-32_155.8	felsic	breccia				WB04-32	155.8	R	
166453	WB04-32_156.7	felsic	breccia	cpy			WB04-32	156.7	R	PD
166454	WB04-32_166.6	felsic	breccia	cpy			WB04-32	166.6	R	
166455	WB04-32_181	felsic	breccia	cpy			WB04-32	181.0	R	PD
166456	WB04-32_184	felsic	breccia	cpy			WB04-32	184.0	R	PD
166457	WB04-32_199.4	felsic	breccia	cpy			WB04-32	199.4	R	PD
166458	WB04-32_207.1	felsic	breccia	cpy			WB04-32	207.1	R	PD
166459	WB04-32_231.7	felsic	breccia				WB04-32	231.7	R	
166460	WB04-32_243	mafic	basalt				WB04-32	243.0	R	
166461	WB04-32_257.6	felsic	monzonite				WB04-32	257.6	R	
166462	WB04-32_268.5	felsic	breccia				WB04-32	268.5	R	
166463	WB04-32_272.6	felsic	breccia				WB04-32	272.6	R	PD
166464	WB04-32_315.1	felsic	breccia				WB04-32	315.1	R	
166465	WB04-32_348.6	felsic	breccia	cpy			WB04-32	348.6	R	PD
166466	WB04-33_5.6	felsic	breccia				WB04-33	5.6	R	
166467	WB04-35_146	felsic	monzonite				WB04-35	146.0	R	
166468	WB04-35_147	felsic	monzonite				WB04-35	147.0	R	
166469	WB04-35_161	felsic	breccia				WB04-35	161.0	R	
166470	WB04-35_181.6	felsic	monzonite				WB04-35	181.6	R	
166471	WB04-40_40.9	felsic	monzonite				WB04-40	40.9	R	
166472	WB04-40_65	felsic	breccia	cpy			WB04-40	65.0	R	
166473	WB04-40_68.1	felsic	breccia	cpy			WB04-40	68.1	R	PD
166474	WB04-40_69	felsic	breccia	cpy			WB04-40	69.0	R	
166475	WB04-40_69.3	felsic	breccia				WB04-40	69.3	R	
166476	WB04-40_76.3	felsic	breccia	cpy			WB04-40	76.3	R	

Thin Section	Polished block	Northing	Easting	Azimuth	Dip	Other preps	Other Comments
1TS		5354.5	2886.2	246	-85		
		5354.5	2886.2	246	-85		
1TS		5434.6	2630	60	-50		
1TS		5434.6	2630	60	-50	LASI thick section off glass in paper box #1	
1TS		5434.6	2630	60	-50		gnt alteration
		5434.6	2630	60	-50		
		5434.6	2630	60	-50		py mylonite
		5434.6	2630	60	-50		
		5434.6	2630	60	-50	thick section on glass in wooden box #1	
1TS		5434.6	2630	60	-50	thinnie and thick section on glass in wooden box #1, LASI thick section off glass in paper box #1	
1TS		5407.7	2964.8	240	-60		
1TS		5407.7	2964.8	240	-60		stage 5 epi-vein, chalcedony
	PB	5407.7	2964.8	240	-60	LASI thick section off glass in paper box #1, LAICPMS mount	
		5407.7	2964.8	240	-60	S-isotope	
1TS		5407.7	2964.8	240	-60		
	PB	5407.7	2964.8	240	-60	LAICPMS mount, S-isotope	
		5407.7	2964.8	240	-60		
		5407.7	2964.8	240	-60	S-isotope	
1TS		5407.7	2964.8	240	-60	C-O isotope	
		5407.7	2964.8	240	-60	S-isotope (sulfate)	
1TS		5407.7	2964.8	240	-60	LASI thick section off glass in paper box #1,S-isotope (sulfate+ sulfide)	
		5407.7	2964.8	240	-60		bladed sulfate vein
		5407.7	2964.8	240	-60		
		5407.7	2964.8	240	-60	S-isotope (sulfate)	
1TS		5407.7	2964.8	240	-60		
		5407.7	2964.8	240	-60	C-O isotope,S-isotope (sulfate)	
1TS		5407.7	2964.8	240	-60		
		5407.7	2964.8	240	-60	S-isotope (sulfate)	
1TS		5465.1	2683.2	240	-60		
		5511	2760.4	240	-60		
1TS		5511	2760.4	240	-60		
		5511	2760.4	240	-60		
		5511	2760.4	240	-60		
1TS	PB	5448.62	2654.74	60	-50	LAICPMS mount	stage 5 epi vein
1TS		5448.62	2654.74	60	-50		
	PB	5448.62	2654.74	60	-50	LAICPMS mount, S-isotope	
1TS		5448.62	2654.74	60	-50		
		5448.62	2654.74	60	-50		MBx
1TS		5448.62	2654.74	60	-50	double size thinnie and thick section in plastic box	

Appendix F continued

UTas #	Field Number	Composition	Rock Name	Ore mineral 1	Ore mineral 2	Ore mineral 3	Drill Hole	Depth (m)	Hand specimen	Powder
166477	WB04-40_78	felsic	breccia				WB04-40	78.0	R	
166478	WB04-40_78.5	felsic	breccia	cpy			WB04-40	78.5	R	
166479	WB04-47_280	felsic	monzonite				WB04-47	280.0	R	
166480	WB04-47_284.5	felsic	monzonite	cpy			WB04-47	284.5	R	PD
166481	WB04-47_301.9	felsic	monzonite				WB04-47	301.9	R	
166482	WB04-49_26.3	felsic	monzonite				WB04-49	26.3	R	
166483	WB04-49_127.4	felsic	monzonite	cpy			WB04-49	127.4	R	PD
166484	WB04-49_136.7	felsic	breccia	cpy			WB04-49	136.7	R	
166485	WB04-49_162.3	felsic	breccia	cpy			WB04-49	162.3	R	PD
166486	WB04-49_162.5	felsic	breccia	cpy			WB04-49	162.5	R	
166487	WB04-49_168	felsic	breccia	cpy			WB04-49	168.0	R	
166488	WB04-49_170.7	felsic	breccia				WB04-49	170.7	R	
166489	WB04-52_117.7	felsic	breccia				WB04-52	117.7	R	
166490	WB04-52_121.1	felsic	breccia	cpy			WB04-52	121.1	R	PD
166491	WB04-52_124.0	felsic	breccia				WB04-52	124.0	R	
166492	WB04-52_136.4	felsic	breccia				WB04-52	136.4	R	
166493	WB04-52_142.8	felsic	monzonite	cpy			WB04-52	142.8	R	PD
166494	WB04-52_150.7	felsic	breccia				WB04-52	150.7	R	
166495	WB04-52_153	felsic	breccia				WB04-52	153.0	R	
166496	WB04-64_221.8	carboante	carbonate				WB04-64	221.8	R	
166497	WB04-73_17.4	felsic	monzonite				WB04-73	17.4	R	
166498	WB04-73_24.2	felsic	diorite				WB04-73	24.2	R	PD
166499	WB04-73_33	felsic	monzonite				WB04-73	33.0	R	
166500	WB04-73_55	felsic	monzonite				WB04-73	55.0	R	
166501	WB04-73_62	felsic	diorite				WB04-73	62.0	R	
166502	WB04-73_111.2	felsic	monzonite				WB04-73	111.2	R	
166503	WB04-73_146.8	felsic	monzonite				WB04-73	146.8	R	PD
166504	WB04-73_151.9-152.1	felsic	breccia				WB04-73	151.9-152.1	R	
166505	WB04-73_168.8	felsic	monzonite				WB04-73	168.8	R	
166506	WB04-73_210.7	felsic	monzonite				WB04-73	210.7	R	
166507	WB04-73_223	felsic	monzonite				WB04-73	223.0	R	
166508	WB04-73_231.8	felsic	monzonite				WB04-73	231.8	R	
166509	WB04-73_244.4	felsic	monzonite				WB04-73	244.4	R	
166510	WB04-73_260.7	felsic	diorite				WB04-73	260.7	R	
166511	WB04-73_269.1	felsic	breccia	cpy			WB04-73	269.1	R	PD
166512	WB04-73_274.1	felsic	monzonite	cpy			WB04-73	274.1	R	
166513	WB04-81_106.5	felsic	monzonite	cpy			WB04-81	106.5	R	PD
166514	WB04-81_113.5	felsic	monzonite	cpy			WB04-81	113.5	R	
166515	WB04-81_125.5	felsic	monzonite	cpy			WB04-81	125.5	R	
166516	WB04-88_203.3	felsic	breccia	cpy			WB04-88	203.3	R	PD

Thin Section	Polished block	Northing	Easting	Azimuth	Dip	Other preps	Other Comments
1TS		5448.62	2654.74	60	-50		
		5448.62	2654.74	60	-50		
		5306.95	2672.25	60	-50		cb cement
1TS	PB	5306.95	2672.25	60	-50	LAICPMSmount, S-isotope	
		5306.95	2672.25	60	-50		stage 4 vein
		6460.2	2823.15	240	-60		
		6460.2	2823.15	240	-60	S-isotope	
		6460.2	2823.15	240	-60		
1TS		6460.2	2823.15	240	-60	S-isotope	
		6460.2	2823.15	240	-60		cb cement
		6460.2	2823.15	240	-60		
		6460.2	2823.15	240	-60		cb cement
		5490.36	2770.93	240	-60		garnet alteration
		5490.36	2770.93	240	-60	S-isotope	cb cement
		5490.36	2770.93	240	-60		
1TS		5490.36	2770.93	240	-60		
		5490.36	2770.93	240	-60		
		5490.36	2770.93	240	-60		cb cement
1TS		5490.36	2770.93	240	-60		
1TS		5313.46	2718.07	60	-50		bladed carbonate?
		5217.76	2641.29	240	-45		
1TS		5217.76	2641.29	240	-45	C-O isotope	
		5217.76	2641.29	240	-45		
1TS		5217.76	2641.29	240	-45	LASI thick section off glass in paper box #1	
		5217.76	2641.29	240	-45		
		5217.76	2641.29	240	-45		
1TS		5217.76	2641.29	240	-45	LASI thick section off glass in paper box #1	
1TS		5217.76	2641.29	240	-45	C-O isotope	
1TS		5217.76	2641.29	240	-45		
1TS		5217.76	2641.29	240	-45	LASI thick section off glass in paper box #1	
1TS		5217.76	2641.29	240	-45		
1TS		5217.76	2641.29	240	-45		
		5217.76	2641.29	240	-45		
		5217.76	2641.29	240	-45		
	PB	5217.76	2641.29	240	-45	LAICPMS mount, S-isotope	
		5217.76	2641.29	240	-45	LASI thick section off glass in paper box #1	
1TS		5275.052	2898.481	60	-50		
		5275.052	2898.481	60	-50		
		5275.052	2898.481	60	-50		
	PB	5244.58	2846.88	60	-50	S-isotope, LAICPMS mount	

Appendix F continued

UTas #	Field Number	Composition	Rock Name	Ore mineral 1	Ore mineral 2	Ore mineral 3	Drill Hole	Depth (m)	Hand specimen	Powder
166517	WB04-95_28.6	felsic	monzonite				WB04-95	28.6	R	
166518	WB04-95_31.6	felsic	monzonite	cpy	bn		WB04-95	31.6	R	
166519	WB04-95_35.93	felsic	monzonite	cpy	bn		WB04-95	35.9	R	
166520	WB04-95_38.2	felsic	monzonite	cpy	bn		WB04-95	38.2	R	
166521	WB04-95_42.4	felsic	monzonite	cpy	bn		WB04-95	42.4	R	
166522	WB04-95_43.8	felsic	breccia	cpy	bn		WB04-95	43.8	R	
166523	WB04-95_49.37	felsic	breccia	cpy	bn		WB04-95	49.4	R	
166524	WB04-95_54.6	felsic	breccia	cpy	bn		WB04-95	54.6	R	
166525	WB04-95_66.5	felsic	mylonite	cpy	bn		WB04-95	66.5	R	
166526	WB04-95_69.7	felsic	breccia	cpy	bn		WB04-95	69.7	R	
166527	WB04-95_83.9	felsic	breccia	cpy	bn		WB04-95	83.9	R	
166528	WB04-95_89.4	felsic	breccia	cpy	bn		WB04-95	89.4	R	
166529	WB04-95_107.14	felsic	breccia	cpy	bn		WB04-95	107.1	R	
166530	WB04-95_115.7	felsic	monzonite	cpy			WB04-95	115.7	R	
166531	WB04-95_130.15	felsic	breccia				WB04-95	130.2	R	
166532	WB04-95_134	felsic	breccia	cpy			WB04-95	134.0	R	
166533	WB04-95_161.5	felsic	monzonite				WB04-95	161.5	R	
166534	WB04-95_168.6	felsic	breccia	cpy			WB04-95	168.6	R	
166535	WB04-95_181.6	felsic	breccia				WB04-95	181.6	R	
166536	WB04-95_187.4	felsic	breccia	cpy			WB04-95	187.4	R	PD
166537	WB04-95_208.5	felsic	monzonite	cpy			WB04-95	208.5	R	
166538	WB04-95_219.35	felsic	breccia				WB04-95	219.4	R	
166539	WB04-95_221	felsic	breccia				WB04-95	221.0	R	PD
166540	WB04-95_225.3	felsic	breccia	cpy			WB04-95	225.3	R	
166541	WB04-95_227.7	felsic	breccia	cpy			WB04-95	227.7	R	
166542	WB04-95_255.3	felsic	monzonite				WB04-95	255.3	R	
166543	WB04-95_266.2	felsic	monzonite				WB04-95	266.2	R	
166544	WB04-95_281.1	felsic	monzonite				WB04-95	281.1	R	
166545	WB04-95_304.6	felsic	monzonite				WB04-95	304.6	R	
166546	WB04-95_311.8	felsic	monzonite				WB04-95	311.8	R	
166547	WB04-96_191.4	felsic	monzonite				WB04-96	191.4	R	
166548	WB04-96_209.9	felsic	monzonite				WB04-96	209.9	R	
166549	WB04-108_3.98	felsic	breccia				WB04-108	4.0	R	
166550	WB04-108_22.56	felsic	breccia				WB04-108	22.6	R	
166551	WB04-108_25.5	felsic	breccia				WB04-108	25.5	R	

Thin Section	Polished block	Northing	Easting	Azimuth	Dip	Other preps	Other Comments
1TS		5339.75	2913.97	0	-90	thick section on glass in wooden box #1	
		5339.75	2913.97	0	-90		part of breccia halo
2TS		5339.75	2913.97	0	-90	thick section off glass in paper box #1, 2 thinnies a&b, LAICPMS mount	part of breccia halo
		5339.75	2913.97	0	-90		part of breccia halo
		5339.75	2913.97	0	-90		cb cement
		5339.75	2913.97	0	-90		
1TS		5339.75	2913.97	0	-90	thick section on glass in wooden box #1	
		5339.75	2913.97	0	-90		
	PB	5339.75	2913.97	0	-90	S-isotope, thick section x 2, 1 in wooden box #1 and 1 off glass in paper box #1, LAICPMS mount	stage 3 mylonite
		5339.75	2913.97	0	-90		
		5339.75	2913.97	0	-90		cb cement
1TS		5339.75	2913.97	0	-90	stage 3-4 albite vein, thick section in wooden box #1	
	PB	5339.75	2913.97	0	-90	S-isotope,LAICPMS mount, thick sectionsx 2 , 1 in wooden box #1, 1 off the glass in paper box #1	cb cement
1TS		5339.75	2913.97	0	-90		
		5339.75	2913.97	0	-90		
		5339.75	2913.97	0	-90		
		5339.75	2913.97	0	-90		
	PB	5339.75	2913.97	0	-90	LAICPMS mount	
		5339.75	2913.97	0	-90		pre-breccia alteration in clast
1TS	PB	5339.75	2913.97	0	-90	LAICPMS mount x 2 for S and cb, cb LAIXPMS mount is in paper box #1, thick section in paper box #1, S-isotope	
1TS		5339.75	2913.97	0	-90		
		5339.75	2913.97	0	-90		stage 5 vein breccia with hydrothermal components
		5339.75	2913.97	0	-90	S-isotope (sulfate)	
		5339.75	2913.97	0	-90		
		5339.75	2913.97	0	-90		
		5339.75	2913.97	0	-90		stage 5 epi vein
1TS		5339.75	2913.97	0	-90		stage 4 vein
		5339.75	2913.97	0	-90		
		5339.75	2913.97	0	-90		
		5339.75	2913.97	0	-90		
		5207.879	2941.122	60	-50		stringers
		5207.879	2941.122	60	-50		
		5546.064	2565.619	0	-90		MBX
1TS		5546.064	2565.619	0	-90		MBX
1TS		5546.064	2565.619	0	-90		

Appendix F continued

UTas #	Field Number	Composition	Rock Name	Ore mineral 1	Ore mineral 2	Ore mineral 3	Drill Hole	Depth (m)	Hand specimen	Powder
166552	WB04-108_39.1	felsic	monzonite				WB04-108	39.1	R	
166553	WB04-108_49.4	felsic	monzonite				WB04-108	49.4	R	
166554	WB04-108_50.5	felsic	monzonite				WB04-108	50.5	R	
166555	WB04-108_91.9	felsic	breccia				WB04-108	91.9	R	
166556	WB04-108_94.9	felsic	breccia				WB04-108	94.9	R	
166557	WB04-108_95.6	felsic	breccia				WB04-108	95.6	R	
166558	WB04-108_101	felsic	monzonite				WB04-108	101.0	R	
166559	WB04-108_108.4	felsic	monzonite				WB04-108	108.4	R	
166560	WB04-108_111.39	felsic	monzonite				WB04-108	111.4	R	
166561	WB04-108_114.43	felsic	monzonite				WB04-108	114.4	R	
166562	WB04-108_132.28	felsic	breccia				WB04-108	132.3	R	
166563	WB04-108_148.8	felsic	breccia				WB04-108	148.8	R	
166564	WB04-108_154.6	felsic	monzonite				WB04-108	154.6	R	
166565	WB04-108_161.9	felsic	breccia				WB04-108	161.9	R	
166566	WB04-108_173.4	felsic	breccia				WB04-108	173.4	R	
166567	WB04-108_187.3	felsic	breccia				WB04-108	187.3	R	
166568	WB04-108_200.4	felsic	breccia				WB04-108	200.4	R	
166569	WB04-108_220.4	felsic	monzonite				WB04-108	220.4	R	
166570	WB04-108_225.2	felsic	monzonite	cpy			WB04-108	225.2	R	
166571	WB04-108_236.2	felsic	monzonite				WB04-108	236.2	R	
166572	WB04-108_239.1	felsic	breccia				WB04-108	239.1	R	
166573	WB04-108_257.8	felsic	breccia				WB04-108	257.8	R	
166574	WB04-108_258.9	felsic	brecccia				WB04-108	258.9	R	
166575	WB04-108_283.9	felsic	monzonite				WB04-108	283.9	R	
166576	WB04-108_297.3	felsic	monzonite				WB04-108	297.3	R	
166577	WB04-108_302.1	felsic	breccia	cpy			WB04-108	302.1	R	
166578	WB04-108_304	felsic	breccia	cpy			WB04-108	304.0	R	
166579	WB04-108_307.2	felsic	breccia				WB04-108	307.2	R	
166580	WB04-108_313.3	felsic	breccia				WB04-108	313.3	R	
166581	WB04-108_315.8	felsic	breccia	cpy			WB04-108	315.8	R	
166582	WB04-108_316.1	felsic	breccia				WB04-108	316.1	R	PD
166583	WB04-108_326.1	felsic	breccia				WB04-108	326.1	R	
166584	WB04-108_331	felsic	breccia				WB04-108	331.0	R	
166585	WB04-108_334	felsic	breccia				WB04-108	344.4	R	
166586	WB04-108_345.5	felsic	breccia				WB04-108	345.5	R	
166587	WB04-108_351.6	felsic	monzonite				WB04-108	351.6	R	
166588	WB04-108_361.4	felsic	breccia				WB04-108	361.4	R	
166589	WB04-108_369.1	felsic	breccia				WB04-108	369.1	R	
166590	WB04-108_391.3	felsic	breccia				WB04-108	391.3	R	
166591	WB04-108_394.5	felsic	breccia				WB04-108	394.5	R	

Thin Section	Polished block	Northing	Easting	Azimuth	Dip	Other preps	Other Comments
		5546.064	2565.619	0	-90		
1TS		5546.064	2565.619	0	-90		monzonite with xenolith
		5546.064	2565.619	0	-90		sparse-mod Kfd -phyric monzonite
		5546.064	2565.619	0	-90		MBx
		5546.064	2565.619	0	-90		MBx
		5546.064	2565.619	0	-90		MBx + mafic xenolith
		5546.064	2565.619	0	-90		stage 5 vein with phyllic alteration
1TS		5546.064	2565.619	0	-90		trachyte?
1TS		5546.064	2565.619	0	-90	LAICPMS mount	stage 5 vein
		5546.064	2565.619	0	-90		monzonite with xenolith
		5546.064	2565.619	0	-90	LAICPMS mount	
		5546.064	2565.619	0	-90	LAICPMS mount	
1TS		5546.064	2565.619	0	-90		monzonite with xenolith
1TS		5546.064	2565.619	0	-90	thick section and LAICPMS mount for Cb traces in paper box #1	
		5546.064	2565.619	0	-90		
		5546.064	2565.619	0	-90		JV clast
		5546.064	2565.619	0	-90		MBx
1TS		5546.064	2565.619	0	-90		
		5546.064	2565.619	0	-90		stage 3 cpy
1TS		5546.064	2565.619	0	-90		
1TS		5546.064	2565.619	0	-90	LASI thick section off glass in paper box #1	
1TS		5546.064	2565.619	0	-90		
		5546.064	2565.619	0	-90		healed fault breccia
		5546.064	2565.619	0	-90		moderate Kfld-phyric monzonite
		5546.064	2565.619	0	-90	S-isotope	
1TS		5546.064	2565.619	0	-90	double wide thin section in plastic box	
1TS		5546.064	2565.619	0	-90	double wide thick section in plastic box, LAICPMS mount	
1TS		5546.064	2565.619	0	-90		
1TS		5546.064	2565.619	0	-90		
1TS		5546.064	2565.619	0	-90	thick section on glass in wooden box #2	
		5546.064	2565.619	0	-90	S-isotope (sulfate)	
		5546.064	2565.619	0	-90		cb cement
1TS		5546.064	2565.619	0	-90	double wide thick and thick sections in plastic box	
1TS		5546.064	2565.619	0	-90		bladed sulfate vein
1TS		5546.064	2565.619	0	-90	thick section off glass in paper box #1	
		5546.064	2565.619	0	-90		hnbld monzonite with xenoliths
		5546.064	2565.619	0	-90		
		5546.064	2565.619	0	-90		stage 4 ankeraite-solomite vein and alteration
1TS		5546.064	2565.619	0	-90	double wide thinnie in plastic box	mafic clasts
		5546.064	2565.619	0	-90		

Appendix F continued

UTas #	Field Number	Composition	Rock Name	Ore mineral 1	Ore mineral 2	Ore mineral 3	Drill Hole	Depth (m)	Hand specimen	Powder
166590	WB04-108_391.3	felsic	breccia				WB04-108	391.3	R	
166591	WB04-108_394.5	felsic	breccia				WB04-108	394.5	R	
166592	WB04-108_401	felsic	breccia				WB04-108	401.0	R	
166593	WB04-108_401.4	felsic	breccia				WB04-108	401.4	R	
166594	WB04-108_410	felsic	breccia				WB04-108	410.0	R	
166595	WB04-108_416.3	felsic	breccia				WB04-108	416.3	R	
166596	WB04-108_418.8	felsic	monzonite				WB04-108	418.8	R	
166597	WB04-108_419	felsic	breccia				WB04-108	419.0	R	
166598	WB04-108_420.3	felsic	monzonite				WB04-108	420.3	R	
166599	WB04-108_430.4	felsic	breccia				WB04-108	430.4	R	
166600	WB04-108_431.8	felsic	breccia				WB04-108	431.8	R	
166601	WB04-108_441.8	felsic	breccia				WB04-108	441.8	R	PD
166602	WB04-111_187.4	felsic	monzonite				WB04-111	187.4	R	
166603	WB04-111_198.8	felsic	monzonite				WB04-111	198.8	R	
166604	WB04-111_203.5	felsic	breccia	cpy			WB04-111	203.5	R	
166605	WB04-111_206.4	felsic	breccia				WB04-111	206.4	R	
166606	WB04-111_206.9	felsic	breccia				WB04-111	206.9	R	
166607	WB04-111_211.7	felsic	breccia				WB04-111	211.7	R	
166608	WB04-111_215.6	felsic	breccia				WB04-111	215.6	R	
166609	WB04-111_217.4	felsic	breccia	cpy			WB04-111	217.4	R	
166610	WB04-111_219.9	felsic	breccia	cpy	bn		WB04-111	219.9	R	
166611	WB04-111_224.5	felsic	breccia	cpy			WB04-111	224.5	R	
166612	WB04-111_236.25	felsic	breccia	cpy			WB04-111	236.3	R	
166613	WB04-111_237.8	felsic	breccia				WB04-111	237.8	R	
166614	WB04-111_248.8	felsic	breccia				WB04-111	248.8	R	
166615	WB04-111_251.9	felsic	breccia				WB04-111	251.8	R	
166616	WB04-111_253.2	felsic	breccia				WB04-111	253.2	R	
166617	WB04-111_253.6	felsic	breccia	bn			WB04-111	253.6	R	
166618	WB04-111_254.8	felsic	breccia				WB04-111	254.8	R	
166619	WB04-111_256	felsic	monzonite				WB04-111	256.0	R	
166620	WB04-114_97.1	felsic	monzonite				WB04-114	97.1	R	
166621	WB04-114_100.9	felsic	monzonite				WB04-114	100.9	R	
166622	WB04-114_113.4	felsic	monzonite	cpy			WB04-114	113.4	R	PD
166623	WB04-114_125.4	felsic	monzonite				WB04-114	125.4	R	
166624	WB04-114_132	felsic	monzonite				WB04-114	132.0	R	
166625	WB04-115_369.5	felsic	monzonite	cpy			WB04-115	369.5	R	
166626	WB04-115_371	felsic	breccia	cpy	bn		WB04-115	371.0	R	
166627	WB04-115_372.3	felsic	breccia	cpy	bn		WB04-115	372.3	R	
166628	WB04-115_384	felsic	breccia	cpy			WB04-115	384.0	R	
166629	WB04-115_385.5	felsic	breccia	cpy	bn		WB04-115	385.5	R	
166630	WB04-115_386.4	felsic	breccia	cpy			WB04-115	386.4	R	PD

Thin Section	Polished block	Northing	Easting	Azimuth	Dip	Other preps	Other Comments
1TS		5546.064	2565.619	0	-90	double wide thinnie in plastic box	mafic clasts
		5546.064	2565.619	0	-90		
1TS		5546.064	2565.619	0	-90		
1TS		5546.064	2565.619	0	-90	thick section in wooden box #2	cb cement
		5546.064	2565.619	0	-90		
1TS		5546.064	2565.619	0	-90	LASI thick section off glass in paper box #1	
1TS		5546.064	2565.619	0	-90		equigranular monzonite, cut by gnt vein
1TS		5546.064	2565.619	0	-90		
		5546.064	2565.619	0	-90		equigranular monzonite, cut by gnt vein
1TS		5546.064	2565.619	0	-90		Kfeld flooding alteration
		5546.064	2565.619	0	-90		Kfeld flooding alteration
		5546.064	2565.619	0	-90	S-isotope (sulfate)	
		5453.5	2603.33	60	-70		
1TS		5453.5	2603.33	60	-70	LAICPMS mount	stage 5 epithermal vein with bladed texture
1TS		5453.5	2603.33	60	-70		
1TS		5453.5	2603.33	60	-70		
		5453.5	2603.33	60	-70		
		5453.5	2603.33	60	-70		
1TS		5453.5	2603.33	60	-70		
		5453.5	2603.33	60	-70		
		5453.5	2603.33	60	-70		mafic JV clast?
1TS		5453.5	2603.33	60	-70	thick section in wooden box #2, LAICPMS mount	
1TS		5453.5	2603.33	60	-70		
1TS		5453.5	2603.33	60	-70		cb cement
		5453.5	2603.33	60	-70		
1TS		5453.5	2603.33	60	-70		stage 3 galena vein
		5453.5	2603.33	60	-70	C-O isotope	
		5453.5	2603.33	60	-70		
1TS		5453.5	2603.33	60	-70		
1TS		5453.5	2603.33	60	-70		crowded Kfl-phyric monzonite
		5243.76	2938.44	60	-50		
		5243.76	2938.44	60	-50		
		5243.76	2938.44	60	-50		
1TS		5243.76	2938.44	60	-50		
		5243.76	2938.44	60	-50		truncated mgt vein
1TS		5522.5	2719.23	240	-80		
		5522.5	2719.23	240	-80		
		5522.5	2719.23	240	-80		cb cement
		5522.5	2719.23	240	-80		
1TS		5522.5	2719.23	240	-80	LAICPMS mount (thinnie) for cb in paper box #2,	cb cement
		5522.5	2719.23	240	-80	S-isotope (sulfate)	

Appendix F continued

UTas #	Field Number	Composition	Rock Name	Ore mineral 1	Ore mineral 2	Ore mineral 3	Drill Hole	Depth (m)	Hand specimen	Powder
166631	WB04-115_403.7	felsic	breccia	cpy			WB04-115	403.7	R	
166632	WB04-115_406.3	felsic	breccia	cpy			WB04-115	406.3	R	
166633	WB04-115_407.7	felsic	breccia	cpy			WB04-115	407.7	R	
166634	WB04-115_409	felsic	breccia	cpy	bn		WB04-115	409.0	R	PD
166635	WB04-115_413.9	felsic	breccia				WB04-115	413.9	R	
166636	WB04-115_415.9	felsic	breccia	cpy			WB04-115	415.9	R	
166637	WB04-122_311.5	felsic	breccia	cpy	bn		WB04-122	311.5	R	
166638	WB04-122_313.5	felsic	breccia	cpy	bn		WB04-122	313.5	R	
166639	WB04-122_313.5b	felsic	breccia				WB04-122	313.5	R	
166640	WB04-122_316.2	felsic	breccia	cpy			WB04-122	316.2	R	
166641	WB04-122_323.3	felsic	breccia				WB04-122	323.3	R	
166642	WB04-122_334.1	felsic	breccia	cpy	bn		WB04-122	334.1	R	
166643	WB04-122_344.5	felsic	breccia	cpy	bn		WB04-122	344.5	R	PD
166644	WB04-122_346.0-345.3	felsic	breccia				WB04-122	346.0-345.3	R	
166645	WB04-122_350	felsic	breccia	cpy			WB04-122	350.0	R	
166646	WB04-122_354.4-354.6	felsic	breccia	cpy	bn		WB04-122	354.4-354.6	R	
166647	WB04-122_355.6	felsic	monzonite	cpy			WB04-122	355.6	R	
166648	WB04-122_360.7	felsic	breccia	cpy	bn		WB04-122	360.7	R	
166649	WB04-122_366.6	felsic	diorite				WB04-122	366.6	R	
166650	WB04-122_367.1	felsic	diorite	cpy			WB04-122	367.1	R	
166651	WB04-122_371.8	felsic	monzonite				WB04-122	371.8	R	
166652	WB04-122_375.4	felsic	breccia	cpy			WB04-122	375.4	R	
166653	WB04-122_384.4	felsic	monzonite	cpy	bn		WB04-122	384.4	R	
166654	WB04-131_365.8	felsic	breccia	cpy			WB04-131	365.8	R	
166655	WB04-131_376.2	felsic	breccia	cpy			WB04-131	376.2	R	
166656	WB04-131_379.4	felsic	breccia				WB04-131	379.4	R	
166657	WB04-131_400.3	felsic	monzonite				WB04-131	400.3	R	
166658	WB04-131_408.4	felsic	breccia				WB04-131	408.4	R	
166659	WB04-141_87.6	felsic	monzonite				WB04-141	87.6	R	
166660	WB04-141_103.9	felsic	breccia				WB04-141	103.9	R	
166661	WB04-141_126	felsic	breccia				WB04-141	126.0	R	
166662	WB04-141_133.5	felsic	breccia				WB04-141	133.5	R	
166663	WB04-141_136	felsic	breccia				WB04-141	136.0	R	
166664	WB04-150_424.4	felsic	breccia				WB04-150	424.4	R	
166665	WB04-150_445.5	felsic	breccia				WB04-150	445.5	R	
166666	WB04-150_453.4	felsic	breccia				WB04-150	453.4	R	
166667	WB04-150_459.9	felsic	breccia				WB04-150	459.9	R	
166668	WB04-150_485.8	felsic	breccia				WB04-150	485.8	R	

Thin Section	Polished block	Northing	Easting	Azimuth	Dip	Other preps	Other Comments
		5522.5	2719.23	240	-80		
		5522.5	2719.23	240	-80		
		5522.5	2719.23	240	-80		
1TS		5522.5	2719.23	240	-80	S-isotope	
		5522.5	2719.23	240	-80		
		5522.5	2719.23	240	-80		
1TS		5429.66	2560.34	60	-70	LASI - thick section off glass in paper box #2, LAICPMS mount	
1TS		5429.66	2560.34	60	-70		
		5429.66	2560.34	60	-70		
		5429.66	2560.34	60	-70		
1TS		5429.66	2560.34	60	-70		bladed anhydrite vein
1TS		5429.66	2560.34	60	-70		
		5429.66	2560.34	60	-70	S-isotope (sulfate)	
1TS		5429.66	2560.34	60	-70		mafic clast
		5429.66	2560.34	60	-70		
1TS		5429.66	2560.34	60	-70		
		5429.66	2560.34	60	-70		stage 3 cpy has cut eMz contact
		5429.66	2560.34	60	-70		
1TS		5429.66	2560.34	60	-70		
1TS		5429.66	2560.34	60	-70	LASI thick section off glass in paper box #2	stage 3 cpy + vein
		5429.66	2560.34	60	-70		
		5429.66	2560.34	60	-70		
		5429.66	2560.34	60	-70	stage 3 cpy + bn along coherent contact	
1TS		5677.22	2632.41	240	-60		
		5677.22	2632.41	240	-60	LAICPMS mount, LASI thick section off glass in paper box #2	
		5677.22	2632.41	240	-60	C-O isotope,	
		5677.22	2632.41	240	-60		phyllic alteration
		5677.22	2632.41	240	-60		
1TS		5567.756	2753.628	60	-70		amgydales
1TS		5567.756	2753.628	60	-70		MBx
		5567.756	2753.628	60	-70		MBx, stage 4 pink cb vein breccia
		5567.756	2753.628	60	-70	LASI thick section off glass in paper box #2	MBx
		5567.756	2753.628	60	-70		MBx
		5714.3	2611.23	240	-60		stage 4 infill
1TS		5714.3	2611.23	240	-60		
		5714.3	2611.23	240	-60	C-O isotope	
1TS		5714.3	2611.23	240	-60		gnt alteration
		5714.3	2611.23	240	-60	thick section off glass (LAICPMS cb mount) in paper box #2	

Appendix F continued

UTas #	Field Number	Composition	Rock Name	Ore mineral 1	Ore mineral 2	Ore mineral 3	Drill Hole	Depth (m)	Hand specimen	Powder
166669	WB04-152_515.1	felsic	breccia				WB04-152	515.1	R	
166670	WB04-152_540.1	mafic	basalt				WB04-152	540.1	R	
166671	WB04-152_549.6	felsic	monzonite				WB04-152	549.6	R	
166672	WB04-152_563.5	felsic	breccia				WB04-152	563.5	R	
166673	WB04-152_565.9	felsic	breccia				WB04-152	565.9	R	
166674	WB04-156_61.9	felsic	breccia				WB04-156	61.9	R	
166675	WB04-156_73.6	felsic	monzonite				WB04-156	73.6	R	
166676	WB04-156_87.6	felsic	monzonite				WB04-156	87.6	R	
166677	WB04-172_102.5	felsic	monzonite	cpy			WB04-172	102.5	R	PD
166678	WB04-192_312	felsic	breccia	cpy			WB04-192	312.0	R	PD
166679	WB04-192_321.2	felsic	breccia	cpy	bn		WB04-192	321.2	R	PD
166680	WB05-188_6.5	felsic	breccia				WB05-188	6.5	R	
166681	WB05-188_11	felsic	breccia				WB05-188	11.0	R	
166682	WB05-188_18	felsic	breccia				WB05-188	18.0	R	
166683	WB05-188_22.85	felsic	breccia	cpy			WB05-188	22.9	R	
166684	WB05-188_23	felsic	breccia	cpy			WB05-188	23.0	R	PD
166685	WB05-188_23.5	felsic	breccia				WB05-188	23.5	R	PD
166686	WB05-188_24.3	felsic	breccia	cpy			WB05-188	24.3	R	
166687	WB05-188_35.6	felsic	breccia				WB05-188	35.6	R	
166688	WB05-188_45.2	felsic	breccia	cpy			WB05-188	45.2	R	
166689	WB05-188_46.2	felsic	breccia				WB05-188	46.2	R	
166690	WB05-188_51.5	felsic	breccia	cpy			WB05-188	51.5	R	
166691	WB05-188_59.1	felsic	breccia	cpy			WB05-188	59.1	R	
166692	WB05-188_59.48	felsic	breccia	cpy	bn		WB05-188	59.5	R	
166693	WB05-188_60.1	felsic	breccia	cpy			WB05-188	60.1	R	
166694	WB05-188_68.25	felsic	breccia	cpy	bn		WB05-188	68.3	R	
166695	WB05-188_76.65	felsic	breccia	cpy			WB05-188	76.7	R	
166696	WB05-188_88.9	felsic	breccia	cpy			WB05-188	88.9	R	
166697	WB05-188_97.35	felsic	breccia	cpy	bn		WB05-188	97.4	R	
166698	WB05-188_104.18	felsic	breccia	bn			WB05-188	104.2	R	
166699	WB05-188_118.2	felsic	breccia	cpy	bn		WB05-188	118.2	R	
166700	WB05-188_129.45	felsic	breccia	cpy	bn		WB05-188	129.5	R	
166701	WB05-188_130.65	felsic	breccia	cpy	bn		WB05-188	130.7	R	
166702	WB05-188_134.15	mafic	basalt				WB05-188	134.2	R	
166703	WB05-188_138.55	felsic	breccia	cpy	bn		WB05-188	138.6	R	
166704	WB05-188_149	felsic	breccia	cpy			WB05-188	149.0	R	
166705	WB05-188_153.7	felsic	breccia	cpy			WB05-188	153.7	R	
166706	WB05-188_159.7	felsic	breccia	cpy			WB05-188	159.7	R	PD
166707	WB05-188_221.9	felsic	monzonite				WB05-188	221.9	R	

Thin Section	Polished block	Northing	Easting	Azimuth	Dip	Other preps	Other Comments
1TS		5756.5	2585.4	240	-60	LAICPMS mount, LASI thick section in paper box #2	
1TS		5756.5	2585.4	240	-60		xenolith
		5756.5	2585.4	240	-60		
		5756.5	2585.4	240	-60		
		5756.5	2585.4	240	-60	LASI thick section off glass in paper box #2	
1TS		5625.8	2359	60	-70	Thick section in wooden box #2,LASI thick section off glass in paper box #2	
1TS		5625.8	2359	60	-70		
		5625.8	2359	60	-70	C-O isotope	
		5508.9	2550.83	60	-70	S-isotope	
1TS		5473.47	2499.78	60	-70	S-isotope, LAICPMSmount	
		5473.47	2499.78	60	-70	S-isotope	
1TS		5407.55	2783.36	0	-90		
1TS		5407.55	2783.36	0	-90		
		5407.55	2783.36	0	-90		
		5407.55	2783.36	0	-90		
		5407.55	2783.36	0	-90	C-O isotope, thick sections off glass in paper box #2	
		5407.55	2783.36	0	-90	S-isotope, C-O isotope, thick sections off glass in paper box #2	
		5407.55	2783.36	0	-90		
1TS		5407.55	2783.36	0	-90		
		5407.55	2783.36	0	-90		sratge 3 cpy veins
1TS		5407.55	2783.36	0	-90		
		5407.55	2783.36	0	-90		sratge 3 cpy veins
		5407.55	2783.36	0	-90		
		5407.55	2783.36	0	-90	thick section in wooden box #2, LAICPMS mount	
		5407.55	2783.36	0	-90		
1TS		5407.55	2783.36	0	-90		
		5407.55	2783.36	0	-90		
		5407.55	2783.36	0	-90		
		5407.55	2783.36	0	-90		
		5407.55	2783.36	0	-90		
		5407.55	2783.36	0	-90	thick section off glass in paper box #2, LAICPMS mount	
		5407.55	2783.36	0	-90		cb cement
		5407.55	2783.36	0	-90		cb cement
		5407.55	2783.36	0	-90		AP dyke
		5407.55	2783.36	0	-90		cb cement
1TS		5407.55	2783.36	0	-90	thick section in wooden box #2	
		5407.55	2783.36	0	-90		
1TS		5407.55	2783.36	0	-90		
		5407.55	2783.36	0	-90		

Appendix F continued

UTas #	Field Number	Composition	Rock Name	Ore mineral 1	Ore mineral 2	Ore mineral 3	Drill Hole	Depth (m)	Hand specimen	Powder
166704	WB05-188_149	felsic	breccia	cpy			WB05-188	149.0	R	
166705	WB05-188_153.7	felsic	breccia	cpy			WB05-188	153.7	R	
166706	WB05-188_159.7	felsic	breccia	cpy			WB05-188	159.7	R	PD
166707	WB05-188_221.9	felsic	monzonite				WB05-188	221.9	R	
166708	WB05-188_224	felsic	monzonite				WB05-188	224.0	R	
166709	WB05-188_244.3	felsic	monzonite				WB05-188	244.3	R	
166710	WB05-188_247.2	felsic	monzonite				WB05-188	247.2	R	
166711	WB05-188_268.6	felsic	monzonite				WB05-188	268.6	R	
166712	WB05-188_274.9	felsic	monzonite				WB05-188	274.9	R	
166713	WB05-188_300.1	felsic	monzonite				WB05-188	300.1	R	
166714	WB05-188_320.1	felsic	monzonite				WB05-188	320.1	R	
166715	WB05-188_323.18	felsic	monzonite				WB05-188	323.2	R	
166716	WB05-188_325.3	felsic	monzonite				WB05-188	325.3	R	
166717	WB05-188_330.33	felsic	monzonite				WB05-188	330.3	R	
166718	WB05-188_338	felsic	monzonite				WB05-188	338.0	R	
166719	WB05-188_384.8	felsic	monzonite				WB05-188	384.8	R	
166720	WB05-188_390.9	felsic	monzonite				WB05-188	390.9	R	
166721	WB05-188_395.8	felsic	monzonite				WB05-188	395.8	R	
166722	WB05-188_505.1	felsic	monzonite				WB05-188	505.1	R	
166723	WB05-188_511.2	felsic	monzonite				WB05-188	511.2	R	
166724	WB05-188_519.5	felsic	monzonite				WB05-188	519.5	R	
166725	WB05-188_565.8	felsic	monzonite				WB05-188	565.8	R	
166726	WB05-188_572.6	mafic	basalt				WB05-188	572.6	R	
166727	WB05-188_614.16	mafic	basalt				WB05-188	614.2	R	
166728	WB05-188_632.37	felsic	monzonite				WB05-188	632.4	R	
166729	WB05-188_683.18	felsic	monzonite				WB05-188	683.2	R	
166730	WB05-205_144.5	felsic	monzonite				WB05-205	144.5	R	
166731	WB05-210_418.2	felsic	breccia				WB05-210	418.2	R	
166732	WB05-210_418.6	felsic	breccia				WB05-210	418.5	R	
166733	WB05-210_423	felsic	breccia	cpy			WB05-210	423.0	R	
166734	WB05-210_424.3	felsic	breccia	cpy			WB05-210	424.3	R	
166735	WB05-210_425.8	felsic	breccia	cpy			WB05-210	425.8	R	
166736	WB05-210_426	felsic	breccia	cpy			WB05-210	426.0	R	
166737	WB05-210_445.3	felsic	breccia	cpy			WB05-210	445.3	R	
166738	WB05-210_465.4	felsic	breccia	cpy			WB05-210	465.4	R	
166739	WB05-210_467	felsic	diorite				WB05-210	467.0		
166740	WB05-210_472	felsic	breccia	cpy			WB05-210	472.0	R	PD
166741	WB05-210_481.6	felsic	breccia	cpy			WB05-210	481.6	R	
166742	WB05-210_481.6b	felsic	breccia				~~WB05-210~~	~~487.7~~	R	
166743	WB05-210_491.5	felsic	breccia	cpy			WB05-210	491.5	R	
166744	WB05-210_491.8	felsic	breccia				WB05-210	491.8	R	

Thin Section	Polished block	Northing	Easting	Azimuth	Dip	Other preps	Other Comments
1TS		5407.55	2783.36	0	-90	thick section in wooden box #2	
		5407.55	2783.36	0	-90		
1TS		5407.55	2783.36	0	-90		
		5407.55	2783.36	0	-90		
1TS		5407.55	2783.36	0	-90		
		5407.55	2783.36	0	-90		
1TS		5407.55	2783.36	0	-90		
1TS		5407.55	2783.36	0	-90		Sparesly Kfd-phyric monzonite
1TS		5407.55	2783.36	0	-90		
1TS		5407.55	2783.36	0	-90		hld-bearing equigranular monzonite
		5407.55	2783.36	0	-90		
		5407.55	2783.36	0	-90		
		5407.55	2783.36	0	-90		
1TS		5407.55	2783.36	0	-90		equigranular monzonite with amgydales
1TS		5407.55	2783.36	0	-90		
1TS		5407.55	2783.36	0	-90		
1TS		5407.55	2783.36	0	-90		
1TS		5407.55	2783.36	0	-90		
		5407.55	2783.36	0	-90		
		5407.55	2783.36	0	-90		
1TS		5407.55	2783.36	0	-90		
1TS		5407.55	2783.36	0	-90		crowded Kfd-phyric monzonite
1TS		5407.55	2783.36	0	-90		
		5407.55	2783.36	0	-90		
		5407.55	2783.36	0	-90		
		5407.55	2783.36	0	-90		
1TS		5286.07	3021.45	130	-70		
1TS		5286.07	3021.45	130	-70		
		5286.07	3021.45	130	-70		healed fault breccia
1TS		5286.07	3021.45	130	-70		
1TS		5286.07	3021.45	130	-70	double wide thinnie and thick sections in plastic box, LSICPMS mount, thick section off glass in paper box #2	
1TS		5286.07	3021.45	130	-70	thinnie and thick section in wooden box #2	
		5286.07	3021.45	130	-70		
		5286.07	3021.45	130	-70		
		5286.07	3021.45	130	-70	thinnie is carbon-coated	
1TS		5286.07	3021.45	130	-70		
1TS		5286.07	3021.45	130	-70		
		5286.07	3021.45	130	-70		cb cement
		5286.07	3021.45	130	-70		
		5286.07	3021.45	130	-70		
		5286.07	3021.45	130	-70	LAICPMS mount (thinnie) for Cb traces and thick section mount in paper box #2	cb cement

Appendix F continued

UTas #	Field Number	Composition	Rock Name	Ore mineral 1	Ore mineral 2	Ore mineral 3	Drill Hole	Depth (m)	Hand specimen	Powder
166742	WB05-210_481.6b	felsic	breccia				WB05-210	487.7	R	
166743	WB05-210_491.5	felsic	breccia	cpy			WB05-210	491.5	R	
166744	WB05-210_491.8	felsic	breccia				WB05-210	491.8	R	
166745	WB05-210_494.7	felsic	breccia				WB05-210	494.7	R	
166746	WB05-210_497.7	felsic	monzodiorite				WB05-210	497.7	R	
166747	WB05-210_498.6	felsic	breccia				WB05-210	498.6	R	
166748	WB05-210_511.7	felsic	breccia	cpy			WB05-210	511.7	R	
166749	WB05-210_515.9	felsic	breccia	cpy			WB05-210	515.7	R	
166750	WB05-210_516.3	felsic	breccia	cpy			WB05-210	516.3	R	
166751	WB05-210_519.3	felsic	breccia	cpy			WB05-210	519.3	R	
166752	WB05-210_522	felsic	mylonite	cpy			WB05-210	522.0	R	
166753	WB05-210_535.6	mafic	basalt				WB05-210	535.6	R	
166754	WB05-210_536	felsic	breccia				WB05-210	536.0	R	
166755	WB05-210_549.5	felsic	breccia				WB05-210	549.5	R	
166756	WB05-210_561.6	felsic	breccia				WB05-210	561.6	R	
166757	WB05-210_561.9	felsic	breccia	cpy			WB05-210	561.9	R	
166758	WB05-213_478.6	felsic	breccia	cpy			WB05-213	478.6	R	
166759	WB05-213_479.1	felsic	breccia	cpy			WB05-213	479.1	R	
166760	WB05-213_483.4	felsic	breccia	cpy			WB05-213	483.4	R	
166761	WB05-213_487.7	felsic	breccia	cpy			WB05-213	487.7	R	
166762	WB05-213_489.1	felsic	monzonite				WB05-213	489.1	R	
166763	WB05-213_493.4	felsic	breccia	cpy			WB05-213	493.4	R	
166764	WB05-213_495.2	felsic	breccia	cpy			WB05-213	495.2	R	
166765	WB05-213_515.8	felsic	breccia	cpy			WB05-213	515.8	R	
166766	WB05-213_517.9	felsic	monzonite				WB05-213	517.9	R	
166767	WB05-213_520.9	felsic	breccia	cpy			WB05-213	520.9	R	
166768	WB05-213_522.4	felsic	breccia	cpy			WB05-213	522.4	R	
166769	WB05-213_529.44	felsic	breccia	cpy			WB05-213	529.4	R	
166770	WB05-213_538.8	felsic	breccia				WB05-213	538.8	R	PD
166771	WB05-213_544.7	felsic	breccia				WB05-213	544.7	R	
166772	WB05-213_553.2	felsic	breccia				WB05-213	553.2	R	
166773	WB05-213_555.2	mafic	basalt				WB05-213	555.2	R	
166774	WB05-213_560	felsic	breccia				WB05-213	560.0	R	
166775	WB05-213_563.8	felsic	breccia	cpy			WB05-213	563.8	R	
166776	WB05-213_576.3	felsic	monzonite				WB05-213	576.3	R	
166777	WB05-213_583.7	felsic	monzonite				WB05-213	583.7	R	
166778	WB05-213_586.2	felsic	breccia				WB05-213	586.2	R	

Thin Section	Polished block	Northing	Easting	Azimuth	Dip	Other preps	Other Comments
		5286.07	3021.45	130	-70		
		5286.07	3021.45	130	-70		
		5286.07	3021.45	130	-70	LAICPMS mount (thinnie) for Cb traces and thick section mount in paper box #2	cb cement
1TS		5286.07	3021.45	130	-70		
		5286.07	3021.45	130	-70		
		5286.07	3021.45	130	-70	S-isotope (sulfate)	
		5286.07	3021.45	130	-70		
1TS		5286.07	3021.45	130	-70		
1TS		5286.07	3021.45	130	-70	double wide thinnie and thick sections in plastic box	
1TS		5286.07	3021.45	130	-70	double wide thinnie and thick sections in plastic box	cb cement
1TS		5286.07	3021.45	130	-70		cpy mylonite
1TS		5286.07	3021.45	130	-70		AP dyke
1TS		5286.07	3021.45	130	-70		
		5286.07	3021.45	130	-70		
1TS		5286.07	3021.45	130	-70		
		5286.07	3021.45	130	-70		
		5493.8	2776.24	240	-80		
		5493.8	2776.24	240	-80	S-isotope (sulfate)	
1TS		5493.8	2776.24	240	-80	double wide thinnie in plastic box	
1TS		5493.8	2776.24	240	-80	LAICPMS mount,LASI thick section off glass in paper box #2	
		5493.8	2776.24	240	-80		stage 2 cpy-py veins
1TS		5493.8	2776.24	240	-80	LASI thick section off glass in paper box #2	
		5493.8	2776.24	240	-80		
1TS		5493.8	2776.24	240	-80	double wide thinnie in plastic box	
1TS		5493.8	2776.24	240	-80		sparsely Kfd-phyric monzonite with amgydale
1TS		5493.8	2776.24	240	-80		
		5493.8	2776.24	240	-80		
		5493.8	2776.24	240	-80		
		5493.8	2776.24	240	-80	S-isotope (sulfate)	
1TS		5493.8	2776.24	240	-80	double wide thinnie and thick section in plastic box	cb cement
		5493.8	2776.24	240	-80		
1TS		5493.8	2776.24	240	-80		AP dyke
1TS		5493.8	2776.24	240	-80		
		5493.8	2776.24	240	-80	LASI thick section off glass in paper box #2, LAICMS mount	
		5493.8	2776.24	240	-80		
		5493.8	2776.24	240	-80	double wide thinnie and thick section in plastic box	truncated vein
1TS		5493.8	2776.24	240	-80		pre-breccia alteration

Appendix F continued

UTas #	Field Number	Composition	Rock Name	Ore mineral 1	Ore mineral 2	Ore mineral 3	Drill Hole	Depth (m)	Hand specimen	Powder
166778	WB05-213_586.2	felsic	breccia				WB05-213	586.2	R	
166779	WB05-213_595.7	felsic	breccia				WB05-213	595.7	R	
166780	WB05-213_596.5	felsic	breccia	cpy			WB05-213	596.5	R	
166781	WB05-213_597	felsic	breccia				WB05-213	597.0	R	
166782	WB05-213_616.5	felsic	breccia				WB05-213	616.5	R	
166783	WB05-213_619.5	felsic	breccia				WB05-213	619.5	R	
166784	WB05-213_621.7	felsic	breccia				WB05-213	621.7	R	
166785	WB05-213_626.9	felsic	breccia				WB05-213	626.9	R	
166786	WB05-213_633.8	felsic	breccia	cpy			WB05-213	633.8	R	
166787	WB05-213_634.6	felsic	breccia				WB05-213	634.6	R	
166788	WB05-213_640.7	felsic	monzonite				WB05-213	640.7	R	
166789	WB05-213_646.8	felsic	breccia				WB05-213	646.8	R	
166790	WB05-213_664	felsic	breccia				WB05-213	664.0	R	
166791	WB05-213_670.9	felsic	breccia				WB05-213	670.9	R	
166792	WB05-223_81.5	felsic	breccia				WB05-223	81.5	R	
166793	WB05-223_103.1	felsic	breccia				WB05-223	103.1	R	
166794	WB05-223_117.5	felsic	breccia				WB05-223	117.5	R	
166795	WB05-223_118.0	felsic	breccia				WB05-223	118.0	R	
166796	WB07-239_8.7	felsic	breccia				WB07-239	8.7	R	
166797	WB07-239_9.0	felsic	breccia				WB07-239	9.0	R	
166798	WB07-239_9.1	felsic	breccia				WB07-239	9.1	R	
166799	WB07-239_12.8	felsic	breccia				WB07-239	12.8	R	
166800	WB07-239_14.5	felsic	breccia				WB07-239	14.5	R	
166801	WB07-239_17.5	felsic	breccia				WB07-239	17.5	R	
166802	WB07-239_19.4	felsic	breccia				WB07-239	19.4	R	
166803	WB07-239_19.7	felsic	breccia				WB07-239	19.7	R	
166804	WB07-239_19.9	felsic	breccia				WB07-239	19.9	R	
166805	WB07-239_28.8	felsic	breccia				WB07-239	28.8	R	
166806	WB07-239_33.7	felsic	breccia				WB07-239	33.7	R	
166807	WB07-239_45.7	felsic	breccia				WB07-239	45.7	R	
166808	WB07-239_51.2	felsic	breccia				WB07-239	51.2	R	
166809	WB07-239_59.3	felsic	breccia				WB07-239	59.3	R	
166810	WB07-239_66.2	felsic	breccia				WB07-239	66.2	R	
166811	WB07-239_95.5	felsic	breccia				WB07-239	95.5	R	
166812	WB07-239_100.1	felsic	breccia				WB07-239	100.1	R	
166813	WB07-239_100.2	felsic	breccia				WB07-239	100.2	R	
166814	WB07-239_104	felsic	breccia				WB07-239		R	
166815	WB07-239_110.2	felsic	breccia				WB07-239	110.2	R	
166816	WB07-239_118.2	felsic	breccia				WB07-239	118.2	R	
166817	WB07-239_124.3	felsic	breccia				WB07-239	124.3	R	
166818	WB07-239_125.5	felsic	breccia				WB07-239	125.5	R	
166819	WB07-239_137.7	felsic	breccia				WB07-239	137.7	R	

Thin Section	Polished block	Northing	Easting	Azimuth	Dip	Other preps	Other Comments
1TS		5493.8	2776.24	240	-80		pre-breccia alteration
1TS		5493.8	2776.24	240	-80	double wide thinnie and thick section in plastic box	
		5493.8	2776.24	240	-80		
		5493.8	2776.24	240	-80		
		5493.8	2776.24	240	-80		
		5493.8	2776.24	240	-80		rounded mafic clast
		5493.8	2776.24	240	-80		pre-breccia alteration
2TS		5493.8	2776.24	240	-80		
		5493.8	2776.24	240	-80		
		5493.8	2776.24	240	-80	thick section in wooden box #2, LASI thick section in paper box #2	
		5493.8	2776.24	240	-80		
		5493.8	2776.24	240	-80		
		5493.8	2776.24	240	-80		
		5493.8	2776.24	240	-80		
		5764	2264.19	240	-60	thick section off glass in paper box #2	
1TS		5764	2264.19	240	-60		
1TS		5764	2264.19	240	-60		
1TS		5764	2264.19	240	-60		
							cross bedding
							graded breccia
							graded breccia
							graded breccia
							3 pieces
							graded breccia
							graded breccia
							graded breccia
							cross bedding
							graded breccia
							graded breccia
							graded breccia
							JV clasts?
							JV clasts?
							unconformity?
							alteration front
							fault
							hydrothermal breccia

Appendix F continued

UTas #	Field Number	Composition	Rock Name	Ore mineral 1	Ore mineral 2	Ore mineral 3	Drill Hole	Depth (m)	Hand specimen	Powder
166820	WB07-239_142.1	felsic	breccia				WB07-239	142.1	R	
166821	WB07-239_178.9	felsic	breccia				WB07-239	178.9	R	
166822	WB07-239_220.5	felsic	breccia				WB07-239	220.5	R	
166823	WB07-239_226.4	felsic	breccia				WB07-239	226.4	R	
166824	WB07-239_280.9	felsic	breccia	cpy			WB07-239	280.9	R	
166825	WB07-239_284.0	felsic	breccia	cpy			WB07-239	284.0	R	
166826	WB07-239_357.2	felsic	breccia	cpy			WB07-239	357.2	R	
166827	WB07-239_360.8	felsic	breccia				WB07-239	360.8	R	
166828	WB07-239_387.0	felsic	breccia	cpy			WB07-239	387.0	R	
166829	NEZboil	felsic	monzonite				HPass-field sample		R	
166830	NEZ 936-11	felsic	breccia	cpy	tn		HPass-field sample		R	PD
166831	DC-cb-cm3	felsic	breccia				HPass-field sample		R	
166832	NEZ epi	felsic	breccia				HPass-field sample		R	
166833	NEZ sept 25	felsic	breccia	cpy			HPass-field sample		R	
166834	Mt.Polley - 1	felsic	ore	cpy	bn		HPass-field sample		R	
166835	JV clast 07("pit sample" - in thesis)	felsic	breccia				HPass-field sample		R	
166836	AP-NW2b-07	mafic	basalt				HPass-field sample		R	
166837	Slab 1	felsic	ore	cpy	bn		HPass-field sample		R	
166838	slab 2	felsic	ore	cpy	bn		HPass-field sample		R	
166839	NEZdol	carbonate	marble				HPass-field sample		R	
166840	LS-Morehead	carbonate	marble				HPass-field sample		R	
166841	LS-Likley	carbonate	marble				HPass-field sample			PD
166842	Post -Bx dikes (M.Jackson, 2008 collection)	mafic	basalt				WB04-106	457.3	R	
166843	Post -Bx dikes (M.Jackson, 2008 collection)	felsic	monzonite				WB04-138	32.3	R	
166844	Post -Bx dikes (M.Jackson, 2008 collection)	felsic	diorite				WB04-138	76.7	R	

Thin Section	Polished block	Northing	Easting	Azimuth	Dip	Other preps	Other Comments
							hydrothermal breccia
							hydrothermal breccia
							hydrothermal breccia
							hydrothermal breccia
							hydrothermal breccia
							hydrothermal breccia
							hydrothermal breccia
							hydrothermal breccia
							hydrothermal breccia
1TS						S isotopes, C-O isotopes, LA-ICP-MS mount , thick sections off glass in paper box #2, CAS	
1TS						S isotopes, C-O isotopes, LA-ICP-MS mount (cb+sulfide), Cb LAICPMS mount and thinnie in paper box #2, double wide thick section in plastic box (carbon coated),	stage 5 collorofrm cpy+tn
							stage 5 epi breccia
							stage 5 epi breccia
							sulfide ore
							JV clast
1TS						LA-ICP-MS mount	stage 5 veins in AP dike
							sulfide ore
							sulfide ore
1TS						C-O isotopes,	marble clast
1TS						C-O isotopes, thin section in paper box #2	regional limestone
1TS						C-O isotopes, thin section in paper box #2	regional limestone
							Augite porphyry
1TS						thin section in paper box #2	Hornblends Monz
							Plag microporphyry

Appendix F continued

UTas #	Field Number	Composition	Rock Name	Ore mineral 1	Ore mineral 2	Ore mineral 3	Drill Hole	Depth (m)	Hand specimen	Powder
166845	Post -Bx dikes (M.Jackson, 2008 collection)	felsic	monzonite				WB04-138	199.5	R	
166846	Post -Bx dikes (M.Jackson, 2008 collection)	felsic	monzonite				WB04-149	29	R	
166847	Post -Bx dikes (M.Jackson, 2008 collection)	felsic	monzonite				WB04-155	165.2	R	
166946	Post -Bx dikes (M.Jackson, 2008 collection)	felsic	monzonite				WB04-155	279.9	R	
166947	Post -Bx dikes (M.Jackson, 2008 collection)	mafic	basalt				WB04-155	311.5	R	
166948	Post -Bx dikes (M.Jackson, 2008 collection)	mafic	breccia				WB04-155	352.4	R	
166949	Post -Bx dikes (M.Jackson, 2008 collection)	intermediate	monzonite				WB04-155	455.3	R	
166950	Post -Bx dikes (M.Jackson, 2008 collection)	intermediate	monzonite				WB04-158	247	R	
166951	APT1-Mt. Polley Complex	felsic	syenite				Chris Rees-field sample 2007		R	
166952	APT2-Mt. Polley Complex	felsic	diorite				Chris Rees-field sample 2007		R	
166953	APT3-Mt. Polley Complex	felsic	diorite				Chris Rees-field sample 2007		R	
166954	APT4-Mt. Polley Complex	felsic	monzonite				Chris Rees-field sample 2007		R	
166955	APT5-Mt. Polley Complex	felsic	mozodioirte				Chris Rees-field sample 2007		R	
166956	APT7-Mt. Polley Complex	felsic	monzonite				Chris Rees-field sample 2007		R	
166957	APT8-Mt. Polley Complex	felsic	diorite				Chris Rees-field sample 2007		R	

Thin Section	Polished block	Northing	Easting	Azimuth	Dip	Other preps	Other Comments
1TS						thin section in paper box #2	Biotite Monz
							eMz
							Sparse Monz porphyry
							trachyte (aphanitic monz)
							Mafic dykes
							"altered mafic" clast
							Crowded Monz porphyry
							Plag & Ksp Monz porphyry
						location: "borrow pit", south of Mt. Polley Mine site	orbicular pseudoleucite nepheline syneite of the Bootkjack Stock, Unit Bns
						592758E, 5822205N	Diorite or monzodiorite, unit Pd2
						591662E, 5823737N	Diorite or monzodiorite, unit Pd1
						591739E, 5823807N	K-feldspar-phyric monzonite, unit Pkm
						591800E, 5823430N	Moderately Kf-alteted monzodiorite (diorite? Monzodiorite?) of unit Pmdu , typical of much of Mt. Polley , slightly Plagioclase-phyric , quite rich in lithic inlcusions
						591734E, 5823173N	Monzointe of unit Pmz, Pmz is differntiated from other monzonitic rocks in Pmdu by its more homogeneous , equigranular texture, better defined ferromagmesiam minerals and lack of inclusions
						590915E, 5823527N	coarse grained , equigranular pyroxene-bioite, diorite of unit Pd1

Appendix F continued

UTas #	Field Number	Composition	Rock Name	Ore mineral 1	Ore mineral 2	Ore mineral 3	Drill Hole	Depth (m)	Hand specimen	Powder
166958	APT9-Mt. Polley Complex	felsic	monzonite				Chris Rees-field sample 2007		R	
166959	APT10-Mt. Polley Complex	felsic	monzonite				Chris Rees-field sample 2007		R	
166960	APT11-Mt. Polley Complex	felsic	monzonite				Chris Rees-field sample 2007		R	

Thin Section	Polished block	Northing	Easting	Azimuth	Dip	Other preps	Other Comments
						590985E, 5825159N	Hornblend Monzonite (-monzodiorite?) from Polley Lake Rd, lumped in with unit Pmdu
						592675E, 5824932N	altered monzonite-monzodiorite of uni Pmdu, from Leak Zone
						592904E, 5824771N	megacrystic K-feldspar-phyric monzonite, unit Pkm, 15mwide dike